

Nitrogen oxides and their involvement in photochemical processes throughout the troposphere

Dissertation

zur Erlangung des Grades
'Doktor rerum naturalium (Dr. rer. nat.)'
im Promotionsfach Chemie

am Fachbereich Chemie, Pharmazie und Geowissenschaften der
Johannes Gutenberg-Universität Mainz

angefertigt am Max-Planck-Institut für Chemie
Max Planck Graduate Center

vorgelegt von

Clara Maria Nussbaumer

geboren am 28.11.1996 in Bonn

Mainz, May 11, 2023

1. Gutachter:

2. Gutachter:

Tag der mündlichen Prüfung: 05.07.2023

Declaration

I hereby declare that I wrote the dissertation submitted without any unauthorized external assistance and used only sources acknowledged in the work. All textual passages which are appropriated verbatim or paraphrased from published and unpublished texts as well as all information obtained from oral sources are duly indicated and listed in accordance with bibliographical rules. In carrying out this research, I complied with the rules of standard scientific practice as formulated in the statutes of Johannes Gutenberg-University Mainz to insure standard scientific practice.

Clara Maria Nussbaumer
Mainz, May 11, 2023

Acknowledgment

Abstract

Nitrogen oxides (NO_x) describe the sum of nitric oxide (NO) and nitrogen dioxide (NO_2) which are important trace gases in the troposphere, the layer closest to the earth's surface. NO_x has a profound influence on atmospheric photochemical processes which majorly impact local air quality and the formation of tropospheric ozone, which in turn affects the earth's radiative budget and global warming. This work presents several studies on the sources and distribution of nitrogen oxides and their involvement in photochemical processes throughout the troposphere with the aim to improve our understanding of its role in tropospheric photochemistry and its effects on human health and climate change.

The first study presented in this work investigates the occurrence of deep convection in the presence and in the absence of lightning in a developing tropical cyclone based on in situ observations of nitric oxide (NO) and other trace gases during the research aircraft campaign CAFE Africa (Chemistry of the Atmospheric Field Experiment in Africa) which took place in August and September 2018 over West Africa and the Atlantic Ocean. It is shown that the amount of lightning, indicated by peaks in NO mixing ratios, decreases with increasing strength of the observed tropical cyclone. At an advanced stage of the cyclone, only NO free air from the marine boundary layer transported upwards through deep convection can be observed from the airborne platform in the upper troposphere.

The second study presents the development of a new photolytic converter for improved photolysis-chemiluminescence measurements of nitrogen dioxide (NO_2), particularly for aircraft applications where additional challenges such as rapidly changing ambient conditions are encountered. A conventional photolytic converter was employed for NO_2 measurements during the research aircraft campaign CAFE Africa, which failed due to wall effects impacting the instrumental background and the occurrence of memory effects associated with ambient mixing ratios of NO and humidity. Instead, an improved converter made from quartz glass can overcome these drawbacks showing improved laboratory results.

The third study presented in this work shows the findings on how NO_x impacts the formation of formaldehyde (HCHO) and ozone (O_3) based on three ground site measurement campaigns across Europe. These are the HUMPPA (Hyytiälä United Measurements of Photochemistry and Particles) campaign in Finland in 2010, the HOPE (Hohenpeißenberg Photochemistry Experiment) campaign in Germany in 2012 and the CYPHEX campaign in Cyprus (Cyprus Photochemistry Experiment) in 2014. It is shown that the oxidation of isoprene, methanol, acetaldehyde and methane accounts for the production of HCHO at all three sites. Acetaldehyde and methane form HCHO via methyl peroxy radicals (CH_3O_2) which is favored in the presence of excess NO over the competing reaction forming methyl hydrogen peroxide (CH_3OOH). This ratio, described by $\alpha(\text{CH}_3\text{O}_2)$, is found to provide valuable insight into the sensitivity of O_3 to its precursors.

The fourth study investigates the impact of NO_x reductions in the upper troposphere due to reduced air traffic during the European COVID-19 lockdowns. It is based on the research aircraft campaign BLUESKY which took place over Europe in May and June 2020, in comparison to the UTOPIAN (Upper Tropospheric Ozone: Processes Involving HO_x and NO_x) and the HOOVER (HO_x over Europe) aircraft campaigns in 2003/04 and 2006/07, respectively. The study is based on in situ observations during the three aircraft campaigns and modeling simulations

by the ECHAM5 (fifth generation European Centre Hamburg general circulation model, version 5.3.02)/MESSy2 (second generation Modular Earth Submodel System, version 2.54.0) Atmospheric Chemistry (EMAC) model. By the help of $\alpha(\text{CH}_3\text{O}_2)$, it is shown that O_3 chemistry changed from a VOC (volatile organic compound) sensitivity in 2003/04 to a NO_x sensitivity as an outcome of upper tropospheric NO_x reductions induced by the COVID-19 lockdowns.

The fifth study presented in this work evaluates the impact of NO_x on O_3 sensitivity in the upper tropical troposphere across all longitudes, based on EMAC modeling simulations. Lightning is shown to be the only significant source of NO_x in the upper tropical troposphere and the driver of the dominating O_3 sensitivity. Regions characterized by frequent lightning such as South America and Central Africa show a strong VOC sensitivity, while regions where lightning is sparse such as South East Asia are clearly NO_x -sensitive. The results additionally indicate that $\alpha(\text{CH}_3\text{O}_2)$ is a universal indicator for O_3 sensitivity throughout the entire troposphere while the most common definition in literature, the correlation of ozone production ($P(\text{O}_3)$) with NO_x , is only valid at the surface.

The sixth study as part of this work investigates emissions of NO_x from the surface based on in situ observations of NO_x concentrations and the vertical wind speed during the aircraft campaign RECAP-CA (Re-Evaluating the Chemistry of Air Pollutants in California) which took place in California in June 2021. NO_x fluxes are calculated via wavelet transformation, which is a sub-type of eddy covariance, and compared to the local emission inventory provided by the California Air Resources Board (CARB). It is shown that NO_x fluxes over Los Angeles exhibit a strong weekend effect and while on the same order of magnitude, can show strong local deviations from the emission inventory.

This work underlines the importance of nitrogen oxides in different parts of the troposphere. Understanding sources, and photochemistry at the surface, as presented in two studies, is essential for improving local air quality and therefore human and plant health. Upper tropospheric processes that involve NO_x , which is presented in the remaining four studies, can provide insights into weather phenomena, such as the formation of tropical cyclones, and the sensitivity of O_3 affecting the radiative budget and therefore global warming.

Zusammenfassung

Stickoxide (NO_x) repräsentieren die Summe aus Stickstoffmonoxid (NO) und Stickstoffdioxid (NO_2) und sind wichtige Spurengase in der Troposphäre, der der Erdoberfläche am nächsten liegenden Schicht. NO_x hat einen tiefgreifenden Einfluss auf die atmosphärischen, photochemischen Prozesse, die große Auswirkungen auf die lokale Luftqualität, sowie die Bildung von troposphärischem Ozon haben und dadurch den Strahlungshaushalt und die Erderwärmung beeinflussen. Diese Arbeit präsentiert mehrere Studien zu den Quellen und der Verteilung von Stickoxiden, sowie ihre Beteiligung an den photochemischen Prozessen in der gesamten Troposphäre mit dem Ziel unser Verständnis der Rolle von Stickoxiden in der troposphärischen Photochemie, sowie ihre Auswirkungen auf die menschliche Gesundheit und den Klimawandel zu verbessern.

Die erste Studie, die in dieser Arbeit präsentiert wird, untersucht das Auftreten von tiefer Konvektion in An- und Abwesenheit von Blitzen in einem entstehenden tropischen Zyklon. Die Studie basiert auf in situ Beobachtungen von Stickstoffmonoxid und anderen Spurengasen während der Forschungsflugzeugkampagne CAFE Africa (Chemistry of the Atmospheric Field Experiment in Africa), die im August und September 2018 über Westafrika und dem Atlantischen Ozean stattgefunden hat. Es wird gezeigt, dass die Menge an Blitzen, angegeben durch das Auftreten von Höchstwerten im NO Mischungsverhältnis, mit zunehmender Stärke des beobachteten tropischen Zyklons abnimmt. In einem fortgeschrittenen Stadium des Zyklons wird ausschließlich NO freie Luft, die aus der marinen Grenzschicht durch tiefe Konvektion nach oben transportiert wird, in der oberen Troposphäre beobachtet.

Die zweite Studie präsentiert die Entwicklung eines neuen, photolytischen Konverters für verbesserte Photolyse-Chemilumineszenz Messungen von Stickstoffdioxid (NO_2), insbesondere in Hinblick auf Flugzeuganwendungen, für die zusätzliche Herausforderungen wie zum Beispiel schnell wechselnde Umgebungsbedingungen vorliegen. Ein konventioneller photolytischer Konverter wurde für NO_2 Messungen während der CAFE Africa Flugzeugkampagne verwendet, die auf Grund von Wandeffekten, die den instrumentellen Hintergrund und das Auftreten von Speichereffekten im Zusammenhang mit den NO Mischungsverhältnissen und der Feuchtigkeit der Umgebungsluft beeinflussen, scheiterten. Stattdessen kann ein neuer Konverter aus Quarzglas diese Nachteile überwinden und zeigt verbesserte Laborergebnisse.

Die dritte Studie, die in dieser Arbeit präsentiert wird, zeigt Erkenntnisse wie NO_x die Bildung von Formaldehyd (HCHO) und Ozon (O_3) beeinflusst, basierend auf drei Bodenfeldkampagnen in Europa. Diese sind die HUMPPA (Hyytiälä United Measurements of Photochemistry and Particles) Kampagne 2010 in Finnland, die HOPE (Hohenpeißenberg Photochemistry Experiment) Kampagne 2012 in Deutschland und die CYPHEX (Cyprus Photochemistry Experiment) Kampagne 2014 in Zypern. Es wird gezeigt, dass die Oxidation von Isopren, Methanol, Acetaldehyd und Methan die Produktion von HCHO an allen drei Orten repräsentiert. Acetaldehyd und Methan bilden HCHO über Methylperoxradikale (CH_3O_2). Dieser Reaktionsweg ist bei Vorliegen von NO im Überschuss gegenüber der konkurrierenden Reaktion zu Methylwasserstoffperoxid (CH_3OOH) begünstigt. Dieses Verhältnis, beschrieben durch $\alpha(\text{CH}_3\text{O}_2)$, kann einen wertvollen Einblick in die Sensitivität von O_3 auf seine Vorläufer liefern.

Die vierte Studie untersucht den Einfluss von NO_x Reduktionen in der oberen Troposphäre durch verringerten Luftverkehr während der europäischen COVID-19 Lockdowns basierend auf der For-

schungsflugzeugkampagne BLUESKY, die im Mai und Juni 2020 über Europe stattgefunden hat, im Vergleich mit der UTOPIAN (Upper Tropospheric Ozone: Processes Involving HO_x and NO_x) und der HOOVER (HO_x over Europe) Flugzeugkampagnen 2003/04 und 2006/07. Die Studie basiert auf in situ Beobachtungen während der drei Flugzeugkampagnen und Modellsimulationen durch das ECHAM5 (fifth generation European Centre Hamburg general circulation model, version 5.3.02)/MESSy2 (second generation Modular Earth Submodel System, version 2.54.0) Atmosphärenchemie (EMAC) Model. Mit der Hilfe von $\alpha(\text{CH}_3\text{O}_2)$ wird gezeigt, dass die Ozonchemie von einer VOC (flüchtige organische Substanz) Sensitivität 2003/04 zu einer NO_x Sensitivität als Folge von NO_x Reduktionen in der oberen Troposphäre durch die COVID-19 Lockdowns übergegangen ist.

Die fünfte Studie, die in dieser Arbeit präsentiert wird, analysiert den Einfluss von NO_x auf die O_3 Sensitivität in der oberen tropischen Troposphäre über alle Längengrade, basierend auf EMAC Modellsimulationen. Es wird gezeigt, dass Blitze die einzig signifikante Quelle von NO_x in der oberen tropischen Troposphäre sind und maßgeblich die dominierende Ozonsensitivität beeinflussen. Regionen, die durch frequentierte Blitze charakterisiert sind, wie zum Beispiel Südamerika und Zentralafrika, zeigen eine starke VOC Sensitivität, während Regionen, in denen Blitze selten sind, wie zum Beispiel Südostasien, eindeutig NO_x sensitiv sind. Die Ergebnisse zeigen außerdem, dass $\alpha(\text{CH}_3\text{O}_2)$ ein universeller Indikator für die O_3 Sensitivität in der gesamten Troposphäre ist, während die gebräuchlichste Definition in der Literatur, die Korrelation der Ozonproduktion ($P(\text{O}_3)$) mit NO , nur am Boden gültig ist.

Die sechste Studie als Teil dieser Arbeit untersucht NO_x Emissionen von der Oberfläche basierend auf in situ Beobachtungen von NO_x Konzentrationen und der vertikalen Windgeschwindigkeit während der Flugzeugkampagne RECAP-CA (Re-Evaluating the Chemistry of Air Pollutants in California), die im Juni 2021 in Kalifornien stattgefunden hat. NO_x Flüsse werden mittels Wavelet-Transformation, einer Unterart der Eddy Kovarianz, berechnet und mit dem lokalen Emissionskataster des California Air Resources Boards (CARB) verglichen. Es wird gezeigt, dass NO_x Flüsse in Los Angeles einen starken Wochenendeffekt aufweisen und, obwohl sie die gleiche Größenordnung besitzen, lokal starke Abweichungen vom Emissionskataster zeigen können.

Diese Arbeit unterstreicht die Wichtigkeit von Stickoxiden in unterschiedlichen Teilen der Troposphäre. Es ist unabdingbar die Quellen und die Photochemie am Boden zu verstehen, wie in zwei der präsentierten Studien, um die lokale Luftqualität und damit die Gesundheit von Menschen und Pflanzen zu verbessern. Prozesse in der oberen Troposphäre, die NO_x involvieren, wie in den verbleibenden vier Studien untersucht wird, können Einblicke in Wetterphänomene, wie zum Beispiel die Bildung von tropischen Zyklonen, geben, sowie in die Sensitivität von O_3 , die den Strahlungshaushalt und damit die Erderwärmung beeinflusst.

Contents

Abstract	vii
Zusammenfassung	ix
1 Motivation	1
2 Introduction	3
2.1 The earth's atmosphere	3
2.2 The role of nitrogen oxides (NO_x) in the troposphere	4
2.2.1 Photostationary state (PSS)	4
2.2.2 Atmospheric sources and distribution	5
2.2.3 Formation of O_3	8
2.2.4 Formation of HCHO	11
2.2.5 Chemical regime throughout the troposphere	12
2.3 Airborne and ground-based measurements of NO_x	14
2.3.1 Laser induced fluorescence (LIF)	14
2.3.2 Photolysis-chemiluminescence (P-CL)	15
2.3.3 Challenges in NO_2 measurements	16
3 Results	19
3.1 Overview	19
3.2 Deep convection and lightning in a developing hurricane	21
3.3 Optimization of airborne NO_2 measurements	37
3.4 Photochemical production of formaldehyde and ozone across Europe	57
3.5 Impact of the COVID-19 lockdown on photochemical processes in the upper troposphere over Europe	79
3.6 Ozone sensitivity in the upper tropical troposphere	97
3.7 Airborne NO_x flux measurements over Los Angeles	125
3.8 List of publications	147
4 Supplement	149
4.1 Supplement of Section 3.2	149
4.2 Supplement of Section 3.3	163
4.3 Supplement of Section 3.4	171
4.4 Supplement of Section 3.5	191
4.5 Supplement of Section 3.6	201
4.6 Supplement of Section 3.7	221
References	229

1 Motivation

Atmospheric trace gases, and the chemistry they are involved in, significantly influence the habitability of our planet and the survival of its species. In the troposphere, this has two major aspects, which are the local air quality affecting human, animal and plant health and the abundance of greenhouse gases contributing to global warming and climate change. Nitrogen oxides ($\text{NO}_x \equiv \text{NO} + \text{NO}_2$) play a key role in tropospheric photochemistry. Understanding its sources, monitoring its distribution and investigating its influence on air quality and global warming are the central aspects of this work.

The foundation of investigating NO_x in the troposphere are reliable and accurate measurements. While this is mostly the case for nitric oxide (NO), nitrogen dioxide (NO_2) measurements remain a challenge [1,2]. These difficulties have been studied as part of this work and a new instrument component was developed which shows significant improvements, particularly for upper tropospheric measurements [2].

NO_x is a precursor to tropospheric ozone (O_3) which, at the surface, is a hazard to human health and additionally a greenhouse gas, which severely influences the earth's radiative budget, particularly in the upper troposphere [3–5]. The photochemical production and the sensitivity of O_3 to its precursors is studied in various locations in order to obtain a broader understanding. One study focuses on processes at the surface at three different European sites in Germany, Finland and Cyprus [6]. Besides the production of O_3 , it also investigates the formation of formaldehyde (HCHO) in which NO_x plays a key role. The distribution across possible reactions pathways is dependent on ambient mixing ratios of NO_x and can provide insights into the dominating O_3 sensitivity. Another study evaluates O_3 formation in the upper troposphere over Europe based on three aircraft campaigns across almost two decades. A particular focus is the impact of the COVID-19 European lockdowns, mostly reduced air traffic, which are shown to have a strong influence on the O_3 sensitivity in the upper troposphere, providing insights into effects of potential future changes of nitrogen oxides [7]. Based on these findings a study using modeled data from the EMAC atmospheric chemistry - general circulation model investigates O_3 sensitivity to NO_x , with particular focus on lightning emissions, in the upper tropical troposphere across all longitudes [8].

Besides its consideration from a chemistry perspective, lightning in the upper tropical troposphere occurs in combination with deep convective processes – the updraft of air from the boundary layer to the top of the troposphere. The dependence of deep convection and lightning is studied based on in situ observations in a developing tropical weather system over West Africa and the Atlantic Ocean, later transitioning into a hurricane causing devastating damage to human life and property at the U.S. South East Coast [9].

While it is important to study the photochemistry of nitrogen oxides throughout the entire troposphere, it is also highly relevant to investigate the sources. The studies mentioned above identify lightning as the major NO_x source in the upper tropical troposphere and NO_x aircraft emissions in the upper troposphere in the northern hemisphere over Europe. The sources of NO_x at the surface, particularly in urban areas, are much more versatile and more difficult to quantify, but a crucial component in local air quality control. NO_x fluxes, representing an emission per area and time, are studied over Los Angeles based on airborne NO_x and vertical wind speed measurements. The calculation is performed using wavelet transformation based on the eddy covariance method

Figure 1 provides a simplified overview of the studies performed as part of this work and their importance in tropospheric processes and chemistry. This work aims to investigate the role of nitrogen oxides in various parts of the troposphere and to discuss their impact on us humans and our planet.

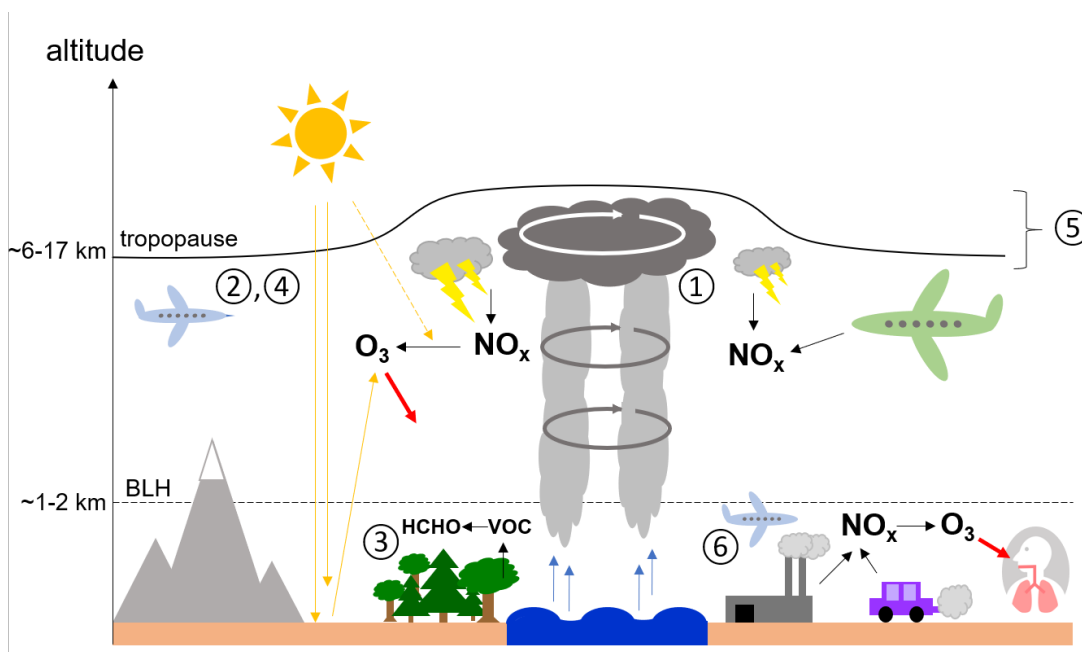


Figure 1: Simplified overview of the studies performed as part of this work. ① Studies of deep convection and lightning in a tropical cyclone, ② Improvements of airborne NO_2 measurements, ③ Formaldehyde and ozone formation at the surface, ④ Influence of the COVID-19 lockdowns on ozone formation in the upper troposphere over Europe, ⑤ Ozone sensitivity in the upper tropical troposphere across all longitudes and ⑥ NO_x emissions from Los Angeles via direct airborne measurements. This figure was self-created.

2 Introduction

2.1 The earth's atmosphere

The atmosphere describes the gaseous blanket of the earth and can be subdivided into several layers, characterized by the vertical temperature profile, whereby each temperature inversion marks the beginning of a new atmospheric layer [11,12]. An overview of the atmospheric layers and temperature developments can be seen in Figure 2 [12,13].

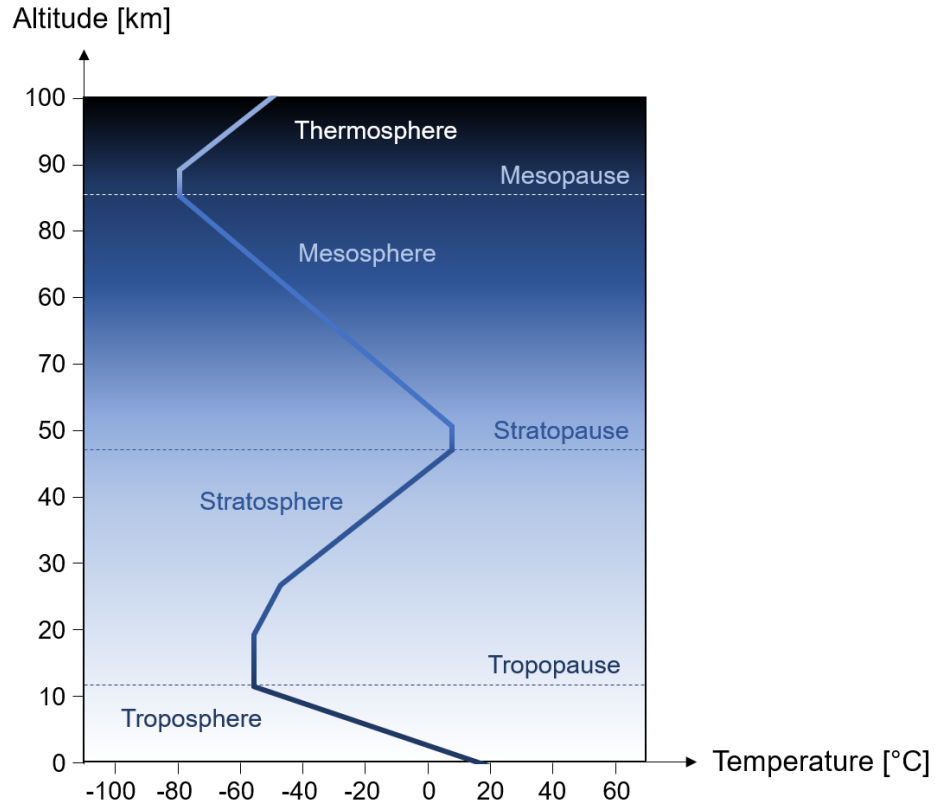


Figure 2: Schematic overview of the atmospheric layers and the vertical temperature profile. The exact values depend on the location on the globe. This figure was self-created based on [12] and [13].

The troposphere represents the layer closest to the surface and features decreasing temperature with altitude by an average rate of $6.5^{\circ}\text{C km}^{-1}$ up to the tropopause which marks the transition to the overlaying stratosphere [12]. The altitude of the tropopause is largely dependent on the season and its latitudinal position and varies from 6–8 km at the poles to around 15–17 km in the tropics [11,14]. Throughout the atmosphere, pressure and density decrease roughly exponentially with altitude, so that 80 % (by weight) of the atmospheric air is accumulated in the troposphere, which only makes up a small volume fraction of the entire atmosphere [12,15]. The earth's surface is heated through absorption of the sun's radiation and in turn warms the air masses close to it, which rise, expand due to decreasing pressure and cool down – an adiabatic change of state explaining the tropospheric temperature gradient [16]. The troposphere additionally holds the

majority of the atmospheric water content and is characterized by strong vertical mixing, which leads to the occurrence of multiple meteorological events [14].

The following layer, the stratosphere, reaches from the tropopause up to around 50 km. It is characterized by increasing temperature with altitude and poor vertical mixing. This temperature inversion results from ozone molecules (O_3) absorbing UV radiation by the sun, a process that is vital to life on the earth's surface. The stratosphere holds 19 % of the atmospheric trace gases and 90 % of its ozone, mostly accumulated in the ozone layer [12, 17]. UV light from the sun leads to the homolytic cleavage of diatomic oxygen. Via the reaction with an oxygen molecule, the resulting oxygen radical forms O_3 , which in turn can be photolytically cleaved to molecular oxygen and a radical, restarting the cycle. That way, approximately 98 % of the sun's radiation is filtered and only the remaining 2 % reaches the troposphere, making life on earth possible [12, 18].

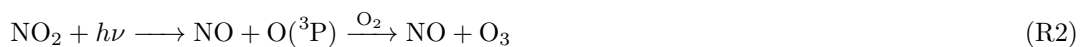
Above the stratopause follows the mesosphere, which is again characterized by decreasing temperature with altitude, reaching a minimum of around -90°C at the mesopause ($\sim 80\text{--}85\text{ km}$), which marks the transition to the thermosphere. The temperature in the thermosphere increases again with altitude due to absorption of solar radiation via N_2 and O_2 dissociation [11, 12, 15, 16].

This work focuses on photochemical processes involving nitrogen oxides in the troposphere, which holds most of the atmospheric mass and its trace gases, and (together with the stratosphere) forms the most important layers of the atmosphere affecting the earth's climate and its living beings.

2.2 The role of nitrogen oxides (NO_x) in the troposphere

2.2.1 Photostationary state (PSS)

Nitrogen oxides (NO_x), the sum of nitric oxide (NO) and nitrogen dioxide (NO_2), play a major role in the photochemical processes taking place in the troposphere. NO and NO_2 can rapidly interconvert via the reaction of NO with ozone (O_3), forming NO_2 and its back-reaction starting with the photolysis of NO_2 as shown in Reactions (R1) and (R2), respectively [11].

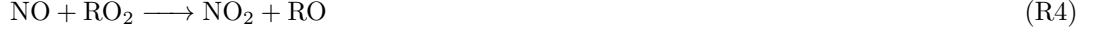


In photostationary state (PSS), this interconversion does not affect the NO_x or the O_3 budget and can be described by the Leighton ratio as shown in Equation (1) with the rate constant k of Reaction (R1) and the photolysis frequency j of Reaction (R2) [19].

$$\frac{k_{\text{NO}+\text{O}_3} \times [\text{NO}] \times [\text{O}_3]}{j_{\text{NO}_2} \times [\text{NO}_2]} = \phi \approx 1 \quad (1)$$

For polluted regions this correlation needs to be expanded by the oxidation of NO by peroxy radicals forming NO_2 besides Reaction (R1), which we show in Reactions (R3) and (R4) [1, 20, 21]. In the

upper troposphere, RO_2 can be mostly represented by methyl peroxy radicals (CH_3O_2) [8, 22].



The (extended) Leighton ratio can for example be used to estimate NO_2 mixing ratios from NO and O_3 measurements. Particularly in the upper troposphere, NO_2 measurements are a challenge due to thermal interferences of reservoir species, which we present in Nussbaumer et al. (2021) [2] and can be found in Section 3.3.

2.2.2 Atmospheric sources and distribution

NO_x is mostly emitted as NO and converted to NO_2 in the atmosphere by the reactions shown in the previous section [12]. There are various sources throughout the troposphere with peak emissions at the surface and in the upper troposphere, which can be either anthropogenic or biogenic. In the lower troposphere, NO_x is mostly emitted from anthropogenic combustion processes, including internal combustion engines and industrial activity, accounting for approximately two thirds of the overall NO_x emissions [23]. High temperatures during combustion enable the reaction of molecular nitrogen (N_2) and oxygen (O_2) from the air to form NO . Further emissions of NO_x from the surface include biomass burning and soil emissions.

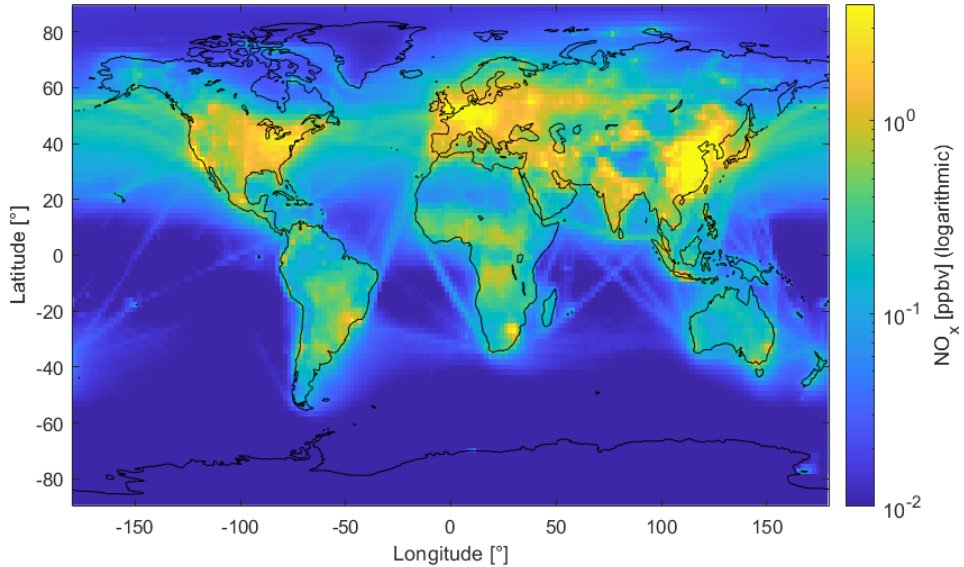


Figure 3: Global distribution of NO_x at the surface as a 20-year average (2000-2019). The data is presented on a logarithmic scale which allows for a more detailed view of areas characterized by low mixing ratios, such as the maritime regions. This figure was self-created based on modeled NO_x data as obtained from Dr. Andrea Pozzer.

Figure 3 presents the global distribution of NO_x as an average from 2000 to 2019, based on daily values at local noon. This figure was created using modeled data of the ECHAM5 (fifth generation European Centre Hamburg general circulation model, version 5.3.02)/MESSy2 (second generation Modular Earth Submodel System, version 2.54.0) Atmospheric Chemistry (EMAC) model [24]. Elevated mixing ratios can be observed in major cities across all continents and for important shipping routes, mostly in the Northern Pacific and Atlantic Oceans.

At the surface, particularly in urban areas, NO_x emissions have the highest impact on local air quality and therefore on human health. In order to develop concepts for decreasing the pollutant load and improving local air quality it is important to not only monitor the ambient mixing ratios of trace gases, but also to investigate its sources in detail. Local emission inventories can provide estimates on NO_x fluxes, that is a mass emitted per surface area and time, which need to be validated by measurements [25]. Nussbaumer et al. (2023) [10] presents direct airborne NO_x flux measurements over Los Angeles based on the research aircraft campaign RECAP-CA (Re-Evaluating the Chemistry of Air Pollutants in California) in June 2021 which can be found in Section 3.7.

In the upper troposphere, NO_x has two major sources which are aircraft (anthropogenic) and lightning [23, 26]. The amount of NO_x that is emitted from lightning is highly uncertain and estimates range from 2 to 8 Tg/year [27]. The free troposphere between the top of the boundary layer and the beginning of the upper troposphere does not hold any particular emission sources and mixing ratios at these altitudes are usually small.

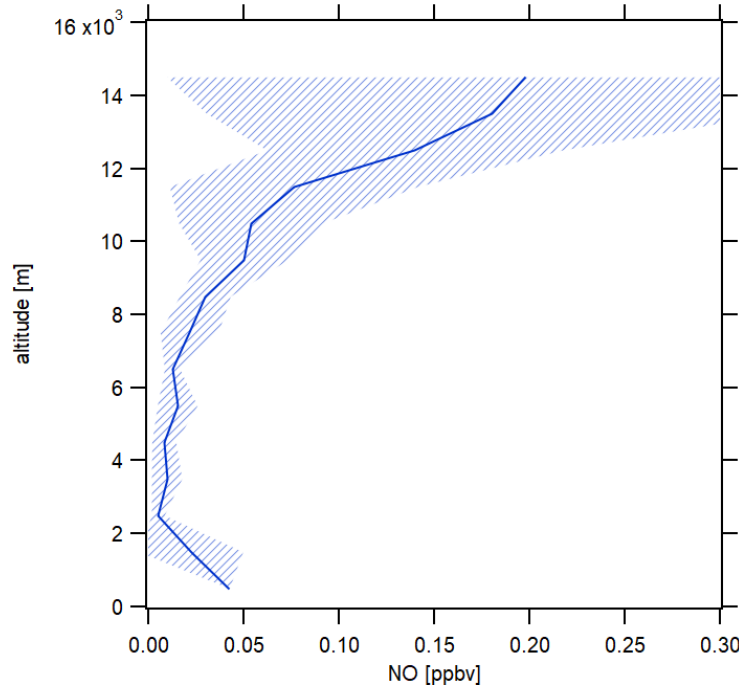


Figure 4: Vertical profile of NO during the aircraft campaign CAFE Africa over West Africa and the Atlantic Ocean in August and September 2018. This figure was self-created based on NO measurements during CAFE Africa. A vertical profile of CAFE Africa NO data can also be found in Tadic et al. (2021) [22].

The different sources of NO_x throughout the troposphere lead to a typical C-shape of its vertical profile. Figure 4 shows the vertical profile of NO based on measurements during the research aircraft campaign CAFE Africa (Chemistry of the Atmosphere Field Experiment in Africa) which took place in August and September 2018 around Cape Verde. Due to its remote location, surface emission of NO are sparse and the vertical profile therefore only shows a small elevation in the lower troposphere with average mixing ratios of less than 50 pptv. The expected increase in mixing ratios in the upper troposphere is particularly pronounced due to the observation of strong lightning events. The average observed mixing ratio between 13 and 14 km is approximately 200 pptv with an 1σ variability in the order of 100 %. This is typical for lightning in the remote upper troposphere as lightning strokes generate highly variable amounts of NO and deep convection can additionally transport NO free air from the marine boundary layer upwards. Section 3.2 (Nussbaumer et al. (2021) [9]) provides more details on a study analyzing lightning events in combination with the occurrence of deep convection during CAFE Africa in regard to the formation of a hurricane.

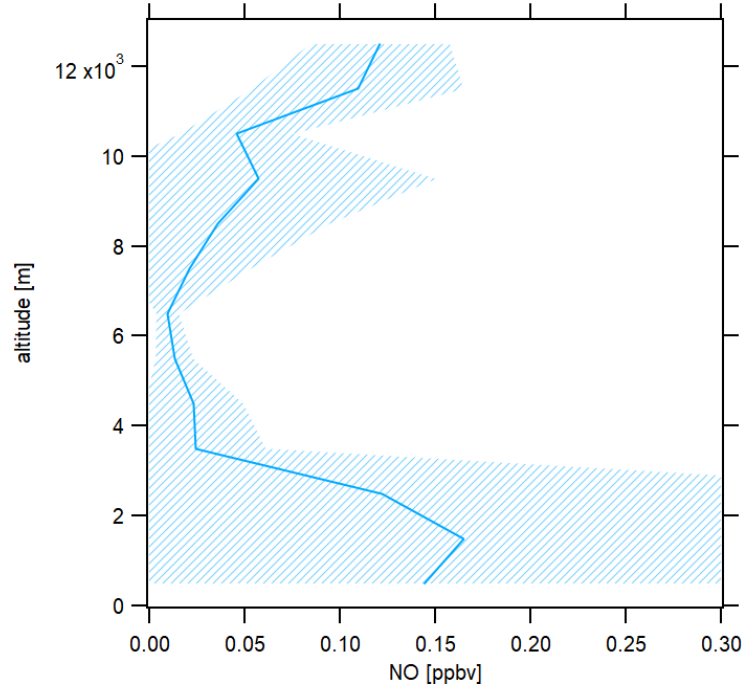


Figure 5: Vertical profile of NO during the aircraft campaign BLUESKY over Europe in May and June 2020. This figure was self-created based on NO measurements during BLUESKY. A vertical profile of BLUESKY NO data can also be found in the supplementary material of Nussbaumer et al. (2022) [7].

A different example of a vertical profile of NO is shown in Figure 5 based on measurements during the aircraft campaign BLUESKY in May and June 2020 over Europe. Since Europe is a densely populated continent, mixing ratios close to the surface are much higher compared to Africa and the Atlantic Ocean during the research campaign CAFE Africa as presented in Figure 4. Average values are around 150 pptv in the lower troposphere, decrease to near zero in the free troposphere and increase again in the upper troposphere. The average NO mixing ratio between 12 and 13 km is 120 pptv and therefore similar to the surface. While lightning plays a major role in the

tropical upper troposphere, in the northern mid-latitudes upper tropospheric NO mostly results from aircraft emissions as lightning events are more sparse [27,28]. NO mixing ratios over Europe and implications of the COVID-19 lockdowns on the upper tropospheric photochemistry involving NO and O₃ are discussed in detail in Nussbaumer et al. (2022) [7] which can be found in Section 3.5.

2.2.3 Formation of O₃

NO_x and volatile organic compounds (VOCs) are the two main precursors to tropospheric O₃ [23, 29, 30]. There are two important reasons to study ozone and its dependence on NO_x and VOCs in the troposphere. First, O₃ at the earth’s surface is a health hazard to plants and humans when inhaled as it can cause various diseases affecting the respiratory and cardiovascular system [5,31]. A detailed analysis of O₃ formation at three different ground measurement sites across Europe, which are Finland, Germany and Cyprus, characterized by various background conditions is provided in Nussbaumer et al. (2021) [6], and can be found in Section 3.4. Second, O₃ is a greenhouse gas and contributes significantly to the earth’s radiative budget – particularly in the upper troposphere – affecting global warming and climate change [3, 4]. In Nussbaumer et al. (2023) [8], the mechanisms influencing ozone formation in the upper tropical troposphere with particular focus on NO_x emissions from lightning are discussed in detail, which can be found in Section 3.6.

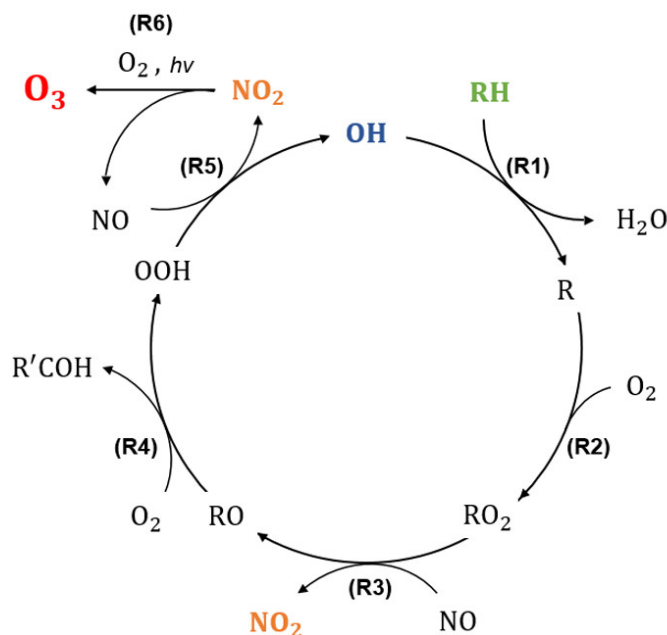


Figure 6: HO_x cycle, presenting how an OH radical catalyzes the formation of O₃ from NO and a VOC (RH) [32]. Reprinted (adapted) with permission from Nussbaumer and Cohen, Environ. Sci. Technol. 2020, 54, 24, 15652–15659. Copyright 2020 American Chemical Society.

Figure 6 (reprinted (adapted) from [32], Copyright 2020 American Chemical Society) shows how ozone is formed from a VOC, here represented by RH whereby R is an organic rest, and NO in the presence of O₂. The reaction scheme is well known in literature and has been reported many

times (e.g. [23, 33]). The cycle, referred to as the HO_x cycle (HO_x representing the sum of OH and HO_2), is catalyzed by an OH radical. In the first step, OH reacts with RH (a VOC) under H abstraction to form H_2O and R. The organic radical reacts with oxygen from the air and generates an organic peroxy radical (RO_2). RO_2 subsequently oxidizes NO to NO_2 and is in turn reduced to RO, which forms HO_2 in the presence of oxygen. In the last step of the cycle, HO_2 oxidizes NO to NO_2 while the OH radical is regenerated. In the presence of sunlight and oxygen the two NO_2 molecules formed within one turn around the HO_x cycle can form two O_3 molecules. NO_2 and O_3 are often investigated as a sum O_x , as they can rapidly interconvert in the presence of sunlight and each represents the oxidized species. The catalytic HO_x cycle can be interrupted by multiple termination reactions which include self-reactions of peroxy radicals and HO_x , the formation of nitrate species or the reaction of NO_2 and OH to form nitric acid (HNO_3) [23, 32]. The possible termination reactions are presented in Reactions (R5)–(R11).



Ozone has several loss pathways, including the reaction with OH, HO_2 and photolysis, as shown in Reaction (R12)–(R14) [11, 23]. Reaction (R14) only yields a net loss of ozone, if $\text{O}(^1\text{D})$ reacts with H_2O to form OH radicals. If it collides with N_2 or O_2 from the air, $\text{O}(^3\text{P})$ is formed which subsequently reacts back to ozone with oxygen. The share of $\text{O}(^1\text{D})$ that forms OH in competition with the back reaction to O_3 can be described by $\alpha(\text{O}(^1\text{D}))$ as shown in Equation (2), whereby k represents the rate constants for each individual reaction [34]. In the lower troposphere, deposition to the earth’s surface can be considered another loss mechanism. The reaction with NO to form NO_2 (Reaction (R1)) is usually not considered when calculating ozone loss as its reverse reaction (Reaction (R2)) represents an ozone production pathway.



$$\alpha(\text{O}({}^1\text{D})) = \frac{k_{\text{O}({}^1\text{D})+\text{H}_2\text{O}} \times [\text{H}_2\text{O}]}{k_{\text{O}({}^1\text{D})+\text{N}_2} \times [\text{N}_2] + k_{\text{O}({}^1\text{D})+\text{O}_2} \times [\text{O}_2] + k_{\text{O}({}^1\text{D})+\text{H}_2\text{O}} \times [\text{H}_2\text{O}]} \quad (2)$$

Figure 7 provides an overview of the ozone production $P(\text{O}_3)$ (green) and loss $L(\text{O}_3)$ pathways (orange) typically assumed for studies on O_3 in the upper troposphere [22, 34, 35].

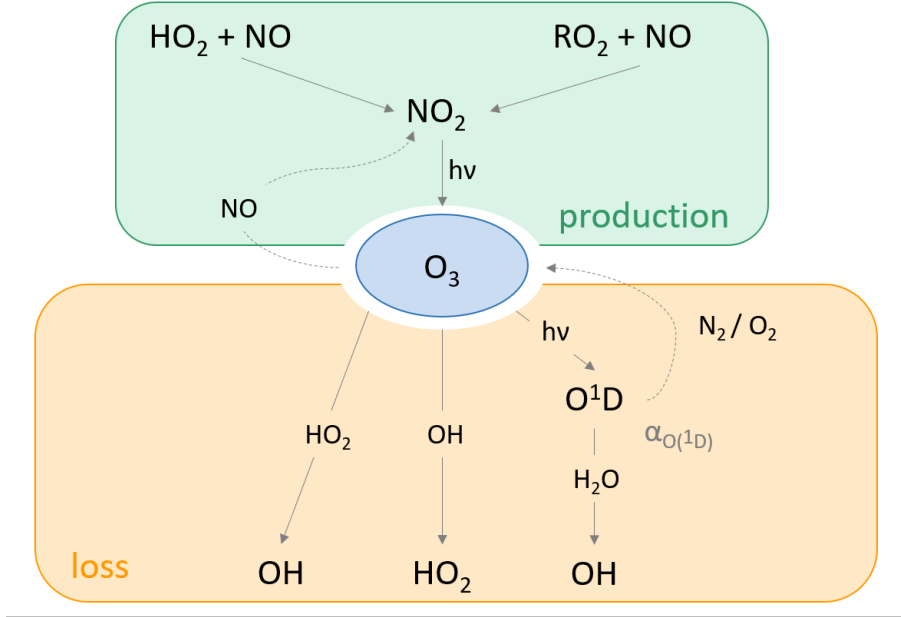


Figure 7: Overview of ozone production (green) and loss pathways (orange) typically applied for the upper troposphere. This figure was self-created based on Nussbaumer et al. (2021, 2022, 2023) [6–8].

At high altitudes (upper troposphere), reliable NO_2 measurements are difficult to obtain [1, 2]. Considering $\text{NO}_2\text{-O}_3\text{-NO}$ photostationary state, the production of ozone can be represented by the reaction of NO with HO_2 and RO_2 (mostly CH_3O_2), which yields NO_2 , and O_3 after photolysis. Equations (3)–(5) present the calculations of $P(\text{O}_3)$, $L(\text{O}_3)$ and the net ozone production rate (NOPR) with the rate constants k and the photolysis frequency j .

$$P(\text{O}_3) = [\text{NO}] \times (k_{\text{NO}+\text{HO}_2} \times [\text{HO}_2] + k_{\text{NO}+\text{CH}_3\text{O}_2} \times [\text{CH}_3\text{O}_2]) \quad (3)$$

$$L(\text{O}_3) = [\text{O}_3] \times (k_{\text{O}_3+\text{HO}_2} \times [\text{HO}_2] + k_{\text{O}_3+\text{OH}} \times [\text{OH}] + \alpha(\text{O}({}^1\text{D})) \times j(\text{O}({}^1\text{D}))) \quad (4)$$

$$\begin{aligned} \text{NOPR} &= P(\text{O}_3) - L(\text{O}_3) \\ &= [\text{NO}] \times (k_{\text{NO}+\text{HO}_2} \times [\text{HO}_2] + k_{\text{NO}+\text{CH}_3\text{O}_2} \times [\text{CH}_3\text{O}_2]) \\ &\quad - [\text{O}_3] \times (k_{\text{O}_3+\text{HO}_2} \times [\text{HO}_2] + k_{\text{O}_3+\text{OH}} \times [\text{OH}] + \alpha(\text{O}({}^1\text{D})) \times j(\text{O}({}^1\text{D}))) \end{aligned} \quad (5)$$

The presented method is used to calculate net ozone production over Europe [7] and in the upper tropical troposphere on a global scale [8], which can be found in Sections 3.5 and 3.6, respectively. Calculations of net ozone production across Europe at the surface [6] are presented in Section 3.4. For this study – due to the availability of reliable NO_2 measurements at the surface – $P(\text{O}_3)$ is calculated via the photolysis of NO_2 . For $L(\text{O}_3)$, the reaction with NO and deposition to the surface are then added as loss mechanisms. The reliability of NO_2 measurements depending on the altitude and additional parameters within the troposphere is discussed in detail in Section 3.3.

2.2.4 Formation of HCHO

Another important trace gas in the troposphere is formaldehyde (HCHO). In secondary processes, which dominate in remote locations due to the short atmospheric lifetime of HCHO , it is formed from almost any VOC oxidized by OH or O_3 , or via photolysis [36–38]. Approximately half of the production pathways additionally involve NO , and HCHO is therefore closely related to the processes that also control the availability of O_3 [6]. Figure 8 presents a simplified overview of the production (green) and loss pathways (orange) of formaldehyde.

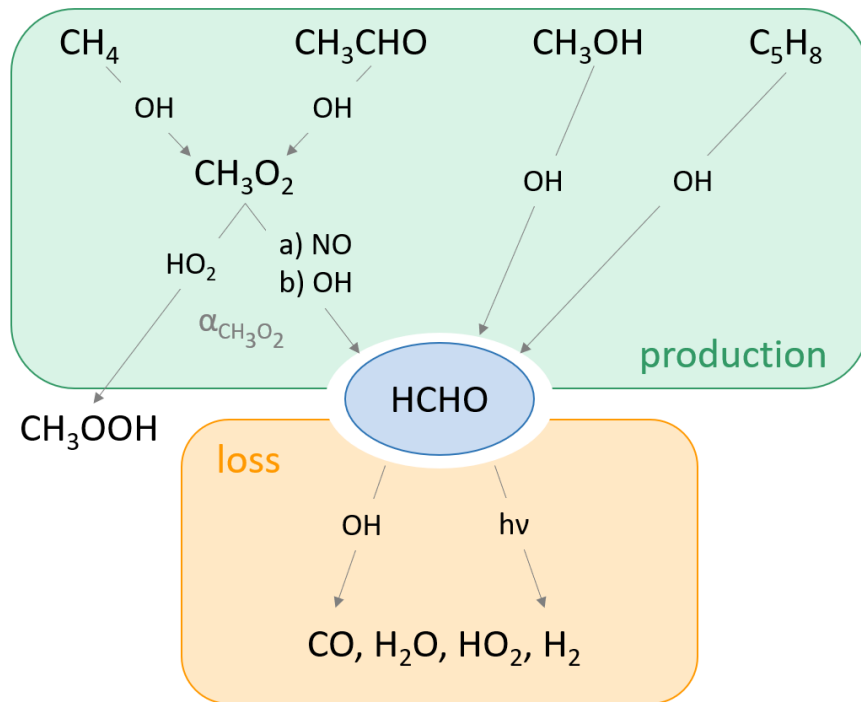


Figure 8: Simplified overview of formaldehyde production (green) and loss pathways (orange). This figure was self-created based on Nussbaumer et al. (2021) [6].

At the surface, besides photolysis and the reaction with OH , deposition is additionally considered a loss mechanism [36]. Methane (CH_4), acetaldehyde (CH_3CHO), methanol (CH_3OH) and isoprene (C_5H_8) are found to be the main precursors of HCHO based on ground measurements at three different sites across Europe which is presented in detail in Section 3.4 [6]. Methanol and isoprene form HCHO directly via oxidation by OH radicals. Methane and acetaldehyde are first oxidized to

methyl peroxy radicals (CH_3O_2). In a second step the reaction with NO (and OH) yields HCHO, competing with the reaction with HO_2 to form methyl hydroperoxide (CH_3OOH). The ratio of CH_3O_2 that forms HCHO is represented by $\alpha(\text{CH}_3\text{O}_2)$ as shown in Equation (6) [6–8].

$$\alpha(\text{CH}_3\text{O}_2) = \frac{k_{\text{CH}_3\text{O}_2+\text{NO}} \times [\text{NO}] + k_{\text{CH}_3\text{O}_2+\text{OH}} \times [\text{OH}]}{k_{\text{CH}_3\text{O}_2+\text{NO}} \times [\text{NO}] + k_{\text{CH}_3\text{O}_2+\text{OH}} \times [\text{OH}] + k_{\text{CH}_3\text{O}_2+\text{HO}_2} \times [\text{HO}_2]} \quad (6)$$

The reaction of CH_3O_2 with NO does not only lead to the formation of HCHO via CH_3O , but also to NO_2 which subsequently forms O_3 , as shown in Figure 7. The competing reaction of CH_3O_2 with HO_2 presents a termination reaction of the HO_x cycle, as shown in Reaction (R7). Besides evaluating the formation of HCHO, $\alpha(\text{CH}_3\text{O}_2)$ therefore provides information on the sensitivity of O_3 , which we will discuss in detail in the following section.

2.2.5 Chemical regime throughout the troposphere

The correlation of O_3 and its precursors is non-linear and therefore, changes in ambient NO_x and VOCs can have various impacts on O_3 mixing ratios, depending on the local background conditions [11, 39–41]. Due to the implications of ozone for both air quality and climate change it is highly relevant to study its sensitivity in response to short- and long-term changes of NO_x and VOCs. The dependence of O_3 formation on its precursors at the surface is presented in Figure 9.

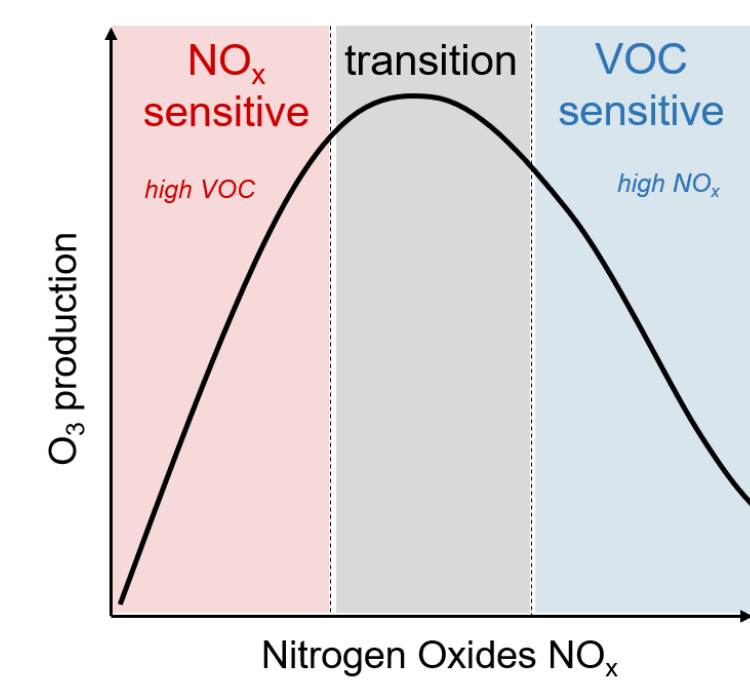


Figure 9: Non-linear correlation between ozone production and its precursors NO_x and VOCs at the surface. This figure was self-created based on Pusede et al. (2012) [41], Nussbaumer et al. (2020) [32] and Nussbaumer et al. (2023) [8].

For low ambient mixing ratios of NO_x , O_3 production linearly depends on nitrogen oxides, which is referred to as NO_x -sensitive regime. The NO_x to VOC ratio is small and the system is only sensitive to changes in NO_x , while changes in VOC do not impact $P(\text{O}_3)$. For high ambient mixing ratios of NO_x and an elevated NO_x to VOC ratio, $P(\text{O}_3)$ decreases with increases in NO_x . Chemistry under these conditions is referred to as VOC-sensitive regime. Peak production of ozone marks the transition between the two chemical regimes and the exact position depends on ambient VOC levels [29, 41]. The course of $P(\text{O}_3)$ with NO_x as shown in Figure 9 can be explained by the HO_x cycle and its termination reactions. When the availability of NO_x is limited, the HO_x cycle is promoted. OH radicals predominately react with RH (a VOC), leading to the formation of HO_2 and RO_2 which form NO_2 via the reaction with NO, and subsequently O_3 via photolysis. Peroxy radicals are abundant and therefore, increases in NO directly affect increases in O_3 formation. The main termination reactions of the HO_x cycle for a NO_x -sensitive regime are self-reactions of peroxy radicals (R6)–(R8). When the availability of VOCs is limited and NO_x is present in excess, the termination reaction (R11) of the HO_x cycle becomes relevant. Instead of the reaction of OH radicals with VOCs promoting $P(\text{O}_3)$, OH reacts with NO_2 to form HNO_3 , which terminates the HO_x cycle [11, 23, 32, 42]. Various techniques exist to determine the dominant chemical regime including the weekend ozone effect, the ozone production efficiency, the H_2O_2 to HNO_3 ratio or the HCHO to NO_2 ratio to name some examples [43–46]. A detailed description of these techniques can be found in Nussbaumer et al. (2023) [8] which is presented in Section 3.6.

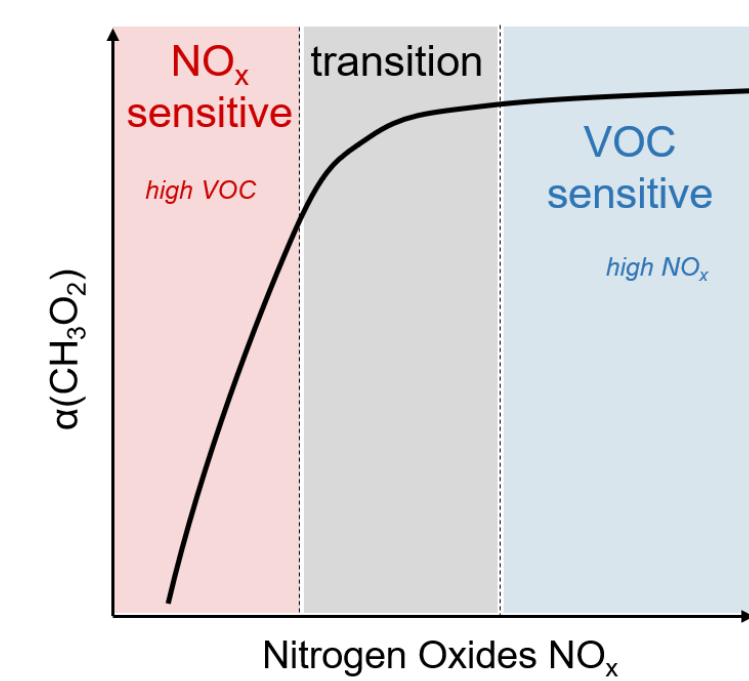


Figure 10: Determining the dominant chemical regime using the correlation of $\alpha(\text{CH}_3\text{O}_2)$ with NO_x – valid throughout the entire troposphere. This figure was self-created based on Nussbaumer et al. (2023) [8].

In the upper troposphere, this definition of the dominant chemical regime is no longer valid because the termination reaction of OH and NO_2 forming nitric acid plays a minor role at low temperatures

and the NO_2 mixing ratios are much lower compared to the surface. Instead, the development of $\alpha(\text{CH}_3\text{O}_2)$ with NO_x can indicate the dominating O_3 sensitivity which can be seen in Figure 10. For low ambient mixing ratios of NO_x , $\alpha(\text{CH}_3\text{O}_2)$ increases linearly with increasing NO_x , i.e. a NO_x -sensitive regime. In analogy to the definition via $P(\text{O}_3)$ (as shown in Figure 9), peroxy radicals are abundant in comparison to NO_x and increases in NO promote the formation of O_3 and of HCHO . CH_3O_2 reacts both with HO_2 and NO . For high ambient NO_x , all available CH_3O_2 radicals react with NO to form O_3 and HCHO and changes in NO_x do not affect $\alpha(\text{CH}_3\text{O}_2)$ or ambient O_3 levels anymore. Detailed analyses of $\alpha(\text{CH}_3\text{O}_2)$ and its suitability to indicate the dominant chemical regime throughout the entire troposphere and on a global scale are discussed in detail in Sections 3.4 [6] (lower troposphere in Finland, Germany and Cyprus), 3.5 [7] (upper troposphere over Europe) and 3.6 [8] (upper tropical troposphere).

2.3 Airborne and ground-based measurements of NO_x

Multiple methods for measuring nitrogen oxides exist, which include e.g. absorption spectroscopy, differential optical absorption spectroscopy (DOAS), laser induced fluorescence (LIF) and catalytic or photolysis-chemiluminescence (P-CL) [47]. Airborne measurements, which are central to this work as most of the included studies deal with photochemical processes involving nitrogen oxides throughout the troposphere, face particular challenges due to variations in altitude, pressure and temperature, high velocities of the measuring platform, as well as a large variation of mixing ratios due to the large areas and altitudes which can be covered. Therefore, requirements for aircraft NO_x measurements include low detection limits, high data accuracy, the ability of in situ measurements, high data resolution, low weight and volume of the instrument, independence of ambient conditions (as far as possible) and low energy consumption [47]. This section briefly presents two methods enabling atmospheric measurements of nitrogen oxides which are laser induced fluorescence (LIF) and chemiluminescence. These methods are most often applied on airborne platforms as they provide low detection limits and high compatibility with requirements for airborne measurements. The focus is hereby on NO_x measurements via photolysis-chemiluminescence which were performed and improved as part of this work.

2.3.1 Laser induced fluorescence (LIF)

Laser induced fluorescence (LIF) is a method enabling measurements of atmospheric trace gases via laser excitation. Different sub-methods can be distinguished. A direct method for NO_2 detection is the single-photon LIF. NO_2 is excited by a laser and forms excited-state NO_2^* . During its relaxation, a fluorescent signal ($> 700 \text{ nm}$) is emitted, which can be detected by a photomultiplier tube (PMT). The signal is proportional to sampled NO_2 concentrations in the measured air and can be converted to mixing ratios via a calibration gas standard [47–50]. For NO , both single and two-photon LIF detection is possible, whereby a laser excites the molecule once or twice (two different wavelengths), respectively. The fluorescent emission is detected during de-excitation providing specific information on the NO molecule [47]. NO_x can also be measured indirectly via the methods described above when NO and NO_2 are first converted to NO_2 and NO , respectively. For photofragmentation two-photon NO_2 LIF, NO_2 is photolyzed to NO and $\text{O}(^3\text{P})$ by a laser prior to NO detection. NO can first be oxidized to NO_2 through addition of O_3 in excess and

subsequently be detected via NO₂ LIF detection [10, 51]. NO_x data obtained via laser induced fluorescence measurements are presented in Section 3.7 and Nussbaumer et al. (2023) [10].

2.3.2 Photolysis-chemiluminescence (P-CL)

In contrast to the fluorescence method described in the previous section, chemiluminescence is a chemical method to measure nitrogen oxides in the atmosphere. It is a direct method for NO and an indirect method for NO₂ detection. NO from the sampled air is converted to excited-state NO₂* with excess O₃ in the main reaction chamber. A photon is emitted when falling back to the ground state, which is detected by a PMT. The signal counts are proportional to the amount of NO in the sample and can be converted to mixing ratios via instrument calibration with bottled NO. For the NO₂ measurement, NO₂ is converted to NO prior to the reaction with O₃ and PMT detection [1, 2, 52]. This is possible via catalytic or photolytic conversion. The catalytic method is based on a redox-reaction e.g. with molybdenum as reducing agent: $\text{Mo} + 3\text{NO}_2 \longrightarrow \text{MoO}_3 + 3\text{NO}$. Drawbacks of the catalytic conversion include high temperatures usually – around 300–350 °C – which makes this method not selective to NO₂ [53, 54]. For the photolytic method, NO₂ is converted to NO using light of a wavelength close to the peak absorption cross section of NO₂, which is 398 nm [47, 52]. The yield of this conversion is referred to as the conversion efficiency C_e and depends mostly on the light intensity and residence time in the converter. The PMT detects the sum of NO in the sample and the share (NO_c) of NO₂ converted to NO, defined by the conversion efficiency. NO₂ can then be calculated from simultaneous measurements of NO and NO_c, as shown in Equation (7) [2].

$$[\text{NO}_2] = \frac{[\text{NO}_c] - [\text{NO}]}{C_e} \quad (7)$$

Some other species including alkenes can also generate a chemiluminescent signal after reaction with O₃, which occurs on a longer time scale compared to the reaction of NO with O₃. Therefore, regular pre-chamber measurements are performed, for which O₃ is added to the sample flow and reacts with NO before entering the main reaction chamber. In the latter, only the side reactions then generate a chemiluminescent signal, which can be subtracted from the measurements excluding the pre-chamber set-up [1, 35].

The instrument used to perform studies in the scope of this work is a two-channel photolysis-chemiluminescence instrument. It was originally purchased from ECO Physics (Dürnten, Switzerland; CLD 790 SR) and modified manually multiple times. It is described in detail in Tadic et al. (2020) [35] and Nussbaumer et al. (2021) [2], the latter of which is provided in Section 3.3. Figure 11 presents a sketch of the instrument’s structure, which was adapted from Tadic et al. (2020) [35]. The gas supplies are shown in yellow. The O₂ supply ensures the formation of O₃ for the chemiluminescent reaction. The synthetic air supply (SynAir) allows for background measurements, and together with the NO supply for instrument calibrations. The NO₂ supply is usually not employed. Mass flow controllers (MFCs) adjust the desired flow rates (usually 1.5 SLM per channel). The pre-chambers are shown in orange, the main reaction chambers in light gray and

the photolytic converter, which is present in the channel measuring NO_x , is presented in light blue.

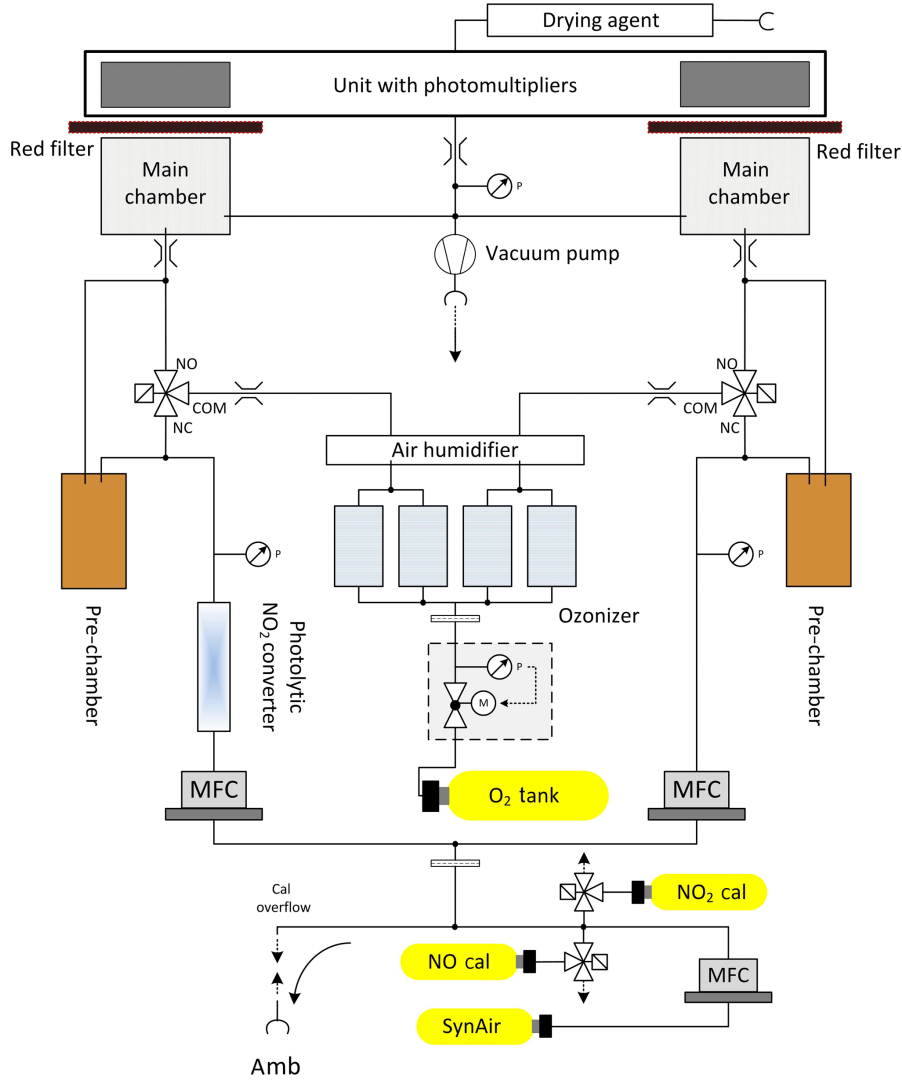


Figure 11: Sketch of the photolysis-chemiluminescence instrument which was used to perform NO_x measurements in the scope of this work. This figure was adapted from Tadic et al. (2020) [35].

2.3.3 Challenges in NO_2 measurements

Tropospheric measurements of NO are reliable and well-implemented and can reach detection limits in the low single-digit pptv range. In contrast, NO_2 measurements, particularly in the upper troposphere, where mixing ratios are low, are still a major challenge. This is mostly due to thermal interferences of NO_2 reservoir species, which include for example methyl peroxyxynitrate (MPN), pernitric acid (PNA) and peroxyacetyl nitrate (PAN) [1, 2]. These can occur in the photolytic converter of photolysis-chemiluminescence instruments, where temperatures are usually elevated due to the light for NO_2 conversion, but also in any other instrument part with increased temperatures. The share of reservoir species that release NO_2 in the instrument can be estimated

via first-order decay, as shown in Equation (8) whereby k is the rate constant of the decay and t is the residence time.

$$\text{artifact} = 1 - \exp(-k \times t) \times 100\% \quad (8)$$

Exemplary, for a residence time of 1 s at an instrument part with a temperature of 30 °C and a pressure of 1000 hPa, $\sim 11\%$ of PNA and 93 % of MPN, that are present in the sampled air, would release NO₂. This problem arises both in LIF, as well as chemiluminescence instruments [1,2,55]. A challenge, which has been reported and observed in previous field campaigns for measurements via photolysis-chemiluminescence, is a memory effect on the walls of the photolytic converter [56,57]. As part of this work a new improved photolytic converter was developed, which is presented in detail Nussbaumer et al. (2021) [2] and can be found in Section 3.3.

3 Results

3.1 Overview

This work consists of six studies, four of which have been published in peer reviewed journals. The remaining two studies have been submitted to *Atmospheric Chemistry & Physics* and are currently under review at *EGUsphere*. I am the first author of all published and submitted papers. I have analyzed all data, prepared the manuscripts and figures and revised the published papers according to the referees' comments. A detailed overview of all author contributions can be found in each subsection. This section presents the results of each study. Section 4 provides the supplementary material.

All studies, which are part of this work, deal with the effects of nitrogen oxides throughout the troposphere, including their sources and their involvement in photochemical processes, particularly focusing on the role as a precursor to tropospheric ozone.

Section 3.2 presents the role of NO_x as a meteorological indicator, showing lightning and convective events in a developing tropical cyclone over the Atlantic Ocean off the coast of West Africa. It is shown that deep convection, transporting air from the marine boundary layer to the upper troposphere, occurs in the developing cyclone independent of its strength, while the number of lightning events decreases with increasing storm strength based on measurements during the aircraft campaign CAFE Africa 2018. The study which was published in the journal *Atmospheric Chemistry & Physics* is the first to present in situ observations of lightning and convection in a developing cyclone.

Section 3.3 presents a study on improving NO_2 measurements with particular focus on airborne applications, which still presents a considerable challenge up to today. A new photolytic converter made from quartz glass was developed, which shows advantages for photolysis-chemiluminescence measurements through reduced wall effects. The paper presenting this work was published in the journal *Atmospheric Measurement Techniques* and is the first to thoroughly analyze and point out major disadvantages in the use of a conventional photolytic converter on research aircraft.

Section 3.4 shows the role of NO_x in the formation of formaldehyde and ozone at the surface, where these trace gases have major implications for air quality as well as human and plant health. It is shown that while almost any VOC can form HCHO, four are sufficient to represent HCHO production at three measurement sites across Europe in Finland, Germany and Cyprus. These four VOCs are methane, acetaldehyde, methanol and isoprene. A new indicator – $\alpha(\text{CH}_3\text{O}_2)$ – is presented to analyze dominating O_3 sensitivity based on NO and HO_x measurements. This study was published in the journal *Atmospheric Chemistry & Physics* and presents the first calculation of HCHO production from in situ measurements in Europe.

Section 3.5 presents the impact of reduced mixing ratios of NO_x as a result of less air traffic during the European COVID-19 lockdowns on ozone formation and its sensitivity in the upper troposphere based on the indicator $\alpha(\text{CH}_3\text{O}_2)$ which was first introduced in Section 3.4. It is shown, that the dominant chemical regime in the upper troposphere has shifted from a VOC sensitivity to a transition regime over the past 15 years due to general emission reductions, and to a NO_x sensitivity as a result of the COVID-19 lockdowns. This study was published in the journal *Atmospheric Chemistry & Physics* and is the first to investigate changes in O_3 sensitivity as an outcome of the COVID-19 lockdowns in the upper troposphere.

Based on the findings of Sections 3.4 and 3.5 and the use of $\alpha(\text{CH}_3\text{O}_2)$ as an indicator for O_3 sensitivity, Section 3.6 investigates the impact of NO_x on O_3 formation and its precursor sensitivity in the upper tropical troposphere (UTT) on a global scale. It is shown that lightning is the only significant source of NO_x and majorly controls O_3 sensitivity in the UTT. Additionally, it is found that the most common indicator for O_3 sensitivity found in literature cannot be applied in the upper troposphere, but only at the surface. Instead, $\alpha(\text{CH}_3\text{O}_2)$ is valid throughout the entire troposphere and has major advantages over previous indicators, which has never been shown in literature before. This study was submitted to the journal *Atmospheric Chemistry & Physics*.

Following a detailed investigation of NO_x sources in the upper troposphere, Section 3.7 presents an evaluation of NO_x sources at the surface based on direct airborne observations of fluxes over Los Angeles. Knowing the exact NO_x sources and their magnitude is essential for emission control and thus the improvement of local air quality. Based on measurements of NO_x mixing ratios and the vertical wind speed, NO_x fluxes are calculated via wavelet transformation and compared to an emission inventory, showing some local discrepancies. The manuscript presenting this study was submitted to the journal *Atmospheric Chemistry & Physics* and is the first to investigate NO_x fluxes based on aircraft measurements over Los Angeles.

3.2 Deep convection and lightning in a developing hurricane

This chapter has been published in the journal *Atmospheric Chemistry & Physics* as a measurement report. I am the first author of this paper. I have analyzed all data presented, I have made the figures and I have prepared and revised the manuscript. The co-authors were involved in the presented research campaign CAFE Africa (Africa 2018) and in proofreading the manuscript. Detailed author contributions can be found at the end of the paper in the section *Author contributions*.

How to cite: Nussbaumer, C. M., Tadic, I., Dienhart, D., Wang, N., Edtbauer, A., Ernle, L., Williams, J., Obersteiner, F., Gutiérrez-Álvarez, I., Harder, H., Lelieveld, J., and Fischer, H.: Measurement report: In situ observations of deep convection without lightning during the tropical cyclone Florence 2018, *Atmos. Chem. Phys.*, 21, 7933–7945, <https://doi.org/10.5194/acp-21-7933-2021>, **2021**.

submitted: 28 Jan 2021

published: 25 May 2021

The supplementary material for this publication can be found in Section 4.1.

Atmos. Chem. Phys., 21, 7933–7945, 2021
<https://doi.org/10.5194/acp-21-7933-2021>
 © Author(s) 2021. This work is distributed under
 the Creative Commons Attribution 4.0 License.



Atmospheric
Chemistry
and Physics
Open Access
EGU

Measurement report: In situ observations of deep convection without lightning during the tropical cyclone Florence 2018

Clara M. Nussbaumer¹, Ivan Tadic¹, Dirk Dienhart¹, Nijing Wang¹, Achim Edtbauer¹, Lisa Ernle¹, Jonathan Williams^{1,2}, Florian Obersteiner³, Isidoro Gutiérrez-Álvarez⁴, Hartwig Harder¹, Jos Lelieveld^{1,2}, and Horst Fischer¹

¹Department of Atmospheric Chemistry, Max Planck Institute for Chemistry, Mainz, Germany

²Climate and Atmosphere Research Center, The Cyprus Institute, Nicosia, Cyprus

³Institute of Meteorology and Climate Research – Atmospheric Trace Gases and Remote Sensing (IMK-ASF), Karlsruhe Institute of Technology, Karlsruhe, Germany

⁴Department of Integrated Sciences, Center for Natural Resources, Health and Environment (RENSMA), University of Huelva, Huelva, Spain

Correspondence: Clara M. Nussbaumer (clara.nussbaumer@mpic.de)

Received: 28 January 2021 – Discussion started: 8 February 2021

Revised: 14 April 2021 – Accepted: 22 April 2021 – Published: 25 May 2021

Abstract. Hurricane Florence was the sixth named storm in the Atlantic hurricane season 2018. It caused dozens of deaths and major economic damage. In this study, we present in situ observations of trace gases within tropical storm Florence on 2 September 2018, after it had developed a rotating nature, and of a tropical wave observed close to the African continent on 29 August 2018 as part of the research campaign CAFE Africa (Chemistry of the Atmosphere: Field Experiment in Africa) with HALO (High Altitude and Long Range Research Aircraft). We show the impact of deep convection on atmospheric composition by measurements of the trace gases nitric oxide (NO), ozone (O₃), carbon monoxide (CO), hydrogen peroxide (H₂O₂), dimethyl sulfide (DMS) and methyl iodide (CH₃I) and by the help of color-enhanced infrared satellite imagery taken by GOES-16. While both systems, i.e., the tropical wave and the tropical storm, are deeply convective, we only find evidence for lightning in the tropical wave using both in situ NO measurements and data from the World Wide Lightning Location Network (WWLLN).

1 Introduction

Tropical cyclones are low-pressure systems evolving over warm tropical waters usually close to the Equator ($\pm 20^\circ$ latitude) – an area which includes the so-called Intertrop-

ical Convergence Zone (ITCZ) (Frank and Roundy, 2006; Deutscher Wetterdienst, 2020). The ITCZ is a global band of convection where southeasterly and northeasterly trade winds converge. It is characterized by rapidly changing weather events. Air heated by the sun near the Equator rises, creating low pressures near the surface, which initiates flows from adjacent areas (Waliser and Gautier, 1993; Wang and Magnusdottir, 2006; Deutscher Wetterdienst, 2020). In this region of high ocean temperature and intense solar radiation, humid air can rise deeply into the troposphere up to 15 km and higher (Collier and Hughes, 2011; Deutscher Wetterdienst, 2020). This is associated with the formation of deep, convective cumulonimbus clouds accompanied by heavy rainfall and thunderstorm activity (Zipser, 1994; Xu and Zipser, 2012). In the early stages, these systems are referred to as tropical waves or disturbances which together with low wind shear and high ocean temperature of 26.5 °C or higher can form tropical cyclones (Frank and Roundy, 2006; Shapiro and Goldenberg, 1998; National Ocean Service, 2020b). Wu and Takahashi (2018) suggested that simultaneous occurrence of convection and vorticity in disturbances favors tropical cyclone formation. However, the exact formation mechanism of tropical cyclones from tropical waves is not fully understood today (Wu and Takahashi, 2018; Frank and Roundy, 2006). Tropical cyclones are characterized by their rotating nature around a center originating

Published by Copernicus Publications on behalf of the European Geosciences Union.

from Coriolis forces and the balance of the pressure gradient (Smith et al., 2005; Gray, 1975). Consequently, tropical cyclones in the Northern Hemisphere spin counterclockwise and in the Southern Hemisphere clockwise, while rotating systems do not develop within about 5° latitude of the Equator (National Ocean Service, 2020a; Gray, 1975). Tropical cyclones are categorized and named according to the maximum sustained wind speed and their geographic origin. A tropical cyclone formed over the Atlantic Ocean – most often west of the African continent – with a maximum wind speed of 64 knots (118 km/h) and higher is defined as a hurricane according to the Beaufort scale. Lower wind speeds of up to 34 knots (63 km/h) characterize a tropical depression. Tropical cyclones with intermediate wind speed (34 to 63 knots) are referred to as tropical storms (DeMaria et al., 2012; National Weather Service, 2020).

Deep convection can affect trace gas concentrations in the upper troposphere which was, for example, shown by Dickerson et al. (1987), who reported increased concentrations of NO, CO, O₃ and other reactive species in a thunderstorm outflow over the Midwestern United States in 1985, and Barth et al. (2015), with the latter based on observations during the DC3 (Deep Convective Clouds and Chemistry) field campaign. Similar observations were made by Bucci et al. (2020), who reported convective uplift in the upper troposphere/lower stratosphere based on the StratoClim aircraft campaign over Nepal in 2017. It is usually observed along with lightning. Collision of light ice particles moving upwards in cumulonimbus clouds and graupel particles moving downwards due to gravity in the presence of supercooled water induces electric charge separation which accumulates and discharges spontaneously as a lightning flash (Lal et al., 2014; Liu et al., 2012). Lightning events are frequent over tropical continental areas such as South America or Africa where cloud-to-cloud lightning contributes to around 90 % (Williams and Satori, 2004; Price and Rind, 1993). While lightning events over the ocean are less frequent, they are subject to extensive research with regards to the occurrence in tropical cyclones. Zipser (1994) reported significantly reduced lightning activity over tropical oceans despite heavy rainfall from convective clouds in comparison to tropical continental and coastal areas with similar rainfall based on shipborne observations during the GARP Atlantic Tropical Experiment (GATE, where GARP represents the Global Atmospheric Research Program) in 1974. Lal et al. (2014) observed higher lightning activity over continental compared to oceanic areas based on satellite data from 2000 to 2011. These results are in line with other published work, e.g., Cecil et al. (2014), Xu and Zipser (2012) and Xu et al. (2010). Regarding tropical cyclones, DeMaria et al. (2012) reported more intense lightning activity in tropical storms compared to hurricanes based on lightning data from the World Wide Lightning Location Network (WWLLN) and satellite data on tropical cyclones which is in agreement with findings from Abarca et al. (2011), who reported a decrease in lightning

density with increasing storm strength. DeMaria et al. (2012) additionally found greater lightning activity in intensifying compared to weakening storms, which was also reported by Zhang et al. (2015).

Measurements of nitric oxide (NO) in the upper troposphere can provide indirect evidence on the recent occurrence of lightning. The heat developed in lightning flashes allows the abundant N₂ and O₂ to atomize and then recombine to form NO (Murray, 2016; Huntrieser et al., 2011). In the upper troposphere, lightning is the main source of NO by around 80 %, whereas it only contributes about 10 % to the overall global NO budget (Schumann and Huntrieser, 2007; Murray, 2016). Over the ocean, the only significant NO emissions are from lightning, ships and aircraft (Bond et al., 2002; Masiol and Harrison, 2014). NO sources over land are more versatile including anthropogenic emissions from industry, vehicles and biomass burning (partly natural) as well as natural sources from lightning and soil, with the natural sources dominating over West Africa (Pacífico et al., 2019; Knippertz et al., 2015). One lightning flash produces approximately $(2\text{--}40) \times 10^{25}$ molecules of NO, which together with NO_x as NO_x have a lifetime of several days near the Equator (Pollack et al., 2016; Schumann and Huntrieser, 2007; Levy et al., 1999).

Other trace gases can be used to detect convective injection from the marine boundary layer into the upper troposphere. These include near-surface emissions of carbon monoxide (CO) from the photolysis of dissolved organic matter (DOM) (Stubbins et al., 2006) and methyl iodide (CH₃I), which is produced by algae and phytoplankton as well as aqueous photochemical processes and is released from the ocean with an atmospheric lifetime of 4–7 d (Tegtmeier et al., 2013; Bell et al., 2002). Another possible source could be dust originated from the African continent which enters the sea or comes in contact with sea water vapor and produces methyl iodide as described by Williams et al. (2007). One possible explanation for the formation of CH₃I is a substitution reaction of methoxy-group-containing species and iodide from seawater under the presence of iron ions from dust. However, the mechanism is not yet fully understood (Williams et al., 2007). Furthermore, phytoplankton forms dimethylsulfoniopropionate (DMSP) in seawater, which is degraded to dimethyl sulfide (DMS) and emitted from the ocean's surface (Simó and Dachs, 2002; Gondwe et al., 2003). Its lifetime ranges from 1–2 d and depends on the atmospheric abundance of OH and NO₃ which oxidize DMS (Breider et al., 2010). OH concentrations in turn are controlled by nitrogen oxides (NO_x = NO + NO₂) and ozone. The latter is formed by photolysis of NO₂ with O₂ and depends on ambient NO and hydrocarbons (Nussbaumer and Cohen, 2020). Photolysis of O₃ and reaction with water vapor yield OH (Levy, 1971; Lelieveld and Dentener, 2000; Tegtmeier et al., 2013). NO_x from lightning plays a key role in OH formation in the free troposphere (Lelieveld et al., 2018; Brune et al., 2018). On the other hand, in NO_x-poor conditions, e.g., in the ma-

rine boundary layer close to the surface, the concentrations of peroxyradicals can build up, leading to O_3 destruction and high levels of H_2O_2 (Ayers et al., 1992). Due to a strong surface uptake loss of H_2O_2 , concentrations peak at mid-range altitudes (Weller and Schrems, 1993).

Hurricane Florence was the sixth named storm in the Atlantic hurricane season of 2018 (AL062018) (Stewart and Berg, 2019). It developed from a tropical wave over West Africa, which was first reported on 28 August by the National Hurricane Center (NHC) Miami (FL, USA) (National Hurricane Center, 2018c). On 31 August, a tropical depression developed which was upgraded to a tropical storm by the NHC on 1 September (National Hurricane Center, 2018a; Stewart and Berg, 2019). The tropical cyclone grew to hurricane strength on 4 September (National Hurricane Center, 2018b). Hurricane Florence reached its maximum wind speed of 130 knots (category 4 hurricane) on 11 September and made landfall on 14 September in North Carolina. It claimed overall more than 50 deaths and caused USD 24 billion worth of damage mainly from flooding in North Carolina and South Carolina (Stewart and Berg, 2019; Paul et al., 2019).

Some studies have investigated trace gas concentrations and convective uplift in the upper troposphere through aircraft observations. Newell et al. (1996) reported in situ observations of deep convection in Typhoon Mireille in 1991 which they found to be strongest in the wall cloud region. They additionally detected enhanced NO concentrations in the eye wall area and suggested lightning as a source based on observations reported by Davis et al. (1996). Roux et al. (2020) found the convective uplift of boundary layer air as well as the inflow of lower stratospheric air to the upper troposphere based on measurements of CO, O_3 and H_2O during aircraft typhoon observations over Taipei in 2016. In contrast, studies of lightning activity within convective systems over the ocean and in tropical cyclones are predominantly based on satellite data and ground-based observations from the WWLLN (University of Washington, 2020; Abreu et al., 2010; Bürgesser, 2017; Hutchins et al., 2012b; Bucsele et al., 2019). Generally, data from in situ chemical measurements in the upper troposphere are sparse, and to our knowledge, the in situ aircraft observation of deep convection in tropical cyclones accompanied by and in the absence of lightning depending on the stage of development has not been reported before. In this study, we present airborne in situ observations of trace gases within a tropical wave on 29 August 2018 and of the tropical storm Florence on 2 September 2018 based on measurements during the aircraft campaign CAFE Africa (Chemistry of the Atmosphere: Field Experiment in Africa). The data are examined for evidence of the chemical impacts of deep convection and lightning activity.

2 Observations

The research campaign CAFE Africa took place from August to September 2018 over West Africa and the central eastern Atlantic. Fourteen measurement flights (MFs) were performed with HALO (High Altitude and Long Range Research Aircraft) starting from the campaign base in Sal on Cabo Verde (16.75° N, 22.95° W). A detailed description of the campaign is provided by Tadic et al. (2021).

In this paper, we report observations based on three measurement flights – MF10, MF12 and MF14. Figure 1 shows an overview of the geographical locations of the three flights including satellite images obtained from NASA Worldview on the day of observation. The images were taken by the VIIRS (Visible Infrared Imaging Radiometer Suite) instrument carried by the NASA/NOAA satellite Suomi NPP (National Polar-orbiting Partnership) based on a daily resolution (NASA Worldview, 2020). MF10 was carried out on 24 August 2018 and was chosen as comparison flight as parts of it were in close geographical proximity to MF14. We have restricted our analysis to data from MF10 which were obtained in these parts in a similar geographical area and altitude range as MF14 (as shown in Fig. 1a). MF12 was carried out on 29 August 2018 and passed over a tropical low-pressure system which had recently moved off the West African coast. Tropical cyclone Florence was passed over on 2 September 2018 in the scope of MF14 west of the Cabo Verde islands after it was upgraded to a tropical storm.

The research aircraft carried multiple instruments for the measurement of various atmospheric trace gases including NO, O_3 , CO, H_2O_2 , CH_3I and DMS. NO was measured via chemiluminescence (detector from ECO Physics CLD 790 SR, Dürnten, Switzerland) with a relative uncertainty of 6 % and a detection limit of 5 ppt_v (Tadic et al., 2020). O_3 mixing ratios were analyzed by UV absorption and chemiluminescence with the FAIRO instrument (chemiluminescence data with a total uncertainty of 2.5 %; Zahn et al., 2012). CO was measured via quantum cascade laser absorption spectroscopy with an uncertainty of 4.3 % (Schiller et al., 2008). H_2O_2 mixing ratios were measured via dual-enzyme detection (modified Aero-Laser AL2021, Garmisch-Partenkirchen, Germany) with a total measurement uncertainty of 9 % and a detection limit of 15 ppt_v (Hottmann et al., 2020). DMS was measured via proton-transfer-reaction time-of-flight mass spectrometry (PTR-TOF-MS-8000, Ionicon Analytik GmbH, Innsbruck, Austria) with a detection limit of 15 ppt_v (Wang et al., 2020; Edtbauer et al., 2020). CH_3I was measured with a custom-built fast gas-chromatography-mass-spectrometry system described by Bourtsoukidis et al. (2017) with a detection limit of 0.5 ppt_v. Backward trajectories were calculated using the Lagrangian particle dispersion model FLEXPART 10.2 (Stohl et al., 2005; Pissot et al., 2019). Lightning data were obtained from the WWLLN (University of Washington, 2020). Satellite images were acquired from NASA Worldview (2020). Color-enhanced

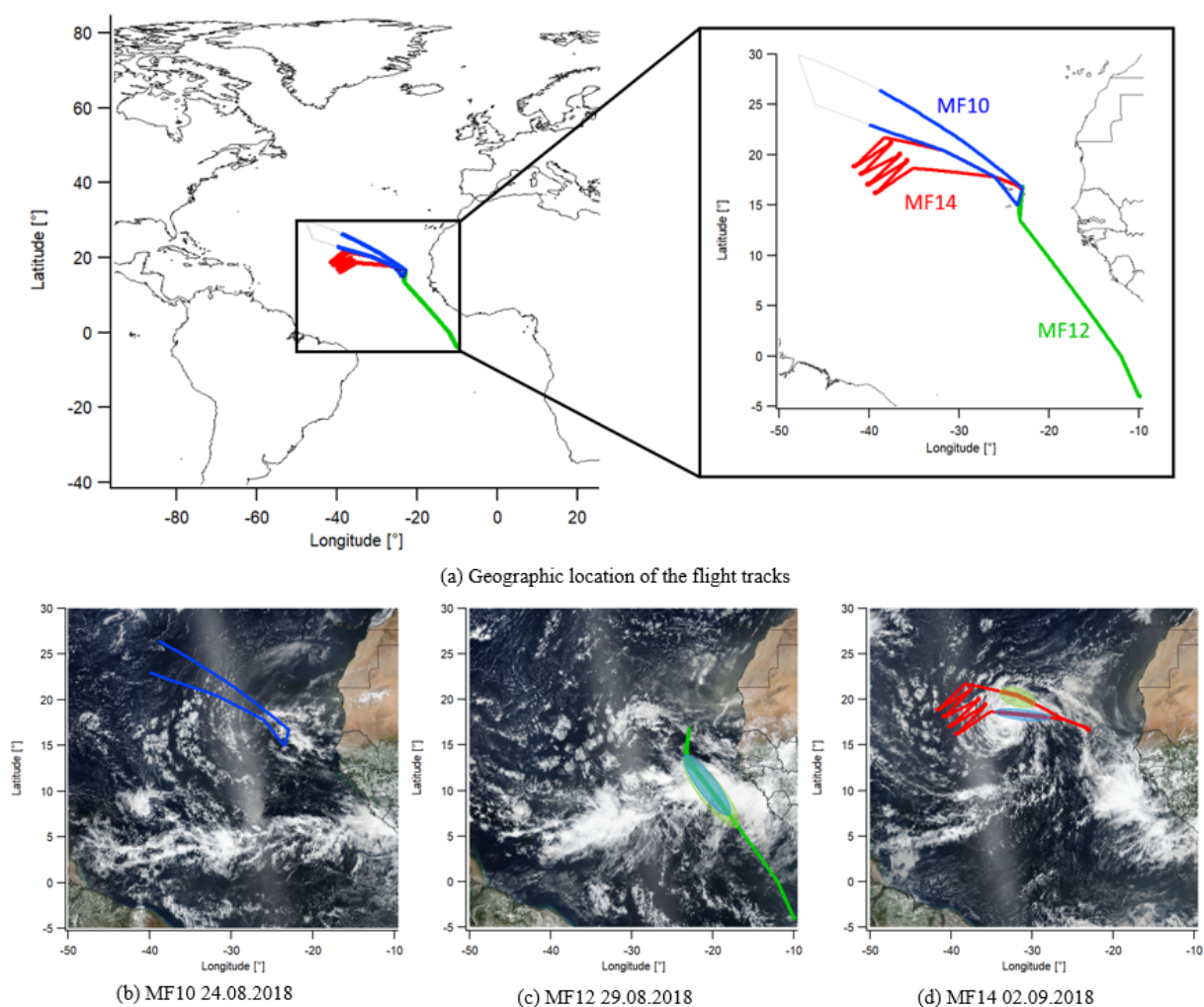


Figure 1. Overview of the flight tracks including satellite images obtained on the day of observation from the NASA Worldview application (NASA Worldview, 2020). Blue: MF10 on 24 August as comparison flight. Green: MF12 on 29 August over the tropical wave. Red: MF14 on 2 September over tropical storm Florence. Marked areas indicate convection.

infrared imagery were obtained from the Naval Research Laboratory and from the Real-Time Tropical Cyclone web page maintained by the Cooperative Institute for Research in the Atmosphere (CIIRA), Colorado State University, and NOAA's Center for Satellite Research, Fort Collins, Colorado (Naval Research Laboratory, 2020; CIIRA and NOAA, 2018).

3 Results and discussion

3.1 Cloud top

Figure 2 shows the color-enhanced infrared imagery obtained from the Naval Research Laboratory including the flight

tracks for MF12 and MF14. The satellite images are colored according to the temperature deduced from IR emissions of cloud tops in degrees Celsius ($^{\circ}\text{C}$) as measured by the satellite GOES-16 (Geostationary Operational Environmental Satellite). The flight track is colored according to the IR temperature scale showing the ambient temperature measured on the research aircraft, which was mainly between -50 and -60 $^{\circ}\text{C}$. The IR images give information on the occurrence of convective clouds. It can be assumed that the IR temperature of a cloud top is equal to the ambient temperature at that altitude. Accordingly, lower IR temperatures represent clouds at higher altitudes. The flight altitude for MF12 at 18:00 UTC shown in Fig. 2a was 14.4 km while passing over an area of elevated clouds. The corresponding temper-

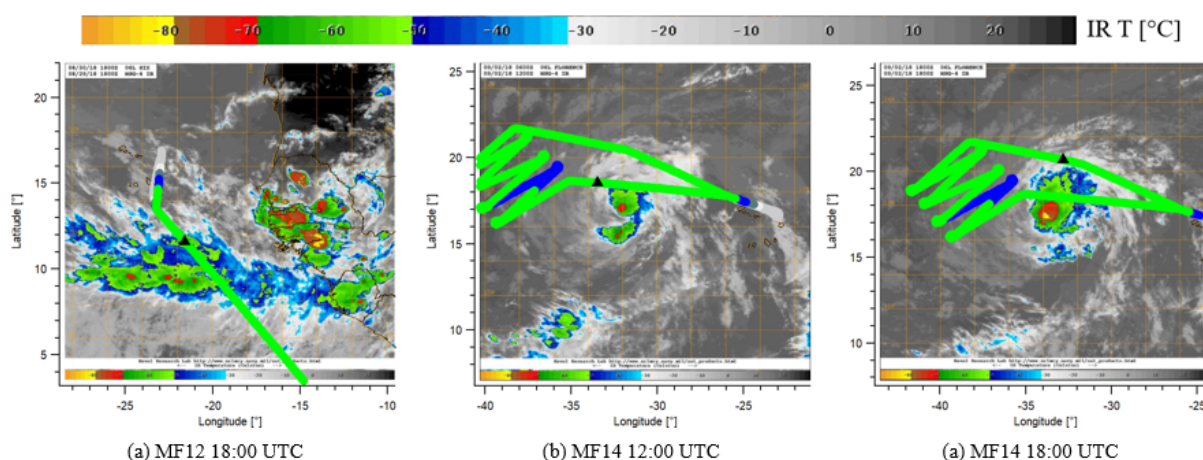


Figure 2. Flight tracks with color-enhanced infrared imagery obtained from the Naval Research Laboratory Tropical Cyclone page (Naval Research Laboratory, 2020) for MF12 and MF14 (no image availability before MF12 18:00 UTC). The altitude of the flight tracks is colored according to the IR temperature legend. The temperature during most parts of the flight was between -50 and -60 °C. Black triangles show the according position of the research aircraft for the time of the background IR image.

ature was -68 ± 1 °C, so the aircraft was likely above the cloud top. For MF12, the same area was passed in the morning at an altitude of 12.9 km, but no IR image is available. The temperature was -56 ± 1 °C. Assuming a similar cloud elevation in the morning, the research aircraft was at a similar altitude as the cloud top. The flight altitude for MF14 at 12:00 and at 18:00 UTC as shown in Fig. 2b and c was 13.2 km, and the temperature was -58 ± 1 °C. The colored IR images show an IR temperature between -40 and -50 °C at the current aircraft position (black triangle), which indicates that the research aircraft was above but close to cloud top at both occasions.

3.2 Trace gas measurements

Deep convective transport generally occurs in cumulonimbus systems accompanied by high cloud tops. Figure 3 shows the temporal development of the observed trace gases during MF12 and MF14. An overview of MF10 can be found in Fig. S1 of the Supplement. Blue and green shadowed plot areas show the time intervals when the research aircraft had passed areas of high cloud tops as shown in Fig. 2. The respective geographical positions of the aircraft are highlighted in Fig. 1c and d. Indicators for deep convection from the marine boundary layer are enhanced concentrations of CO, DMS, H_2O_2 and CH_3I as well as reduced O_3 at the flight altitude. In the absence of lightning, we expect decreased concentrations of NO in convective areas due to the vertical transport of NO-poor marine boundary layer air. In contrast, we expect enhanced NO concentrations in the presence of lightning (Pollack et al., 2016; Ridley et al., 2004; Lange et al., 2001; DeCaria et al., 2000; Chameides et al., 1987). For MF12, O_3 was low while pass-

ing the area of enhanced cloud tops after take-off with an average of 41 ± 2 ppb_v (10:30–11:45 UTC). The IR satellite image subsequently shows lower cloud tops, and the measured O_3 concentrations at the same flight altitude of 12.9 km were on average 69 ± 15 ppb_v (11:45–12:55 UTC). The same area of high cloud tops was passed on the way back at a higher flight altitude of 14.4 km. Before entering the area, O_3 was on average 76 ± 5 ppb_v (16:15–17:00 UTC) and then decreased to 46 ± 11 ppb_v (17:05–18:15 UTC). For MF14, the research aircraft also passed an area of elevated cloud tops after take-off (11:20–12:05 UTC) and before landing (17:50–18:25 UTC) with O_3 average concentrations of 34 ± 2 and 36 ± 2 ppb_v, respectively, at a flight altitude of 13.2 km. O_3 concentrations measured between these areas were higher by around 30 % with 48 ± 10 ppb_v at an altitude of 12.6 ± 0.3 km. At similar altitudes, MF10 showed O_3 concentrations of 72 ± 6 ppb_v. Besides the observed convective influence from the O_3 measurements, concentrations were overall larger for MF10 and MF12 compared to MF14. This is likely a response to NO concentrations which influence O_3 production as discussed further below.

For MF12, DMS was significantly enhanced when passing the area of high cloud tops in the morning with a maximum value of 33 ppt_v and varying between 0 and 18 ppt_v at the same flight altitude outside this area. No DMS was detected when passing the convective area in the evening, which is possibly due to the higher altitude of the research aircraft compared to the morning hours. The IR cloud top images in Fig. 2a show that the aircraft was likely above the cloud top while the convective influence is highest within the cloud. DMS concentrations during MF14 were on average 27 ± 17 and 14 ± 9 ppt_v passing the first and the sec-

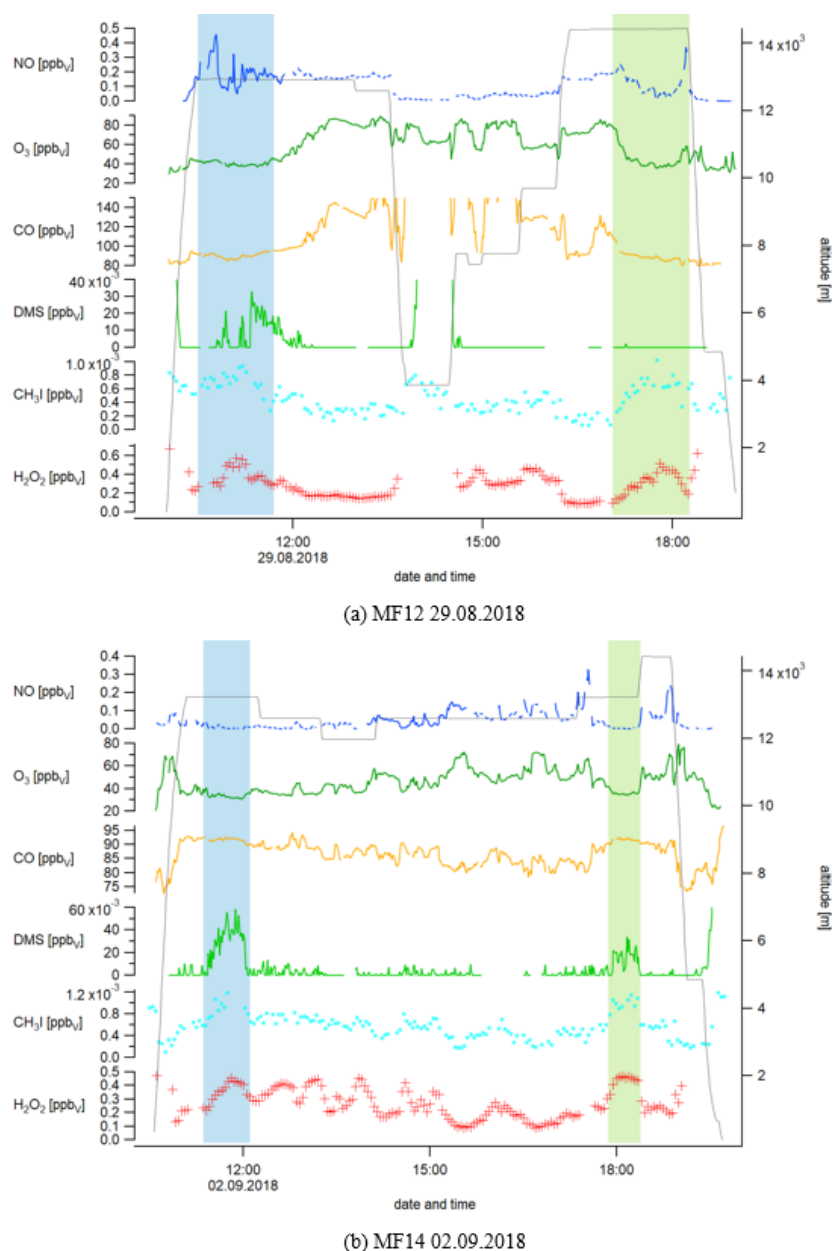


Figure 3. Overview of the temporal development of the observed trace gases NO, O₃, CO, DMS, CH₃I and H₂O₂ during measurement flights MF12 and MF14. Blue and green bars show the time intervals for which the research aircraft had passed high cloud tops (compare Fig. 1c and d). The overview for MF10 can be found in Fig. S1 of the Supplement.

ond high cloud top area, respectively, and below the detection limit in between, which clearly shows the effect of convection from the marine boundary layer. A maximum value of 58 ppt_v was reached passing the first cloud top area, which was higher compared to the MF12 maximum. For MF10, DMS concentrations were below the detection limit at com-

parable altitudes for the whole flight. CH₃I and H₂O₂, too, reached maximum concentrations when passing high cloud top areas during MF12 and MF14 and lower values at similar altitudes with lower cloud tops. NO concentrations were 169 ± 85 ppt_v for MF10 at 13.6 ± 0.7 km. For the identified convective areas during MF14, NO was close to zero (0–

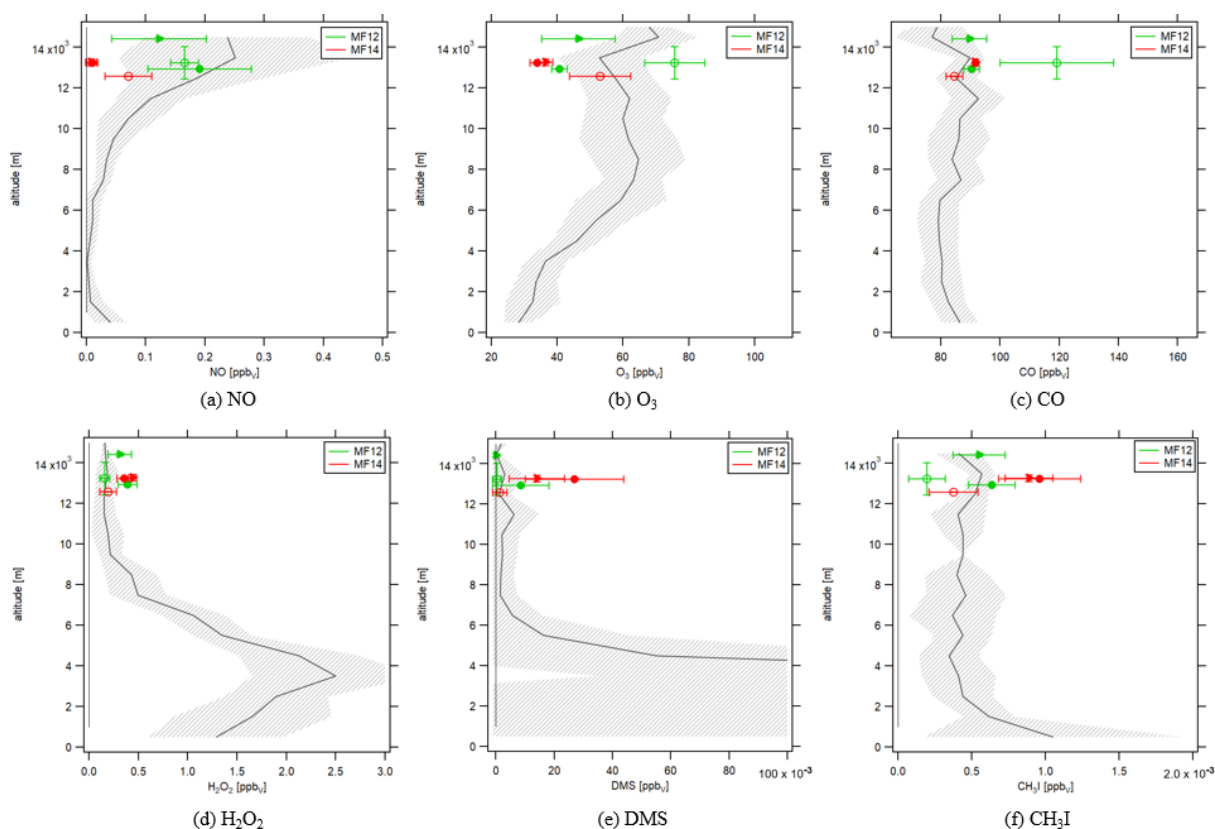


Figure 4. Vertical profiles of the background trace gas concentrations during CAFE Africa around Cabo Verde (gray) and the average trace gas concentrations for convective (filled symbols) and non-convective (open symbols) areas during MF12 (green) and MF14 (red).

37 ppt_v) and slightly enhanced in between with an average value of 56 ± 50 ppt_v. These observations demonstrate the occurrence of convection and the absence of lightning. In contrast, MF12 showed clear signs of lightning, particularly when passing the identified convective area in the morning. The measured NO concentrations showed characteristic spikes with a maximum of 459 ppt_v, which is by more than 1 order of magnitude higher than the detected signals during MF14. NO concentrations for MF12 outside the convective areas were 169 ± 21 ppt_v, which is very similar to NO levels during MF10. Backward trajectories for MF10 and MF12 (outside of convection) (Fig. S2 of the Supplement) show that the air originated from the African continent where lightning is frequent. Together with the absence of large spikes as observed for MF12 in the area of high cloud tops – an indicator for fresh lightning – the increased background level of NO for MF10 and MF12 was likely due to aged nitric oxide from thunderstorm activity over the ITCZ, mainly West Africa. Possible explanations for the lower NO background concentration during MF14 could be that the flight path was further away from coastal Africa and that the

flight data were influenced by convective processes with upward transport of low NO air from the marine boundary layer. Assuming dominant NO_x-limited chemistry as suggested by Tadic et al. (2021), low NO background levels induce low O₃ levels. In the convective areas during MF14 with particularly low NO concentrations, an O₃ destruction regime might have been present. In contrast, high NO background levels during MF10 and MF12 led to the observed high O₃ background as mentioned earlier. CO background levels for MF10 were 84 ± 7 ppbv. For MF14, CO was enhanced when passing high cloud tops with 92 ± 1 ppbv, and lower in between these areas with 86 ± 3 ppbv, which emphasizes the updraft of CO-rich air from the earth's surface. CO concentrations in the high cloud top areas for MF12 were comparable to those for MF14 but significantly lower compared to adjacent areas with low cloud tops observed in the Southern Hemisphere. From these observations, it seems that the inflow to the thunderstorms was in the Northern Hemisphere, while the background mixing ratios of CO were higher in the Southern Hemisphere due to biomass burning.

Figures S3 and S4 of the Supplement show the flight tracks of MF12 and MF14, respectively, color-coded according to the measured trace gas concentrations which underlines the geographic allocation of the convective areas.

3.3 Deep convection

Figure 4 shows the vertical concentration profiles of atmospheric trace gases averaged for all CAFE Africa take-offs and landings on Cabo Verde in gray. Flights before sunrise and after sunset were excluded for NO, O₃, CO, H₂O₂ and DMS. Figure S5a of the Supplement shows an overview of all data points that were included. Generally, for take-off and landing the data points before reaching and after leaving a constant flight altitude, respectively, were considered. CH₃I data were available for MF11, MF12, MF14 and MF15. Each data point in the vertical profile is the average of all data measured at this altitude ± 500 m, providing a background profile of atmospheric trace gases around Cabo Verde. Please note that these profiles represent background conditions in the Northern Hemisphere. Southern Hemisphere profiles generally show higher mixing ratios for CO and O₃ due to biomass burning over southern Africa and throughout the hemisphere (Fig. S6 of the Supplement). Red colors represent MF14 and green colors show MF12. Filled symbols represent areas with convection, and open symbols represent areas without convection according to the results from Sect. 3.2. For filled symbols, we differentiate between circles for the first passing of a convective area and triangles for the second passing. An overview of the symbols representing certain flight sections can be found in Fig. S5b of the Supplement. Figure 4a shows NO concentrations which are lowest at low altitudes and increase with height. Ground-level concentrations were slightly enhanced due to airport emissions but can be assumed negligible at ground-level altitudes over the ocean surface. The large enhancement and increased variability of NO at altitudes above 10 km was due to the overall effect of lightning associated with the position of the ITCZ just south of the Cabo Verde islands (Fig. 2 of Tadic et al., 2021). Average NO concentrations for MF14 in convective areas were close to zero – emphasizing the vertical updraft of NO-poor air from the marine boundary layer – while NO in the non-convective area was enhanced. All data points for MF12 are within the variability range of the background profile, which is what we expect for non-convective areas. For the MF12 convective areas, two opposing trends appear which are the vertical transport of NO-poor air from ground-level altitudes and the generation of fresh NO at high altitudes through lightning. From Fig. 3a, we suggested the occurrence of fresh lightning primarily for the early passing of the convective area. This is in accordance with the green circle (first passing) being situated at higher NO levels compared to the green triangle (second passing). O₃ concentrations are shown in Fig. 4b. Ground-level O₃ was low, increasing with altitude up to 8 km, and reaching a concentration of 61 ± 6 ppb_v aloft.

Average concentrations in convective areas were reduced for both MF12 and MF14, while they were enhanced in non-convective areas. Low-altitude CO concentrations were enhanced through ocean emissions and transport from the continent and led to a slight increase in concentrations in convective areas. As described above, the non-convective area of MF12 was heavily influenced by a biomass burning plume. The H₂O₂ background profile shown in Fig. 4d peaks at around 3–4 km altitude where the NO profile is lowest. NO-poor air induces an O₃ destructive regime, enhancing the abundance of peroxyradicals forming H₂O₂. Ground-level H₂O₂ was lower due to surface uptake. Non-convective areas of MF12 and MF14 are well represented by the H₂O₂ background profile, while concentrations in convective areas were enhanced. DMS and CH₃I (Fig. 4e and f) were elevated at low altitudes due to ocean emissions and possibly dust emissions and decreased with altitude. Again, concentrations of trace gases in convective areas showed an enhancement compared to non-convective areas. Figure S7 of the Supplement presents the background profiles including average concentrations of MF10 and MF14. As expected, values for MF10 are well described by the background profiles. For the trace gases CO, H₂O₂ and DMS, open symbols (representing non-convective average concentrations) for MF10 and MF14 are situated very close to the background profile. Filled symbols for MF14 are enhanced, which corroborates the effect of convection. For O₃ and NO, convective average concentrations were significantly reduced, while again open symbols fall within the variability range of the background profile. NO concentrations for MF14 were slightly lower compared to MF10 for non-convective areas due to the reasons discussed above.

While the discussed trace gases usually have a relatively short lifetime of the order of days, it is also possible that convection has occurred in a different location, and the trace gases were transported to the point of observation through advection. Backward trajectories can be used to examine this hypothesis. Figures S8 and S9 of the Supplement show the color-enhanced infrared satellite images of MF14 including the flight track and the backward trajectories for the prior 5 d. Black crosses mark the location of each calculated “air parcel” on its trajectory at the time when the satellite image was taken. It is shown that the backward trajectories are crossing the convective clouds of the developing cyclone several times. In contrast, Fig. S10 of the Supplement shows the analogous images for a section of the flight track further west where convection was not observed. The calculated air parcels on the backward trajectories were ahead of the developing cyclone at all times and never passed a convective system.

3.4 Lightning

In Sect. 3.1, 3.2 and 3.3, we have presented evidence on the occurrence of deep convection during MF12 and MF14. We

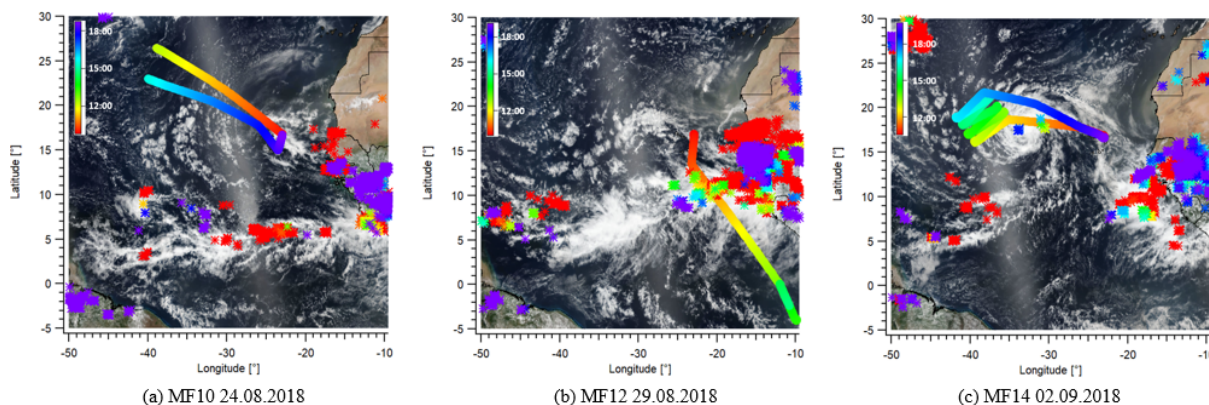


Figure 5. Lightning flashes shown as asterisks detected by the WWLLN on 24 and 29 August and 2 September 2018. Flashes and flight tracks are color-coded according to the time of day (Red shows morning hours and blue shows evening hours.) Background satellite images were obtained from the NASA Worldview application (NASA Worldview, 2020).

have hypothesized from the observed NO concentrations in the convective areas that the low-pressure system observed during MF12 included lightning, while the tropical storm observed during MF14 did not show any lightning activity. Figure 5 shows the lightning strokes as asterisks and the flight tracks as lines for MF10 (Fig. 5a), MF12 (Fig. 5b) and MF14 (Fig. 5c) color-coded according to the time of day obtained from the WWLLN. The WWLLN provides real-time lightning data covering almost the entire globe including oceans and remote locations. This is accompanied by a lower detection efficiency compared to local networks. Several studies have investigated this topic suggesting a WWLLN global detection efficiency of around 10 % with constant improvements through an increasing number of stations (Holzworth et al., 2019; Bürgesser, 2017; Virts et al., 2013; Abarca et al., 2010). Allen et al. (2019) calculated a detection efficiency of around 12 % for tropical Africa (long. -30 to 90° , lat. -30 to 30°) and of around 30 % for tropical America (long. -150 to -30° , lat. -30 to 30°) for 2011. At the same time, the WWLLN is capable of detecting almost any storm with lightning (Hutchins et al., 2012a; Jacobson et al., 2006). As expected, no lightning strokes were observed during MF10. For MF12, many lightning strokes were detected in the area with deep convection – many of which occurred in spatial and temporal proximity to the research aircraft. Figure 5b only shows the outbound flight part of MF12 as the inbound flight was stacked and much of the lightning occurred between take-off and noon. Finally, for MF14, very few lightning strokes were detected by the WWLLN in the area of the tropical storm, which is in accordance with the low observed NO concentrations.

4 Conclusions

In this study, we have presented in situ observations of a tropical cyclone which developed into hurricane Florence during the Atlantic hurricane season 2018. A nascent low-pressure system was observed during a measurement flight with HALO on 29 August and after a tropical storm had developed on 2 September. We observed deep convection for both the tropical wave and the tropical storm, based on in situ observations, supported by color-enhanced infrared imagery taken by the satellite GOES-16. Measured NO concentrations suggest significant occurrence of lightning only in the tropical wave but not in the tropical storm. This hypothesis is confirmed by the lightning strokes detected through the WWLLN. Our result is consistent with previous studies, e.g., DeMaria et al. (2012), Zhang et al. (2015) and Abarca et al. (2011), who found decreasing lightning activities with increasing cyclone strength. While these studies are based on satellite and ground-based observations, we present the first in situ observations in support of this hypothesis demonstrating that convective injection of marine boundary layer air can occur without NO production from lightning. In future, more in situ observations of deep convection and lightning activity in tropical cyclones with varying strength should be performed and reported in order to consolidate and expand the present knowledge of lightning in deep convective systems and its role in atmospheric chemistry.

Data availability. Data measured during the flight campaign CAFE Africa are available to all scientists agreeing to the CAFE Africa data protocol. Lightning data are available upon request from the World Wide Lightning Location Network.

Supplement. The supplement related to this article is available online at: <https://doi.org/10.5194/acp-21-7933-2021-supplement>.

Author contributions. HF had the idea. CMN and HF designed the study. CMN analyzed the data and wrote the article. IT measured and provided the NO and CO data. DD measured and provided the H₂O₂ data. JW, AE, NW and LE measured and provided the DMS and CH₃I data. O₃ data were received from FO. HH and IGA calculated the backward trajectories. HF, JL, HH and JW significantly contributed to planning and operating the research campaign.

Competing interests. The authors declare that they have no conflict of interest.

Acknowledgements. We would like to thank Uwe Parchatka for his assistance with the measurement of NO, Bettina Hottmann for her support of the measurement of H₂O₂ and Efstratios Bourtsoukidis for his assistance with the measurement of methyl iodide during CAFE Africa. We acknowledge the collaboration with the DLR (German Aerospace Center) during CAFE Africa. We acknowledge the Cooperative Institute for Research in the Atmosphere, Colorado State University, and NOAA's Center for Satellite Research, Fort Collins, Colorado, for using imagery from the Real-Time Tropical Cyclone web page. We acknowledge the Naval Research Laboratory for providing IR satellite images on the NRL Tropical Cyclone Page. The authors wish to thank the World Wide Lightning Location Network (<http://wwlln.net>, last access: 18 December 2020), which is a collaboration among over 50 universities and institutions, for providing the lightning location data used in this paper. We acknowledge the use of imagery from the NASA Worldview application (<https://worldview.earthdata.nasa.gov>, last access: 7 December 2020), which is part of the NASA Earth Observing System Data and Information System (EOSDIS). This work was supported by the Max Planck Graduate Center (MPGC) with the Johannes Gutenberg-Universität Mainz.

Financial support. The article processing charges for this open-access publication were covered by the Max Planck Society.

Review statement. This paper was edited by Christopher Cantrell and reviewed by two anonymous referees.

References

- Abarca, S. F., Corbosiero, K. L., and Galarneau Jr., T. J.: An evaluation of the worldwide lightning location network (WWLLN) using the national lightning detection network (NLDN) as ground truth, *J. Geophys. Res.-Atmos.*, 115, D18206, <https://doi.org/10.1029/2009JD013411>, 2010.
- Abarca, S. F., Corbosiero, K. L., and Vollaro, D.: The World Wide Lightning Location Network and convective activity in tropical cyclones, *Mon. Weather Rev.*, 139, 175–191, <https://doi.org/10.1175/2010MWR3383.1>, 2011.
- Abreu, D., Chandan, D., Holzworth, R., and Strong, K.: A performance assessment of the World Wide Lightning Location Network (WWLLN) via comparison with the Canadian Lightning Detection Network (CLDN), *Atmos. Meas. Tech.*, 3, 1143–1153, <https://doi.org/10.5194/amt-3-1143-2010>, 2010.
- Allen, D. J., Pickering, K. E., Bucseles, E., Krotkov, N., and Holzworth, R.: Lightning NO_x production in the tropics as determined using OMI NO₂ retrievals and WWLLN stroke data, *J. Geophys. Res.-Atmos.*, 124, 13498–13518, <https://doi.org/10.1029/2018JD029824>, 2019.
- Ayers, G., Penkett, S., Gillett, R., Bandy, B., Galbally, I., Meyer, C., Elsworth, C., Bentley, S., and Forgan, B.: Evidence for photochemical control of ozone concentrations in unpolluted marine air, *Nature*, 360, 446–449, <https://doi.org/10.1038/360446a0>, 1992.
- Barth, M. C., Cantrell, C. A., Brune, W. H., Rutledge, S. A., Crawford, J. H., Huntrieser, H., Carey, L. D., MacGorman, D., Weisman, M., Pickering, K. E., Bruning, E., Anderson, B., Apel, E., Biggerstaff, M., Campos, T., Campuzano-Jost, P., Cohen, R., Crounse, J., Day, D. A., Diskin, G., Flocke, F., Fried, A., Garland, C., Heikes, B., Honomichl, S., Hornbrook, R., Huey, L. G., Jimenez, J. L., Lang, T., Lichtenstern, M., Mikoviny, T., Nault, B., O'Sullivan, D., Pan, L. L., Peischl, J., Pollack, I., Richter, D., Riener, D., Ryerson, T., Schlager, H., Clair, J. S., Walega, J., Weibring, P., Weinheimer, A., Wennberg, P., Wisthaler, A., Wooldridge, P. J., and Ziegler, C.: The deep convective clouds and chemistry (DC3) field campaign, *Bull. Am. Meteorol. Soc.*, 96, 1281–1309, <https://doi.org/10.1175/BAMS-D-13-00290.1>, 2015.
- Bell, N., Hsu, L., Jacob, D. J., Schultz, M., Blake, D., Butler, J., King, D., Lobert, J., and Maier-Reimer, E.: Methyl iodide: Atmospheric budget and use as a tracer of marine convection in global models, *J. Geophys. Res.-Atmos.*, 107, D17, <https://doi.org/10.1029/2001JD001151>, 2002.
- Bond, D. W., Steiger, S., Zhang, R., Tie, X., and Orville, R. E.: The importance of NO_x production by lightning in the tropics, *Atmos. Environ.*, 36, 1509–1519, [https://doi.org/10.1016/S1352-2310\(01\)00553-2](https://doi.org/10.1016/S1352-2310(01)00553-2), 2002.
- Bourtsoukidis, E., Helleis, F., Tomsche, L., Fischer, H., Hofmann, R., Lelieveld, J., and Williams, J.: An aircraft gas chromatograph–mass spectrometer System for Organic Fast Identification Analysis (SOFIA): design, performance and a case study of Asian monsoon pollution outflow, *Atmos. Meas. Tech.*, 10, 5089–5105, <https://doi.org/10.5194/amt-10-5089-2017>, 2017.
- Breider, T., Chipperfield, M., Richards, N., Carslaw, K., Mann, G., and Spracklen, D.: Impact of BrO on dimethylsulfide in the remote marine boundary layer, *Geophys. Res. Lett.*, 37, L02807, <https://doi.org/10.1029/2009GL040868>, 2010.
- Brune, W. H., Ren, X., Zhang, L., Mao, J., Miller, D. O., Anderson, B. E., Blake, D. R., Cohen, R. C., Diskin, G. S., Hall, S. R., Hanisco, T. F., Huey, L. G., Nault, B. A., Peischl, J., Pollack, I., Ryerson, T. B., Shingler, T., Sorooshian, A., Ullmann, K., Wisthaler, A., and Wooldridge, P. J.: Atmospheric oxidation in the presence of clouds during the Deep Convective Clouds and Chemistry (DC3) study, *Atmos. Chem. Phys.*, 18, 14493–14510, <https://doi.org/10.5194/acp-18-14493-2018>, 2018.

- Bucci, S., Legras, B., Sellitto, P., D'Amato, F., Viciani, S., Montori, A., Chiarugi, A., Ravegnani, F., Ulanovsky, A., Cairo, F., and Stroh, F.: Deep-convective influence on the upper troposphere–lower stratosphere composition in the Asian monsoon anticyclone region: 2017 StratoClim campaign results, *Atmos. Chem. Phys.*, 20, 12193–12210, <https://doi.org/10.5194/acp-20-12193-2020>, 2020.
- Bucsela, E. J., Pickering, K. E., Allen, D. J., Holzworth, R. H., and Krotkov, N. A.: Midlatitude lightning NO_x production efficiency inferred from OMI and WLLN data, *J. Geophys. Res.-Atmos.*, 124, 13475–13497, <https://doi.org/10.1029/2018JD029824>, 2019.
- Bürgesser, R. E.: Assessment of the world wide lightning location network (WLLN) detection efficiency by comparison to the lightning imaging sensor (LIS), *Q. J. Roy. Meteorol. Soc.*, 143, 2809–2817, <https://doi.org/10.1002/qj.3129>, 2017.
- Cecil, D. J., Buechler, D. E., and Blakeslee, R. J.: Gridded lightning climatology from TRMM-LIS and OTD: Dataset description, *Atmos. Res.*, 135, 404–414, <https://doi.org/10.1016/j.atmosres.2012.06.028>, 2014.
- Chameides, W., Davis, D., Bradshaw, J., Rodgers, M., Sandholm, S., and Bai, D.: An estimate of the NO_x production rate in electrified clouds based on NO observations from the GTE/CITE 1 fall 1983 field operation, *J. Geophys. Res.-Atmos.*, 92, 2153–2156, <https://doi.org/10.1029/JD092iD02p02153>, 1987.
- CIRA and NOAA: AL062018 – Major Hurricane FLORENCE, available at: https://rammb-data.cira.colostate.edu/tc_realtime/storm.asp?storm_id=al062018 (last access: 17 December 2020), 2018.
- Collier, A. B. and Hughes, A. R.: Lightning and the African ITCZ, *J. Atmos. Sol.-Terr. Phys.*, 73, 2392–2398, <https://doi.org/10.1016/j.jastp.2011.08.010>, 2011.
- Davis, D., Crawford, J., Chen, G., Chameides, W., Liu, S., Bradshaw, J., Sandholm, S., Sachse, G., Gregory, G., Anderson, B., Barrick, J., Bachmeier, A., Collins, J., Browell, E., Blake, D., Rowland, S., Kondo, Y., Singh, H., Talbot, R., Heikes, B., Merrill, J., Rodriguez, J., and Newell, R. E.: Assessment of ozone photochemistry in the western North Pacific as inferred from PEM-West A observations during the fall 1991, *J. Geophys. Res.-Atmos.*, 101, 2111–2134, <https://doi.org/10.1029/95JD02755>, 1996.
- DeCaria, A. J., Pickering, K. E., Stenchikov, G. L., Scala, J. R., Stith, J. L., Dye, J. E., Ridley, B. A., and Laroche, P.: A cloud-scale model study of lightning-generated NO_x in an individual thunderstorm during STERAO-A, *J. Geophys. Res.-Atmos.*, 105, 11601–11616, <https://doi.org/10.1029/2000JD900033>, 2000.
- DeMaria, M., DeMaria, R. T., Knaff, J. A., and Molnar, D.: Tropical cyclone lightning and rapid intensity change, *Mon. Weather Rev.*, 140, 1828–1842, <https://doi.org/10.1175/MWR-D-11-00236.1>, 2012.
- Deutscher Wetterdienst: Wetterlexikon – Intertropische Konvergenzzone, available at: <https://www.dwd.de/DE/service/lexikon/Functions/glossar.html?lv2=101224&lv3=101278>, last access: 18 December 2020.
- Dickerson, R. R., Huffman, G., Luke, W., Nunnermacker, L., Pickering, K., Leslie, A., Lindsey, C., Slinn, W., Kelly, T., Daum, P., Delany, A. C., Greenberg, J. P., Zimmerman, P. R., Boatman, J. F., Ray, J. D., and Stedman, D. H.: Thunderstorms: An important mechanism in the transport of air pollutants, *Science*, 235, 460–465, <https://doi.org/10.1126/science.235.4787.460>, 1987.
- Edtbauer, A., Stöner, C., Pfannerstill, E. Y., Berasategui, M., Walter, D., Crowley, J. N., Lelieveld, J., and Williams, J.: A new marine biogenic emission: methane sulfonamide (MSAM), dimethyl sulfide (DMS), and dimethyl sulfone (DMSO₂) measured in air over the Arabian Sea, *Atmos. Chem. Phys.*, 20, 6081–6094, <https://doi.org/10.5194/acp-20-6081-2020>, 2020.
- Frank, W. M. and Roundy, P. E.: The role of tropical waves in tropical cyclogenesis, *Mon. Weather Rev.*, 134, 2397–2417, <https://doi.org/10.1175/MWR3204.1>, 2006.
- Gondwe, M., Krol, M., Gieskes, W., Klaassen, W., and De Baar, H.: The contribution of ocean-leaving DMS to the global atmospheric burdens of DMS, MSA, SO_2 , and NSS SO_4^- , *Global Biogeochem. Cy.*, 17, 1056, <https://doi.org/10.1029/2002GB001937>, 2003.
- Gray, W. M.: Tropical cyclone genesis, *Atmos. Sci. Paper*, PhD thesis, 234, chap. 4, p. 37, 1975.
- Holzworth, R., McCarthy, M., Brundell, J., Jacobson, A., and Rodger, C.: Global distribution of superbolts, *J. Geophys. Res.-Atmos.*, 124, 9996–10005, <https://doi.org/10.1029/2019JD030975>, 2019.
- Hottmann, B., Hafermann, S., Tomsche, L., Marno, D., Martinez, M., Harder, H., Pozzer, A., Neumaier, M., Zahn, A., Bohn, B., Stratmann, G., Ziereis, H., Lelieveld, J., and Fischer, H.: Impact of the South Asian monsoon outflow on atmospheric hydroperoxides in the upper troposphere, *Atmos. Chem. Phys.*, 20, 12655–12673, <https://doi.org/10.5194/acp-20-12655-2020>, 2020.
- Huntrieser, H., Schlager, H., Lichtenstern, M., Stock, P., Hamburger, T., Höller, H., Schmidt, K., Betz, H.-D., Ulanovsky, A., and Ravegnani, F.: Mesoscale convective systems observed during AMMA and their impact on the NO_x and O_3 budget over West Africa, *Atmos. Chem. Phys.*, 11, 2503–2536, <https://doi.org/10.5194/acp-11-2503-2011>, 2011.
- Hutchins, M., Holzworth, R., Brundell, J., and Rodger, C.: Relative detection efficiency of the world wide lightning location network, *Radio Sci.*, 47, RS6005, <https://doi.org/10.1029/2012RS005049>, 2012a.
- Hutchins, M. L., Holzworth, R. H., Rodger, C. J., and Brundell, J. B.: Far-field power of lightning strokes as measured by the World Wide Lightning Location Network, *J. Atmos. Ocean. Technol.*, 29, 1102–1110, <https://doi.org/10.1175/JTECH-D-11-00174.1>, 2012b.
- Jacobson, A. R., Holzworth, R., Harlin, J., Dowden, R., and Lay, E.: Performance assessment of the world wide lightning location network (WLLN), using the Los Alamos sferic array (LASA) as ground truth, *J. Atmos. Ocean. Technol.*, 23, 1082–1092, <https://doi.org/10.1175/JTECH1902.1>, 2006.
- Knippertz, P., Evans, M. J., Field, P. R., Fink, A. H., Lioussé, C., and Marsham, J. H.: The possible role of local air pollution in climate change in West Africa, *Nat. Clim. Change*, 5, 815–822, <https://doi.org/10.1038/NCLIMATE2727>, 2015.
- Lal, D. M., Ghude, S. D., Singh, J., and Tiwari, S.: Relationship between size of cloud ice and lightning in the tropics, *Adv. Meteorol.*, 2014, 471864, <https://doi.org/10.1155/2014/471864>, 2014.
- Lange, L., Hoor, P., Helas, G., Fischer, H., Brunner, D., Scheeren, B., Williams, J., Wong, S., Wohlfrom, K.-H., Arnold, F., Ström, J., Krejci, R., Lelieveld, J., and Andreae, M. O.: Detection of

- lightning-produced NO in the midlatitude upper troposphere during STREAM 1998, *J. Geophys. Res.-Atmos.*, 106, 27777–27785, <https://doi.org/10.1029/2001JD900210>, 2001.
- Lelieveld, J. and Dentener, F. J.: What controls tropospheric ozone?, *J. Geophys. Res.-Atmos.*, 105, 3531–3551, <https://doi.org/10.1029/1999JD901011>, 2000.
- Lelieveld, J., Bourtsoukidis, E., Brühl, C., Fischer, H., Fuchs, H., Harder, H., Hofzumahaus, A., Holland, F., Marno, D., Neumaier, M., Pozzer, A., Schlager, H., Williams, J., Zahn, A., and Ziereis, H.: The South Asian monsoon–pollution pump and purifier, *Science*, 361, 270–273, <https://doi.org/10.1126/science.aar2501>, 2018.
- Levy, H.: Normal atmosphere: Large radical and formaldehyde concentrations predicted, *Science*, 173, 141–143, <https://doi.org/10.1126/science.173.3992.141>, 1971.
- Levy, H., Moxim, W., Klonecki, A., and Kasibhatla, P.: Simulated tropospheric NO_x: Its evaluation, global distribution and individual source contributions, *J. Geophys. Res.-Atmos.*, 104, 26279–26306, <https://doi.org/10.1029/1999JD900442>, 1999.
- Liu, C., Cecil, D. J., Zipser, E. J., Kronfeld, K., and Robertson, R.: Relationships between lightning flash rates and radar reflectivity vertical structures in thunderstorms over the tropics and subtropics, *J. Geophys. Res.-Atmos.*, 117, D06212, <https://doi.org/10.1029/2011JD017123>, 2012.
- Masiol, M. and Harrison, R. M.: Aircraft engine exhaust emissions and other airport-related contributions to ambient air pollution: A review, *Atmos. Environ.*, 95, 409–455, <https://doi.org/10.1016/j.atmosenv.2014.05.070>, 2014.
- Murray, L. T.: Lightning NO_x and impacts on air quality, *Curr. Pollut. Reports*, 2, 115–133, <https://doi.org/10.1007/s40726-016-0031-7>, 2016.
- NASA Worldview: NASA Worldview, available at: <https://worldview.earthdata.nasa.gov/>, last access: 7 December 2020.
- National Hurricane Center: Tropical Weather Outlook 800AM EDT Sat Sep 1 2018, available at: <https://www.nhc.noaa.gov/archive/text/TWOAT/2018/TWOAT.201809011153.txt> (last access: 21 December 2020), 2018a.
- National Hurricane Center: Tropical Weather Outlook 200PM EDT Tue Sep 4 2018, available at: <https://www.nhc.noaa.gov/archive/text/TWOAT/2018/TWOAT.201809041734.txt> (last access: 21 December 2020), 2018b.
- National Hurricane Center: Tropical Weather Outlook 200AM EDT Tue Aug 28 2018, available at: <https://www.nhc.noaa.gov/archive/text/TWOAT/2018/TWOAT.201808280536.txt> (last access: 21 December 2020), 2018c.
- National Ocean Service: What is the difference between a hurricane and a typhoon?, available at: <https://oceanservice.noaa.gov/facts/cyclone.html> (last access: 18 December 2020), 2020a.
- National Ocean Service: How do hurricanes form?, available at: <https://oceanservice.noaa.gov/facts/how-hurricanes-form.html> (last access: 18 December 2020), 2020b.
- National Weather Service: Tropical Definitions, available at: https://www.weather.gov/mob/tropical_definitions, last access: 18 December 2020.
- Naval Research Laboratory: NRL Tropical Cyclone Page, available at: https://www.nrlmry.navy.mil/tc-bin/tc_home2.cgi, last access: 21 December 2020.
- Newell, R., Hu, W., Wu, Z.-X., Zhu, Y., Akimoto, H., Anderson, B., Browell, E., Gregory, G., Sachse, G., Shipham, M., Bachmeier, A. S., Bandy, A. R., Thornton, D. C., Blake, D. R., Rowland, F. S., Bradshaw, J. D., Crawford, J. H., Davis, D. D., Sandholm, S. T., Brockett, W., DeGreef, L., Lewis, D., McCormick, D., Monitz, E., Collins Jr., J. E., Heikes, B. G., Merrill, J. T., Kelly, K. K., Liu, S. C., Kondo, Y., Koike, M., Liu, C.-M., Sakamaki, F., Singh, H. B., Dibb, J. E., and Talbot, R. W.: Atmospheric sampling of Supertyphoon Mireille with NASA DC-8 aircraft on September 27, 1991, during PEM-West A, *J. Geophys. Res.-Atmos.*, 101, 1853–1871, <https://doi.org/10.1029/95JD01374>, 1996.
- Nussbaumer, C. M. and Cohen, R. C.: The Role of Temperature and NO_x in Ozone Trends in the Los Angeles Basin, *Environ. Sci. Technol.*, 54, 15652–15659, <https://doi.org/10.1021/acs.est.0c04910>, 2020.
- Pacifico, F., Delon, C., Jambert, C., Durand, P., Morris, E., Evans, M. J., Lohou, F., Derrien, S., Donnou, V. H. E., Houeto, A. V., Reñares Martínez, I., and Brilouet, P.-E.: Measurements of nitric oxide and ammonia soil fluxes from a wet savanna ecosystem site in West Africa during the DACCWA field campaign, *Atmos. Chem. Phys.*, 19, 2299–2325, <https://doi.org/10.5194/acp-19-2299-2019>, 2019.
- Paul, S., Ghebreyesus, D., and Sharif, H. O.: Brief communication: Analysis of the fatalities and socio-economic impacts caused by Hurricane Florence, *Geosciences*, 9, 58, <https://doi.org/10.3390/geosciences9020058>, 2019.
- Pisso, I., Sollum, E., Grythe, H., Kristiansen, N. I., Casiani, M., Eckhardt, S., Arnold, D., Morton, D., Thompson, R. L., Groot Zwaftink, C. D., Evangeliou, N., Sodemann, H., Haimberger, L., Henne, S., Brunner, D., Burkhardt, J. F., Fouilloux, A., Brioude, J., Philipp, A., Seibert, P., and Stohl, A.: The Lagrangian particle dispersion model FLEX-PART version 10.4, *Geosci. Model Dev.*, 12, 4955–4997, <https://doi.org/10.5194/gmd-12-4955-2019>, 2019.
- Pollack, I., Homeyer, C., Ryerson, T., Aikin, K., Peischl, J., Apel, E., Campos, T., Flocke, F., Hornbrook, R., Knapp, D., Montzka, D., Weinheimer, A., Riemer, Diskin, D., Sachse, G., Mikoviny, T., Wisthaler, A., Bruning, E., MacGorman, D., Cummings, K., Pickering, K., Huntrieser, H., Lichtenstern, M., Schlager, H., and Barth, M.: Airborne quantification of upper tropospheric NO_x production from lightning in deep convective storms over the United States Great Plains, *J. Geophys. Res.-Atmos.*, 121, 2002–2028, <https://doi.org/10.1002/2015JD023941>, 2016.
- Price, C. and Rind, D.: What determines the cloud-to-ground lightning fraction in thunderstorms?, *Geophys. Res. Lett.*, 20, 463–466, <https://doi.org/10.1029/93GL00226>, 1993.
- Ridley, B., Ott, L., Pickering, K., Emmons, L., Montzka, D., Weinheimer, A., Knapp, D., Grahek, F., Li, L., Heymsfield, G., McGill, M., Kucera, P., Mahoney, M. J., Baumgardner, D., Schultz, M., and Brasseur, G.: Florida thunderstorms: A faucet of reactive nitrogen to the upper troposphere, *J. Geophys. Res.-Atmos.*, 109, D17305, <https://doi.org/10.1029/2004JD004769>, 2004.
- Roux, F., Clark, H., Wang, K.-Y., Rohs, S., Sauvage, B., and Nédélec, P.: The influence of typhoons on atmospheric composition deduced from IAGOS measurements over Taipei, *Atmos. Chem. Phys.*, 20, 3945–3963, <https://doi.org/10.5194/acp-20-3945-2020>, 2020.
- Schiller, C., Bozem, H., Gurk, C., Parchatka, U., Königstedt, R., Harris, G., Lelieveld, J., and Fischer, H.: Applications of

- quantum cascade lasers for sensitive trace gas measurements of CO, CH₄, N₂O and HCHO, *Appl. Phys. B*, 92, 419–430, <https://doi.org/10.1007/s00340-008-3125-0>, 2008.
- Schumann, U. and Huntrieser, H.: The global lightning-induced nitrogen oxides source, *Atmos. Chem. Phys.*, 7, 3823–3907, <https://doi.org/10.5194/acp-7-3823-2007>, 2007.
- Shapiro, L. J. and Goldenberg, S. B.: Atlantic sea surface temperatures and tropical cyclone formation, *J. Clim.*, 11, 578–590, [https://doi.org/10.1175/1520-0442\(1998\)011<0578:ASSTAT>2.0.CO;2](https://doi.org/10.1175/1520-0442(1998)011<0578:ASSTAT>2.0.CO;2), 1998.
- Simó, R. and Dachs, J.: Global ocean emission of dimethylsulfide predicted from biogeophysical data, *Global Biogeochem. Cy.*, 16, 26–1, <https://doi.org/10.1029/2001GB001829>, 2002.
- Smith, R. K., Montgomery, M. T., and Zhu, H.: Buoyancy in tropical cyclones and other rapidly rotating atmospheric vortices, *Dynam. Atmos. Ocean.*, 40, 189–208, <https://doi.org/10.1016/j.dynatmoce.2005.03.003>, 2005.
- Stewart, S. and Berg, R.: National Hurricane Center Tropical Cyclone Report Hurricane Florence, available at: https://www.nhc.noaa.gov/data/tcr/AL062018_Florence.pdf (last access: 18 December 2020), 2019.
- Stohl, A., Forster, C., Frank, A., Seibert, P., and Wotawa, G.: Technical note: The Lagrangian particle dispersion model FLEXPART version 6.2, *Atmos. Chem. Phys.*, 5, 2461–2474, <https://doi.org/10.5194/acp-5-2461-2005>, 2005.
- Stubbins, A., Uher, G., Law, C. S., Mopper, K., Robinson, C., and Upstill-Goddard, R. C.: Open-ocean carbon monoxide photoproduction, *Deep-Sea Res. Pt. II*, 53, 1695–1705, <https://doi.org/10.1016/j.dsr2.2006.05.011>, 2006.
- Tadic, I., Crowley, J. N., Dienhart, D., Eger, P., Harder, H., Hottmann, B., Martinez, M., Parchatka, U., Paris, J.-D., Pozzer, A., Rohloff, R., Schuladen, J., Shenolikar, J., Tauer, S., Lelieveld, J., and Fischer, H.: Net ozone production and its relationship to nitrogen oxides and volatile organic compounds in the marine boundary layer around the Arabian Peninsula, *Atmos. Chem. Phys.*, 20, 6769–6787, <https://doi.org/10.5194/acp-20-6769-2020>, 2020.
- Tadic, I., Nussbaumer, C., Bohn, B., Harder, H., Marno, D., Martinez, M., Obersteiner, F., Parchatka, U., Pozzer, A., Rohloff, R., Lelieveld, J., and Fischer, H.: The role of nitric oxide in net ozone production in the upper tropical troposphere above the Atlantic Ocean and West Africa, *Atmospheric Chemistry and Physics Discussions* [preprint], <https://doi.org/10.5194/acp-2021-52>, in review, 2021.
- Tegtmeier, S., Krüger, K., Quack, B., Atlas, E., Blake, D., Boenisch, H., Engel, A., Hepach, H., Hossaini, R., Navarro, M., Raimund, S., Sala, S., Shi, Q., and Ziska, F.: The contribution of oceanic methyl iodide to stratospheric iodine, *Atmos. Chem. Phys.*, 13, 11869–11886, <https://doi.org/10.5194/acp-13-11869-2013>, 2013.
- University of Washington: WWLLN World Wide Lightning Location Network, available at: <http://wwlln.net/>, last access: 18 December 2020.
- Virts, K. S., Wallace, J. M., Hutchins, M. L., and Holzworth, R. H.: Highlights of a new ground-based, hourly global lightning climatology, *Bull. Am. Meteorol. Soc.*, 94, 1381–1391, <https://doi.org/10.1175/BAMS-D-12-00082.1>, 2013.
- Waliser, D. E. and Gautier, C.: A satellite-derived climatology of the ITCZ, *J. Clim.*, 6, 2162–2174, [https://doi.org/10.1175/1520-0442\(1993\)006<2162:ASDCOT>2.0.CO;2](https://doi.org/10.1175/1520-0442(1993)006<2162:ASDCOT>2.0.CO;2), 1993.
- Wang, C.-C. and Magnusdottir, G.: The ITCZ in the central and eastern Pacific on synoptic time scales, *Mon. Weather Rev.*, 134, 1405–1421, <https://doi.org/10.1175/MWR3130.1>, 2006.
- Wang, N., Edtbauer, A., Stöner, C., Pozzer, A., Bourtsoukidis, E., Ernle, L., Dienhart, D., Hottmann, B., Fischer, H., Schuladen, J., Crowley, J. N., Paris, J.-D., Lelieveld, J., and Williams, J.: Measurements of carbonyl compounds around the Arabian Peninsula: overview and model comparison, *Atmos. Chem. Phys.*, 20, 10807–10829, <https://doi.org/10.5194/acp-20-10807-2020>, 2020.
- Weller, R. and Schrems, O.: H₂O₂ in the marine troposphere and seawater of the Atlantic Ocean (48° N–63° S), *Geophys. Res. Lett.*, 20, 125–128, <https://doi.org/10.1029/93GL00065>, 1993.
- Williams, E. and Satori, G.: Lightning, thermodynamic and hydrological comparison of the two tropical continental chimneys, *J. Atmos. Sol.-Terr. Phys.*, 66, 1213–1231, <https://doi.org/10.1016/j.jastp.2004.05.015>, 2004.
- Williams, J., Gros, V., Atlas, E., Maciejczyk, K., Batsaikhan, A., Schöler, H., Forster, C., Quack, B., Yassaa, N., Sander, R., and Van Dingenen, R.: Possible evidence for a connection between methyl iodide emissions and Saharan dust, *J. Geophys. Res.-Atmos.*, 112, D07302, <https://doi.org/10.1029/2005JD006702>, 2007.
- Wu, L. and Takahashi, M.: Contributions of tropical waves to tropical cyclone genesis over the western North Pacific, *Clim. Dynam.*, 50, 4635–4649, <https://doi.org/10.1007/s00382-017-3895-3>, 2018.
- Xu, W. and Zipser, E. J.: Properties of deep convection in tropical continental, monsoon, and oceanic rainfall regimes, *Geophys. Res. Lett.*, 39, L07802, <https://doi.org/10.1029/2012GL051242>, 2012.
- Xu, W., Zipser, E. J., Liu, C., and Jiang, H.: On the relationships between lightning frequency and thundercloud parameters of regional precipitation systems, *J. Geophys. Res.-Atmos.*, 115, D12203, <https://doi.org/10.1029/2009JD013385>, 2010.
- Zahn, A., Weppner, J., Widmann, H., Schlote-Holubek, K., Burger, B., Kühner, T., and Franke, H.: A fast and precise chemiluminescence ozone detector for eddy flux and airborne application, *Atmos. Meas. Tech.*, 5, 363–375, <https://doi.org/10.5194/amt-5-363-2012>, 2012.
- Zhang, W., Zhang, Y., Zheng, D., Wang, F., and Xu, L.: Relationship between lightning activity and tropical cyclone intensity over the northwest Pacific, *J. Geophys. Res.-Atmos.*, 120, 4072–4089, <https://doi.org/10.1002/2014JD022334>, 2015.
- Zipser, E. J.: Deep cumulonimbus cloud systems in the tropics with and without lightning, *Mon. Weather Rev.*, 122, 1837–1851, [https://doi.org/10.1175/1520-0493\(1994\)122<1837:DCCSIT>2.0.CO;2](https://doi.org/10.1175/1520-0493(1994)122<1837:DCCSIT>2.0.CO;2), 1994.

3.3 Optimization of airborne NO₂ measurements

This chapter has been published in the journal *Atmospheric Measurement Techniques* as a research article. I am the first author of this paper. I have performed all laboratory measurements. I have developed the new photolytic converter by the help of UP and HF. I have analyzed all data presented, I have made the figures and I have prepared and revised the manuscript. The co-authors were involved in the presented research campaign CAFE Africa and in proofreading the manuscript. Detailed author contributions can be found at the end of the paper in the section *Author contributions*.

How to cite: Nussbaumer, C. M., Parchatka, U., Tadic, I., Bohn, B., Marno, D., Martinez, M., Rohloff, R., Harder, H., Kluge, F., Pfeilsticker, K., Obersteiner, F., Zöger, M., Doerich, R., Crowley, J. N., Lelieveld, J., and Fischer, H.: Modification of a conventional photolytic converter for improving aircraft measurements of NO₂ via chemiluminescence, *Atmos. Meas. Tech.*, 14, 6759–6776, <https://doi.org/10.5194/amt-14-6759-2021>, **2021**.

submitted: 22 Jun 2021

published: 20 Oct 2021

The supplementary material for this publication can be found in Section 4.2.

Atmos. Meas. Tech., 14, 6759–6776, 2021
<https://doi.org/10.5194/amt-14-6759-2021>
 © Author(s) 2021. This work is distributed under
 the Creative Commons Attribution 4.0 License.



Modification of a conventional photolytic converter for improving aircraft measurements of NO₂ via chemiluminescence

Clara M. Nussbaumer¹, Uwe Parchatka¹, Ivan Tadic¹, Birger Bohn², Daniel Marno¹, Monica Martinez¹, Roland Rohloff¹, Hartwig Harder¹, Flora Kluge³, Klaus Pfeilsticker³, Florian Obersteiner⁴, Martin Zöger⁵, Raphael Doerich¹, John N. Crowley¹, Jos Lelieveld^{1,6}, and Horst Fischer¹

¹Max Planck Institute for Chemistry, Department of Atmospheric Chemistry, 55128 Mainz, Germany

²Institute of Energy and Climate Research, IEK-8: Troposphere, Forschungszentrum Jülich GmbH, 52428 Jülich, Germany

³Institute of Environmental Physics, Heidelberg University, 69120 Heidelberg, Germany

⁴Karlsruhe Institute of Technology, 76021 Karlsruhe, Germany

⁵Flight Experiments, German Aerospace Center (DLR), 82234 Oberpfaffenhofen, Germany

⁶Climate and Atmosphere Research Center, The Cyprus Institute, Nicosia, Cyprus

Correspondence: Clara M. Nussbaumer (clara.nussbaumer@mpic.de)

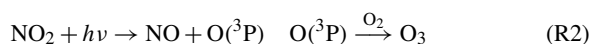
Received: 22 June 2021 – Discussion started: 14 July 2021

Revised: 9 September 2021 – Accepted: 22 September 2021 – Published: 20 October 2021

Abstract. Nitrogen oxides (NO_x ≡ NO + NO₂) are centrally involved in the photochemical processes taking place in the Earth's atmosphere. Measurements of NO₂, particularly in remote areas where concentrations are of the order of parts per trillion by volume (pptv), are still a challenge and subject to extensive research. In this study, we present NO₂ measurements via photolysis–chemiluminescence during the research aircraft campaign CAFE Africa (Chemistry of the Atmosphere – Field Experiment in Africa) 2018 around Cabo Verde and the results of laboratory experiments to characterize the photolytic converter used. We find the NO₂ reservoir species MPN (methyl peroxy nitrate) to produce the only relevant thermal interference in the converter under the operating conditions during CAFE Africa. We identify a memory effect within the conventional photolytic converter (type 1) associated with high NO concentrations and rapidly changing water vapor concentrations, accompanying changes in altitude during aircraft measurements, which is due to the porous structure of the converter material. As a result, NO₂ artifacts, which are amplified by low conversion efficiencies, and a varying instrumental background adversely affect the NO₂ measurements. We test and characterize an alternative photolytic converter (type 2) made from quartz glass, which improves the reliability of NO₂ measurements in laboratory and field studies.

1 Introduction

Nitrogen oxides (NO_x) represent the sum of NO (nitric oxide) and NO₂ (nitrogen dioxide), which can rapidly interconvert in the atmosphere in the presence of sunlight and O₃ (ozone) as shown in Reactions (R1) and (R2) (Jacob, 1999).



Considering only these two reactions in atmospheric NO_x chemistry, the so-called Leighton ratio represents NO₂, NO and O₃ in the photostationary state (PSS) as shown in Eq. (1) (Leighton, 1961). $k_{\text{NO}+\text{O}_3}$ is the rate coefficient of Reaction (R1), and j_{NO_2} is the photolysis frequency for NO₂ in Reaction (R2).

$$\frac{k_{\text{NO}+\text{O}_3} \times [\text{NO}] \times [\text{O}_3]}{j_{\text{NO}_2} \times [\text{NO}_2]} = \phi \approx 1 \quad (1)$$

Several studies have shown that the Leighton ratio as presented in Eq. (1) is only valid for highly polluted environments, whereas in other regions, besides O₃, oxidized halogen species and peroxy radicals (HO₂ and RO₂) significantly contribute to the oxidation of NO to NO₂ and require an extension of the Leighton expression for a reliable calculation of PSS NO₂ concentrations, as presented in Sect. 2.4.

(Mannschreck et al., 2004; Griffin et al., 2007; Ma et al., 2017; Reed et al., 2016).

NO_x can be emitted from either natural or anthropogenic sources, with the latter dominating globally. Natural emissions include, for example, biogenic soil emissions, biomass burning and lightning. Anthropogenic emissions are mainly from combustion processes in vehicles or from power and industrial plants, which contribute almost two-thirds to the global burden (Pusede et al., 2015; Ganzeveld et al., 2002; Logan, 1983). Nitrogen oxides are, together with volatile organic compounds, important precursors to tropospheric ozone, which can be a hazard to plant, animal and human health, causing multiple diseases regarding the cardiovascular and respiratory system (Nussbaumer and Cohen, 2020; Nuvolone et al., 2018; Lippmann, 1989). NO_x additionally promotes the formation of acid rain (through conversion to HNO_3) – hazardous to many ecosystems – and is a threat to human health itself (Boningari and Smirniotis, 2016; Greaver et al., 2012). Beyond that, NO_x controls the abundance of OH radicals, which regulate the oxidizing capacity of the atmosphere (Levy, 1971; Lelieveld and Dentener, 2000). Due to the health implications and the impact on atmospheric photochemical processes, it is highly relevant to measure and monitor ambient NO_x concentrations with sophisticated instruments that provide reliable concentration measurements, especially in remote areas where NO and NO_2 are low. More specifically, this requires a low instrumental background, which, particularly for NO_2 , is often impacted by unwanted chemical processes that can lead to artifact signals (Reed et al., 2016; Andersen et al., 2021; Jordan et al., 2020).

Many different measurement techniques have been deployed to measure nitrogen oxides such as cavity-enhanced absorption spectroscopy (and variants – e.g., cavity-attenuated phase-shift spectroscopy, Ge et al., 2013; Kebabian et al., 2005; cavity ring-down spectroscopy, O’Keefe and Deacon, 1988; other techniques, Zheng et al., 2018), differential optical absorption spectroscopy (Hüneke et al., 2017; Winer and Biermann, 1994) and laser-induced fluorescence (Thornton et al., 2000; Javed et al., 2019) for NO_2 or absorption spectroscopy for NO (Ventrillard et al., 2017). However, detection of NO and NO_2 via chemiluminescence (CLD) is likely the most common technique for the measurement of nitrogen oxides in the atmosphere and is distinguished by the simultaneous in situ measurement of both NO and NO_2 , low detection limits, and deployability in research aircraft at high altitudes for measurements in the upper troposphere (Pollack et al., 2010; Reed et al., 2016; Tadic et al., 2020). The measurement principle is based on the reaction of nitric oxide and ozone, which yields electronically excited NO_2 (NO_2^*) that (along with physical quenching) returns to the electronic ground state by fluorescence whereby a photon of a wavelength $> 600\text{ nm}$ is emitted, which can be detected by a photomultiplier tube. The resulting signal is proportional to the initial NO concentration (Clough and Thrush, 1967). For nitrogen dioxide detection, NO_2 is first converted

to NO. The standard method for this conversion is the use of a catalytic converter, in which NO_2 passes through a heated molybdenum converter where it is reduced by Mo to NO ($\text{Mo} + 3\text{NO}_2 \rightarrow \text{MoO}_3 + \text{NO}$). However, high temperatures ($300\text{--}350^\circ\text{C}$) in the converter along with catalytic surface effects lead to interferences with other atmospheric compounds that can be converted to NO_2 , such as HONO (nitrous acid), HNO_3 (nitric acid) or PAN (peroxyacetyl nitrate), and bias the measurement (Demerjian, 2000; Villena et al., 2012; Jung et al., 2017). An alternative and widespread method is the use of a photolytic converter (photolysis–chemiluminescence: P-CL), also referred to as blue light converter, which utilizes LEDs emitting at a wavelength of around 395 nm to dissociate NO_2 to NO (Pollack et al., 2010; Reed et al., 2016; Tadic et al., 2020; Ryerson et al., 2000). Interferences (as described above) in the blue light converter are still possible but to a significantly lesser extent. Reed et al. (2016) investigated potential interferences in a photolytic converter related to the presence of PAN, methyl peroxy nitrate (MPN, $\text{CH}_3\text{O}_2\text{NO}_2$) or pernitric acid (PNA, HO_2NO_2). These compounds are NO_2 reservoir species, and their decomposition (to NO_2) is dependent on the temperature, pressure and residence time in the blue light converter (Nault et al., 2015; Fischer et al., 2014). Please note that none of these compounds are photolyzed in the blue light converter and are only subject to thermal decomposition (Reed et al., 2016; Tadic et al., 2020). Generally, increasing temperature and increasing residence time promote the decay of thermally unstable trace gases and the release of NO_2 , which is further described in Sect. 2.5 (Reed et al., 2016). With increasing residence time in the converter and high atmospheric HONO / NO_2 ratios, photolysis of HONO could become relevant, as recently shown by Gingerysty et al. (2021).

The CLD detects a signal (which we call the NO_c signal) composed of the ambient NO concentration and the ambient NO_2 concentration multiplied by the conversion efficiency C_e according to Eq. (2).

$$[\text{NO}_c] = [\text{NO}] + C_e \times [\text{NO}_2] \quad (2)$$

The conversion efficiency describes the fraction of NO_2 that is converted to NO in the converter and can be thought of as the NO yield from NO_2 . Its value is dependent on the optical output of the LEDs as well as the NO_2 residence time and the pressure in the converter. C_e is therefore in competition with unwanted formation of NO_2 from NO_2 reservoir species. For example, a longer residence time increases the conversion efficiency but could potentially increase the quantity of NO_2 reservoir species that decay in the converter, which takes place according to first-order kinetics, as described in more detail in Sect. 2.5. The NO_2 concentration is calculated from the difference in the signal with and without use of the photolytic converter: $[\text{NO}_2] = ([\text{NO}_c] - [\text{NO}]) / C_e$ (Sadanaga et al., 2010; Tadic et al., 2020; Ryerson et al., 2000).

While NO measurements are generally reliable and well-understood, NO₂ measurement techniques utilizing the conversion of NO₂ to NO are subject to extensive research. Hosaynali Beygi et al. (2011) found a strong deviation from the Leighton ratio at low NO_x concentrations between 5 and 25 pptv despite the inclusion of HO₂, RO₂ and halogen oxides, suggesting the occurrence of a so far unknown atmospheric oxidant. Frey et al. (2015) also reported higher measured NO₂/NO ratios than expected from PSS based on measurements in Antarctica and hypothesized the presence of an additional oxidant or a measurement bias. This is in line with findings and suggestions by Silvern et al. (2018) based on observations during the aircraft campaign SEAC⁴RS over the United States of America. Reed et al. (2016) examined the described deviation through the laboratory investigation of potential NO₂ interferences of thermally unstable trace gases such as peroxyacyl nitrate (PAN) within the photolytic converter in comparison to laser-induced fluorescent NO₂ measurement and found that this could contribute to the higher-than-expected NO₂ concentrations measured by P-CL instruments. Jordan et al. (2020) investigated interferences in a photolytic converter made from quartz glass and showed how the converter conditions affect the conversion efficiency and the artifact signal (caused by NO₂ reservoir species). The correct adjustment of the conditions, preferably including low pressure, high flow rates and small temperature variations, can minimize interferences, which was also concluded by Reed et al. (2016). Andersen et al. (2021) reported the measurement of a significant NO₂ measurement bias during ground-based observations in the remote marine tropical troposphere with a conventional blue light converter, which was related to its porous walls. They were able to eliminate this effect by implementation of a photolytic converter made from quartz glass, which reduced the overall measurement uncertainty by around 50 %. The use of quartz glass in a blue light converter was also reported by Pollack et al. (2010), who compared the commercially available converter BLC-A manufactured by Droplet Measurement Technologies to other photolytic converters.

An additional challenge is the significant decrease in the NO₂/NO ratio with altitude. At the surface during daytime, NO₂ concentrations are approximately 2 to 4 times higher than NO concentrations. The NO₂/NO ratio decreases by around 1 order of magnitude when going from the lower to the upper troposphere, which increases the uncertainty when deriving NO₂ mixing ratios using Eq. (2) (Travis et al., 2016; Silvern et al., 2018; Logan et al., 1981). At the same time, the concentration of NO₂ reservoir species such as PNA or MPN is significantly higher in the upper troposphere compared to that at the surface, and consequently interferences are more likely to occur at high altitudes (Nault et al., 2015; Kim et al., 2007). These aspects result in particularly strict requirements regarding airborne NO₂ measurements.

In this study, we describe a modified blue light converter (BLC) (type 1) originally purchased from Droplet Measure-

ment Technologies, which we have deployed in NO₂ measurements via photolysis–chemiluminescence during the research aircraft campaign CAFE Africa (Chemistry of the Atmosphere: Field Experiment in Africa) and also in laboratory investigations. We show how high NO concentrations and rapidly changing water vapor concentrations affect the instrumental background and induce a memory effect that cannot be corrected retrospectively. This is particularly relevant to aircraft measurements during which water vapor concentrations are subject to rapid changes due to variations in flight altitude, but also to all other application areas. The photolytic converter and similar designs are widely used for field measurements of NO₂ all across the world (e.g., Andersen et al., 2021; Jung et al., 2017; Xu et al., 2013; Breuninger et al., 2013; Fuchs et al., 2010; Reidmiller et al., 2010; Crowley et al., 2010; Sather et al., 2006) and can provide reliable results for stationary use and locations with only little variation in ambient NO and low humidity levels, but they suffer from enhanced uncertainty in other applications. We propose the elimination of any direct contact points between the sample gas and the porous inner converter surface and have developed an alternative photolytic converter entirely made from quartz glass (type 2). Highly reflective properties are achieved by an outer mantle made from optical PTFE (polytetrafluoroethylene, also known as Teflon). The type 2 quartz converter shows promising results in the laboratory regarding its application in field studies for more reliable NO₂ measurements. We do not claim to be the first to present an alternative quartz glass converter for P-CL measurement of NO₂. However, we are the first to point out the technical difficulties of the application of conventional NO₂ converters in airborne studies and believe the presented results to be a guidepost for future NO₂ aircraft measurements via photolysis–chemiluminescence.

2 Observations and methods

2.1 Instrument

All NO_x measurements were performed using a modified two-channel chemiluminescence instrument originally purchased from ECO Physics (Dürnten, Switzerland; CLD 790 SR), as described by Tadic et al. (2020) (Fig. 2 presents the instrument schematic), operated at a total gas flow of 3 SLM, equally divided into the two channels. NO concentrations are measured in the first channel, also referred to as the NO channel, through formation of NO₂^{*} via reaction with O₃. The resulting excited NO₂^{*} emits a photon (> 600 nm) detected by a photomultiplier tube and preamplifier setup, and it is recorded as counts per second. The second channel, also referred to as the NO_c channel, is structurally identical except for the implementation of a photolytic converter, which converts a known fraction of NO₂ to NO prior to the reaction with O₃ and is operated at a constant pressure

of 110 hPa (105 hPa during the CAFE Africa field experiment). NO_2 concentrations are obtained from the difference in counts from each channel and the conversion efficiency C_e as described above (see Eq. 2). We use a blue light converter (type 1) purchased from Droplet Measurement Technologies in 2005 (later Air Quality Design, now Teledyne API) equipped with UV LEDs emitting at a wavelength of 397 nm (FWHM = 14 nm, as characterized in the laboratory), which is shown in Fig. 1a. The converter was designed for airborne applications. The inner material is made of porous, optically active PTFE (polytetrafluoroethylene) for providing highly reflective properties. To reduce surface effects the converter was equipped with a quartz cylinder covering approximately half of the PTFE surface (the gas still has contact with the PTFE surface in the ring channel and through the head piece). Please note that this modification was made prior to the CAFE Africa research campaign within a limited time frame and did not have the desired outcome. The sample gas enters the converter sideways into the ring channel and reaches the inner tube via the PTFE head piece, which has four circular recesses, one for each UV LED. The sample gas outlet proceeds analogously. The inner volume of the converter is $V = 78 \text{ cm}^3$, which gives a residence time of $t = (V \times 60 \text{ s min}^{-1}) / F \times p / p_{\text{standard}} = (78 \text{ cm}^3 \times 60 \text{ s min}^{-1}) / (1500 \text{ cm}^3 \text{ min}^{-1}) \times 110 \text{ hPa} / 1013 \text{ hPa} = 0.34 \text{ s}$. The conversion efficiency for this type 1 photolytic converter operated under the conditions described above is approximately 20 % ($j = 0.66 \text{ s}^{-1}$), which was determined via gas-phase titration (GPT) of NO with ozone. The results obtained with the described type 1 converter were compared to an alternative photolytic converter completely made from quartz glass (type 2), which is shown in Fig. 1b. For maintaining the reflective properties of the type 1 blue light converter, the type 2 quartz converter was jacketed with optical PTFE, which provides diffuse reflectance of > 99 % in the wavelength range 350–1500 nm (SphereOptics GmbH, 2017). The PTFE material was found to provide a higher conversion efficiency in the converter compared to aluminum foil and additionally provides a stable housing for the sensitive quartz tube. The volume of the type 2 converter is 77 cm^3 , which gives a residence time of $t = 0.33 \text{ s}$ and a conversion efficiency of approximately 14 % ($j = 0.46 \text{ s}^{-1}$) under the operating conditions. The applied LEDs were purchased from LED ENGIn (San Jose, California, USA) (high-efficiency VIOLET LED emitter LZ1-10UB00-01U6, 2–2.2 W, 395–400 nm peak wavelength). Please note that the low conversion efficiencies in both converters result from the operation at low pressures, which we have implemented to pursue aircraft measurements during which altitude changes are accompanied by pressure variations. Operating the converter at lower than minimum ambient pressure levels (max. $\sim 15 \text{ km}$ flight altitude) has the benefit of a constant conversion efficiency. The fractional dissociation of thermally unstable NO_x reservoir species increases with increasing pressure in the converter, which can be seen in Fig. S1a in the Sup-

plement. On the other hand, a higher conversion efficiency would be desirable for improved accuracy of the measurement. The main difference between the two converters is that the sample gas flow does not have direct contact with the porous surface of the material for the type 2 quartz converter. Additionally, the sample gas flow in the type 2 quartz converter does not have contact with the LEDs, which likely minimizes the sample gas heating and consequently the thermal interferences when passing through the converter. The reaction chambers (where the reaction of NO and O_3 takes place) are operated at a constant temperature of 25°C and a pressure of 9–10 mbar in order to minimize quenching of NO_2^* by other molecules. The dry ozone flow is humidified with water vapor for maintaining a constant humidity level at all times.

Besides the photons emitted from relaxation of NO_2^* , the PMT (photomultiplier tube) signal also includes detected photons from interference reactions, for example the reaction of O_3 with alkenes (Alam et al., 2020), as well as a dark current signal. Therefore, a pre-chamber measurement is operated for 20 s every 5 min with ozone added to the sample gas flow. The residence time in the pre-chamber allows for the reaction of O_3 and NO as well as the relaxation of NO_2^* before entering the main reaction chamber (pre-chamber efficiency > 96 % for the NO channel and $\sim 100\%$ for the NO_c channel). It is not long enough to convert interfering compounds, which then occurs in the following main chamber. Consequently, during pre-chamber measurements, the PMT signal only includes the interfering signal and the dark current signal (Ridley and Howlett, 1974; ECO PHYSICS AG, 2002). We subtracted the interpolated signal obtained during pre-chamber measurements from the signal detected during main chamber measurements in order to obtain the signal generated from NO. The material of both the pre-chamber and the main chamber is gold-plated stainless steel.

The instrumental background of each channel is determined via zero (synthetic) air measurements from a gas cylinder and can be converted to mixing ratios using calibration measurements with a known NO concentration, which define the sensitivity ($\text{counts s}^{-1} \text{ ppbv}^{-1}$ – parts per billion by volume) of each channel to NO, as shown in Eq. (3) (after pre-chamber corrections). The signal detected from zero air measurement ($\text{counts}(\text{zero air})$) is subtracted from the signal detected from NO calibration ($\text{counts}(\text{NO calibration})$) and divided by the absolute concentration of the NO calibration ($c(\text{NO calibration})$) to calculate the sensitivity. Dividing the signal detected from zero air measurements by this value gives the instrumental background concentration in mixing ratios, e.g., ppbv. The precision is determined from the reproducibility of the NO calibrations and is 3 % (1σ). The NO concentration is $4.96 \pm 0.21 \text{ ppmv}$, which gives a 4 % uncertainty on the secondary standard used. The resulting NO calibration mixing ratio is $15.8 \pm 0.7 \text{ ppbv}$. The detection limit is given by the reproducibility of the zero air measurements, which is around 5 pptv for the NO channel and the NO_c chan-

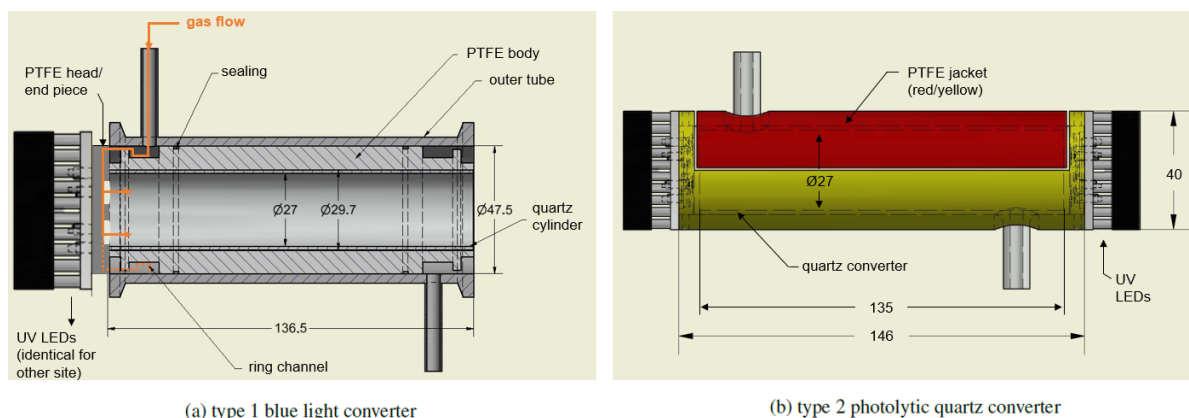


Figure 1. Sketches of the photolytic converters applied in this study.

nel using the type 2 quartz converter. The detection limit is higher when using the type 1 converter, but it is difficult to determine due to the observed memory effects and is estimated at > 10 pptv.

$$\text{sensitivity} = \frac{\text{counts(NO calibration)} - \text{counts(zero air)}}{c(\text{NO calibration})}$$

$$c(\text{background}) = \frac{\text{counts(zero air)}}{\text{sensitivity}} \quad (3)$$

Please note that the utilized zero air can include a trace concentration of NO_x . The manufacturer specifies the maximum concentration of NO_x to be 0.1 ppmv (parts per million by volume) (Westfalen Gas Schweiz GmbH, 2021).

2.2 CAFE Africa field experiment

The CAFE Africa research campaign took place in August and September 2018 and included 14 measurement flights (MF03–MF16), which were performed with the HALO (High Altitude Long Range) research aircraft starting from the campaign base in Sal on Cabo Verde (16.75°N , 22.95°W). We included data measured during the measurement flights MF10, MF12, MF13, MF14 and MF15 in this analysis (MF11 was a nighttime flight and therefore excluded) for which CLD NO_2 measurements were available. An overview of the flight tracks is presented in Fig. 2. A bypass line provided the instruments with air from the aircraft inlet for which the residence time depended on the ambient pressure level (for high altitudes < 0.1 s). The sample line temperature was approximately 25°C . More details on the campaign can be found in Tadic et al. (2021).

NO and NO_2 were measured via photolysis–chemiluminescence with the instrument described in Sect. 2.1 using the type 1 conventional blue light converter equipped with the quartz glass cylinder, operated at a temperature of 313 K and a pressure of 105 hPa (0.32 s residence time). Please note that it was not possible to measure the

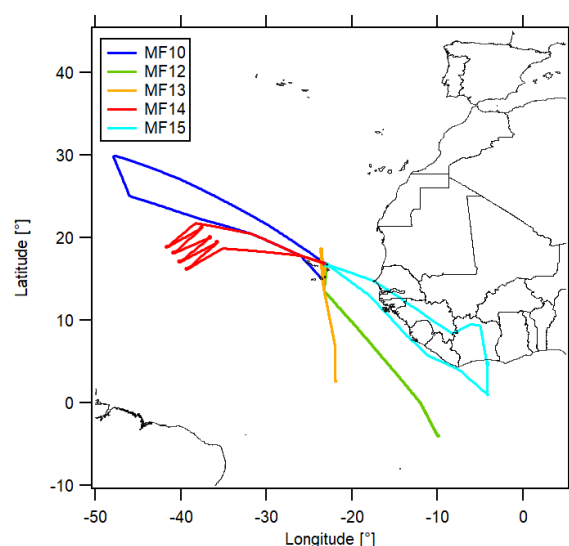


Figure 2. Geographic overview of the measurement flight tracks included in this analysis.

temperature inside the converter. Instead, the temperature of the gas outflow from the converter in the ring channel was measured, which we equate to the inner temperature. Zero air measurements and NO calibrations using a secondary NO standard (cylinder concentration of 1.187 ± 0.036 ppmv and calibration mixing ratio of 2.97 ± 0.09 ppbv) were performed regularly to determine the variability in the instrumental background and the sensitivity of the channels. The ambient measurement was interrupted every 1–2 h by a 1 min zero air measurement, followed by 1 min NO calibration and another 1 min zero air measurement. These calibration background cycles (CB cycles) were performed four to six times during each measurement flight. We linearly interpolated these

instrumental background and calibration measurements to each entire flight. The NO data were processed as described by Tadic et al. (2021) (5 pptv detection limit at 1 min integration time and 6 % relative uncertainty, 1σ). Please note that the instrumental background for the NO data was determined at 5.0 ± 5.3 pptv during a nighttime measurement on 26 August 2018 of NO as presented by Tadic et al. (2021) and previously described by Lee et al. (2009). The instrumental background determined via zero air measurement was similar with 4 ± 7 pptv (Tadic, 2021) (measured four to six times per MF). For the NO₂ data, the NO_c channel sensitivity and the instrumental background concentration were calculated after pre-chamber correction according to Eq. (3). The ambient NO_c signal was divided by the channel sensitivity accordingly. Final NO₂ concentrations were determined via Eq. (4); this includes subtraction of the calculated (and interpolated) NO_c instrumental background concentration and the NO concentration in the NO channel and dividing by the conversion efficiency of the blue light converter, which was 24.2 ± 2.8 % during the campaign.

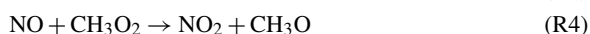
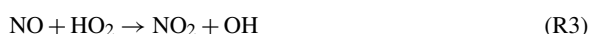
$$c(\text{NO}_2) = \frac{c(\text{NO}_c) - c(\text{background}_{\text{NO}_c}) - c(\text{NO})}{C_e} \quad (4)$$

2.3 Further measurements

Additional measurements of atmospheric trace gases during CAFE Africa including O₃, CO, CH₄, HO₂, OH, NO₂ and water vapor as well as the photolysis frequencies j_{NO_2} and j_{PNA} were used in this study. O₃ was measured via UV absorption and chemiluminescence with the FAIRO (Fast AIRborne Ozone) instrument (total measurement uncertainty of 2.5 %; Zahn et al., 2012). CO and CH₄ were measured via quantum cascade laser absorption spectroscopy (total measurement uncertainty of 4.3 % and 0.3 %, respectively; Schiller et al., 2008). HO₂ and OH were measured with the custom-built HORUS (Hydroxyl Radical measurement Unit based on fluorescence Spectroscopy) instrument via fluorescence spectroscopy (Novelli et al., 2014; Marno et al., 2020). Please note that these data are still preliminary, and the measurement uncertainty is estimated at 50 %. Additional NO₂ concentrations for comparison were measured via differential optical absorption spectroscopy (miniDOAS) with a detection limit of about 5 pptv and an uncertainty depending on the altitude and cloud cover of typically 40 pptv (Hüneke et al., 2017; Kluge et al., 2020). Water vapor was measured via direct absorption by the tunable diode laser system SHARC (Sophisticated Hygrometer for Atmospheric Research) (accuracy of 5 %, detection limit typically in the range of 2–3 ppmv) (Kaufmann et al., 2018). The photolysis frequencies were calculated from actinic flux densities measured with a spectral radiometer (Meteorologie Consult GmbH, Metcon, Koenigstein, Germany) (uncertainty < 15 %) (Bohn and Lohse, 2017). Please note that all measurement data were converted to a uniform timescale with a 1 min time resolution as a basis for this analysis.

2.4 NO₂ calculations

For calculating the photostationary-state NO₂ concentrations during CAFE Africa, we assume that NO₂ production occurs through reaction of NO with O₃ (Reaction R1), HO₂ (Reaction R3) and RO₂ (Reaction R4). Tadic et al. (2021) showed that RO₂ is well-represented by CH₃O₂ during CAFE Africa via model simulations (80 % at 200 hPa of altitude and up to 90 % below), which we therefore use as surrogate for describing all organic peroxy radicals. In analogy to Leighton (1961), we describe NO₂ loss by photodissociation as shown in Reaction (R2). Other loss pathways for NO₂, for example, via OH can be neglected (< 1 %) (Bozem et al., 2017).



NO₂ concentration in photostationary state can therefore be obtained via Eq. (5), whereas the concentration of CH₃O₂ is calculated with the help of Eq. (6), which was derived by Bozem et al. (2017). For the calculation via Eq. (6) we assume that CH₃O₂ and HO₂ formation occurs through CH₄ and CO oxidation, respectively. We estimate an uncertainty of around 20 % resulting from these assumptions. Propagating the measurement uncertainties of HO₂, CH₄ and CO suggests a 50 % uncertainty in the calculated CH₃O₂ data. The NO₂ PSS data have an uncertainty of 22 % regarding the trace gas measurements according to Gaussian error propagation (uncertainty of rate coefficients is considered negligible).

$$[\text{NO}_2]^{\text{PSS}} = \frac{[\text{NO}] \times (k_{\text{NO}+\text{O}_3} \times [\text{O}_3] + k_{\text{NO}+\text{HO}_2} \times [\text{HO}_2] + k_{\text{NO}+\text{CH}_3\text{O}_2} \times [\text{CH}_3\text{O}_2])}{j_{\text{NO}_2}} \quad (5)$$

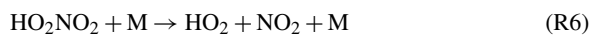
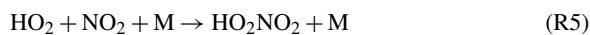
$$[\text{CH}_3\text{O}_2] = \frac{k_{\text{CH}_4+\text{OH}} \times [\text{CH}_4]}{k_{\text{CO}+\text{OH}} \times [\text{CO}]} \times [\text{HO}_2] \quad (6)$$

The temperature-dependent rate coefficients were obtained from the data sheets of the IUPAC Task Group on Atmospheric Chemical Kinetic Data Evaluation (2021) (Atkinson et al., 2004, 2006).

2.5 Calculation of NO₂ reservoir species

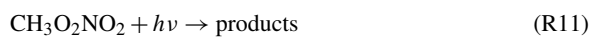
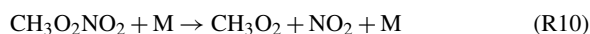
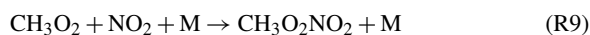
We consider the NO₂ reservoir species PAN (peroxyacetyl nitrate), MPN (methyl peroxy nitrate) and PNA (pernitric acid). PAN was measured during CAFE Africa via chemical ionization mass spectrometry (CIMS) (Phillips et al., 2013). MPN and PNA were not measured and instead estimated via photostationary-state calculations as suggested by Murphy et al. (2004). PNA (HO₂NO₂) production occurs through reaction of HO₂ and NO₂ (R5), while PNA loss is described by Reactions (R6)–(R8) either through thermal decomposition, photolysis or reaction with OH (Veres et al., 2015; IUPAC Task Group on Atmospheric Chemical Kinetic Data Evaluation, 2021; Atkinson et al., 2004). PSS HO₂NO₂ concentra-

tions can then be calculated via Eq. (7). k is the rate coefficient for each reaction and j_{PNA} is the photolysis frequency for Reaction (R7).



$$[\text{HO}_2\text{NO}_2]^{\text{PSS}} = \frac{k_5 \times [\text{HO}_2][\text{NO}_2]^{\text{PSS}}}{k_6 + j_{\text{PNA}} + k_8 \times [\text{OH}]} \quad (7)$$

MPN production and loss terms are in analogy to PNA, as shown in Reactions (R9)–(R11), except for the reaction with OH, which is negligible (Nault et al., 2015; Browne et al., 2011; Murphy et al., 2004; Bahta et al., 1982). The calculation in PSS is performed via Eq. (8). k represents the rate coefficients and j_{MPN} is the photolysis frequency for Reaction (R11). During CAFE Africa, only the photolysis frequency j_{PNA} was evaluated because reliable molecular data for MPN were missing. As suggested by Murphy et al. (2004) we assume identical UV cross sections of MPN and PNA and therefore j_{MPN} to be identical to j_{PNA} .



$$[\text{CH}_3\text{O}_2\text{NO}_2]^{\text{PSS}} = \frac{k_9 \times [\text{CH}_3\text{O}_2][\text{NO}_2]^{\text{PSS}}}{k_{10} + j_{\text{MPN}}} \quad (8)$$

In the photolytic converter, PNA, MPN and PAN can decompose to NO_2 depending on the temperature, pressure and residence time t according to first-order kinetics. The resulting NO_2 artifact is determined via Eq. (9).

$$\begin{aligned} [\text{NO}_2]_{\text{artifact}} = & [\text{HO}_2\text{NO}_2]^{\text{PSS}} \times (1 - \exp(-k_6 \times t)) \\ & + [\text{CH}_3\text{O}_2\text{NO}_2]^{\text{PSS}} \times (1 - \exp(-k_{10} \times t)) \\ & + [\text{CH}_3\text{COO}_2\text{NO}_2] \\ & \times (1 - \exp(-k_{\text{CH}_3\text{COO}_2\text{NO}_2+\text{M}} \times t)) \end{aligned} \quad (9)$$

Gaussian error propagation gives an uncertainty of 55 % for the calculated PNA and MPN data. We use the residence time according to the volume and the flow rate in the photolytic converter as described earlier. The actual value could deviate from the calculated one due to unknown flow dynamics and temperature gradients. Assuming 30 % uncertainty in the residence time gives an overall uncertainty of around 60 % in the NO_2 formed from PNA and MPN in the photolytic converter.

3 Results and discussion

3.1 Aircraft measurements

3.1.1 NO_2 reservoir species

Figure 3a shows the vertical concentration profiles of the NO_2 reservoir species PNA and MPN according to photo-stationary steady-state calculations (Eqs. 7 and 8) as well as PAN measurements during CAFE Africa. MPN concentrations were close to zero at low altitudes up to 10 km and increased above, reaching 57 ± 40 pptv between 13 and 14 km of altitude. The concentration increased further aloft but had a large variability. PNA mixing ratios were low below 8 and above 12 km of altitude and showed peak concentrations of 54 ± 21 pptv between 9 and 10 km. PAN increased from ground level to mid-range altitudes, with a maximum of 383 ± 283 pptv at 4–5 km. Concentrations subsequently decreased with altitude, reaching 92 ± 44 pptv at 14–15 km. Figure 3b shows the NO_2 artifact concentrations resulting from thermal decomposition of the reservoir species in the type 1 blue light converter according to first-order decay. It can be seen that only relevant artifact signals originated from MPN, more than 50 % of which decomposed to NO_2 at the conditions present in the converter; 3 % of the ambient PNA was converted to NO_2 . Even though atmospheric PAN concentrations, particularly at mid-range altitudes, were high, temperature, pressure and residence time in the blue light converter were too low for PAN to decay to NO_2 . As an overview, Fig. 3c shows the temperature-dependent decay $(1 - c/c_0)$ of the discussed NO_2 reservoir species in the converter. The calculation is based on constant pressure (105 hPa) and residence time (0.32 s). The temperature in the converter is shown with the black dashed line. Increasing temperature increases the decomposition share. It can be seen that, for PAN and PNA, the converter temperature would need to be significantly higher to observe a relevant decay (10 % decay of PNA at $> 50^\circ\text{C}$ and of PAN at $\sim 80^\circ\text{C}$). In contrast, for MPN, small changes in the temperature have a strong effect on the decomposing share ($4\%(\text{C}^\circ)^{-1}$ at the steepest point). We show the time- and pressure-dependent decay of PAN, PNA and MPN in Fig. S1. PAN and PNA decay only slightly depending on pressure at the given temperature and residence time. Please note that the residence time and the pressure are correlated, which we have neglected in this calculation. Based on these results, we recommend the implementation of a monitoring system for both temperature and pressure within the photolytic converter, which is difficult to implement in the type 1 blue light converter but allows for a more accurate calculation of the decomposing share and consequently a reliable correction of the NO_2 signal.

We have subtracted the NO_2 artifact signal arising from the decomposition of MPN and PNA from the CLD NO_2 concentrations. Please note that the data coverage for the NO_2 artifact from MPN is 55 % and from PNA is 48 % (difference

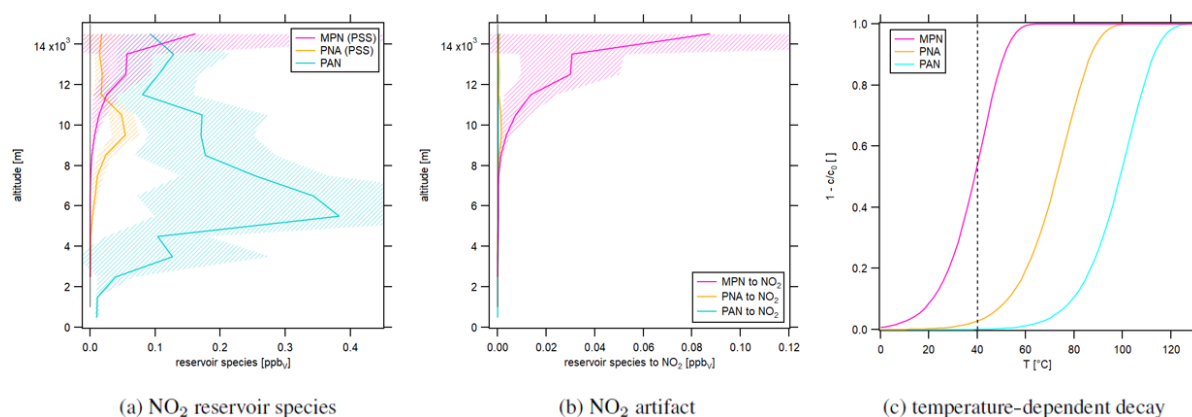


Figure 3. Vertical profiles of (a) NO₂ reservoir species MPN, PNA (from PSS calculations) and PAN (measured during CAFE Africa) as well as (b) NO₂ artifacts in the blue light converter from reservoir species according to first-order decay. The shaded plot areas present the 1σ standard deviation resulting from averaging the concentrations at each considered altitude range. (c) Temperature-dependent decay of the NO₂ reservoir species in the type 1 blue light converter.

due to OH data coverage). We have interpolated the data used in the following sections to reach full coverage of the CLD NO₂ concentrations. Sometimes the data were incomplete at the start or the end of a measurement flight in which case we considered the averaged NO₂ artifact signal according to the vertical profile shown in Fig. 3b as a function of the altitude.

3.1.2 Atmospheric NO₂ concentrations

Figure 4a shows the vertical profile of NO₂ concentrations measured via CLD in green, miniDOAS measurements in purple and NO₂ from PSS calculations in red. Calculated PSS NO₂ concentrations were on average 17 ± 14 pptv and approximately constant over the considered altitude range. At high altitudes, NO₂ from decomposing reservoir species exceeded the PSS values by around a factor of 5. NO₂ concentrations measured by the miniDOAS instrument were 95 ± 31 ppt at ground level and decreased with altitude up to 2 km. They were constant at 15 ± 16 pptv between 2 and 10 km of altitude and agreed to within $\sim 85\%$ to the calculated values. Concentrations increased again above, reaching 54 ± 31 pptv between 11 and 12 km, and decreased aloft with values similar to PSS NO₂ between 14 and 15 km. Average NO₂ concentrations measured by the CLD were 49 ± 76 pptv below 10 km of altitude where decomposition of reservoir species did not play a role and decreased with altitude above. Figure 4b shows the calculated difference in NO₂ concentrations between PSS calculations and miniDOAS measurements in black and between PSS calculations and CLD measurements in gray. It is notable that NO₂ concentrations from PSS and miniDOAS measurements were nearly identical apart for a difference with a maximum value of 48 ± 4 pptv between 10 and 13 km of altitude. In contrast, CLD NO₂ concentrations were higher by 45 ± 62 pptv compared to the cal-

culation up to 10 km of altitude and lower at higher altitudes with a maximum deviation of more than 100 pptv between 14 and 15 km. Figure 4a shows that the NO₂ CLD mixing ratios are negative at high altitudes. This is an indicator of a wrongly measured instrumental background signal in the second channel. If the determined instrumental background was too high, Eq. (4) could return underestimated or even negative NO₂ concentrations. However, the CLD NO₂ data were not generally too small, but even enhanced at lower altitudes compared to PSS and miniDOAS data, which may indicate the contribution of additional factors that we investigate in the following with the help of NO, H₂O and NO₂ concentrations in the course of selected measurement flights. For comparison, Fig. 4c shows the CLD NO₂ data with and without the calculated artifact signal. It can be seen that the data are already negative before the subtraction of decomposing NO₂ reservoir species.

3.1.3 Influence of atmospheric water vapor

Atmospheric water vapor concentrations are highest at ground level and decrease with increasing altitude. As an example, the vertical concentration profile of atmospheric water vapor during CAFE Africa is shown in Fig. S2. Accordingly, altitude changes during aircraft measurements introduce rapid changes in relative humidity to the instruments on board.

Figure 5 shows a time series of NO, water vapor, and calculated and measured NO₂ concentrations during the measurement flights MF10 (Fig. 5a) and MF12 (Fig. 5b). NO concentrations varied between 0.005 and 0.56 ppbv for MF10 and between 0.005 and 0.46 ppbv for MF12. We have recently shown that enhanced NO concentrations in the morning and afternoon of MF12 were due to local, recent light-

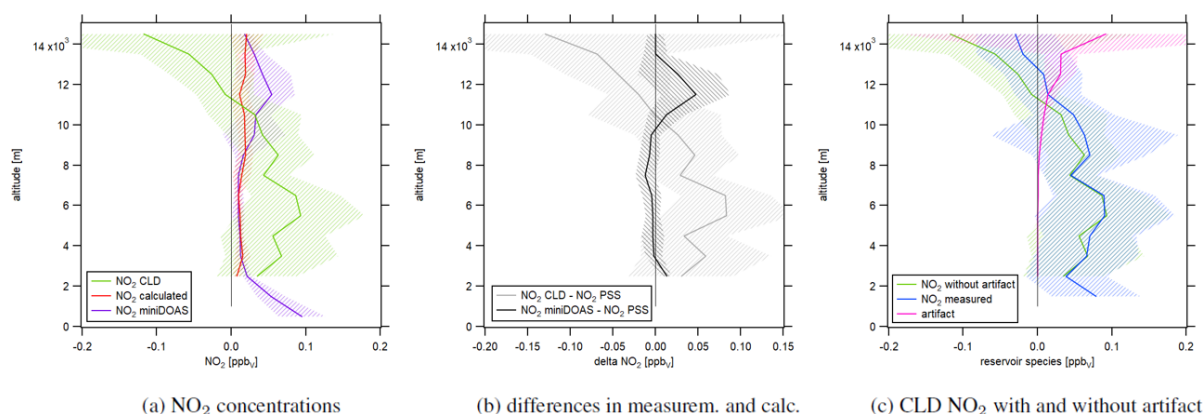


Figure 4. Vertical profiles of (a) NO₂ concentrations measured by the CLD, measured by miniDOAS and calculated via Eq. (5). (b) The difference in NO₂ concentrations from PSS calculations and measurements and (c) CLD NO₂ concentrations with and without an artifact. The shaded plot areas present the 1 σ standard deviation resulting from averaging concentrations at each considered altitude range.

ning activity (Nussbaumer et al., 2021). For MF10, enhanced NO concentrations at high altitudes had their source over the African continent. At low altitudes, NO concentrations were close to zero as there were no significant NO emissions in the marine boundary layer. Water vapor concentrations showed the expected inverse correlation with the flight altitude, with mixing ratios below the detection limit at high altitudes. As already suggested by the vertical NO₂ concentration profiles in Fig. 4a, NO₂ concentrations obtained from CLD measurements were lower than NO₂ concentrations from miniDOAS measurements and PSS calculations (and sometimes even below zero) at high altitudes and higher at low altitudes. Please note that the CLD NO₂ data shown in Fig. 5 were processed as described earlier. This includes the interpolation of the instrumental background and calibration measurements, which were performed six times for MF10 and four times for MF12. A potential variation of the instrumental background or the sensitivity of the channels between two CB cycles would therefore be unaccounted for. We show the instrumental background measurements in the top data trace of each panel in Fig. 5 by red dots and the interpolation as a red dashed line. For MF10, the measured instrumental background in the NO_c channel varied between 85 and 127 pptv and for MF12 between 87 and 109 pptv. In comparison, the instrumental background in the NO channel varied between 1 and 11 pptv for MF10 and between –2 and 6 pptv for MF12. We show the instrumental background for MF10 and MF12 in each channel in Fig. S3. Calculated PSS NO₂ concentrations ranged between 1 and 93 pptv for MF10 and between 2 and 46 pptv for MF12. Local maxima mainly accompanied peaks of nitric oxide, which is a result of the NO dependence of Eq. (5). NO₂ concentrations measured by the miniDOAS instrument varied between 2 and 39 pptv for MF10. For MF12, concentrations were 15 ± 16 pptv and generally lower for low altitudes and higher for high alti-

tudes. NO₂ concentrations measured by the CLD instrument ranged from –224 to 317 pptv for MF10 and from –153 to 384 pptv for MF12. It is striking that the maxima were obtained simultaneously with a sharp decrease in altitude accompanied by an increase in water vapor concentration. For each measurement flight shown here, this phenomenon was observed twice, indicated by the orange dashed lines. For example, the research aircraft descended from 12.6 to 3.9 km at 13:30 UTC during MF12. At the same time, the CLD NO₂ concentration increased from an average of 23 ± 14 pptv between 13:00 and 13:30 UTC to its maximum of 384 pptv at 13:45 UTC when reaching the new lower flight altitude. Water vapor measurements were incomplete before 13:00 UTC, but it can be assumed that they were constant and close to zero at 12.6 km of altitude, rising to $9.5 \pm 0.7 \times 10^3$ ppmv on average after reaching 3.9 km (+15 min). Similar observations were made for MF12 at 18:30 UTC and for MF10 at around 13:30 and 18:00 UTC, in each case accompanied by a decrease in altitude and an increase in water vapor concentrations. The observed NO₂ peaks appeared only for the CLD measurement and not for the values from PSS calculation or miniDOAS measurement, which underlines the instrumental cause. The time series for the measurement flights MF13, MF14 and MF15 shows similar results and can be found in Fig. S4.

We hypothesize that these observations were influenced by a surface effect in the type 1 blue light converter, which has a highly porous inner surface as described earlier. This material can adsorb atmospheric compounds, such as NO, and desorb them at a later stage (for example, supported by an increase in humidity), which we will refer to as memory effect in the following. In a series of laboratory studies, we have investigated the impact of NO concentrations and humidity on the effects described above, particularly in regard to the instrumental background.

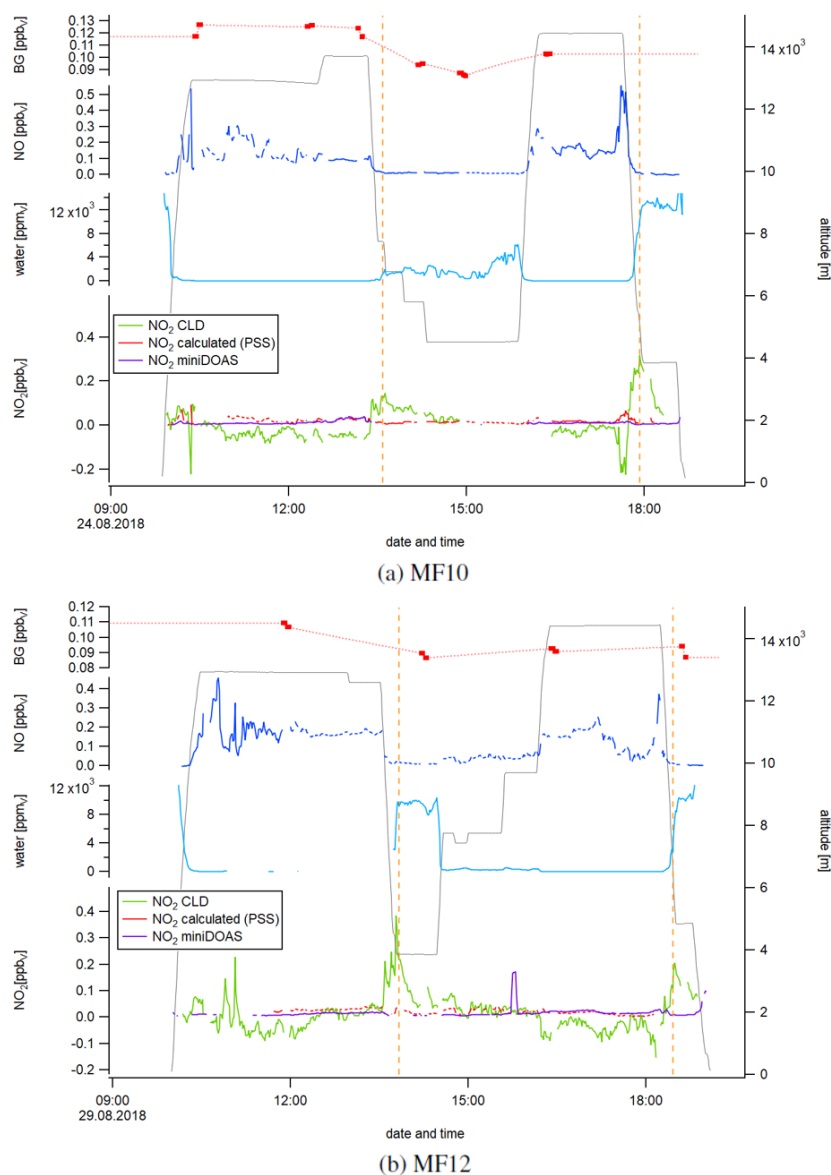


Figure 5. Temporal development of the instrumental background (BG) in the NO_c channel, NO, water vapor, and calculated and measured NO_2 for measurement flights 10 and 12. The orange dashed lines indicate the simultaneous occurrence of a rapid decrease in altitude, an increase in water vapor concentration and a peak in the NO_2 CLD data.

3.2 Laboratory experiments and implications for CAFE Africa

We propose that the memory effect described in the previous section is strongly affected by NO molecules and is dependent on changes in the introduced relative humidity. In order to show this, we have conducted different experiments in the laboratory to investigate the instrumental background produced by the photolytic converter in the NO_c channel. Be-

side NO and H_2O , we suggest that one or more additional factors affect the observed instrumental background signal, which are connected to the light of the LEDs and which we discuss at the end of this section.

For the first set of experiments, we exposed the converter (LEDs switched on) to 15.8 ppbv of NO for 2 h followed by 4 h zero air measurements. The first experiment was carried out under dry conditions, sampling NO and zero air directly

from the gas cylinder. For the second experiment, we introduced water vapor by passing zero air through a washing bottle with deionized water before entering the instrument. The thus obtained relative humidity was $\sim 95\%$ at ambient temperature and decreased over time with decreasing water temperature (through evaporation). For the third and fourth experiment, zero air was humidified only for the zero air measurement and the NO measurement, respectively. We repeated the latter, introducing a lower relative humidity of $\sim 35\%$, and obtained the same result.

Figure 6 shows the temporal development of the instrumental background signal in the NO_c channel after 2 h of NO measurement with a concentration of 15.8 ppbv. The red line shows the experiment under dry conditions, and the blue line presents the experiment under humid conditions. For the yellow line, we performed the NO measurement under dry conditions and the following instrumental background measurement under humid conditions. The green line shows a humid NO measurement and dry instrumental background measurement. Figure 6a presents the results obtained with the type 1 blue light converter. All experiments showed a decreasing instrumental background signal over time in the NO_c channel. For comparison, the instrumental background signal in the NO channel over time is presented in Fig. S5. The lines show no significant trend over time. This indicates that the converter adsorbs NO molecules, for example during NO measurements, and desorbs them during zero air measurements. At $t = 0$ min, the instrumental background signals for all experiments were approximately the same between 90 and 100 pptv but showed a different development over time. The strongest decline by around 25 % over 250 min was observed for a dry instrumental background measurement after a humid NO measurement (green curve). For the opposite case, a humid instrumental background measurement after a dry NO measurement, the signal decreased by around 5 % over the observed time period (yellow curve). Performing the whole experiment under dry or humid conditions (red and blue curve, respectively) had a similar outcome, with an instrumental background signal decrease of approximately 10 %. These observations indicate that the instrumental background measurements in the NO_c channel, which were performed during CAFE Africa and used for the data processing according to Eq. (4), were consistently too high as they were only run for 2×1 min (per CB cycle) and therefore did not represent the actual instrumental background but an artifact signal. In the laboratory, we observed the strongest effect for a dry instrumental background measurement following a humid NO measurement, which was a likely scenario for the ambient monitoring during CAFE Africa as zero air for an instrumental background measurement was sampled from a gas cylinder (dry conditions) and the measured ambient concentration was subject to ambient meteorological conditions. This would explain the occurrence of negative NO_2 concentrations obtained from CLD measurements as mentioned earlier. These experiments also suggest that wa-

ter molecules might not just promote adsorptive or desorptive processes, but also participate in the surface allocation themselves and compete with NO. Following this hypothesis, the surface spaces would fill with NO during an NO measurement under dry conditions and with both NO and H_2O molecules under wet conditions. A subsequent instrumental background measurement under dry conditions would then lead to NO (and possibly H_2O) desorption. For a subsequent instrumental background measurement under humid conditions, H_2O molecules could actively replace NO molecules because of their higher surface affinity, leading to a temporally longer “leakage” of NO and a slower decrease in the instrumental background signal. The described effect would be highest for a dry NO measurement, which gives the maximum NO surface coverage and a wet zero air measurement (yellow), while it would be lowest for the opposite case for which we observed the lowest instrumental background signal after 250 min (green). This hypothesis fits well with the observations during CAFE Africa presented in Sect. 3.1.3; we observed a sharp increase in the NO_2 signal along with rapid increases in water vapor concentration. H_2O molecules could replace adsorbed NO molecules (or other atmospheric compounds), which were detected by the CLD as an artifact signal. Because of the conversion efficiency of 24.4 % of the type 1 blue light converter, the signal difference from the NO and NO_c channel was multiplied by a factor of around 4 (compare Eq. 4). Therefore, the resulting NO_2 signal was distorted by 4 times the actual desorbed NO, explaining the large peaks accompanying altitude descents. As we do not observe these effects in the NO channel (and the two channels are structurally identical), we can exclude that any of the humidity effects are caused by components in the instrument other than the photolytic converter.

We repeated the same laboratory experiments using the type 2 photolytic converter. The resulting temporal development of the instrumental background is presented in Fig. 6b, which shows significant improvements compared to the type 1 converter. The instrumental background in the NO_c channel was many times smaller for the type 2 quartz converter, with mixing ratios of around 10 to 15 pptv, and was, most importantly, constant over time. For stationary long-term experiments it could be possible to measure the instrumental background on the scale of hours. However, for aircraft measurements and the accompanying rapid air mass changes due to the high aircraft velocity, it is vital to obtain a reliable instrumental background measurement within a short time interval, which would be possible with the type 2 converter. Furthermore, changes in humidity did not seem to impact the measurement as all four experiments show the same result. This, too, suggests the suitability of the type 2 converter in aircraft measurements or more generally in field studies impacted by high and changing humidities.

Performing zero air measurements after NO_2 measurements had a similar outcome for each of the applied converters. The instrumental background measurement in the type

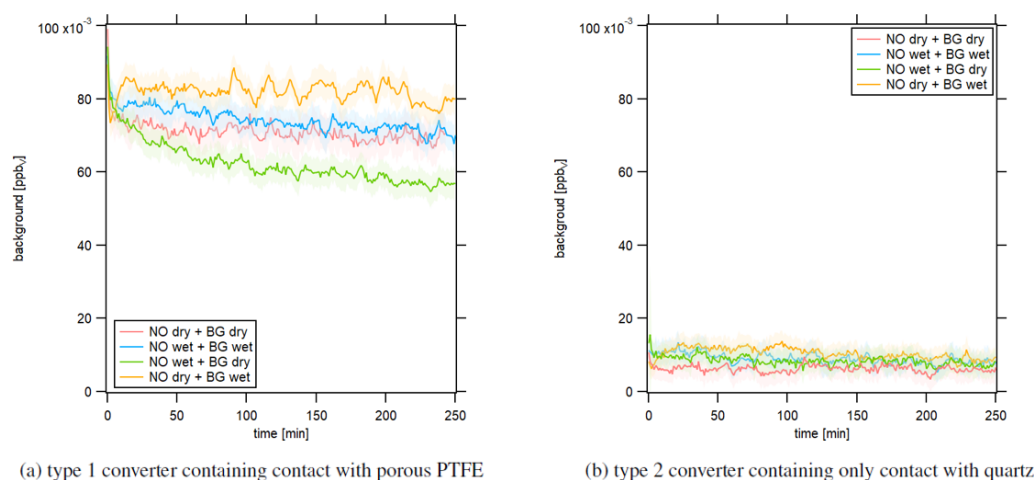


Figure 6. Instrumental background in response to dry and humid conditions after 2 h of NO calibration at 15.8 ppbv in the NO_c channel. The LEDs of the photolytic converter were switched on.

1 blue light converter showed a decreasing trend over time, while it was constant and significantly smaller in the type 2 quartz converter.

Our assumption that the observed effect is – at least partly – associated with NO molecules is supported by an experiment wherein we heated the type 1 blue light converter with switched-off LEDs with a heat gun and observed a sharp increase in the NO_c channel during zero air measurement (following NO calibration measurement). The increase in temperature promoted the desorptive process and had to include NO molecules. Otherwise, the CLD would not have detected any increase in the signal as the converters' LEDs were switched off and NO_2 could not form NO via the photolytic reaction. We show the result of the heating experiment in Fig. 7a. The converter surface was heated for 2 min (under constant movement of the heat gun) at a distance of around 10 cm during zero air measurement. We estimate the surface temperature to not have exceeded 200 °C. We observed a peak NO concentration of 2 ppbv (NO_c instrumental background was 0 ppbv). In comparison, Fig. 7b shows the experiment repeated with the type 2 quartz converter, which showed a small increase in the NO_c signal, too, but approximately 1 order of magnitude smaller compared to the type 1 blue light converter. The qualitative outcome of this experiment was the same with the LEDs switched on as well as with preceding NO_2 (instead of NO) measurement. Please note that a direct comparison of experiments regarding adsorptive and desorptive processes with switched-on and -off LEDs is difficult because the operation of the LEDs increases the temperature within the converter, which, as shown above, strongly impacts the surface allocation.

Beyond that, we performed an experiment to investigate how NO calibration measurements affect subsequent zero air measurements in response to different NO concentrations.

Figure 8 shows the influence of the preceding NO concentration level on the following first 5 min of zero air measurement. We have performed 30 min NO calibrations with NO concentrations between 0.25 and 10 ppbv. Red data points represent the instrumental background of the NO channel, and green data points show the instrumental background of the NO_c channel. Instrumental background concentrations in the NO channel were independent of preceding NO concentrations. In contrast, for the type 1 blue light converter, instrumental background concentrations in the NO_c channel increased with increasing NO concentrations and leveled off for high values, as shown in Fig. 8a. Measured NO concentrations during CAFE Africa were between 0 and 1 ppbv and were therefore situated in the rising part of the curve. That shows that instrumental background measurements during CAFE Africa were not only too high, but also depended on the preceding NO concentration. We tried to retrospectively correct the NO_2 data with a lower instrumental background as obtained from laboratory investigations after several hours of zero air sampling. However, it was not possible to quantify the effect of varying the preceding NO levels. Additionally, the impact of humidity had the exact opposite effect on the NO_2 measurements. While the higher-than-actual instrumental background led to lower-than-actual NO_2 concentrations, increases in humidity triggered higher-than-actual NO_2 concentrations. Figure 8b shows that the development of the instrumental background in the NO_c channel did not depend on the preceding NO concentrations for the type 2 quartz converter. The instrumental background was 12 ± 1 pptv and constant over the whole experiment. The detected instrumental background signal for the NO_c channel disappeared when switching off the light of the UV LEDs. A possible explanation can be a trace concentration of NO_2 in the utilized synthetic air as mentioned earlier.

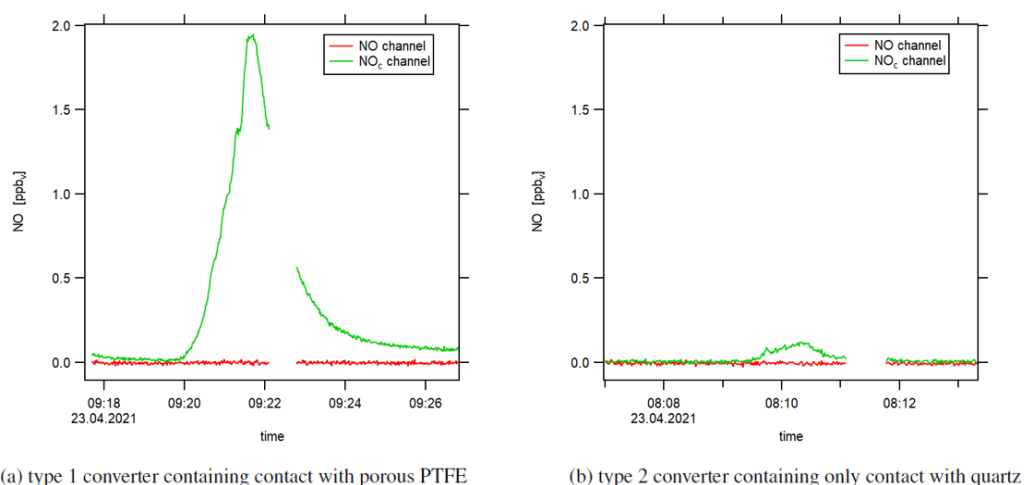


Figure 7. Instrumental background (zero air measurement) when heating the switched-off photolytic converter with a heat gun. The small data gaps are due to pre-chamber measurements.

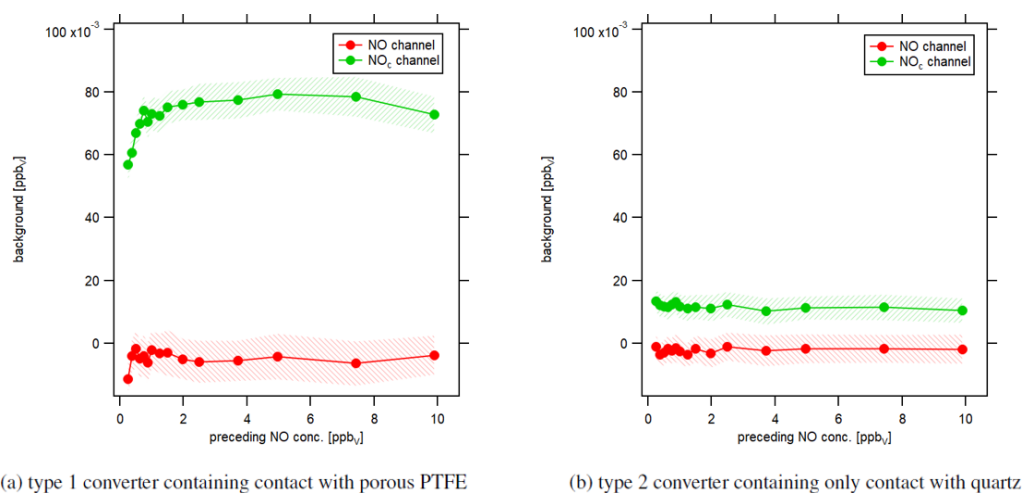


Figure 8. Instrumental background in response to different preceding NO concentrations under dry conditions. Each data point shows the level of the signal of the first 5 min of instrumental background measurements after NO calibrations.

While we have shown above that NO and humidity strongly affect the instrumental background measurements in the type 1 blue light converter, it is likely that there are other factors contributing to the observed effects, too. When switching off the LEDs in the type 1 converter, the observed instrumental background decreased rapidly (too rapidly for a sole temperature effect), which we present in Fig. S6a. This suggests that the light of the LEDs impacts the instrumental background in the NO_c channel. Many other compounds can be photolyzed to form NO, such as PAN, ClNO_2 or BrONO_2 . However, their absorption cross sections suggest no interference at 397 nm, which is the spectral output maximum of the LEDs (Reed et al., 2016; Pollack et al., 2010). Only small

interference could occur with HONO and NO_3 at the edge of the spectral output, and this would require the presence of these compounds in the converter, which should not be the case for the described laboratory investigations but is conceivable given the memory effect observations. For comparison, Fig. S6b shows that the effect of switching the LEDs on and off during zero air measurement is marginal when using the type 2 quartz converter. We have performed an uptake experiment for HNO_3 (nitric acid) to investigate the adsorptive capacity of the converters. HNO_3 in zero air (2500 sccm) was first routed through a bypass, and after reaching a constant signal, the gas flow was changed to include the converter. The HNO_3 concentration behind the converter was moni-

tored via chemical ionization mass spectrometry (CIMS). Figure S7a and b show the resulting adsorption behavior for the type 1 and the type 2 converter, respectively. When directing the gas flow through the type 1 converter, the detected HNO_3 flux decreased rapidly by around a factor of 4, and we did not observe the signal return to its initial value within 40 min (which is when we terminated the experiment). This indicates a high absorptive capacity or a decay of HNO_3 in the converter (or both). Integration of the HNO_3 flux shows that the converter took up approximately 1.7×10^{16} HNO_3 molecules in the considered time frame. In contrast, for the type 2 converter, the HNO_3 flux decreased, too, but returned to its initial value within 10 min, while it adsorbed only $\sim 1.7 \times 10^{15}$ HNO_3 molecules. The observed adsorption capacity can be minimized by coating the quartz surface with FEP (fluorinated ethylene propylene), which provides a highly hydrophobic surface (Neuman et al., 1999; Liebmman et al., 2017). The number of adsorbed HNO_3 molecules was a factor of 4–5 smaller compared to the non-coated quartz converter (Fig. S7c). We did not observe any differences between the coated and non-coated quartz converter regarding the experiments investigating the role of NO and humidity presented above. This uptake experiment shows the high adsorptive capacity of the type 1 blue light converter in comparison to the type 2 quartz converter. In the case of HNO_3 , which could have been adsorbed by the type 1 converter, e.g., during stratospheric measurements, we hypothesize a potential source of NO or NO_2 through, for example, surface-catalyzed chemistry, possibly involving the light of the LEDs or elevated temperature. Again, this experiment underlines the superiority of the type 2 quartz converter over the type 1 blue light converter and suggests applicability for ambient and airborne measurements.

4 Conclusions

In this study, we have investigated a modified conventional blue light converter (type 1) with a highly reflective and porous inner surface made from optical PTFE regarding its application during the research aircraft campaign CAFE Africa, which took place in August and September 2018 around Cabo Verde. We have identified a memory effect in the blue light converter, which is affected by humidity, especially rapid changes in water vapor concentrations, and preceding NO levels; this is particularly relevant for the low NO_2/NO ratio in the upper troposphere. More specifically, this includes the subtraction of a fluctuating, higher-than-actual instrumental background in the NO_c channel, yielding negative NO_2 values and humidity-triggered spontaneous desorption of stored molecules appearing as large NO_2 peaks; both effects are amplified by the low conversion efficiency. The high adsorptive capacity regarding other atmospheric trace gases such as HNO_3 and the light of the LEDs could additionally play a role in the observed ef-

fects. Because of the complex correlations between these parameters it is not possible to retrospectively correct the NO_2 signal measured during CAFE Africa to receive reliable data. If a conventional blue light converter is still in use, we would suggest avoiding constant altitude changes in aircraft applications. Instead, we highly recommend the application of an alternative photolytic converter made from quartz glass (type 2) in order to prevent the gas flow from coming into contact with the porous PTFE surface, which can additionally be coated with FEP to obtain highly hydrophobic properties. Laboratory results indicate a high suitability of the alternative converter in aircraft measurements, which, looking into the future, should be investigated in detail in order to improve in-field NO_2 measurements. With an improved instrumental background, other important questions of current atmospheric NO_2 research, such as deviations from photostationary-state NO_2 in remote locations or interferences from NO_y species, could be addressed and investigated more easily.

Data availability. Data measured during the flight campaign CAFE Africa are available at <https://keeper.mpg.de> (last access: 17 May 2021, registration required) to all scientists agreeing to the CAFE Africa data protocol.

Supplement. The supplement related to this article is available online at: <https://doi.org/10.5194/amt-14-6759-2021-supplement>.

Author contributions. HF had the idea. CMN and HF designed the study. CMN analyzed the data and wrote the paper. CMN performed the laboratory experiments. CMN, UP and HF designed the type 2 quartz converter. IT provided CLD NO_x , CO and CH_4 data for CAFE Africa. Photolysis frequencies were received from BB, DM, MM, RR and HH measured and provided the OH and HO_2 data. KP and FK measured and provided the NO_2 miniDOAS data. FO measured and provided the O_3 data. H_2O data were received from MZ. RD and JNC measured and provided the PAN data. HF, JL and HH made a large contribution to the operation and planning of the aircraft campaign.

Competing interests. Hartwig Harder is a member of the editorial board of *Atmospheric Measurement Techniques*.

Disclaimer. Publisher's note: Copernicus Publications remains neutral with regard to jurisdictional claims in published maps and institutional affiliations.

Acknowledgements. We acknowledge the collaboration with the DLR (German Aerospace Center) during CAFE Africa. This work was supported by the Max Planck Graduate Center with the Johannes Gutenberg-Universität Mainz (MPGC). Flora Kluge and

Klaus Pfeilsticker acknowledge the support given by the Deutsche Forschungsgemeinschaft (DFG) through the projects PF 384-16, PF 384-17 and PF 384-19.

Financial support. The article processing charges for this open-access publication were covered by the Max Planck Society.

Review statement. This paper was edited by Keding Lu and reviewed by three anonymous referees.

References

- Alam, M. S., Crilley, L. R., Lee, J. D., Kramer, L. J., Pfrang, C., Vázquez-Moreno, M., Ródenas, M., Muñoz, A., and Bloss, W. J.: Interference from alkenes in chemiluminescent NO_x measurements, *Atmos. Meas. Tech.*, 13, 5977–5991, <https://doi.org/10.5194/amt-13-5977-2020>, 2020.
- Andersen, S. T., Carpenter, L. J., Nelson, B. S., Neves, L., Read, K. A., Reed, C., Ward, M., Rowlinson, M. J., and Lee, J. D.: Long-term NO_x measurements in the remote marine tropical troposphere, *Atmos. Meas. Tech.*, 14, 3071–3085, <https://doi.org/10.5194/amt-14-3071-2021>, 2021.
- Atkinson, R., Baulch, D. L., Cox, R. A., Crowley, J. N., Hampson, R. F., Hynes, R. G., Jenkin, M. E., Rossi, M. J., and Troe, J.: Evaluated kinetic and photochemical data for atmospheric chemistry: Volume I – gas phase reactions of O_x , HO_x , NO_x and SO_x species, *Atmos. Chem. Phys.*, 4, 1461–1738, <https://doi.org/10.5194/acp-4-1461-2004>, 2004.
- Atkinson, R., Baulch, D. L., Cox, R. A., Crowley, J. N., Hampson, R. F., Hynes, R. G., Jenkin, M. E., Rossi, M. J., Troe, J., and IUPAC Subcommittee: Evaluated kinetic and photochemical data for atmospheric chemistry: Volume II – gas phase reactions of organic species, *Atmos. Chem. Phys.*, 6, 3625–4055, <https://doi.org/10.5194/acp-6-3625-2006>, 2006.
- Bahta, A., Simonaitis, R., and Hecklen, J.: Thermal decomposition kinetics of methyl peroxyxynitrate ($\text{CH}_3\text{O}_2\text{NO}_2$), *J. Phys. Chem.-US*, 86, 1849–1853, 1982.
- Bohn, B. and Lohse, I.: Calibration and evaluation of CCD spectroradiometers for ground-based and airborne measurements of spectral actinic flux densities, *Atmos. Meas. Tech.*, 10, 3151–3174, <https://doi.org/10.5194/amt-10-3151-2017>, 2017.
- Boningari, T. and Smirniotis, P. G.: Impact of nitrogen oxides on the environment and human health: Mn-based materials for the NO_x abatement, *Curr. Opin. Chem. Eng.*, 13, 133–141, <https://doi.org/10.1016/j.coche.2016.09.004>, 2016.
- Bozem, H., Butler, T. M., Lawrence, M. G., Harder, H., Martinez, M., Kubistin, D., Lelieveld, J., and Fischer, H.: Chemical processes related to net ozone tendencies in the free troposphere, *Atmos. Chem. Phys.*, 17, 10565–10582, <https://doi.org/10.5194/acp-17-10565-2017>, 2017.
- Breuninger, C., Meixner, F. X., and Kesselmeier, J.: Field investigations of nitrogen dioxide (NO_2) exchange between plants and the atmosphere, *Atmos. Chem. Phys.*, 13, 773–790, <https://doi.org/10.5194/acp-13-773-2013>, 2013.
- Browne, E. C., Perring, A. E., Wooldridge, P. J., Apel, E., Hall, S. R., Huey, L. G., Mao, J., Spencer, K. M., Clair, J. M. St., Weinheimer, A. J., Wisthaler, A., and Cohen, R. C.: Global and regional effects of the photochemistry of $\text{CH}_3\text{O}_2\text{NO}_2$: evidence from ARCTAS, *Atmos. Chem. Phys.*, 11, 4209–4219, <https://doi.org/10.5194/acp-11-4209-2011>, 2011.
- Clough, P. and Thrush, B. A.: Mechanism of chemiluminescent reaction between nitric oxide and ozone, *T. Faraday Soc.*, 63, 915–925, <https://doi.org/10.1039/TF9676300915>, 1967.
- Crowley, J. N., Schuster, G., Pouvesle, N., Parchatka, U., Fischer, H., Bonn, B., Bingemer, H., and Lelieveld, J.: Nocturnal nitrogen oxides at a rural mountain-site in south-western Germany, *Atmos. Chem. Phys.*, 10, 2795–2812, <https://doi.org/10.5194/acp-10-2795-2010>, 2010.
- Demerjian, K. L.: A review of national monitoring networks in North America, *Atmos. Environ.*, 34, 1861–1884, [https://doi.org/10.1016/S1352-2310\(99\)00452-5](https://doi.org/10.1016/S1352-2310(99)00452-5), 2000.
- ECO PHYSICS AG: CLD 790 SR User-Manual, Dürnten, Switzerland, 2002.
- Fischer, E. V., Jacob, D. J., Yantosca, R. M., Sulprizio, M. P., Millet, D. B., Mao, J., Paulot, F., Singh, H. B., Roiger, A., Ries, L., Talbot, R. W., Dzepina, K., and Pandey Deolal, S.: Atmospheric peroxyacetyl nitrate (PAN): a global budget and source attribution, *Atmos. Chem. Phys.*, 14, 2679–2698, <https://doi.org/10.5194/acp-14-2679-2014>, 2014.
- Frey, M. M., Roscoe, H. K., Kukui, A., Savarino, J., France, J. L., King, M. D., Legrand, M., and Preunkert, S.: Atmospheric nitrogen oxides (NO and NO_2) at Dome C, East Antarctica, during the OPAL campaign, *Atmos. Chem. Phys.*, 15, 7859–7875, <https://doi.org/10.5194/acp-15-7859-2015>, 2015.
- Fuchs, H., Ball, S. M., Bohn, B., Brauers, T., Cohen, R. C., Dorn, H.-P., Dubé, W. P., Fry, J. L., Häsel, R., Heitmann, U., Jones, R. L., Kleffmann, J., Mentel, T. F., Müsgen, P., Rohrer, F., Rollins, A. W., Ruth, A. A., Kiendler-Scharr, A., Schlosser, E., Shillings, A. J. L., Tillmann, R., Varma, R. M., Venables, D. S., Vilena Tapia, G., Wahner, A., Wegener, R., Wooldridge, P. J., and Brown, S. S.: Intercomparison of measurements of NO_2 concentrations in the atmosphere simulation chamber SAPHIR during the NO3Comp campaign, *Atmos. Meas. Tech.*, 3, 21–37, <https://doi.org/10.5194/amt-3-21-2010>, 2010.
- Ganzeveld, L., Lelieveld, J., Dentener, F., Krol, M., Bouwman, A., and Roelofs, G.-J.: Global soil-biogenic NO_x emissions and the role of canopy processes, *J. Geophys. Res.-Atmos.*, 107, ACH-9, <https://doi.org/10.1029/2001JD000684>, 2002.
- Ge, B., Sun, Y., Liu, Y., Dong, H., Ji, D., Jiang, Q., Li, J., and Wang, Z.: Nitrogen dioxide measurement by cavity attenuated phase shift spectroscopy (CAPS) and implications in ozone production efficiency and nitrate formation in Beijing, China, *J. Geophys. Res.-Atmos.*, 118, 9499–9509, <https://doi.org/10.1002/jgrd.50757>, 2013.
- Gingerysty, N. J., Odame-Ankrah, C. A., Jordan, N., and Osthoff, H. D.: Interference from HONO in the measurement of ambient air NO_2 via photolytic conversion and quantification of NO , *J. Environ. Sci.*, 107, 184–193, <https://doi.org/10.1016/j.jes.2020.12.011>, 2021.
- Greaver, T. L., Sullivan, T. J., Herrick, J. D., Barber, M. C., Baron, J. S., Cosby, B. J., Deerhake, M. E., Dennis, R. L., Dubois, J.-J. B., Goodale, C. L., Herlihy, A. T., Lawrence, G. B., Liu, L., Lynch, J. A., and Novak, K. J.: Ecological effects of nitrogen and sulfur air pollution in the US: what do we know?, *Front. Ecol. Environ.*, 10, 365–372, <https://doi.org/10.1890/110049>, 2012.

- Griffin, R. J., Beckman, P. J., Talbot, R. W., Sive, B. C., and Varner, R. K.: Deviations from ozone photostationary state during the International Consortium for Atmospheric Research on Transport and Transformation 2004 campaign: Use of measurements and photochemical modeling to assess potential causes, *J. Geophys. Res.-Atmos.*, 112, D10S07, <https://doi.org/10.1029/2006JD007604>, 2007.
- Hosaynali Beygi, Z., Fischer, H., Harder, H. D., Martinez, M., Sander, R., Williams, J., Brookes, D. M., Monks, P. S., and Lelieveld, J.: Oxidation photochemistry in the Southern Atlantic boundary layer: unexpected deviations of photochemical steady state, *Atmos. Chem. Phys.*, 11, 8497–8513, <https://doi.org/10.5194/acp-11-8497-2011>, 2011.
- Hüneke, T., Aderhold, O.-A., Bounin, J., Dorf, M., Gentry, E., Grossmann, K., Grooß, J.-U., Hoor, P., Jöckel, P., Kennner, M., Knapp, M., Knecht, M., Lörks, D., Ludmann, S., Matthes, S., Raecke, R., Reichert, M., Weimar, J., Werner, B., Zahn, A., Ziereis, H., and Pfeilsticker, K.: The novel HALO mini-DOAS instrument: inferring trace gas concentrations from airborne UV/visible limb spectroscopy under all skies using the scaling method, *Atmos. Meas. Tech.*, 10, 4209–4234, <https://doi.org/10.5194/amt-10-4209-2017>, 2017.
- IUPAC Task Group on Atmospheric Chemical Kinetic Data Evaluation: Evaluated Kinetic Data, available at: <http://iupac.pole-ether.fr>, last access: 2 February 2021.
- Jacob, D. J.: Introduction to atmospheric chemistry, Princeton University Press, Princeton, USA, 1999.
- Javed, U., Kubistin, D., Martinez, M., Pollmann, J., Rudolf, M., Parchatka, U., Reiffs, A., Thieser, J., Schuster, G., Horbanski, M., Pöhler, D., Crowley, J. N., Fischer, H., Lelieveld, J., and Harder, H.: Laser-induced fluorescence-based detection of atmospheric nitrogen dioxide and comparison of different techniques during the PARADE 2011 field campaign, *Atmos. Meas. Tech.*, 12, 1461–1481, <https://doi.org/10.5194/amt-12-1461-2019>, 2019.
- Jordan, N., Garner, N. M., Matchett, L. C., Tokarek, T. W., Osthoff, H. D., Odame-Ankrah, C. A., Grimm, C. E., Pickrell, K. N., Swainson, C., and Rosentreter, B. W.: Potential interferences in photolytic nitrogen dioxide converters for ambient air monitoring: Evaluation of a prototype, *J. Air Waste Manage.*, 70, 753–764, <https://doi.org/10.1080/10962247.2020.1769770>, 2020.
- Jung, J., Lee, J., Kim, B., and Oh, S.: Seasonal variations in the NO₂ artifact from chemiluminescence measurements with a molybdenum converter at a suburban site in Korea (downwind of the Asian continental outflow) during 2015–2016, *Atmos. Environ.*, 165, 290–300, <https://doi.org/10.1016/j.atmosenv.2017.07.010>, 2017.
- Kaufmann, S., Voigt, C., Heller, R., Jurkat-Witschas, T., Krämer, M., Rolf, C., Zöger, M., Giez, A., Buchholz, B., Ebert, V., Thornberry, T., and Schumann, U.: Intercomparison of midlatitude tropospheric and lower-stratospheric water vapor measurements and comparison to ECMWF humidity data, *Atmos. Chem. Phys.*, 18, 16729–16745, <https://doi.org/10.5194/acp-18-16729-2018>, 2018.
- Kebabian, P. L., Herndon, S. C., and Freedman, A.: Detection of nitrogen dioxide by cavity attenuated phase shift spectroscopy, *Anal. Chem.*, 77, 724–728, <https://doi.org/10.1021/ac048715y>, 2005.
- Kim, S., Huey, L. G., Stickel, R., Tanner, D., Crawford, J. H., Olson, J. R., Chen, G., Brune, W., Ren, X., Leshner, R., Wooldridge, P. J., Bertram, T. H., Perring, A., Cohen, R. C., Lefer, B. L., Shetter, R. E., Avery, M., Diskin, G., and Sokolik, I.: Measurement of HO₂NO₂ in the free troposphere during the Intercontinental Chemical Transport Experiment–North America 2004, *J. Geophys. Res.-Atmos.*, 112, <https://doi.org/10.1029/2006JD007676>, 2007.
- Kluge, F., Hüneke, T., Knecht, M., Lichtenstern, M., Rotermund, M., Schlager, H., Schreiner, B., and Pfeilsticker, K.: Profiling of formaldehyde, glyoxal, methylglyoxal, and CO over the Amazon: normalized excess mixing ratios and related emission factors in biomass burning plumes, *Atmos. Chem. Phys.*, 20, 12363–12389, <https://doi.org/10.5194/acp-20-12363-2020>, 2020.
- Lee, J., Moller, S., Read, K., Lewis, A., Mendes, L., and Carpenter, L.: Year-round measurements of nitrogen oxides and ozone in the tropical North Atlantic marine boundary layer, *J. Geophys. Res.*, 114, D21302, <https://doi.org/10.1029/2009JD011878>, 2009.
- Leighton, P.: Photochemistry of air pollution, Academic Press, Inc., New York, USA, 1961.
- Lelieveld, J. and Dentener, F. J.: What controls tropospheric ozone?, *J. Geophys. Res.-Atmos.*, 105, 3531–3551, 2000.
- Levy, H.: Normal atmosphere: Large radical and formaldehyde concentrations predicted, *Science*, 173, 141–143, <https://doi.org/10.1126/science.173.3992.141>, 1971.
- Liebmann, J. M., Schuster, G., Schuladen, J. B., Sobanski, N., Lelieveld, J., and Crowley, J. N.: Measurement of ambient NO₃ reactivity: design, characterization and first deployment of a new instrument, *Atmos. Meas. Tech.*, 10, 1241–1258, <https://doi.org/10.5194/amt-10-1241-2017>, 2017.
- Lippmann, M.: Health effects of ozone a critical review, *JAPCA J. Air Waste Ma.*, 39, 672–695, <https://doi.org/10.1080/08940630.1989.10466554>, 1989.
- Logan, J. A.: Nitrogen oxides in the troposphere: Global and regional budgets, *J. Geophys. Res.-Oceans*, 88, 10785–10807, <https://doi.org/10.1029/JC088iC15p10785>, 1983.
- Logan, J. A., Prather, M. J., Wofsy, S. C., and McElroy, M. B.: Tropospheric chemistry: A global perspective, *J. Geophys. Res.-Oceans*, 86, 7210–7254, <https://doi.org/10.1029/JC086iC08p07210>, 1981.
- Ma, Y., Lu, K., Chou, C. C.-K., Li, X., and Zhang, Y.: Strong deviations from the NO–NO₂–O₃ photostationary state in the Pearl River Delta: Indications of active peroxy radical and chlorine radical chemistry, *Atmos. Environ.*, 163, 22–34, <https://doi.org/10.1016/j.atmosenv.2017.05.012>, 2017.
- Mannschreck, K., Gilge, S., Plass-Duelmer, C., Fricke, W., and Berresheim, H.: Assessment of the applicability of NO–NO₂–O₃ photostationary state to long-term measurements at the Hohenpeissenberg GAW Station, Germany, *Atmos. Chem. Phys.*, 4, 1265–1277, <https://doi.org/10.5194/acp-4-1265-2004>, 2004.
- Marno, D., Ernest, C., Hens, K., Javed, U., Klimach, T., Martinez, M., Rudolf, M., Lelieveld, J., and Harder, H.: Calibration of an airborne HO_x instrument using the All Pressure Altitude-based Calibrator for HO_x Experimentation (APACHE), *Atmos. Meas. Tech.*, 13, 2711–2731, <https://doi.org/10.5194/amt-13-2711-2020>, 2020.
- Murphy, J. G., Thornton, J. A., Wooldridge, P. J., Day, D. A., Rosen, R. S., Cantrell, C., Shetter, R. E., Lefer, B., and Cohen, R. C.: Measurements of the sum of HO₂NO₂ and CH₃O₂NO₂ in the remote troposphere, *Atmos. Chem. Phys.*, 4, 377–384, <https://doi.org/10.5194/acp-4-377-2004>, 2004.

- Nault, B. A., Garland, C., Pusede, S. E., Wooldridge, P. J., Ullmann, K., Hall, S. R., and Cohen, R. C.: Measurements of $\text{CH}_3\text{O}_2\text{NO}_2$ in the upper troposphere, *Atmos. Meas. Tech.*, 8, 987–997, <https://doi.org/10.5194/amt-8-987-2015>, 2015.
- Neuman, J., Huey, L., Ryerson, T., and Fahey, D.: Study of inlet materials for sampling atmospheric nitric acid, *Environ. Sci. Technol.*, 33, 1133–1136, <https://doi.org/10.1021/es980767f>, 1999.
- Novelli, A., Hens, K., Tatum Ernest, C., Kubistin, D., Regelin, E., Elste, T., Plass-Dülmer, C., Martinez, M., Lelieveld, J., and Harder, H.: Characterisation of an inlet pre-injector laser-induced fluorescence instrument for the measurement of atmospheric hydroxyl radicals, *Atmos. Meas. Tech.*, 7, 3413–3430, <https://doi.org/10.5194/amt-7-3413-2014>, 2014.
- Nussbaumer, C. M. and Cohen, R. C.: The Role of Temperature and NO_x in Ozone Trends in the Los Angeles Basin, *Environ. Sci. Technol.*, 54, 15652–15659, <https://doi.org/10.1021/acs.est.0c04910>, 2020.
- Nussbaumer, C. M., Tadic, I., Dienhart, D., Wang, N., Edtbauer, A., Ernle, L., Williams, J., Obersteiner, F., Gutiérrez-Álvarez, I., Harder, H., Lelieveld, J., and Fischer, H.: Measurement report: In situ observations of deep convection without lightning during the tropical cyclone Florence 2018, *Atmos. Chem. Phys.*, 21, 7933–7945, <https://doi.org/10.5194/acp-21-7933-2021>, 2021.
- Nuvolone, D., Petri, D., and Voller, F.: The effects of ozone on human health, *Environ. Sci. Pollut. R.*, 25, 8074–8088, <https://doi.org/10.1007/s11356-017-9239-3>, 2018.
- O’Keefe, A. and Deacon, D. A.: Cavity ring-down optical spectrometer for absorption measurements using pulsed laser sources, *Rev. Sci. Instrum.*, 59, 2544–2551, <https://doi.org/10.1063/1.1139895>, 1988.
- Phillips, G. J., Pouvesle, N., Thieser, J., Schuster, G., Axinte, R., Fischer, H., Williams, J., Lelieveld, J., and Crowley, J. N.: Peroxyacetyl nitrate (PAN) and peroxyacetic acid (PAA) measurements by iodide chemical ionisation mass spectrometry: first analysis of results in the boreal forest and implications for the measurement of PAN fluxes, *Atmos. Chem. Phys.*, 13, 1129–1139, <https://doi.org/10.5194/acp-13-1129-2013>, 2013.
- Pollack, I. B., Lerner, B. M., and Ryerson, T. B.: Evaluation of ultra-violet light-emitting diodes for detection of atmospheric NO_2 by photolysis-chemiluminescence, *J. Atmos. Chem.*, 65, 111–125, <https://doi.org/10.1007/s10874-011-9184-3>, 2010.
- Pusede, S. E., Steiner, A. L., and Cohen, R. C.: Temperature and recent trends in the chemistry of continental surface ozone, *Chem. Rev.*, 115, 3898–3918, <https://doi.org/10.1021/cr5006815>, 2015.
- Reed, C., Evans, M. J., Di Carlo, P., Lee, J. D., and Carpenter, L. J.: Interferences in photolytic NO_2 measurements: explanation for an apparent missing oxidant?, *Atmos. Chem. Phys.*, 16, 4707–4724, <https://doi.org/10.5194/acp-16-4707-2016>, 2016.
- Reidmiller, D. R., Jaffe, D. A., Fischer, E. V., and Finley, B.: Nitrogen oxides in the boundary layer and free troposphere at the Mt. Bachelor Observatory, *Atmos. Chem. Phys.*, 10, 6043–6062, <https://doi.org/10.5194/acp-10-6043-2010>, 2010.
- Ridley, B. and Howlett, L.: An instrument for nitric oxide measurements in the stratosphere, *Rev. Sci. Instrum.*, 45, 742–746, <https://doi.org/10.1063/1.1686726>, 1974.
- Ryerson, T., Williams, E., and Fehsenfeld, F.: An efficient photolysis system for fast-response NO_2 measurements, *J. Geophys. Res.-Atmos.*, 105, 26447–26461, <https://doi.org/10.1029/2000JD900389>, 2000.
- Sadanaga, Y., Fukumori, Y., Kobashi, T., Nagata, M., Takanaka, N., and Bandow, H.: Development of a selective light-emitting diode photolytic NO_2 converter for continuously measuring NO_2 in the atmosphere, *Anal. Chem.*, 82, 9234–9239, <https://doi.org/10.1021/ac101703z>, 2010.
- Sather, M. E., Slonecker, E. T., Kronmiller, K. G., Williams, D. D., Daughtrey, H., and Mathew, J.: Evaluation of short-term Ogawa passive, photolytic, and federal reference method sampling devices for nitrogen oxides in El Paso and Houston, Texas, *J. Environ. Monitor.*, 8, 558–563, <https://doi.org/10.1039/b601113f>, 2006.
- Schiller, C., Bozem, H., Gurk, C., Parchatka, U., Königstedt, R., Harris, G., Lelieveld, J., and Fischer, H.: Applications of quantum cascade lasers for sensitive trace gas measurements of CO , CH_4 , N_2O and HCHO , *Appl. Phys. B-Lasers O.*, 92, 419–430, 2008.
- Silvern, R., Jacob, D., Travis, K., Sherwen, T., Evans, M., Cohen, R., Laughner, J., Hall, S., Ullmann, K., Crounse, J., Wennberg, P. O., Peischl, J., and Pollack, I. B.: Observed NO/NO_2 ratios in the upper troposphere imply errors in $\text{NO}-\text{NO}_2-\text{O}_3$ cycling kinetics or an unaccounted NO_x reservoir, *Geophys. Res. Lett.*, 45, 4466–4474, <https://doi.org/10.1029/2018GL077728>, 2018.
- SphereOptics GmbH: Introduction Diffuse Reflecting Materials, available at: https://sphereoptics.de/en/product/introduction-diffuse-reflecting-materials/?gclid=EAIaIQobChMI9cGJkfh87AIVjql3Ch2jMQ0TEAAYASAAEgJSyvD_BwE (last access: 2 February 2021), 2017.
- Tadic, I.: Photochemical studies on low- and high- NO_x regimes with respect to ozone formation during AQABA and CAFE-Africa, PhD thesis, Mainz, Germany, 2021.
- Tadic, I., Crowley, J. N., Dienhart, D., Eger, P., Harder, H., Hottmann, B., Martinez, M., Parchatka, U., Paris, J.-D., Pozzer, A., Rohloff, R., Schuladen, J., Shenolikar, J., Tauer, S., Lelieveld, J., and Fischer, H.: Net ozone production and its relationship to nitrogen oxides and volatile organic compounds in the marine boundary layer around the Arabian Peninsula, *Atmos. Chem. Phys.*, 20, 6769–6787, <https://doi.org/10.5194/acp-20-6769-2020>, 2020.
- Tadic, I., Nussbaumer, C. M., Bohn, B., Harder, H., Marno, D., Martinez, M., Obersteiner, F., Parchatka, U., Pozzer, A., Rohloff, R., Zöger, M., Lelieveld, J., and Fischer, H.: Central role of nitric oxide in ozone production in the upper tropical troposphere over the Atlantic Ocean and western Africa, *Atmos. Chem. Phys.*, 21, 8195–8211, <https://doi.org/10.5194/acp-21-8195-2021>, 2021.
- Thornton, J. A., Wooldridge, P. J., and Cohen, R. C.: Atmospheric NO_2 : In situ laser-induced fluorescence detection at parts per trillion mixing ratios, *Anal. Chem.*, 72, 528–539, <https://doi.org/10.1021/ac9908905>, 2000.
- Travis, K. R., Jacob, D. J., Fisher, J. A., Kim, P. S., Marais, E. A., Zhu, L., Yu, K., Miller, C. C., Yantosca, R. M., Sulprizio, M. P., Thompson, A. M., Wennberg, P. O., Crounse, J. D., St. Clair, J. M., Cohen, R. C., Laughner, J. L., Dibb, J. E., Hall, S. R., Ullmann, K., Wolfe, G. M., Pollack, I. B., Peischl, J., Neuman, J. A., and Zhou, X.: Why do models overestimate surface ozone in the Southeast United States?, *Atmos. Chem. Phys.*, 16, 13561–13577, <https://doi.org/10.5194/acp-16-13561-2016>, 2016.
- Ventrillard, I., Gorroategi-Carbajo, P., and Romanini, D.: Part per trillion nitric oxide measurement by optical feedback cavity-

- enhanced absorption spectroscopy in the mid-infrared, *Appl. Phys. B-Lasers O.*, 123, 1–8, <https://doi.org/10.1007/s00340-017-6750-7>, 2017.
- Veres, P. R., Roberts, J. M., Wild, R. J., Edwards, P. M., Brown, S. S., Bates, T. S., Quinn, P. K., Johnson, J. E., Zamora, R. J., and de Gouw, J.: Peroxynitric acid (HO_2NO_2) measurements during the UBWOS 2013 and 2014 studies using iodide ion chemical ionization mass spectrometry, *Atmos. Chem. Phys.*, 15, 8101–8114, <https://doi.org/10.5194/acp-15-8101-2015>, 2015.
- Villena, G., Bejan, I., Kurtenbach, R., Wiesen, P., and Kleffmann, J.: Interferences of commercial NO_2 instruments in the urban atmosphere and in a smog chamber, *Atmos. Meas. Tech.*, 5, 149–159, <https://doi.org/10.5194/amt-5-149-2012>, 2012.
- Westfalen Gas Schweiz GmbH: Synth. Luft, KW frei T50 MFI, <https://shop.westfalen.com/ch/de/Home/Gase/Sondergase/Synthetische-Luft-KW-frei/p/S09110150>, last access: 26 March 2021.
- Winer, A. and Biermann, H.: Long pathlength differential optical absorption spectroscopy (DOAS) measurements of gaseous HONO, NO_2 and HCNO in the California South Coast Air Basin, *Res. Chem. Intermediat.*, 20, 423–445, 1994.
- Xu, Z., Wang, T., Xue, L., Louie, P. K., Luk, C. W., Gao, J., Wang, S., Chai, F., and Wang, W.: Evaluating the uncertainties of thermal catalytic conversion in measuring atmospheric nitrogen dioxide at four differently polluted sites in China, *Atmos. Environ.*, 76, 221–226, <https://doi.org/10.1016/j.atmosenv.2012.09.043>, 2013.
- Zahn, A., Weppner, J., Widmann, H., Schlote-Holubek, K., Burger, B., Kühner, T., and Franke, H.: A fast and precise chemiluminescence ozone detector for eddy flux and airborne application, *Atmos. Meas. Tech.*, 5, 363–375, <https://doi.org/10.5194/amt-5-363-2012>, 2012.
- Zheng, K., Zheng, C., Zhang, Y., Wang, Y., and Tittel, F. K.: Review of incoherent broadband cavity-enhanced absorption spectroscopy (IBBCEAS) for gas sensing, *Sensors*, 18, 3646, <https://doi.org/10.3390/s18113646>, 2018.

3.4 Photochemical production of formaldehyde and ozone across Europe

This chapter has been published in the journal *Atmospheric Chemistry & Physics* as a measurement report. I am the first author of this paper. I have analyzed all data presented, I have made the figures and I have prepared and revised the manuscript. The co-authors were involved in the presented research campaigns HUMPPA (Finland 2010), HOPE (Germany 2012) and CYPHEX (Cyprus 2014) and in proofreading the manuscript. Detailed author contributions can be found at the end of the paper in the section *Author contributions*.

How to cite: Nussbaumer, C. M., Crowley, J. N., Schuladen, J., Williams, J., Hafermann, S., Reiffs, A., Axinte, R., Harder, H., Ernest, C., Novelli, A., Sala, K., Martinez, M., Mallik, C., Tomsche, L., Plass-Dülmer, C., Bohn, B., Lelieveld, J., and Fischer, H.: Measurement report: Photochemical production and loss rates of formaldehyde and ozone across Europe, *Atmos. Chem. Phys.*, 21, 18413–18432, <https://doi.org/10.5194/acp-21-18413-2021>, **2021**.

submitted: 18 Aug 2021

published: 17 Dec 2021

The supplementary material for this publication can be found in Section 4.3.



Measurement report: Photochemical production and loss rates of formaldehyde and ozone across Europe

Clara M. Nussbaumer¹, John N. Crowley¹, Jan Schuladen¹, Jonathan Williams^{1,2}, Sascha Hafermann¹,
 Andreas Reiffs¹, Raoul Axinte¹, Hartwig Harder¹, Cheryl Ernest^{1,a}, Anna Novelli^{1,b}, Katrin Sala¹,
 Monica Martinez¹, Chinmay Mallik^{1,c}, Laura Tomsche^{1,d}, Christian Plass-Dülmer³, Birger Bohn⁴,
 Jos Lelieveld^{1,2}, and Horst Fischer¹

¹Department of Atmospheric Chemistry, Max Planck Institute for Chemistry, 55128 Mainz, Germany

²Climate and Atmosphere Research Center, The Cyprus Institute, Nicosia, Cyprus

³Meteorological Observatory Hohenpeissenberg (MOHp), German Meteorological Service,
 83282 Hohenpeissenberg, Germany

⁴Institute of Energy and Climate Research – Troposphere (IEK-8), Forschungszentrum Jülich GmbH,
 52428 Jülich, Germany

^anow at: Department of Neurology, University Medical Center of the Johannes Gutenberg University Mainz,
 55131 Mainz, Germany

^bnow at: Institute of Energy and Climate Research – Troposphere (IEK-8), Forschungszentrum Jülich GmbH,
 52428 Jülich, Germany

^cnow at: Department of Atmospheric Science, Central University of Rajasthan, Rajasthan 305817, India

^dnow at: Institute of Atmospheric Physics, German Aerospace Center,
 82234 Weßling-Oberpfaffenhofen, Germany

Correspondence: Clara M. Nussbaumer (clara.nussbaumer@mpic.de)

Received: 18 August 2021 – Discussion started: 10 September 2021

Revised: 26 October 2021 – Accepted: 4 November 2021 – Published: 17 December 2021

Abstract. Various atmospheric sources and sinks regulate the abundance of tropospheric formaldehyde (HCHO), which is an important trace gas impacting the HO_x ($\equiv \text{HO}_2 + \text{OH}$) budget and the concentration of ozone (O_3). In this study, we present the formation and destruction terms of ambient HCHO and O_3 calculated from in situ observations of various atmospheric trace gases measured at three different sites across Europe during summertime. These include a coastal site in Cyprus, in the scope of the Cyprus Photochemistry Experiment (CYPHEX) in 2014, a mountain site in southern Germany, as part of the Hohenpeissenberg Photochemistry Experiment (HOPE) in 2012, and a forested site in Finland, where measurements were performed during the Hyytiälä United Measurements of Photochemistry and Particles (HUMPPA) campaign in 2010. We show that, at all three sites, formaldehyde production from the OH oxidation of methane (CH_4), acetaldehyde (CH_3CHO), isoprene (C_5H_8) and methanol (CH_3OH) can almost completely balance the observed loss via photolysis, OH oxidation and dry deposition. Ozone chemistry is clearly controlled by nitrogen oxides ($\text{NO}_x \equiv \text{NO} + \text{NO}_2$) that include O_3 production from NO_2 photolysis and O_3 loss via the reaction with NO. Finally, we use the HCHO budget calculations to determine whether net ozone production is limited by the availability of VOCs (volatile organic compounds; VOC-limited regime) or NO_x (NO_x -limited regime). At the mountain site in Germany, O_3 production is VOC limited, whereas it is NO_x limited at the coastal site in Cyprus. The forested site in Finland is in the transition regime.

1 Introduction

Formaldehyde (HCHO) is an important atmospheric trace gas which provides insight into various photochemical processes taking place in the Earth's atmosphere. It has both anthropogenic sources, such as industrial and vehicle emissions, and natural sources including, for example, biomass burning or volatile organic compound (VOC) precursors, with natural sources dominating in remote locations (Luecken et al., 2018; Anderson et al., 2017; Stickler et al., 2006; Wittrock et al., 2006; Lowe and Schmidt, 1983). The majority of these HCHO sources is secondary, and due to its short lifetime, the atmospheric transport of HCHO from primary (direct) emissions (e.g., biomass burning or industry) to remote locations can be mostly neglected (Fortems-Cheiney et al., 2012; Vigouroux et al., 2009; Anderson et al., 2017). Loss processes of HCHO include deposition, reaction with OH and photolysis yielding mainly HO₂, CO and H₂ (Anderson et al., 2017). HCHO production paths are more diverse and include oxidation processes of almost any VOC, including acetone (CH₃COCH₃), methane (CH₄), acetaldehyde (CH₃CHO), methanol (CH₃OH), isoprene (C₅H₈), methyl hydroperoxide (CH₃OOH), ethene (C₂H₄) (these selected species are included in this study due to the availability of measurement data) and many more, the majority of which are initiated by the OH radical during the day (Stickler et al., 2006; Wittrock et al., 2006). Net production processes of formaldehyde, therefore, influence the HO_x (HO_x ≡ OH + HO₂) budget, which, in turn, controls the atmospheric oxidizing capacity (Luecken et al., 2018). This includes the regulation of the atmospheric ozone (O₃) abundance, a trace gas with adverse health effects for humans, animals and plants, leading to cardiovascular and respiratory diseases and the decrease in life expectancy (Nuvolone et al., 2018; Lippmann, 1989). It is, therefore, important to understand the processes influencing and contributing to HCHO and O₃ formation and loss processes in the Earth's atmosphere (see also Figs. 1 and 2 for an overview of the reactions considered in this study).

Previous studies have investigated the processes contributing to HCHO production from secondary sources. Palmer et al. (2003) identified isoprene, methane and methanol to be the main HCHO precursors over the United States of America, contributing over 80 % in the GEOS-CHEM model (Goddard Earth Observing System global 3-D model of tropospheric chemistry). Anderson et al. (2017) evaluated HCHO concentrations in the tropical western Pacific and found methane and acetaldehyde to be the main precursors of HCHO, based on box model simulations. Fried et al. (2011) identified methane to be the main precursor of HCHO in remote regions, based on model simulations and measurements during the INTEx-B campaign (Intercontinental Transport Experiment – Phase B) in 2006. Sumner et al. (2001) investigated the HCHO budget at a forest in Pellston, Michigan (USA), based on observations in the scope of PROPHET

(Program for Research on Oxidants: Photochemistry, Emission and Transport) in 1998. They identified isoprene to be the main HCHO precursor, contributing around 80 %. Dienhart et al. (2021) investigated the relationship between OH reactivity and HCHO production rates during the shipborne campaign AQABA (Air Quality and Climate Change in the Arabian Basin) around the Arabian Peninsula in 2017, which they found to be highest in polluted areas, suggesting a high diversity of HCHO precursors. Kaiser et al. (2015) studied OH reactivities and HCHO concentrations in the Po Valley, based on zeppelin measurements during the research campaign PEGASOS (Pan-European Gas-AeroSols Climate Interaction Study) in 2012 in comparison with model simulations, and attributed the discrepancies to possible primary HCHO emissions from agriculture.

Tropospheric ozone chemistry is dependent on the O₃ precursors NO_x (NO_x ≡ NO + NO₂) and volatile organic compounds (VOCs). Depending on the ambient concentrations of NO_x and VOCs, net ozone formation can either be NO_x or VOC limited. A NO_x limitation is usually dominant for low NO_x concentrations in which increasing NO_x leads to an increase in O₃ formation. For high NO_x concentrations, ozone formation is usually VOC limited, and an increase in ambient NO_x reduces O₃ formation through loss of HO_x as OH is converted to HNO₃ (Pusede et al., 2015; Nussbaumer and Cohen, 2020). Consequently, changes in ambient NO_x concentrations can either increase or decrease O₃ or – at a transition between both regimes – have only a weak net effect on the O₃ production. In urban environments, the chemical regime can be characterized using the weekend effect, which describes the ozone response to decreasing NO_x emissions at weekends, as reported by Pusede and Cohen (2012), Nussbaumer and Cohen (2020), Pires (2012), Wang et al. (2014) and many more (Levitt and Chock, 1976; Seguel et al., 2012; Sadanaga et al., 2011). Another measure for identifying the prevailing chemical regime is the ratio of HCHO and NO₂, which has been determined via satellite measurements in various studies (Sillman, 1995; Jin et al., 2020; Martin et al., 2004; Duncan et al., 2010; Jin and Holloway, 2015). Sillman (1995) initially suggested a threshold of 0.28 for the ratio HCHO/NO_y (NO_y is here the sum of NO_x, HNO₃, peroxyacetyl nitrates and alkyl nitrates), below which the chemistry is VOC limited, based on model simulations for Lake Michigan and the northeastern corridor (USA). Martin et al. (2004) investigated the ratio of the HCHO/NO₂ column based on satellite observations and found a threshold of 1. This is in agreement with findings from Duncan et al. (2010), who suggested a threshold of 1 for a VOC-limited regime, a threshold of 2 for a NO_x-limited regime and a transition in between both using remote sensing. Schroeder et al. (2017) present in situ measurements of HCHO and NO₂ to determine the dominant regime and point out that exact thresholds are geographically variable due to locally different atmospheric composition and ambient conditions, such as VOC variety or humidity.

In this study, we evaluate the formaldehyde and ozone budget during the field experiment CYPHEX (Cyprus Photochemistry Experiment), which took place in July 2014 at a coastal site in Cyprus (Ineia), based on in situ trace gas observations of NO, NO₂, O₃, OH, HO₂, CH₄, CH₃OH (methanol), C₅H₈ (isoprene), CH₃CHO (acetaldehyde), CH₃COCH₃ (acetone), CH₃OOH (methyl hydroperoxide), C₂H₄ (ethene), CH₃SCH₃ (DMS) and HCHO (Derstroff et al., 2017; Meusel et al., 2016; Mallik et al., 2018). We compare the results with two other field campaigns in central and northern Europe, namely the Hohenpeißenberg Photochemistry Experiment (HOPE 2012; Novelli et al., 2017) at a mountain site in Germany and the Hyytiälä United Measurements of Photochemistry and Particles (HUMPPA 2010; Williams et al., 2011) at a boreal forest site in Finland. Only a few studies have evaluated the HCHO budget mainly through model simulations. To our knowledge, there is only one study, by Sumner et al. (2001), that has previously presented HCHO budget calculations from in situ trace gas observations in the USA in 1998. We are first to present HCHO budget calculations from in situ measurements across Europe and show that, in all three locations, HCHO production can be predominantly accounted for by the oxidation of methane, methanol, acetaldehyde and isoprene.

2 Observations and methods

2.1 HCHO chemistry calculations

Figure 1 shows an overview of the main production and loss processes for formaldehyde which we consider in this study and for which measurements were obtained during the field campaign CYPHEX (see Sect. 2.3.1 for further details). The relationships we derive in this study are based on boundary layer conditions, and we, therefore, assume no relevant intrusion from higher altitudes. Acetone and methane can form methyl radicals (CH₃) through oxidation by OH or photolysis, which are subsequently oxidized to methyl peroxy radicals (CH₃O₂) by molecular oxygen (O₂). Another pathway yielding CH₃O₂ is the OH oxidation of acetaldehyde which forms CH₃C(O) in the first step and which can then be oxidized to CH₃C(O)O₂ when O₂ is present. CH₃C(O)O₂ yields CH₃O₂ through a reaction with nitric oxide (NO) or the hydroperoxyl radical (HO₂) via CH₃CO₂. The CH₃O₂ yield from the reaction of CH₃C(O)O₂ with HO₂ is approximately 50 % (*k_c*). Other reaction pathways result in the formation of CH₃C(O)OH (*k_a*) and CH₃C(O)OOH (*k_b*; IUPAC Task Group on Atmospheric Chemical Kinetic Data Evaluation, 2019). We calculate the overall fraction $\alpha_{\text{CH}_3\text{CHO}}$ of acetaldehyde oxidation that results in CH₃O₂ formation via Eq. (1).

$$\alpha_{\text{CH}_3\text{CHO}} = \frac{k_{\text{CH}_3\text{C(O)O}_2+\text{NO}} \times [\text{NO}] + k_{\text{c}} \times [\text{HO}_2]}{k_{\text{CH}_3\text{C(O)O}_2+\text{NO}} \times [\text{NO}] + k_{\text{a}} \times [\text{HO}_2] + k_{\text{b}} \times [\text{HO}_2] + k_{\text{c}} \times [\text{HO}_2]}. \quad (1)$$

Additionally, methyl hydroperoxide (CH₃OOH) forms CH₃O₂ via OH oxidation (60 %; or reacts directly to HCHO via photolysis or OH-initiated oxidation, 40 %; IUPAC Task Group on Atmospheric Chemical Kinetic Data Evaluation, 2007). CH₃O₂ can then either react with HO₂ to form CH₃OOH or yield HCHO through a reaction with NO or OH via CH₃O (Anderson et al., 2017; Stickler et al., 2006; Lowe and Schmidt, 1983; Fittschen et al., 2014). The importance of the CH₃O₂ loss via OH in remote locations has recently been shown in several studies, and the reaction primarily yields HCHO (Lightfoot et al., 1992; Assaf et al., 2017, 2016; Fittschen et al., 2014; Yan et al., 2016). For simplification, we assume this yield to be 100 %, which slightly increases the uncertainty of the calculation but is negligible given the small fraction of CH₃O₂ that reacts with OH (< 10 % for CYPHEX). In our study, we use the rate constant *k_{CH3O2+OH}* recommended by the IUPAC Task Group on Atmospheric Chemical Kinetic Data Evaluation (2017). Table S1 in the Supplement gives an overview of all rate constants used in this study, most of which were taken from IUPAC Task Group on Atmospheric Chemical Kinetic Data Evaluation (2021). The fraction of CH₃O₂ that forms HCHO ($\alpha_{\text{CH}_3\text{O}_2}$) is dependent on the ambient concentrations of HO₂, NO and OH and can be calculated via Eq. (2). CH₃O₂ loss via self-reaction is negligibly small and, therefore, not included. The reaction with NO₂ forming CH₃O₂NO₂ can also be excluded due to its thermal instability in the boundary layer.

$$\alpha_{\text{CH}_3\text{O}_2} = \frac{k_{\text{CH}_3\text{O}_2+\text{NO}} \times [\text{NO}] + k_{\text{CH}_3\text{O}_2+\text{OH}} \times [\text{OH}]}{k_{\text{CH}_3\text{O}_2+\text{NO}} \times [\text{NO}] + k_{\text{CH}_3\text{O}_2+\text{OH}} \times [\text{OH}] + k_{\text{CH}_3\text{O}_2+\text{HO}_2} \times [\text{HO}_2]}. \quad (2)$$

Isoprene oxidation results in the formation of HCHO through the intermediate products methyl vinyl ketone and methacrolein, as described by Wolfe et al. (2016). The HCHO yield from isoprene (α_{Isoprene}) is dependent on the ambient NO concentration and varies between around 30 % for low NO_x and 60 % for high NO_x (RO₂ reacts primarily with NO; Atkinson et al., 2006; Palmer et al., 2003; Sumner et al., 2001). We calculate the HCHO yield via Eq. (3) and estimate [HO₂] ≈ [RO₂], as suggested by Sumner et al. (2001). This assumption is justified when looking at O₃ production (*P*(O₃)) terms. *P*(O₃) can either be calculated via the photolytic reaction of NO₂, as presented in Sect. 2.2, or via the reaction of HO₂ or RO₂ with NO. We equate the two terms, using the rate constant of the reaction of NO and CH₃O₂ as estimate for the reaction of NO and RO₂, and calculate RO₂. We show the diurnal profiles of HO₂ and calculate RO₂ in Fig. S1a in the Supplement. Conversely, we calculate *P*(O₃) for both cases, equating RO₂ to HO₂, which show close agreement, and can be seen in Fig. S1b. This is also confirmed by findings from Crowley et al. (2018) (presented in Fig. 9), based on model simulations of HO₂ and RO₂ during HUMPPA. The yield can vary between 34 % (in the absence

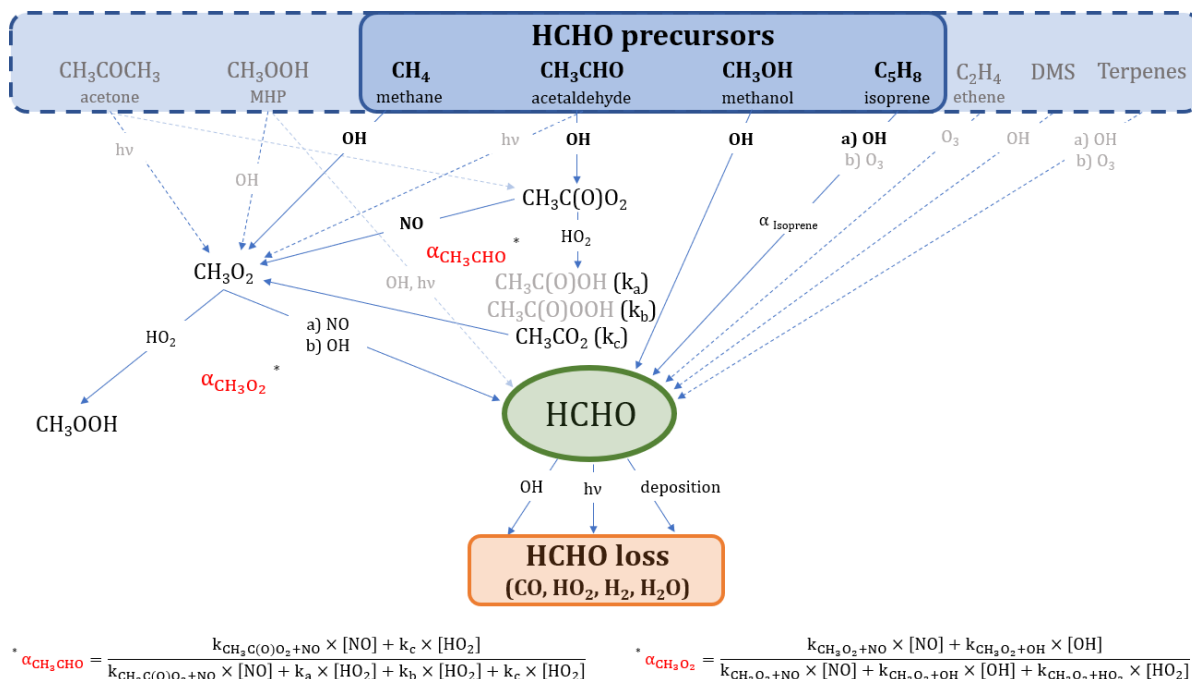


Figure 1. Overview of the chemical and photolytic reactions which lead to HCHO production and loss, considering the trace gases measured during the CYPHEX field experiment. The black and bold font identifies the species which contribute mainly ($\sim 80\%$) to HCHO formation according to the findings in this study. For a better overview, we have omitted intermediate steps with a 100 % yield which are, instead, described in the main text.

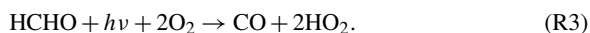
of NO) and 57 % (when NO chemistry dominates the fate of the RO₂ formed), according to Eq. (3), which was originally determined experimentally by Miyoshi et al. (1994). We discuss the effects of the threshold values in Sect. 3.1. C₅H₈(OH)O₂ is the peroxy radical resulting from isoprene oxidation and has six relevant isomers which can undergo multiple reactions yielding HCHO and many other products (Wennberg et al., 2018; Schwantes et al., 2020). Additionally, the formation of HCHO from isoprene does not occur instantaneously (as, for example, from methane or other VOC), but is likely time dependent. However, the consideration of this time-dependent formation and the detailed evaluation of the reactions paths from each peroxy radical isomer is beyond the scope of this study, and we, therefore, adapt the methodology presented by Sumner et al. (2001) to estimate the HCHO production from isoprene.

$$\alpha_{\text{Isoprene}} = 0.34 + 0.23 \times \left(\frac{k_{\text{C}_5\text{H}_8(\text{OH})\text{O}_2 + \text{NO} \times [\text{NO}]}{k_{\text{C}_5\text{H}_8(\text{OH})\text{O}_2 + \text{NO} \times [\text{NO}] + k_{\text{C}_5\text{H}_8(\text{OH})\text{O}_2 + \text{HO}_2 \times [\text{HO}_2] + k_{\text{C}_5\text{H}_8(\text{OH})\text{O}_2 + \text{RO}_2 \times [\text{RO}_2]} \right). \quad (3)$$

Methanol reacts with OH yielding HCHO via CH₂OH and CH₃O and following oxidation by O₂ (Anderson et al., 2017; Stickler et al., 2006). Ethene is a precursor to HCHO through

OH oxidation or ozonolysis (Alam et al., 2011; Atkinson et al., 2006). A potential source of HCHO in marine environments is dimethyl sulfide (DMS) via OH oxidation (Ayers et al., 1997; Urbanski et al., 1997). Terpenes, such as limonene or α -/ β -pinene emitted from plants, can additionally be HCHO sources, as described by Lee et al. (2006).

Reactions (R1)–(R3) present the chemical loss processes of HCHO through OH oxidation and two different photolysis pathways. In addition, HCHO dry deposition – the uptake of HCHO by the Earth’s surface – plays a role in HCHO loss, particularly during the night (Anderson et al., 2017; Posanzini et al., 2002; Sumner et al., 2001; Wesely and Hicks, 2000). While HCHO loss can also occur via wet deposition, as, for example, described by Seyfioglu et al. (2006), or via liquid-phase reactions in cloud droplets, as shown by Franco et al. (2021), this study investigates summertime campaigns without significant precipitation.



We will show in the scope of this work that reactions of methane, acetaldehyde, methanol and isoprene with OH almost completely account for HCHO production in the envi-

ronments considered in this paper across Europe. We have highlighted these pathways in Fig. 1 in a black and bold font. Equations (4) and (5) show the calculation of the basic production $P(\text{HCHO})_{\text{basic}}$ (compared to the reactions shown in Fig. 1) and the loss $L(\text{HCHO})$ terms. The k values represent the rate coefficients, $j(\text{HCHO})$ is the summed photolysis frequency for Reactions (R2) and (R3), v_d describes the dry deposition velocity in centimeters per second (cm s^{-1}) and BLH is the boundary layer height in centimeters.

$$\begin{aligned}
 P(\text{HCHO})_{\text{basic}} &= P_{\text{CH}_4+\text{OH}} + P_{\text{CH}_3\text{CHO}+\text{OH}} + P_{\text{CH}_3\text{OH}+\text{OH}} + P_{\text{C}_5\text{H}_8+\text{OH}} \\
 &= [\text{OH}] \times ([\text{CH}_4] \times k_{\text{CH}_4+\text{OH}} \times \alpha_{\text{CH}_3\text{O}_2} + [\text{CH}_3\text{CHO}] \\
 &\quad \times k_{\text{CH}_3\text{CHO}+\text{OH}} \times \alpha_{\text{CH}_3\text{O}_2} \times \alpha_{\text{CH}_3\text{CHO}} + [\text{CH}_3\text{OH}] \\
 &\quad \times k_{\text{CH}_3\text{OH}+\text{OH}} + [\text{C}_5\text{H}_8] \times k_{\text{C}_5\text{H}_8+\text{OH}} \times \alpha_{\text{Isoprene}}). \quad (4)
 \end{aligned}$$

$$\begin{aligned}
 L(\text{HCHO}) &= L_{\text{HCHO}+\text{OH}} + L_{\text{HCHO}+h\nu} + L_{\text{deposition}} \\
 &= [\text{HCHO}] \times \left([\text{OH}] \times k_{\text{HCHO}+\text{OH}} \right. \\
 &\quad \left. + j(\text{HCHO}) + \frac{v_d(\text{HCHO})}{\text{BLH}} \right). \quad (5)
 \end{aligned}$$

Changes in the HCHO concentration are represented by Eq. (6), which include the production and loss from Eqs. (4)–(5), a transport term $T(\text{HCHO})$, such as advection or entrainment (can be positive or negative), and a term for primary emissions (Fischer et al., 2019).

$$\frac{d[\text{HCHO}]}{dt} = P(\text{HCHO})_{\text{basic}} - L(\text{HCHO}) + T(\text{HCHO}) + P_{\text{emission}}. \quad (6)$$

2.2 O₃ chemistry calculations

Figure 2 presents the main processes contributing to O₃ formation and loss. The only significant chemical source of tropospheric O₃ is the photolysis of nitrogen dioxide (NO₂), which is converted to NO and O(³P) under the influence of sunlight. The reaction of O(³P) with molecular oxygen (O₂) subsequently yields O₃ (Jacob, 1999). NO₂, in turn, is generated from the oxidation of NO by ozone or peroxy radicals (HO₂ and RO₂; Pusede et al., 2015).

Ozone loss processes include the reaction with NO forming NO₂, conversion with OH or HO₂ to HO₂ and OH, respectively, deposition processes and photolysis. O₃ photolysis yields O(¹D), which is deactivated to O(³P) (and then O₃) via collision with nitrogen (N₂) and oxygen (O₂). O₃ loss occurs when O(¹D) reacts with water to form OH. The fraction of this reaction is presented by $\alpha_{\text{O}^1\text{D}}$ as shown in Eq. (7) (Bozem et al., 2017). The reaction of O₃ and NO₂ to form NO₃ could potentially yield a net loss of O₃ when being photolyzed back to NO_x. However, only around 10 % of the NO₃ photolysis leads to NO formation (which results

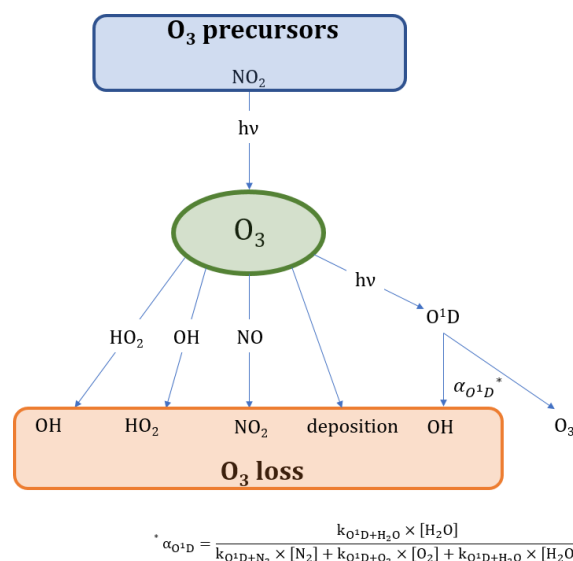


Figure 2. Overview of the chemical and photolytic reactions which lead to O₃ production and loss.

in a O₃ net loss; Stockwell and Calvert, 1983). Additionally, the reaction is likely negligible during the day, as O₃ reacts much more rapidly with NO.

$$\alpha_{\text{O}^1\text{D}} = \frac{k_{\text{O}^1\text{D}+\text{H}_2\text{O}} \times [\text{H}_2\text{O}]}{k_{\text{O}^1\text{D}+\text{N}_2} \times [\text{N}_2] + k_{\text{O}^1\text{D}+\text{O}_2} \times [\text{O}_2] + k_{\text{O}^1\text{D}+\text{H}_2\text{O}} \times [\text{H}_2\text{O}]}. \quad (7)$$

Equations (8) and (9) present the calculations for O₃ production and loss.

$$\begin{aligned}
 P(\text{O}_3) &= P_{\text{NO}_2+h\nu} = [\text{NO}_2] \times j(\text{NO}_2) \quad (8) \\
 L(\text{O}_3) &= L_{\text{O}_3+\text{NO}} + L_{\text{O}_3+\text{OH}} + L_{\text{O}_3+\text{HO}_2} \\
 &\quad + L_{\text{O}_3+h\nu} + L_{\text{deposition}} \\
 &= [\text{O}_3] \times \left([\text{NO}] \times k_{\text{O}_3+\text{NO}} + [\text{OH}] \times k_{\text{O}_3+\text{OH}} \right. \\
 &\quad \left. + [\text{HO}_2] \times k_{\text{O}_3+\text{HO}_2} + j(\text{O}^1\text{D}) \times \alpha_{\text{O}^1\text{D}} + \frac{v_d(\text{O}_3)}{\text{BLH}} \right). \quad (9)
 \end{aligned}$$

As for HCHO, net changes in O₃ are represented by production, loss and a transport term (either positive or negative), as shown in Eq. (10).

$$\frac{d[\text{O}_3]}{dt} = P(\text{O}_3) - L(\text{O}_3) + T(\text{O}_3). \quad (10)$$

2.3 Field experiments

We have analyzed trace gases and further measurement parameters with regard to the HCHO and O₃ budget at three different measurement sites across Europe, which are located in Cyprus (CYPHEX campaign, 2014), southern Ger-

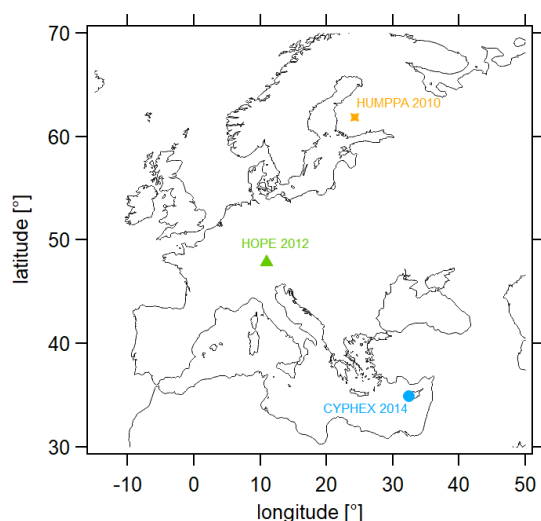


Figure 3. Geographic locations of the measurement sites included in this analysis. CYPHEX – 34.96° N, 32.38° E, 650 m.a.s.l. (above sea level) and UTC+128 min (mean local time); HOPE – 47.80° N, 11.01° E, 980 m.a.s.l. and UTC+44 min; HUMPPA – 61.85° N, 24.28° E, 181 m.a.s.l. and UTC+96 min.

many (HOPE campaign, 2012) and Finland (HUMPPA campaign, 2010). Their geographic locations are shown in Fig. 3. We provide details on each campaign in the following sections. Please note that all times are in UTC (coordinated universal time). The time difference between 12:00 UTC and mean local noon is UTC+128 min for Cyprus, UTC+44 min for Germany and UTC+96 min for Finland (Fischer et al., 2019).

2.3.1 CYPHEX campaign in 2014

The Cyprus Photochemistry Experiment (CYPHEX) took place in Ineia, Cyprus, in July and August 2014. The measurement site was situated on a hilltop 650 m.a.s.l. (34.96° N, 32.38° E) in a remote location, with low population in the surrounding areas. The distance to the coastline of the Mediterranean Sea is approximately 10 km in the north and in the west. A detailed description of the measurement site can be found in Derstroff et al. (2017), Meusel et al. (2016) and Mallik et al. (2018). In this study, we consider the campaign days for which the trace gas measurements were available simultaneously, which is the time period 22–31 July 2014. NO and NO₂ were measured via photolytic chemiluminescence (detector from ECO PHYSICS AG CLD 790 SR, Dürnten, Switzerland, and photolytic converter from Droplet Measurement Technologies, Boulder, CO, USA) with a total uncertainty of 20 % and 30 % and a detection limit of 5 and 20 pptv (parts per trillion by volume), respectively (Hosaynali Beygi et al., 2011; Tadic et al., 2020). O₃ was measured via UV photometry (model 49 O₃ analyzer, Thermo

Environmental Instruments, USA) with a detection limit of 2 ppbv (parts per billion by volume) and a total uncertainty of 5 %. OH and HO₂ were measured via laser-induced fluorescence spectroscopy with the custom-built HORUS (HydrOxyl Radical measurement Unit based on fluorescence Spectroscopy) instrument (accuracy of 28.5 % and 36 % and a detection limit of 1×10^6 molec. cm^{−3} and 0.8 pptv, respectively; Marno et al., 2020; Novelli et al., 2014). HCHO was measured via the Hantzsch method with a commercial instrument (Aero-Laser GmbH, model AL 4021, Garmisch-Partenkirchen, Germany) with a detection limit of 38 pptv and a total uncertainty of 16 % (Kormann et al., 2003). C₂H₄ and CH₄ were determined via gas chromatography flame ionization detection (GC 5000 VOC, AMA Instruments GmbH, Ulm, Germany). CH₄ measurements had a detection limit of 20 ppbv and a total uncertainty of 2 %, and C₂H₄ measurements had a detection limit of 1–8 pptv and a total uncertainty of 10 % (Sobanski et al., 2016; Mallik et al., 2018). Isoprene was measured via gas chromatography mass spectrometry (MSD 5973, Agilent Technologies, Inc., Böblingen, Germany) with a detection limit of 1 pptv and a total uncertainty of 14.5 % (Derstroff et al., 2017). Oxygenated VOC (OVOC) was measured via proton transfer reaction time-of-flight mass spectrometry (PTR-TOF-MS; Ionicon Analytik GmbH, Innsbruck, Austria; CH₃OH – 242 pptv limit of detection (LOD) and 37 % total uncertainty (TU); CH₃COCH₃ – 97 pptv LOD and 10 % TU; CH₃CHO – 85 pptv LOD and 22 % TU; DMS – 18 pptv LOD and 12 % TU; the TU is 4 %–7 % higher for a relative humidity below 25 %; Veres et al., 2013; Graus et al., 2010). CH₃OOH was measured via high-performance liquid chromatography with a detection limit of 25 pptv and a total uncertainty of 9 %. Photolysis frequencies were determined with a single monochromator spectral radiometer (Meteorologie Consult GmbH, Königstein, Germany) with a total uncertainty of around 10 %. The photolysis frequencies for acetaldehyde $j(\text{CH}_3\text{CHO})$ and formaldehyde $j(\text{HCHO})$ were determined via parameterizations based on $j(\text{NO}_2)$ and $j(\text{O}^1\text{D})$, according to Eq. (S1) in the Supplement, with the coefficients presented in Table S2. The latter were derived from least squares fits to photolysis frequencies from a large set of spectroradiometer measurements at Jülich, Germany (Bohn et al., 2008), under all weather conditions and were originally derived for the HUMPPA campaign. In this work, more recent quantum yields for the HCHO photolysis as recommended by IUPAC (2013) were used with an estimated uncertainty of 20 %. An example for the performance of the parameterization is shown in Fig. S2. An overview of all measured trace gases, including the measurement uncertainty and the time resolution of the data used in this study, can be found in Table S3. For the point-by-point calculations, the data were interpolated to the OH time stamp with a 4 min time resolution. All stated detection limits refer to the time resolution shown in Table S3.

2.3.2 HOPE campaign in 2012

The Hohenpeißenberg Photochemistry Experiment (HOPE) took place from June to September 2012 in Hohenpeißenberg, Germany at the Global Atmospheric Watch meteorological observatory (47.80° N, 11.01° E). The measurement location was situated on a hilltop, 980 m a.s.l., in a remote and vegetated area. More details on the campaign and the site location can be found in Novelli et al. (2017). O₃, HCHO, OH and HO₂ were measured with the same methods as described for the CYPHEX campaign in Sect. 2.3.1. NO and NO₂ were measured via (photolysis) chemiluminescence by the German Weather Service, with an estimated uncertainty of 10 %. CH₄ was measured via GC-FID (gas chromatography–flame ionization detector). Isoprene and OVOC were determined via a custom-built GC (Agilent Technologies, Inc.) FID/MS (mass spectrometry) system (Novelli et al., 2017; Werner et al., 2013). $j(\text{NO}_2)$ and $j(\text{O}^1\text{D})$ were measured with filter radiometers (Meteo-rologie Consult GmbH, Königstein, Germany) with an uncertainty of 10 % (Bohn et al., 2008). $j(\text{HCHO})$ was determined via parameterization (Sect. 2.3.1). BLH (boundary layer height) measurements were not performed and instead adopted from Fischer et al. (2019), which are 1500 m for daytime ($j(\text{NO}_2) > 10^{-3} \text{ s}^{-1}$) and 200 m for nighttime ($j(\text{NO}_2) < 10^{-3} \text{ s}^{-1}$). These values were derived from BLH measurements at other locations during summertime, including the CYPHEX and the HUMPPA measurement site, and at a site in central Germany situated at a comparable altitude. We assume that this estimate increases the uncertainty from 20 % (BLH measurements) to 30 %. We determined the deposition velocity v_d from the HCHO nighttime loss, as previously performed by Fischer et al. (2019), for H₂O₂. The loss rate coefficient k_d was determined from the [HCHO] decrease from 21:00–01:30 UTC divided by the average HCHO concentration [HCHO]_{av} during this time interval. Multiplication with the nighttime BLH (200 m) then yielded the deposition velocity according to Eq. (11). The HCHO loss via deposition during nighttime is independent of the BLH (see Eqs. 5 and 11).

$$v_d = \frac{k_{d,\text{night}} \times \text{BLH}_{\text{night}}}{x} = \frac{\frac{d[\text{HCHO}]}{dt}}{[\text{HCHO}]_{\text{av}} \times x} \times \text{BLH}_{\text{night}}. \quad (11)$$

Please note that v_d derived this way represents a lower limit of the nighttime loss rate, as HCHO could be formed from NO₃ and O₃ chemistry (for example, from ozone and isoprene) at night (Crowley et al., 2018). The factor x considers the inconsistent mixing of the boundary layer at night, for which x was 2, assuming a linear gradient between the top and the bottom of the boundary layer. During the day, x equaled 1 (Shepson et al., 1992; Fischer et al., 2019). As we determined the loss rate from the nighttime decrease in HCHO, the daytime deposition velocity was twice the nighttime deposition velocity according to Eq. (11), which

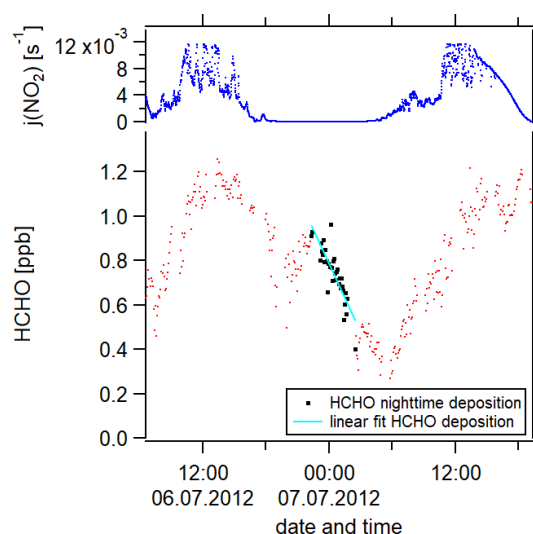


Figure 4. The determination of the deposition velocity is based on the HCHO nighttime loss, which is here exemplarily shown for 1 night during the campaign HOPE (2012) in Hohenpeißenberg, southern Germany.

gives $v_d(\text{day}) = 0.94 \text{ cm s}^{-1}$ and $v_d(\text{night}) = 0.47 \text{ cm s}^{-1}$. Literature values for daytime deposition velocities range between 0.36 and 1.5 cm s^{-1} and for nighttime between 0.18 and 0.65 cm s^{-1} (Sumner et al., 2001; Stickler et al., 2007; DiGangi et al., 2011; Ayers et al., 1997). We, therefore, consider our calculation to yield reasonable estimates.

We have performed this calculation for 9 nights. Figure 4 exemplarily shows the nighttime loss of HCHO for 1 night during the HOPE campaign. Red data points represent the HCHO mixing ratios, the black color highlights the data points which we included in our analysis (nighttime HCHO loss) and the cyan line is the linear fit of these data points. An overview of the nights thus analyzed can be found in Fig. S3b. The uncertainty of each calculation results from the single uncertainties of $\frac{d[\text{HCHO}]}{dt}$, [HCHO]_{av} and the nighttime BLH. The uncertainty of $\frac{d[\text{HCHO}]}{dt}$ is composed of the HCHO measurement uncertainty (16 %) and the uncertainty of the fit (30 % upper limit) with the latter dominating. The uncertainty of [HCHO]_{av} is based on the HCHO measurement uncertainty and the HCHO averaging (20 % upper limit). Again, the uncertainty of the averaging prevails over the measurement uncertainty. The uncertainty of the BLH is 30 %. Gaussian error propagation gives an overall uncertainty of $\sqrt{30\%^2 + 30\%^2 + 20\%^2} = 47\%$ from the calculation. Besides the uncertainty resulting from the calculation, an additional uncertainty arises from the atmospheric variability which describes ambient, instrumentally independent variations in the considered trace gases and parameters caused by, for example, atmospheric turbulence. The uncertainty from the atmospheric variability represented by the 1σ stan-

dard deviation of the mean over the considered 9 nights is 54 %, which exceeds the uncertainty from the calculation. We, therefore, estimate the uncertainty of v_d to be 54 %. Please note that, in our uncertainty analysis, we consider the arising statistical errors but not the systematic errors which are not quantifiable but could potentially increase the overall uncertainty. An overview of all uncertainties and the time resolution of the measured trace gases can be found in Table S3. Absolute H₂O concentrations were estimated from the measured relative humidity via the Magnus formula over water. Please note that some trace gases were not available simultaneously or only for a short overlap. We, therefore, present the averaged diurnal profiles.

2.3.3 HUMPPA campaign in 2010

The Hyytiälä United Measurements of Photochemistry and Particles (HUMPPA) campaign took place in July and August 2010 at SMEAR II (Station for Measuring Ecosystem–Atmosphere Relation) in Hyytiälä, Finland (61.85° N, 24.28° E, 181 m a.s.l.). The site is located in a remote area in a boreal forest. A detailed description of the campaign can be found in Williams et al. (2011). The measurement methods for NO_x, O₃, HCHO and CH₄ were the same as those presented for the CYPHEX campaign. CH₃OH was measured via a cold trap PTR-MS with a detection limit of around 50 pptv (integration time of 5 min). Acetaldehyde was measured via PTR-MS with a detection limit of 50 pptv (integration time of 6 min; Williams et al., 2011). Isoprene was measured via GC (GC 6890A, Agilent Technologies, Inc.) coupled to a mass selective detector (MSD 5973 inert, Agilent Technologies, Inc.) with an uncertainty of around 15 %. Highly constrained box model simulations, which were in fair agreement with experimental data, were available for OH and HO₂, as described by Crowley et al. (2018), with an uncertainty in the order of 30 %–40 %. $j(\text{NO}_2)$ and $j(\text{O}^1\text{D})$ were measured with filter radiometers (Meteorologie Consult GmbH, Königstein, Germany) with an uncertainty of around 10 %; $j(\text{HCHO})$ was determined via parameterization (analogous to CYPHEX and HOPE). H₂O was measured with an infrared light absorption analyzer (URAS 4 H₂O, Hartmann & Braun AG, Frankfurt am Main, Germany). The BLH was measured by radio soundings, as presented by Ouwersloot et al. (2012), ranging from 200 m during nighttime (here $j(\text{NO}_2) < 10^{-3} \text{ s}^{-1}$) to 1500 m during daytime (here $j(\text{NO}_2) < 10^{-3} \text{ s}^{-1}$; Fischer et al., 2019). The deposition velocity was determined analogously to the HOPE campaign, based on the nighttime HCHO loss on the basis of 14 nights, and was 0.85 cm s^{-1} during the day and 0.43 cm s^{-1} during the night. The uncertainty of the calculation results from the single uncertainties of $\frac{d[\text{HCHO}]}{dt}$ (16 %), $[\text{HCHO}]_{\text{av}}$ (33 %) and the nighttime BLH (20 %). Gaussian error propagation gives an overall uncertainty of 42 % from the calculation. The atmospheric variability equals 54 %. We, therefore, estimate the total uncertainty of the deposition ve-

locity to be 54 %. An overview of all considered nights and the respective HCHO loss is presented in Fig. S3c. The deposition velocity of ozone was adopted from Rannik et al. (2012) for the time period during calendar weeks 25–34 of the year and a relative humidity below 70 %, which is 0.491 cm s^{-1} for daytime and 0.069 cm s^{-1} for nighttime. A modeling study by Emmerichs et al. (2021) presents the average values in the same order of magnitude (~ 0.2 – 0.3 cm s^{-1} for July and August). Again, uncertainties and time resolution are shown in Table S3. Similar to the HOPE campaign, some trace gases were not available simultaneously, and we, therefore, present the averaged diurnal profiles.

3 Results and discussion

3.1 Net HCHO production during CYPHEX in 2014

HCHO concentrations during the CYPHEX campaign ranged between 0.3 and 1.9 ppbv (1.1 ± 0.4 ppbv on average), with a maximum in the diel cycle during morning hours (04:00 UTC) and a minimum in the afternoon (15:00 UTC). Please note the mean local time difference stated in Sect. 2.3 and Fig. 3. The temporal development of HCHO concentrations during the campaign and the respective $j(\text{NO}_2)$ values (to illustrate the daily cycle) are shown in Fig. S3a. Figure S4a presents the diurnal average of HCHO, including its rate of change $\frac{d[\text{HCHO}]}{dt}$. The uncertainty is dominated by the atmospheric variability which is on average 27 % for daytime HCHO.

Figure 5 shows the time series of the HCHO production terms (Fig. 5a), the HCHO loss terms (Fig. 5b) and the net HCHO production (Fig. 5c) during the CYPHEX research campaign in Cyprus in July 2014. We calculated the HCHO production terms for all measured gas-phase precursors shown in Fig. 1. The individual production terms are shown in Fig. S5. The total measurement uncertainties were determined via Gaussian error propagation and were 28 % for HCHO production (31 % for only considering the OH oxidation of methane, methanol, isoprene and acetaldehyde) and 26 % for HCHO loss. Table S4 provides an overview of all calculated uncertainties. We present two example step-by-step calculations via Gaussian error propagation in Eqs. (S2)–(S8). All other calculations were made accordingly. We have neglected the uncertainties for the HCHO yield from isoprene, $\alpha_{\text{CH}_3\text{O}_2}$ and $\alpha_{\text{CH}_3\text{CHO}}$ and instead present a sensitivity study for these parameters later in this section. Dark green colors show the overall HCHO production as the sum of all single production terms. All production terms show a diurnal cycle which follows the course of the photolysis frequency $j(\text{NO}_2)$, which we show in Fig. 5d. Photolysis reactions do not take place after sunset, and oxidation reactions are dependent on the abundance of OH radicals, which is low during nighttime. Therefore, HCHO production approaches zero during nighttime. Due to data gaps, a full diurnal profile was only available for 23, 28 and

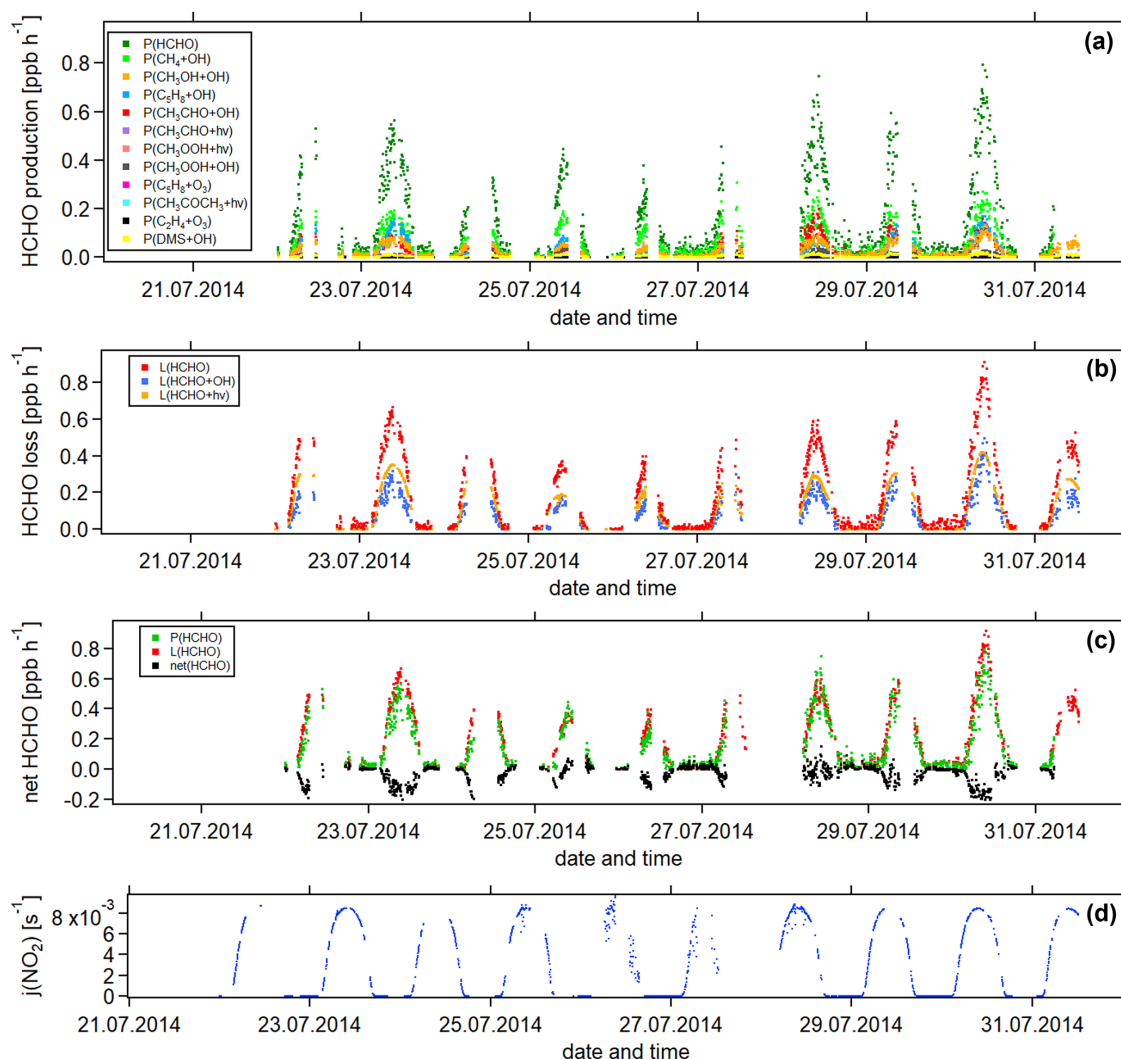


Figure 5. Temporal development of (a) HCHO production terms, (b) HCHO loss terms and (c) net HCHO from 22 July to 31 July 2014 during the CYPHEX research campaign in Cyprus. The NO₂ photolysis frequency $j(\text{NO}_2)$ is shown in panel (d) as an illustration of the diurnal cycle. All times are in UTC.

30 July, where the overall HCHO production reached maxima between 0.6 and 0.8 ppbv h⁻¹. The reactions of methane, methanol, isoprene and acetaldehyde with OH dominated the HCHO production processes. This is additionally illustrated in Fig. 6, which presents the daily average share (including day- and nighttime values) of each production term based on a balance to the overall loss rate. HCHO production was, therefore, dominated by the reaction of methane and OH (almost a third), followed by the oxidation of acetaldehyde contributing around 15 % and the OH oxidations of isoprene and methanol, both contributing around 14 %. These four species together represented 75 % of the overall HCHO production

required to balance the sinks. The production through the OH oxidation of methyl hydroperoxide and dimethyl sulfide and through the reaction of isoprene and ozone contributed by around 1 %–2 % each. The remaining species each yielded less than 1 % of the overall HCHO. Less than 20 % was unaccounted for (the rest in Fig. 6). This part also includes HCHO production from terpenes via oxidation through OH or O₃. The yields from these reactions vary greatly in the literature. Considering the yields from OH oxidation, suggested by Lee et al. (2006), from laboratory investigations, limonene, β - and α -pinene would account for 3 %, 2 % and 1 % of the overall HCHO production, respectively. The isoprene yield

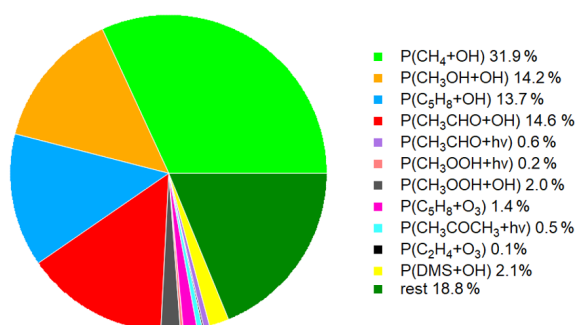


Figure 6. Chemical production terms of HCHO during CYPHEX, including daily averages of all data.

is limited to a value between 34 % and 57 %. The lower limit would give a HCHO production from isoprene of 11 %, and the upper limit would yield 19 %. The value for $\alpha_{\text{CH}_3\text{O}_2}$ can theoretically be between 0 % and 100 % but is likely situated at the upper end due to the availability of NO. As an example, a 20 % decrease in $\alpha_{\text{CH}_3\text{O}_2}$ would give a HCHO production from CH₃O₂ of 38 % (compared to 47 % for the calculated $\alpha_{\text{CH}_3\text{O}_2}$). A 20 % increase would yield 57 % on average and decrease the rest to less than 10 %. For $\alpha_{\text{CH}_3\text{CHO}}$, a 20 % decrease and increase would give a HCHO yield from acetaldehyde of 12 % and 18 %, respectively, assuming a constant $\alpha_{\text{CH}_3\text{O}_2}$. Please note that the uncertainty of the absolute values used to create this pie chart is dominated by the atmospheric and diurnal variability in the single terms and is of the order of 100 %.

HCHO loss was determined from the reaction with OH and photolysis. Red colors in Fig. 5b show the overall calculated HCHO loss. Similar to the HCHO production, HCHO loss via OH and photolysis only plays a role during the daytime. At night, dry deposition is the only HCHO loss mechanism, and the deposition velocity v_d can be determined from the nighttime decrease in ambient HCHO concentrations, as shown by Sumner et al. (2001). However, we often observed increasing HCHO concentrations during nighttime, particularly before sunrise. The reason for this nighttime HCHO increase is not yet fully understood. The role of the deposition processes at elevated altitudes is not yet fully understood but is likely influenced by flows along mountain slopes and horizontal advection on hilltops. For hilltops, incoming air through advection likely originated from areas without deposition (too high above the ground; Derstroff et al., 2017). Please note that the effect of deposition processes could also be counteracted by a nighttime HCHO source, such as terpene oxidation by ozone or advection. The determined value for the deposition can, therefore, be seen as being a lower estimate (Crowley et al., 2018). As we do not observe the net loss of HCHO at night during the CYPHEX campaign, we estimate the dry deposition to be negligible. Figure 5c shows the overall HCHO production and loss rates, as well as

the difference between both, which we refer to as net HCHO production, in black. Production and loss showed a good balance with values of $\pm 0.2 \text{ ppbv h}^{-1}$. On most days, HCHO loss prevailed over HCHO production, based on measured precursors.

In order to better account for diurnal changes, we investigated the daily cycle of HCHO production and loss rates based on hourly averages over all measurement days. Figure 7 shows the diurnal profiles of the main HCHO production terms (Fig. 7a) as determined above, the HCHO loss terms (Fig. 7b) and net HCHO production (Fig. 7c). The solid lines represent the hourly averages of the point-by-point calculation of the production and loss terms. The uncertainty is composed of the measurement uncertainty and the atmospheric variability, where the latter is demonstrated by the 1σ error shades. For HCHO production, the measurement uncertainty was 31 %, and the daytime atmospheric variability was 40 % (61 % for day and night). For HCHO loss, the uncertainties were 26 % and 34 % (57 %), respectively. In both cases, the overall uncertainty was dominated by the atmospheric variability. The dashed lines show the hourly production and loss terms calculated from the hourly averaged trace gas concentrations. The uncertainty from the atmospheric variability was 22 % (34 %) for HCHO production and 25 % (52 %) for HCHO loss and is exemplarily indicated by an error bar for one point for each production and loss term in Fig. 7. Both methods have advantages and disadvantages. The point-by-point calculation allows for a simultaneous consideration of all measurement parameters. Potential atmospheric changes or incidents such as wind, precipitation or rare primary emission events are reflected by all parameters as they are monitored at the same time. On the other hand, this method reduces the number of data points used as only one single missing species prevents the calculation of the overall term. In order to increase the number of results, we have interpolated the values for the isoprene yield (data coverage 81 %), $\alpha_{\text{CH}_3\text{CHO}}$ and $\alpha_{\text{CH}_3\text{O}_2}$ (data coverage 64 %). Calculating production and loss terms from the hourly averaged trace gas concentrations allows for the inclusion of all measured parameters but could potentially increase the uncertainty of the estimate, depending on the duration and overlap of the single measurements. However, in this case, the data were limited to 1 week in July with mainly simultaneous measurements of all parameters, and we, therefore, do not expect large uncertainties. The similarity of the results, as shown in Fig. 7, indicates that both methods provide reasonable results.

For HCHO production, the daily maxima of around $0.4\text{--}0.45 \text{ ppbv h}^{-1}$ were reached between 09:00 and 10:00 UTC, which was coincident with the maximum of the photolysis frequency $j(\text{NO}_2)$. HCHO production from methane dominated the overall production term, with a maximum of close to 0.2 ppbv h^{-1} , followed by acetaldehyde, isoprene and methanol. HCHO loss peaked around 09:00 UTC, with a value of 0.5 ppbv h^{-1} , with around 55 % contribution from

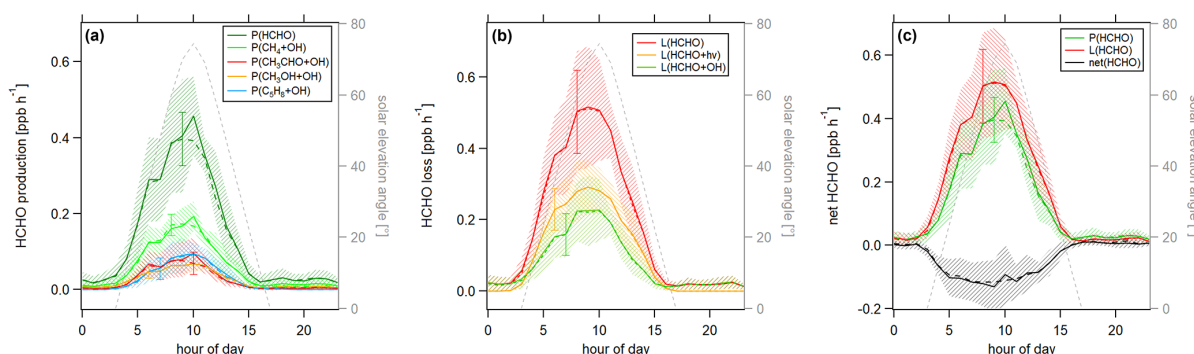


Figure 7. Diurnal profiles of (a) HCHO production $P(\text{HCHO})$, (b) HCHO loss $L(\text{HCHO})$ and (c) HCHO net terms during the CYPHEX campaign in 2014. Solid lines show the hourly averaged HCHO production and loss terms, based on the point-by-point calculation of simultaneous parameter measurements. The uncertainty from the atmospheric variability is represented by the 1σ error shades. For the dashed lines, all measurement parameters were averaged first, followed by the calculation of hourly HCHO production and loss terms. The uncertainty is based on the atmospheric variability of all parameters and is exemplarily shown by the error bar for one point for each production and loss term. The gray dashed line represents the diurnal solar elevation angle at the measurement site, as determined by help of the NOAA Solar Calculator (2021).

photolysis and 45 % from OH oxidation. Figure 7c shows that the calculated production term for HCHO can almost completely balance the loss, which, assuming that the major loss processes are well constrained, leads to the conclusion that HCHO production can be approximated by OH oxidation of methane, acetaldehyde, isoprene and methanol. This is in line with the HCHO rate of change presented in Fig. S4a which oscillated around zero. Therefore, transport processes and primary emissions during CYPHEX can likely be excluded.

3.2 Net O₃ production during CYPHEX in 2014

Ozone varied between 46 and 104 ppbv during the CYPHEX campaign (70 ± 13 ppbv on average), with a diel maximum at 04:00 UTC and a minimum at 15:00 UTC. The time series of O₃ concentrations is presented in Fig. S6a. The diel mean, including the rate of change $d\text{O}_3/dt$, can be found in Fig. S7a. The uncertainty is dominated by the atmospheric variability, which is on average 16 % (1σ) for O₃.

Figure 8 shows the diurnal cycle of the production and loss rates for ozone, analogous to Fig. 7. Solid lines show the hourly averaged point-by-point calculations of the O₃ production and loss terms. The 1σ error shades present the atmospheric variability, which was 59 % for O₃ production and 37 % for O₃ daytime loss (44 % for day and night). The measurement uncertainties were 32 % and 16 %, respectively, and the overall uncertainty was, therefore, dominated by the atmospheric variability. Dashed lines show the O₃ production and loss terms based on the hourly averaged measurement parameters. The uncertainty resulting from the averaging of the individual parameters is exemplarily shown by the error bar for one point and is similar to the atmospheric variability

obtained by the point-by-point method (57 % for $P(\text{O}_3)$ and 35 % (49 %) for $L(\text{O}_3)$). Figure 8a shows O₃ production represented by the photolysis of NO₂. Figure 8b shows the O₃ loss terms. O₃ loss through reaction with NO was dominant, followed by photolysis. The loss via OH and HO₂ was negligibly small. O₃ net production during the CYPHEX campaign was, therefore, clearly dominated by nitrogen oxides chemistry. Figure 8c shows the net O₃ production. O₃ production and loss were similar throughout the day, with peak values of 4–7 ppbv h^{−1} between 05:00 and 10:00 UTC. Net O₃ production was between −1 and 1 ppbv h^{−1}. Please note that we have excluded the NO₂ data from 24 July between 13:15 and 16:15 UTC due to a singular high-concentration event. The large spike in NO₂ (O₃ titration of NO) is likely the result of sampling air impacted by the exhaust from a diesel generator which provided on-site power and was located about 200 m from the containers housing the instruments. We show O₃ net production, including all NO₂ data points, in Fig. S9a. O₃ production is directly proportional to the NO₂ concentration, according to Eq. (8), which explains the large afternoon production peak. We show the diel profile of NO₂ concentrations with and without the afternoon peak in Fig. S9b. Production and loss terms for O₃ were balanced, and the O₃ rate of change oscillated around zero (Fig. S7a), suggesting that the diel variability was likely not impacted by transport processes.

3.3 Comparison with HOPE (2012) and HUMPPA (2010)

3.3.1 Net HCHO production

We have shown, in Sect. 3.1 and 3.2, that the hourly averaging of measurement parameters and subsequent calculation

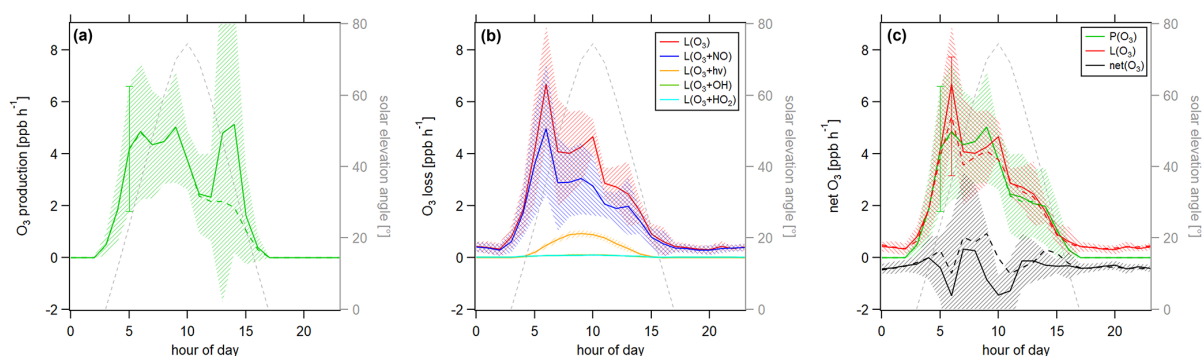


Figure 8. Diurnal profiles of (a) ozone production $P(\text{O}_3)$, (b) ozone loss $L(\text{O}_3)$ and (c) ozone net terms during the CYPHEX campaign in 2014. Solid lines show the hourly averaged O₃ production and loss terms, based on the point-by-point calculation of simultaneous parameter measurements. The uncertainty from the atmospheric variability is represented by the 1σ error shades. For the dashed lines, all measurement parameters were averaged first, followed by the calculation of hourly O₃ production and loss terms. The uncertainty is mostly dominated by the atmospheric variability in all parameters and is exemplarily shown by the error bar for one point for each production and loss term. Please find the temporal development of production and loss terms throughout the campaign in Fig. S8.

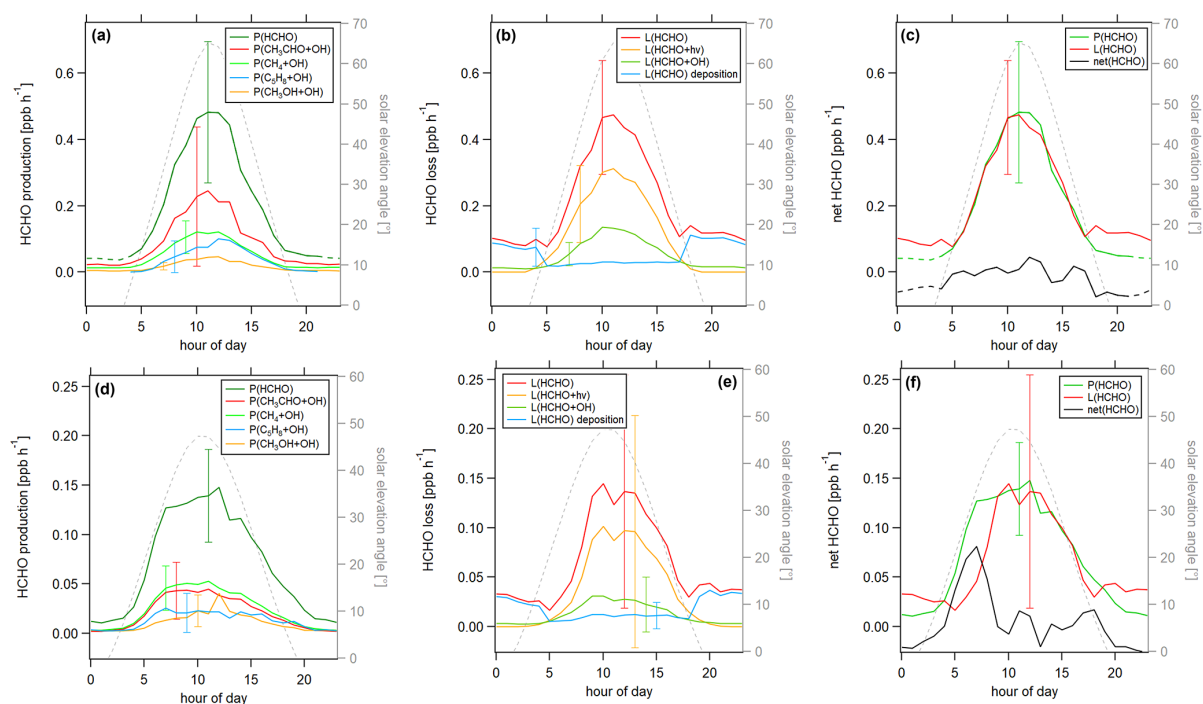


Figure 9. Diurnal profiles of HCHO production $P(\text{HCHO})$ and loss $L(\text{HCHO})$ terms during the HOPE campaign 2012 (top row) and the HUMPPA campaign 2010 (bottom row). (a) $P(\text{HCHO})$, (b) $L(\text{HCHO})$, (c) net HCHO, (d) $P(\text{HCHO})$, (e) $L(\text{HCHO})$ and (f) net(HCHO).

of production and loss terms yielded reliable results during the CYPHEX campaign. For HUMPPA and HOPE, we have pursued this approach regarding the calculations of HCHO and O₃ production and loss terms, as the simultaneous data availability for all measurement parameters was too low for a point-by-point analysis.

HCHO mixing ratios during the HOPE campaign varied between 0.1 and 3.2 ppbv (1.1 ± 0.5 ppbv on average), with a maximum in the diel cycle at 15:00 UTC and a minimum at 06:00 UTC. The average mixing ratio was similar to the average mixing ratio during the CYPHEX campaign, but the variability was higher, which is likely due to the longer time

period of available data which was about 4 weeks for HOPE (compared to a bit more than 1 week for CYPHEX), including, e.g., larger temperature variations. HCHO mixing ratios in Hyytiälä during the HUMPPA campaign ranged between 0.03 and 5.7 ppbv, with an average of 0.4 ± 0.5 ppbv. The variability is high because of biomass burning events in Russia which were detected at the site in Finland on 26–30 July and 9 August, as described by Williams et al. (2011). The large HCHO peaks detected on these days can also be seen in Fig. S3c. Figure S4b and c present the diurnal cycles for HCHO, including the rate of change $\frac{d(\text{HCHO})}{dt}$ during HOPE and HUMPPA. The uncertainty is dominated by the atmospheric variability represented by the 1σ standard deviation, which is, on average, 44 % for HCHO for HOPE and 106 % for HUMPPA.

Figure 9 shows the HCHO production and loss rates for the two campaigns. For all cases, the uncertainty was dominated by the atmospheric variability (1σ), which was 42 % for daytime HCHO production and 40 % for daytime HCHO loss in Hohenpeißenberg and 38 % and 77 % in Hyytiälä, respectively. The measurement uncertainty was around 30 % to 40 %. We present the atmospheric variability with the error bars in Fig. 9. For better clarity, we only show one error bar for each term. An overview of all calculated uncertainties can be found in Table S4. HCHO production during HOPE is shown in Fig. 9a. The maximum production rate of 0.48 ppbv h^{-1} was reached between 11:00 and 12:00 UTC, and a comparison to $j(\text{NO}_2)$ shows good agreement with local noon. The production of HCHO was dominated by the oxidation of acetaldehyde, which contributed to the peak production by around 50 %, followed by methane, isoprene and methanol. We show a pie chart representing the contribution of the single HCHO production terms during HOPE in Fig. S10a. HCHO loss is shown in Fig. 9b. The maximum loss rate of HCHO was 0.46 ppbv h^{-1} . During the day, HCHO loss was dominated by photolysis and oxidation, while, at nighttime, deposition was the main loss path for formaldehyde in Hohenpeißenberg. Figure 9c shows HCHO net production during HOPE. The calculated production of HCHO slightly prevailed over its loss. At 11:00 UTC, HCHO loss was > 95 % of HCHO production. Overall absolute loss and production terms were very similar compared to the results obtained for the site in Cyprus. The main difference is the composition of the HCHO production, which was dominated by the oxidation of acetaldehyde in Hohenpeißenberg and by the oxidation of methane in Cyprus. HCHO production and loss during the HUMPPA campaign are shown in Fig. 9d–f. HCHO production reached a peak value of 0.15 ppbv h^{-1} at 12:00 UTC. Methane and acetaldehyde contributed to the overall production by approximately equal parts, followed by isoprene and methanol. Figure S10b shows the share of the individual HCHO production terms during HUMPPA. Axinte (2016) showed that the contribution from terpene oxidation to HCHO production was small (1 %–2 % each), which is in line with our findings for the

CYPHEX campaign. HCHO loss was dominated by photolysis during the day and by dry deposition at night. Figure 9f shows that HCHO production and loss were in good agreement throughout the day (~ 90 %), apart from the morning hours 06:00–07:00 UTC when HCHO production prevailed over its loss by around 2 to 3 times, indicating a missing loss term, most likely due to dilution with HCHO-poor air during the rise of the planetary boundary layer in the early morning hours (accompanied by a peak in the HCHO rate of change as shown in Fig. S4b). Overall production and loss terms for HCHO were around 3 times smaller compared to the values obtained for the sites in Germany and Cyprus. We also observed smaller concentrations of CH₄, OH radicals and HCHO. It is notable that HCHO production was slightly higher than the loss for both the HUMPPA and the HOPE campaign. This is also reflected by peaks in the rate of change (0.1 – 0.2 ppbv h^{-1}) in the morning/midday hours (Fig. S4b and c) and could indicate a transport effect from areas with lower HCHO concentration, e.g., entrainment, according to Eq. (6). For HUMPPA, this idea is supported when excluding the data impacted by biomass burning, which we show in Fig. S11a. It can be seen that HCHO production prevailed over its loss, suggesting a missing loss term. The difference was highest in the morning hours, with approximately 0.1 ppbv h^{-1} , and decreased throughout the day indicating, e.g., a vertical dilution from higher, HCHO-poor altitudes. For comparison, Fig. S11b shows the HCHO production and loss terms when only considering data impacted by biomass burning. Due to high HCHO mixing ratios, the loss terms were substantially higher compared to its production. In periods influenced by biomass burning, the highest HCHO yield was from acetaldehyde (averaged diel mixing ratios of 1.1 ppbv compared to 0.6 ppbv without biomass burning); when excluding biomass burning, the yield from methane was slightly higher.

3.3.2 Net O₃ production

Ozone concentrations in Hohenpeißenberg were, on average, 44 ± 11 ppbv, with a minimum of 5 ppbv and a maximum of 97 ppbv. The campaign-averaged diel profile displayed a peak of 48 ppbv at 16:00 UTC and a minimum of 39 ppbv at 07:00 UTC. In Hyytiälä, ozone concentrations were between 20 and 76 ppbv and 42 ± 11 ppbv on average. A diel peak of 49 ppbv was reached between 15:00 and 16:00 UTC and a minimum of 34 ppbv at 05:00 UTC. The temporal development of ozone concentrations during the campaigns and the diurnal averages can be found in Figs. S6 and S7. The uncertainty is dominated by the atmospheric variability (1σ) which is, on average, 24 % for O₃ for HOPE and 23 % for HUMPPA.

Figure 10 shows the ozone production and loss terms for the research campaigns HOPE and HUMPPA. The overall uncertainty was again dominated by the atmospheric variability (1σ), which was 58 % for the daytime O₃ produc-

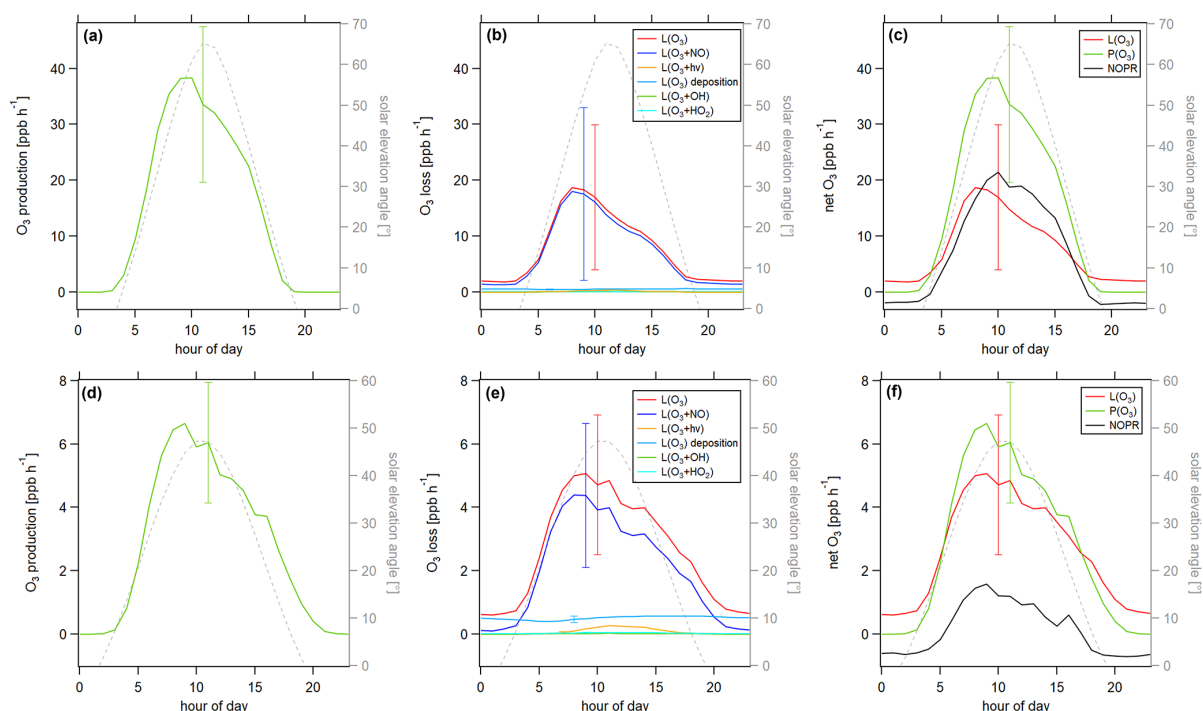


Figure 10. Diurnal profiles of O₃ production $P(\text{O}_3)$ and loss $L(\text{O}_3)$ terms during the HOPE campaign 2012 (top row) and the HUMPPA campaign 2010 (bottom row). (a) $P(\text{O}_3)$, (b) $L(\text{O}_3)$, (c) net O₃, (d) $P(\text{O}_3)$, (e) $L(\text{O}_3)$ and (f) net O₃.

tion and 90 % for the daytime O₃ loss in Hohenpeißenberg and 44 % and 51 %, respectively, in Hyytiälä. In comparison, the measurement uncertainty regarding overall production and loss was between 10 % and 15 %. A detailed overview of the uncertainties can be found in Table S4. We adopted the dry deposition velocity for ozone in Hyytiälä from Rannik et al. (2012). No literature values for the ozone dry deposition in Hohenpeißenberg were available. Therefore, we applied the same values as for the HUMPPA campaign, which increased the uncertainty of the analysis. However, the fraction of ozone dry deposition of the overall loss was small. For the applied deposition velocity, dry deposition contributed by around 4 % during the daytime. For a change in v_d of ± 100 %, the fraction varied between 2 % and 7 %. We, therefore, assume a maximum additional uncertainty of 5 % resulting from this estimate. Ozone production in Hohenpeißenberg reached peak values of 38 ppbv h⁻¹. In contrast, ozone loss showed a maximum of only 21 ppbv h⁻¹, most of which was due to the reaction with NO. In Hyytiälä, ozone production was 6.7 ppbv h⁻¹ at its diurnal maximum, while ozone loss reached 5.1 ppbv h⁻¹ and was mainly composed of the loss via NO, followed by dry deposition. The differences between production and loss terms could again indicate a transport effect, according to Eq. (10), as described for HCHO. The rate of change for O₃ showed peak val-

ues (2–3 ppbv h⁻¹) during the morning/midday hours, which was not observed for the CYPHEX campaign (Fig. S7). O₃ production and loss terms during HUMPPA and CYPHEX were similar, while the values were significantly higher during HOPE. O₃ production in Hohenpeißenberg was almost 1 order of magnitude higher compared to the other sites, which was likely due to the higher ambient NO_x concentrations. The net O₃ production (the difference between O₃ production and loss) at each site could give a hint regarding the dominant chemical ozone regime. For HOPE, net O₃ production was significantly above zero, with diurnal maximum values of around 20 ppbv h⁻¹ at 10:00 UTC, which could indicate a VOC limitation. In contrast, net O₃ production was close to zero for CYPHEX, and the ozone regime was more likely NO_x limited. We will discuss the dominant chemical ozone regime in detail in the following section.

3.4 Chemical regime

Various methods exist to determine the prevailing chemical ozone regime (i.e., the net efficiency of production or loss), one of which is the ratio of formaldehyde and nitrogen dioxide. We have calculated the diel HCHO/NO₂ ratios for all three measurement sites, which is shown in Fig. 11a. The HCHO/NO₂ ratio was highest in Cyprus with 8.0 ± 2.4 , followed by 1.4 ± 0.7 in Hyytiälä and 0.7 ± 0.2 in Hohen-

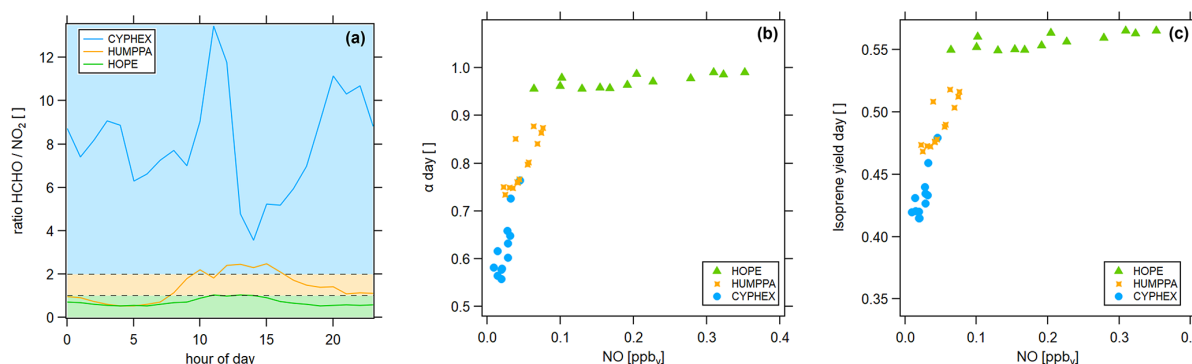


Figure 11. Determination of the dominant chemical regime via (a) the HCHO/NO₂ ratio (colored areas indicate the dominant chemical regime, according to Duncan et al. (2010), which are blue (HCHO/NO₂ > 2) for a NO_x limitation, green (HCHO/NO₂ < 1) for a VOC limitation and yellow (1 < HCHO/NO₂ < 2) for the transition), (b) the fraction of methyl peroxy radicals forming HCHO and (c) the HCHO yield from isoprene.

peißenberg. According to findings by Martin et al. (2004) and Duncan et al. (2010) these values indicate a dominant NO_x-limited regime during CYPHEX and a dominant VOC-limited regime during HOPE. The regime during HUMPPA was likely transitioning between both limitations. We show two additional approaches for determining the present chemical regime in Fig. 11. In Fig. 11b, we present the daytime averages of $\alpha_{\text{CH}_3\text{O}_2}$ versus the NO concentration. All campaigns show a linear correlation. Daytime average NO concentrations during CYPHEX ranged from 1 to 45 pptv, accompanied by an increase in $\alpha_{\text{CH}_3\text{O}_2}$ from around 55 % to 75 %, giving a slope of 5.54 ppbv⁻¹. The slope for the increase in $\alpha_{\text{CH}_3\text{O}_2}$ with NO is approximately half for the HUMPPA campaign, with a value of 2.52 ppbv⁻¹. The NO concentration ranged from 22 to 76 pptv, along with an increase in $\alpha_{\text{CH}_3\text{O}_2}$ from 73 % to 87 %. Finally, for the HOPE campaign, NO concentrations and its range were highest with values between 60 and 350 pptv. At the same time, $\alpha_{\text{CH}_3\text{O}_2}$ showed the smallest increase by only 3 percentage points. The resulting slope was the smallest, with a value of 0.11 ppbv⁻¹. $\alpha_{\text{CH}_3\text{O}_2}$ indicates the share of CH₃O₂ that forms HCHO, predominantly through the reaction with NO. The competing reaction is the conversion with HO₂ to CH₃OOH. A high value for $\alpha_{\text{CH}_3\text{O}_2}$, which is not (or only a little) responsive to a changing NO concentration, indicates a VOC limited regime, while in a NO_x-limited regime, small changes in ambient NO have a large effect on the HCHO formation from CH₃O₂. Analogously, we show the HCHO yield from isoprene, according to Eq. (3), versus NO concentrations in Fig. 11c, which we suggest as an indicator for the present chemical regime too. For the CYPHEX campaign, the isoprene yield was most responsive to ambient NO concentrations with a slope of 1.61 ppbv⁻¹, indicating a NO_x limitation. In contrast, the isoprene yield during the HOPE campaign was almost non-responsive to changing NO, indicating a VOC limitation (slope of 0.05 ppbv⁻¹). Al-

though specialized instrumentation is still necessary to measure NO, OH and HO₂, these methods to determine the dominant chemical regime only require the knowledge of a small number of trace gas concentrations and the ambient temperature.

4 Conclusions

In this study, we have analyzed the photochemical processes contributing to formaldehyde and ozone production and loss across Europe based on in situ trace gas observations during three different stationary field campaigns in Cyprus (CYPHEX in 2014), Germany (HOPE in 2012) and Finland (HUMPPA in 2010). Very consistently across all sites, we found that formaldehyde loss can be predominantly accounted for by the production via the OH oxidation of methane, acetaldehyde, isoprene and methanol. Formaldehyde loss is represented by photolysis, OH oxidation and, to a small extent, by dry deposition. Ozone chemistry is mainly controlled by nitrogen oxides. The production can be described by NO₂ photolysis, and the loss is mainly a function of NO reduction and, to a smaller extent, of photolysis and dry deposition. We found a good agreement between O₃ production and loss in Cyprus and Finland, while the production was approximately double its loss in southern Germany. Finally, we have presented several different approaches for determining the prevalent chemical regime, which included the HCHO/NO₂ ratio, and the fraction of CH₃O₂ forming HCHO, and the HCHO yield from isoprene in its dependence on the ambient NO concentration. We identify a VOC-limited regime during the HOPE campaign in Germany and a NO_x-limited regime during the CYPHEX campaign in Cyprus, whereas chemistry during the HUMPPA campaign in Finland was likely at a transitional point.

While ongoing research on HCHO photochemical processes has continuously widened the contributors to possible production paths and the complexity of calculations and models, we show that the consideration of only four precursor VOCs is capable of almost completely representing the HCHO production term at various sites across Europe. We encourage extending the HCHO budget calculations based on in situ trace gas observations to more sites worldwide as a simple, but effective, tool to monitor photochemical processes and air quality, including the dominant chemical regime.

Data availability. All data generated and analyzed for this study are available from KEEPER (2021; <https://keeper.mpdl.mpg.de/>, last access: 6 December 2021) upon request to the authors.

Supplement. The supplement related to this article is available online at: <https://doi.org/10.5194/acp-21-18413-2021-supplement>.

Author contributions. HF had the idea. CMN and HF designed the study. CMN analyzed the data and wrote the paper. JS, JNC and BB provided J values. CPD provided trace gas measurements for HOPE. JNC provided OH and HO₂ model data for HUMPPA. JW provided VOC data. HH, CE, AN, KT, MM, CM and LT provided OH and HO₂ data for CYPHEX and HOPE. HCHO data were measured and provided by AR and RA. SH provided CH₃OOH data. NO_x and O₃ data were obtained from HF. JL significantly contributed to planning the research campaigns.

Competing interests. The contact author has declared that neither they nor their co-authors have any competing interests.

Disclaimer. Publisher's note: Copernicus Publications remains neutral with regard to jurisdictional claims in published maps and institutional affiliations.

Acknowledgements. We acknowledge all researchers and supporting personnel who participated in the CYPHEX campaign in 2014, the HOPE campaign in 2012 and the HUMPPA campaign in 2010. We would like to thank Pekka Rantala (University of Helsinki), for providing the CH₃CHO data for HUMPPA. This work was supported by the Max Planck Graduate Center with the Johannes Gutenberg-Universität Mainz (MPGC).

Financial support. The article processing charges for this open-access publication were covered by the Max Planck Society.

Review statement. This paper was edited by John Liggio and reviewed by two anonymous referees.

References

- Alam, M. S., Camredon, M., Rickard, A. R., Carr, T., Wyche, K. P., Hornsby, K. E., Monks, P. S., and Bloss, W. J.: Total radical yields from tropospheric ethene ozonolysis, *Phys. Chem. Chem. Phys.*, 13, 11002–11015, <https://doi.org/10.1039/C0CP02342F>, 2011.
- Anderson, D., Nicely, J., Wolfe, G., Hanisco, T., Salawitch, R., Canty, T., Dickerson, R., Apel, E., Baidar, S., Bannan, T., Blake, N. J., Chen, D., Dix, B., Fernandez, R. P., Hall, S. R., Hornbrook, R. S., Huey, L. G., Josse, B., Jöckel, P., Kinnison, D. E., Koenig, T. K., Breton, M. L., Marécal, V., Morgenstern, O., Oman, L. D., Pan, L. L., Percival, C., Plummer, D., Revell, L. E., Rozanov, E., Saiz-Lopez, A., Stenke, A., Sudo, K., Tilmes, S., Ullmann, K., Volkamer, R., Weinheimer, A. J., and Zeng, G.: Formaldehyde in the tropical western Pacific: Chemical sources and sinks, convective transport, and representation in CAM-Chem and the CCMi models, *J. Geophys. Res.-Atmos.*, 122, 11201–11226, <https://doi.org/10.1002/2016JD026121>, 2017.
- Assaf, E., Song, B., Tomas, A., Schoemaeker, C., and Fittschen, C.: Rate constant of the reaction between CH₃O₂ radicals and OH radicals revisited, *J. Phys. Chem. A*, 120, 8923–8932, <https://doi.org/10.1021/acs.jpca.6b07704>, 2016.
- Assaf, E., Sheps, L., Whalley, L., Heard, D., Tomas, A., Schoemaeker, C., and Fittschen, C.: The reaction between CH₃O₂ and OH radicals: product yields and atmospheric implications, *Environ. Sci. Technol.*, 51, 2170–2177, <https://doi.org/10.1021/acs.est.6b06265>, 2017.
- Atkinson, R., Baulch, D. L., Cox, R. A., Crowley, J. N., Hampson, R. F., Hynes, R. G., Jenkin, M. E., Rossi, M. J., Troe, J., and IUPAC Subcommittee: Evaluated kinetic and photochemical data for atmospheric chemistry: Volume II – gas phase reactions of organic species, *Atmos. Chem. Phys.*, 6, 3625–4055, <https://doi.org/10.5194/acp-6-3625-2006>, 2006.
- Axinte, R. D.: The oxidation photochemistry and transport of hydrogen peroxide and formaldehyde at three sites in Europe: trends, budgets and 3-D model simulations, PhD thesis, Johannes Gutenberg-Universität Mainz, <https://doi.org/10.25358/openscience-3313>, 2016.
- Ayers, G., Gillett, R., Granek, H., De Serves, C., and Cox, R.: Formaldehyde production in clean marine air, *Geophys. Res. Lett.*, 24, 401–404, <https://doi.org/10.1029/97GL00123>, 1997.
- Bohn, B., Corlett, G. K., Gillmann, M., Sanghavi, S., Stange, G., Tensing, E., Vrekoussis, M., Bloss, W. J., Clapp, L. J., Kortner, M., Dorn, H.-P., Monks, P. S., Platt, U., Plass-Dülmer, C., Mihalopoulos, N., Heard, D. E., Clemitshaw, K. C., Meixner, F. X., Prevot, A. S. H., and Schmitt, R.: Photolysis frequency measurement techniques: results of a comparison within the ACCENT project, *Atmos. Chem. Phys.*, 8, 5373–5391, <https://doi.org/10.5194/acp-8-5373-2008>, 2008.
- Bozem, H., Butler, T. M., Lawrence, M. G., Harder, H., Martinez, M., Kubistin, D., Lelieveld, J., and Fischer, H.: Chemical processes related to net ozone tendencies in the free troposphere, *Atmos. Chem. Phys.*, 17, 10565–10582, <https://doi.org/10.5194/acp-17-10565-2017>, 2017.
- Crowley, J. N., Pouvesle, N., Phillips, G. J., Axinte, R., Fischer, H., Petäjä, T., Nölscher, A., Williams, J., Hens, K., Harder, H., Martinez-Harder, M., Novelli, A., Kubistin, D., Bohn, B., and Lelieveld, J.: Insights into HO_x and RO_x chemistry in the bo-

- real forest via measurement of peroxyacetic acid, peroxyacetic nitric anhydride (PAN) and hydrogen peroxide, *Atmos. Chem. Phys.*, 18, 13457–13479, <https://doi.org/10.5194/acp-18-13457-2018>, 2018.
- Dierstoff, B., Hüser, I., Bourtsoukidis, E., Crowley, J. N., Fischer, H., Gromov, S., Harder, H., Janssen, R. H. H., Kesselmeier, J., Lelieveld, J., Mallik, C., Martinez, M., Novelli, A., Parchatka, U., Phillips, G. J., Sander, R., Sauvage, C., Schuladen, J., Stöner, C., Tomsche, L., and Williams, J.: Volatile organic compounds (VOCs) in photochemically aged air from the eastern and western Mediterranean, *Atmos. Chem. Phys.*, 17, 9547–9566, <https://doi.org/10.5194/acp-17-9547-2017>, 2017.
- Dienhart, D., Crowley, J. N., Bourtsoukidis, E., Edtbauer, A., Eger, P. G., Ernle, L., Harder, H., Hottmann, B., Martinez, M., Parchatka, U., Paris, J.-D., Pfannerstill, E. Y., Rohloff, R., Schuladen, J., Stöner, C., Tadic, I., Tauer, S., Wang, N., Williams, J., Lelieveld, J., and Fischer, H.: Measurement report: Observation-based formaldehyde production rates and their relation to OH reactivity around the Arabian Peninsula, *Atmos. Chem. Phys. Discuss.* [preprint], <https://doi.org/10.5194/acp-2021-304>, in review, 2021.
- DiGangi, J. P., Boyle, E. S., Karl, T., Harley, P., Turnipseed, A., Kim, S., Cantrell, C., Maudlin III, R. L., Zheng, W., Flocke, F., Hall, S. R., Ullmann, K., Nakashima, Y., Paul, J. B., Wolfe, G. M., Desai, A. R., Kajii, Y., Guenther, A., and Keutsch, F. N.: First direct measurements of formaldehyde flux via eddy covariance: implications for missing in-canopy formaldehyde sources, *Atmos. Chem. Phys.*, 11, 10565–10578, <https://doi.org/10.5194/acp-11-10565-2011>, 2011.
- Duncan, B. N., Yoshida, Y., Olson, J. R., Sillman, S., Martin, R. V., Lamsal, L., Hu, Y., Pickering, K. E., Retscher, C., Allen, D. J., and Crawford, J. H.: Application of OMI observations to a space-based indicator of NO_x and VOC controls on surface ozone formation, *Atmospheric Environment*, 44, 2213–2223, <https://doi.org/10.1016/j.atmosenv.2010.03.010>, 2010.
- Emmerichs, T., Kerkweg, A., Ouwersloot, H., Fares, S., Mammarella, I., and Taraborrelli, D.: A revised dry deposition scheme for land-atmosphere exchange of trace gases in ECHAM/MESSy v2.54, *Geosci. Model Dev.*, 14, 495–519, <https://doi.org/10.5194/gmd-14-495-2021>, 2021.
- Fischer, H., Axinte, R., Bozem, H., Crowley, J. N., Ernest, C., Gilge, S., Hafermann, S., Harder, H., Hens, K., Janssen, R. H. H., Königstedt, R., Kubistin, D., Mallik, C., Martinez, M., Novelli, A., Parchatka, U., Plass-Dülmer, C., Pozzer, A., Regelin, E., Reiffs, A., Schmidt, T., Schuladen, J., and Lelieveld, J.: Diurnal variability, photochemical production and loss processes of hydrogen peroxide in the boundary layer over Europe, *Atmos. Chem. Phys.*, 19, 11953–11968, <https://doi.org/10.5194/acp-19-11953-2019>, 2019.
- Fittschen, C., Whalley, L. K., and Heard, D. E.: The reaction of CH₃O₂ radicals with OH radicals: a neglected sink for CH₃O₂ in the remote atmosphere, *Environ. Sci. Technol.*, 48, 7700–7701, <https://doi.org/10.1021/es502481q>, 2014.
- Fortems-Cheiney, A., Chevallier, F., Pison, I., Bousquet, P., Saunois, M., Szopa, S., Cressot, C., Kurosu, T. P., Chance, K., and Fried, A.: The formaldehyde budget as seen by a global-scale multi-constraint and multi-species inversion system, *Atmos. Chem. Phys.*, 12, 6699–6721, <https://doi.org/10.5194/acp-12-6699-2012>, 2012.
- Franco, B., Blumenstock, T., Cho, C., Clarisse, L., Clerbaux, C., Coheur, P.-F., De Mazière, M., De Smedt, I., Dorn, H.-P., Emmerichs, T., Fuchs, H., Gkatzelisand, G., Griffith, D. W. T., Gromov, S., Hannigan, J. W., Hase, F., Hohaus, T., Jones, N., Kerkweg, A., Kiendler-Scharr, A., Lutsch, E., Mahieu, E., Novelli, A., Ortega, I., Paton-Walsh, C., Pommier, M., Pozzer, A., Reimer, D., Rosanka, S., Sander, R., Schneider, M., Strong, K., Tillmann, R., Van Roozendae, M., Vereecken, L., Vigouroux, C., Wahner, A., and Taraborrelli, D.: Ubiquitous atmospheric production of organic acids mediated by cloud droplets, *Nature*, 593, 233–237, <https://doi.org/10.1038/s41586-021-03462-x>, 2021.
- Fried, A., Cantrell, C., Olson, J., Crawford, J. H., Weibring, P., Walega, J., Richter, D., Junkermann, W., Volkamer, R., Sinreich, R., Heikes, B. G., O'Sullivan, D., Blake, D. R., Blake, N., Meinardi, S., Apel, E., Weinheimer, A., Knapp, D., Perring, A., Cohen, R. C., Fuelberg, H., Shetter, R. E., Hall, S. R., Ullmann, K., Brune, W. H., Mao, J., Ren, X., Huey, L. G., Singh, H. B., Hair, J. W., Riemer, D., Diskin, G., and Sachse, G.: Detailed comparisons of airborne formaldehyde measurements with box models during the 2006 INTEX-B and MILAGRO campaigns: potential evidence for significant impacts of unmeasured and multi-generation volatile organic carbon compounds, *Atmospheric Chemistry and Physics*, 11, 11867–11894, 2011.
- Graus, M., Müller, M., and Hansel, A.: High resolution PTR-TOF: quantification and formula confirmation of VOC in real time, *J. Am. Soc. Mass Spectr.*, 21, 1037–1044, <https://doi.org/10.1016/j.jasms.2010.02.006>, 2010.
- Hosaynali Beygi, Z., Fischer, H., Harder, H. D., Martinez, M., Sander, R., Williams, J., Brookes, D. M., Monks, P. S., and Lelieveld, J.: Oxidation photochemistry in the Southern Atlantic boundary layer: unexpected deviations of photochemical steady state, *Atmos. Chem. Phys.*, 11, 8497–8513, <https://doi.org/10.5194/acp-11-8497-2011>, 2011.
- IUPAC: https://iupac-aeris.ipsl.fr/show_datasheets.php?category=Organic+photolysis (last access: 8 December 2021), 2013.
- IUPAC Task Group on Atmospheric Chemical Kinetic Data Evaluation: Data Sheet HO_x VOC34, available at: <http://iupac.pole-ether.fr> (last access: 5 July 2021), 2007.
- IUPAC Task Group on Atmospheric Chemical Kinetic Data Evaluation: Data Sheet HO_x VOC95, available at: <http://iupac.pole-ether.fr> (last access: 9 June 2021), 2017.
- IUPAC Task Group on Atmospheric Chemical Kinetic Data Evaluation: Data Sheet HO_x VOC54, available at: <http://iupac.pole-ether.fr> (last access: 9 June 2021), 2019.
- IUPAC Task Group on Atmospheric Chemical Kinetic Data Evaluation: Evaluated Kinetic Data, available at: <http://iupac.pole-ether.fr> (last access: 5 July 2021), 2021.
- Jacob, D. J.: Introduction to atmospheric chemistry, Princeton University Press, Princeton, USA, 1999.
- Jin, X. and Holloway, T.: Spatial and temporal variability of ozone sensitivity over China observed from the Ozone Monitoring Instrument, *J. Geophys. Res.-Atmos.*, 120, 7229–7246, <https://doi.org/10.1002/2015JD023250>, 2015.
- Jin, X., Fiore, A., Boersma, K. F., Smedt, I. D., and Valin, L.: Inferring Changes in Summertime Surface Ozone–NO_x–VOC Chemistry over US Urban Areas from Two Decades of Satellite and Ground-Based Observations, *Environ. Sci. Technol.*, 54, 6518–6529, <https://doi.org/10.1021/acs.est.9b07785>, 2020.

- Kaiser, J., Wolfe, G. M., Bohn, B., Broch, S., Fuchs, H., Ganzeveld, L. N., Gomm, S., Häseler, R., Hofzumahaus, A., Holland, F., Jäger, J., Li, X., Lohse, I., Lu, K., Prévôt, A. S. H., Rohrer, F., Wegener, R., Wolf, R., Mentel, T. F., Kiendler-Scharr, A., Wahner, A., and Keutsch, F. N.: Evidence for an unidentified non-photochemical ground-level source of formaldehyde in the Po Valley with potential implications for ozone production, *Atmos. Chem. Phys.*, 15, 1289–1298, <https://doi.org/10.5194/acp-15-1289-2015>, 2015.
- KEEPER: <https://keeper.mpd.mpg.de/>, last access: 6 December 2021.
- Kormann, R., Fischer, H., de Reus, M., Lawrence, M., Brühl, Ch., von Kuhlmann, R., Holzinger, R., Williams, J., Lelieveld, J., Warneke, C., de Gouw, J., Heland, J., Ziereis, H., and Schlager, H.: Formaldehyde over the eastern Mediterranean during MINOS: Comparison of airborne in-situ measurements with 3D-model results, *Atmos. Chem. Phys.*, 3, 851–861, <https://doi.org/10.5194/acp-3-851-2003>, 2003.
- Lee, A., Goldstein, A. H., Kroll, J. H., Ng, N. L., Varutbangkul, V., Flagan, R. C., and Seinfeld, J. H.: Gas-phase products and secondary aerosol yields from the photooxidation of 16 different terpenes, *J. Geophys. Res.*, 111, D17305, <https://doi.org/10.1029/2006JD007050>, 2006.
- Levitt, S. B. and Chock, D. P.: Weekday-weekend pollutant studies of the Los Angeles basin, *JAPCA J. Air Waste Ma.*, 26, 1091–1092, 1976.
- Lightfoot, P. D., Cox, R. A., Crowley, J. N., Destriau, M., Hayman, G. D., Jenkin, M. E., Moortgat, G. K., and Zabel, F.: Organic peroxy radicals: kinetics, spectroscopy and tropospheric chemistry, *Atmos. Env. A-Gen.*, 26, 1805–1961, [https://doi.org/10.1016/0960-1686\(92\)90423-I](https://doi.org/10.1016/0960-1686(92)90423-I), 1992.
- Lippmann, M.: Health effects of ozone a critical review, *JAPCA*, 39, 672–695, <https://doi.org/10.1080/08940630.1989.10466554>, 1989.
- Lowe, D. C. and Schmidt, U.: Formaldehyde (HCHO) measurements in the nonurban atmosphere, *J. Geophys. Res.-Oceans*, 88, 10844–10858, <https://doi.org/10.1029/JC088iC15p10844>, 1983.
- Luecken, D., Napelenok, S., Strum, M., Scheffe, R., and Phillips, S.: Sensitivity of ambient atmospheric formaldehyde and ozone to precursor species and source types across the United States, *Environ. Sci. Technol.*, 52, 4668–4675, <https://doi.org/10.1021/acs.est.7b05509>, 2018.
- Mallik, C., Tomsche, L., Bourtsoukidis, E., Crowley, J. N., Derstroff, B., Fischer, H., Hafermann, S., Hüser, I., Javed, U., Keßel, S., Lelieveld, J., Martinez, M., Meusel, H., Novelli, A., Phillips, G. J., Pozzer, A., Reiffs, A., Sander, R., Taraborrelli, D., Sauvage, C., Schuladen, J., Su, H., Williams, J., and Harder, H.: Oxidation processes in the eastern Mediterranean atmosphere: evidence from the modelling of HO_x measurements over Cyprus, *Atmos. Chem. Phys.*, 18, 10825–10847, <https://doi.org/10.5194/acp-18-10825-2018>, 2018.
- Marno, D., Ernest, C., Hens, K., Javed, U., Klimach, T., Martinez, M., Rudolf, M., Lelieveld, J., and Harder, H.: Calibration of an airborne HO_x instrument using the All Pressure Altitude-based Calibrator for HO_x Experimentation (APACHE), *Atmos. Meas. Tech.*, 13, 2711–2731, <https://doi.org/10.5194/amt-13-2711-2020>, 2020.
- Martin, R. V., Fiore, A. M., and Van Donkelaar, A.: Space-based diagnosis of surface ozone sensitivity to anthropogenic emissions, *Geophys. Res. Lett.*, 31, L06120, <https://doi.org/10.1029/2004GL019416>, 2004.
- Meusel, H., Kuhn, U., Reiffs, A., Mallik, C., Harder, H., Martinez, M., Schuladen, J., Bohn, B., Parchatka, U., Crowley, J. N., Fischer, H., Tomsche, L., Novelli, A., Hoffmann, T., Janssen, R. H. H., Hartogensis, O., Pikridas, M., Vrekoussis, M., Bourtsoukidis, E., Weber, B., Lelieveld, J., Williams, J., Pöschl, U., Cheng, Y., and Su, H.: Daytime formation of nitrous acid at a coastal remote site in Cyprus indicating a common ground source of atmospheric HONO and NO, *Atmos. Chem. Phys.*, 16, 14475–14493, <https://doi.org/10.5194/acp-16-14475-2016>, 2016.
- Miyoshi, A., Hatakeyama, S., and Washida, N.: OH radical-initiated photooxidation of isoprene: An estimate of global CO production, *J. Geophys. Res.-Atmos.*, 99, 18779–18787, <https://doi.org/10.1029/94JD01334>, 1994.
- NOAA Solar Calculator: <https://gml.noaa.gov/grad/solcalc/>, last access: 8 July 2021.
- Novelli, A., Hens, K., Tatum Ernest, C., Kubistin, D., Regelin, E., Elste, T., Plass-Dülmer, C., Martinez, M., Lelieveld, J., and Harder, H.: Characterisation of an inlet pre-injector laser-induced fluorescence instrument for the measurement of atmospheric hydroxyl radicals, *Atmos. Meas. Tech.*, 7, 3413–3430, <https://doi.org/10.5194/amt-7-3413-2014>, 2014.
- Novelli, A., Hens, K., Tatum Ernest, C., Martinez, M., Nölscher, A. C., Sinha, V., Paasonen, P., Petäjä, T., Sipilä, M., Elste, T., Plass-Dülmer, C., Phillips, G. J., Kubistin, D., Williams, J., Vereecken, L., Lelieveld, J., and Harder, H.: Estimating the atmospheric concentration of Criegee intermediates and their possible interference in a FAGE-LIF instrument, *Atmos. Chem. Phys.*, 17, 7807–7826, <https://doi.org/10.5194/acp-17-7807-2017>, 2017.
- Nussbaumer, C. M. and Cohen, R. C.: The Role of Temperature and NO_x in Ozone Trends in the Los Angeles Basin, *Environ. Sci. Technol.*, 54, 15652–15659, <https://doi.org/10.1021/acs.est.0c04910>, 2020.
- Nuvolone, D., Petri, D., and Voller, F.: The effects of ozone on human health, *Environ. Sci. Pollut. R.*, 25, 8074–8088, <https://doi.org/10.1007/s11356-017-9239-3>, 2018.
- Ouwensloot, H. G., Vilà-Guerau de Arellano, J., Nölscher, A. C., Krol, M. C., Ganzeveld, L. N., Breitenberger, C., Mammarella, I., Williams, J., and Lelieveld, J.: Characterization of a boreal convective boundary layer and its impact on atmospheric chemistry during HUMPPA-COPEC-2010, *Atmos. Chem. Phys.*, 12, 9335–9353, <https://doi.org/10.5194/acp-12-9335-2012>, 2012.
- Palmer, P. I., Jacob, D. J., Fiore, A. M., Martin, R. V., Chance, K., and Kurosu, T. P.: Mapping isoprene emissions over North America using formaldehyde column observations from space, *J. Geophys. Res.*, 108, 4180, <https://doi.org/10.1029/2002JD002153>, 2003.
- Pires, J. C. M.: Ozone weekend effect analysis in three European urban areas, *CLEAN Soil Air Water*, 40, 790–797, <https://doi.org/10.1002/clen.201100410>, 2012.
- Possanzini, M., Di Palo, V., and Cecinato, A.: Sources and photodecomposition of formaldehyde and acetaldehyde in Rome ambient air, *Atmos. Environ.*, 36, 3195–3201, [https://doi.org/10.1016/S1352-2310\(02\)00192-9](https://doi.org/10.1016/S1352-2310(02)00192-9), 2002.
- Pusede, S. E. and Cohen, R. C.: On the observed response of ozone to NO_x and VOC reactivity reductions in San Joaquin Valley California 1995–present, *Atmos. Chem. Phys.*, 12, 8323–8339, <https://doi.org/10.5194/acp-12-8323-2012>, 2012.

- Pusede, S. E., Steiner, A. L., and Cohen, R. C.: Temperature and recent trends in the chemistry of continental surface ozone, *Chem. Rev.*, 115, 3898–3918, <https://doi.org/10.1021/cr5006815>, 2015.
- Rannik, Ü., Altimir, N., Mammarella, I., Bäck, J., Rinne, J., Ruuskanen, T. M., Hari, P., Vesala, T., and Kulmala, M.: Ozone deposition into a boreal forest over a decade of observations: evaluating deposition partitioning and driving variables, *Atmos. Chem. Phys.*, 12, 12165–12182, <https://doi.org/10.5194/acp-12-12165-2012>, 2012.
- Sadanaga, Y., Sengen, M., Takenaka, N., and Bandow, H.: Analyses of the ozone weekend effect in Tokyo, Japan: regime of oxidant (O₃ + NO₂) production, *Aerosol Air Qual. Res.*, 12, 161–168, <https://doi.org/10.4209/aaqr.2011.07.0102>, 2011.
- Schroeder, J. R., Crawford, J. H., Fried, A., Walega, J., Weinheimer, A., Wisthaler, A., Müller, M., Mikoviny, T., Chen, G., Shook, M., Blake, D. R., and Tonnesen, G. S.: New insights into the column CH₂O/NO₂ ratio as an indicator of near-surface ozone sensitivity, *J. Geophys. Res.-Atmos.*, 122, 8885–8907, <https://doi.org/10.1002/2017JD026781>, 2017.
- Schwantes, R. H., Emmons, L. K., Orlando, J. J., Barth, M. C., Tyn-dall, G. S., Hall, S. R., Ullmann, K., St. Clair, J. M., Blake, D. R., Wisthaler, A., and Bui, T. P. V.: Comprehensive isoprene and terpene gas-phase chemistry improves simulated surface ozone in the southeastern US, *Atmos. Chem. Phys.*, 20, 3739–3776, <https://doi.org/10.5194/acp-20-3739-2020>, 2020.
- Seguel, R. J., Morales S., R. G. E., and Leiva G., M. A.: Ozone weekend effect in Santiago, Chile, *Environ. Pollut.*, 162, 72–79, <https://doi.org/10.1016/j.envpol.2011.10.019>, 2012.
- Seyfioglu, R., Odabasi, M., and Cetin, E.: Wet and dry deposition of formaldehyde in Izmir, Turkey, *Sci. Total Environ.*, 366, 809–818, <https://doi.org/10.1016/j.scitotenv.2005.08.005>, 2006.
- Shepson, P. B., Bottenheim, J. W., Hastie, D. R., and Venkatram, A.: Determination of the relative ozone and PAN deposition velocities at night, *Geophys. Res. Lett.*, 19, 1121–1124, <https://doi.org/10.1029/92GL01118>, 1992.
- Sillman, S.: The use of NO_y, H₂O₂, and HNO₃ as indicators for ozone-NO_x-hydrocarbon sensitivity in urban locations, *J. Geophys. Res.-Atmos.*, 100, 14175–14188, <https://doi.org/10.1029/94JD02953>, 1995.
- Sobanski, N., Tang, M. J., Thieser, J., Schuster, G., Pöhler, D., Fischer, H., Song, W., Sauvage, C., Williams, J., Fachinger, J., Berkes, F., Hoor, P., Platt, U., Lelieveld, J., and Crowley, J. N.: Chemical and meteorological influences on the lifetime of NO₃ at a semi-rural mountain site during PARADE, *Atmos. Chem. Phys.*, 16, 4867–4883, <https://doi.org/10.5194/acp-16-4867-2016>, 2016.
- Stickler, A., Fischer, H., Williams, J., De Reus, M., Sander, R., Lawrence, M., Crowley, J., and Lelieveld, J.: Influence of summertime deep convection on formaldehyde in the middle and upper troposphere over Europe, *J. Geophys. Res.*, 111, D14308, <https://doi.org/10.1029/2005JD007001>, 2006.
- Stickler, A., Fischer, H., Bozem, H., Gurk, C., Schiller, C., Martinez-Harder, M., Kubistin, D., Harder, H., Williams, J., Eerdekens, G., Yassaa, N., Ganzeveld, L., Sander, R., and Lelieveld, J.: Chemistry, transport and dry deposition of trace gases in the boundary layer over the tropical Atlantic Ocean and the Guyanas during the GABRIEL field campaign, *Atmos. Chem. Phys.*, 7, 3933–3956, <https://doi.org/10.5194/acp-7-3933-2007>, 2007.
- Stockwell, W. R. and Calvert, J. G.: The mechanism of NO₃ and HONO formation in the nighttime chemistry of the urban atmosphere, *J. Geophys. Res.-Oceans*, 88, 6673–6682, <https://doi.org/10.1029/JC088iC11p06673>, 1983.
- Sumner, A. L., Shepson, P. B., Couch, T. L., Thornberry, T., Carroll, M. A., Sillman, S., Pippin, M., Bertman, S., Tan, D., Faloon, I., Brune, W., Young, V., Cooper, O., Moody, J., and Stockwell, W.: A study of formaldehyde chemistry above a forest canopy, *J. Geophys. Res.-Atmos.*, 106, 24387–24405, <https://doi.org/10.1029/2000JD900761>, 2001.
- Tadic, I., Crowley, J. N., Dienhart, D., Eger, P., Harder, H., Hottmann, B., Martinez, M., Parchatka, U., Paris, J.-D., Pozzer, A., Rohloff, R., Schuladen, J., Shenolikar, J., Tauer, S., Lelieveld, J., and Fischer, H.: Net ozone production and its relationship to nitrogen oxides and volatile organic compounds in the marine boundary layer around the Arabian Peninsula, *Atmos. Chem. Phys.*, 20, 6769–6787, <https://doi.org/10.5194/acp-20-6769-2020>, 2020.
- Urbanski, S. P., Stickel, R. E., Zhao, Z., and Wine, P. H.: Mechanistic and kinetic study of formaldehyde production in the atmospheric oxidation of dimethyl sulfide, *Journal of the Chemical Society, Faraday Transactions*, 93, 2813–2819, <https://doi.org/10.1039/A701380I>, 1997.
- Veres, P. R., Faber, P., Drewnick, F., Lelieveld, J., and Williams, J.: Anthropogenic sources of VOC in a football stadium: Assessing human emissions in the atmosphere, *Atmos. Environ.*, 77, 1052–1059, <https://doi.org/10.1016/j.atmosenv.2013.05.076>, 2013.
- Vigouroux, C., Hendrick, F., Stavrakou, T., Dils, B., De Smedt, I., Hermans, C., Merlaud, A., Scolas, F., Senten, C., Vanhaelewyn, G., Fally, S., Carleer, M., Metzger, J.-M., Müller, J.-F., Van Roozendaal, M., and De Mazière, M.: Ground-based FTIR and MAX-DOAS observations of formaldehyde at Réunion Island and comparisons with satellite and model data, *Atmos. Chem. Phys.*, 9, 9523–9544, <https://doi.org/10.5194/acp-9-9523-2009>, 2009.
- Wang, Y. H., Hu, B., Ji, D. S., Liu, Z. R., Tang, G. Q., Xin, J. Y., Zhang, H. X., Song, T., Wang, L. L., Gao, W. K., Wang, X. K., and Wang, Y. S.: Ozone weekend effects in the Beijing–Tianjin–Hebei metropolitan area, China, *Atmos. Chem. Phys.*, 14, 2419–2429, <https://doi.org/10.5194/acp-14-2419-2014>, 2014.
- Wennberg, P. O., Bates, K. H., Crounse, J. D., Dodson, L. G., McVay, R. C., Mertens, L. A., Nguyen, T. B., Praske, E., Schwantes, R. H., Smarte, M. D., St. Clair, J. M., Teng, A. P., Zhang, X., and Seinfeld, J. H.: Gas-phase reactions of isoprene and its major oxidation products, *Chem. Rev.*, 118, 3337–3390, <https://doi.org/10.1021/acs.chemrev.7b00439>, 2018.
- Werner, A., Plass-Dülmer, C., Englert, J., Michl, K., and Tensing, E.: VOCs at Hohenpeißenberg during HOPE 2012, EGU General Assembly, Vienna, Austria, 7–12 April 2013, EGU2013-8175, 2013.
- Wesely, M. and Hicks, B.: A review of the current status of knowledge on dry deposition, *Atmos. Environ.*, 34, 2261–2282, [https://doi.org/10.1016/S1352-2310\(99\)00467-7](https://doi.org/10.1016/S1352-2310(99)00467-7), 2000.
- Williams, J., Crowley, J., Fischer, H., Harder, H., Martinez, M., Petäjä, T., Rinne, J., Bäck, J., Boy, M., Dal Maso, M., Hakala, J., Kajos, M., Keronen, P., Rantala, P., Aalto, J., Aaltonen, H., Paatero, J., Vesala, T., Hakola, H., Levula, J., Pohja, T., Herrmann, F., Auld, J., Mesarchaki, E., Song, W., Yassaa, N., Nölscher, A., Johnson, A. M., Custer, T., Sinha, V., Thieser,

- J., Pouvesle, N., Taraborrelli, D., Tang, M. J., Bozem, H., Hosaynali-Beygi, Z., Axinte, R., Oswald, R., Novelli, A., Kubistin, D., Hens, K., Javed, U., Trawny, K., Breitenberger, C., Hidalgo, P. J., Ebben, C. J., Geiger, F. M., Corrigan, A. L., Russell, L. M., Ouwersloot, H. G., Vilà-Guerau de Arellano, J., Ganzeveld, L., Vogel, A., Beck, M., Bayerle, A., Kampf, C. J., Bertelmann, M., Köllner, F., Hoffmann, T., Valverde, J., González, D., Riekkola, M.-L., Kulmala, M., and Lelieveld, J.: The summertime Boreal forest field measurement intensive (HUMPPA-COPEC-2010): an overview of meteorological and chemical influences, *Atmos. Chem. Phys.*, 11, 10599–10618, <https://doi.org/10.5194/acp-11-10599-2011>, 2011.
- Wittrock, F., Richter, A., Oetjen, H., Burrows, J. P., Kanakidou, M., Myriokefalitakis, S., Volkamer, R., Beirle, S., Platt, U., and Wagner, T.: Simultaneous global observations of glyoxal and formaldehyde from space, *Geophys. Res. Lett.*, 33, L16804, <https://doi.org/10.1029/2006GL026310>, 2006.
- Wolfe, G. M., Kaiser, J., Hanisco, T. F., Keutsch, F. N., de Gouw, J. A., Gilman, J. B., Graus, M., Hatch, C. D., Holloway, J., Horowitz, L. W., Lee, B. H., Lerner, B. M., Lopez-Hilfiker, F., Mao, J., Marvin, M. R., Peischl, J., Pollack, I. B., Roberts, J. M., Ryerson, T. B., Thornton, J. A., Veres, P. R., and Warneke, C.: Formaldehyde production from isoprene oxidation across NO_x regimes, *Atmos. Chem. Phys.*, 16, 2597–2610, <https://doi.org/10.5194/acp-16-2597-2016>, 2016.
- Yan, C., Kocavska, S., and Krasnoperov, L. N.: Kinetics of the reaction of CH₃O₂ radicals with OH studied over the 292–526 K temperature range, *J. Phys. Chem. A*, 120, 6111–6121, <https://doi.org/10.1021/acs.jpca.6b04213>, 2016.

3.5 Impact of the COVID-19 lockdown on photochemical processes in the upper troposphere over Europe

This chapter has been published in the journal *Atmospheric Chemistry & Physics* as a research article. I am the first author of this paper. I have analyzed all data presented, I have made the figures and I have prepared and revised the manuscript. The co-authors were involved in the presented research campaign BLUESKY (Europe 2020) and in proofreading the manuscript. Detailed author contributions can be found at the end of the paper in the section *Author contributions*.

How to cite: Nussbaumer, C. M., Pozzer, A., Tadic, I., Röder, L., Obersteiner, F., Harder, H., Lelieveld, J., and Fischer, H.: Tropospheric ozone production and chemical regime analysis during the COVID-19 lockdown over Europe, *Atmos. Chem. Phys.*, 22, 6151–6165, <https://doi.org/10.5194/acp-22-6151-2022>, **2022**.

submitted: 09 Dec 2021

published: 11 May 2022

The supplementary material for this publication can be found in Section 4.4.



Tropospheric ozone production and chemical regime analysis during the COVID-19 lockdown over Europe

Clara M. Nussbaumer¹, Andrea Pozzer¹, Ivan Tadic¹, Lenard Röder¹, Florian Obersteiner²,
Hartwig Harder¹, Jos Lelieveld^{1,3}, and Horst Fischer¹

¹Department of Atmospheric Chemistry, Max Planck Institute for Chemistry, 55128 Mainz, Germany

²Institute of Meteorology and Climate Research – Atmospheric Trace Gases and Remote Sensing (IMK-ASF),
Karlsruhe Institute of Technology, 76021 Karlsruhe, Germany

³Climate and Atmosphere Research Center, The Cyprus Institute, Nicosia, Cyprus

Correspondence: Clara M. Nussbaumer (clara.nussbaumer@mpic.de)

Received: 9 December 2021 – Discussion started: 21 December 2021

Revised: 12 April 2022 – Accepted: 15 April 2022 – Published: 11 May 2022

Abstract. The COVID-19 (coronavirus disease 2019) European lockdowns have led to a significant reduction in the emissions of primary pollutants such as NO (nitric oxide) and NO₂ (nitrogen dioxide). As most photochemical processes are related to nitrogen oxide (NO_x ≡ NO + NO₂) chemistry, this event has presented an exceptional opportunity to investigate its effects on air quality and secondary pollutants, such as tropospheric ozone (O₃). In this study, we present the effects of the COVID-19 lockdown on atmospheric trace gas concentrations, net ozone production rates (NOPRs) and the dominant chemical regime throughout the troposphere based on three different research aircraft campaigns across Europe. These are the UTOPIHAN (Upper Tropospheric Ozone: Processes Involving HO_x and NO_x) campaigns in 2003 and 2004, the HOOVER (HO_x over Europe) campaigns in 2006 and 2007, and the BLUESKY campaign in 2020, the latter performed during the COVID-19 lockdown. We present in situ observations and simulation results from the ECHAM5 (fifth-generation European Centre Hamburg general circulation model, version 5.3.02)/MESSy2 (second-generation Modular Earth Sub-model System, version 2.54.0) Atmospheric Chemistry (EMAC), model which allows for scenario calculations with business-as-usual emissions during the BLUESKY campaign, referred to as the “no-lockdown scenario”. We show that the COVID-19 lockdown reduced NO and NO₂ mixing ratios in the upper troposphere by around 55 % compared to the no-lockdown scenario due to reduced air traffic. O₃ production and loss terms reflected this reduction with a deceleration in O₃ cycling due to reduced mixing ratios of NO_x, while NOPRs were largely unaffected. We also study the role of methyl peroxyradicals forming HCHO (α-CH₃O₂) to show that the COVID-19 lockdown shifted the chemistry in the upper-troposphere–tropopause region to a NO_x-limited regime during BLUESKY. In comparison, we find a volatile organic compound (VOC)-limited regime to be dominant during UTOPIHAN.

1 Introduction

COVID-19 (coronavirus disease 2019) describes the disease accompanying an infection with the SARS-CoV-2 (severe acute respiratory syndrome coronavirus-2) virus. The disease is highly infectious and can have severe health consequences, including premature death, particularly for the elderly and people with pre-existing conditions (WHO, 2021). On 11 March 2020, COVID-19 was declared a pandemic

by the World Health Organization (WHO, 2020a, b). As a response, in many countries worldwide – including the European continent – governments initiated a shutdown of the daily life for minimizing the spread of the virus, which is referred to as a COVID-19 lockdown. Among others, this included a reduction in vehicular and industrial activities as well as sharp restrictions on air travel accompanied by a reduction in atmospheric pollutants such as nitrogen oxides (NO_x ≡ NO + NO₂) (Venter et al., 2020; Kroll et al., 2020;

Chossière et al., 2021; Onyeaka et al., 2021; Salma et al., 2020; Matthias et al., 2021; Forster et al., 2020).

NO and NO₂ are important atmospheric trace gases as they are involved in almost all photochemical processes taking place in the earth's atmosphere. NO_x directly impacts the production of tropospheric ozone (O₃), which is a hazard to human and plant health (Nuvolone et al., 2018; Mills et al., 2018). Together with volatile organic compound (VOC) oxidation, NO forms NO₂ within the HO_x cycle, catalyzed by an OH radical. Under the influence of sunlight, NO₂ can subsequently form O₃ through the reaction with molecular oxygen, as shown in Reaction (R1) (Leighton, 1971; Crutzen, 1988; Lelieveld and Dentener, 2000; Pusede and Cohen, 2012; Pusede et al., 2015; Nussbaumer and Cohen, 2020).



Various termination reactions such as the formation of HNO₃ from OH and NO₂ or other radical recombinations cause ozone chemistry to be non-linear, which means that a reduction in ambient NO_x can either increase or decrease O₃ production (Calvert and Stockwell, 1983; Pusede et al., 2015). For low ambient NO_x levels, a NO_x reduction usually causes a decrease in O₃ production, which is referred to as a NO_x-limited chemical regime. In contrast, a NO_x reduction increases O₃ production when a VOC-limited chemical regime is dominant – usually at high ambient NO_x levels (Sillman et al., 1990; National Research Council, 1992; Pusede and Cohen, 2012). In the transition region between the two regimes, changes in NO_x do not (or only slightly) impact O₃ production rates (Wang et al., 2018). Earlier studies on evaluating correlations of NO_x and O₃ in the troposphere include Liu et al. (1987), Logan (1985) and Lin et al. (1988), reporting a non-linear dependence that varies with ambient levels of hydrocarbons and NO_x.

Many different methods enable the determination of the dominant chemical regime, such as the use of the weekend ozone effect, which considers the response of O₃ to NO_x reductions on weekends, or the ratio of HCHO to NO₂, with various approaches from in situ observations, remote sensing and model simulations (e.g., Jin et al., 2020; Pusede and Cohen, 2012; Nussbaumer and Cohen, 2020; Duncan et al., 2010). We have recently shown that the fraction α of methyl peroxyradicals (CH₃O₂) forming formaldehyde (HCHO) in correlation with ambient NO concentrations is capable of indicating the dominant chemical regime based on three different field campaigns across Europe in Finland (HUMPPA 2012), Germany (HOPE 2012) and Cyprus (CYPHEX 2014) (Nussbaumer et al., 2021). CH₃O₂ formed from, for example, the oxidation of acetaldehyde (CH₃CHO) or methane (CH₄) can either react with NO or OH radicals to form HCHO or undergo the competing reaction with HO₂ to form methyl hydroperoxide (CH₃OOH). For more details, please see Fig. 1 in Nussbaumer et al. (2021). $\alpha_{\text{CH}_3\text{O}_2}$ consequently depends on the ambient concentrations of NO, OH

and HO₂ and the respective rate constants for the reaction with CH₃O₂, the latter of which were taken from the IUPAC Task Group on Atmospheric Chemical Kinetic Data Evaluation (2021). Self-reaction of CH₃O₂ as a contributor to CH₃O₂ loss forming HCHO is negligible. The calculation of $\alpha_{\text{CH}_3\text{O}_2}$ is presented in Eq. (1).

$$\alpha_{\text{CH}_3\text{O}_2} = \frac{k_{\text{CH}_3\text{O}_2+\text{NO}} \times [\text{NO}] + k_{\text{CH}_3\text{O}_2+\text{OH}} \times [\text{OH}]}{k_{\text{CH}_3\text{O}_2+\text{NO}} \times [\text{NO}] + k_{\text{CH}_3\text{O}_2+\text{OH}} \times [\text{OH}] + k_{\text{CH}_3\text{O}_2+\text{HO}_2} \times [\text{HO}_2]} \quad (1)$$

Low values for $\alpha_{\text{CH}_3\text{O}_2}$ with a high response to NO are an indicator for a NO_x-limited regime, whereas high values for $\alpha_{\text{CH}_3\text{O}_2}$ with little response to changing NO represent a VOC limitation (Fig. 11 in Nussbaumer et al., 2021). Investigating the dominant chemical regime is an important method for analyzing photochemical processes and air quality.

Previous studies have explored changes in air quality, trace gas emissions and the dominant chemical regime during the COVID-19 lockdown in Europe. Menut et al. (2020) reported NO₂ reductions between 30 % and 50 % for various western European countries in the course of March 2020, with both decreasing and increasing O₃ concentrations in response, depending on the location, based on surface in situ observations and model simulations. Ordóñez et al. (2020) observed decreased NO₂ and increased O₃ concentrations in central Europe in March and April 2020 based on in situ observations compared to 2015–2019. While they found NO₂ reductions to be mainly attributed to the COVID-19 lockdown, O₃ enhancements were predominantly affected by meteorological changes. Chossière et al. (2021) presented evidence of NO₂ reductions during the COVID-19 lockdown in Europe and O₃ changes dependent on the dominant chemical regime through investigation of HCHO/NO₂ ratios based on in situ and satellite observations. Similar studies were performed by Matthias et al. (2021), Mertens et al. (2021), Balamurugan et al. (2021), Grange et al. (2021) and many more.

Besides the changes within the dominant chemical regime through NO_x reductions, i.e., increasing ozone within a VOC-limited regime and decreasing ozone within a NO_x-limited regime, the COVID-19 lockdown could have potentially changed the dominant chemical regime from VOC- to NO_x-limited as pointed out by Kroll et al. (2020) and Gaubert et al. (2021). Cazorla et al. (2021) found a lockdown-induced change from a VOC- to a NO_x-limited regime in Quito (Ecuador) based on the share of precursor loss to HNO₃ and H₂O₂. The latter is dominant for NO_x-limited chemistry (Kleinman et al., 2001). A change from a VOC- to a NO_x-limited regime was also reported by Zhu et al. (2021) in China based on HCHO-to-NO₂ ratios (NO_x limitation for ratios above 2 according to Duncan et al., 2010).

Most of the literature on pollutant reductions during the COVID-19 lockdown focuses on near-surface air quality, and only few studies consider the free troposphere. Steinbrecht et al. (2021), Chang et al. (2022) and Bouarar et al. (2021)

reported decreases in O_3 concentrations in the free troposphere based on in situ observations and modeling studies in the Northern Hemisphere. Bouarar et al. (2021) found that reduced air traffic – a unique incidence after strongly increasing aircraft activities over the past decades, as shown by Lee et al. (2021) – can explain around a third of the observed O_3 decrease in 2020, the remaining contributions coming from ground-level reductions and meteorological differences. Reduced O_3 in the free troposphere was also reported by Clark et al. (2021) around Frankfurt airport. Cristofanelli et al. (2021) reported lower O_3 concentrations above the planetary boundary layer (PBL) in 2020 compared to the 1996–2019 average at Monte Cimone in Italy, which is in line with findings by the World Meteorological Organization (2021), extended to include two mountain sites in Germany.

In this study, we present atmospheric trace gas concentrations, net ozone production rates and an analysis on the dominant chemical regime based on in situ observations during the research aircraft campaign BLUESKY, which took place in May and June 2020 over Europe, and model simulations. During this time period, aircraft activity was still strongly limited due to the COVID-19 lockdown. We compare the results to model simulations assuming business-as-usual emissions not impacted by government restrictions, which we refer to as the “no-lockdown scenario”. Additionally, we present results of two previous aircraft campaigns, which are UTOPIHAN (Upper Tropospheric Ozone: Processes Involving HO_x and NO_x) in 2003/04 and HOOVER (HO_x over Europe) in 2006/07. While many studies have been published on emissions reductions and the effect on secondary pollutants during the COVID-19 lockdown, only a few studies have investigated changes in the dominant chemical regime, and to our knowledge we are the first to report a shift to NO_x -limited chemistry in the upper troposphere. This can demonstrate the consequences of emission changes in VOCs (including methane) and NO_x for tropospheric ozone.

2 Observations and methods

2.1 Calculations of net ozone production rates (NOPRs)

Besides the chemical regime, production and loss processes of O_3 are effective tools in exploring relevant photochemistry. As already demonstrated in Reaction (R1), O_3 is formed via NO_2 photolysis. Under the assumption of photostationary state, this term can be equated with the reactions of NO with O_3 , HO_2 and RO_2 (Hosaynali Beygi et al., 2011). The resulting term for O_3 production $P(O_3)$ is shown in Eq. (2) (Tadic et al., 2020; Leighton, 1971); $j(NO_2)$ is the photolysis frequency of NO_2 , and k describes the respective rate constant (for this work taken from the IUPAC Task Group on Atmospheric Chemical Kinetic Data Evaluation,

2021).

$$P(O_3) = [NO_2] \times j(NO_2) = [NO] \times (k_{O_3+NO} \times [O_3] + k_{NO+HO_2} \times [HO_2] + \sum_z k_{NO+R_zO_2} \times [R_zO_2]) \quad (2)$$

We assume R_zO_2 (the sum of all peroxy radicals) to be represented by CH_3O_2 , which we find to be a reasonable approximation when comparing modeled CH_3O_2 to the overall modeled RO_2 as shown in Fig. S1 in the Supplement, exemplarily for the BLUESKY campaign. Above 800 hPa, CH_3O_2 represents more than 90 % of RO_2 . Below 800 hPa, it still accounts for more than 70 % on average. CH_3O_2 can be calculated via Eq. (3) as derived by Bozem et al. (2017a). While the model can simulate CH_3O_2 mixing ratios, Eq. (3) is required when working with experimental data as CH_3O_2 was not directly measured.

$$[CH_3O_2] = \frac{k_{CH_4+OH} \times [CH_4]}{k_{CO+OH} \times [CO]} \times [HO_2] \quad (3)$$

O_3 loss occurs via the reaction with NO , OH and HO_2 and via photolysis and can be calculated as presented in Eq. (4). The photolysis of O_3 first yields O^1D , which reacts back to O_3 through collision with O_2 or N_2 and causes an O_3 loss through reaction with H_2O . The share of O_3 that is effectively lost through O_3 photolysis is described by α_{O^1D} in Eq. (5) (Bozem et al., 2017a). Additional loss due to reactions of O_3 with alkenes and the loss of NO_2 due to formation of HNO_3 or peroxy nitrates are negligibly small, particularly in the upper troposphere.

$$L(O_3) = [O_3] \times (k_{O_3+NO} \times [NO] + k_{O_3+HO_2} \times [HO_2] + k_{O_3+OH} \times [OH] + \alpha_{O^1D} \times j(O^1D)) \quad (4)$$

$$\alpha_{O^1D} = \frac{k_{O^1D+H_2O} \times [H_2O]}{k_{O^1D+N_2} \times [N_2] + k_{O^1D+O_2} \times [O_2] + k_{O^1D+H_2O} \times [H_2O]} \quad (5)$$

Net ozone production rates (NOPRs) are then calculated from the difference in $P(O_3)$ and $L(O_3)$, whereas $P(O_3)$ can be expressed via either NO_2 or NO reaction terms. The term $k_{O_3+NO} \times [O_3] \times [NO]$ can be neglected for the latter as it is equally present in $P(O_3)$ and $L(O_3)$.

$$\begin{aligned} \text{NOPR} &= P(O_3) - L(O_3) = [NO_2] \times j(NO_2) \\ &\quad - [O_3] \times (k_{O_3+NO} \times [NO] + k_{O_3+HO_2} \\ &\quad \times [HO_2] + k_{O_3+OH} \times [OH] + \alpha_{O^1D} \times j(O^1D)) \\ &= [NO] \times (k_{NO+HO_2} \times [HO_2] + k_{NO+CH_3O_2} \\ &\quad \times [CH_3O_2]) - [O_3] \times (k_{O_3+HO_2} \times [HO_2] \\ &\quad + k_{O_3+OH} \times [OH] + \alpha_{O^1D} \times j(O^1D)) \end{aligned} \quad (6)$$

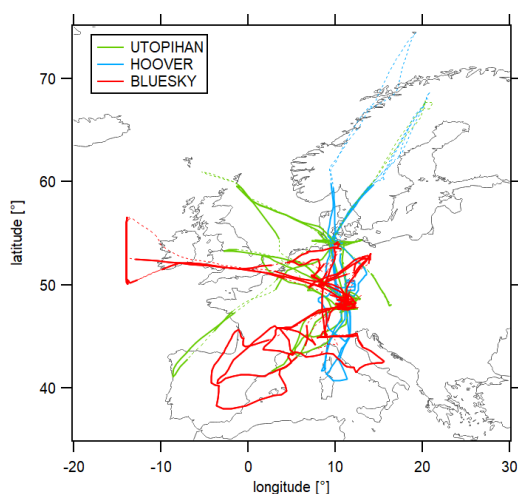


Figure 1. Overview of the flight tracks of the considered aircraft campaigns: UTOPIHAN (2003 and 2004) in green, HOOVER (2006 and 2007) in blue and BLUESKY (2020) in red. Solid lines present the data considered in this study (filtered for troposphere and south of 60°N), and dashed lines show the complete flight tracks.

2.2 Field experiments

We have investigated in situ trace gas observations from three different research aircraft campaigns, which are the UTOPIHAN campaigns in 2003/04, the HOOVER campaigns in 2006/07 and the BLUESKY campaign in 2020. Figure 1 shows an overview of the flight tracks over Europe. We have filtered the data for the tropospheric region with the help of the modeled tropopause pressure (see Sect. 2.3) and south of 60°N as there were no data points for the BLUESKY campaign further north. Dashed lines show the complete flight tracks during each campaign, and solid lines show the data which we have considered in this study. The experimental data were obtained with a time resolution of 1 min and subsequently adjusted to fit the model resolution of 6 min. For this, each sixth experimental data point (which fit the model timescale) and the data points from ± 2 min were averaged. The remaining data points were discarded.

2.2.1 UTOPIHAN 2003/04

The UTOPIHAN (Upper Tropospheric Ozone: Processes Involving HO_x and NO_x) campaigns took place in June/July 2003 and March 2004 starting from Oberpfaffenhofen airport in Germany (48.08° N, 11.28° E) with the GFD (Gesellschaft für Flugziieldarstellung, Hohn, Germany) research aircraft Learjet 35A (Colomb et al., 2006; Klippel et al., 2011; Stickler et al., 2006). NO and O_3 were measured via chemiluminescent detection (CLD 790 SR, ECO Physics, Dürnten, Switzerland). NO data have a precision of 6.5 %, an accu-

racy of ≤ 25 % and a detection limit of < 0.01 ppbv. O_3 data have a precision of 1 % and an accuracy of 5 %; $j(\text{NO}_2)$ was determined via filter radiometers (Meterologie Consult GmbH, Königstein, Germany) with a precision of 1 % and an accuracy of 15 %. CO measurements were obtained from a tunable diode laser absorption spectrometer with a detection limit of 0.26 ppbv (30 s time resolution) and an accuracy of 3.6 % (6 s time resolution) (Kormann et al., 2005).

2.2.2 HOOVER 2006/07

The HOOVER (HO_x over Europe) campaigns took place in October 2006 and July 2007 using the GFD research aircraft Learjet 35A with the campaign base in Hohn, Germany (54.31° N, 9.53° E) (Klippel et al., 2011; Bozem et al., 2017b, a; Regelin et al., 2013). NO and O_3 measurements were performed via chemiluminescence (CLD 790 SR, ECO Physics, Dürnten, Switzerland) with a precision of 7 % and 4 %, an accuracy of 12 % and 2 %, and a detection limit of 0.2 and 2 ppbv, respectively (30 s time resolution) (Hosaynali Beygi et al., 2011). CO and CH_4 were measured via quantum cascade laser absorption spectroscopy with an accuracy of 1.1 % and 0.6 % and detection limits of 0.2 and 6 ppbv, respectively (2 s time resolution) (Schiller et al., 2008). OH and HO_2 measurements were performed via laser-induced fluorescence with the HORUS (HydrOxyl Radical measurement Unit based on fluorescence Spectroscopy) instrument with an accuracy of 18 % and detection limits of 0.016 and 0.33 pptv, respectively (1 min time resolution) (Regelin et al., 2013). Photolysis frequencies were measured using filter radiometers (Meterologie Consult GmbH, Königstein, Germany) with a precision of 1 % and an accuracy of 15 % (1 s time resolution). H_2O was measured via IR absorption with a typical accuracy of 1 % (modified LI-6262, LI-COR Inc., Lincoln, USA) (Gurk et al., 2008; LI-COR, Inc., 1996).

2.2.3 BLUESKY 2020

The BLUESKY campaign took place in May and June 2020 over Europe. Eight flights were carried out using the HALO (High Altitude Long Range) research aircraft starting from the campaign base in Oberpfaffenhofen, Germany. The goal of the campaign was to examine the effects of the COVID-19 lockdown on the troposphere and lower stratosphere over European cities, rural areas and the transatlantic flight corridor. More details can be found in Reifenberg et al. (2022) and Voigt et al. (2022). While most restrictions across Europe were in place in March and April 2020, May and June emissions, particularly from air travel but also from ground-based sources such as on-road traffic, were still affected by the COVID-19 lockdowns (Schlosser et al., 2020; Brockmann Lab, 2022; Hasegawa, 2022; EUROCONTROL, 2022). NO was measured via chemiluminescence (CLD 790 SR, ECO Physics, Dürnten, Switzerland) with a total uncertainty of

15 % and a detection limit of 5 pptv (1 min time resolution) (Tadic et al., 2020).

O₃ measurements were performed with the FAIRO (Fast AIRborne Ozone) instrument, which allows fast detection via chemiluminescence that is calibrated in situ by UV photometry (2.5 % combined uncertainty, 5 Hz time resolution) (Zahn et al., 2012). CO was measured via the quantum cascade laser spectrometer TRISTAR (Tracer In Situ TDLAS for Atmospheric Research) with an uncertainty of 3 % (1 min time resolution) (Schiller et al., 2008).

2.3 Modeling study

The modeled data were obtained from the ECHAM5 (fifth-generation European Centre Hamburg general circulation model, version 5.3.02)/MESSy2 (second-generation Modular Earth Submodel System, version 2.54.0) Atmospheric Chemistry (EMAC) model, which is described in Jöckel et al. (2016) and Reifenberg et al. (2022).

We use data of NO, NO₂, O₃, OH, HO₂, CO, CH₄, CH₃O₂, H₂O, $j(\text{NO}_2)$, $j(\text{O}^1\text{D})$ temperature and pressure, modeled along the flight tracks of the described research aircraft campaigns UTOPIHAN, HOOVER and BLUESKY. The data were filtered for the troposphere using the modeled tropopause pressure. Stratospheric data were discarded. In order to evaluate the impact of reduced emissions during the COVID-19 lockdown, the model was used to simulate a scenario with usual emissions for the BLUESKY campaign, which we refer to as the “no-lockdown scenario”. For details of the model setup please see the paper by Reifenberg et al. (2022).

3 Results and discussion

This analysis is structured as follows: as a full set of in situ observations necessary for a regime analysis and calculating net ozone production rates, which includes NO, O₃, OH, HO₂, CO, CH₄, H₂O, $j(\text{NO}_2)$ and $j(\text{O}^1\text{D})$, is only available for the HOOVER campaign, we first show that the model and experimental data are in close agreement for this campaign. We conclude from this finding that the model is generally capable of reproducing the experimental data and therefore use the model data in our following analysis. In the second step, we provide a comparison between the three campaigns as well as the no-lockdown scenario regarding the individual trace gases and net ozone production rates. We finally present our results of the analysis of the dominant chemical regime, based on $\alpha_{\text{CH}_3\text{O}_2}$.

3.1 Comparison of the model and experiment

Figure 2 shows a comparison of in situ observations (orange) and model simulations (blue) for the HOOVER campaign as vertical profiles. The shaded areas present the 1 σ standard

deviations, and the numbers of data points available for each altitude bin are shown in Tables S1 and S2 in the Supplement.

Figure 2a presents the vertical profile of NO, which shows the typical tropospheric C-shape distribution with the highest values at the surface (e.g., vehicle and industrial emissions) and the upper troposphere (e.g., aircraft and lightning emissions). Ground-level mixing ratios (0–1000 m) were around 0.4 ppbv and decreased with altitude to values of $37 \pm 27(1\sigma)$ pptv and 47 ± 32 pptv for the model and the experiment, respectively, between 3 and 9 km altitude. The only relevant deviation between the model and experiment was between 10 and 11 km altitude with mixing ratios of 0.20 ± 0.03 ppbv and 0.39 ± 0.32 ppbv, respectively.

Figure 2b shows the measured and modeled O₃ mixing ratios, which were lowest at ground level, with 43.7 ± 14.5 ppbv and 36.4 ± 12.8 ppbv for the model and experiment and increased with altitude up to 128.1 ± 22.7 ppbv and 97.5 ± 15.6 ppbv, respectively. Model values were approximately 20 % higher compared to the measured data but showed the same vertical shape. The observed positive O₃ bias of the modeled data is an issue almost all global models suffer from in the Northern Hemisphere and which has not been entirely understood yet (Revell et al., 2018; Young et al., 2018; Jöckel et al., 2016; Parrish et al., 2014).

CO vertical profiles are shown in Fig. 2c and were highest at the surface, with 146.4 ± 63.2 ppbv and 128.0 ± 42.3 ppbv for the model and experiment, respectively, and decreased with altitude to around 70 ppbv in the upper troposphere. HO_x ($\equiv \text{OH} + \text{HO}_2$) is presented in Fig. 2d and e. HO₂ mixing ratios showed a maximum value of around 20 pptv between 2 and 3 km altitude and decreased aloft to values of around 2 pptv in the upper troposphere. The model and experiment showed close agreement. OH mixing ratios were mostly below 1 pptv. Similar to NO, the main deviation between the model and experiment was between 10 and 11 km altitude, where measured values were higher by around 0.5 pptv. Nevertheless, the error bars representing the 1 σ standard deviation of the averages overlapped at all altitudes.

Figure 2f shows the vertical profiles of CH₄, which did not show any particular gradient with altitude. Mixing ratios were 1809 ± 19 ppbv for the model simulation and 1815 ± 40 ppbv for the experiment throughout the campaign. CH₄ is needed for calculating CH₃O₂ via Eq. (3), which we show in Fig. 2g in orange compared to the model simulation of CH₃O₂. Figure 2h and i present the photolysis frequencies $j(\text{NO}_2)$ and $j(\text{O}^1\text{D})$, which show close agreement for the model and experiment. We show the vertical profiles for H₂O, temperature and pressure in Fig. S2. Again, model simulation can represent the experimental data well.

For the UTOPIHAN and the BLUESKY campaigns only a limited number of observations are available. Similar to the HOOVER campaigns, NO, O₃ and CO can be well approximated by the model simulations, which we present in Figs. S3 and S4. Tropospheric ozone is slightly overesti-

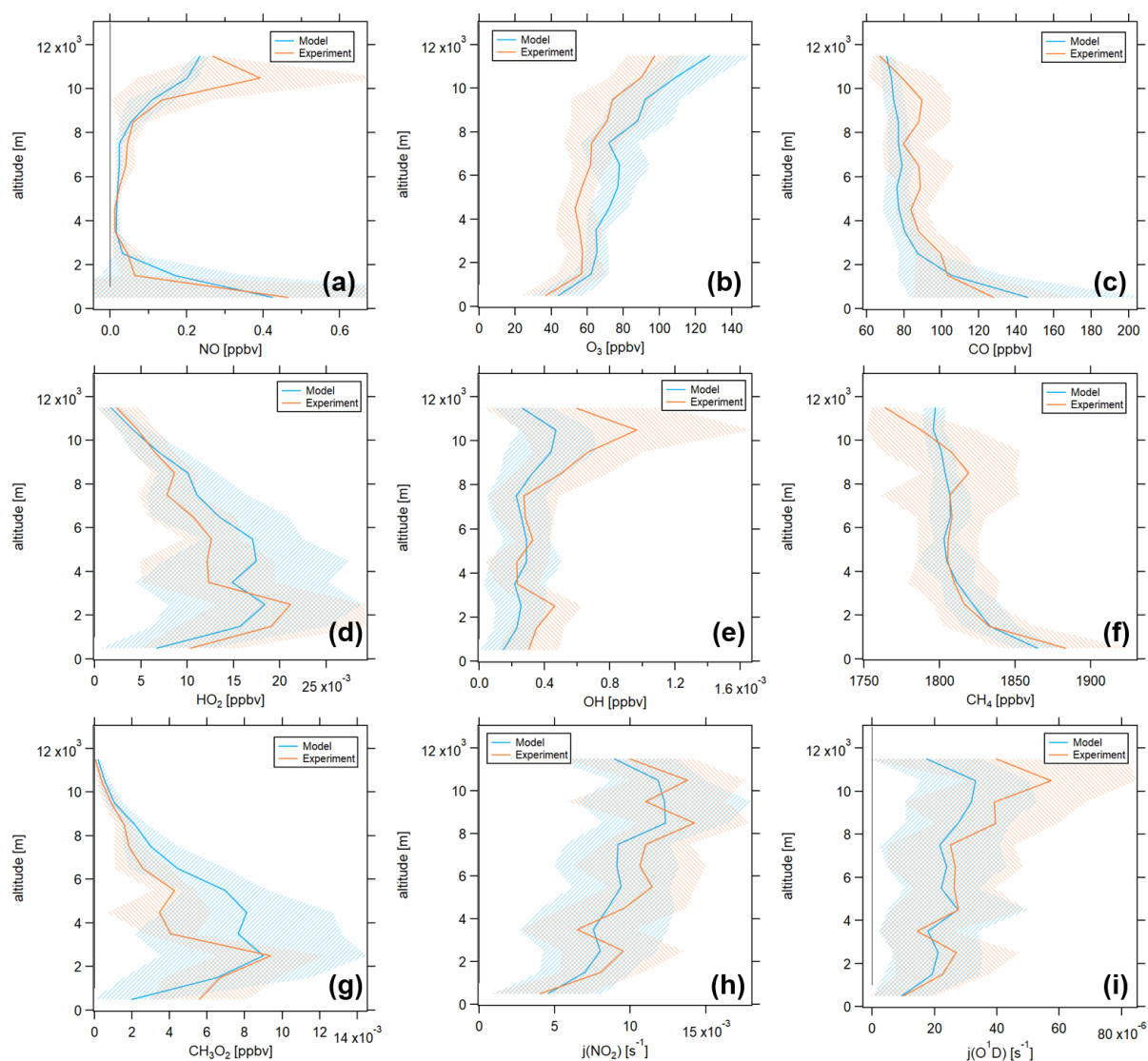


Figure 2. Vertical profiles of in situ observations and model data of the atmospheric trace gases (a) NO, (b) O₃, (c) CO, (d) HO₂, (e) OH, (f) CH₄ and (g) CH₃O₂ and the photolysis rates (h) $j(\text{NO}_2)$ and (i) $j(\text{O}^1\text{D})$ during the HOOVER campaign for estimating the model performance. Blue colors show modeled data by EMAC along the HOOVER campaign flight track (model) and orange colors show experimental data (experiment). The orange trace in panel (g) shows the calculation of CH₃O₂ from experimental CH₄, CO and HO₂ via Eq. (3). The shaded areas represent the 1σ standard deviation from averaging the data points at each altitude bin. The numbers of data points averaged per altitude bin are displayed in Tables S1 and S2 in the Supplement.

mated, which we attribute to the simplified representation of multiphase chemistry (clouds) in the present model version, which underpredicts chemical ozone loss (Rosanka et al., 2021). Based on these results, we conclude that the model is generally capable of representing the in situ observations well and use the model data for all following analyses.

3.2 Campaign comparison

3.2.1 Trace gases

Figure 3 presents the vertical profiles of some selected trace gases during the research aircraft campaigns UTOPIHAN (green), HOOVER (blue) and BLUESKY (red) which were obtained from model simulations. Yellow lines show the no-

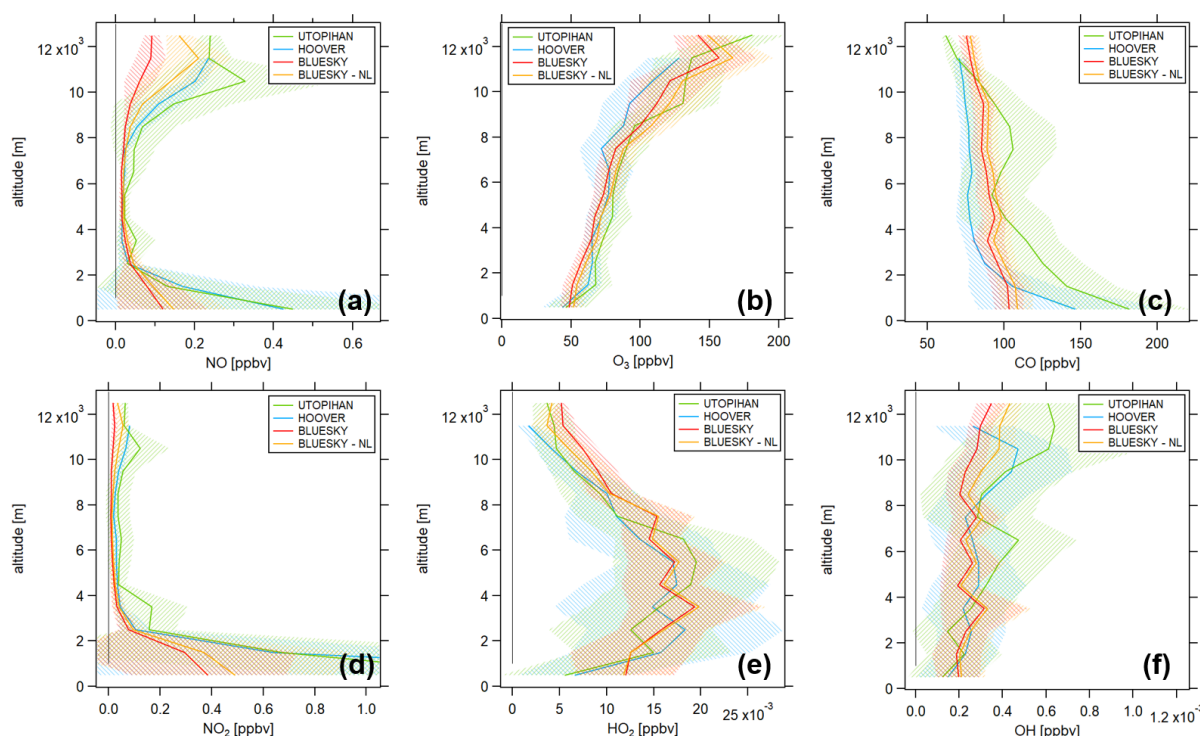


Figure 3. Vertical profiles of the atmospheric trace gases (a) NO, (b) O₃, (c) CO, (d) NO₂, (e) HO₂ and (f) OH for the campaigns UTOPIHAN (green), HOOVER (blue) and BLUESKY (red) and the no-lockdown (NL) scenario (yellow). All data shown here are from EMAC model simulations along the flight track of each research campaign. Two separate simulations were run on the flight path of BLUESKY, one with lockdown and one with business-as-usual emissions. The shaded areas represent the 1σ standard deviation from averaging the data points at each altitude bin. The numbers of data points averaged per altitude bin are displayed in Table S2.

lockdown (NL) scenario for the BLUESKY campaign in 2020.

The vertical profiles of NO are presented in Fig. 3a. For all campaigns, we observe the typical C shape as described for the HOOVER campaigns in Sect. 3.1. Surface (0–1000 m) mixing ratios were similar for UTOPIHAN and HOOVER, with 0.45 ± 0.37 (1σ) ppbv and 0.43 ± 0.74 ppbv, respectively. In comparison, the ground-level concentration of NO during BLUESKY was 0.12 ± 0.11 ppbv. The differences in NO mixing ratios between the campaigns are the outcome of the general emission reduction due to legislative limitation of nitrogen oxides and other hazardous pollutants over the past decades as the campaigns took place 15–20 years apart. We show the decrease in NO_x emissions in the model over the past 2 decades in Fig. S5. Assuming the no-lockdown scenario during BLUESKY, NO ground-level mixing ratios were 0.15 ± 0.14 ppbv and therefore 25 % higher compared to actual mixing ratios (20 % emission reduction). This difference between lockdown and no-lockdown mixing ratios is slightly lower compared to the findings by other studies, for example by Donzelli et al. (2021), who found a NO decrease of 35 %–65 % in Valencia,

Spain, or by Higham et al. (2021), who reported a NO decrease of 55 % in the UK compared to 2019. A possible reason can be that the BLUESKY aircraft campaign took place in May and June 2020, whereas the main lockdown period across Europe occurred rather in March and April. Emissions were still reduced in the following months, but likely to a smaller extent. NO was low and similar for all campaigns between 3 and 8 km altitude, a region without any particular NO sources, with most values below 50 pptv. Above 10 km, NO mixing ratios were 0.29 ± 0.19 ppbv for UTOPIHAN, 0.21 ± 0.03 ppbv for HOOVER and 0.08 ± 0.04 ppbv for BLUESKY. In comparison, NO mixing ratios for the no-lockdown scenario were 0.17 ± 0.08 ppbv above 10 km altitude. This corresponds to an emission reduction of 55 % and results in both absolute and relative NO reductions in the upper troposphere being much higher compared to ground-level reductions. The observed NO reduction in the upper troposphere can be attributed to reduced air traffic, which we show in Fig. 4. In addition to the vertical profiles of NO for BLUESKY (red) and BLUESKY-NL (yellow), we present the modeled BLUESKY-NL scenario without aircraft emissions in blue. In the lower troposphere, where aircraft emis-

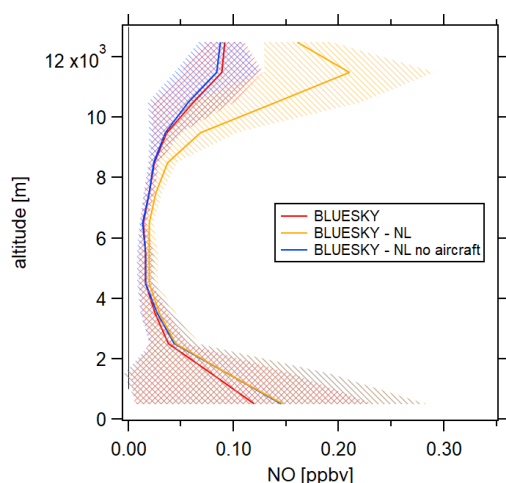


Figure 4. NO vertical profiles for BLUESKY (red), for the BLUESKY no-lockdown scenario (yellow) and for the BLUESKY no-lockdown scenario without aircraft emissions (blue) (model data). Upper-tropospheric NO reductions observed for BLUESKY can be attributed to reduced air traffic during the COVID-19 lockdowns.

sions do not play a significant role, this profile is identical to the BLUESKY-NL scenario. In the upper troposphere, it is very similar to the BLUESKY scenario (including the air travel restrictions), showing that reduced air traffic causes the observed NO decrease.

Figure 3b presents the O_3 vertical profiles. For all campaigns, O_3 mixing ratios were lowest at ground level, with values of around 50 ppbv, and increased with increasing altitude up to around 140 ppbv above 10 km altitude. No significant differences between the campaigns can be observed. While ozone concentrations are dependent on various effects such as precursor levels (including NO_x and VOCs) or meteorology, seasonal variations with a maximum around summertime and a minimum during winter months are also of importance (Logan, 1985). The campaigns shown here include different seasons: the HOOVER campaigns took place in October and July, and the UTOPIHAN campaigns include data from July and March. Figure S6 shows the vertical profiles of ozone separated into different seasons, for both modeled and measured data. Comparing late spring/early summer data of the three field campaigns reveals that O_3 levels during BLUESKY were lower compared to HOOVER and UTOPIHAN, which is in line with findings from Clark et al. (2021), Chang et al. (2022), Bouarar et al. (2021) and Miyazaki et al. (2021).

CO vertical profiles can be seen in Fig. 3c. Ground-level mixing ratios were 181.4 ± 39.4 ppbv for UTOPIHAN, 146.4 ± 63.2 ppbv for HOOVER and slightly lower with 103.2 ± 9.2 ppbv for BLUESKY. Mixing ratios slightly decreased with altitude. Above 3 km altitude, CO for HOOVER

was lower compared to the other campaigns (mostly between 70 and 80 ppbv). Mixing ratios for UTOPIHAN were slightly higher up to 11 km altitude (between 90 and 110 ppbv) compared to BLUESKY (between 80 and 100 ppbv), but generally, significant differences are not evident.

Figure 3d shows the vertical profiles of NO_2 mixing ratios. Similar to NO, ground-level NO_2 mixing ratios were highest for UTOPIHAN and HOOVER, with 1.57 ± 0.77 ppbv and 2.58 ± 2.72 ppbv, respectively. In contrast, mixing ratios for BLUESKY were 0.39 ± 0.30 ppbv and 0.49 ± 0.38 ppbv considering the no-lockdown scenario, which yields a 20 % NO_2 lockdown reduction, as observed for NO. We show the NO_2 range 0–1 ppbv for enabling the campaign distinction at low mixing ratios and present the full range in Fig. S7. As expected for NO_2 , mixing ratios decreased with increasing altitude. No differences between the campaigns can be observed for mid-range altitudes. In the upper troposphere, NO_2 mixing ratios for the individual campaigns showed the same behavior as for NO. Above 10 km altitude, NO_2 was on average 100.6 ± 93.2 pptv for UTOPIHAN, 70.5 ± 13.5 pptv for HOOVER and 43.1 ± 23.1 pptv for the no-lockdown scenario for BLUESKY. In comparison, BLUESKY NO_2 mixing ratios were 19.9 ± 9.8 pptv, which corresponds to a 55 % reduction. In contrast to NO, NO_2 reductions were relatively higher in the upper troposphere but absolutely higher at the surface.

Figure 3e and f show the vertical profiles of HO_x . HO_2 mixing ratios were highest at mid-range altitudes (2–6 km), with values up to 20 pptv, and decreased aloft. OH mixing ratios were lowest at the surface (0.1–0.2 pptv) and increased with altitude. Above 10 km altitude, OH mixing ratios were 0.62 ± 0.38 pptv for UTOPIHAN, 0.40 ± 0.24 pptv for HOOVER, 0.30 ± 0.06 pptv for BLUESKY and 0.39 ± 0.08 pptv for the no-lockdown scenario.

3.2.2 Net ozone production rates

Figure 5 shows the vertical profiles of O_3 production and loss terms. All calculations were performed using model data (justified by the findings from Sect. 3.1) as a full set of in situ observations is only available for HOOVER, but not for UTOPIHAN and BLUESKY. Figure 5a presents net ozone production rates, which were highest at the surface, with values between 1 and 2 ppbv h^{-1} , but had large atmospheric variabilities, represented by the 1σ variability shades from the vertical bin averaging. NOPRs then decreased with increasing altitude. For the HOOVER campaigns, O_3 loss dominated between 3 and 6 km altitude, with NOPRs of -58.9 ± 73.4 pptv h^{-1} . Negative NOPRs were also found for BLUESKY between 4 and 7 km, with -18.7 ± 12.9 pptv h^{-1} , and for UTOPIHAN as well as the no-lockdown BLUESKY scenario between 5 and 6 km. NOPRs were mostly positive and constant aloft. Above 10 km altitude, NOPRs were 91.7 ± 260.9 pptv h^{-1}

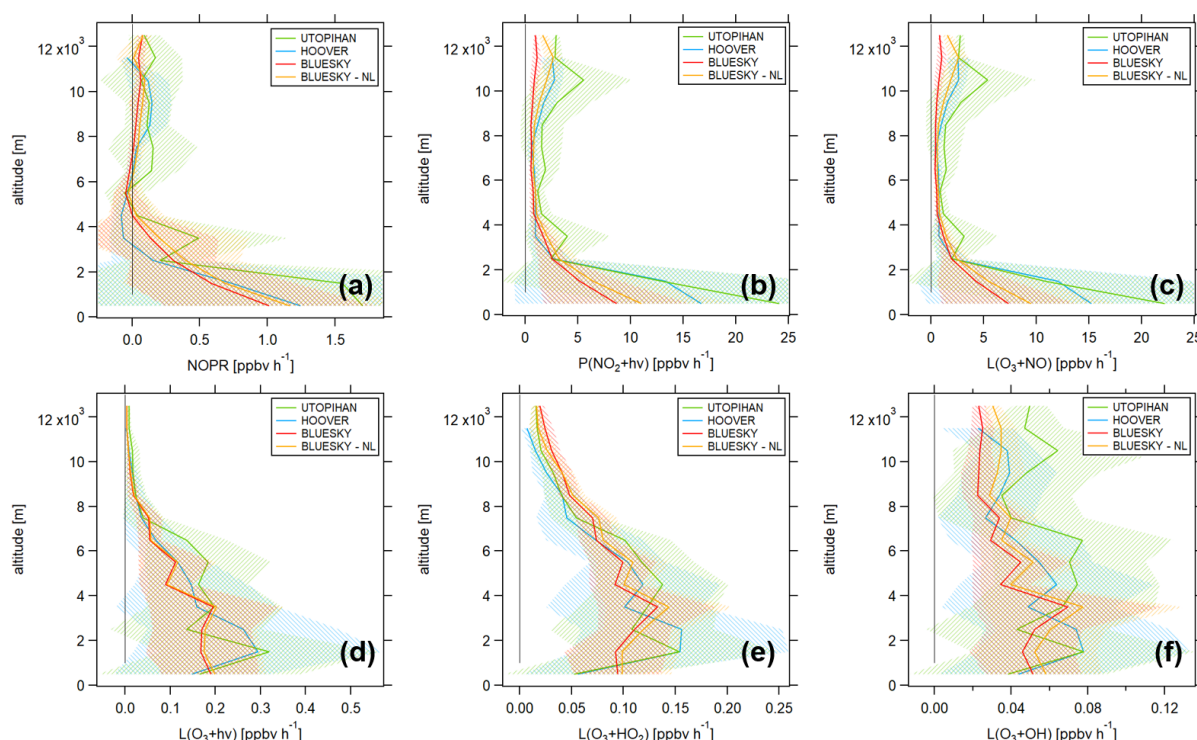


Figure 5. Vertical profiles of (a) net ozone production rates, (b) O_3 production via NO_2 photolysis, (c) O_3 loss via reaction with NO, (d) O_3 loss via photolysis, (e) O_3 loss via reaction with HO_2 and (f) O_3 loss via reaction with OH for the campaigns UTOPIHAN (green), HOOVER (blue) and BLUESKY (red) and the no-lockdown (NL) scenario (yellow). The number of data points averaged per altitude bin are displayed in Table S2.

for UTOPIHAN (51 data points), $71.2 \pm 151.5 \text{ pptv h}^{-1}$ for HOOVER (25 data points), $60.7 \pm 39.7 \text{ pptv h}^{-1}$ for BLUESKY (130 data points) and $61.4 \pm 99.8 \text{ pptv h}^{-1}$ for the no-lockdown scenario. The error ranges are large and overlapping, and therefore significant differences between the campaigns cannot be observed.

Figure 5b shows O_3 production. We calculated the $P(\text{O}_3)$ via the photolysis of NO_2 . In contrast, NO_2 is not available experimentally for the HOOVER campaign, in which case the approximation via the extended Leighton ratio as shown in Eq. (2) is necessary. Modeled $P(\text{O}_3)$ via NO_2 photolysis and measured $P(\text{O}_3)$ via reaction of NO with O_3 , OH and HO_2 are in good agreement, which we show in Fig. 6. The only relevant deviation is observed at ground level, where the experimental value is significantly higher compared to the modeled value. However, only three data points were available for the calculation, with a 1σ standard deviation of the averaging of $> 100\%$. Similar to NOPRs in Fig. 5a, ground-level $P(\text{O}_3)$ shows large variability, with absolute values of around 10 ppbv h^{-1} for BLUESKY and values of around 20 ppbv h^{-1} for UTOPIHAN and HOOVER. The production term then decreased with altitude for each campaign. Significant differences between the campaigns

can only be observed at high altitudes. Above 10 km, $P(\text{O}_3)$ was $4.55 \pm 3.82 \text{ ppbv h}^{-1}$ for UTOPIHAN (51 data points) and $2.68 \pm 0.90 \text{ ppbv h}^{-1}$ for HOOVER (25 data points). For BLUESKY with the no-lockdown scenario, $P(\text{O}_3)$ was $2.17 \pm 0.95 \text{ ppbv h}^{-1}$ (130 data points), and in comparison, lockdown values were on average $0.97 \pm 0.41 \text{ ppbv h}^{-1}$, which corresponds to a 55 % reduction in ozone production. We observed the same relative reduction as for NO and NO_2 mixing ratios.

Figure 5c presents the vertical profiles of O_3 loss via the reaction with NO, which show a similar course compared to the $P(\text{O}_3)$ profiles. Above 10 km, O_3 loss via reaction with NO was largest for UTOPIHAN, with $4.37 \pm 3.82 \text{ ppbv h}^{-1}$, followed by HOOVER, with $2.56 \pm 0.87 \text{ ppbv h}^{-1}$. For BLUESKY, a loss of $0.86 \pm 0.42 \text{ ppbv h}^{-1}$ was observed during the lockdown and a loss of $2.05 \pm 1.02 \text{ ppbv h}^{-1}$ for the no-lockdown scenario. Figure 5d–f present additional considered loss pathways for O_3 via photolysis and via the reactions with HO_2 and OH. It can be seen that these O_3 losses are negligibly small in comparison to the loss via NO, and no significant differences between the campaigns were present.

Consequently, net production of ozone was dominated by NO_x chemistry for all campaigns, and variations in produc-

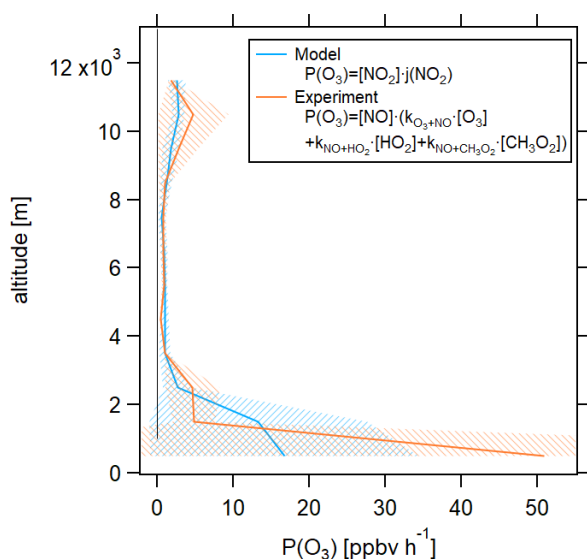


Figure 6. Modeled and experimental vertical profiles of $P(\text{O}_3)$ for HOOVER. Modeled $P(\text{O}_3)$ was calculated via NO_2 photolysis, and experimental $P(\text{O}_3)$ was calculated via the extended Leighton ratio as shown in Eq. (2).

tion and loss terms corresponded to the mixing ratios of NO and NO_2 as presented in Fig. 3. In the campaign comparison, higher NO_x concentrations (as for example for UTOPIHAN) lead to higher production and loss terms of O_3 and vice versa. For the BLUESKY campaign, this analysis shows that the lockdown did not affect net ozone production rates but instead impacted the cycling of O_3 such that both production and loss rates were decreased through the reduced availability of NO and NO_2 in the upper troposphere.

3.3 Chemical regime

As described above, the share of methyl peroxyradicals forming formaldehyde $\alpha_{\text{CH}_3\text{O}_2}$ can be a measure for the dominant chemical regime when correlated with NO mixing ratios. We have previously validated this method in a comparison to the established method of analyzing the HCHO/NO_2 ratio (Nussbaumer et al., 2021). HCHO can be formed by almost any hydrocarbon and is therefore a proxy for VOCs, which are often not measured in their entirety. Likewise, $\alpha_{\text{CH}_3\text{O}_2}$ – representing the HCHO yield from methyl peroxy radicals – is capable of revealing the dominant chemical regime without the knowledge of ambient VOC levels. Figure 7a shows the vertical profiles of $\alpha_{\text{CH}_3\text{O}_2}$ for all available data points for all campaigns based on the model simulation. $\alpha_{\text{CH}_3\text{O}_2}$ values were close to 1 at the surface and decreased with altitude up to around 5 km, where values of around 0.6 were observed, with no significant differences between the campaigns. $\alpha_{\text{CH}_3\text{O}_2}$ increased again aloft,

whereas it was lowest for the BLUESKY campaign. Above 10 km, $\alpha_{\text{CH}_3\text{O}_2}$ was 0.97 ± 0.03 for UTOPIHAN, 0.98 ± 0.01 for HOOVER and 0.96 ± 0.04 for the no-lockdown scenario for BLUESKY. In comparison, $\alpha_{\text{CH}_3\text{O}_2}$ was lower for BLUESKY, with 0.90 ± 0.06 .

Figure 7b and c present $\alpha_{\text{CH}_3\text{O}_2}$ in correlation with NO mixing ratios below 2 km altitude and above 10 km altitude, respectively, based on model results. Below 2 km altitude, $\alpha_{\text{CH}_3\text{O}_2}$ ranged between 0.5 and 1.0 over the NO range of 0–1 ppbv. No significant trends or differences can be observed. We show $\alpha_{\text{CH}_3\text{O}_2}$ between 2 and 10 km altitude in Fig. S8, which does not present any differences between the campaigns either. In contrast, above 10 km altitude, tropospheric $\alpha_{\text{CH}_3\text{O}_2}$ showed a different behavior for each campaign. For an easier distinction, we show each campaign in an individual panel in Fig. S9. For UTOPIHAN, $\alpha_{\text{CH}_3\text{O}_2}$ was high and almost non-responsive to changing NO mixing ratios, with a slope of $\Delta\alpha/\Delta\text{NO} = 0.09 \pm 0.02 \text{ ppbv}^{-1}$. In contrast, $\alpha_{\text{CH}_3\text{O}_2}$ for BLUESKY was between 0.75 and 1. Small changes in NO mixing ratios caused large changes in $\alpha_{\text{CH}_3\text{O}_2}$, with a slope of $1.12 \pm 0.08 \text{ ppbv}^{-1}$. For the no-lockdown scenario the response of $\alpha_{\text{CH}_3\text{O}_2}$ to NO was intermediate between UTOPIHAN and BLUESKY with a slope of $0.37 \pm 0.03 \text{ ppbv}^{-1}$. These observations suggest that a VOC-limited chemical regime was present during the UTOPIHAN campaign in the upper troposphere and a transition regime during the BLUESKY no-lockdown scenario, likely due to emission control over time. For BLUESKY, we observe a distinct NO_x limitation in the upper troposphere, which is related to the lockdown conditions. Aircraft NO_x emissions are much larger than aircraft VOC emissions (Schumann, 2002). We can therefore expect reduced air traffic to effect lower NO_x/VOC ratios, shifting chemistry towards a NO_x -limited regime. Lamprecht et al. (2021) reported ground-level reductions in several aromatic VOCs during the COVID-19 lockdown to be comparable to NO_x reductions in Europe, implicating a steady NO_x/VOC level and therefore no changes in the dominating chemical regime, which is in line with our findings for the lower troposphere. Only few data points were available for HOOVER, which were observed at similar NO levels, and the response of $\alpha_{\text{CH}_3\text{O}_2}$ to NO can therefore not be investigated. While the NOPRs did not change under lockdown conditions due to compensating effects in the NO_x chemistry, we can expect impacts on tropospheric ozone from changes in VOCs (including CH_4) relevant for future emission scenarios. The effects of NO_x aircraft emissions on O_3 and CH_4 have been previously discussed for pre-lockdown conditions in Khodayari et al. (2014) and Khodayari et al. (2015), who present increased methane loss rates and a shorter lifetime as a response to increased OH concentrations from aviation as well as higher ozone production rates. Having investigated NOPRs in this study, lockdown effects on CH_4 loss in the upper troposphere induced by reduced air traffic could be subject to future studies.

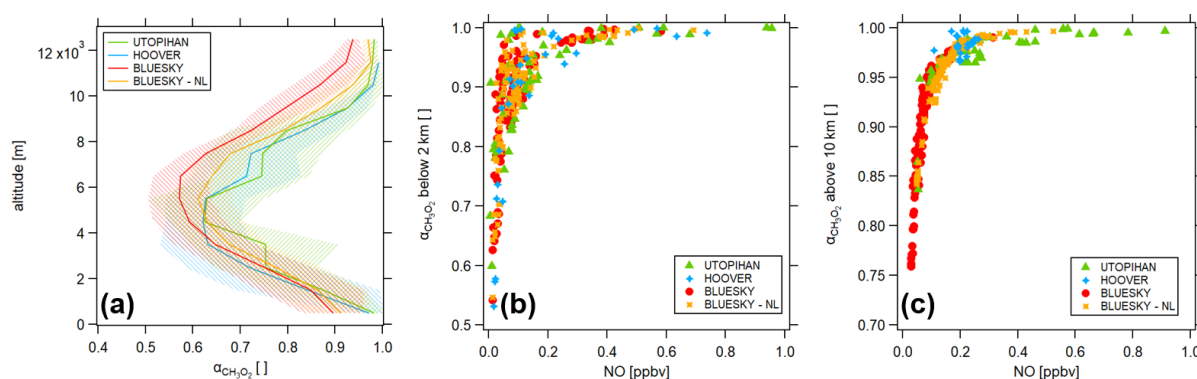


Figure 7. $\alpha_{\text{CH}_3\text{O}_2}$ for the campaigns UTOPIHAN (green), HOOVER (blue) and BLUESKY (red) and the no-lockdown (NL) scenario (yellow) (a) as a vertical profile, (b) in correlation with NO below 2 km and (c) in correlation with NO above 10 km.

4 Conclusions

In this study, we present in situ observations of atmospheric trace gases and model simulations from the EMAC model for three different aircraft campaigns across Europe: the UTOPIHAN campaigns in 2003/04, the HOOVER campaigns in 2006/07 and the BLUESKY campaign in 2020, including a modeled “no-lockdown scenario” with business-as-usual emissions for the latter. We found that model results can reproduce in situ observations well and thus could be used for further analysis which benefits from a more complete set of parameters and a higher data coverage. While observations for O_3 , CO and HO_x were very similar for all campaigns, NO_x showed significant differences, particularly in the upper troposphere, where mixing ratios were highest for UTOPIHAN and HOOVER, followed by the no-lockdown scenario for BLUESKY. Observed NO and NO_2 emissions during the BLUESKY campaign were approximately 55 % lower compared to the modeled no-lockdown scenario, which are attributed to reduced aircraft activity at these altitudes due to the COVID-19 travel restrictions. We found a similar trend in production and loss terms of O_3 , which were dominated by NO_x chemistry. The COVID-19 lockdown caused a significant deceleration in O_3 cycling, whereas net ozone production rates were not affected by the emission reductions. Finally, we showed that chemistry in the upper troposphere was VOC-limited during the UTOPIHAN campaign, NO_x -limited during the BLUESKY campaign and in a transition regime for the BLUESKY no-lockdown scenario. While ground-level chemistry regimes were not found to be affected, the COVID-19 lockdown caused the predominant chemistry to shift from a transition regime to a clear NO_x -limited regime at high altitudes.

We found that the three aircraft campaigns, performed over a period of 17 years, represent the range from VOC- to NO_x -limited tropospheric ozone chemistry, which can help analyze the impacts of anthropogenic emission scenarios. We

encourage future studies to investigate the dominating chemical regime in the upper troposphere, a topic which has not received much attention in the literature so far, in order to get a deeper understanding of photochemical processes and the dominant ozone chemistry in a range of the atmosphere which receives its main NO_x emissions from air traffic and lightning. The COVID-19 lockdown has been a unique opportunity to examine the effect of sharp reductions in primary pollutants on our atmosphere and could be a guidepost for future air policy in an effort to decrease anthropogenic emissions and to decelerate global warming.

Data availability. Data measured during the flight campaigns BLUESKY, UTOPIHAN and HOOVER are available upon request at <https://keeper.mpg.de/> (last access: 9 May 2022) to all scientists agreeing to the respective data protocols. The model results used in this study are available upon request to the author.

Supplement. The supplement related to this article is available online at: <https://doi.org/10.5194/acp-22-6151-2022-supplement>.

Author contributions. CMN and HF had the idea and designed the study. CMN analyzed the data and wrote the manuscript. AP provided the modeling data. IT provided NO data for BLUESKY. CO data for BLUESKY were received from LR. O_3 data for BLUESKY were obtained from FO. HH provided HO_x data for HOOVER. JL and HF were significantly involved in planning and operating the research campaign.

Competing interests. At least one of the (co-)authors is a member of the editorial board of *Atmospheric Chemistry and Physics*. The peer-review process was guided by an independent editor, and the authors also have no other competing interests to declare.

Disclaimer. Publisher's note: Copernicus Publications remains neutral with regard to jurisdictional claims in published maps and institutional affiliations.

Special issue statement. This article is part of the special issue "BLUESKY atmospheric composition measurements by aircraft during the COVID-19 lockdown in spring 2020". It is not associated with a conference.

Acknowledgements. We acknowledge Simon Reifenberg for preparing the input data for EMAC. This work was supported by the Max Planck Graduate Center (MPGC) with the Johannes Gutenberg-Universität Mainz.

Financial support. The article processing charges for this open-access publication were covered by the Max Planck Society.

Review statement. This paper was edited by Stefania Gilardoni and reviewed by two anonymous referees.

References

- Balamurugan, V., Chen, J., Qu, Z., Bi, X., Gensheimer, J., Shekhar, A., Bhattacharjee, S., and Keutsch, F. N.: Tropospheric NO₂ and O₃ response to COVID-19 lockdown restrictions at the national and urban scales in Germany, *J. Geophys. Res.-Atmos.*, 126, 1–15, <https://doi.org/10.1029/2021JD035440>, 2021.
- Bouarar, I., Gaubert, B., Brasseur, G. P., Steinbrecht, W., Doumbia, T., Tilmes, S., Liu, Y., Stavrakou, T., Deroubaix, A., Darras, S., Granier, C., Lacey, F., Müller, J.-F., Shi, X., Elguindi, N., and Wang, T.: Ozone Anomalies in the Free Troposphere During the COVID-19 Pandemic, *Geophys. Res. Lett.*, 48, e2021GL094204, <https://doi.org/10.1029/2021GL094204>, 2021.
- Bozem, H., Butler, T. M., Lawrence, M. G., Harder, H., Martinez, M., Kubistin, D., Lelieveld, J., and Fischer, H.: Chemical processes related to net ozone tendencies in the free troposphere, *Atmos. Chem. Phys.*, 17, 10565–10582, <https://doi.org/10.5194/acp-17-10565-2017>, 2017a.
- Bozem, H., Pozzer, A., Harder, H., Martinez, M., Williams, J., Lelieveld, J., and Fischer, H.: The influence of deep convection on HCHO and H₂O₂ in the upper troposphere over Europe, *Atmos. Chem. Phys.*, 17, 11835–11848, <https://doi.org/10.5194/acp-17-11835-2017>, 2017b.
- Brockmann Lab: Covid-19 Mobility Project, <http://covid-19-mobility.org/>, last access: 9 March 2022.
- Calvert, J. G. and Stockwell, W. R.: Deviations from the O₃–NO–NO₂ photostationary state in tropospheric chemistry, *Can. J. Chem.*, 61, 983–992, <https://doi.org/10.1139/v83-174>, 1983.
- Cazorla, M., Herrera, E., Palomeque, E., and Saud, N.: What the COVID-19 lockdown revealed about photochemistry and ozone production in Quito, Ecuador, *Atmos. Pollut. Res.*, 12, 124–133, <https://doi.org/10.1016/j.apr.2020.08.028>, 2021.
- Chang, K.-I., Cooper, O. R., Gaudel, A., Allaart, M., Ancellet, G., Clark, H., Godin-Beekmann, S., Leblanc, T., Van Malderen, R., Nédélec, P., Petropavlovskikh, I., Steinbrecht, W., Stübi, R., Tarasick, D. W., and Torres, C.: Impact of the COVID-19 Economic Downturn on Tropospheric Ozone Trends: An Uncertainty Weighted Data Synthesis for Quantifying Regional Anomalies Above Western North America and Europe, *AGU Advances*, 3, e2021AV000542, <https://doi.org/10.1029/2021AV000542>, 2022.
- Chossière, G. P., Xu, H., Dixit, Y., Isaacs, S., Eastham, S. D., Allroggen, F., Speth, R. L., and Barrett, S. R.: Air pollution impacts of COVID-19-related containment measures, *Sci. Adv.*, 7, 1–10, <https://doi.org/10.1126/sciadv.abe1178>, 2021.
- Clark, H., Bennouna, Y., Tsvilidou, M., Wolff, P., Sauvage, B., Barret, B., Le Flochmoën, E., Blot, R., Boulanger, D., Cousin, J.-M., Nédélec, P., Petzold, A., and Thouret, V.: The effects of the COVID-19 lockdowns on the composition of the troposphere as seen by In-service Aircraft for a Global Observing System (IAGOS) at Frankfurt, *Atmos. Chem. Phys.*, 21, 16237–16256, <https://doi.org/10.5194/acp-21-16237-2021>, 2021.
- Colomb, A., Williams, J., Crowley, J., Gros, V., Hofmann, R., Salisbury, G., Klüpfel, T., Kormann, R., Stickler, A., Forster, C., and Lelieveld, J.: Airborne measurements of trace organic species in the upper troposphere over Europe: the impact of deep convection, *Environ. Chem.*, 3, 244–259, <https://doi.org/10.1071/EN06020>, 2006.
- Cristofanelli, P., Arduni, J., Serva, F., Calzolari, F., Bonasoni, P., Busetto, M., Maione, M., Sprenger, M., Trisolino, P., and Putero, D.: Negative ozone anomalies at a high mountain site in northern Italy during 2020: a possible role of COVID-19 lockdowns?, *Environ. Res. Lett.*, 16, 074029, <https://doi.org/10.1088/1748-9326/ac0b6a>, 2021.
- Crutzen, P. J.: Tropospheric ozone: An overview, in: *Mathematical and Physical Sciences*, 1st edn., edited by: Isaksen, I. S. A., Vol. 227, Springer, 3–32, https://doi.org/10.1007/978-94-009-2913-5_1, 1988.
- Donzelli, G., Cioni, L., Cancellieri, M., Llopis-Morales, A., and Morales-Suárez-Varela, M.: Relations between air quality and COVID-19 lockdown measures in Valencia, Spain, *Int. J. Env. Res. Pub. He.*, 18, 2296, <https://doi.org/10.3390/ijerph18052296>, 2021.
- Duncan, B. N., Yoshida, Y., Olson, J. R., Sillman, S., Martin, R. V., Lamsal, L., Hu, Y., Pickering, K. E., Retscher, C., Allen, D. J., and Crawford, J. H.: Application of OMI observations to a space-based indicator of NO_x and VOC controls on surface ozone formation, *Atmos. Environ.*, 44, 2213–2223, <https://doi.org/10.1016/j.atmosenv.2010.03.010>, 2010.
- EUROCONTROL: COVID-19 impact on the European air traffic network, <https://www.eurocontrol.int/covid19>, last access: 9 March 2022.
- Forster, P. M., Forster, H. I., Evans, M. J., Gidden, M. J., Jones, C. D., Keller, C. A., Lamboll, R. D., Le Quéré, C., Rogelj, J., Rosen, D., Schleussner, C.-F., Richardson, T. B., Smith, C. J., and Turnock, S. T.: Current and future global climate impacts resulting from COVID-19, *Nat. Clim. Change*, 10, 913–919, <https://doi.org/10.1038/s41558-020-0883-0>, 2020.
- Gaubert, B., Bouarar, I., Doumbia, T., Liu, Y., Stavrakou, T., Deroubaix, A., Darras, S., Elguindi, N., Granier, C., Lacey, F., Müller, J.-F., Shi, X., Tilmes, S., Wang, T., and Brasseur, G. P.: Global changes in secondary atmospheric pollutants during the 2020 COVID-19 pandemic, *J. Geophys. Res.-Atmos.*, 126, 1–22, <https://doi.org/10.1029/2020JD034213>, 2021.

- Grange, S. K., Lee, J. D., Drysdale, W. S., Lewis, A. C., Hueglin, C., Emmenegger, L., and Carslaw, D. C.: COVID-19 lockdowns highlight a risk of increasing ozone pollution in European urban areas, *Atmos. Chem. Phys.*, 21, 4169–4185, <https://doi.org/10.5194/acp-21-4169-2021>, 2021.
- Gurk, Ch., Fischer, H., Hoor, P., Lawrence, M. G., Lelieveld, J., and Wernli, H.: Airborne in-situ measurements of vertical, seasonal and latitudinal distributions of carbon dioxide over Europe, *Atmos. Chem. Phys.*, 8, 6395–6403, <https://doi.org/10.5194/acp-8-6395-2008>, 2008.
- Hasegawa, T.: Effects of Novel Coronavirus (COVID-19) on Civil Aviation: Economic Impact Analysis, https://www.icao.int/sustainability/Documents/Covid-19/ICAO_coronavirus_Econ_Impact.pdf, last access: 9 March 2022.
- Higham, J., Ramírez, C. A., Green, M., and Morse, A.: UK COVID-19 lockdown: 100 days of air pollution reduction?, *Air Qual. Atmos. Health*, 14, 325–332, <https://doi.org/10.1007/s11869-020-00937-0>, 2021.
- Hosaynali Beygi, Z., Fischer, H., Harder, H. D., Martinez, M., Sander, R., Williams, J., Brookes, D. M., Monks, P. S., and Lelieveld, J.: Oxidation photochemistry in the Southern Atlantic boundary layer: unexpected deviations of photochemical steady state, *Atmos. Chem. Phys.*, 11, 8497–8513, <https://doi.org/10.5194/acp-11-8497-2011>, 2011.
- IUPAC Task Group on Atmospheric Chemical Kinetic Data Evaluation: Evaluated Kinetic Data, <http://iupac.pole-ether.fr>, last access: 3 November 2021.
- Jin, X., Fiore, A., Boersma, K. F., Smedt, I. D., and Valin, L.: Inferring Changes in Summertime Surface Ozone–NO_x–VOC Chemistry over U.S. Urban Areas from Two Decades of Satellite and Ground-Based Observations, *Environ. Sci. Technol.*, 54, 6518–6529, <https://doi.org/10.1021/acs.est.9b07785>, 2020.
- Jöckel, P., Tost, H., Pozzer, A., Kunze, M., Kirner, O., Brenninkmeijer, C. A. M., Brinkop, S., Cai, D. S., Dyroff, C., Eckstein, J., Frank, F., Garny, H., Gottschaldt, K.-D., Graf, P., Grewe, V., Kerkweg, A., Kern, B., Matthes, S., Mertens, M., Meul, S., Neu-maier, M., Nützel, M., Oberländer-Hayn, S., Ruhnke, R., Runde, T., Sander, R., Scharffe, D., and Zahn, A.: Earth System Chemistry integrated Modelling (ESCiMo) with the Modular Earth Submodel System (MESSy) version 2.51, *Geosci. Model Dev.*, 9, 1153–1200, <https://doi.org/10.5194/gmd-9-1153-2016>, 2016.
- Khodayari, A., Tilmes, S., Olsen, S. C., Phoenix, D. B., Wuebbles, D. J., Lamarque, J.-F., and Chen, C.-C.: Aviation 2006 NO_x-induced effects on atmospheric ozone and HO_x in Community Earth System Model (CESM), *Atmos. Chem. Phys.*, 14, 9925–9939, <https://doi.org/10.5194/acp-14-9925-2014>, 2014.
- Khodayari, A., Olsen, S. C., Wuebbles, D. J., and Phoenix, D. B.: Aviation NO_x-induced CH₄ effect: Fixed mixing ratio boundary conditions versus flux boundary conditions, *Atmos. Environ.*, 113, 135–139, <https://doi.org/10.1016/j.atmosenv.2015.04.070>, 2015.
- Kleinman, L. I., Daum, P. H., Lee, Y.-N., Nunnermacker, L. J., Springston, S. R., Weinstein-Lloyd, J., and Rudolph, J.: Sensitivity of ozone production rate to ozone precursors, *Geophys. Res. Lett.*, 28, 2903–2906, <https://doi.org/10.1029/2000GL012597>, 2001.
- Klippel, T., Fischer, H., Bozem, H., Lawrence, M. G., Butler, T., Jöckel, P., Tost, H., Martinez, M., Harder, H., Regelin, E., Sander, R., Schiller, C. L., Stickler, A., and Lelieveld, J.: Distribution of hydrogen peroxide and formaldehyde over Central Europe during the HOOVER project, *Atmos. Chem. Phys.*, 11, 4391–4410, <https://doi.org/10.5194/acp-11-4391-2011>, 2011.
- Kormann, R., Königstedt, R., Parchatka, U., Lelieveld, J., and Fischer, H.: QUALITAS: A mid-infrared spectrometer for sensitive trace gas measurements based on quantum cascade lasers in CW operation, *Rev. Sci. Instrum.*, 76, 075102, <https://doi.org/10.1063/1.1931233>, 2005.
- Kroll, J. H., Heald, C. L., Cappa, C. D., Farmer, D. K., Fry, J. L., Murphy, J. G., and Steiner, A. L.: The complex chemical effects of COVID-19 shutdowns on air quality, *Nat. Chem.*, 12, 777–779, <https://doi.org/10.1038/s41557-020-0535-z>, 2020.
- Lamprecht, C., Graus, M., Striednig, M., Sticher, M., and Karl, T.: Decoupling of urban CO₂ and air pollutant emission reductions during the European SARS-CoV-2 lockdown, *Atmos. Chem. Phys.*, 21, 3091–3102, <https://doi.org/10.5194/acp-21-3091-2021>, 2021.
- Lee, D. S., Fahey, D., Skowron, A., Allen, M., Burkhardt, U., Chen, Q., Doherty, S., Freeman, S., Forster, P., Fuglestad, J., Gettelman, A., Leon, R. D., Lim, L., Lund, M., Millar, R., Owen, B., Penner, J., Pitari, G., Prather, M., Sausen, R., and Wilcox, L.: The contribution of global aviation to anthropogenic climate forcing for 2000 to 2018, *Atmos. Environ.*, 244, 117834, <https://doi.org/10.1016/j.atmosenv.2020.117834>, 2021.
- Leighton, P. A.: Photochemistry of air pollution, Academic Press Inc., 2nd edn., New York, ISBN 9780323156455, 1971.
- Lelieveld, J. and Dentener, F. J.: What controls tropospheric ozone?, *J. Geophys. Res.-Atmos.*, 105, 3531–3551, <https://doi.org/10.1029/1999JD901011>, 2000.
- LI-COR, Inc.: LI-6262 CO₂/H₂O Analyzer Operating and Service Manual, <https://www.licor.com/documents/umazybyhzal840pf63a1137qz7ofib> (last access: 6 December 2021), 1996.
- Lin, X., Trainer, M., and Liu, S.: On the nonlinearity of the tropospheric ozone production, *J. Geophys. Res.-Atmos.*, 93, 15879–15888, <https://doi.org/10.1029/JD093iD12p15879>, 1988.
- Liu, S., Trainer, M., Fehsenfeld, F., Parrish, D., Williams, E., Fahey, D. W., Hübler, G., and Murphy, P. C.: Ozone production in the rural troposphere and the implications for regional and global ozone distributions, *J. Geophys. Res.-Atmos.*, 92, 4191–4207, <https://doi.org/10.1029/JD092iD04p04191>, 1987.
- Logan, J. A.: Tropospheric ozone: Seasonal behavior, trends, and anthropogenic influence, *J. Geophys. Res.-Atmos.*, 90, 10463–10482, <https://doi.org/10.1029/JD090iD06p10463>, 1985.
- Matthias, V., Quante, M., Arndt, J. A., Badeke, R., Fink, L., Petrik, R., Feldner, J., Schwarzkopf, D., Link, E.-M., Ramacher, M. O. P., and Wedemann, R.: The role of emission reductions and the meteorological situation for air quality improvements during the COVID-19 lockdown period in central Europe, *Atmos. Chem. Phys.*, 21, 13931–13971, <https://doi.org/10.5194/acp-21-13931-2021>, 2021.
- Menut, L., Bessagnet, B., Siour, G., Mailler, S., Pennel, R., and Cholakian, A.: Impact of lockdown measures to combat Covid-19 on air quality over western Europe, *Sci. Total Environ.*, 741, 140426, <https://doi.org/10.1016/j.scitotenv.2020.140426>, 2020.
- Mertens, M., Jöckel, P., Matthes, S., Nützel, M., Grewe, V., and Sausen, R.: COVID-19 induced lower-

- tropospheric ozone changes, *Environ. Res. Lett.*, 16, 1–9, <https://doi.org/10.1088/1748-9326/abf191>, 2021.
- Mills, G., Pleijel, H., Malley, C. S., Sinha, B., Cooper, O. R., Schultz, M. G., Neufeld, H. S., Simpson, D., Sharps, K., Feng, Z., Gerosa, G., Harmens, H., Kobayashi, K., Saxena, P., Paoletti, E., Sinha, V., and Xu, X.: Tropospheric Ozone Assessment Report: Present-day tropospheric ozone distribution and trends relevant to vegetation, *Elementa*, 6, 47, <https://doi.org/10.1525/elementa.302>, 2018.
- Miyazaki, K., Bowman, K., Sekiya, T., Takigawa, M., Neu, J. L., Sudo, K., Osterman, G., and Eskes, H.: Global tropospheric ozone responses to reduced NO_x emissions linked to the COVID-19 worldwide lockdowns, *Sci. Adv.*, 7, 1–14, <https://doi.org/10.1126/sciadv.abf7460>, 2021.
- National Research Council – Committee on Tropospheric Ozone: Rethinking the ozone problem in urban and regional air pollution, 1st edn., National Academy Press, Washington D.C., <https://doi.org/10.17226/1889>, 1992.
- Nussbaumer, C. M. and Cohen, R. C.: The Role of Temperature and NO_x in Ozone Trends in the Los Angeles Basin, *Environ. Sci. Technol.*, 54, 15652–15659, <https://doi.org/10.1021/acs.est.0c04910>, 2020.
- Nussbaumer, C. M., Crowley, J. N., Schuladen, J., Williams, J., Hafermann, S., Reiffs, A., Axinte, R., Harder, H., Ernest, C., Novelli, A., Sala, K., Martinez, M., Mallik, C., Tomsche, L., Plass-Dülmer, C., Bohn, B., Lelieveld, J., and Fischer, H.: Measurement report: Photochemical production and loss rates of formaldehyde and ozone across Europe, *Atmos. Chem. Phys.*, 21, 18413–18432, <https://doi.org/10.5194/acp-21-18413-2021>, 2021.
- Nuvolone, D., Petri, D., and Voller, F.: The effects of ozone on human health, *Environ. Sci. Pollut. Res.*, 25, 8074–8088, <https://doi.org/10.1007/s11356-017-9239-3>, 2018.
- Onyeaka, H., Anumudu, C. K., Al-Sharify, Z. T., Egele-Godswill, E., and Mbaegbu, P.: COVID-19 pandemic: A review of the global lockdown and its far-reaching effects, *Sci. Prog.*, 104, 1–18, <https://doi.org/10.1177/00368504211019854>, 2021.
- Ordóñez, C., Garrido-Perez, J. M., and García-Herrera, R.: Early spring near-surface ozone in Europe during the COVID-19 shutdown: Meteorological effects outweigh emission changes, *Sci. Total Environ.*, 747, 14322, <https://doi.org/10.1016/j.scitotenv.2020.141322>, 2020.
- Parrish, D., Lamarque, J.-F., Naik, V., Horowitz, L., Shindell, D., Staehelin, J., Derwent, R., Cooper, O., Tanimoto, H., Volz-Thomas, A., Gilge, S., Scheel, H.-E., Steinbacher, M., and Fröhlich, M.: Long-term changes in lower tropospheric baseline ozone concentrations: Comparing chemistry-climate models and observations at northern midlatitudes, *J. Geophys. Res.-Atmos.*, 119, 5719–5736, <https://doi.org/10.1002/2013JD021435>, 2014.
- Pusede, S. and Cohen, R.: On the observed response of ozone to NO_x and VOC reactivity reductions in San Joaquin Valley California 1995–present, *Atmos. Chem. Phys.*, 12, 8323–8339, <https://doi.org/10.5194/acp-12-8323-2012>, 2012.
- Pusede, S. E., Steiner, A. L., and Cohen, R. C.: Temperature and recent trends in the chemistry of continental surface ozone, *Chem. Rev.*, 115, 3898–3918, <https://doi.org/10.1021/cr5006815>, 2015.
- Regelin, E., Harder, H., Martinez, M., Kubistin, D., Tatum Ernest, C., Bozem, H., Klippel, T., Hosaynali-Beygi, Z., Fischer, H., Sander, R., Jöckel, P., Königstedt, R., and Lelieveld, J.: HO_x measurements in the summertime upper troposphere over Europe: a comparison of observations to a box model and a 3-D model, *Atmos. Chem. Phys.*, 13, 10703–10720, <https://doi.org/10.5194/acp-13-10703-2013>, 2013.
- Reifenberg, S. F., Martin, A., Kohl, M., Hamryszczak, Z., Tadic, I., Röder, L., Crowley, D., Fischer, H., Kaiser, K., Schneider, J., Dörich, R., Crowley, J. N., Tomsche, L., Marsing, A., Voigt, C., Zahn, A., Pöhlker, C., Hollanda, B., Krüger, O., Pöschl, U., Pöhlker, M., Lelieveld, J., and Pozzer, A.: Impact of reduced emissions on direct and indirect aerosol radiative forcing during COVID-19 lockdown in Europe, in preparation, 2022.
- Revell, L. E., Stenke, A., Tummon, F., Feinberg, A., Rozanov, E., Peter, T., Abraham, N. L., Akiyoshi, H., Archibald, A. T., Butchart, N., Deushi, M., Jöckel, P., Kinnison, D., Michou, M., Morgenstern, O., O'Connor, F. M., Oman, L. D., Pitari, G., Plummer, D. A., Schofield, R., Stone, K., Tilmes, S., Visioni, D., Yamashita, Y., and Zeng, G.: Tropospheric ozone in CCMi models and Gaussian process emulation to understand biases in the SOCOLv3 chemistry–climate model, *Atmos. Chem. Phys.*, 18, 16155–16172, <https://doi.org/10.5194/acp-18-16155-2018>, 2018.
- Rosanka, S., Sander, R., Franco, B., Wespes, C., Wahner, A., and Taraborrelli, D.: Oxidation of low-molecular-weight organic compounds in cloud droplets: global impact on tropospheric oxidants, *Atmos. Chem. Phys.*, 21, 9909–9930, <https://doi.org/10.5194/acp-21-9909-2021>, 2021.
- Salma, I., Vörösmarty, M., Gyöngyösi, A. Z., Thén, W., and Weidinger, T.: What can we learn about urban air quality with regard to the first outbreak of the COVID-19 pandemic? A case study from central Europe, *Atmos. Chem. Phys.*, 20, 15725–15742, <https://doi.org/10.5194/acp-20-15725-2020>, 2020.
- Schiller, C., Bozem, H., Gurk, C., Parchatka, U., Königstedt, R., Harris, G., Lelieveld, J., and Fischer, H.: Applications of quantum cascade lasers for sensitive trace gas measurements of CO , CH_4 , N_2O and HCHO , *Appl. Phys. B*, 92, 419–430, <https://doi.org/10.1007/s00340-008-3125-0>, 2008.
- Schlosser, F., Maier, B. F., Jack, O., Hinrichs, D., Zachariae, A., and Brockmann, D.: COVID-19 lockdown induces disease-mitigating structural changes in mobility networks, *P. Natl. Acad. Sci. USA*, 117, 32883–32890, <https://doi.org/10.1073/pnas.2012326117>, 2020.
- Schumann, U.: Aircraft emissions, in: *Encyclopedia of global environmental change*, 3, edited by: Ian Douglas, John Wiley & Sons Ltd, Chichester, 178–186, ISBN 0471977969, 2002.
- Sillman, S., Logan, J. A., and Wofsy, S. C.: The sensitivity of ozone to nitrogen oxides and hydrocarbons in regional ozone episodes, *J. Geophys. Res.-Atmos.*, 95, 1837–1851, <https://doi.org/10.1029/JD095iD02p01837>, 1990.
- Steinbrecht, W., Kubistin, D., Plass-Dülmer, C., Davies, J., Tarasick, D. W., Gathen, P. v. d., Deckelmann, H., Jepsen, N., Kivi, R., Lyall, N., Palm, M., Notholt, J., Kois, B., Oelsner, P., Allaart, M., Piders, A., Gill, M., Malderen, R. V., Delcloo, A. W., Sussmann, R., Mahieu, E., Servais, C., Romanens, G., Stübi, R., Ancellet, G., Godin-Beekmann, S., Yamanouchi, S., Strong, K., Johnson, B., Cullis, P., Petropavlovskikh, I., Hannigan, J. W., Hernandez, J.-L., Rodriguez, A. D., Nakano, T., Chouza, F., Leblanc, T., Torres, C., Garcia, O., Röhring, A. N., Schneider, M., Blumenstock, T., Tully, M., Paton-Walsh, C., Jones, N., Querel, R., Strahan, S., Stauffer, R. M.,

- Thompson, A. M., Inness, A., Engelen, R., Chang, K.-L., and Cooper, O. R.: COVID-19 crisis reduces free tropospheric ozone across the Northern Hemisphere, *Geophys. Res. Lett.*, 48, 1–11, <https://doi.org/10.1029/2020GL091987>, 2021.
- Stickler, A., Fischer, H., Williams, J., De Reus, M., Sander, R., Lawrence, M., Crowley, J., and Lelieveld, J.: Influence of summertime deep convection on formaldehyde in the middle and upper troposphere over Europe, *J. Geophys. Res.-Atmos.*, 111, 1–17, <https://doi.org/10.1029/2005JD007001>, 2006.
- Tadic, I., Crowley, J. N., Dienhart, D., Eger, P., Harder, H., Hottmann, B., Martinez, M., Parchatka, U., Paris, J.-D., Pozzer, A., Rohloff, R., Schuladen, J., Shenolikar, J., Tauer, S., Lelieveld, J., and Fischer, H.: Net ozone production and its relationship to nitrogen oxides and volatile organic compounds in the marine boundary layer around the Arabian Peninsula, *Atmos. Chem. Phys.*, 20, 6769–6787, <https://doi.org/10.5194/acp-20-6769-2020>, 2020.
- Venter, Z. S., Aunan, K., Chowdhury, S., and Lelieveld, J.: COVID-19 lockdowns cause global air pollution declines, *P. Natl. Acad. Sci. USA*, 117, 18984–18990, <https://doi.org/10.1073/pnas.2006853117>, 2020.
- Voigt, C., Lelieveld, J., Schlager, H., Schneider, J., Curtius, J., Meerkötter, R., Sauer, D., Bugliaro, L., Bohn, B., Crowley, J. N., Erbertseder, T., Groß, S., Li, Q., Mertens, M., Pöhlker, M., Pozzer, A., Schumann, U., Tomsche, L., Williams, J., Zahn, A., Andreae, M., Borrmann, S., Brüner, T., Dörich, R., Dörnbrack, A., Edtbauer, A., Ernle, L., Fischer, H., Giez, A., Granzin, M., Grewe, V., Hahn, V., Harder, H., Heinritzi, M., Holanda, B., Jöckel, P., Kaiser, K., Krüger, O., Lucke, J., Marsing, A., Martin, A., Matthes, S., Pöhlker, C., Pöschl, U., Reifenberg, S., Ringsdorf, A., Scheibe, M., Tadic, I., Zauner-Wieczorek, M., Henke, R., and Rapp, M.: BLUESKY aircraft mission reveals reduction in atmospheric pollution during the 2020 Corona lockdown, *B. Am. Meteorol. Soc.*, in review, 2022.
- Wang, P., Chen, Y., Hu, J., Zhang, H., and Ying, Q.: Attribution of tropospheric ozone to NO_x and VOC emissions: considering ozone formation in the transition regime, *Environ. Sci. Technol.*, 53, 1404–1412, <https://doi.org/10.1021/acs.est.8b05981>, 2018.
- WHO: WHO Director-General's opening remarks at the media briefing on COVID-19 – 11 March 2020, <https://www.who.int/director-general/speeches> (last access: 2 November 2021), 2020a.
- WHO: Coronavirus disease 2019 (COVID-19) Situation Report – 51, https://www.who.int/docs/default-source/coronaviruse/situation-reports/20200311-sitrep-51-covid-19.pdf?sfvrsn=1ba62e57_10 (last access: 2 November 2021), 2020b.
- WHO: Coronavirus disease 2019 (COVID-19), https://www.who.int/health-topics/coronavirus#tab=tab_1, last access: 2 November 2021.
- World Meteorological Organization: WMO Air Quality and Climate Bulletin – No. 1, September 2021, edited by: Cooper, O. R., Sokhi, R. S., Nicely, J. M., Carmichael, G., Darmanov, A., Laj, P., and Liggio, J., https://library.wmo.int/index.php?lvl=notice_display&id=21942#.YTIzN9 (last access: 18 March 2022), 2021.
- Young, P. J., Naik, V., Fiore, A. M., Gaudel, A., Guo, J., Lin, M., Neu, J., Parrish, D., Rieder, H., Schnell, J., et al.: Tropospheric Ozone Assessment Report: Assessment of global-scale model performance for global and regional ozone distributions, variability, and trends, *Elementa*, 6, 10, <https://doi.org/10.1525/elementa.265>, 2018.
- Zahn, A., Weppner, J., Widmann, H., Schlote-Holubek, K., Burger, B., Kühner, T., and Franke, H.: A fast and precise chemiluminescence ozone detector for eddy flux and airborne application, *Atmos. Meas. Tech.*, 5, 363–375, <https://doi.org/10.5194/amt-5-363-2012>, 2012.
- Zhu, S., Poetzsch, J., Shen, J., Wang, S., Wang, P., and Zhang, H.: Comprehensive insights into O_3 changes during the COVID-19 from O_3 formation regime and atmospheric oxidation capacity, *Geophys. Res. Lett.*, 48, 1–11, <https://doi.org/10.1029/2021GL093668>, 2021.

3.6 Ozone sensitivity in the upper tropical troposphere

This chapter has been submitted to the journal *Atmospheric Chemistry & Physics* as a research article and is currently under review at *EGUsphere*. I am the first author of this paper. I have analyzed all data presented, I have made the figures and I have prepared the manuscript. Detailed author contributions can be found at the end of the paper in the section *Author contributions*.

How to cite: Nussbaumer, C. M., Fischer, H., Lelieveld, J. and Pozzer, A.: What controls ozone sensitivity in the upper tropical troposphere?, *EGUsphere* [preprint], <https://doi.org/10.5194/egusphere-2023-816>, **2023**.

submitted: 24 Apr 2023

The supplementary material for this publication can be found in Section 4.5.

<https://doi.org/10.5194/egusphere-2023-816>

Preprint. Discussion started: 4 May 2023

© Author(s) 2023. CC BY 4.0 License.



What controls ozone sensitivity in the upper tropical troposphere?

Clara M. Nussbaumer¹, Horst Fischer¹, Jos Lelieveld^{1,2}, and Andrea Pozzer^{1,2}

¹Max Planck Institute for Chemistry, Department of Atmospheric Chemistry, Mainz, Germany

²Climate and Atmosphere Research Center, The Cyprus Institute, Nicosia, Cyprus

Correspondence: Clara Nussbaumer (clara.nussbaumer@mpic.de)

Abstract.

Ozone is after water vapor, the second most important contributor to the radiative energy budget of the upper troposphere (UT). Therefore, observing and understanding the processes contributing to ozone production are important for monitoring the progression of climate change. Nitrogen oxides ($\text{NO}_x \equiv \text{NO} + \text{NO}_2$) and volatile organic compounds (VOC) are two main tropospheric precursors to ozone formation. Depending on their abundances, ozone production can be sensitive to changes in either of these two precursors. Here, we focus on processes contributing to ozone chemistry in the upper tropical troposphere between 30°S and 30°N latitude, where changes in ozone have a relatively large impact on anthropogenic radiative forcing. Based on modeled trace gas mixing ratios and meteorological parameters simulated by the EMAC atmospheric chemistry - general circulation model, we analyze a variety of commonly applied metrics including ozone production rates ($\text{P}(\text{O}_3)$), the formaldehyde (HCHO) to NO_2 ratio and the share of methyl peroxyradicals (CH_3O_2) forming HCHO ($\alpha(\text{CH}_3\text{O}_2)$), for their ability to describe the chemical regime. We show that the distribution of trace gases in the tropical UT is strongly influenced by the varying locations of deep convection throughout the year, and we observe peak values for NO_x and $\text{P}(\text{O}_3)$ over the continental areas of South America and Africa where lightning is frequent. We find that $\text{P}(\text{O}_3)$ and its response to NO is unsuitable for determining the dominant regime in the upper troposphere. Instead, $\alpha(\text{CH}_3\text{O}_2)$ and the HCHO/ NO_2 ratio in combination with ambient NO levels perform well as metrics to indicate whether NO_x or VOC sensitivity is prevalent. A sensitivity study with halving, doubling and excluding lightning NO_x demonstrates that lightning and its distribution in the tropics are the major determinants of the chemical regimes and ozone formation in the upper tropical troposphere.

1 Introduction

Ozone (O_3) is abundant in the stratosphere and makes life on earth possible by absorbing highly energetic UV radiation emitted by the sun (Rowland, 1991; Staehelin et al., 2001). In the troposphere, on the other hand, high O_3 levels have adverse effects on human health, plant growth and climate (Ainsworth et al., 2012; Cooper et al., 2014; Nuvolone et al., 2018). Ground-level tropospheric ozone has received particular attention due to its role in causing cardiovascular and respiratory diseases (Nuvolone et al., 2018). Additionally, ozone can be detrimental to plants through limiting stomatal conductance and therefore the capability of to perform plants photosynthesis (Ainsworth et al., 2012; Mills et al., 2018). Ozone in the free troposphere is subject to particular focus due to its radiative forcing efficiency as a greenhouse gas and its contribution to global warming and climate change. In the upper troposphere (UT), ozone is the second most important greenhouse gas after water vapor and

<https://doi.org/10.5194/egusphere-2023-816>

Preprint. Discussion started: 4 May 2023

© Author(s) 2023. CC BY 4.0 License.



changes in ozone exert (and will continue to exert) a particularly large impact on the earth's radiative forcing – especially in the tropopause region and the tropical UT (Lacis et al., 1990; Mohnen et al., 1993; Wuebbles, 1995; Lelieveld and van Dorland, 1995; van Dorland et al., 1997; Staehelin et al., 2001; Iglesias-Suarez et al., 2018).

30 While transport from the stratosphere contributes significantly to ozone in the upper troposphere, the formation of O_3 from its precursors nitrogen oxides (NO_x) and volatile organic compounds (VOCs), might still be the predominant source of ozone in this layer of the atmosphere (Lelieveld and Dentener, 2000; Cooper et al., 2014; Pusede et al., 2015). In the lower troposphere, NO_x mostly originates from combustion processes such as vehicle engines and industrial activity. Soil emissions, partly natural and partly from agricultural activity, additionally contribute to NO_x sources at the surface. In the upper troposphere, NO_x is derived from lightning and aircraft (Pusede et al., 2015). VOC sources are even more diverse and range from biogenic vegetation emissions to anthropogenic emissions like combustion processes or volatile chemical products, such as paints, detergents, cosmetics (McDonald et al., 2018). Within a photochemical cycle catalyzed by OH radicals, VOCs and nitric oxide (NO) molecules form nitrogen dioxide (NO_2), which can subsequently react with O_3 in the presence of oxygen and sunlight as shown in the overall reaction (R1) (Leighton, 1961; Crutzen, 1988).



Deviations from the HO_x cycle, including self-reactions of peroxy radicals and the reaction of OH with NO_2 forming HNO_3 , can terminate the formation of ozone. A detailed description of the HO_x cycle and its termination reactions can, for example, be found in Pusede and Cohen (2012), Pusede et al. (2015) and Nussbaumer and Cohen (2020).

Depending on the availability of its precursors, ozone formation can either be sensitive to the levels of NO_x or VOC. While terms like NO_x or VOC -“limited” -“sensitive” and -“saturated” are widely used in the literature in reference to chemical ozone regimes, there is no unified definition, as pointed out in a review by Sillman (1999) more than two decades ago. When it comes to the upper troposphere, most of the indicators for either regime are no longer valid.

Initial descriptions of ozone chemistry and the coining of the term “regime” date back to the late 1980s with studies by Liu et al. (1987), Lin et al. (1988) and Sillman et al. (1990). The most common definition for chemical regimes in the literature is based on the response of ozone production ($P(O_3)$) to changes in its precursors based on the ozone isopleths, which is described in review articles and textbooks (National Research Council, 1992; Seinfeld and Pandis, 1998; Sillman, 1999; Seinfeld, 2004). Correspondingly, in low- NO_x environments increases in NO_x lead to increases in O_3 , while changes in VOCs have little to no impact – a NO_x -sensitive regime. In high- NO_x environments increases in NO_x affect decreases in O_3 – a VOC-sensitive regime (or NO_x -saturated regime). Within an NO_x -sensitive regime, OH radicals primarily react with VOCs and promote the catalytic HO_x cycle and the formation of O_3 . The self-reaction of peroxy radicals is the main termination reaction. With increasing NO_x levels and the transition to a VOC-sensitive regime, the termination reaction of OH with NO_2 to form HNO_3 becomes dominant, affecting the anti-proportional correlation of NO_x and O_3 .

Various indicators have been reported in the literature to determine the dominant regime. Some studies have directly addressed the production of O_3 (or odd oxygen (O_x) $\equiv O_3 + NO_2$) in response to changing NO_x (Brasseur et al., 1996; Jaeglé

<https://doi.org/10.5194/egusphere-2023-816>

Preprint. Discussion started: 4 May 2023

© Author(s) 2023. CC BY 4.0 License.



et al., 1999; Tonnesen and Dennis, 2000a; Tadic et al., 2021). Other studies considered the so-called ozone production efficiency (OPE), which evaluates how many ozone molecules are formed by NO_x before it is removed to reaction products such as HNO_3 or PAN (peroxyacetyl nitrate) (Liu et al., 1987; Trainer et al., 1993; Wang et al., 2018a). Low OPEs indicate a VOC-sensitive and high OPEs a NO_x -sensitive regime. Similar approaches such as the ratio of O_3 and reactive nitrogen species (NO_y) or NO_z ($\equiv \text{NO}_y - \text{NO}_x$) have also been reported (Milford et al., 1994; Sillman, 1995; Fischer et al., 2003; Peralta et al., 2021; Wang et al., 2022). A common method for determining the dominant regime in urban environments is the weekend ozone effect, where the response of O_3 levels to decreasing NO_x mixing ratios on weekends is monitored (e.g., Fujita et al. (2003); Pusede and Cohen (2012); Nussbaumer and Cohen (2020); Sicard et al. (2020); Gough and Anderson (2022)). Another indicator is the ratio between formaldehyde (HCHO) and NO_2 . Sillman (1995) originally suggested the ratio HCHO/NO_y ($\text{NO}_y \equiv \text{NO}_x + \text{HNO}_3 + \text{organic nitrates}$) as a metric, which was later adjusted to the HCHO/NO_2 ratio. This metric evaluates the reaction of OH radicals with VOCs (ultimately leading to HCHO as a reaction intermediate) enhancing O_3 production in competition with the reaction of OH radicals with NO_2 , which decelerates O_3 formation (Tonnesen and Dennis, 2000b). The HCHO/NO_2 ratio has been widely applied in the literature based on ground-based measurements and satellite observations (e.g., Duncan et al. (2010); Jin et al. (2020); Xue et al. (2022)). The ratio of hydrogen peroxide (H_2O_2) to HNO_3 is another metric used for regime analysis. Also initially suggested by Sillman (1995), it compares the HO_2 self-reaction (forming H_2O_2) with the reaction of OH and NO_2 , both leading to termination of the HO_x cycle. While the HO_2 self-reaction dominates over the formation of HNO_3 as a termination reaction, O_3 increases linearly with NO_x . Recent studies using $\text{H}_2\text{O}_2/\text{HNO}_3$ include Wang et al. (2018b), Vermeuel et al. (2019) and Liu et al. (2021). The HCHO/NO_2 and $\text{H}_2\text{O}_2/\text{HNO}_3$ ratios, as well as the OPE require absolute values as reference points to determine the regime, which can vary depending on the ambient conditions; background mixing ratios are a major drawback of these metrics. Dyson et al. (2022) recently analyzed the dominant regime in Beijing using a method that considers the loss of OH, HO_2 and RO_2 radicals via reaction with NO_x in comparison to the overall production of these radical species. The production thereby equals the overall radical loss via reaction with NO_x , self-reaction and aerosol uptake, an idea which has been previously described by Sakamoto et al. (2019). Within a VOC-sensitive regime, HO_2 is predominantly lost via the reaction with NO, while in a NO_x -sensitive regime, aerosol uptake plays a significant role in HO_2 loss. Dyson et al. (2022) found the transition to occur around 0.1 ppbv of NO. Cazorla and Brune (2009) and Hao et al. (2023) reported direct measurements of $\text{P}(\text{O}_3)$ in a reaction chamber through observing changes in O_x in a certain time interval. This technique can be used to determine the dominant chemical regime when correlated with ambient NO mixing ratios.

Some studies (including Jaeglé et al. (1998), Wennberg et al. (1998) and Jaeglé et al. (1999)) have analyzed the dominant chemical regime in the UT. These studies focus on the U.S. and the North Atlantic and consistently report a linear correlation between $\text{P}(\text{O}_3)$ and NO_x based on aircraft observations, deducing a NO_x -sensitive regime, while model simulations predict a $\text{P}(\text{O}_3)$ decrease with high NO_x . One explanation for these observations could be that these studies, published around 25 years ago, overestimated the NO_x loss. We know today that the reaction rate of NO_2 and OH is much lower than previously assumed (Mollner et al., 2010; Henderson et al., 2012; Nault et al., 2016). The loss reaction of NO_2 with OH to HNO_3 does not play a significant role under the conditions in the upper troposphere (in contrast to low-altitude) so that the typical

<https://doi.org/10.5194/egusphere-2023-816>

Preprint. Discussion started: 4 May 2023

© Author(s) 2023. CC BY 4.0 License.



definition for a VOC-sensitive regime where O_3 production decreases with increasing NO_x does not apply anymore. Khodayari et al. (2018) reported an NO_x -saturated (VOC-sensitive) regime based on a modeling sensitivity study, where a decreasing O_3 burden was observed with increasing lightning NO_x . We suggest that this observed anti-correlation might not result from increased NO_x loss as applicable for surface conditions, and might instead be an outcome of decreasing HO_2 with increasing NO . Pickering et al. (1990) reported a VOC-sensitive regime over the U.S. at 11 km altitude based on measurements in June 1985 and model simulations. A study by Dahlmann et al. (2011) indicates increasing $P(O_3)$ with increasing NO at 250 hPa over Europe, implying a NO_x -sensitive regime following the common definition. Shah et al. (2023) analyzed the relationship between the NO_y/NO ratio and O_3 mixing ratios and assumed an NO_x -sensitive regime over the Central U.S. based on a flight during the DC3 research campaign in 2012. Liang et al. (2011) analyzed changes in net ozone production with NO_x in the Arctic troposphere and found a proportional relationship up to 10 ppbv NO_x based on box model calculations and observations.

While all studies have briefly touched upon the dominant chemical regime in the upper troposphere, a thorough analysis and a definition that is valid throughout the troposphere have not yet been reported. In view of ozone's major implications for the earth's radiative energy budget and climate change (particularly in the UT), O_3 sensitivity is highly relevant for understanding and monitoring which precursors and processes are most important for the O_3 budget at high altitudes in the troposphere.

In Nussbaumer et al. (2021a), we introduced a new metric $\alpha(CH_3O_2)$ for determining the dominant regime, which presents the ratio of methyl peroxyradicals (CH_3O_2) forming HCHO with NO versus the reaction of CH_3O_2 with HO_2 . We have applied this metric to ground-based observations at three different sites in Europe and for aircraft observations during the 2022 BLUESKY research campaign in the upper troposphere over Europe (Nussbaumer et al., 2022). We found a change at high altitudes from a VOC- to a NO_x -sensitive regime over the past two decades up to 2020, promoted by emission reductions during the COVID-19 pandemic.

In this study, we use $\alpha(CH_3O_2)$ to analyze the dominant regime in the upper tropical troposphere between $30^\circ S$ and $30^\circ N$ latitude based on modeled trace-gas mixing ratios and meteorological parameters by the EMAC atmospheric chemistry - general circulation model. We additionally investigate the effects of NO_x produced by lightning in six different tropical areas: the Pacific Ocean, South America, the Atlantic Ocean, Africa, the Indian Ocean and South East Asia. Finally, we provide a new definition for NO_x - and VOC-sensitive regimes, which is valid throughout the troposphere.

2 Methods

2.1 Calculations of ozone production ($P(O_3)$) and loss ($L(O_3)$) rates

The calculation of ozone production ($P(O_3)$) and loss ($L(O_3)$) rates was performed as presented in Section 2.1 of Nussbaumer et al. (2022). Briefly, ozone production $P(O_3)$ is described by the reaction of NO with HO_2 and peroxy radicals R_zO_2 (Equation (1)); the latter can be approximated by CH_3O_2 in the upper troposphere. CH_3O_2 accounts for $85 \pm 5\%$ of R_zO_2 , represented by the sum of CH_3O_2 , $C_2H_5O_2$ (ethylperoxy radicals), CH_3CO_3 (peroxyacetyl radicals), $CH_3COCH_2O_2$ (acetylperoxy radicals), iso- $C_3H_7O_2$ (iso-propylperoxy radicals), $C_5H_6O_3$ (isoprene (hydroxy) peroxy radicals), $C_4H_7O_4$ (methyl vinyl ketone / methacrolein peroxy radicals) and $LHOC_3H_6O_2$ (hydroxyperoxy radicals from propene + OH).

<https://doi.org/10.5194/egusphere-2023-816>
 Preprint. Discussion started: 4 May 2023
 © Author(s) 2023. CC BY 4.0 License.



$$P(O_3) = k_{NO+HO_2} \times [HO_2] \times [NO] + \sum_z k_{NO+R_zO_2} \times [R_zO_2][NO] \quad (1)$$

Ozone loss $L(O_3)$ is calculated as shown in Equation (2) via the reaction of O_3 with HO_2 and OH and via photolysis. The latter
 130 only yields an effective ozone loss if $O(^1D)$ (resulting from O_3 photolytic cleavage) reacts with H_2O instead of colliding with
 O_2 or N_2 (and reforming O_3). This share is represented by $\alpha_{O(^1D)}$ in Equation (3).

$$L(O_3) = k_{O_3+HO_2} \times [HO_2] \times [O_3] + k_{O_3+OH} \times [OH] \times [O_3] + \alpha_{O(^1D)} \times j(O^1D) \times [O_3] \quad (2)$$

$$\alpha_{O^1D} = \frac{k_{O^1D+H_2O} \times [H_2O]}{k_{O^1D+N_2} \times [N_2] + k_{O^1D+O_2} \times [O_2] + k_{O^1D+H_2O} \times [H_2O]} \quad (3)$$

The resulting net ozone production rate (NOPR) is then calculated by subtracting ozone loss from its production as shown in
 135 Equation (4).

$$\begin{aligned} NOPR &= P(O_3) - L(O_3) \\ &= [NO] \times (k_{NO+HO_2} \times [HO_2] + k_{NO+CH_3O_2} \times [CH_3O_2]) \\ &\quad - [O_3] \times (k_{O_3+HO_2} \times [HO_2] + k_{O_3+OH} \times [OH] + \alpha_{O^1D} \times j(O^1D)) \end{aligned} \quad (4)$$

2.2 Calculations of $\alpha(CH_3O_2)$

$\alpha(CH_3O_2)$ represents the share of methyl peroxyradicals forming HCHO with NO and OH versus the reaction with HO_2
 yielding CH_3OOH and is calculated as shown in Equation (5).

$$\alpha_{CH_3O_2} = \frac{k_{CH_3O_2+NO} \times [NO] + k_{CH_3O_2+OH} \times [OH]}{k_{CH_3O_2+NO} \times [NO] + k_{CH_3O_2+OH} \times [OH] + k_{CH_3O_2+HO_2} \times [HO_2]} \quad (5)$$

We demonstrated in previous studies that $\alpha(CH_3O_2)$ can be used as a metric to determine the dominant chemical regime
 (Nussbaumer et al., 2021a, 2022). While the formation of HCHO from CH_3O_2 enhances O_3 formation, the reaction of CH_3O_2
 with HO_2 represents a termination reaction of the HO_x cycle and therefore decelerates $P(O_3)$. The progression of $\alpha(CH_3O_2)$
 in dependence of the ambient NO mixing ratio is shown in Figure 1. The black line presents the average $\alpha(CH_3O_2)$ across
 145 all longitudes and between $30^\circ S$ and $30^\circ N$ latitude at 200 hPa altitude for daily values from 2000 to 2019 binned to the NO
 mixing ratios. It therefore describes the background behavior of NO vs $\alpha(CH_3O_2)$ for all data used in this study. The grey error
 shades show the 1σ standard deviation resulting from the averaging. At low NO mixing ratios (here <0.1 ppbv), $\alpha(CH_3O_2)$
 changes rapidly even with small changes in NO. The resulting slope of the linear fit of the data is 3.75 ± 0.44 ppbv $^{-1}$. In this
 range, CH_3O_2 reacts both with NO and with HO_2 (and with itself). With increasing availability of NO, the reaction of CH_3O_2

<https://doi.org/10.5194/egusphere-2023-816>

Preprint. Discussion started: 4 May 2023

© Author(s) 2023. CC BY 4.0 License.

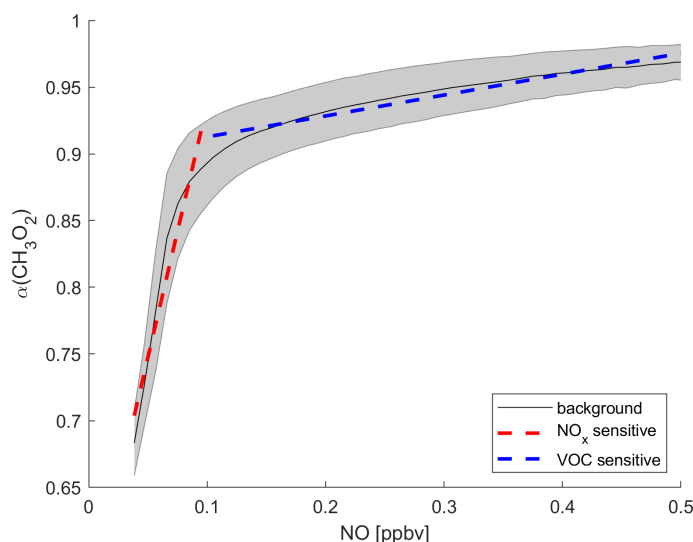


Figure 1. Demonstration of how $\alpha(\text{CH}_3\text{O}_2)$ can be used as a metric to determine the dominant chemical regime. The black line shows the tropical background $\alpha(\text{CH}_3\text{O}_2)$ binned to NO mixing ratios. The grey error shades show the 1σ standard deviation. The red and blue dashed lines represent a NO_x -sensitive and a VOC-sensitive regime, respectively.

150 with NO and therefore the amount of O_3 formed is enhanced. This regime is referred to as NO_x -sensitive. In comparison, for higher NO mixing ratios (here >0.1 ppbv), $\alpha(\text{CH}_3\text{O}_2)$ only shows minor changes with increasing NO and is almost constant. The resulting slope is $0.16 \pm 0.01 \text{ ppbv}^{-1}$. In this range, NO is so abundant that CH_3O_2 reacts primarily with NO and changes in NO have almost no impact on the reaction. The amount of O_3 formed is limited by the abundance of CH_3O_2 , which itself is formed by a precursor VOC and no longer increases with increasing NO. This regime is referred to as VOC-sensitive.

155 Depending on where in this graph the data points from specific areas are located, it is possible to identify if a NO_x - or a VOC-sensitive regime is dominant.

2.3 Modeling study

The data analyzed in this study were produced by model simulations using the ECHAM5 (fifth generation European Centre Hamburg general circulation model, version 5.3.02)/MESSy2 (second-generation Modular Earth Submodel System, version 160 2.54.0) Atmospheric Chemistry (EMAC) model. Details on the EMAC model can be found in Jöckel et al. (2016). We applied EMAC in the T63L47MA-resolution, i.e., with a spherical truncation of T63 (corresponding to a quadratic Gaussian grid of 1.875 by 1.875 degrees in latitude and longitude) with 47 vertical hybrid pressure levels up to 0.01 hPa. Roughly 22 levels are included in the troposphere depending on the latitude, and the model has a time step of 6 minutes. The dynamics of the EMAC model have been weakly nudged in the troposphere (Jeuken et al., 1996) towards the ERA5 meteorological reanalysis 165 data (Hersbach et al., 2020) of the European Centre for Medium-Range Weather Forecasts (ECMWF) to represent the actual

<https://doi.org/10.5194/egusphere-2023-816>

Preprint. Discussion started: 4 May 2023

© Author(s) 2023. CC BY 4.0 License.

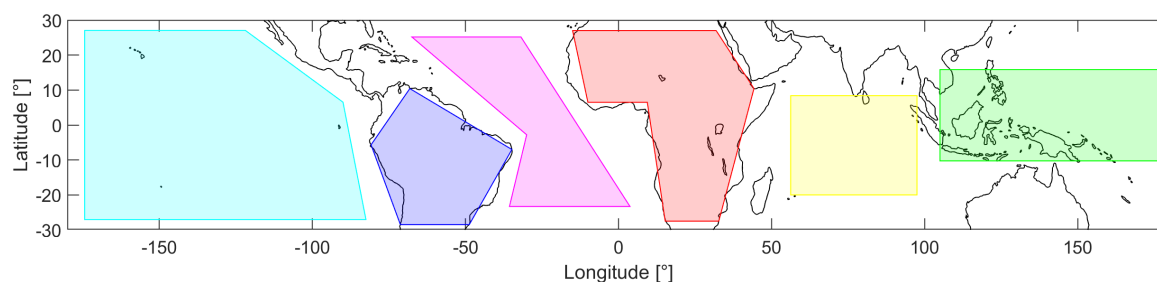


Figure 2. Overview of the defined areas in the tropics between 30° S and 30° N latitude: Pacific Ocean (cyan), South America (blue), Atlantic Ocean (pink), Africa (red), Indian Ocean (yellow) and South East Asia (green).

day-to-day meteorology in the troposphere. The set-up adopted here is similar to the one presented in Reifenberg et al. (2022), using the anthropogenic emissions CAMS-GLOB-ANTv4.2 (Granier et al., 2019), with varying monthly values for the period 2000–2019. The model has been extensively evaluated for ozone (e.g., Jöckel et al., 2016), showing a systematic though minor overestimation of the model compared to observations, which is a common feature in chemistry general circulation models of this complexity (Young et al., 2013). Comparison of the model results against numerous field campaigns (e.g., Lelieveld et al., 2018; Tadic et al., 2021; Nussbaumer et al., 2022) reveals a good agreement between observations and model results of NO_x and VOCs for locations in the UT. The reference simulation covers the time period 2000–2019 with hourly output of trace gas mixing ratios of O_3 , NO , NO_2 , OH , HO_2 , CH_3O_2 , HCHO , CO , CH_4 and H_2O , as well as the photolysis rates $j(\text{NO}_2)$ and $j(\text{O}^1\text{D})$ and meteorological parameters such as temperature and pressure, necessary for calculating net ozone production rates and $\alpha(\text{CH}_3\text{O}_2)$. The data were post-processed to obtain daily values at local noon time and calculated for 200 hPa (upper troposphere) using bilinear interpolation between the hybrid pressure model levels.

For detailed analysis, six different areas are defined and their geographic extent is shown in Figure 2. These areas refer to the Pacific Ocean (cyan), South America (blue), the Atlantic Ocean (pink), Africa (red), the Indian Ocean (yellow) and South East Asia (green).

3 Results and Discussion

3.1 Development of trace gases over time

The analyzed trace gases do not show statistically significant trends over time from 2000 to 2019 at 200 hPa, which we show in Figure S1 of the Supplement. We find small global increases of some trace gases, e.g., average NO and HO_2 mixing ratios increase by $\sim 5\%$ and average NO_2 and O_3 mixing ratios by up to 10% from 2000 to 2019. Global mean temperature increases by approximately 1 °C over the 20 year period. Even though slight trends can be detected, the variability is high and the 1σ standard deviation (grey shaded) is significantly larger than the variation over time and we therefore used a daily climatology from the 20-year period in order to simplify the calculations.

<https://doi.org/10.5194/egusphere-2023-816>

Preprint. Discussion started: 4 May 2023

© Author(s) 2023. CC BY 4.0 License.



3.2 Tropical distribution

3.2.1 NO_x

Figure 3 shows the distribution of NO in the upper tropical troposphere (at 200 hPa). We find large changes throughout the year, which are related to the seasonality of deep convection and the location of the intertropical convergence zone (ITCZ). In order to illustrate the differences, we subdivide the data into four periods, December–February (DJF), March–May (MAM), June–August (JJA) and September–November (SON). Each grid cell extends over $1.875^\circ \times 1.875^\circ$ latitude and longitude and represents a 20-year average of the respective period. During DJF, NO mixing ratios are highest over South America, southern Africa and northern Australia with average peak values between 0.3 and 0.4 ppbv. Over the other tropical regions, NO mixing ratios are much lower with average values of 0.09 ± 0.01 ppbv over the Pacific and the Indian Oceans, 0.12 ± 0.02 ppbv over the Atlantic Ocean, 0.10 ± 0.03 ppbv over North Africa and 0.08 ± 0.01 ppbv over South East Asia. Generally, the mixing ratios over land are much higher than those over the ocean, and the mixing ratios north of the equator are lower with an average value of 0.09 ± 0.03 ppbv compared to south of the equator with 0.14 ± 0.06 ppbv. During MAM, NO mixing ratios over South America are similar to those during DJF with average values of 0.21 ± 0.05 ppbv. NO mixing ratios over Africa are much higher compared to DJF with 0.28 ± 0.11 ppbv on average and peak values of 0.53 ppbv. The relatively high mixing ratios relocate from South to Central Africa from DJF to MAM and also over the Arabian Peninsula and South Asia, including India. Mixing ratios over Australia are around 0.15 ppbv and therefore approximately half of those during DJF and are similar over South East Asia.

During JJA, peak NO mixing ratios are found north of the equator over Central America and North Africa. Average NO mixing ratios are 0.14 ± 0.07 ppbv in the northern and 0.09 ± 0.02 ppbv in the southern tropical hemisphere. The distribution therefore changes drastically compared to DJF. During SON, NO mixing ratios are similar to MAM and peak over South America and Central Africa. The highest NO mixing ratios are found in the locations of predominant deep convection, which vary throughout the year. During DJF, deep convection dominates in the southern hemisphere, and during JJA it is most prevalent in the northern hemisphere. In July, deep convection is highest over Central America, North Africa and South Asia (northern India). In January, it is predominant over South America, Central to South Africa and North Australia (Yan, 2005). The areas where these convective processes are prevailing define the ITCZ where north- and southeasterly trade winds converge. Increased thunderstorm activity explains the occurrence of peak NO mixing ratios. Various studies have reported significantly increased lightning over land compared to the ocean, which is in line with the distribution of NO as shown in Figure 3 (Christian et al., 2003; Rudlosky and Virts, 2021; Nussbaumer et al., 2021b). South East Asia is often referred to as the “maritime” continent. This region experiences frequent cumulonimbus activity, but the convective available potential energy (CAPE) is less compared with that over the South American and in particular the African land masses. This region therefore shows lower NO mixing ratios throughout the year. The relative distribution of NO₂ is very similar to NO, which we show in Figure S2 of the Supplement. On average, NO₂ mixing ratios are around a factor of 7 lower compared to NO.

<https://doi.org/10.5194/egusphere-2023-816>

Preprint. Discussion started: 4 May 2023

© Author(s) 2023. CC BY 4.0 License.

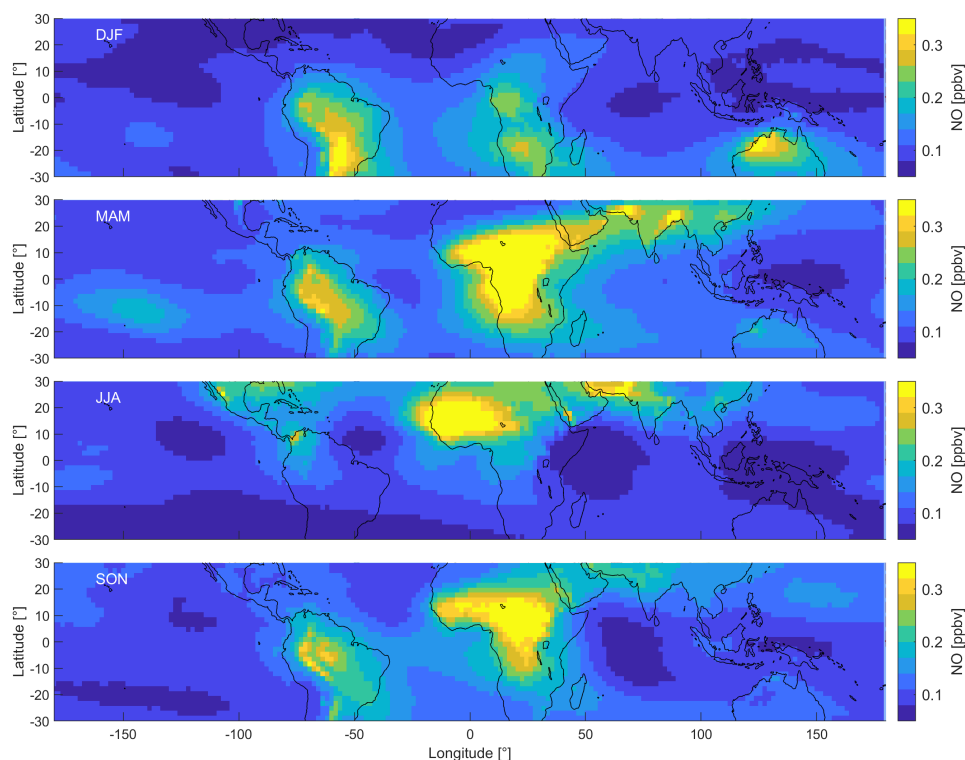


Figure 3. Distribution of NO in the tropical UT between 30° S and 30° N for December–February (DJF), March–May (MAM), June–August (JJA) and September–November (SON).

220 3.2.2 HO₂

Figure 4 shows the DJF and JJA distributions of HO₂. An overview of all four periods can be found in Figure S3 of the Supplement. Similar to NO, the spatial DJF distributions of HO₂ mixing ratios show peak values between 15 and 20 pptv over South America and South Africa. While NO shows minimum values over South East Asia and the Indian Ocean, HO₂ mixing ratios are elevated with average values of 13 ± 1 pptv and 12 ± 1 pptv, respectively. Mixing ratios are lower over the Pacific and the Atlantic Oceans with $8-9 \pm 1$ pptv on average and north of $\sim 20^{\circ}$ N. During JJA, HO₂ mixing ratios are elevated over the Indian Ocean, South Asia and Central America, including the Atlantic and Pacific Ocean around 10° N latitude. HO₂ is relatively low over South America and Africa. During MAM and SON, HO₂ is mostly intermediate between DJF and JJA and does not show any noteworthy features. Mixing ratios of CH₃O₂ show a very similar distribution to HO₂ across the tropical UT and range from ~ 0.5 to 4 pptv, which we show in Figure S4 of the Supplement.

<https://doi.org/10.5194/egusphere-2023-816>

Preprint. Discussion started: 4 May 2023

© Author(s) 2023. CC BY 4.0 License.

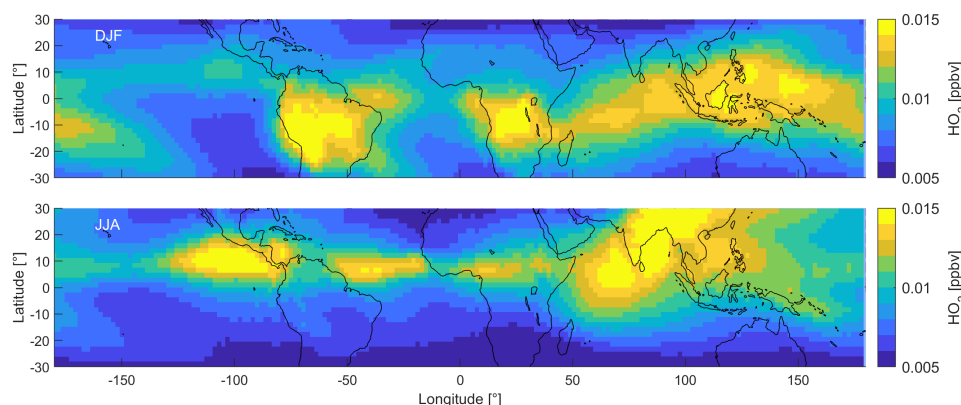


Figure 4. Distribution of HO_2 in the tropical UT between 30°S and 30°N during DJF (top panel) and JJA (bottom panel).

230 3.2.3 NOPR

The tropical UT distribution of net ozone production rates is closely related to the distribution of NO (Figure 3). We show the model-calculated results for each period in Figure S5 of the Supplement. During DJF, NOPRs peak over South America with average values of $0.77 \pm 0.20 \text{ ppbv h}^{-1}$ and maximum values above 1 ppbv h^{-1} over southern Africa and northern Australia. In the course of the year and the local variations in deep convection, NOPR peaks move northwards, reaching the northernmost point in JJA, and moving southwards again in SON and DJF. During DJF, NOPRs are $0.36 \pm 0.21 \text{ ppbv h}^{-1}$ and $0.23 \pm 0.09 \text{ ppbv h}^{-1}$ in the southern and northern tropical hemisphere, respectively. During JJA, NOPRs are $0.17 \pm 0.06 \text{ ppbv h}^{-1}$ in the southern tropical hemisphere and more than twice as high in the northern tropical hemisphere with $0.36 \pm 0.15 \text{ ppbv h}^{-1}$. The production of O_3 outweighs its loss by a factor of 8 on average for the studied conditions. The difference is larger in regions with peak NOPRs, e.g., over South America with a factor of 11, and smaller in regions with low NOPRs, e.g., over the Pacific Ocean with a factor of around 7. We show the distribution of both $\text{P}(\text{O}_3)$ and $\text{L}(\text{O}_3)$ in Figures S6 and S7 of the Supplement. These results are in line with findings by Apel et al. (2015), who reported enhanced ozone production for high lightning NO_x over the U.S. during a research flight in June 2012 as part of the DC3 campaign.

3.2.4 $\alpha(\text{CH}_3\text{O}_2)$

Figure 5 shows the distribution of $\alpha(\text{CH}_3\text{O}_2)$ in the tropical UT during DJF and JJA. We show all periods in Figure S8 of the Supplement. During DJF, $\alpha(\text{CH}_3\text{O}_2)$ ranges from 0.77 to 0.95 with lowest values over South East Asia and highest values over South Africa and Australia. During JJA, lowest values are obtained over South East Asia, the Indian Ocean and over the Pacific and Atlantic Oceans around 10°N latitude. Maximum values of up to 0.97 are reached over North Africa and the Arabian Peninsula. Therefore, as expected, $\alpha(\text{CH}_3\text{O}_2)$ is proportional to NOPR and NO_x mixing ratios and is anti-proportional to HO_2 mixing ratios. At low NO_x/HO_2 ratios, increases in NO enhance $\alpha(\text{CH}_3\text{O}_2)$, while at high NO_x/HO_2 ratios, changes in NO

<https://doi.org/10.5194/egusphere-2023-816>

Preprint. Discussion started: 4 May 2023

© Author(s) 2023. CC BY 4.0 License.

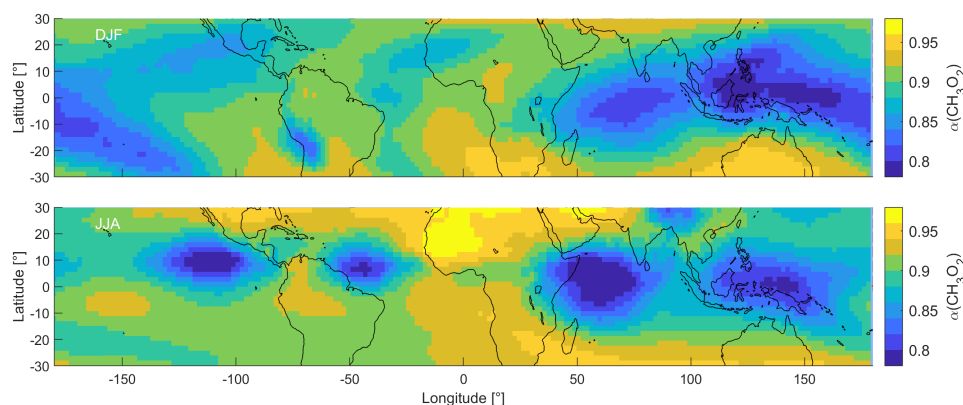


Figure 5. Distribution of $\alpha(\text{CH}_3\text{O}_2)$ in the tropical UT between 30°S and 30°N during DJF (top panel) and JJA (bottom panel).

250 have no or only little effect. We will discuss the implications of $\alpha(\text{CH}_3\text{O}_2)$ for the dominant chemical regime in the tropical UT and specific regions in the following section.

3.3 Chemical regimes

3.3.1 Baseline scenario

Figure 6 presents $\alpha(\text{CH}_3\text{O}_2)$, O_3 and the HCHO/NO_2 ratio binned to NO mixing ratios during DJF, MAM, JJA and SON. The graphs show NO mixing ratios up to 0.5 ppbv, which includes 99.6 % of all data points. The frequency distribution of the NO data can be seen in Figure S9 of the Supplement. The black lines and the grey shades represent the average of all data points binned to NO and the associated 1σ standard deviation. The colored data points show the average of the individual areas as shown in Figure 2. The error bars represent the 1σ variability. Data for the Pacific Ocean are shown in cyan, for South America in blue, for the Atlantic Ocean in magenta, for Africa in red, for the Indian Ocean in yellow and for South East Asia in green.

260 $\alpha(\text{CH}_3\text{O}_2)$ (left column: (a), (d), (g) and (j)) increases strongly with NO for mixing ratios below 0.1 ppbv with a slope of $3.75 \pm 0.44 \text{ ppbv}^{-1}$. For example, an average increase of $\alpha(\text{CH}_3\text{O}_2)$ by 0.1 results from an increase of ambient NO by around 27 pptv. This characterizes the NO_x -sensitive regime. In contrast, for NO mixing ratios higher than 0.1 ppbv NO, increasing NO has only a minor effect on $\alpha(\text{CH}_3\text{O}_2)$ (slope = $0.16 \pm 0.01 \text{ ppbv}^{-1}$), which represents the VOC-sensitive regime. To reach an increase of $\alpha(\text{CH}_3\text{O}_2)$ by 0.1, ambient NO needs to increase by 625 pptv, a factor of >20 higher compared to the low- NO_x regime. Within the NO_x -sensitive regime, predominantly CH_3O_2 reacts with NO, forming O_3 , as well as with HO_2 , which does not result in formation of O_3 . With increasing NO, the share of the reaction with NO (compared to the reaction with HO_2) increases, which in turn enhances O_3 . In contrast, within the VOC-sensitive regime CH_3O_2 radicals mostly react with NO in any case and increases in NO do not affect O_3 . This is illustrated in the middle column of Figure 6 ((b), (e), (h) and (k)): O_3 increases with NO for low NO mixing ratios and reaches a plateau for high NO mixing ratios. While the shift from the NO_x -

265

<https://doi.org/10.5194/egusphere-2023-816>

Preprint. Discussion started: 4 May 2023

© Author(s) 2023. CC BY 4.0 License.

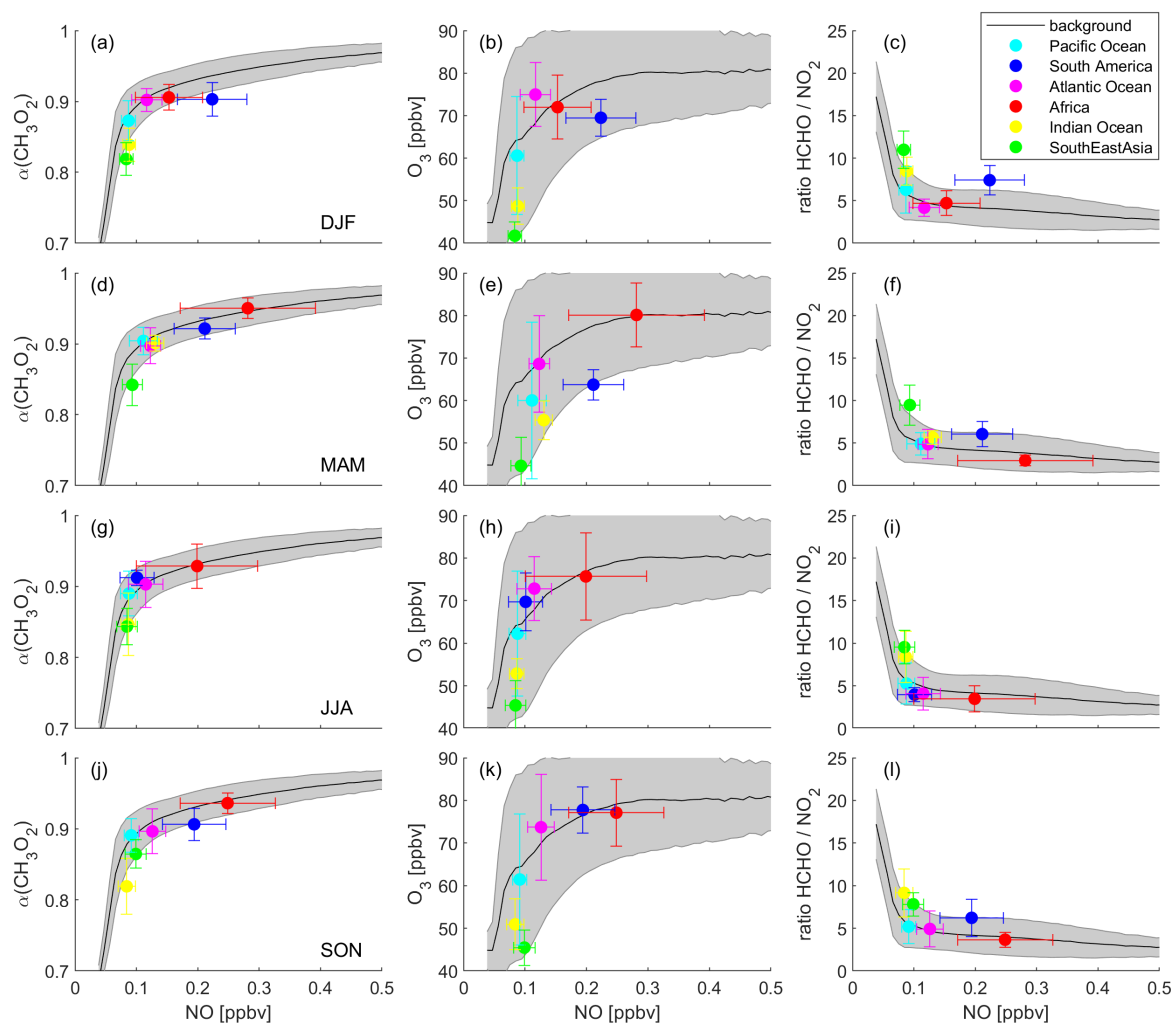


Figure 6. Different metrics to determine the dominant chemical regime. Left column: $\alpha(\text{CH}_3\text{O}_2)$, middle column: O_3 and right column: HCHO/NO_2 ratio, binned to NO mixing ratios for (a)–(c) DJF (December–February), (d)–(f) MAM (March–May), (g)–(i) JJA (June–August) and (j)–(l) SON (September–November). Black lines show averages of all data points and grey shades present the 1σ standard deviation. Colored data points show the averages for the indicated areas and the 1σ variability.

270 to the VOC-sensitive regime is relatively sharp for $\alpha(\text{CH}_3\text{O}_2)$, the transition for O_3 is broader and more difficult to relate to a NO mixing ratio. This graph is illustrative, but should not be used solely for determining the dominant chemical regime. In the right column (Figure 6 (c), (f), (i) and (l)), we present the HCHO/NO_2 ratio binned to NO mixing ratios. In the literature, mostly absolute values for the HCHO/NO_2 ratio are used to determine the chemical regime, for example $\text{HCHO}/\text{NO}_2 > 2$

<https://doi.org/10.5194/egusphere-2023-816>

Preprint. Discussion started: 4 May 2023

© Author(s) 2023. CC BY 4.0 License.



for NO_x sensitivity and $\text{HCHO}/\text{NO}_2 < 1$ for VOC sensitivity (Duncan et al., 2010). These threshold values are not valid in the upper troposphere due to the vertical gradients of the trace gases. However, the HCHO/NO_2 ratio can also indicate the transition from a NO_x - to a VOC-sensitive regime when binned to NO mixing ratios, which does not require any absolute threshold values. Within the NO_x -sensitive regime, the HCHO/NO_2 strongly decreases with small increases in NO, and within the VOC-sensitive regime it is mostly unresponsive to changes in NO. Depending on where in these plots a specific data point or an average of several data points is located, it is possible to derive the dominant chemical regime.

As explained earlier, it is not possible to determine the dominant chemical regime from ozone formation rates $\text{P}(\text{O}_3)$ in the upper troposphere, as the formation of HNO_3 plays a minor role at UT altitudes and therefore does not lead to a decrease in $\text{P}(\text{O}_3)$, which in theory indicates the dominance of VOC over NO_x sensitivity. In fact, $\text{P}(\text{O}_3)$ does decrease for NO mixing ratios above around 0.7 ppbv, but for a different reason, as shown in Figure S10 of the Supplement. Panel (a) presents $\text{P}(\text{O}_3)$ binned to NO, which increases for low NO, reaches a plateau around 0.6–0.7 ppbv NO and decreases at higher NO. Panel (b) shows NO_x loss ($\text{L}(\text{NO}_x)$) rates via OH, HO_2 and CH_3O_2 , which are negligible compared to $\text{P}(\text{O}_3)$ rates as shown in panel (a). Even though $\text{L}(\text{NO}_x)$ increases with increasing NO, it is still only 6 % of the ozone production at 1 ppbv NO. The decrease in $\text{P}(\text{O}_3)$ is therefore not associated with the formation of HNO_3 (as it is in the lower troposphere) but reflects the decrease of HO_2 with increasing NO (see panels (c)-(d)). The peak in $\text{P}(\text{O}_3)$, therefore, does not provide an indication for a regime change.

Figure 6 (a) shows NO vs $\alpha(\text{CH}_3\text{O}_2)$ during DJF. The tropical UT over the Indian Ocean and South East Asia is characterized by NO_x sensitivity with NO mixing ratios between 80 and 90 pptv and an average α of 0.84 and 0.82, respectively. Ozone formation over South America is VOC-sensitive with an average NO mixing ratio of 222 pptv and an α of 0.90. The data points for the Pacific Ocean, the Atlantic Ocean and Africa are close to the transition point of the two regimes, with a tendency of the Pacific Ocean towards NO_x and of the Atlantic Ocean and Africa towards VOC sensitivity. This is in line with Figure 6 (b) which presents NO vs. O_3 mixing ratios. The data points for South East Asia, the Indian Ocean and the Pacific Ocean are located mostly in the up-sloping part of the curve, where O_3 strongly increases with increasing NO. The averages for the Atlantic Ocean, Africa and South America are located towards the flattening of the curve. Figure 6 (c) shows the DJF averages for NO vs. the HCHO/NO_2 ratio. For South East Asia, the Indian Ocean and the Pacific Ocean, NO mixing ratios are below 0.1 ppbv and HCHO/NO_2 ratios are high with values of 6.3, 8.5 and 10.9 ppbv ppbv⁻¹, respectively. For the Atlantic Ocean and Africa, the average NO mixing ratios are higher and the HCHO/NO_2 ratios are lower with values of 4.2 and 4.7 ppbv ppbv⁻¹, respectively. NO mixing ratios over South America are even higher, but the HCHO/NO_2 ratio is also higher with a value of 7.4 ppbv ppbv⁻¹. This underlines the limitation of using absolute threshold values for determining the dominant chemical regime. If a threshold for the regime transition were to be set to, e.g., 5 ppbv ppbv⁻¹, the South American UT would be characterized as NO_x -sensitive, while it clearly shows VOC sensitivity. It is therefore important to consider the metrics used in relation to ambient NO mixing ratios, and it is best to use them in combination with other metrics.

Figure 6 (d) shows $\alpha(\text{CH}_3\text{O}_2)$ binned to NO for MAM data. The UT over South East Asia is NO_x -sensitive with values similar to DJF. Over the Indian Ocean, both the average NO mixing ratio and $\alpha(\text{CH}_3\text{O}_2)$ increase to 130 pptv and 0.90, respectively, being located in the transition regime, together with the Pacific Ocean and the Indian Ocean. Minor changes from DJF to MAM occur over South America, which is still VOC-sensitive. A strong VOC sensitivity is calculated for the UT

<https://doi.org/10.5194/egusphere-2023-816>

Preprint. Discussion started: 4 May 2023

© Author(s) 2023. CC BY 4.0 License.

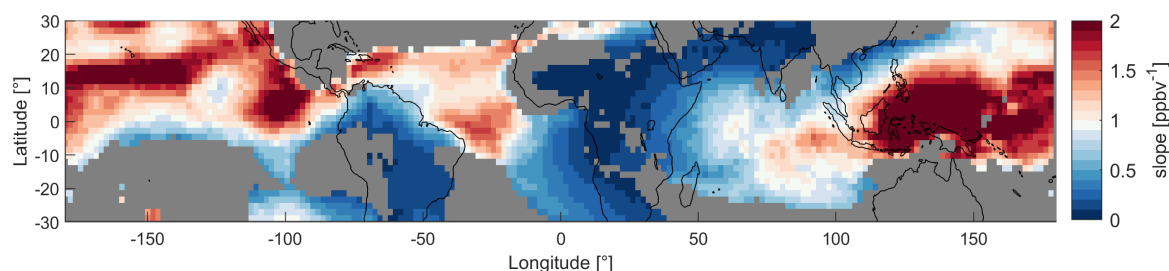


Figure 7. Map of the tropical UT between 30 ° S and 30 ° N colored by the slopes of NO vs $\alpha(\text{CH}_3\text{O}_2)$ of the data in model grid regions. Red colors indicate NO_x and blue colors VOC sensitivity. For gray areas the R^2 of the fit is below 30 %.

over Africa with average NO mixing ratios of 279 pptv and $\alpha(\text{CH}_3\text{O}_2)$ of 0.95. These findings are confirmed by O_3 and the HCHO/ NO_2 ratio binned to NO in Figure 6 (e) and (f). The data for South East Asia, the Pacific Ocean, the Atlantic Ocean and South America are similar to values during DJF. Between DJF and MAM, the values over the Indian Ocean and Africa change to higher NO (131 pptv and 279 pptv) in combination with higher O_3 (55 ppbv and 80 ppbv) and a lower HCHO/ NO_2 ratio (5.7 ppbv ppbv⁻¹ and 3.0 ppbv ppbv⁻¹), associated with a change from the NO_x -sensitive to the transition regime and a change from the transition to the VOC-sensitive regime, respectively.

Figure 6 (g), (h) and (i) show similar graphs for JJA (June–August), indicating NO_x sensitivity for the UT over South East Asia and the Indian Ocean, a transition regime for the Pacific Ocean, the Atlantic Ocean and South America and VOC sensitivity for Africa. During SON (September–November), as shown in Figure 6 (j), (k) and (l), South America shifts back to VOC sensitivity. All other regimes remain unchanged between JJA and SON.

Figure S11 of the Supplement shows the mean values of the specified areas for $\text{P}(\text{O}_3)$ vs. NO. While the computational tools presented above allow for a clear distinction between the regimes depending on location and time of the year, this indicator shows no differences. According to the surface-oriented definition for chemical regimes, all data points would be located in the NO_x -sensitive regime.

Since NO and HO_2 mixing ratios, as well as NOPRs change throughout the year, the varying locations of deep convection also affect the dominant chemical regime. Areas with deep convection are potentially associated with lightning activity, resulting in higher NO mixing ratios that lead to VOC sensitivity. The continental areas of South America and especially Africa experience most lightning and therefore show the most VOC-sensitive regimes (Williams and Satori, 2004). As the cumulonimbus clouds in South East Asia are mostly formed in maritime conditions, the region experiences significantly less lightning and therefore shows NO_x sensitivity all year round. Ozone formation over the oceans is either NO_x -sensitive or in the transition regime as lightning strikes are significantly less frequent in maritime compared to continental areas. Figure 7 presents a geographical distribution of the tropical UT colored by the slopes of the NO vs $\alpha(\text{CH}_3\text{O}_2)$ data in each individual grid region to illustrate the dominating chemical regimes. Here, we present a map for MAM data. In Figure S12 of the Supplement, we show them for all periods. High values for the slopes and red colors (i.e. values well above 1) represent the predominantly

<https://doi.org/10.5194/egusphere-2023-816>

Preprint. Discussion started: 4 May 2023

© Author(s) 2023. CC BY 4.0 License.

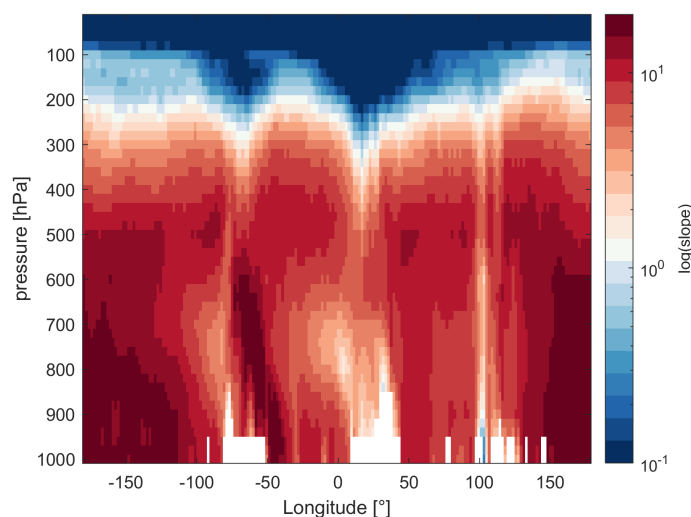


Figure 8. Slopes of NO vs $\alpha(\text{CH}_3\text{O}_2)$ by pressure altitude and longitude on a log scale during the period March–May (MAM) and close to the equator (1°N). Red colors indicate NO_x and blue colors VOC sensitivity. White areas between 800 and 1000 hPa result from the local surface topography.

NO_x -sensitive regime and low values, accompanied by blue colors represent VOC sensitivity. It is not possible to determine an exact threshold slope for the transitioning between regimes. Generally, the more intense the color (red or blue), the more clearly a location is assigned to one of the two regimes. Lighter colors indicate a state closer to the transition regime. Grey areas indicate that the R^2 of the fit is $< 30\%$ which, for example, occurs when the data are arranged in a cloud of points. This depiction is in line with the results from Figure 6. During MAM, blue colors over South America and Africa indicate a VOC-sensitive regime. Red colors over South East Asia show NO_x sensitivity. Finally, over the three oceans we find lighter colors indicating the transition regime. This view also allows for a more detailed differentiation between the areas; for example, the UT over the Atlantic Ocean tends more towards an NO_x -sensitive regime in the northern and towards a VOC-sensitive regime in the southern part.

While we focus on the upper troposphere in this study, $\alpha(\text{CH}_3\text{O}_2)$ remains a suitable indicator for the dominant chemical regime at all altitudes. In Figure 8 we present the slopes of NO vs $\alpha(\text{CH}_3\text{O}_2)$ by pressure altitude and longitudes, as an example for MAM data close to the equator (1°N). White areas at the bottom (between 800 and 1000 hPa) result from the local topography (mountains). For the free troposphere, we find strong NO_x sensitivity with a maximum of 38 ppbv^{-1} . In the upper troposphere lower stratosphere at pressure altitudes between 300 and 100 hPa, we observe the transitioning to a VOC-sensitive regime. For latitudes with strong lightning activity, including areas such as continental South America (-80 to -60° longitude) and Africa (5 to 30° longitude), the transition occurs in the upper troposphere, corresponding to pressure altitudes of 250–300 hPa. For latitudes with low lightning activity, for example, between 130 and 160° longitude (South East Asia), the regime

<https://doi.org/10.5194/egusphere-2023-816>

Preprint. Discussion started: 4 May 2023

© Author(s) 2023. CC BY 4.0 License.



change only occurs at the transition to the lower stratosphere – at a pressure altitude of around 150 hPa – which is characterized by strong NO_x saturation. In Figure S13 of the Supplement we additionally show the dominant chemical regime, indicated by NO vs $\alpha(\text{CH}_3\text{O}_2)$, on a global scale near the surface as the annual average. As we would expect, $\alpha(\text{CH}_3\text{O}_2)$ indicates VOC sensitivity at the surface for all urbanized and industrialized regions characterized by high NO_x emissions and NO_x sensitivity for remote regions. Shipping routes, which are closer to the transition regime, can be distinguished from the pronounced maritime NO_x sensitivity.

3.3.2 Sensitivity study: lightning NO_x

Three additional model runs were performed in order to investigate the impact of lightning NO_x . First, lightning NO_x was completely omitted. In second and third runs, NO_x from lightning was halved and doubled, respectively, compared to the baseline scenario. The emissions of global lightning NO_x in the baseline scenario amount to 6.2 Tg/year (estimated from the climatological data) in agreement with the work of Miyazaki et al. (2014).

Figure 9 shows the three previously discussed metrics (a) $\alpha(\text{CH}_3\text{O}_2)$, (b) O_3 and (c) the HCHO/NO_2 ratio binned to NO mixing ratios for the modeling scenario excluding lightning NO_x . As there are no significant differences between the periods, we show all-year data here. Figure S14 of the Supplement shows the subdivision into DJF, MAM, JJA and SON. The black lines representing the average of all data points show a similar course compared to the baseline scenario including lightning NO_x , but the distinction between the regimes is less pronounced. Figure 9 (a) presents NO vs $\alpha(\text{CH}_3\text{O}_2)$. At low NO mixing ratios, $\alpha(\text{CH}_3\text{O}_2)$ increases with NO , indicating NO_x sensitivity and for higher NO mixing ratios, $\alpha(\text{CH}_3\text{O}_2)$ is only marginally affected by changes in NO , indicating VOC sensitivity. The tropical UT over all selected areas is clearly located within the NO_x -sensitive chemical regime. The average NO mixing ratios range from 17 pptv over South East Asia to 33 pptv over Africa. Compared to the baseline scenario, excluding lightning NO_x leads to a decrease of ambient NO levels by up to one order of magnitude. The average $\alpha(\text{CH}_3\text{O}_2)$ ranges from 0.49 to 0.68 over South East Asia and Africa, respectively. The abundance of HO_2 in comparison to NO is therefore high, and a significant amount of CH_3O_2 undergoes reaction with HO_2 , next to NO . Figure 9 (b) shows O_3 mixing ratios as a function of NO . O_3 mixing ratios first increase as a function of NO , reach a peak at around 0.05 ppbv NO and 85 ppbv O_3 and subsequently change little at higher NO levels. Note that the number of data points decreases rapidly for high NO mixing ratios. Only around 5.5 % of the data points represent NO values of >0.05 ppbv. We show the associated frequency distribution in Figure S15 of the Supplement. As expected, the data points of all selected areas are located at low NO and O_3 levels, at average O_3 mixing ratios ranging from 30 ppbv over South East Asia to 50 ppbv over Africa. Figure 9 (c) shows the HCHO/NO_2 ratio binned to NO mixing ratios. The tendencies of the average values (black line) are again similar to the one for the baseline scenario, but the absolute values for the HCHO/NO_2 ratio are higher. The highest average value occurs over South East Asia with $35.2 \text{ ppbv ppbv}^{-1}$ and the lowest over the Atlantic Ocean with $13.2 \text{ ppbv ppbv}^{-1}$. All data points are therefore clearly located within the NO_x -sensitive regime, which is in line with the findings from the correlation between NO and $\alpha(\text{CH}_3\text{O}_2)$ from Figure 9 (a).

In Figure S16 and S17, we present the three metrics $\alpha(\text{CH}_3\text{O}_2)$, O_3 and the HCHO/NO_2 ratio binned to NO mixing ratios for all periods and locations for halved and doubled lightning NO_x , respectively. The transition region between the regimes occurs

<https://doi.org/10.5194/egusphere-2023-816>

Preprint. Discussion started: 4 May 2023

© Author(s) 2023. CC BY 4.0 License.

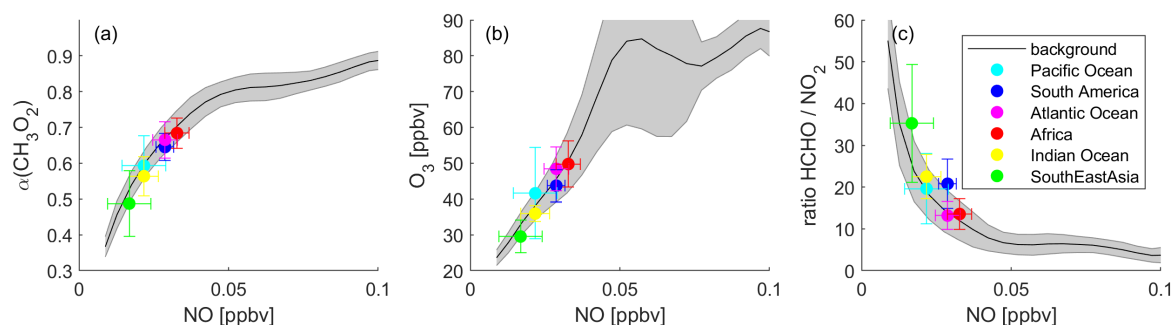


Figure 9. Determination of the dominant chemical regime in the tropical UT in the “no lightning” scenario via (a) $\alpha(\text{CH}_3\text{O}_2)$, (b) O_3 and (c) the HCHO/NO_2 ratio, binned to NO mixing ratios. Black lines show averages of all data points and grey shades present the 1σ standard deviation. Colored data points show the averages for the indicated areas with the 1σ variability.

around 0.1 ppbv and is therefore not meaningfully different from that in the baseline scenario, but the distinction between the regimes is more conspicuous with increasing lightning NO_x emissions. Figure S18 shows the average $\alpha(\text{CH}_3\text{O}_2)$ vs. NO for each considered location and for all modeled lightning NO_x scenarios. As expected, in each location the data points shift to higher values for both NO and $\alpha(\text{CH}_3\text{O}_2)$ with increasing influence of lightning NO_x . When excluding lightning, the dominant regime changes to NO_x -sensitive in all locations. Removing lightning also shows that lightning is by far the dominant source of NO_x in the upper tropical troposphere. In maritime regions where lightning is relatively infrequent, NO_x depends more strongly on advection from continental regions, formation from HNO_3 and aircraft emissions. A model run excluding NO_x emissions from aircraft does not lead to significant differences compared to the baseline scenario, which we present by the black crosses in Figure S18. Excluding lightning shows that NO_x mixing ratios also decrease significantly in maritime environments, including South East Asia where NO_x mixing ratios drop from 90 pptv to 17 pptv on average. This illustrates that in maritime locations in the tropics, i.e., apart from South America and Central Africa, NO_x mixing ratios are largely dependent on transported lightning NO_x . For halved lightning NO_x , NO_x sensitivity also prevails in most locations. Only Africa and South America show a transition regime for the periods of the year with maximum lightning. For doubled lightning NO_x , the qualitative regime observations are similar to the baseline scenario. The UT over Central Africa and South America is mostly VOC-sensitive, over South East Asia and the Indian Ocean it is NO_x -sensitive and this layer is in the transition regime over the Pacific and Atlantic Ocean. Therefore, regions with frequent lightning are VOC-sensitive in the baseline scenario while the doubling of lightning NO_x does not have a large impact in regions where lightning is generally infrequent. In accordance with our prior analysis, O_3 does not increase significantly from the doubling of lightning NO_x . In the VOC-sensitive regime, the black curve representing the average of all data points of NO vs O_3 levels off at around 90 ppbv compared to 80 ppbv for the baseline scenario. This aids our understanding of NO_x and VOC sensitivity in the upper troposphere, as all available HO_2 and CH_3O_2 radicals react with NO within the VOC-sensitive regime and changes in NO_x therefore do not affect changes in O_3 .

<https://doi.org/10.5194/egusphere-2023-816>

Preprint. Discussion started: 4 May 2023

© Author(s) 2023. CC BY 4.0 License.



The sensitivity study of lightning NO_x emphasizes two major aspects. First, lightning is the predominant source of NO_x in the upper tropical troposphere as the mixing ratios drop to near zero when excluding it, and a model run excluding aircraft NO_x does not show significant differences compared to the baseline scenario. Second, lightning and its distribution in the tropics, which is affected by the partitioning of continental and maritime areas and the varying locations of deep convection throughout the year, are the most important determinants of the dominant chemical regime in the UT. Our results additionally indicate that any future changes in lightning will only significantly affect O_3 levels in the upper troposphere if lightning substantially increases in locations where it is currently sparse or if lightning decreases in areas where it is presently frequent.

4 Conclusions

We have investigated the dominance of NO_x and VOC sensitivity in the upper tropical troposphere (200 hPa) between 30°S and 30°N latitude. The analyzed trace gas mixing ratios and meteorological parameters are calculated with the EMAC atmospheric chemistry - general circulation model for a $1.875^\circ \times 1.875^\circ$ horizontal resolution and the years 2000–2019. One model run considers a baseline scenario and three additional ones with halved, doubled and excluded lightning NO_x emissions, respectively. We find that the mixing ratios of the considered trace gases have not changed significantly in the upper troposphere over the past two decades and we therefore evaluate the average of the data which benefits from a higher statistical significance. The distribution of the analyzed trace gases varies with the time of the year and the changing areas of deep convection, confined within the ITCZ. During DJF, maximum convection occurs over South America, Central to South Africa and North Australia and during JJA, over Central America, North Africa and continental Asia. As a consequence, NO_x mixing ratios and net ozone production rates peak over South America, South Africa and North Australia during DJF, over South America and Central Africa during MAM and SON, and over Central America and North Africa during JJA, as deep convection brings increased thunderstorm and lightning activity, particularly over continental areas. The distribution of HO_2 mostly differs from NO_x due to enhanced mixing ratios over South East Asia, where NO_x is low year around.

We analyzed several commonly applied metrics for their potential to determine the dominant chemical regime in the upper troposphere, including ozone production rates $P(\text{O}_3)$, the fraction of methyl peroxyradicals forming formaldehyde $\alpha(\text{CH}_3\text{O}_2)$, and the ratio of HCHO to NO_2 . We show that $\alpha(\text{CH}_3\text{O}_2)$ and the HCHO/NO_2 are good indicators for the chemical regime in the upper troposphere, while $P(\text{O}_3)$ is unsuitable. At the surface, NO_x sensitivity is generally defined by increasing $P(\text{O}_3)$ with NO , and VOC sensitivity by decreasing $P(\text{O}_3)$ with NO . In the upper troposphere, this indicator is no longer valid as the reaction of NO_2 with OH does not play a significant role. Instead, under conditions of NO_x sensitivity CH_3O_2 undergoes reaction with both HO_2 and NO , and increasing NO leads to an enhancement of O_3 . For VOC-sensitive conditions, CH_3O_2 predominantly reacts with NO and as the latter is present in excess it does not influence O_3 mixing ratios. In this case, ozone formation changes are governed by those in VOC, controlling the availability of peroxy radicals. The transition point can be read from the course of $\alpha(\text{CH}_3\text{O}_2)$ and the HCHO/NO_2 ratio as a function of NO abundance. This definition of chemical regimes in terms of NO_x and VOC sensitivity is valid throughout the entire troposphere. When assessing O_3 sensitivity in the upper troposphere based on trace gas measurements, $\alpha(\text{CH}_3\text{O}_2)$ is to be preferred over the HCHO/NO_2 ratio as it can be

<https://doi.org/10.5194/egusphere-2023-816>

Preprint. Discussion started: 4 May 2023

© Author(s) 2023. CC BY 4.0 License.



more easily determined from in-situ data. While NO and HO_x measurements are commonly performed on research aircraft, 440 for example, NO₂ measurements tend to suffer from the unselective detection or artifacts from reservoir species, which makes accurate quantification challenging.

In the ITCZ over continental areas, ozone chemistry is mostly VOC-sensitive. The UT over South America and Africa is therefore VOC-sensitive apart from JJA and DJF, respectively, where chemistry moves towards the transition area. Over maritime areas, including South East Asia, ozone chemistry is mostly NO_x-sensitive or in the transition regime depending 445 on the time of the year. The metrics which are found to be good indicators for the UT, $\alpha(\text{CH}_3\text{O}_2)$, O₃ mixing ratios and the HCHO/NO₂ ratio as a function of NO, show that the transition between a NO_x- and a VOC-sensitive regime occurs around 0.1 ppbv NO. When decreasing or excluding lightning NO_x, the considered areas are mostly dominated by a NO_x-sensitive regime.

We conclude that lightning is the major driver of the dominant ozone chemistry in the upper tropical troposphere. While it is 450 still not fully understood how lightning activity will evolve in the future, it remains important to monitor and understand ozone production in the upper tropical troposphere, a process which has a major impact on the radiative energy budget, and in turn on global warming.

Data availability. Model data will be uploaded to a public data repository upon acceptance of the manuscript.

Author contributions. CMN, HF and AP conceived the study. CMN analyzed the data and wrote the manuscript. AP provided the modeling 455 data. All authors contributed to designing the study and proofreading the manuscript.

Competing interests. At least one of the (co-)authors is a member of the editorial board of Atmospheric Chemistry and Physics.

Acknowledgements. This work was supported by the Max Planck Graduate Center (MPGC) with the Johannes Gutenberg-Universität Mainz.

<https://doi.org/10.5194/egusphere-2023-816>

Preprint. Discussion started: 4 May 2023

© Author(s) 2023. CC BY 4.0 License.



References

- Ainsworth, E. A., Yendrek, C. R., Sitch, S., Collins, W. J., and Emberson, L. D.: The effects of tropospheric ozone on net primary productivity and implications for climate change, *Annual review of plant biology*, 63, 637–661, <https://doi.org/10.1146/annurev-arplant-042110-103829>, 2012.
- Apel, E., Hornbrook, R., Hills, A., Blake, N., Barth, M., Weinheimer, A., Cantrell, C., Rutledge, S., Basarab, B., Crawford, J., Diskin, G., Homeyer, C. R., Campos, T., Flocke, F., Fried, A., Blake, D. R., Brune, W., Pollack, I., Peischl, J., Ryerson, T., Wennberg, P. O., Crounse, J. D., Wisthaler, A., Mikoviny, T., Huey, G., Heikes, B., O’Sullivan, D., and Riemer, D. D.: Upper tropospheric ozone production from lightning NO_x-impacted convection: Smoke ingestion case study from the DC3 campaign, *Journal of Geophysical Research: Atmospheres*, 120, 2505–2523, <https://doi.org/10.1002/2014JD022121>, 2015.
- Brasseur, G. P., Müller, J.-F., and Granier, C.: Atmospheric impact of NO_x emissions by subsonic aircraft: A three-dimensional model study, *Journal of Geophysical Research: Atmospheres*, 101, 1423–1428, <https://doi.org/10.1029/95JD02363>, 1996.
- Cazorla, M. and Brune, W.: Measurement of ozone production sensor, *Atmospheric Measurement Techniques Discussions*, 2, 3339–3368, <https://doi.org/10.5194/amt-3-545-2010>, 2009.
- Christian, H. J., Blakeslee, R. J., Boccippio, D. J., Boeck, W. L., Buechler, D. E., Driscoll, K. T., Goodman, S. J., Hall, J. M., Koshak, W. J., Mach, D. M., and Stewart, M. F.: Global frequency and distribution of lightning as observed from space by the Optical Transient Detector, *Journal of Geophysical Research: Atmospheres*, 108, ACL–4, 2003.
- Cooper, O. R., Parrish, D., Ziemke, J., Balashov, N., Cupeiro, M., Galbally, I., Gilge, S., Horowitz, L., Jensen, N., Lamarque, J.-F., Naik, V., Oltmans, S. J., Schwab, J., Shindell, D. T., Thompson, A. M., Thouret, V., Wang, Y., and Zbinden, R. M.: Global distribution and trends of tropospheric ozone: An observation-based review, *Global distribution and trends of tropospheric ozone, Elementa: Science of the Anthropocene*, 2, <https://doi.org/10.12952/journal.elementa.000029>, 2014.
- Crutzen, P. J.: Tropospheric ozone: An overview, Springer, https://doi.org/10.1007/978-94-009-2913-5_1, 1988.
- Dahlmann, K., Grewe, V., Ponater, M., and Matthes, S.: Quantifying the contributions of individual NO_x sources to the trend in ozone radiative forcing, *Atmospheric Environment*, 45, 2860–2868, <https://doi.org/10.1016/j.atmosenv.2011.02.071>, 2011.
- Duncan, B. N., Yoshida, Y., Olson, J. R., Sillman, S., Martin, R. V., Lamsal, L., Hu, Y., Pickering, K. E., Retscher, C., Allen, D. J., and Crawford, J. H.: Application of OMI observations to a space-based indicator of NO_x and VOC controls on surface ozone formation, *Atmospheric Environment*, 44, 2213–2223, <https://doi.org/10.1016/j.atmosenv.2010.03.010>, 2010.
- Dyson, J. E., Whalley, L. K., Slater, E. J., Woodward-Massey, R., Ye, C., Lee, J. D., Squires, F., Hopkins, J. R., Dunmore, R. E., Shaw, M., Hamilton, J. F., Lewis, A. C., Worrall, S. D., Bacak, A., Mehra, A., Bannan, T. J., Coe, H., Percival, C. J., Ouyang, B., Hewitt, C. N., Jones, R. L., Crilley, L. R., Kramer, L. J., Acton, W. J. F., Bloss, W. J., Saksakulkrai, S., Xu, J., Shi, Z., Harrison, R. M., Kotthaus, S., Grimmond, S., Sun, Y., Xu, W., Yue, S., Wei, L., Fu, P., Wang, X., Arnold, S. R., and Heard, D. E.: Impact of HO₂ aerosol uptake on radical levels and O₃ production during summertime in Beijing, *Atmospheric Chemistry and Physics Discussions*, pp. 1–43, <https://doi.org/10.5194/acp-2022-800>, 2022.
- Fischer, H., Kormann, R., Klüpfel, T., Gurk, C., Königstedt, R., Parchatka, U., Mühle, J., Rhee, T., Brenninkmeijer, C., Bonasoni, P., et al.: Ozone production and trace gas correlations during the June 2000 MINATROC intensive measurement campaign at Mt. Cimone, *Atmospheric Chemistry and Physics*, 3, 725–738, <https://doi.org/10.5194/acp-3-725-2003>, 2003.

<https://doi.org/10.5194/egusphere-2023-816>

Preprint. Discussion started: 4 May 2023

© Author(s) 2023. CC BY 4.0 License.



- Fujita, E. M., Stockwell, W. R., Campbell, D. E., Keislar, R. E., and Lawson, D. R.: Evolution of the magnitude and spatial extent of the weekend ozone effect in California's South Coast Air Basin, 1981–2000, *Journal of the Air & Waste Management Association*, 53, 802–815, <https://doi.org/10.1080/10473289.2003.10466225>, 2003.
- Gough, W. A. and Anderson, V.: Changing Air Quality and the Ozone Weekend Effect during the COVID-19 Pandemic in Toronto, Ontario, Canada, *Climate*, 10, 41, <https://doi.org/10.3390/cli10030041>, 2022.
- Granier, C., Darras, S., Denier van der Gon, H., Doubalova, J., Elguindi, N., Galle, B., Gauss, M., Guevara, M., Jalkanen, J.-P., Kuenen, J., Lioussé, C., Quack, B., Simpson, D., and Sindelarova, K.: The Copernicus Atmosphere Monitoring Service global and regional emissions (April 2019 version), Copernicus Atmosphere Monitoring Service (CAMS) report, <https://doi.org/10.24380/d0bn-kx16>, 2019.
- Hao, Y., Zhou, J., Zhou, J., Wang, Y., Yang, S., Huangfu, Y., Li, X., Zhang, C., Liu, A., Wu, Y., Yang, S., Peng, Y., Qi, J., He, X., Song, X., Chen, Y., Yuan, B., and Shao, M.: Measuring and modelling investigation of the Net Photochemical Ozone Production Rate via an improved dual-channel reaction chamber technique, *Atmospheric Chemistry and Physics Discussions*, pp. 1–32, 2023.
- Henderson, B., Pinder, R., Crooks, J., Cohen, R., Carlton, A., Pye, H., and Vizuete, W.: Combining Bayesian methods and aircraft observations to constrain the HO₂+ NO₂ reaction rate, *Atmospheric Chemistry and Physics*, 12, 653–667, <https://doi.org/10.5194/acp-12-653-2012>, 2012.
- Hersbach, H., Bell, B., Berrisford, P., Hirahara, S., Horányi, A., Muñoz-Sabater, J., Nicolas, J., Peubey, C., Radu, R., Schepers, D., et al.: The ERA5 global reanalysis, *Quarterly Journal of the Royal Meteorological Society*, 146, 1999–2049, 2020.
- Iglesias-Suarez, F., Kinnison, D. E., Rap, A., Maycock, A. C., Wild, O., and Young, P. J.: Key drivers of ozone change and its radiative forcing over the 21st century, *Atmospheric Chemistry and Physics*, 18, 6121–6139, <https://doi.org/10.5194/acp-18-6121-2018>, 2018.
- Jaeglé, L., Jacob, D. J., Brune, W., Tan, D., Faloona, I., Weinheimer, A., Ridley, B., Campos, T., and Sachse, G.: Sources of HO_x and production of ozone in the upper troposphere over the United States, *Geophysical Research Letters*, 25, 1709–1712, <https://doi.org/10.1029/98GL00041>, 1998.
- Jaeglé, L., Jacob, D. J., Brune, W., Faloona, I., Tan, D., Kondo, Y., Sachse, G., Anderson, B., Gregory, G., Vay, S., Singh, H., Blake, D., and Shet, R.: Ozone production in the upper troposphere and the influence of aircraft during SONEX: Approach of NO_x-saturated conditions, *Geophysical Research Letters*, 26, 3081–3084, <https://doi.org/10.1029/1999GL900451>, 1999.
- Jeuken, A., Siegmund, P., Heijboer, L., Feichter, J., and Bengtsson, L.: On the potential of assimilating meteorological analyses in a global climate model for the purpose of model validation, *Journal of Geophysical Research: Atmospheres*, 101, 16 939–16 950, 1996.
- Jin, X., Fiore, A., Boersma, K. F., Smedt, I. D., and Valin, L.: Inferring Changes in Summertime Surface Ozone–NO_x–VOC Chemistry over US Urban Areas from Two Decades of Satellite and Ground-Based Observations, *Environmental science & technology*, 54, 6518–6529, <https://doi.org/10.1021/acs.est.9b07785>, 2020.
- Jöckel, P., Tost, H., Pozzer, A., Kunze, M., Kirner, O., Brenninkmeijer, C. A., Brinkop, S., Cai, D. S., Dyroff, C., Eckstein, J., Frank, F., Garmy, H., Gottschaldt, K.-D., Graf, P., Grewe, V., Kerkweg, A., Kern, B., Matthes, S., Mertens, M., Meul, S., Neumaier, M., Nützel, M., Oberländer-Hayn, S., Ruhnke, R., Runde, T., Sander, R., Scharffe, D., and Zahn, A.: Earth system chemistry integrated modelling (ESCiMo) with the modular earth submodel system (MESSy) version 2.51, *Geoscientific Model Development*, 9, 1153–1200, <https://doi.org/10.5194/gmd-9-1153-2016>, 2016.
- Khodayari, A., Vitt, F., Phoenix, D., and Wuebbles, D. J.: The impact of NO_x emissions from lightning on the production of aviation-induced ozone, *Atmospheric Environment*, 187, 410–416, <https://doi.org/10.1016/j.atmosenv.2018.05.057>, 2018.
- Lacis, A. A., Wuebbles, D. J., and Logan, J. A.: Radiative forcing of climate by changes in the vertical distribution of ozone, *Journal of Geophysical Research: Atmospheres*, 95, 9971–9981, <https://doi.org/10.1029/JD095iD07p09971>, 1990.

<https://doi.org/10.5194/egusphere-2023-816>

Preprint. Discussion started: 4 May 2023

© Author(s) 2023. CC BY 4.0 License.



- Leighton, P.: Photochemistry of air pollution, Academic Press, Inc., New York, 1961.
- Lelieveld, J. and Dentener, F. J.: What controls tropospheric ozone?, *Journal of Geophysical Research: Atmospheres*, 105, 3531–3551, <https://doi.org/10.1029/1999JD901011>, 2000.
- Lelieveld, J. and van Dorland, R.: Ozone chemistry changes in the troposphere and consequent radiative forcing of climate, in: *Atmospheric Ozone as a Climate Gas: General Circulation Model Simulations*, pp. 227–258, Springer, https://doi.org/10.1007/978-3-642-79869-6_16, 1995.
- Lelieveld, J., Bourtsoukidis, E., Brühl, C., Fischer, H., Fuchs, H., Harder, H., Hofzumahaus, A., Holland, F., Marno, D., Neumaier, M., et al.: The South Asian monsoon—pollution pump and purifier, *Science*, 361, 270–273, 2018.
- Liang, Q., Rodriguez, J., Douglass, A., Crawford, J., Olson, J., Apel, E., Bian, H., Blake, D., Brune, W., Chin, M., Colarco, P. R., da Silva, A., Diskin, G. S., Duncan, B. N., G. Huey, L., Knapp, D. J., Montzka, D. D., Nielsen, J. E., Pawson, S., Riemer, D. D., Weinheimer, A. J., and Wisthaler, A.: Reactive nitrogen, ozone and ozone production in the Arctic troposphere and the impact of stratosphere-troposphere exchange, *Atmospheric Chemistry and Physics*, 11, 13 181–13 199, <https://doi.org/10.5194/acp-11-13181-2011>, 2011.
- Lin, X., Trainer, M., and Liu, S.: On the nonlinearity of the tropospheric ozone production, *Journal of Geophysical Research: Atmospheres*, 93, 15 879–15 888, <https://doi.org/10.1029/JD093iD12p15879>, 1988.
- Liu, S., Trainer, M., Fehsenfeld, F., Parrish, D., Williams, E., Fahey, D. W., Hübler, G., and Murphy, P. C.: Ozone production in the rural troposphere and the implications for regional and global ozone distributions, *Journal of Geophysical Research: Atmospheres*, 92, 4191–4207, <https://doi.org/10.1029/JD092iD04p04191>, 1987.
- Liu, Y., Wang, T., Stavrakou, T., Elguindi, N., Doumbia, T., Granier, C., Bouarar, I., Gaubert, B., and Brasseur, G. P.: Diverse response of surface ozone to COVID-19 lockdown in China, *Science of the Total Environment*, 789, 147 739, <https://doi.org/10.1016/j.scitotenv.2021.147739>, 2021.
- McDonald, B. C., De Gouw, J. A., Gilman, J. B., Jathar, S. H., Akherati, A., Cappa, C. D., Jimenez, J. L., Lee-Taylor, J., Hayes, P. L., McKeen, S. A., et al.: Volatile chemical products emerging as largest petrochemical source of urban organic emissions, *Science*, 359, 760–764, <https://doi.org/10.1126/science.aag0524>, 2018.
- Milford, J. B., Gao, D., Sillman, S., Blossey, P., and Russell, A. G.: Total reactive nitrogen (NO_y) as an indicator of the sensitivity of ozone to reductions in hydrocarbon and NO_x emissions, *Journal of Geophysical Research: Atmospheres*, 99, 3533–3542, <https://doi.org/10.1029/93JD03224>, 1994.
- Mills, G., Pleijel, H., Malley, C. S., Sinha, B., Cooper, O. R., Schultz, M. G., Neufeld, H. S., Simpson, D., Sharps, K., Feng, Z., Gerosa, G., Harmens, H., Kobayashi, K., Saxena, P., Paoletti, E., Sinha, V., and Xu, X.: Tropospheric Ozone Assessment Report: Present-day tropospheric ozone distribution and trends relevant to vegetation, *Elementa: Science of the Anthropocene*, 6, <https://doi.org/10.1525/elementa.302>, 2018.
- Miyazaki, K., Eskes, H., Sudo, K., and Zhang, C.: Global lightning NO_x production estimated by an assimilation of multiple satellite data sets, *Atmospheric Chemistry and Physics*, 14, 3277–3305, 2014.
- Mohnen, V., Goldstein, W., and Wang, W.-C.: Tropospheric ozone and climate change, *Air & Waste*, 43, 1332–1334, <https://doi.org/10.1080/1073161X.1993.10467207>, 1993.
- Mollner, A. K., Valluvadasan, S., Feng, L., Sprague, M. K., Okumura, M., Milligan, D. B., Bloss, W. J., Sander, S. P., Martien, P. T., Harley, R. A., McCoy, A. B., and Carter, W. P. L.: Rate of gas phase association of hydroxyl radical and nitrogen dioxide, *Science*, 330, 646–649, <https://doi.org/10.1126/science.1193030>, 2010.

<https://doi.org/10.5194/egusphere-2023-816>

Preprint. Discussion started: 4 May 2023

© Author(s) 2023. CC BY 4.0 License.



- National Research Council: Rethinking the ozone problem in urban and regional air pollution, National Academies Press, <https://doi.org/10.17226/1889>, 1992.
- 570 Nault, B. A., Garland, C., Wooldridge, P. J., Brune, W. H., Campuzano-Jost, P., Crounse, J. D., Day, D. A., Dibb, J., Hall, S. R., Huey, L. G., Jimenez, J. L., Liu, X., Mao, J., Mikoviny, T., Peischl, J., Pollack, I. B., Ren, X., Ryerson, T. B., Scheuer, E., Ullmann, K., Wennberg, P. O., Wisthaler, A., Zhang, L., and Cohen, R. C.: Observational Constraints on the Oxidation of NO_x in the Upper Troposphere, *The Journal of Physical Chemistry A*, 120, 1468–1478, <https://doi.org/10.1021/acs.jpca.5b07824>, 2016.
- Nussbaumer, C. M. and Cohen, R. C.: The Role of Temperature and NO_x in Ozone Trends in the Los Angeles Basin, *Environmental Science & Technology*, 54, 15 652–15 659, <https://doi.org/10.1021/acs.est.0c04910>, 2020.
- 575 Nussbaumer, C. M., Crowley, J. N., Schuladen, J., Williams, J., Hafermann, S., Reiffs, A., Axinte, R., Harder, H., Ernest, C., Novelli, A., Sala, K., Martinez, M., Mallik, C., Tomsche, L., Plass-Dülmer, C., Bohn, B., Lelieveld, J., and Fischer, H.: Measurement report: Photochemical production and loss rates of formaldehyde and ozone across Europe, *Atmospheric Chemistry and Physics Discussions*, pp. 1–29, <https://doi.org/10.5194/acp-2021-694>, 2021a.
- 580 Nussbaumer, C. M., Tadic, I., Dienhart, D., Wang, N., Edtbauer, A., Ernle, L., Williams, J., Obersteiner, F., Gutiérrez-Álvarez, I., Harder, H., Lelieveld, J., and Fischer, H.: Measurement report: In situ observations of deep convection without lightning during the tropical cyclone Florence 2018, *Atmospheric Chemistry and Physics*, 21, 7933–7945, 2021b.
- Nussbaumer, C. M., Pozzer, A., Tadic, I., Röder, L., Obersteiner, F., Harder, H., Lelieveld, J., and Fischer, H.: Tropospheric ozone production and chemical regime analysis during the COVID-19 lockdown over Europe, *Atmospheric Chemistry and Physics*, 22, 6151–6165, <https://doi.org/10.5194/acp-22-6151-2022>, 2022.
- 585 Nuvolone, D., Petri, D., and Voller, F.: The effects of ozone on human health, *Environmental Science and Pollution Research*, 25, 8074–8088, <https://doi.org/10.1007/s11356-017-9239-3>, 2018.
- Peralta, O., Ortíz-Alvarez, A., Torres-Jardón, R., Suárez-Lastra, M., Castro, T., and Ruíz-Suárez, L. G.: Ozone over Mexico City during the COVID-19 pandemic, *Science of The Total Environment*, 761, 143 183, <https://doi.org/10.1016/j.scitotenv.2020.143183>, 2021.
- 590 Pickering, K. E., Thompson, A. M., Dickerson, R. R., Luke, W. T., McNamara, D. P., Greenberg, J. P., and Zimmerman, P. R.: Model calculations of tropospheric ozone production potential following observed convective events, *Journal of Geophysical Research: Atmospheres*, 95, 14 049–14 062, <https://doi.org/10.1029/JD095iD09p14049>, 1990.
- Pusede, S. and Cohen, R.: On the observed response of ozone to NO_x and VOC reactivity reductions in San Joaquin Valley California 1995–present, *Atmospheric Chemistry and Physics*, 12, 8323–8339, <https://doi.org/10.5194/acp-12-8323-2012>, 2012.
- 595 Pusede, S. E., Steiner, A. L., and Cohen, R. C.: Temperature and recent trends in the chemistry of continental surface ozone, *Chemical reviews*, 115, 3898–3918, <https://doi.org/10.1021/cr5006815>, 2015.
- Reifenberg, S. F., Martin, A., Kohl, M., Bacer, S., Hamryszczak, Z., Tadic, I., Röder, L., Crowley, D. J., Fischer, H., Kaiser, K., et al.: Numerical simulation of the impact of COVID-19 lockdown on tropospheric composition and aerosol radiative forcing in Europe, *Atmospheric Chemistry and Physics*, 22, 10 901–10 917, 2022.
- 600 Rowland, S. F.: Stratospheric ozone depletion, *Annual Review of Physical Chemistry*, 42, 731–768, <https://doi.org/10.1146/annurev.pc.42.100191.003503>, 1991.
- Rudlosky, S. D. and Virts, K. S.: Dual geostationary lightning mapper observations, *Monthly Weather Review*, 149, 979–998, 2021.
- Sakamoto, Y., Sadanaga, Y., Li, J., Matsuoka, K., Takemura, M., Fujii, T., Nakagawa, M., Kohno, N., Nakashima, Y., Sato, K., Nakayama, T., Kato, S., Takami, A., Yoshino, A., Murano, K., and Kajii, Y.: Relative and absolute sensitivity analysis on ozone production in Tsukuba, a city in Japan, *Environmental Science & Technology*, 53, 13 629–13 635, <https://doi.org/10.1021/acs.est.9b03542>, 2019.
- 605

<https://doi.org/10.5194/egusphere-2023-816>

Preprint. Discussion started: 4 May 2023

© Author(s) 2023. CC BY 4.0 License.



- Seinfeld, J. H.: Air pollution: A half century of progress, *AIChE Journal*, 50, 1096–1108, <https://doi.org/10.1002/aic.10102>, 2004.
- Seinfeld, J. H. and Pandis, S. N.: *Atmospheric chemistry and physics: from air pollution to climate change*, John Wiley & Sons, 1998.
- Shah, V., Jacob, D. J., Dang, R., Lamsal, L. N., Strode, S. A., Steenrod, S. D., Boersma, K. F., Eastham, S. D., Fritz, T. M., Thompson, C., Peischl, J., Bourgeois, I., Pollack, I. B., Nault, B. A., Cohen, R. C., Campuzano-Jost, P., Jimenez, J. L., Andersen, S. T., Carpenter, L. J., Sherwen, T., and Evans, M. J.: Nitrogen oxides in the free troposphere: implications for tropospheric oxidants and the interpretation of satellite NO₂ measurements, *Atmospheric Chemistry and Physics*, 23, 1227–1257, <https://doi.org/10.5194/acp-23-1227-2023>, 2023.
- Sicard, P., Paoletti, E., Agathokleous, E., Araminiené, V., Proietti, C., Coulibaly, F., and De Marco, A.: Ozone weekend effect in cities: Deep insights for urban air pollution control, *Environmental Research*, 191, 110 193, <https://doi.org/10.1016/j.envres.2020.110193>, 2020.
- Sillman, S.: The use of NO_y, H₂O₂, and HNO₃ as indicators for ozone-NO_x-hydrocarbon sensitivity in urban locations, *Journal of Geophysical Research: Atmospheres*, 100, 14 175–14 188, <https://doi.org/10.1029/94JD02953>, 1995.
- Sillman, S.: The relation between ozone, NO_x and hydrocarbons in urban and polluted rural environments, *Atmospheric Environment*, 33, 1821–1845, [https://doi.org/10.1016/S1352-2310\(98\)00345-8](https://doi.org/10.1016/S1352-2310(98)00345-8), 1999.
- Sillman, S., Logan, J. A., and Wofsy, S. C.: The sensitivity of ozone to nitrogen oxides and hydrocarbons in regional ozone episodes, *Journal of Geophysical Research: Atmospheres*, 95, 1837–1851, <https://doi.org/10.1029/JD095iD02p01837>, 1990.
- Staehelin, J., Harris, N. R., Appenzeller, C., and Eberhard, J.: Ozone trends: A review, *Reviews of Geophysics*, 39, 231–290, <https://doi.org/10.1029/1999RG000059>, 2001.
- Tadic, I., Nussbaumer, C. M., Bohn, B., Harder, H., Marno, D., Martinez, M., Obersteiner, F., Parchatka, U., Pozzer, A., Rohloff, R., et al.: Central role of nitric oxide in ozone production in the upper tropical troposphere over the Atlantic Ocean and western Africa, *Atmospheric Chemistry and Physics*, 21, 8195–8211, 2021.
- Tonnesen, G. S. and Dennis, R. L.: Analysis of radical propagation efficiency to assess ozone sensitivity to hydrocarbons and NO_x: 1. Local indicators of instantaneous odd oxygen production sensitivity, *Journal of Geophysical Research: Atmospheres*, 105, 9213–9225, <https://doi.org/10.1029/1999JD900371>, 2000a.
- Tonnesen, G. S. and Dennis, R. L.: Analysis of radical propagation efficiency to assess ozone sensitivity to hydrocarbons and NO_x: 2. Long-lived species as indicators of ozone concentration sensitivity, *Journal of Geophysical Research: Atmospheres*, 105, 9227–9241, <https://doi.org/10.1029/1999JD900372>, 2000b.
- Trainer, M., Parrish, D., Buhr, M., Norton, R., Fehsenfeld, F., Anlauf, K., Bottenheim, J., Tang, Y., Wiebe, H., Roberts, J., et al.: Correlation of ozone with NO_y in photochemically aged air, *Journal of Geophysical Research: Atmospheres*, 98, 2917–2925, <https://doi.org/10.1029/92JD01910>, 1993.
- van Dorland, R., Dentener, F. J., and Lelieveld, J.: Radiative forcing due to tropospheric ozone and sulfate aerosols, *Journal of Geophysical Research: Atmospheres*, 102, 28 079–28 100, <https://doi.org/10.1029/97JD02499>, 1997.
- Vermeuel, M. P., Novak, G. A., Alwe, H. D., Hughes, D. D., Kaleel, R., Dickens, A. F., Kenski, D., Czarnetzki, A. C., Stone, E. A., Stanier, C. O., et al.: Sensitivity of ozone production to NO_x and VOC along the Lake Michigan coastline, *Journal of Geophysical Research: Atmospheres*, 124, 10 989–11 006, <https://doi.org/10.1029/2019JD030842>, 2019.
- Wang, J., Ge, B., and Wang, Z.: Ozone production efficiency in highly polluted environments, *Current Pollution Reports*, 4, 198–207, <https://doi.org/10.1007/s40726-018-0093-9>, 2018a.
- Wang, P., Chen, Y., Hu, J., Zhang, H., and Ying, Q.: Attribution of tropospheric ozone to NO_x and VOC emissions: considering ozone formation in the transition regime, *Environmental science & technology*, 53, 1404–1412, <https://doi.org/10.1021/acs.est.8b05981>, 2018b.

<https://doi.org/10.5194/egusphere-2023-816>

Preprint. Discussion started: 4 May 2023

© Author(s) 2023. CC BY 4.0 License.



- Wang, P., Zhu, S., Vrekoussis, M., Brasseur, G. P., Wang, S., and Zhang, H.: Is atmospheric oxidation capacity better in indicating tropospheric O₃ formation?, *Frontiers of Environmental Science & Engineering*, 16, 1–7, <https://doi.org/10.1007/s11783-022-1544-5>, 2022.
- 645 Wennberg, P., Hanisco, T., Jaegle, L., Jacob, D., Hints, E., Lanzendorf, E., Anderson, J., Gao, R.-S., Keim, E., Donnelly, S., NEGRO, L. A. D., FAHEY, D. W., MCKEEN, S. A., SALAWITCH, R. J., WEBSTER, C. R., MAY, R. D., HERMAN, R. L., PROFFITT, M. H., MARGITAN, J. J., ATLAS, E. L., SCHAUFFLER, S. M., FLOCKE, F., MCELROY, C. T., , and BUI, T. P.: Hydrogen radicals, nitrogen radicals, and the production of O₃ in the upper troposphere, *science*, 279, 49–53, <https://doi.org/10.1126/science.279.5347.49>, 1998.
- Williams, E. and Satori, G.: Lightning, thermodynamic and hydrological comparison of the two tropical continental chimneys, *Journal of Atmospheric and Solar-Terrestrial Physics*, 66, 1213–1231, <https://doi.org/10.1016/j.jastp.2004.05.015>, 2004.
- 650 Wuebbles, D. J.: Weighing functions for ozone depletion and greenhouse gas effects on climate, *Annual review of energy and the environment*, 20, 45–70, <https://doi.org/10.1146/annurev.eg.20.110195.000401>, 1995.
- Xue, J., Zhao, T., Luo, Y., Miao, C., Su, P., Liu, F., Zhang, G., Qin, S., Song, Y., Bu, N., et al.: Identification of ozone sensitivity for NO₂ and secondary HCHO based on MAX-DOAS measurements in northeast China, *Environment International*, 160, 107 048, <https://doi.org/10.1016/j.envint.2021.107048>, 2022.
- 655 Yan, Y. Y.: Intertropical Convergence Zone (ITCZ), pp. 429–432, Springer Netherlands, Dordrecht, https://doi.org/10.1007/1-4020-3266-8_110, https://doi.org/10.1007/1-4020-3266-8_110, 2005.
- Young, P., Archibald, A., Bowman, K., Lamarque, J.-F., Naik, V., Stevenson, D., Tilmes, S., Voulgarakis, A., Wild, O., Bergmann, D., et al.: Pre-industrial to end 21st century projections of tropospheric ozone from the Atmospheric Chemistry and Climate Model Intercomparison Project (ACCMIP), *Atmospheric Chemistry and Physics*, 13, 2063–2090, 2013.
- 660

3.7 Airborne NO_x flux measurements over Los Angeles

This chapter has been submitted to the journal *Atmospheric Chemistry & Physics* as a measurement report and is currently under review at *EGUsphere*. I am the first author of this paper. I have analyzed all data presented, I have made the figures and I have prepared the manuscript. The co-authors were involved in the presented research campaign RECAP-CA (California 2021) and in proofreading the manuscript. Detailed author contributions can be found at the end of the paper in the section *Author contributions*.

How to cite: Nussbaumer, C. M., Place, B. K., Zhu, Q., Pfannerstill, E. Y., Wooldridge, P., Schulze, B. C., Arata, C., Ward, R., Bucholtz, A., Seinfeld, J. H., Goldstein, A. H., and Cohen, R. C.: Measurement report: Airborne measurements of NO_x fluxes over Los Angeles during the RECAP-CA 2021 campaign, *EGUsphere* [preprint], <https://doi.org/10.5194/egusphere-2023-601>, **2023**.

submitted: 29 Mar 2023

The supplementary material for this publication can be found in Section 4.6.

<https://doi.org/10.5194/egusphere-2023-601>

Preprint. Discussion started: 12 April 2023

© Author(s) 2023. CC BY 4.0 License.



Measurement report: Airborne measurements of NO_x fluxes over Los Angeles during the RECAP-CA 2021 campaign

Clara M. Nussbaumer^{1,2}, Bryan K. Place², Qindan Zhu³, Eva Y. Pfannerstill⁴, Paul Wooldridge², Benjamin C. Schulze⁵, Caleb Arata⁴, Ryan Ward⁵, Anthony Bucholtz⁶, John H. Seinfeld⁵, Allen H. Goldstein^{4,7}, and Ronald C. Cohen^{2,3}

¹Department of Atmospheric Chemistry, Max Planck Institute for Chemistry, 55128 Mainz, Germany

²Department of Chemistry, University of California, Berkeley, Berkeley, CA 94720, USA

³Department of Earth and Planetary Science, University of California, Berkeley, Berkeley, CA 94720, USA

⁴Department of Environmental Science, Policy, and Management, University of California, Berkeley, Berkeley, CA 94720, USA

⁵Department of Environmental Science and Engineering, California Institute of Technology, Pasadena, CA 91125, USA

⁶Department of Meteorology, Naval Postgraduate School, Monterey, CA 93943, USA

⁷Department of Civil and Environmental Engineering, University of California, Berkeley, Berkeley, CA 94720, USA

Correspondence: Clara M. Nussbaumer (clara.nussbaumer@mpic.de) and Ron C. Cohen (rccohen@berkeley.edu)

Abstract.

Nitrogen oxides ($\text{NO}_x \equiv \text{NO} + \text{NO}_2$) are involved in most atmospheric photochemistry, including the formation of tropospheric ozone (O_3). While various methods exist to accurately measure NO_x concentrations, it is still a challenge to quantify the source and flux of NO_x emissions. We present airborne measurements of NO_x and winds used to infer the emission of NO_x across Los Angeles. The measurements were obtained during the research aircraft campaign RECAP-CA (Re-Evaluating the Chemistry of Air Pollutants in California) in June 2021. Geographic allocations of the fluxes are compared to the NO_x emission inventory from the California Air Resources Board (CARB). We find that the NO_x fluxes have a pronounced weekend effect and are highest in the Eastern part of the San Bernardino valley. The comparison of the RECAP-CA and the modeled CARB NO_x fluxes suggest the modeled emissions are too high near the coast and in downtown Los Angeles and too low further inland in the Eastern part of the San Bernardino valley.

1 Introduction

Nitrogen oxides (NO_x), representing the sum of nitric oxide (NO) and nitrogen dioxide (NO_2) are hazardous pollutants and precursor to tropospheric ozone, which is known to have adverse health effects on humans and plants (Boningari and Smirniotis, 2016; Mills et al., 2018; Nuvolone et al., 2018; CARB, 2022b). NO_x is emitted from some natural sources including soil, microbial activity and lightning, but mostly from anthropogenic combustion sources, such as electricity generation facilities and motor vehicles, with the latter dominating in urban environments (Delmas et al., 1997; Pusede et al., 2015). Densely populated cities, such as the megacity Los Angeles, often suffer from poor air quality leading to increases in respiratory diseases and premature mortality (Stewart et al., 2017). Air quality monitoring, public policy and new emission control technologies have

<https://doi.org/10.5194/egusphere-2023-601>

Preprint. Discussion started: 12 April 2023

© Author(s) 2023. CC BY 4.0 License.



been developed and implemented to assess, guide and manage emissions, leading to healthier air in cities (CARB, 2022b).
 20 Significant reductions in NO_x and other primary pollutants have occurred in the U.S. and specifically in Los Angeles over
 the past decades (e.g. Qian et al. (2019); Nussbaumer and Cohen (2020); EPA (2022a)). However, ozone exceedances of the
 national ambient air quality standard (NAAQS) of 0.070 ppm (8-hr maximum) are still frequent in Los Angeles which the
 American Lung Association (2022) found to have the highest ozone pollution in all of the United States (South Coast Air
 Quality Management District, 2017; EPA, 2022c). In the summer months June - September of 2021, O_3 exceeded the NAAQS
 25 on more than half the days. Exceedances were even more frequent in 2020, demonstrating that further precursor reductions are
 imperative (EPA, 2022b).

The combination of emission inventories with models provide insight into the emission reductions needed to achieve healthy
 air and synthesize our understanding of atmospheric dynamics, that describe the flow of emissions from their source through
 the atmosphere, the deposition of chemicals to the earth's surface and the oxidation of molecules. Comparison of predicted con-
 30 centrations of chemicals with this type of combined modeling system provides a guide for the needed reductions in emissions
 to protect public health. Errors and biases in any part of this system can lead to incorrect estimates of the amount of reduction
 needed to achieve a particular goal. Fujita et al. (2013) pointed towards the problem of biased emission inventories regarding
 future predictions of ozone, naming underestimations in early VOC (volatile organic compound) SoCAB (South Coast Air
 Basin) emission inventories and hence modeled VOC/ NO_x that did not match the atmosphere as a key bias in understanding
 35 ozone chemistry.

Direct observational mapping of emissions would allow a more straightforward evaluation of the accuracy of emission in-
 ventories without requiring untangling potential errors in emissions from those of transport or chemistry. Until recently, such
 measurements have been rare because of the difficulty of obtaining and interpreting measurements of emissions in heteroge-
 neous urban environments and especially the difficulty of mapping emissions over the spatial scales needed to assess the full
 40 complement of urban processes. Recently, several experiments have overcome these challenges, measuring NO_x and VOC
 fluxes using aircraft platforms.

Airborne studies on VOC fluxes include Karl et al. (2013) and Misztal et al. (2014) who present fluxes of biogenic VOCs
 based on research flights during the CABERNET (California Airborne BVOC Emission Research in Natural Ecosystem Tran-
 sects) campaign over Californian oak forests in June 2011. Yuan et al. (2015) determined CH_4 and VOC emissions from two
 45 shale gas production plants in the Southern United States based on aircraft measurements in summer 2013. Yu et al. (2017)
 derived isoprene and monoterpene fluxes during the airborne Southeast Atmosphere Study above the U.S. in 2013. Other stud-
 ies presenting VOC fluxes based on aircraft measurements include Karl et al. (2009), Conley et al. (2009), Kaser et al. (2015),
 Wolfe et al. (2015), Gu et al. (2017) and Yu et al. (2017).

Nitrogen oxides fluxes based on airborne measurements are even less common than VOCs. Wolfe et al. (2015) reported NO_x
 50 fluxes based on a measurement flight during the NASA SEAC⁴RS campaign in 2013. Vaughan et al. (2016) and Vaughan et al.
 (2021) reported NO_x fluxes based on this method over the Greater London region during the OPFUE (Ozone Precursors Fluxes
 in an Urban Environment) campaign in July 2014. They compared emission predictions from the National Atmospheric Emis-
 sions Inventory with the calculated NO_x fluxes via wavelet transformation, which they found to be higher than the inventory

<https://doi.org/10.5194/egusphere-2023-601>

Preprint. Discussion started: 12 April 2023

© Author(s) 2023. CC BY 4.0 License.



by up to a factor of 2, underlining the importance of emission inventory validation. Zhu et al. (2023) recently reported NO_x fluxes over the San Joaquin Valley of California based on the RECAP-CA (Re-Evaluating the Chemistry of Air Pollutants in California) aircraft campaign where NO_x from soils was identified key contributor to the overall emission.

In this paper, we present NO_x flux calculations via wavelet transformation from aircraft measurements of NO_x concentrations and the vertical wind speed during the RECAP-CA aircraft campaign over Los Angeles in June 2021. We provide footprint calculations for investigating the origin of the sampled air masses and compare our results to the emission inventory of the California Air Resources Board (CARB).

2 Observations and methods

2.1 RECAP-CA aircraft campaign

The RECAP-CA (Re-Evaluating the Chemistry of Air Pollutants in California) aircraft campaign took place in June 2021 over Los Angeles and the Central Valley of California with the campaign base in Burbank, California (34.20°N , 118.36°W) using the CIRPAS (Center for Interdisciplinary Remotely Piloted Aircraft Studies) Twin Otter aircraft. Details on the research aircraft (Figure S1) can be found in Reid et al. (2001) and Hegg et al. (2005). The ambient air was sampled with an inlet approx. 1 m above the aircraft nose at a sampling speed of around 60 m s^{-1} . The aircraft carried instruments for measurements of meteorological data, nitrogen oxides, volatile organic compounds and greenhouse gases. All flights were carried out between 11:00 and 18:00 local time (LT).

We focus on the measurements over Los Angeles which took place on three weekends (June 6, 12 and 19) and six weekdays (June 1, 4, 10, 11, 18 and 21) in 2021. The flight paths are shown in Figure 1a. All flights were carried out at an altitude of roughly 300–400 m above ground level, covering the coastal region of Los Angeles, parts of Santa Ana county, Los Angeles Downtown and the San Bernardino valley. Flight days were chosen to explore as wide a range of temperature as possible. In addition, about half the flights started with the East-West legs and the other half the coastal North-South legs to gain additional variation in temperature. For further analysis, we separated the covered area in four different segments, as shown in Figure 1b.

2.2 Meteorological measurements

The meteorological instruments on-board the CIRPAS Twin Otter research aircraft were previously described in Karl et al. (2013). Temperature was obtained by a Rosemount Sensor (Emerson Electric Co., St. Louis, Missouri, USA). Dew point temperature was measured by a DewMaster Chilled Mirror Hygrometer (Edgetech Instruments Inc., Hudson, Massachusetts, USA). Differential and barometric pressure sensors (Setra Systems Inc., Boxborough, Massachusetts, USA) were used to determine the pressure. GPS latitude, longitude, altitude, ground speed and track, as well as pitch, heading and roll angle were measured by a C-MIGITS (Miniature Integrated GPS (Global Positioning System)/INS (Inertial Navigation System) Tactical System) III (Systron Donner Inertial Division, Concord, California, USA). A radome flow angle probe provided the true air speed and the 3D wind.

<https://doi.org/10.5194/egusphere-2023-601>

Preprint. Discussion started: 12 April 2023

© Author(s) 2023. CC BY 4.0 License.

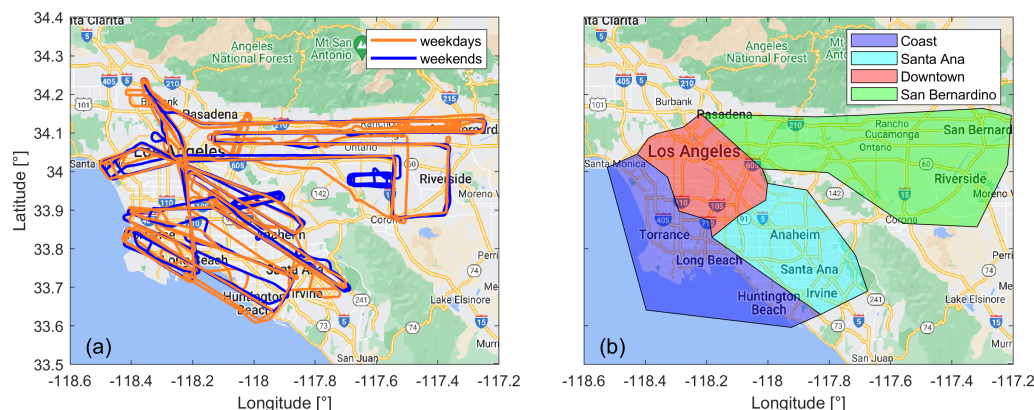


Figure 1. (a) Overview of the flight paths during the RECAP-CA campaign over Los Angeles in June 2021. Blue colors show weekend flights and orange colors show weekday flights. (b) Geographic separation of the covered area in four segments, including the coast (blue), parts of Santa Ana county (light blue), Downtown Los Angeles (red) and the San Bernardino valley (green). © Google Maps 2023.

85 2.3 NO_x measurements

NO_x measurements were carried out using a custom-built three-channel thermal dissociation laser-induced fluorescence (TD-LIF) instrument with a detection limit of ~ 15 pptv (10 s) and a precision (2σ) of $< 7\%$ (Thornton et al., 2000). The instrument is described in detail in Thornton et al. (2000), Day et al. (2002) and Sparks et al. (2019). Briefly, NO₂ is excited in the first channel with a 532 nm Nd³⁺:YVO₄ laser (Explorer One XP, Spectra Physics). The fluorescence resulting from NO₂* de-excitation is detected by a photomultiplier tube as a signal which is approximately proportional to the ambient NO₂ mixing ratio. The proportionality arises because the fluorescence signal and the quenching of the fluorescence both scale with pressure. Calibration with an NO₂ gas standard (5.5 ppm; Praxair) was performed once an hour. The instrument background was determined every 20 minutes using scrubbed ambient air. NO is determined in the second channel through conversion to NO₂ by adding excess ozone (O₃). NO_y species were detected through thermal dissociation at $\sim 500^\circ\text{C}$ to NO₂ in the third channel (Day et al., 2002). Ambient air was sampled at a flow rate of 6 l/min, equally divided into the three instrument channels.

2.4 NO_x flux calculations

The emission of a trace gas is characterized as a flux which is a mass emitted per area and time, e.g. $\text{mg m}^{-2} \text{h}^{-1}$. A flux F can be described as the covariance of the fluctuation in the vertical wind speed ω' and the fluctuation in the concentration of the trace gas of interest c' , as shown in Eq. (1).

$$100 \quad F = \overline{\omega'c'} \quad (1)$$

<https://doi.org/10.5194/egusphere-2023-601>
 Preprint. Discussion started: 12 April 2023
 © Author(s) 2023. CC BY 4.0 License.



Analyses of the covariance of winds and concentrations from tower-based or aircraft-based observations enable the determination of fluxes. With the eddy covariance method, the flux is directly calculated from the measurements as the mean of the product of the deviation of the vertical windspeed from the mean of the vertical wind speed and the deviation of the concentration analogously, as shown in Eq. (2) (e.g. Schaller et al. (2017); Desjardins et al. (2021)).

$$\overline{\omega'c'} = \frac{1}{N} \sum_{x=1}^N (\omega_x - \bar{\omega})(c_x - \bar{c}) \quad (2)$$

Requirements for accurate fluxes with EC are steady state conditions and homogeneous horizontal air masses. Typically an averaging time of at least 30 minutes is used to ensure the full spectrum of eddies are sampled (Schaller et al., 2017; Desjardins et al., 2021). The 30 minutes long averaging time is easily implementable for stationary tower installments. For aircraft observations, the high aircraft velocity and the associated rapid geographical change are inconsistent with the steady state requirement. An alternative is the flux calculation via wavelet transformation. This approach does not require the assumption of stationary conditions as it enables the determination of a flux localized both in time and frequency (Karl et al., 2013; Schaller et al., 2017). A discrete time series such as the vertical wind speed or the concentration of an atmospheric trace gas is convolved with a wavelet function $\psi_{a,b}(t)$ yielding the wavelet coefficient $W(a,b)$ according to Eq. (3) (Torrence and Compo, 1998; Thomas and Foken, 2005; Schaller et al., 2017; Desjardins et al., 2021).

$$W(a,b) = \int_{-\infty}^{\infty} x(t) \psi_{a,b}(t) dt \quad (3)$$

The function $\psi_{a,b}(t)$, Eq. (4), a wavelet, scaled by a and shifted by b , controlling the frequency and the time of the wavelet, respectively. In our study, we use the complex Morlet wavelet ψ_M , Eq. (5), which is the product of a sine and a gaussian function, with $\omega_0 = 6$ and $u = \frac{t-b}{a}$ (Torrence and Compo, 1998; Metzger et al., 2013; Wolfe et al., 2018).

$$\psi_{a,b}(t) = \frac{1}{\sqrt{a}} \times \psi_M\left(\frac{t-b}{a}\right) \quad (4)$$

$$\psi_M(u) = \pi^{-\frac{1}{4}} \times e^{-i\omega_0 u} \times e^{-\frac{u^2}{2}} \quad (5)$$

The expression $|W^2(a,b)|$ represents the power spectrum of the discrete time series, showing each scale a and translation b with the according amplitude. For two different time series, the product of the wavelet coefficients yields the cross power spectrum which when integrated represents the covariance and, in case of the vertical wind speed and the trace gas concentration, the flux (Torrence and Compo, 1998; Metzger et al., 2013; Schaller et al., 2017). The flux is calculated through wavelet transformation via Eq. (6) whereas C_δ is a reconstruction factor equal to 0.776 for the Morlet wavelet. N is the number of

<https://doi.org/10.5194/egusphere-2023-601>
 Preprint. Discussion started: 12 April 2023
 © Author(s) 2023. CC BY 4.0 License.



elements in the time series ($n = 0, 1, \dots, N$) with the time step δt and J is the number of scales ($j = 0, 1, \dots, J$) with the spacing δj (Metzger et al., 2013; Schaller et al., 2017; Desjardins et al., 2021).

$$\overline{\omega'c'} = \frac{\delta t}{C_\delta} \times \frac{\delta j}{N} \times \sum_{n=0}^{N-1} \sum_{j=0}^J \frac{[W_c(a, b) \times W_\omega^*(a, b)]}{a(j)} \quad (6)$$

Both data pre-treatment (of the NO_x and meteorological data) and wavelet analysis were performed following the procedure presented by Vaughan et al. (2021). The time stamp of the meteorological data was interpolated to the NO_x data time stamp with a resolution of 5 Hz. We generated flight segments as input for the wavelet analysis with a 10 km minimum length of continuous measurements. Observations above the boundary layer and thus in the free troposphere were excluded from our analysis as they are assumed to be out of contact with the surface below. Data with an aircraft roll angle larger than 8° or where the altitude changed by more than ~ 100 m across the 10 km were excluded. Due to different inlet sampling locations and computer clocks, the NO_x measurements and the vertical wind speed measurements were slightly time shifted. This lag correction was quantified via the cross covariance of the two time series. The vertical wind speed was then shifted to the NO_x measurements according to the covariance peak. We used the median lag of all segments of the same flight day for the lag correction. In Figure S2 of the Supplement we show an example covariance peak for NO_x and potential temperature θ with the vertical wind speed, respectively, for three segments on June 6.

For the wavelet analysis, we followed the procedure described in detail in Torrence and Compo (1998). The wavelet transform was calculated separately for the vertical wind speed fluctuation ω' and the NO_x concentration fluctuation c' . We used the wavelet software provided by C. Torrence and G. Compo, with the Morlet wavelet ψ_M (described in Eq. (5)), the time step $\delta t = 0.2 \text{ s}^{-1}$, a scale spacing $\delta j = 0.25$ and a scale number of $J = \log_2\left(\frac{N\delta t}{j_{\min}}\right) \times \frac{1}{\delta j}$ (default value, $j_{\min} = 2 \times \delta t$). For example, there would be 36 scales for a segment with 1000 data points. The cross spectrum was obtained through the sum of the product of the real parts of the wavelet transform for c' and ω' and the product of the imaginary parts, which gave the NO_x flux via the weighted sum over all scales according to Eq. (24) in Torrence and Compo (1998). Due to edge effects, the error is particularly high at the beginning and end of each segment which is described by the cone of influence (COI) (Torrence and Compo, 1998). We have discarded data points for which more than 80 % of the spectral information is located within the COI. Note that approximately 50 % of the data points are lost due to edge effects, likely due to short segment lengths and frequent calibrations. For our analysis, we used the 2 km moving mean of the NO_x flux. Figure 2a shows the discrete time series of the NO_x concentration and the vertical wind speed for one segment on 6 June with a length of 30.0 km. The x axis shows the time in seconds from the start of the segment (~ 9 min). Figure 2b shows the cross power spectrum of c' and ω' , with red colors representing positive and blue colors representing negative amplitudes, and the cone of influence by the black dashed line. The 2 km moving mean of the resulting NO_x flux is presented in Figure 2c. We show an example co-spectrum for the NO_x flux and the heat flux in Figure S3 of the Supplement, for three segments on June 6 corresponding to Figure S2.

The overall uncertainty of the calculated NO_x flux is composed of the uncertainty of the measurement of the NO_x concentration and the vertical wind speed as well as the uncertainty associated with the presented method of performing the wavelet transformation, including random and systematic errors (Lenschow et al., 1994; Mann and Lenschow, 1994; Wolfe et al., 2015;

<https://doi.org/10.5194/egusphere-2023-601>

Preprint. Discussion started: 12 April 2023

© Author(s) 2023. CC BY 4.0 License.

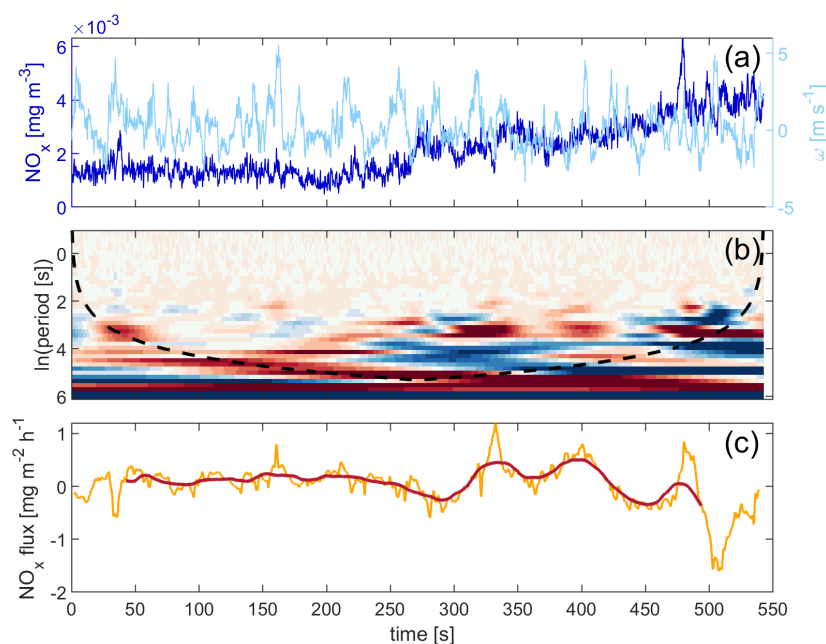


Figure 2. (a) Discrete time series of the NO_x concentration (dark blue) and the vertical wind speed (light blue) for a segment on 6 June. (b) Cross power spectrum with 41 scales and 2777 translations, the latter equaling the number of points in the segment. Red colors represent positive and blue colors represent negative amplitudes. (c) The resulting NO_x flux (orange) and the 2 km moving mean (red).

Vaughan et al., 2021). A detailed error analysis for these observations is provided in Zhu et al. (2023). We find the median and average values of the NO_x flux are dominated by the atmospheric variability and not the measurement uncertainties. The atmospheric variability of NO_x is in the order of 30 % (1σ) which is around 4 times higher compared to the instrumental precision of $<7\%$ (1σ).

2.5 Vertical Divergence

Vertical flux divergence describes the effect that a flux measured at a certain altitude can differ from the surface flux caused for example through chemistry conversions, entrainment from above or horizontal advection, mostly through differing wind speeds with altitude (Wolfe et al., 2018; Vaughan et al., 2021). The characterization of the vertical divergence can be performed by measurements of a vertical profile over a homogeneous surface. Several race tracks stacked at multiple heights were conducted over Los Angeles during RECAP-CA, but none fulfilled the criteria for performing flux calculations as described in Section 2.4 (e.g. roll angle or segment length). A different approach is described in Wolfe et al. (2018) and Zhu et al. (2023) which investigates the calculated NO_x fluxes in dependence of the relative measurement position in the boundary layer over a homogeneous surface. In contrast to the San Joaquin Valley considered in Zhu et al. (2023), the measurements over Los Angeles are not

<https://doi.org/10.5194/egusphere-2023-601>
 Preprint. Discussion started: 12 April 2023
 © Author(s) 2023. CC BY 4.0 License.



homogeneous, neither in space nor in time, due to a high variety of emission sources and a diurnal cycle affected e.g. by rush hour traffic. In Figure S4 of the Supplement we show the calculated NO_x flux across Los Angeles versus the dimensionless altitude z/z_i , where z is the radar altitude of the research aircraft and z_i the boundary layer height. The data points exhibit a decreasing trend (green) with altitude pointing towards the effect of vertical divergence, but show a low statistical significance with an R^2 of only 6 %, likely due to the source heterogeneity, both space- and time-wise. In order to investigate the influence of vertical divergence, we exemplarily perform a correction of the fluxes with the fit derived from Figure S4, using a correction factor as presented in Eq. (15) in Wolfe et al. (2018). The resulting surface flux F_0 can then be calculated as shown in Equation (7), with the measured flux F_z at the altitude z/z_i , the slope m of the linear fit and its y-intercept c .

$$F_0 = \frac{F_z}{1 + \frac{m}{c} * z/z_i} \quad (7)$$

We show the fluxes adjusted for this estimate of the vertical divergence versus the dimensionless altitude in Figure S5 of the Supplement. Data points which are located close to the linear fit can be corrected quite accurately. However, corrections for data points which are located further away from the fit, and particularly those measured close to the boundary layer height, are highly uncertain. As the slope is negative, and the absolute values for slope and y-intercept are almost equal, the denominator in Equation (7) gets extremely small close to the BLH and the correction correspondingly large. Karl et al. (2013) also suggests that fluxes can get uncertain close to the boundary layer height due to entrainment to the free troposphere. Thus for the sensitivity study, we omit data points within the upper 20 % of the boundary layer ($z/z_i \geq 0.8$).

2.6 Footprint calculations

In order to map emissions, we performed footprint calculations which help to identify the areas where the measured air masses originated (Vesala et al., 2008). We used the footprint model KL04-2D, proposed by Kljun et al. (2004), and further developed by Metzger et al. (2012) to include the impact of cross winds. The KL04 model was developed from the 3D backward Lagrangian model KL02 (Kljun et al., 2002). This model was previously applied by Vaughan et al. (2021).

We subdivided the area of observations into a $500 \text{ m} \times 500 \text{ m}$ spatial grid and calculated an average of all data points located in one grid box, separately for each segment. We then performed the footprint calculation for each grid box of each segment, approximately 5,000 footprints for the entire campaign. The footprint calculation is dependent on the wind direction [°], the crosswind fluctuations (standard deviation of the horizontal wind speed) [m/s], the vertical wind fluctuations (standard deviation of the vertical wind speed) [m/s], the friction velocity [m/s], the roughness length [m], the altitude of the measurement above ground level [m] and the height of the planetary boundary layer [m]. The roughness length z_0 is a measure of the surface properties, which we adapted from Burian et al. (2002) and from the World Meteorological Organization (2018) based on the land cover use for Los Angeles. We first generated footprints using the roughness length from the High-Resolution Rapid Refresh (HRRR) model by the National Oceanic and Atmospheric Administration (NOAA, 2021). Based on the dominant land cover type in each footprint, we then applied the roughness length according to Burian et al. (2002) and the World Meteorological Organization (2018). The land use data set was obtained from the Multi-Resolution Land Characteristics Consortium

<https://doi.org/10.5194/egusphere-2023-601>
 Preprint. Discussion started: 12 April 2023
 © Author(s) 2023. CC BY 4.0 License.

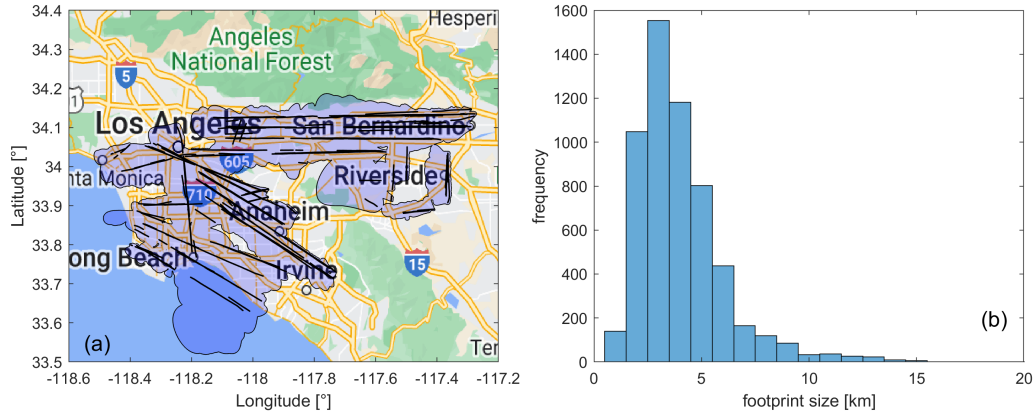


Figure 3. (a) Overview of the 90 % footprint influences for the flight campaign over Los Angeles. © Google Maps 2023. (b) Frequency distribution of the 90 % footprint size which describes the distance perpendicular to the flight track.

(MRLC, 2019). The friction velocity u^* is a measure for the shear stress and can be approximated via the logarithmic wind profile as shown in Eq. (8), where u is the horizontal wind speed, k the Karman constant equaling 0.41 and z the altitude above ground level (Weber, 1999).

$$u^* = u \times k \times \ln\left(\frac{z}{z_0}\right)^{-1} \quad (8)$$

The model output is a spatial grid of the fractional contribution to each footprint normalized to a value of unity. We focused on the 90 % footprint influences and assigned the measured NO_x flux to the NO_x flux of each grid box in the 90 % footprints. We then overlayed all footprint grids separately for weekends and for weekdays and calculated a value for the NO_x flux for each grid box as the weighted average.

Figure 3a presents the 90 % contours of all segments over Los Angeles in blue and the according flight paths in black. The majority of the 90 % footprints captured air masses from a distance of ~ 3 km (perpendicular to the flight track) as shown in the histogram of footprint size in Figure 3b. We observed individual footprints with a size of up to 23 km, for example for 11 June around Redondo Beach which were accompanied by high horizontal wind speeds ($\sim 4 \text{ m s}^{-1}$) and a flight altitude ($\sim 440 \text{ m}$) in the upper part of the boundary layer (BLH of $\sim 545 \text{ m}$). This is in line with the findings by Kljun et al. (2004), demonstrating the impact of the receptor height (Fig. 1 in Kljun et al. (2004)). The smallest footprint with 500 m was observed on 19 June, characterized by a small value for the horizontal wind speed with $\sim 0.5 \text{ m s}^{-1}$.

The influence of the horizontal wind speed on the footprint analysis is also highlighted in Figure 4. The two panels present selected flight segments in geographic proximity over the San Bernardino valley on 6 June (Figure 4a) and on 12 June (Figure 4b). Both days were weekend days and we expect similar NO_x emissions. However, the calculated NO_x flux for the displayed segments was on average $0.18 \pm 0.25 \text{ mg m}^{-2} \text{ h}^{-1}$ for 6 June and $1.66 \pm 1.06 \text{ mg m}^{-2} \text{ h}^{-1}$ for 12 June. At the same time, the

<https://doi.org/10.5194/egusphere-2023-601>

Preprint. Discussion started: 12 April 2023

© Author(s) 2023. CC BY 4.0 License.

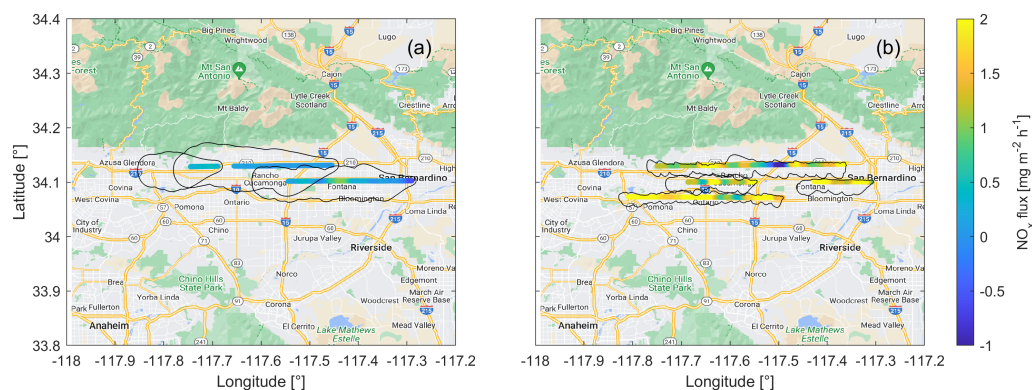


Figure 4. Flight segments in geographic proximity on two weekend days, (a) 6 June and (b) 12 June, with different footprint size. © Google Maps 2023.

footprint size for these segments was more than 4 times larger for 6 June with an average of 8.2 ± 2.1 km, than for 12 June with an average of 1.9 ± 1.0 km. The measured air on 12 June originated from above the highways in the San Bernardino valley. In contrast, on 6 June we also captured air from adjacent, less NO_x sources, such as residential areas, diluting the NO_x polluted air from above the highways and leading to lower NO_x fluxes. While all inputs for the footprint model were roughly similar (e.g. radar altitude 384 m (June 6) and 349 m (June 12); BLH 637 m (June 6) and 600 m (June 12)), the horizontal wind speed was significantly higher on 6 June with an average of 8.2 ± 1.2 m s^{-1} than on June 12 where the average was 2.5 ± 1.0 m s^{-1} . This example also underlines the importance of footprint calculations in the interpretation of the observed fluxes.

2.7 Emission inventory

The California Air Resources Board (CARB) provides an emission inventory for Los Angeles with a 1 hour temporal resolution and a $4 \text{ km} \times 4 \text{ km}$ spatial resolution over 12 vertical layers. The emission inventory is assembled from several sub-models accounting for different emission source categories. These are on-road vehicle emissions, aircraft emission and all other emissions, including for example shipping and port emissions. Mobile emissions are obtained via the ESTA (Emissions Spatial and Temporal Allocator) model (CARB, 2019). Emissions from vehicles, including passenger cars, buses and heavy-duty trucks, are estimated via the EMFAC (Emission FACTor) model based on vehicle registrations and emission rate data for different vehicle types (CARB, 2021, 2022a). In combination with spatial information and temporal data, such as diurnal profiles and day-of-week dependence, the on-road emission inventory can be created via the ESTA model (CARB, 2019). The GATE (Gridded Aircraft Trajectory Emissions) model analogously provides spatially and temporally resolved aircraft emissions (CARB, 2017). Emissions from shipping and port activities, as well as additional point or area sources, are modeled with the SMOKE (Sparse Matrix Operator Kernel Emissions) model (CEMPD, 2022).

<https://doi.org/10.5194/egusphere-2023-601>

Preprint. Discussion started: 12 April 2023

© Author(s) 2023. CC BY 4.0 License.



We are presenting a comparison of the NO_x fluxes calculated from the RECAP-CA campaign measurements with the 2020 CARB emission inventory for Los Angeles, which is a baseline inventory and therefore does not include any effects related to the COVID-19 (coronavirus disease 2019) economic and social upheaval. For each flight day of the 2021 campaign, we include the according day of the week of the emission inventory in 2020. As 2020 was a leap year, the day of year of each considered flight is shifted by two from the 2020 calendar (e.g. Tuesday, 1 June, was the 152nd day of 2021 for which we consider Tuesday, 2 June, the 154th day of 2020, from the emission inventory). We combined the $500 \text{ m} \times 500 \text{ m}$ spatial resolution of the RECAP-CA NO_x fluxes to the $4 \text{ km} \times 4 \text{ km}$ CARB grid for this comparison.

3 Results and Discussion

3.1 NO_x emissions over Los Angeles

NO_x concentrations and NO_x fluxes over Los Angeles are separated into four different geographical regions, as shown in Figure 1b. We analyze the effects of temperature and the planetary boundary layer height, as well as differences between weekend and weekday data. Figure 5 shows the temperature for the different sections, measured on the research aircraft ($380 \pm 63 \text{ m}$ altitude). Lowest temperatures were observed in the coastal section with a median value of 17°C . Temperatures measured over Santa Ana and Downtown were slightly higher with median values around 19°C . Further inland, observed temperatures were highest with a median value of 24°C . Significant differences between the four sections were also observed regarding the boundary layer height (BLH) as presented in Figure 5b. The lowest BLH was found for the coastal section with a median value of 470 m , followed by Santa Ana with 490 m and a median value of 540 m for Downtown. The BLH in the San Bernardino valley was highest with a median value of 590 m . Figure 5c shows NO_x concentrations and Figure 5d shows the corresponding fluxes over Los Angeles, separated into the geographical sections and into weekdays and weekends. Neither NO_x concentrations nor NO_x fluxes were found to be temperature dependent (see Figure S6).

Median concentrations were highest in Downtown with 0.011 mg m^{-3} on weekdays and 0.006 mg m^{-3} on weekends. In the San Bernardino valley, median concentrations were 0.010 mg m^{-3} and 0.007 mg m^{-3} on weekdays and weekends, respectively. The median measured fluxes in Downtown Los Angeles were 0.86 and $0.35 \text{ mg m}^{-2} \text{ h}^{-1}$, respectively for weekdays and weekends. In the San Bernardino valley the median fluxes were $0.97 \text{ mg m}^{-2} \text{ h}^{-1}$ on weekdays and $0.46 \text{ mg m}^{-2} \text{ h}^{-1}$ on weekends. In all of these locations weekend emissions decreased by 50 - 60 % from weekday values.

Concentrations were lower near the coast. Median NO_x concentrations were similar for the coastal section and Santa Ana with around 0.005 mg m^{-3} on weekdays. The weekend values were smaller with $0.003 - 0.004 \text{ mg m}^{-3}$. However, no significant differences could be observed between weekday and weekend fluxes in these regions. Much of the coastal region is over water and the median values of fluxes are near zero on both weekdays and weekends and approximately $0.2 \text{ mg m}^{-2} \text{ h}^{-1}$ on both weekdays and weekends in the Santa Ana region.

While NO_x concentrations were observed to be highest over Downtown Los Angeles, NO_x fluxes were found to be highest in the San Bernardino valley. This effect could be partly caused by the observed differences in the boundary layer height. While

<https://doi.org/10.5194/egusphere-2023-601>

Preprint. Discussion started: 12 April 2023

© Author(s) 2023. CC BY 4.0 License.

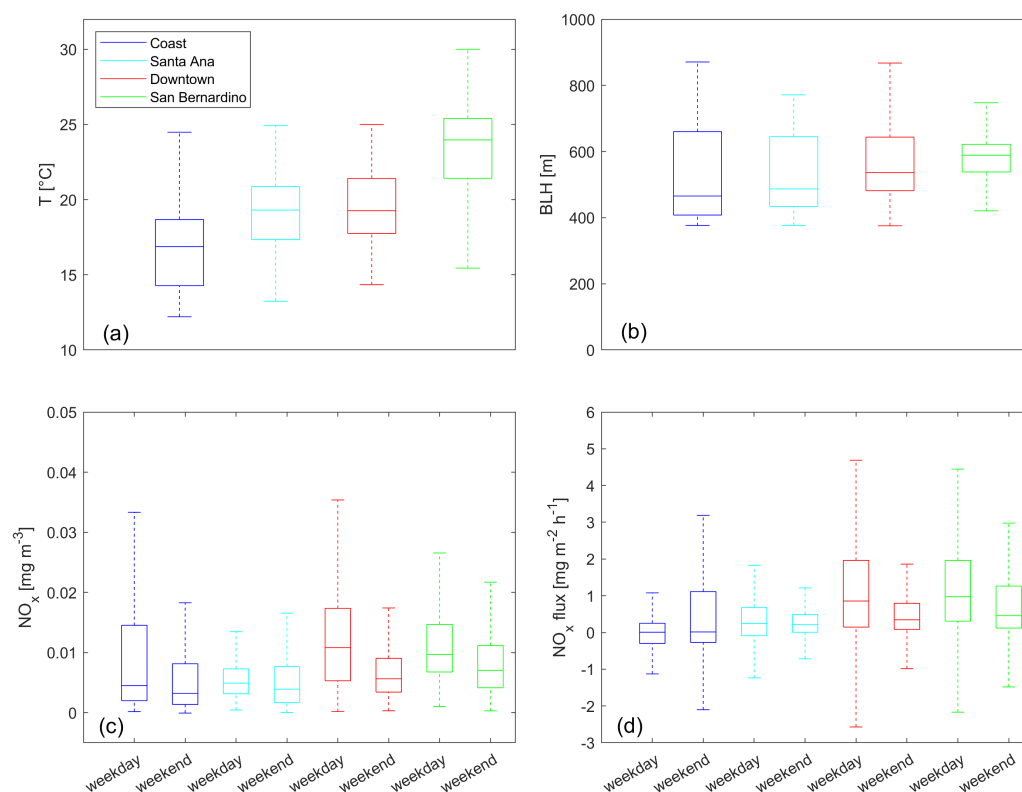


Figure 5. Boxplots for (a) the temperature, (b) the boundary layer height, (c) NO_x concentrations and (d) NO_x fluxes subdivided into four geographical sections according to Figure 1b and into weekday and weekend data. Please note that outliers are not shown.

highest emissions occurred in the San Bernardino valley, the increased planetary BLH (as shown in Figure 5b), should lead to a $\sim 15\%$ lower mixing ratio. The differences in concentrations are likely also due to chemistry and advection.

Using the highway information by the California Department of Transportation (2015), we separated NO_x fluxes into emissions from highway and non-highway grid cells. A $500\text{ m} \times 500\text{ m}$ grid cell is considered a highway emission when it is crossed by a highway. We present the resulting emission grid in Figure S7 of the Supplement. For weekdays, NO_x fluxes from highway grid cells were on average $0.84 \pm 1.43\text{ mg m}^{-2}\text{ h}^{-1}$, approximately 25% higher than NO_x fluxes from non-highway grid cells with an average of $0.67 \pm 1.26\text{ mg m}^{-2}\text{ h}^{-1}$. Weekend NO_x fluxes from highways were on average $0.58 \pm 0.94\text{ mg m}^{-2}\text{ h}^{-1}$. Weekend NO_x emissions from non-highway areas were $0.45 \pm 0.93\text{ mg m}^{-2}\text{ h}^{-1}$. Note the large 1σ standard deviations, indicating the large variability of the fluxes. The median values were lower compared to the mean values (0.57 and $0.29\text{ mg m}^{-2}\text{ h}^{-1}$ for highway and non-highway, respectively, on weekdays and 0.38 and $0.26\text{ mg m}^{-2}\text{ h}^{-1}$ for highway and non-highway, respectively, on weekends), but showed a similar qualitative result with higher emissions from highway compared to non-highway areas.

<https://doi.org/10.5194/egusphere-2023-601>

Preprint. Discussion started: 12 April 2023

© Author(s) 2023. CC BY 4.0 License.



3.2 Comparison to the emission inventory

The comparison between the emission inventory and the calculated NO_x fluxes is shown in Figure 6. We present the week-day data here and show the weekend data in Figure S8 of the Supplement. Panel (a) shows the RECAP-CA NO_x fluxes at $4 \text{ km} \times 4 \text{ km}$, panel (b) presents the CARB emission inventory and in panel (c) we show the difference between the RECAP-CA and the CARB data according to Eq. (9).

$$\Delta \text{NO}_x \text{ flux} = \text{NO}_x \text{ flux}(\text{RECAP}) - \text{NO}_x \text{ flux}(\text{CARB}) \quad (9)$$

As expected from the results presented in Section 3.1 the highest NO_x fluxes were observed in the San Bernardino valley which is characterized by several heavily trafficked highways and warehouses that cause dense diesel truck traffic (Los Angeles Times, 2023). Elevated NO_x emission also occurred in the region around Downtown Los Angeles. The average weekend RECAP-CA NO_x fluxes (Figure S8a) showed a similar emission distribution over Los Angeles compared to the weekday data, but with smaller values. This is in line with the findings presented in Section 3.1.

Figure 6b shows average weekday NO_x fluxes as predicted by the CARB emission inventory. The large NO_x flux in proximity to the coast ($\sim 34.0^\circ \text{ N}$, 118.4° W) with a value close to $8 \text{ mg m}^{-2} \text{ h}^{-1}$ was associated with aircraft emissions from Los Angeles International Airport (LAX). We show the NO_x fluxes as predicted by CARB separated into (a) on-road emissions, (b) aircraft emissions, (c) area sources and (d) emissions from ocean going vessels in Figure S9 of the Supplement. Aircraft NO_x emissions can also be observed in the San Bernardino valley ($\sim 34.1^\circ \text{ N}$, 117.6° W) from Ontario International Airport which is illustrated in Figure S9b. High NO_x fluxes in this area were also associated with on-road emissions, shown in Figure S9a. The Downtown Los Angeles area ($\sim 34.0^\circ \text{ N}$, 118.2° W) also showed high fluxes which originated from on-road and area sources. Elevated NO_x fluxes around Long Beach ($\sim 33.8^\circ \text{ N}$, 118.2° W) were associated with shipping and port emissions. Average weekend NO_x fluxes predicted by the emission inventory are presented in Figure S8b which showed a similar qualitative distribution compared to the weekday data, but were generally lower. Figure 6c presents the difference between the NO_x fluxes from the RECAP-CA campaign and the CARB emission inventory. Red colors represent higher values for the RECAP-CA campaign compared to the emission inventory. Blue colors indicate higher fluxes from the emission inventory. In most places, the NO_x fluxes predicted by the emission inventory were higher compared to the values from the RECAP-CA campaign. This difference was particularly pronounced in the area around Downtown Los Angeles and along the coast. We were not able to capture any airport emissions during the RECAP-CA campaign, as a result the differences in the vicinity of the Los Angeles and Ontario airports should not be interpreted as meaningful. NO_x fluxes around Downtown Los Angeles are dominated by area sources and on-road emissions.

We observed higher NO_x fluxes during the RECAP-CA campaign compared to the emission inventory in the San Bernardino valley. A possible explanation could be the accumulation of distribution and fulfillment centers which are accessible to delivery trucks via multiple highways in this area (Schorung and Lecourt, 2021; Los Angeles Times, 2023). Over the past two decades net sales via distribution centers have grown exponentially (Statista, 2022a). In the U.S., the number of delivered orders by the online retailer amazon has increased by nearly a factor of 6 between 2018 and 2020 (Statista, 2022b). NO_x emissions in

<https://doi.org/10.5194/egusphere-2023-601>
Preprint. Discussion started: 12 April 2023
© Author(s) 2023. CC BY 4.0 License.

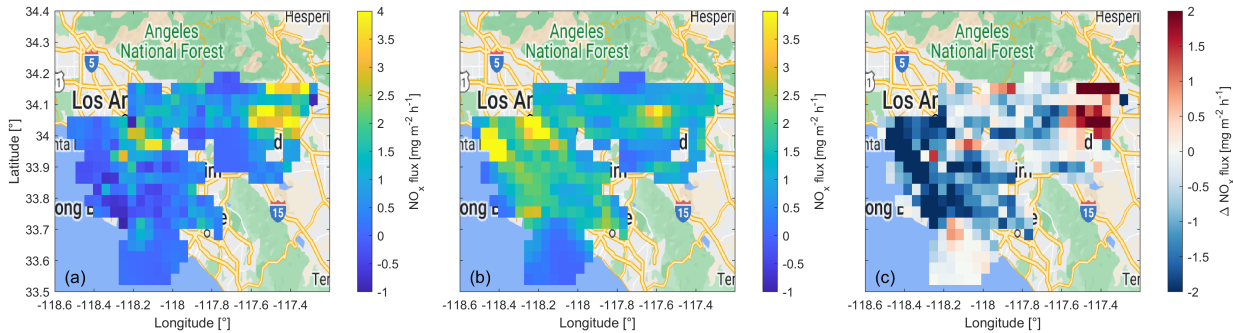


Figure 6. Weekday averages of NO_x emissions across Los Angeles with a $4 \text{ km} \times 4 \text{ km}$ spatial resolution (a) during the RECAP-CA campaign, (b) from the CARB emission inventory and (c) the difference between RECAP-CA and CARB NO_x fluxes. © Google Maps 2023.

proximity to warehouses have likely increased to a similar extent in recent years which might not yet be incorporated in the CARB 2020 emission inventory. Additional research is needed to examine more details of these differences and connect them to specific processes in the inventory and observations.

In Figure S10 and S11 of the Supplement we show the NO_x fluxes corrected for vertical divergence as presented in Section 2.5 in comparison to the CARB emission inventory for weekdays and weekends, respectively. The emission features shown in Figure 6 for the RECAP-CA campaign are more pronounced after applying the factor for vertical correction. High emissions are observed over Downtown Los Angeles and the inland highways in San Bernardino, while the coastal region and Santa Ana show lower, and even negative fluxes. As a result, CARB emissions remain dominant over RECAP-CA fluxes in the coastal region, but are lower around Downtown Los Angeles and in San Bernardino. The median values of the corrected fluxes are around a factor of 3 higher compared to the non-corrected fluxes. The interquartile range increases by even more as a result of the large scatter induced by the correction (compare Figure S5). This sensitivity analysis emphasizes how important the characterization of the vertical flux divergence is and should be subject to future studies.

4 Conclusions

In this study, we have investigated NO_x fluxes via wavelet analysis, based on in-situ observations of NO_x concentrations and the vertical wind speed during the research aircraft campaign RECAP-CA (Re-Evaluating the Chemistry of Air Pollutants in California) which took place in June 2021 over Los Angeles. We identified NO_x concentrations to be highest over Downtown Los Angeles, while we found highest NO_x fluxes in the San Bernardino valley where a high planetary BLH induced a higher dilution of the emitted NO_x . Both NO_x concentrations and NO_x fluxes revealed a weekend effect with higher values on weekdays due to more commuter traffic and more diesel trucks on roads, which was most pronounced over Downtown Los Angeles and the San Bernardino valley. Footprint calculations revealed that the distance of the 90 % influence was on average 4 km, whereby the horizontal wind speed played a dominant role in the footprint size. NO_x emissions predicted by the California

<https://doi.org/10.5194/egusphere-2023-601>

Preprint. Discussion started: 12 April 2023

© Author(s) 2023. CC BY 4.0 License.



340 Air Resources Board (CARB) 2020 were in the same order of magnitude, but on average higher compared to the RECAP-CA
NO_x fluxes. Spatially, the emission inventory particularly overestimated the fluxes in coastal proximity and over Downtown
Los Angeles. In contrast, the emission inventory underestimated the NO_x fluxes over the Eastern part of the San Bernardino
valley.

Data availability. Data measured during the flight campaign, computed fluxes and footprints are available at <https://doi.org/10.5281/zenodo.7786409>
345 (Nussbaumer et al., 2023).

Author contributions. CMN analyzed the data with contributions from BKP, QZ and EYP. CMN wrote the manuscript. All authors con-
tributed to designing the study and proofreading the manuscript.

Competing interests. At least one of the (co-)authors is a member of the editorial board of Atmospheric Chemistry and Physics.

Acknowledgements. We acknowledge Horst Fischer and Lenard Röder for valuable discussions and proofreading of this manuscript. The
350 RECAP-CA aircraft campaign was funded by the California Air Resources Board (20RD003 and 20AQP012) and the South Coast Air
Quality Management District (#20327). The wavelet software was provided by C. Torrence and G. Compo, and is available at URL:
<http://paos.colorado.edu/research/wavelets/>. Plots including Google Maps data were created with a matlab function by Bar-Yehuda, Z. (2022).
This work was supported by the Max Planck Graduate Center with the Johannes Gutenberg-Universität Mainz (MPGC).

<https://doi.org/10.5194/egusphere-2023-601>

Preprint. Discussion started: 12 April 2023

© Author(s) 2023. CC BY 4.0 License.



References

- 355 American Lung Association: Most Polluted Cities, <https://www.lung.org/research/sota/city-rankings/most-polluted-cities>, accessed on 2022-04-08, 2022.
- Bar-Yehuda, Z.: zoharby plot google map, https://github.com/zoharby/plot_google_map, retrieved on 2022-07-11, 2022.
- Boningari, T. and Smirniotis, P. G.: Impact of nitrogen oxides on the environment and human health: Mn-based materials for the NO_x abatement, *Current Opinion in Chemical Engineering*, 13, 133–141, <https://doi.org/10.1016/j.coche.2016.09.004>, 2016.
- 360 Burian, S. J., Brown, M. J., and Velugubantla, S. P.: Roughness length and displacement height derived from building databases, <https://www.osti.gov/biblio/976101>, 2002.
- California Department of Transportation: State Highways (Segments), California, 2015, available at <https://searchworks.stanford.edu/view/x453kn9742>, accessed on 2022-07-15, 2015.
- CARB: GATE Basic Introduction, https://github.com/mmb-carb/GATE_Documentation/blob/master/docs/BASIC_INTRO.md, accessed on 2022-05-30, 2017.
- 365 CARB: ESTA Basic Introduction, https://github.com/mmb-carb/ESTA_Documentation/blob/master/docs/BASIC_INTRO.md, accessed on 2022-05-30, 2019.
- CARB: EMFAC2021 Volume III Technical Document, Tech. rep., Mobile Source Analysis Branch Air Quality Planning and Science Division, https://ww2.arb.ca.gov/sites/default/files/2021-08/emfac2021_technical_documentation_april2021.pdf?utm_medium=email&utm_source=govdelivery, accessed on 2022-05-31, 2021.
- 370 CARB: Welcome to EMFAC, <https://arb.ca.gov/emfac/>, accessed on 2022-05-31, 2022a.
- CARB: Nitrogen Dioxide and Health, <https://ww2.arb.ca.gov/resources/nitrogen-dioxide-and-health>, accessed on 2022-04-07, 2022b.
- CEMPD: SMOKE, <https://github.com/CEMPD/SMOKE/>, center for Environmental Modeling for Policy Development, accessed on 2022-05-31, 2022.
- 375 Conley, S., Faloona, I., Miller, G., Lenschow, D., Blomquist, B., and Bandy, A.: Closing the dimethyl sulfide budget in the tropical marine boundary layer during the Pacific Atmospheric Sulfur Experiment, *Atmospheric Chemistry and Physics*, 9, 8745–8756, <https://doi.org/10.5194/acp-9-8745-2009>, 2009.
- Day, D., Wooldridge, P., Dillon, M., Thornton, J., and Cohen, R.: A thermal dissociation laser-induced fluorescence instrument for in situ detection of NO₂, peroxy nitrates, alkyl nitrates, and HNO₃, *Journal of Geophysical Research: Atmospheres*, 107, ACH-4, <https://doi.org/10.1029/2001JD000779>, 2002.
- 380 Delmas, R., Serça, D., and Jambert, C.: Global inventory of NO_x sources, *Nutrient cycling in agroecosystems*, 48, 51–60, 1997.
- Desjardins, R. L., Worth, D. E., MacPherson, I., Mauder, M., and Bange, J.: Aircraft-Based Flux Density Measurements. In: *Springer Handbook of Atmospheric Measurements*, pp. 1305–1330, Springer International Publishing, Cham, https://doi.org/10.1007/978-3-030-52171-4_48, 2021.
- 385 EPA: Overview of the Clean Air Act and Air Pollution, <https://www.epa.gov/clean-air-act-overview>, accessed on 2022-04-07, 2022a.
- EPA: Air Data - Ozone Exceedances, <https://www.epa.gov/outdoor-air-quality-data/air-data-ozone-exceedances>, accessed on 2022-04-07, 2022b.
- EPA: California Nonattainment/Maintenance Status for Each County by Year for All Criteria Pollutants, https://www3.epa.gov/airquality/greenbook/anayo_ca.html, accessed on 2022-04-08, 2022c.

<https://doi.org/10.5194/egusphere-2023-601>

Preprint. Discussion started: 12 April 2023

© Author(s) 2023. CC BY 4.0 License.



- 390 Fujita, E. M., Campbell, D. E., Stockwell, W. R., and Lawson, D. R.: Past and future ozone trends in California's South Coast Air Basin: Reconciliation of ambient measurements with past and projected emission inventories, *Journal of the Air & Waste Management Association*, 63, 54–69, <https://doi.org/10.1080/10962247.2012.735211>, 2013.
- Gu, D., Guenther, A. B., Shilling, J. E., Yu, H., Huang, M., Zhao, C., Yang, Q., Martin, S. T., Artaxo, P., Kim, S., Seco, R., Stavrou, T., Longo, K. M., Tóta, J., de Souza, R. A. F., Vega, O., Liu, Y., Shrivastava, M., Alves, E. G., Santos, F. C., Leng, G., and
- 395 Hu, Z.: Airborne observations reveal elevational gradient in tropical forest isoprene emissions, *Nature communications*, 8, 15541, <https://doi.org/10.1038/ncomms15541>, 2017.
- Hegg, D. A., Covert, D. S., Jonsson, H., and Covert, P. A.: Determination of the transmission efficiency of an aircraft aerosol inlet, *Aerosol science and technology*, 39, 966–971, <https://doi.org/10.1080/02786820500377814>, 2005.
- Karl, T., Apel, E., Hodzic, A., Riemer, D., Blake, D., and Wiedinmyer, C.: Emissions of volatile organic compounds inferred from airborne
- 400 flux measurements over a megacity, *Atmospheric Chemistry and Physics*, 9, 271–285, <https://doi.org/10.5194/acp-9-271-2009>, 2009.
- Karl, T., Misztal, P., Jonsson, H., Shertz, S., Goldstein, A., and Guenther, A.: Airborne flux measurements of BVOCs above Californian oak forests: Experimental investigation of surface and entrainment fluxes, OH densities, and Damköhler numbers, *Journal of the atmospheric sciences*, 70, 3277–3287, <https://doi.org/10.1175/JAS-D-13-054.1>, 2013.
- Kaser, L., Karl, T., Yuan, B., Mauldin III, R., Cantrell, C., Guenther, A. B., Patton, E., Weinheimer, A. J., Knote, C., Orlando, J., Emmons, L., Apel, E., Hornbrook, R., Shertz, S., Ullmann, K., Hall, S., Graus, M., de Gouw, J., Zhou, X., and Ye, C.: Chemistry-turbulence
- 405 interactions and mesoscale variability influence the cleansing efficiency of the atmosphere, *Geophysical Research Letters*, 42, 10–894, <https://doi.org/10.1002/2015GL066641>, 2015.
- Kljun, N., Rotach, M., and Schmid, H.: A three-dimensional backward Lagrangian footprint model for a wide range of boundary-layer stratifications, *Boundary-Layer Meteorology*, 103, 205–226, <https://doi.org/10.1023/A:1014556300021>, 2002.
- 410 Kljun, N., Calanca, P., Rotach, M., and Schmid, H.: A simple parameterisation for flux footprint predictions, *Boundary-Layer Meteorology*, 112, 503–523, <https://doi.org/10.1023/B:BOUN.0000030653.71031.96>, 2004.
- Lenschow, D., Mann, J., and Kristensen, L.: How long is long enough when measuring fluxes and other turbulence statistics?, *Journal of Atmospheric and Oceanic Technology*, 11, 661–673, [https://doi.org/10.1175/1520-0426\(1994\)011<0661:HLILEW>2.0.CO;2](https://doi.org/10.1175/1520-0426(1994)011<0661:HLILEW>2.0.CO;2), 1994.
- Los Angeles Times: Warehouse boom transformed Inland Empire. Are jobs worth the environmental degradation?, https://www.latimes.com/california/story/2023-02-05/warehouses-big-rigs-fill-inland-empire-streets?utm_id=85748&sfmc_id=1882085, accessed on 2023-03-06,
- 415 2023.
- Mann, J. and Lenschow, D. H.: Errors in airborne flux measurements, *Journal of Geophysical Research: Atmospheres*, 99, 14 519–14 526, <https://doi.org/10.1029/94JD00737>, 1994.
- Metzger, S., Junkermann, W., Mauder, M., Beyrich, F., Butterbach-Bahl, K., Schmid, H. P., and Foken, T.: Eddy-covariance flux measurements with a weight-shift microlight aircraft, *Atmospheric Measurement Techniques*, 5, 1699–1717, <https://doi.org/10.5194/amt-5-1699-2012>, 2012.
- Metzger, S., Junkermann, W., Mauder, M., Butterbach-Bahl, K., Trancón y Widemann, B., Neidl, F., Schäfer, K., Wieneke, S., Zheng, X. H., Schmid, H. P., and Foken, T.: Spatially explicit regionalization of airborne flux measurements using environmental response functions, *Biogeosciences*, 10, 2193–2217, <https://doi.org/10.5194/bg-10-2193-2013>, 2013.
- 425 Mills, G., Pleijel, H., Malley, C. S., Sinha, B., Cooper, O. R., Schultz, M. G., Neufeld, H. S., Simpson, D., Sharps, K., Feng, Z., Gerosa, G., Harmens, H., Kobayashi, K., Saxena, P., Paoletti, E., Sinha, V., and Xu, X.: Tropospheric Ozone Assessment Re-

<https://doi.org/10.5194/egusphere-2023-601>

Preprint. Discussion started: 12 April 2023

© Author(s) 2023. CC BY 4.0 License.



- port: Present-day tropospheric ozone distribution and trends relevant to vegetation, *Elementa: Science of the Anthropocene*, 6, <https://doi.org/10.1525/elementa.302>, 2018.
- Misztal, P. K., Karl, T., Weber, R., Jonsson, H. H., Guenther, A. B., and Goldstein, A. H.: Airborne flux measurements of biogenic isoprene over California, *Atmospheric Chemistry and Physics*, 14, 10 631–10 647, <https://doi.org/10.5194/acp-14-10631-2014>, <https://acp.copernicus.org/articles/14/10631/2014/>, 2014.
- MRLC: Multi-Resolution Land Characteristics (MRLC) Consortium - National Land Cover Database, available at <https://www.mrlc.gov/>, accessed on 2022-05-02, 2019.
- NOAA: The High-Resolution Rapid Refresh (HRRR), <https://rapidrefresh.noaa.gov/hrrr/>, accessed on 2022-05-25, 2021.
- Nussbaumer, C. M. and Cohen, R. C.: The Role of Temperature and NO_x in Ozone Trends in the Los Angeles Basin, *Environmental Science & Technology*, 54, 15 652–15 659, <https://doi.org/10.1021/acs.est.0c04910>, 2020.
- Nussbaumer, C. M., Place, B. K., Zhu, Q., Pfannerstill, E. Y., Wooldridge, P., Schulze, B. C., Arata, C., Ward, R., Bucholtz, A., Seinfeld, J. H., Goldstein, A. H., and Cohen, R. C.: Supporting data for: Measurement report: Airborne measurements of NO_x fluxes over Los Angeles during the RECAP-CA 2021 campaign, <https://doi.org/10.5281/zenodo.7786409>, 2023.
- Nuvolone, D., Petri, D., and Voller, F.: The effects of ozone on human health, *Environmental Science and Pollution Research*, 25, 8074–8088, <https://doi.org/10.1007/s11356-017-9239-3>, 2018.
- Pusede, S. E., Steiner, A. L., and Cohen, R. C.: Temperature and recent trends in the chemistry of continental surface ozone, *Chemical reviews*, 115, 3898–3918, <https://doi.org/10.1021/cr5006815>, 2015.
- Qian, Y., Henneman, L. R., Mulholland, J. A., and Russell, A. G.: Empirical development of ozone isopleths: Applications to Los Angeles, *Environmental Science & Technology Letters*, 6, 294–299, <https://doi.org/10.1021/acs.estlett.9b00160>, 2019.
- Reid, J. S., Jonsson, H. H., Smith, M. H., and Smirnov, A.: Evolution of the vertical profile and flux of large sea-salt particles in a coastal zone, *Journal of Geophysical Research: Atmospheres*, 106, 12 039–12 053, <https://doi.org/10.1029/2000JD900848>, 2001.
- Schaller, C., Göckede, M., and Foken, T.: Flux calculation of short turbulent events – comparison of three methods, *Atmospheric Measurement Techniques*, 10, 869–880, <https://doi.org/10.5194/amt-10-869-2017>, 2017.
- Schorung, M. and Lecourt, T.: Analysis of the spatial logics of Amazon warehouses following a multiscalar and temporal approach. For a geography of Amazon's logistics system in the United States., <https://halshs.archives-ouvertes.fr/halshs-03489397/document>, research report, accessed on 2022-05-31, 2021.
- South Coast Air Quality Management District: Final 2016 air quality management plan, Chapter 2, Tech. rep., South Coast Air Quality Management District, <http://www.aqmd.gov/docs/default-source/clean-air-plans/air-quality-management-plans/2016-air-quality-management-plan/final-2016-aqmp/chapter2.pdf>, accessed on 2022-04-08, 2017.
- Sparks, T. L., Ebben, C. J., Wooldridge, P. J., Lopez-Hilfiker, F. D., Lee, B. H., Thornton, J. A., McDuffie, E. E., Fibiger, D. L., Brown, S. S., Montzka, D. D., Weinheimer, A. J., Schroder, J. C., Campuzano-Jost, P., Jimenez, J. L., and Cohen, R. C.: Comparison of airborne reactive nitrogen measurements during WINTER, *Journal of Geophysical Research: Atmospheres*, 124, 10 483–10 502, <https://doi.org/10.1029/2019JD030700>, 2019.
- Statista: Annual net sales revenue of Amazon from 2004 to 2021, <https://www.statista.com/statistics/266282/annual-net-revenue-of-amazoncom/>, accessed on 2022-06-01, 2022a.
- Statista: Number of packages delivered by Amazon Logistics in the United States from 2018 to 2020 (in billion packages)*, <https://www.statista.com/statistics/1178979/amazon-logistics-package-volume-united-states/>, accessed on 2022-06-01, 2022b.

<https://doi.org/10.5194/egusphere-2023-601>

Preprint. Discussion started: 12 April 2023

© Author(s) 2023. CC BY 4.0 License.



- Stewart, D. R., Saunders, E., Perea, R. A., Fitzgerald, R., Campbell, D. E., and Stockwell, W. R.: Linking air quality and human health effects models: an application to the Los Angeles air basin, *Environmental health insights*, 11, 1178630217737551, <https://doi.org/10.1177/1178630217737551>, 2017.
- Thomas, C. and Foken, T.: Detection of long-term coherent exchange over spruce forest using wavelet analysis, *Theoretical and Applied Climatology*, 80, 91–104, <https://doi.org/10.1007/s00704-004-0093-0>, 2005.
- Thornton, J. A., Wooldridge, P. J., and Cohen, R. C.: Atmospheric NO₂: In situ laser-induced fluorescence detection at parts per trillion mixing ratios, *Analytical Chemistry*, 72, 528–539, <https://doi.org/10.1021/ac9908905>, 2000.
- Torrence, C. and Compo, G. P.: A practical guide to wavelet analysis, *Bulletin of the American Meteorological society*, 79, 61–78, [https://doi.org/10.1175/1520-0477\(1998\)079<0061:APGTWA>2.0.CO;2](https://doi.org/10.1175/1520-0477(1998)079<0061:APGTWA>2.0.CO;2), 1998.
- Vaughan, A. R., Lee, J. D., Misztal, P. K., Metzger, S., Shaw, M. D., Lewis, A. C., Purvis, R. M., Carslaw, D. C., Goldstein, A. H., Hewitt, C. N., Davison, B., and Beevers, Sean D. Karl, T. G.: Spatially resolved flux measurements of NO_x from London suggest significantly higher emissions than predicted by inventories, *Faraday discussions*, 189, 455–472, <https://doi.org/10.1039/c5fd00170f>, 2016.
- Vaughan, A. R., Lee, J. D., Metzger, S., Durden, D., Lewis, A. C., Shaw, M. D., Drysdale, W. S., Purvis, R. M., Davison, B., and Hewitt, C. N.: Spatially and temporally resolved measurements of NO_x fluxes by airborne eddy covariance over Greater London, *Atmospheric Chemistry and Physics*, 21, 15 283–15 298, <https://doi.org/10.5194/acp-21-15283-2021>, 2021.
- Vesala, T., Kljun, N., Rannik, Ü., Rinne, J., Sogachev, A., Markkanen, T., Sabelfeld, K., Foken, T., and Leclerc, M. Y.: Flux and concentration footprint modelling: State of the art, *Environmental Pollution*, 152, 653–666, <https://doi.org/10.1016/j.envpol.2007.06.070>, 2008.
- Weber, R. O.: Remarks on the definition and estimation of friction velocity, *Boundary-Layer Meteorology*, 93, 197–209, <https://doi.org/10.1023/A:1002043826623>, 1999.
- Wolfe, G. M., Hanisco, T. F., Arkinson, H. L., Bui, T. P., Crounse, J. D., Dean-Day, J., Goldstein, A., Guenther, A., Hall, S. R., Huey, G., Jacob, D. J., Karl, T., Kim, P. S., Liu, X., Marvin, M. R., Mikoviny, T., Misztal, P. K., Nguyen, T. B., Peischl, J., Pollack, I., Ryerson, T., St. Clair, J. M., Teng, A., Travis, K. R., Ullmann, K., Wennberg, P. O., and Wisthaler, A.: Quantifying sources and sinks of reactive gases in the lower atmosphere using airborne flux observations, *Geophysical Research Letters*, 42, 8231–8240, <https://doi.org/10.1002/2015GL065839>, 2015.
- Wolfe, G. M., Kawa, S. R., Hanisco, T. F., Hannun, R. A., Newman, P. A., Swanson, A., Bailey, S., Barrick, J., Thornhill, K. L., Diskin, G., DiGangi, J., Nowak, J. B., Sorenson, C., Bland, G., Yungel, J. K., and Swenson, C. A.: The NASA Carbon Airborne Flux Experiment (CARAFE): instrumentation and methodology, *Atmospheric Measurement Techniques*, 11, 1757–1776, <https://doi.org/10.5194/amt-11-1757-2018>, 2018.
- World Meteorological Organization: Flux and concentration footprint modelling: State of the art, 8, World Meteorological Organization, 2018.
- Yu, H., Guenther, A., Gu, D., Warneke, C., Geron, C., Goldstein, A., Graus, M., Karl, T., Kaser, L., Misztal, P., and Bin, Y.: Airborne measurements of isoprene and monoterpene emissions from southeastern US forests, *Science of the Total Environment*, 595, 149–158, <https://doi.org/10.1016/j.scitotenv.2017.03.262>, 2017.
- Yuan, B., Kaser, L., Karl, T., Graus, M., Peischl, J., Campos, T. L., Shertz, S., Apel, E. C., Hornbrook, R. S., Hills, A., Gilman, J. B., Lerner, B. M., Warneke, C., Flocke, F. M., Ryerson, T. B., Guenther, A. B., and de Gouw, J. A.: Airborne flux measurements of methane and volatile organic compounds over the Haynesville and Marcellus shale gas production regions, *Journal of Geophysical Research: Atmospheres*, 120, 6271–6289, <https://doi.org/10.1002/2015JD023242>, 2015.

<https://doi.org/10.5194/egusphere-2023-601>

Preprint. Discussion started: 12 April 2023

© Author(s) 2023. CC BY 4.0 License.



Zhu, Q., Place, B., Pfannerstill, E. Y., Tong, S., Zhang, H., Wang, J., Nussbaumer, C. M., Wooldridge, P., Schulze, B. C., Arata, C., et al.: Direct observations of NO_x emissions over the San Joaquin Valley using airborne flux measurements during RECAP-CA 2021 field campaign, *Atmospheric Chemistry and Physics Discussions*, pp. 1–21, <https://doi.org/10.5194/acp-2023-3>, 2023.

3.8 List of publications

- Nussbaumer, C. M.**, Tadic, I., Dienhart, D., Wang, N., Edtbauer, A., Ernle, L., Williams, J., Obersteiner, F., Gutiérrez-Álvarez, I., Harder, H., Lelieveld, J., and Fischer, H.: Measurement report: In situ observations of deep convection without lightning during the tropical cyclone Florence 2018, *Atmos. Chem. Phys.*, 21, 7933–7945, <https://doi.org/10.5194/acp-21-7933-2021>, **2021**.
- Tadic, I., **Nussbaumer, C. M.**, Bohn, B., Harder, H., Marno, D., Martinez, M., Obersteiner, F., Parchatka, U., Pozzer, A., Rohloff, R., Zöger, M., Lelieveld, J., and Fischer, H.: Central role of nitric oxide in ozone production in the upper tropical troposphere over the Atlantic Ocean and western Africa, *Atmos. Chem. Phys.*, 21, 8195–8211, <https://doi.org/10.5194/acp-21-8195-2021>, **2021**.
- Nussbaumer, C. M.**, Parchatka, U., Tadic, I., Bohn, B., Marno, D., Martinez, M., Rohloff, R., Harder, H., Kluge, F., Pfeilsticker, K., Obersteiner, F., Zöger, M., Doerich, R., Crowley, J. N., Lelieveld, J., and Fischer, H.: Modification of a conventional photolytic converter for improving aircraft measurements of NO₂ via chemiluminescence, *Atmos. Meas. Tech.*, 14, 6759–6776, <https://doi.org/10.5194/amt-14-6759-2021>, **2021**.
- Nussbaumer, C. M.**, Crowley, J. N., Schuladen, J., Williams, J., Hafermann, S., Reiffs, A., Axinte, R., Harder, H., Ernest, C., Novelli, A., Sala, K., Martinez, M., Mallik, C., Tomsche, L., Plass-Dülmer, C., Bohn, B., Lelieveld, J., and Fischer, H.: Measurement report: Photochemical production and loss rates of formaldehyde and ozone across Europe, *Atmos. Chem. Phys.*, 21, 18413–18432, <https://doi.org/10.5194/acp-21-18413-2021>, **2021**.
- Nussbaumer, C. M.**, Pozzer, A., Tadic, I., Röder, L., Obersteiner, F., Harder, H., Lelieveld, J., and Fischer, H.: Tropospheric ozone production and chemical regime analysis during the COVID-19 lockdown over Europe, *Atmos. Chem. Phys.*, 22, 6151–6165, <https://doi.org/10.5194/acp-22-6151-2022>, **2022**.
- Dewald, P., **Nussbaumer, C. M.**, Schuladen, J., Ringsdorf, A., Edtbauer, A., Fischer, H., Williams, J., Lelieveld, J., and Crowley, J. N.: Fate of the nitrate radical at the summit of a semi-rural mountain site in Germany assessed with direct reactivity measurements, *Atmos. Chem. Phys.*, 22, 7051–7069, <https://doi.org/10.5194/acp-22-7051-2022>, **2022**.
- Röder, L. L., Dewald, P., **Nussbaumer, C. M.**, Schuladen, J., Crowley, J. N., Lelieveld, J., and Fischer, H.: Data quality enhancement for field experiments in atmospheric chemistry via sequential Monte Carlo filters, *Atmos. Meas. Tech.*, 16, 1167–1178, <https://doi.org/10.5194/amt-16-1167-2023>, **2023**.
- Zhu, Q., Place, B., Pfannerstill, E. Y., Tong, S., Zhang, H., Wang, J., **Nussbaumer, C. M.**, Wooldridge, P., Schulze, B. C., Arata, C., Bucholtz, A., Seinfeld, J. H., Goldstein, A. H., and Cohen, R. C.: Direct observations of NO_x emissions over the San Joaquin Valley using airborne flux measurements during RECAP-CA 2021 field campaign, *Atmos. Chem. Phys. Discuss.* [preprint], <https://doi.org/10.5194/acp-2023-3>, in review, **2023**.

Nussbaumer, C. M., Place, B. K., Zhu, Q., Pfannerstill, E. Y., Wooldridge, P., Schulze, B. C., Arata, C., Ward, R., Bucholtz, A., Seinfeld, J. H., Goldstein, A. H., and Cohen, R. C.: Measurement report: Airborne measurements of NO_x fluxes over Los Angeles during the RECAP-CA 2021 campaign, *EGUsphere* [preprint], <https://doi.org/10.5194/egusphere-2023-601>, **2023**.

Nussbaumer, C. M., Fischer, H., Lelieveld, J., Pozzer, A.: What controls ozone sensitivity in the upper tropical troposphere?, *EGUsphere* [preprint], <https://doi.org/10.5194/egusphere-2023-816>, **2023**.

4 Supplement

4.1 Supplement of Section 3.2

This chapter provides the Supplement of *Measurement report: In situ observations of deep convection without lightning during the tropical cyclone Florence 2018*, available at:

<https://doi.org/10.5194/acp-21-7933-2021-supplement>

Supplement of Atmos. Chem. Phys., 21, 7933–7945, 2021
<https://doi.org/10.5194/acp-21-7933-2021-supplement>
© Author(s) 2021. CC BY 4.0 License.



Atmospheric
Chemistry
and Physics
Open Access
EGU

Supplement of

Measurement report: In situ observations of deep convection without lightning during the tropical cyclone Florence 2018

Clara M. Nussbaumer et al.

Correspondence to: Clara M. Nussbaumer (clara.nussbaumer@mpic.de)

The copyright of individual parts of the supplement might differ from the article licence.

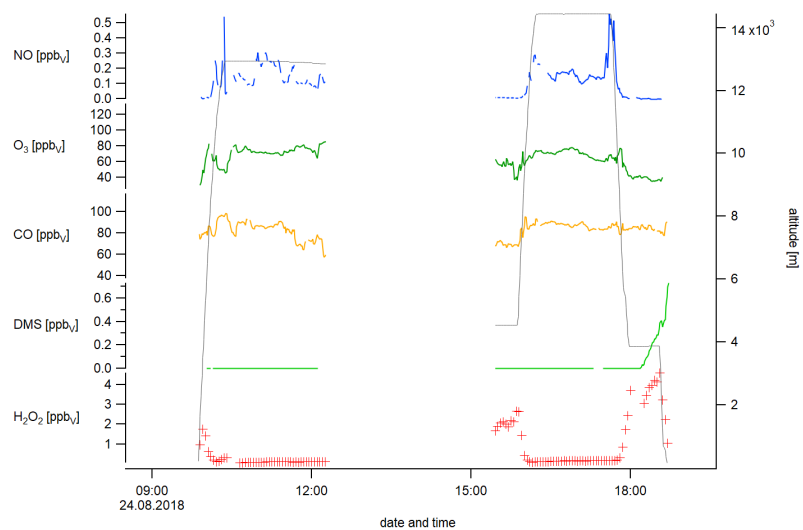


Figure S1. Overview of the temporal development of trace gases during flight MF10 on 24 August 2018.

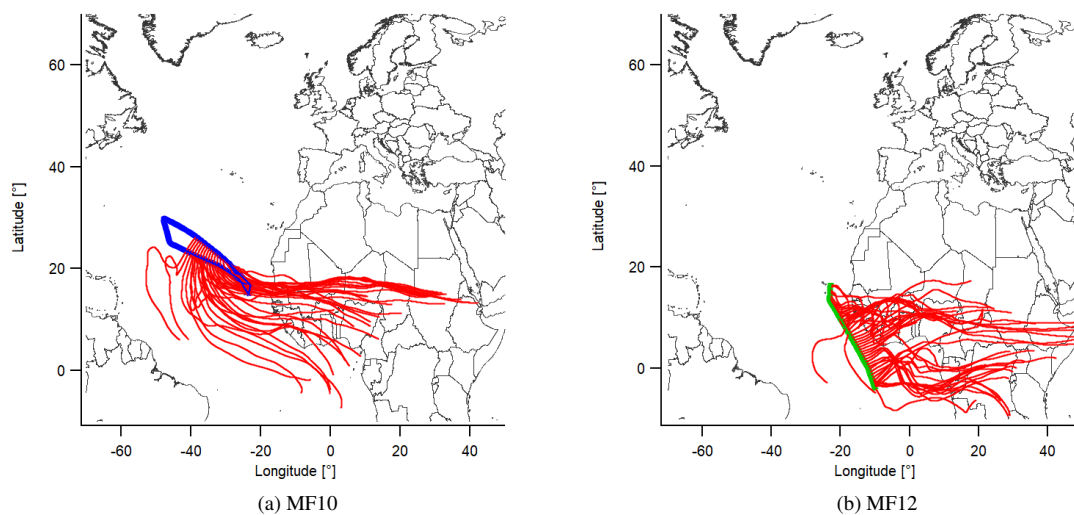


Figure S2. Overview of backward trajectories for MF10 and MF12 which originated from over the African continent where lightning is frequent.

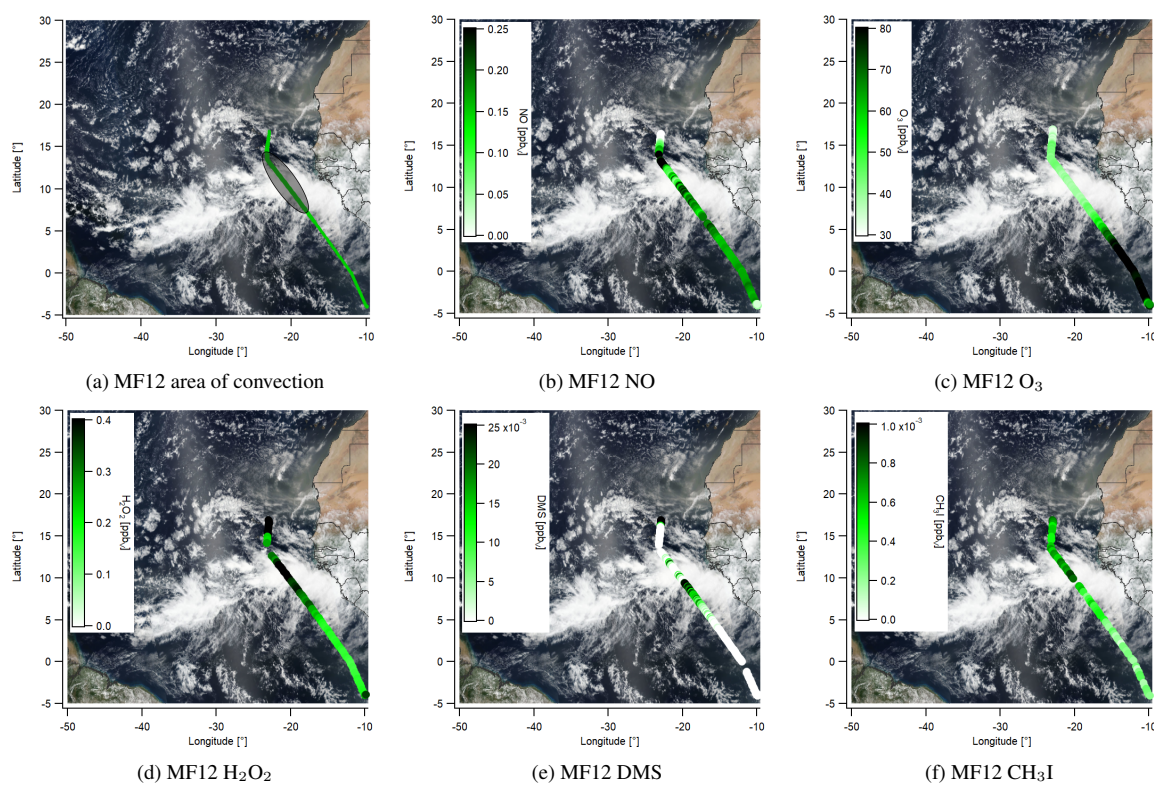


Figure S3. Overview of trace gas concentrations on the flight track of MF12 on 29 August. Out- and inbound flights for MF12 were stacked. Here we show the outbound flight as an example. In the area where we observed deep convection O₃ was reduced and H₂O₂, DMS and CH₃I were elevated. NO was elevated due to lightning. CO is not shown here due to the influence of biomass burning as described in the main text. Background satellite images were obtained from the NASA Worldview application.

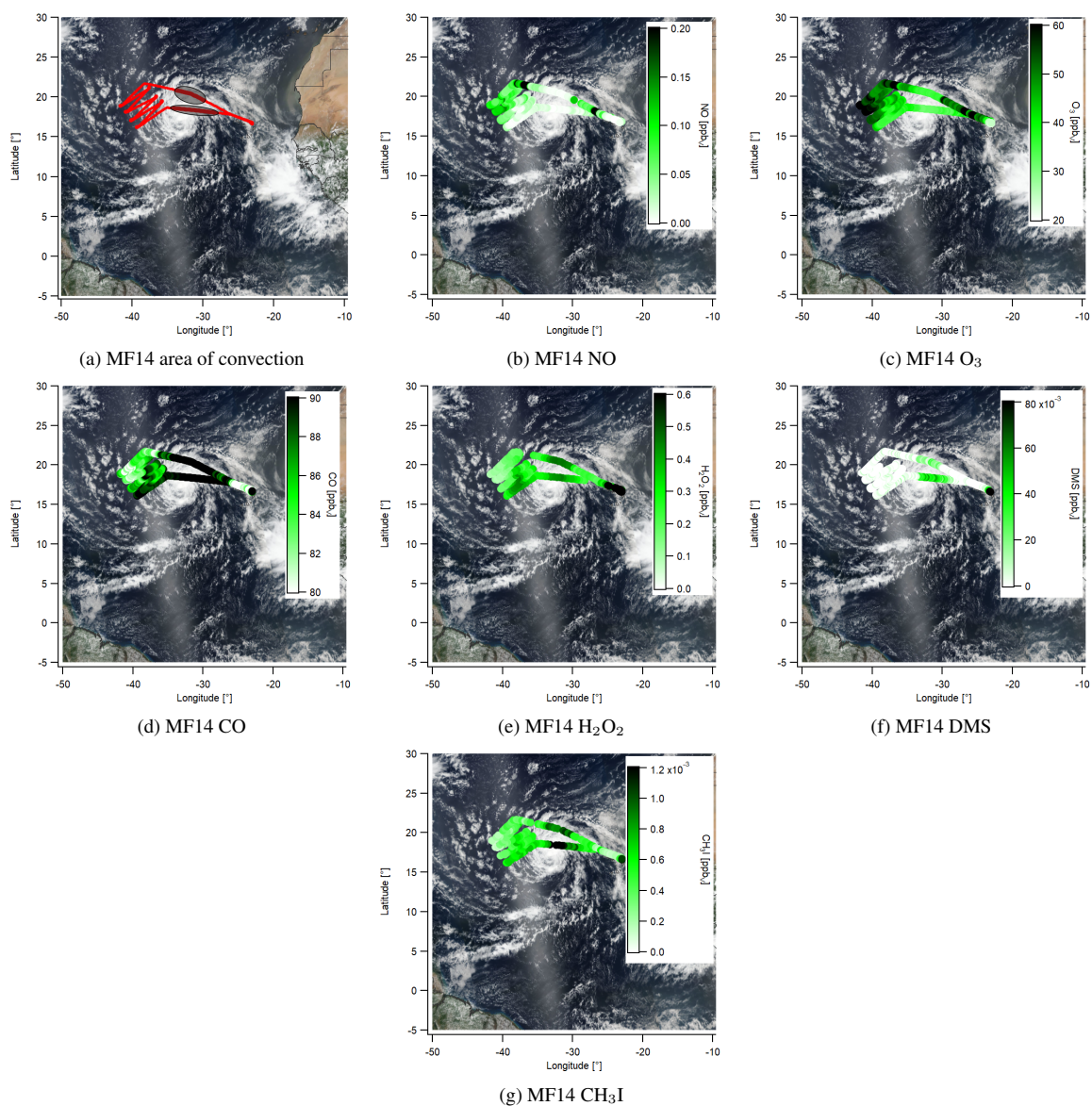


Figure S4. Overview of trace gas concentrations on the flight track of MF14 on 2 September. In the area where we observed deep convection O₃ and NO were reduced while CO, H₂O₂, DMS and CH₃I were elevated. Background satellite images were obtained from the NASA Worldview application.

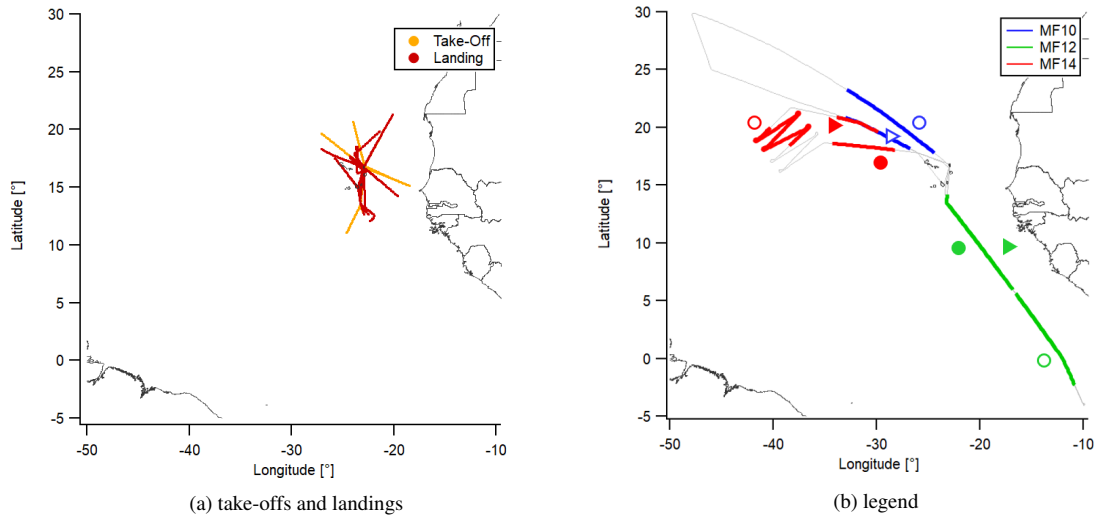


Figure S5. (a) Overview of all take-offs (orange) and landings (red) considered for the background profiles and (b) overview of symbols for the vertical profiles shown in Figure 4 and S7 (b).

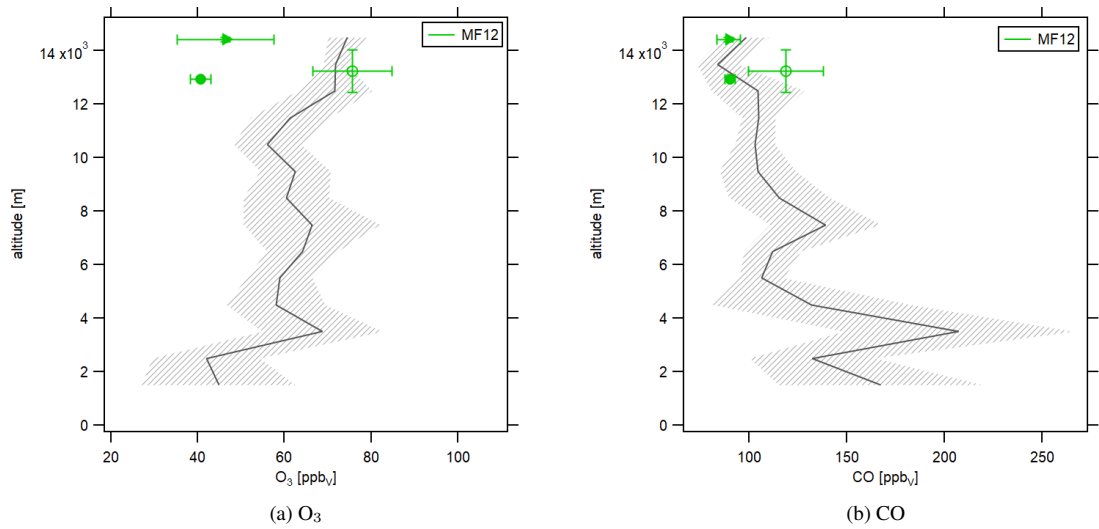


Figure S6. Southern hemisphere (< 5 °N) background profiles for O₃ and CO including MF12 average concentrations (as shown in Figure 4) for comparison.

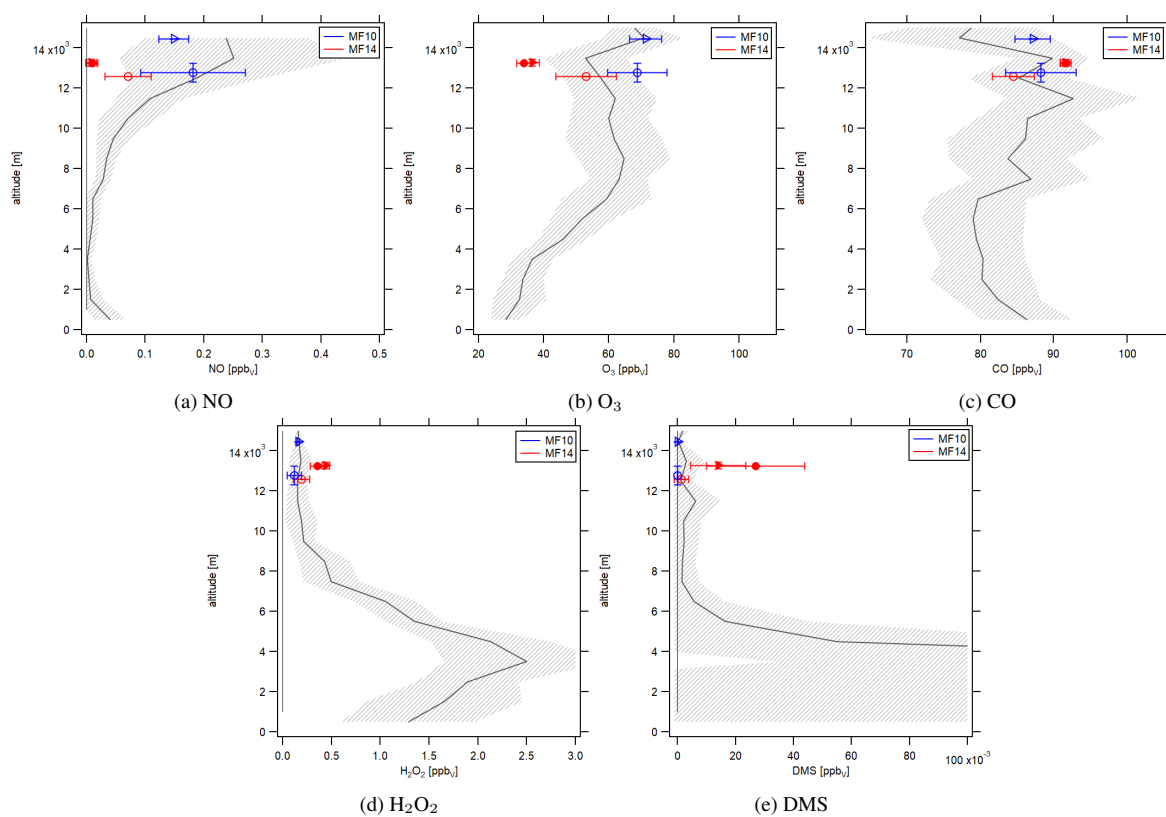
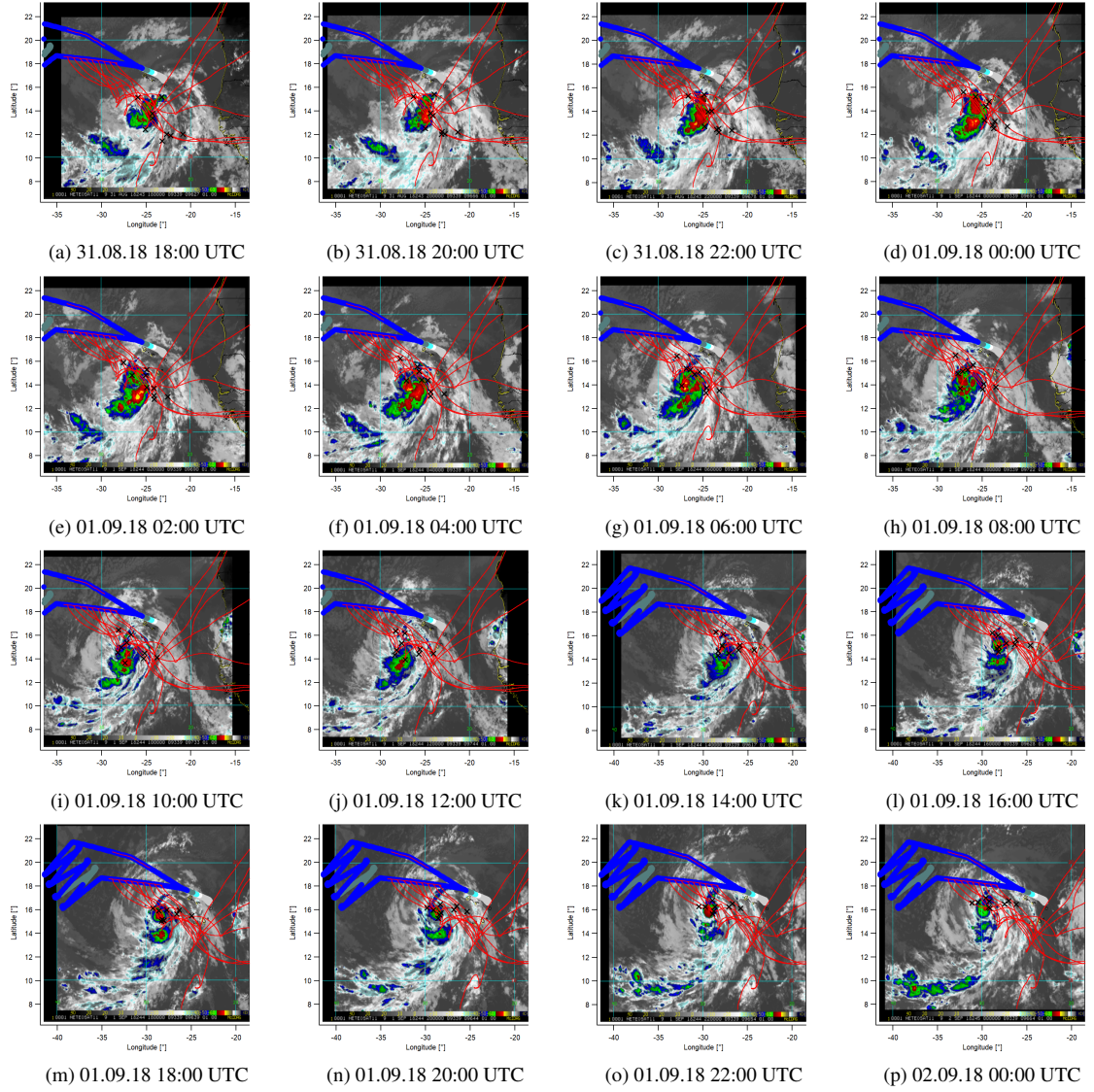


Figure S7. Vertical profiles of background trace gas concentrations during CAFE Africa around Cabo Verde (gray) and average trace gas concentrations for convective (filled symbols) and non-convective (open symbols) areas during MF10 (blue) and MF14 (red). Data on CH₃I are not available for MF10 due to instrumental malfunction.



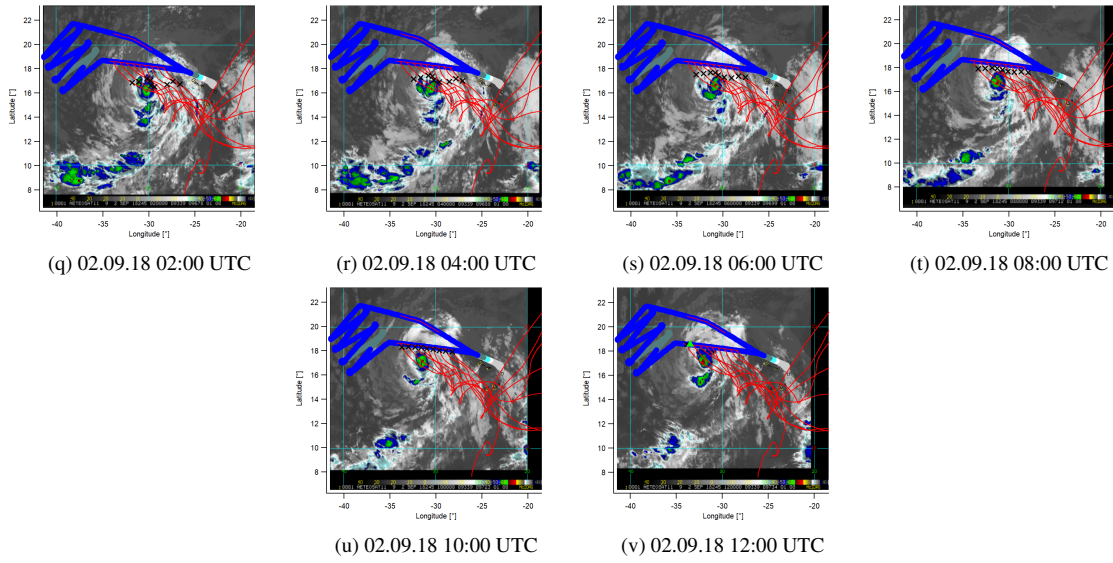
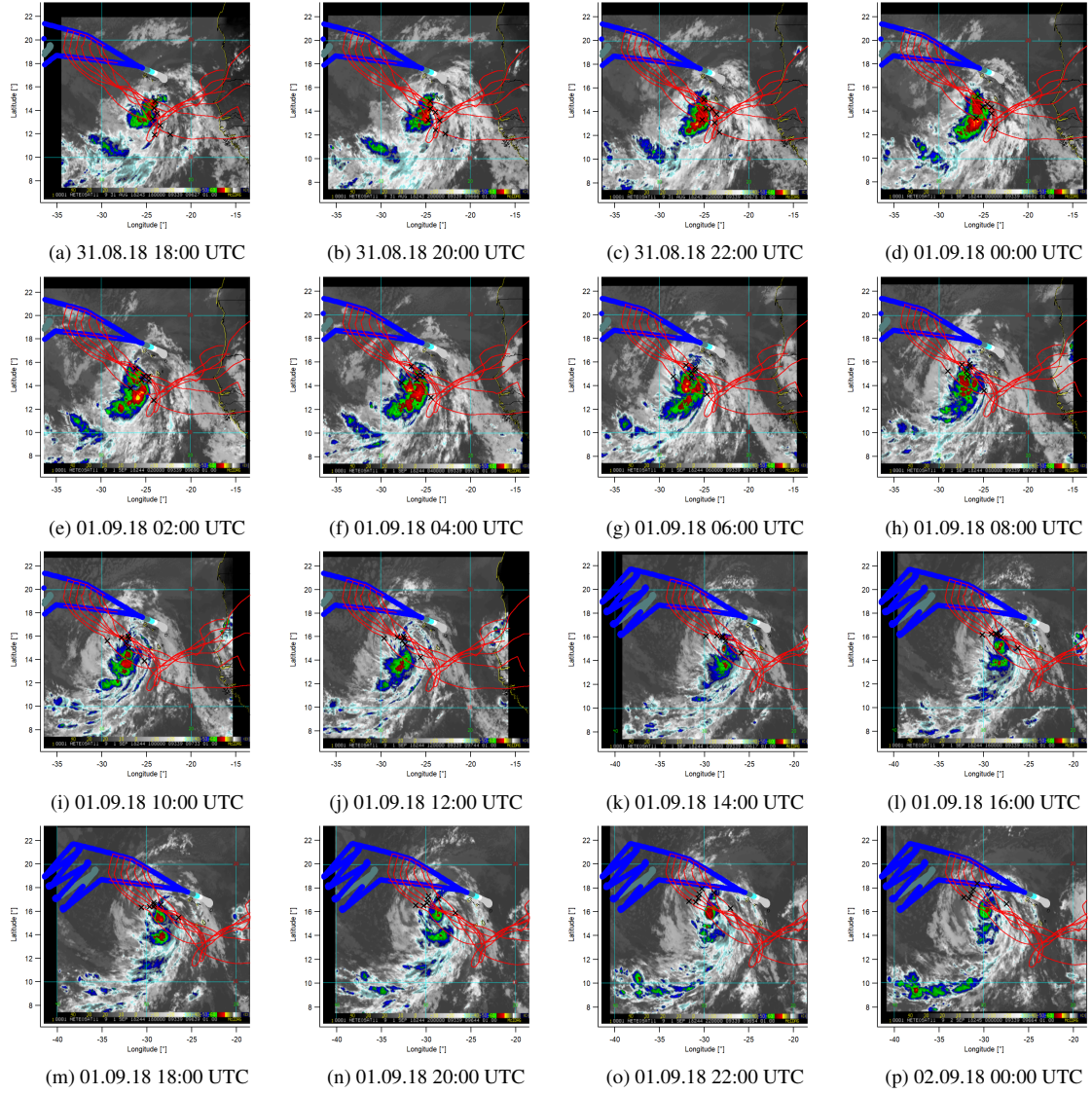


Figure S8. Color enhanced infrared images with flight track and backward trajectories for MF14 from 31.08, 18:00 UTC to 02.09.18 12:00 UTC in 2 h intervals. Black crosses mark the location of each calculated "air parcel" on its backward trajectory at the time of the satellite image. Red lines are the backward trajectories for the air parcels for which we observed convection on the outbound flight. The green triangle marks the current position of the research aircraft. Background satellite IR images were obtained from the TC-Realtime web page maintained by the Cooperative Institute for Research in the Atmosphere, Colorado State University, and NOAA's Center for Satellite Research, Fort Collins Colorado.



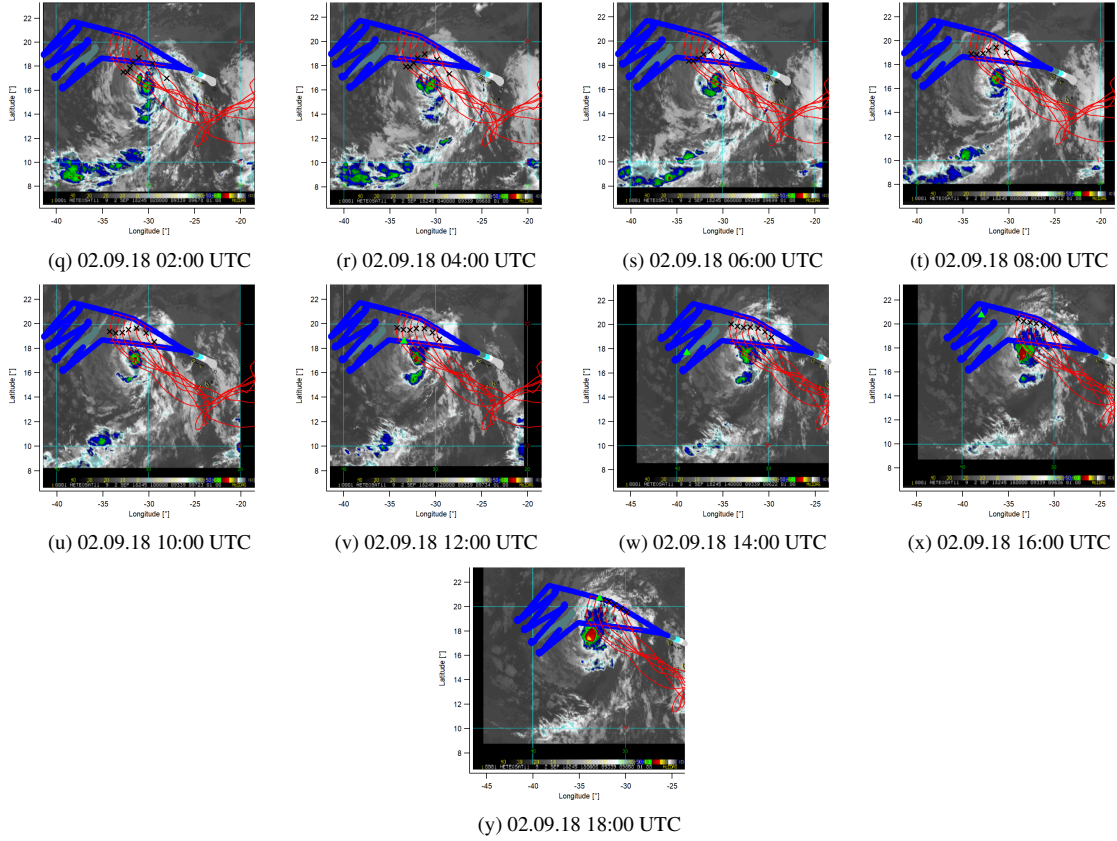
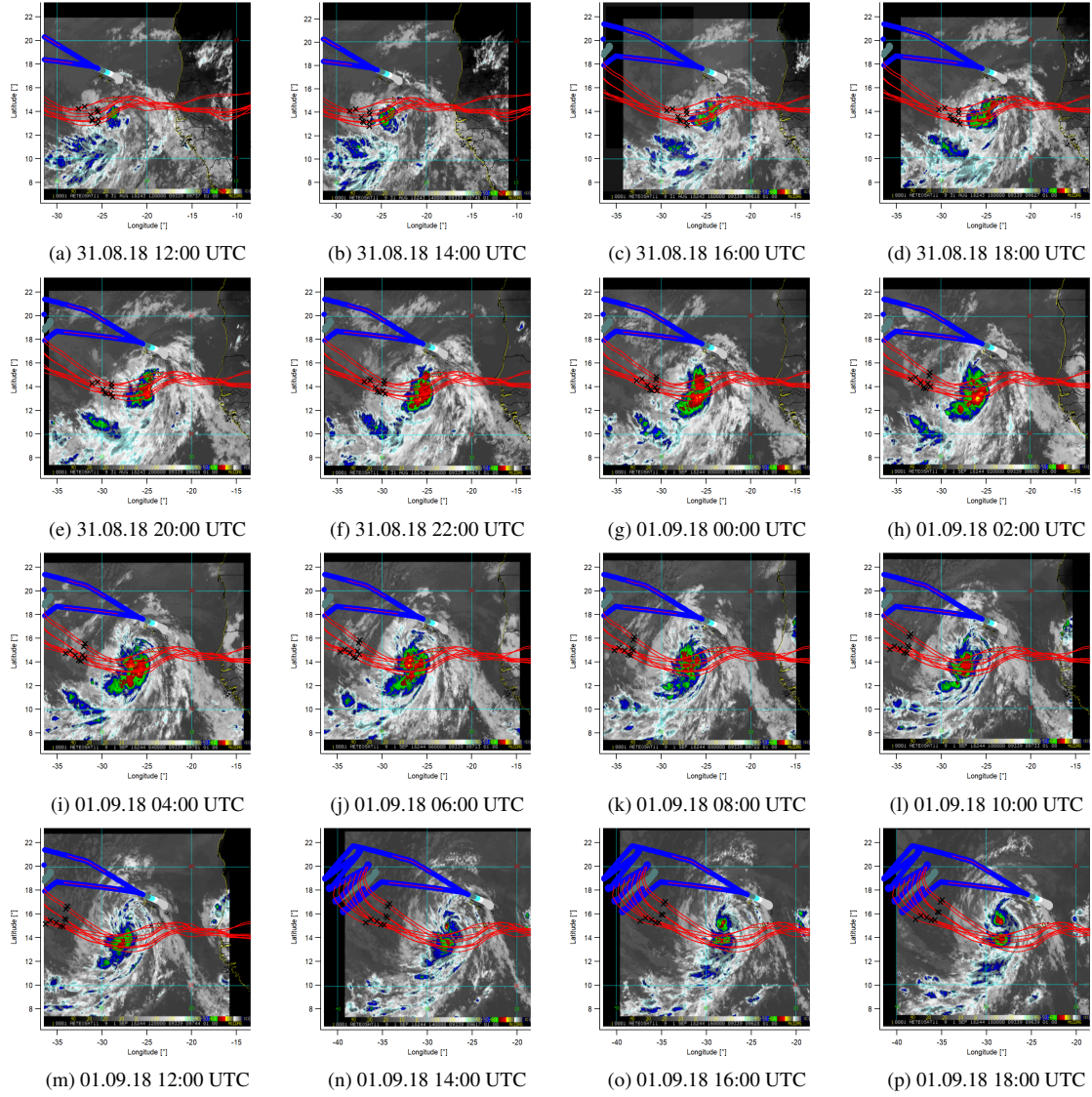


Figure S9. Color enhanced infrared images with flight track and backward trajectories for MF14 from 31.08. 18:00 UTC to 02.09.18 18:00 UTC in 2 h intervals. Black crosses mark the location of each calculated "air parcel" on its backward trajectory at the time of the satellite image. Red lines are the backward trajectories for the air parcels for which we observed convection on the inbound flight. The green triangle marks the current position research aircraft. Background satellite IR images were obtained from the TC-Realtime web page maintained by the Cooperative Institute for Research in the Atmosphere, Colorado State University, and NOAA's Center for Satellite Research, Fort Collins Colorado.



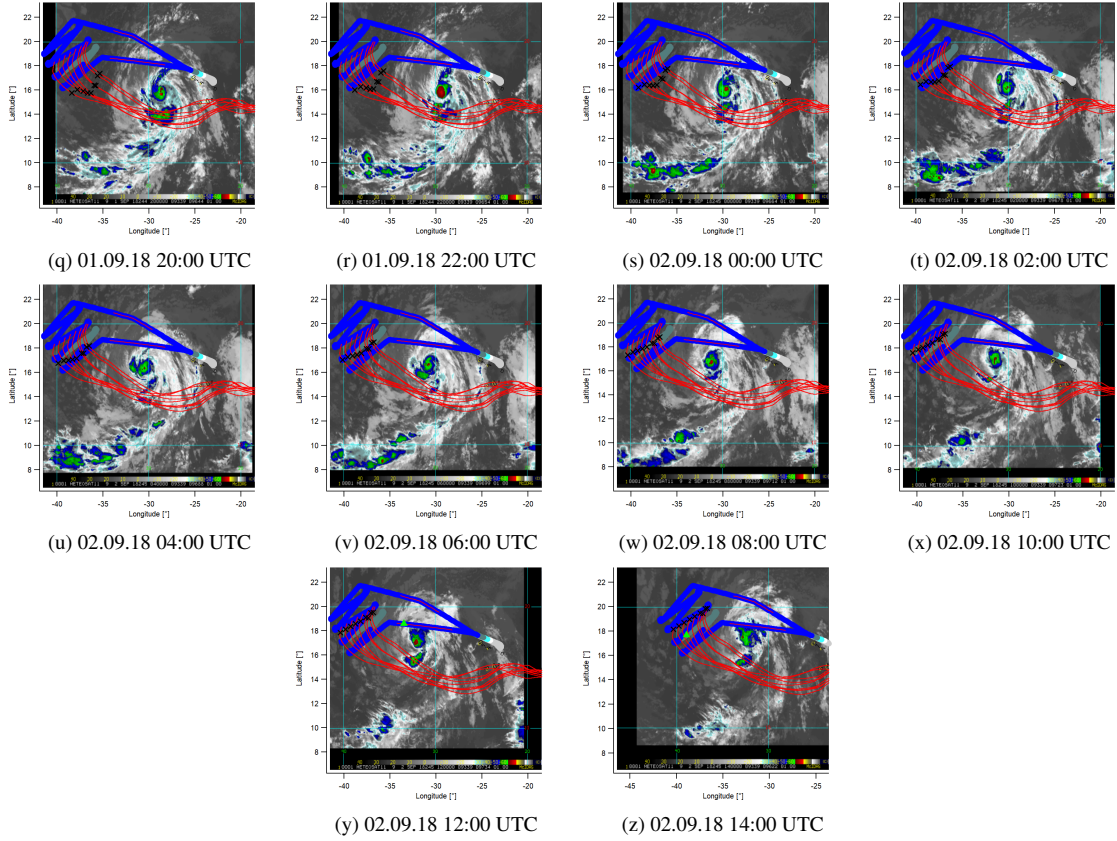


Figure S10. Color enhanced infrared images with flight track and backward trajectories for MF14 from 31.08. 18:00 UTC to 02.09.18 14:00 UTC in 2 h intervals. Black crosses mark the location of each calculated "air parcel" on its backward trajectory at the time of the satellite image. Red lines are the backward trajectories for air parcels for which we did not observe convection. The green triangle marks the current position of the research aircraft. Background satellite IR images were obtained from the TC-Realtime web page maintained by the Cooperative Institute for Research in the Atmosphere, Colorado State University, and NOAA's Center for Satellite Research, Fort Collins Colorado.

4.2 Supplement of Section 3.3

This chapter provides the Supplement of *Modification of a conventional photolytic converter for improving aircraft measurements of NO₂ via chemiluminescence*, available at:

<https://doi.org/10.5194/amt-14-6759-2021-supplement>

Supplement of Atmos. Meas. Tech., 14, 6759–6776, 2021
<https://doi.org/10.5194/amt-14-6759-2021-supplement>
© Author(s) 2021. CC BY 4.0 License.



Atmospheric
Measurement
Techniques

Open Access



Supplement of

Modification of a conventional photolytic converter for improving aircraft measurements of NO₂ via chemiluminescence

Clara M. Nussbaumer et al.

Correspondence to: Clara M. Nussbaumer (clara.nussbaumer@mpic.de)

The copyright of individual parts of the supplement might differ from the article licence.

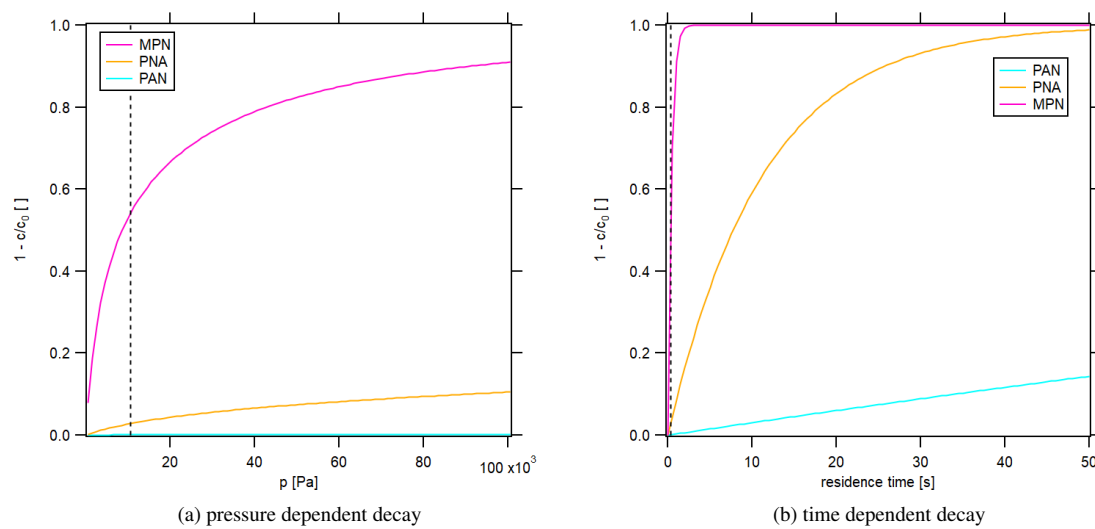


Figure S1. Decay of NO₂ reservoir species in correlation with (a) the pressure and (b) the residence time in the converter.

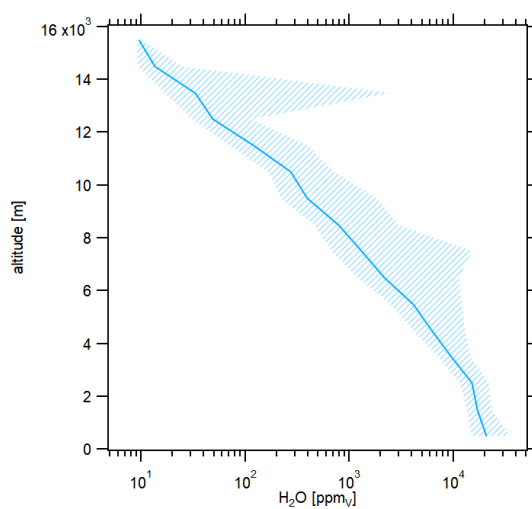


Figure S2. Vertical profile of atmospheric water vapor concentrations.

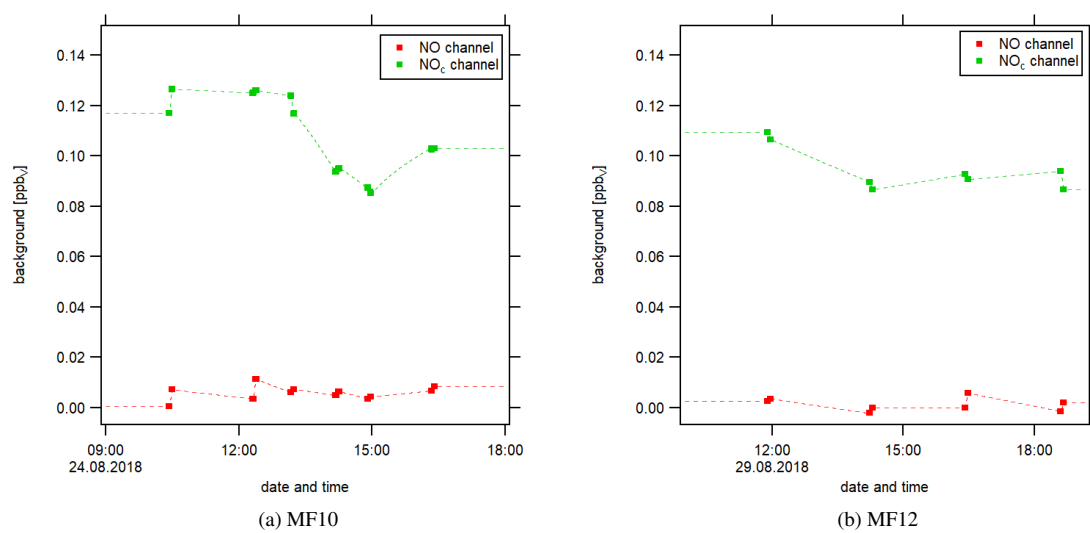
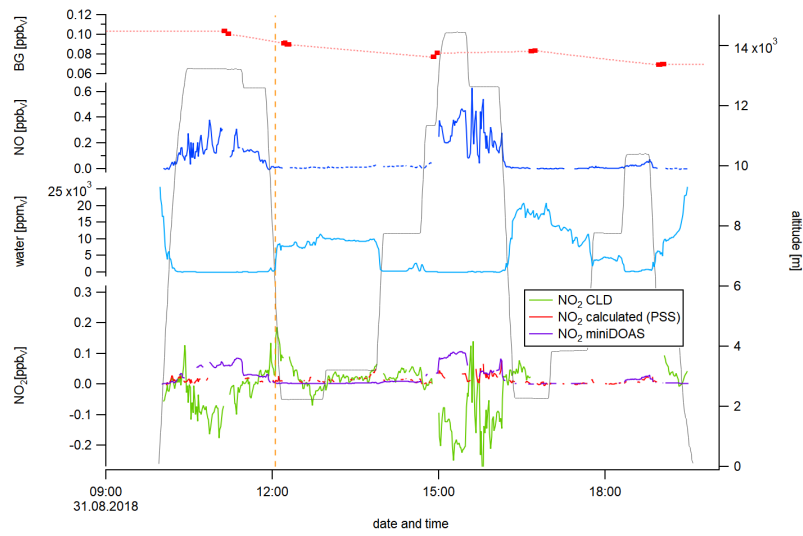
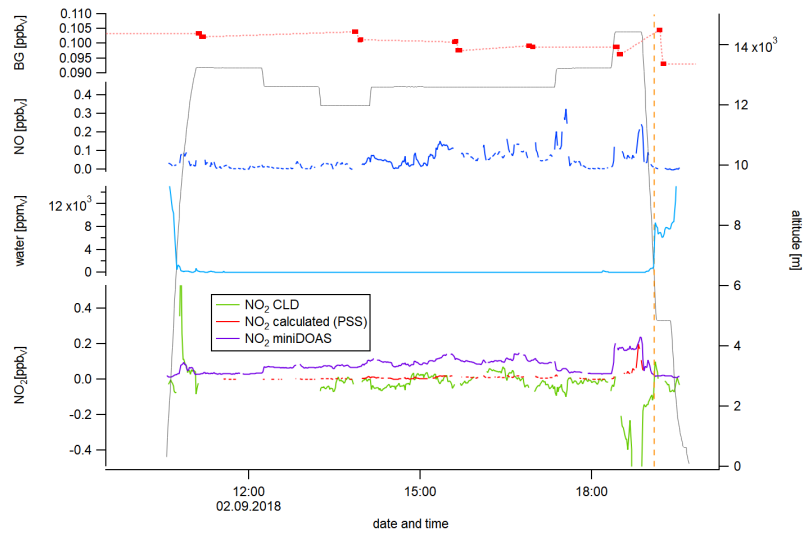


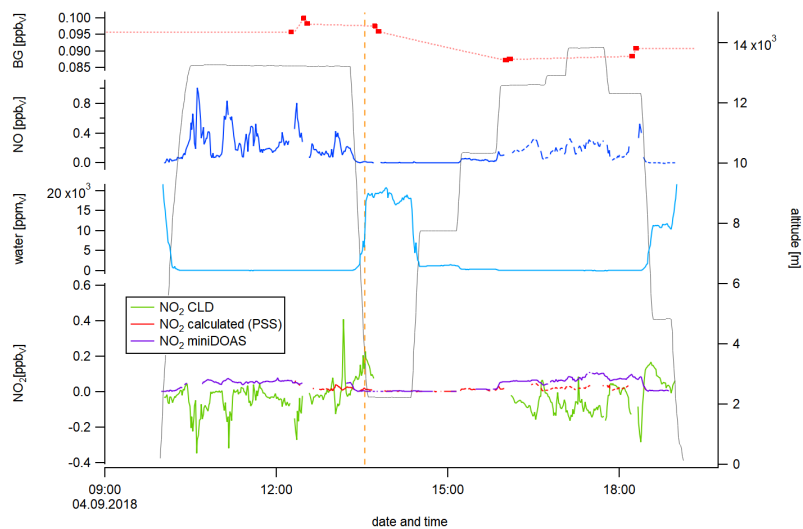
Figure S3. Instrumental background of the NO and the NO_c channel for MF10 and MF12.



(a) MF13



(b) MF14



(c) MF15

Figure S4. Temporal development of NO, water vapor, and calculated and measured NO₂ exemplarily for measurement flights 13, 14 and 15.

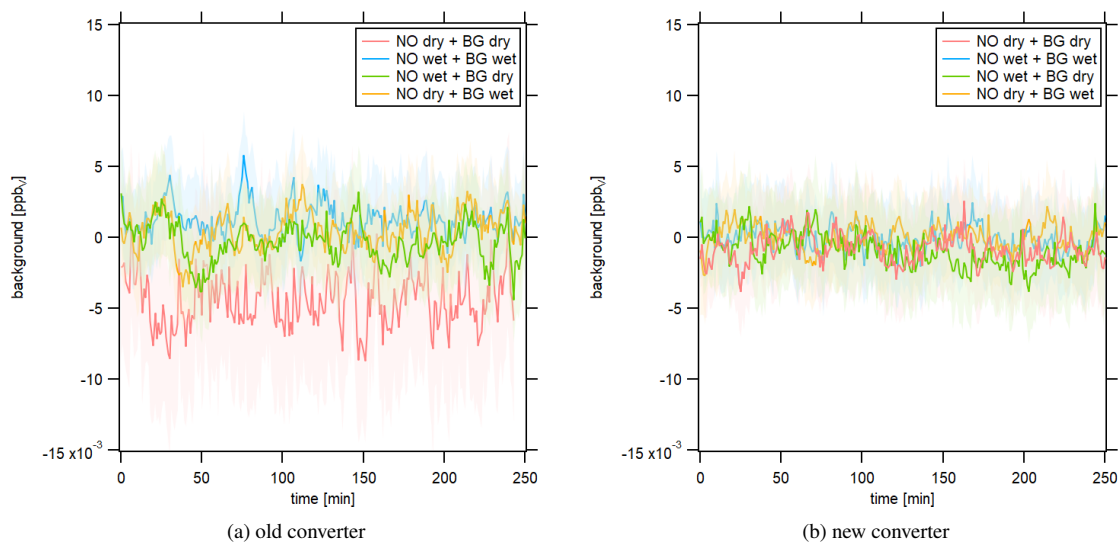


Figure S5. Instrumental background of the first channel in response to dry and humid conditions after 2 h of NO calibration at 15.8 ppbv in analogy to Figure 6 of the manuscript.

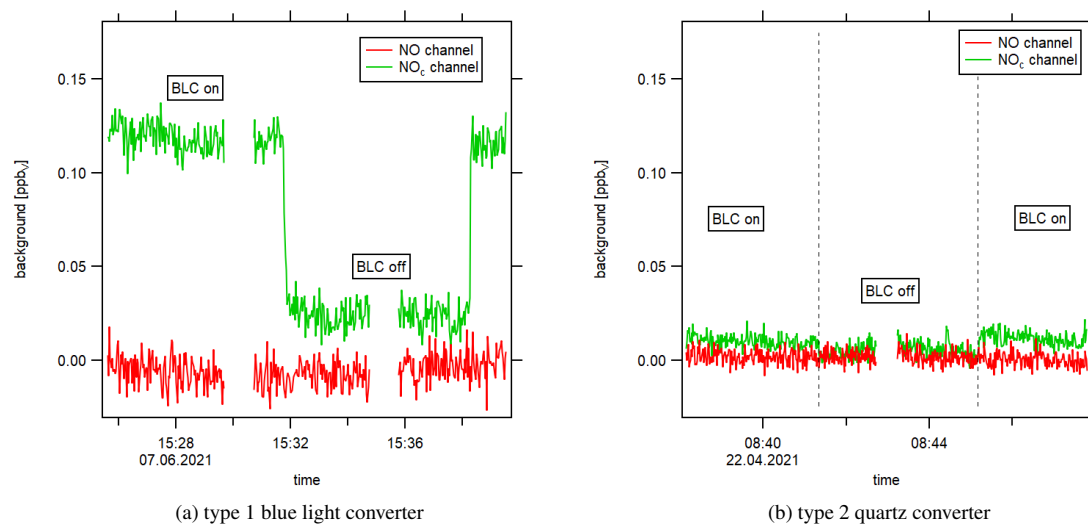


Figure S6. Instrumental background when switching the LEDs in the photolytic converter on and off during zero air measurement.

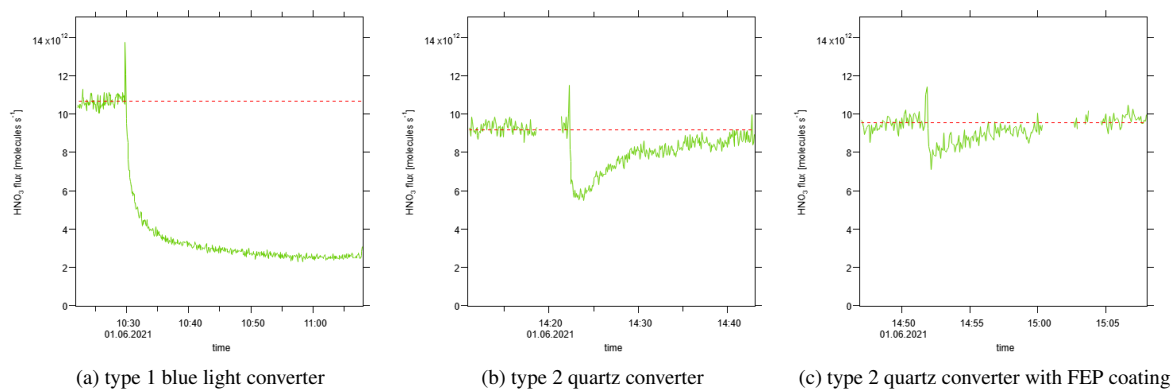


Figure S7. HNO_3 uptake experiment.

4.3 Supplement of Section 3.4

This chapter provides the Supplement of *Measurement report: Photochemical production and loss rates of formaldehyde and ozone across Europe*, available at:

<https://doi.org/10.5194/acp-21-18413-2021-supplement>

Supplement of Atmos. Chem. Phys., 21, 18413–18432, 2021
<https://doi.org/10.5194/acp-21-18413-2021-supplement>
© Author(s) 2021. CC BY 4.0 License.



Atmospheric
Chemistry
and Physics
Open Access
EGU

Supplement of

Measurement report: Photochemical production and loss rates of formaldehyde and ozone across Europe

Clara M. Nussbaumer et al.

Correspondence to: Clara M. Nussbaumer (clara.nussbaumer@mpic.de)

The copyright of individual parts of the supplement might differ from the article licence.

Table S1. Overview of applied rate constants.

rate constant	value / calculation [$\text{cm}^3 \text{ molecule}^{-1} \text{ s}^{-1}$]
$k_{\text{CH}_4+\text{OH}}^1$	$1.85 \times 10^{-12} \times \exp(-1690 \text{ K}/T)$
$k_{\text{CH}_3\text{CHO}+\text{OH}}^1$	$4.7 \times 10^{-12} \times \exp(345 \text{ K}/T)$
$k_{\text{CH}_3\text{OH}+\text{OH}}^1$	$2.85 \times 10^{-12} \times \exp(-345 \text{ K}/T)$
$k_{\text{CH}_3\text{O}_2+\text{NO}}^1$	$2.3 \times 10^{-12} \times \exp(360 \text{ K}/T)$
$k_{\text{CH}_3\text{O}_2+\text{HO}_2}^1$	$3.8 \times 10^{-13} \times \exp(780 \text{ K}/T)$
$k_{\text{CH}_3\text{O}_2+\text{OH}}^1$	$3.7 \times 10^{-11} \times \exp(350 \text{ K}/T)$
$k_{\text{C}_5\text{H}_8(\text{OH})\text{O}_2+\text{NO}}^2$	9.0×10^{-12}
$k_{\text{C}_5\text{H}_8(\text{OH})\text{O}_2+\text{HO}_2}^2$	1.3×10^{-11}
$k_{\text{C}_5\text{H}_8(\text{OH})\text{O}_2+\text{RO}_2}^2$	6.6×10^{-14}
$k_{\text{C}_5\text{H}_8+\text{OH}}^1$	$2.1 \times 10^{-11} \times \exp(465 \text{ K}/T)$
$k_{\text{C}_5\text{H}_8+\text{O}_3}^1$	$1.05 \times 10^{-14} \times \exp(-2000 \text{ K}/T)$
$k_{\text{C}_2\text{H}_4+\text{O}_3}^1$	$6.82 \times 10^{-15} \times \exp(-2500 \text{ K}/T)$
$k_{\text{CH}_3\text{OOH}+\text{OH}}^1$	$5.3 \times 10^{-12} \times \exp(190 \text{ K}/T)$
$k_{\text{DMS}+\text{OH}}^3$	$1.13 \times 10^{-11} \times \exp(-253 \text{ K}/T) + \frac{1.0 \times 10^{-39} \times [\text{O}_2] \times \exp(5820 \text{ K}/T)}{1 + 5.0 \times 10^{-30} \times [\text{O}_2] \times \exp(6280 \text{ K}/T)}$
$k_{\text{HCHO}+\text{OH}}^1$	$5.4 \times 10^{-12} \times \exp(135 \text{ K}/T)$
$k_{\text{O}_3+\text{NO}}^1$	$2.07 \times 10^{-12} \times \exp(-1400 \text{ K}/T)$
$k_{\text{O}_3+\text{OH}}^4$	$1.7 \times 10^{-12} \times \exp(-940 \text{ K}/T)$
$k_{\text{O}_3+\text{HO}_2}^3$	$2.03 \times 10^{-16} \times (T/400 \text{ K})^{4.57} \times \exp(693 \text{ K}/T)$
$k_{\text{O}^1\text{D}+\text{O}_2}^1$	$3.2 \times 10^{-11} \times \exp(67 \text{ K}/T)$
$k_{\text{O}^1\text{D}+\text{N}_2}^1$	$2.15 \times 10^{-11} \times \exp(110 \text{ K}/T)$
$k_{\text{O}^1\text{D}+\text{H}_2\text{O}}^1$	2.14×10^{-10}

¹ IUPAC Task Group; ² Sumner et al., 2001; ³ Atkinson et al., 2004; ⁴ Atkinson et al., 2006;

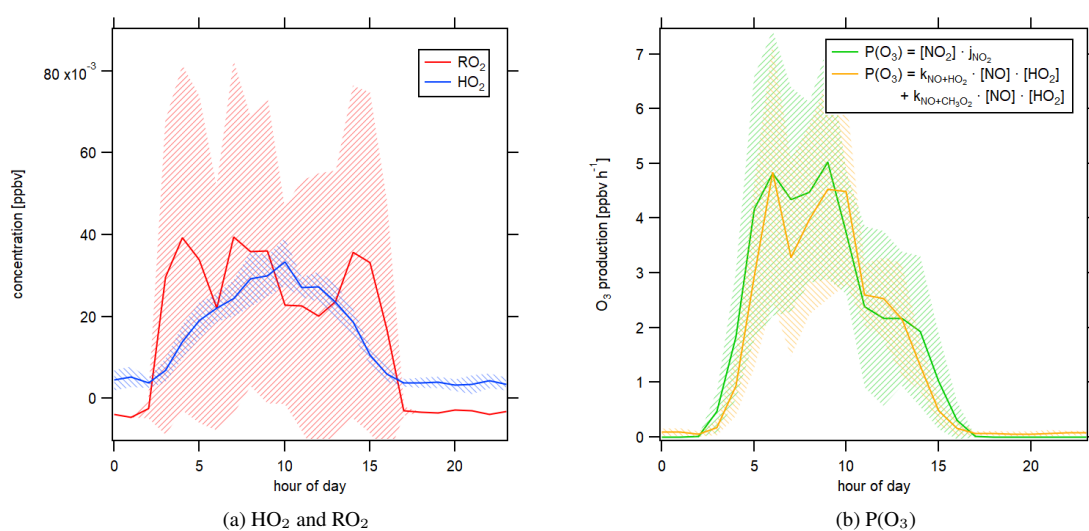


Figure S1. (a) Diurnal profile of HO_2 and calculated RO_2 during CYPHEX through equating $\text{P}(\text{O}_3)$ from NO_2 photolysis and $\text{P}(\text{O}_3)$ from reaction of NO with HO_2 and RO_2 (b) O_3 production calculated via the photolytic reaction of NO_2 , and the reaction of HO_2 and RO_2 with NO , assuming $[\text{HO}_2] = [\text{RO}_2]$. We use the rate constant $k_{\text{NO}+\text{CH}_3\text{O}_2}$ as surrogate for $k_{\text{NO}+\text{RO}_2}$. Both panels show close agreement which justifies the assumption that $[\text{HO}_2] = [\text{RO}_2]$.

Table S2. Coefficients for the calculation of $j(\text{HCHO})$ and $j(\text{CH}_3\text{CHO})$ according to Equation (S1).

species	a_1	a_2 [s]	b_1	b_2 [s]
HCHO	1.719	-1.768×10^4	4.701×10^{-3}	-3.471×10^{-2}
CH ₃ CHO	1.516×10^{-1}	-8.970×10^2	4.567×10^{-5}	1.711×10^{-3}

$$j(\text{species})_{\text{parameter}} = a_1 \times j(\text{O}^1\text{D}) + a_2 \times (j(\text{O}^1\text{D}))^2 + b_1 \times j(\text{NO}_2) + b_2 \times (j(\text{NO}_2))^2 \quad (\text{S1})$$

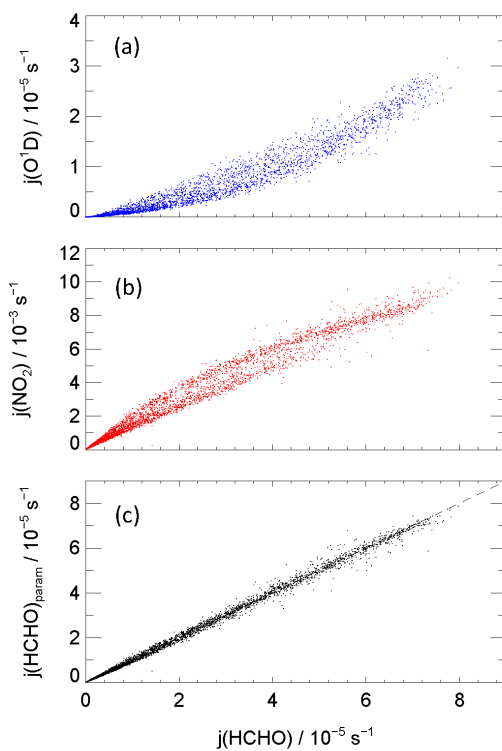
**Figure S2.** Correlations of measured $j(\text{HCHO})$ (molecular plus radical channel) with (a) $j(\text{O}^1\text{D})$ and (b) $j(\text{NO}_2)$ from spectroradiometer measurements. The correlation of measured and parameterized $j(\text{HCHO})$ according to Equation (S1) is shown in panel (c). Only one out of ten data points from the original data set is shown for clarity.

Table S3. Total uncertainties and time resolution of the data used in this study.

trace gas	total uncertainty [%]			time resolution [min]		
	CYPHEX	HOPE	HUMPPA	CYPHEX	HOPE	HUMPPA
NO	20	10	5	5s	1	5
NO ₂	30	10	6	5s	1	5
O ₃	5	5	10	1	1	5
HCHO	16	16	34	10	5	5
CH ₄	2	5	5	1	1	5
OH	28.5	30	30	4	5	10
HO ₂	36	40	40	14s	5	10
C ₂ H ₄	10	-	-	1h	-	-
C ₅ H ₈	14.5	15	15	45	1-4h	5
CH ₃ OH	41	14	20	1	1.5-3h	2h
CH ₃ CHO	27	13	20	1	1.5-3h	30
CH ₃ COCH ₃	17	-	-	1	-	-
DMS	17	-	-	1	-	-
CH ₃ OOH	9	-	-	12	-	-
j(O ¹ D)	10	10	10	10	1	30
j(NO ₂)	10	10	10	10	1	5
j(HCHO)	20	20	20	10	1	5
j(CH ₃ CHO)	20	-	-	10	-	-
j(CH ₃ COCH ₃)	20	-	-	10	-	-
j(CH ₃ OOH)	20	-	-	10	-	-
BLH	-	20	20	-	-	-
v_d	-	54	54	-	-	-

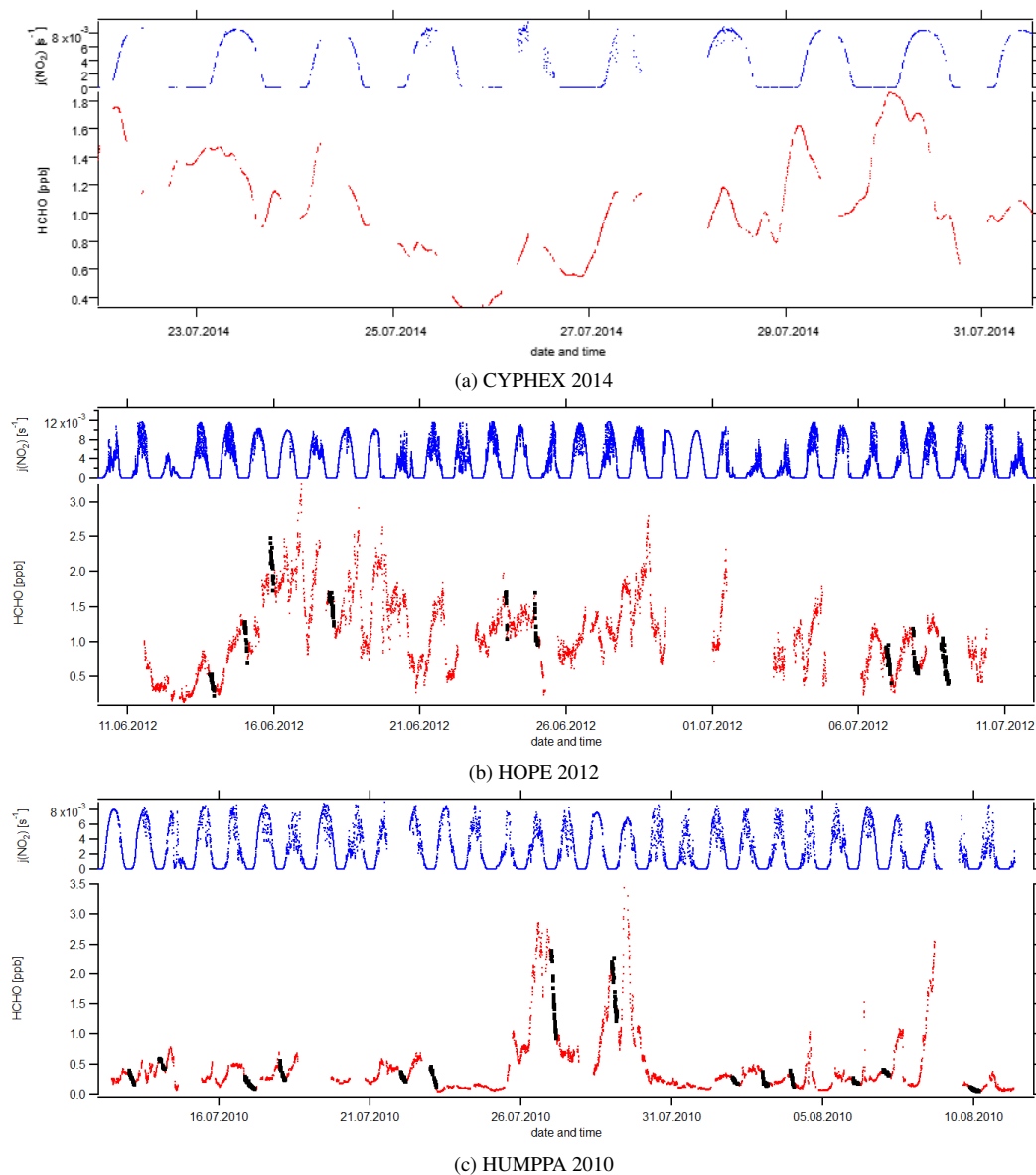


Figure S3. Temporal development of the HCHO concentration and the NO_2 photolysis frequency during each research campaign. For HOPE and HUMPPA, these plots can be used for determining the HCHO deposition velocity at nighttime.

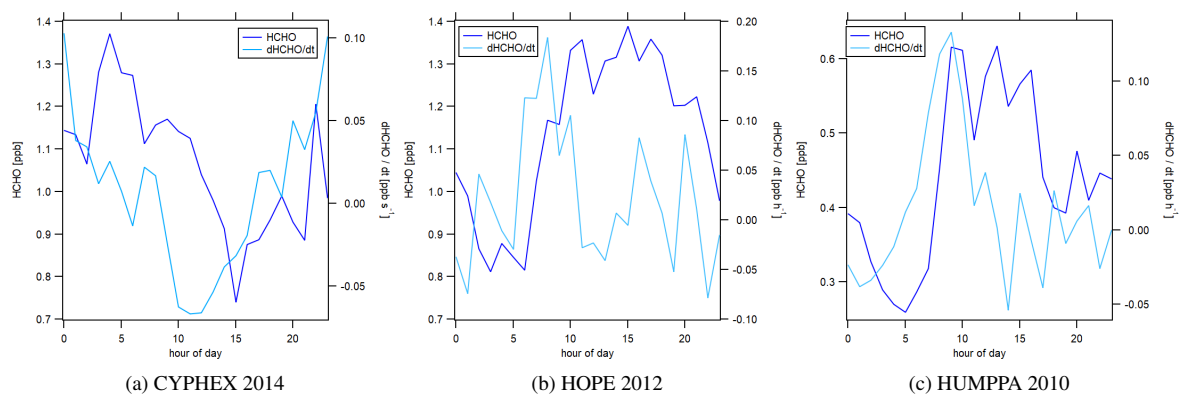
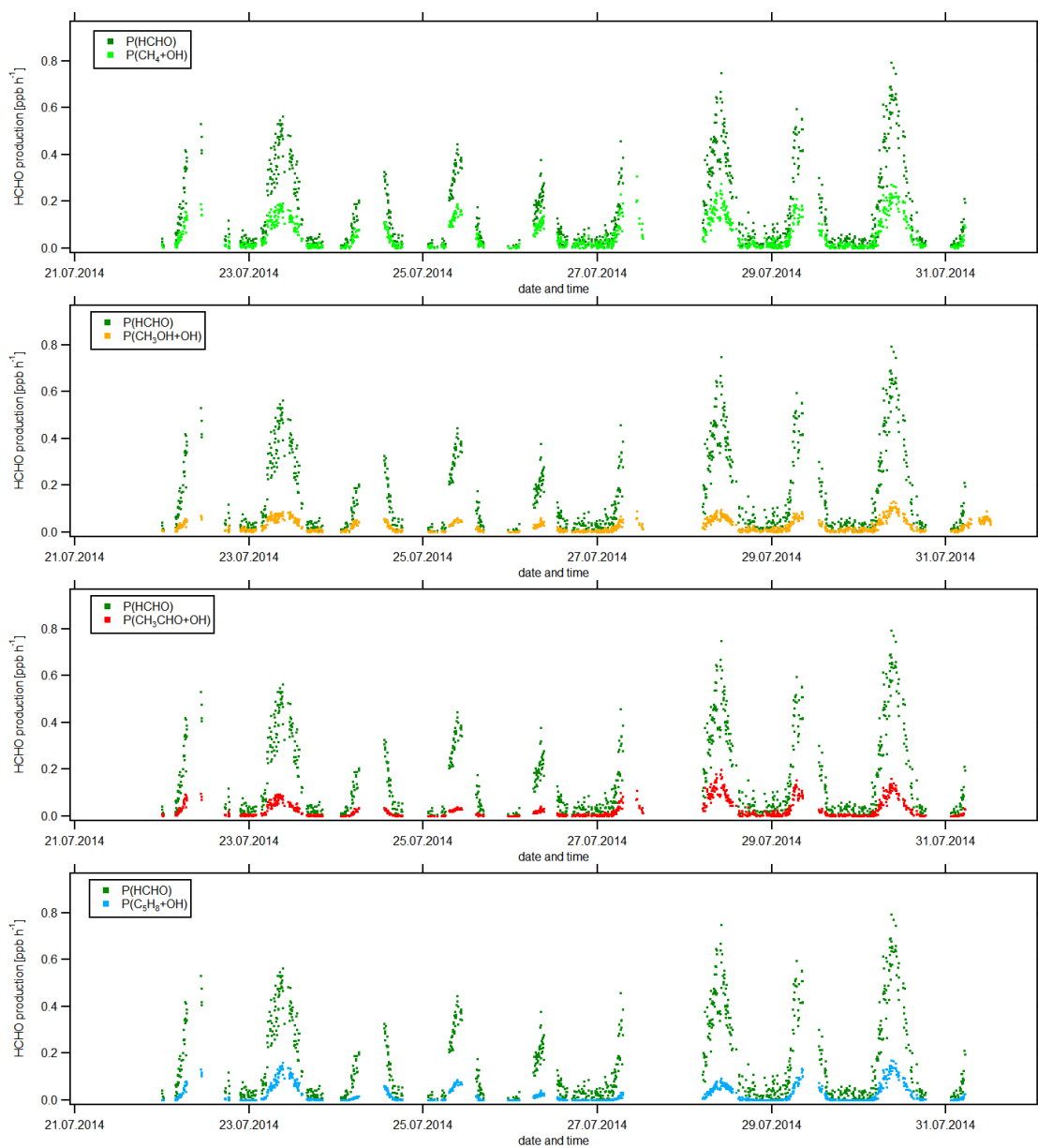
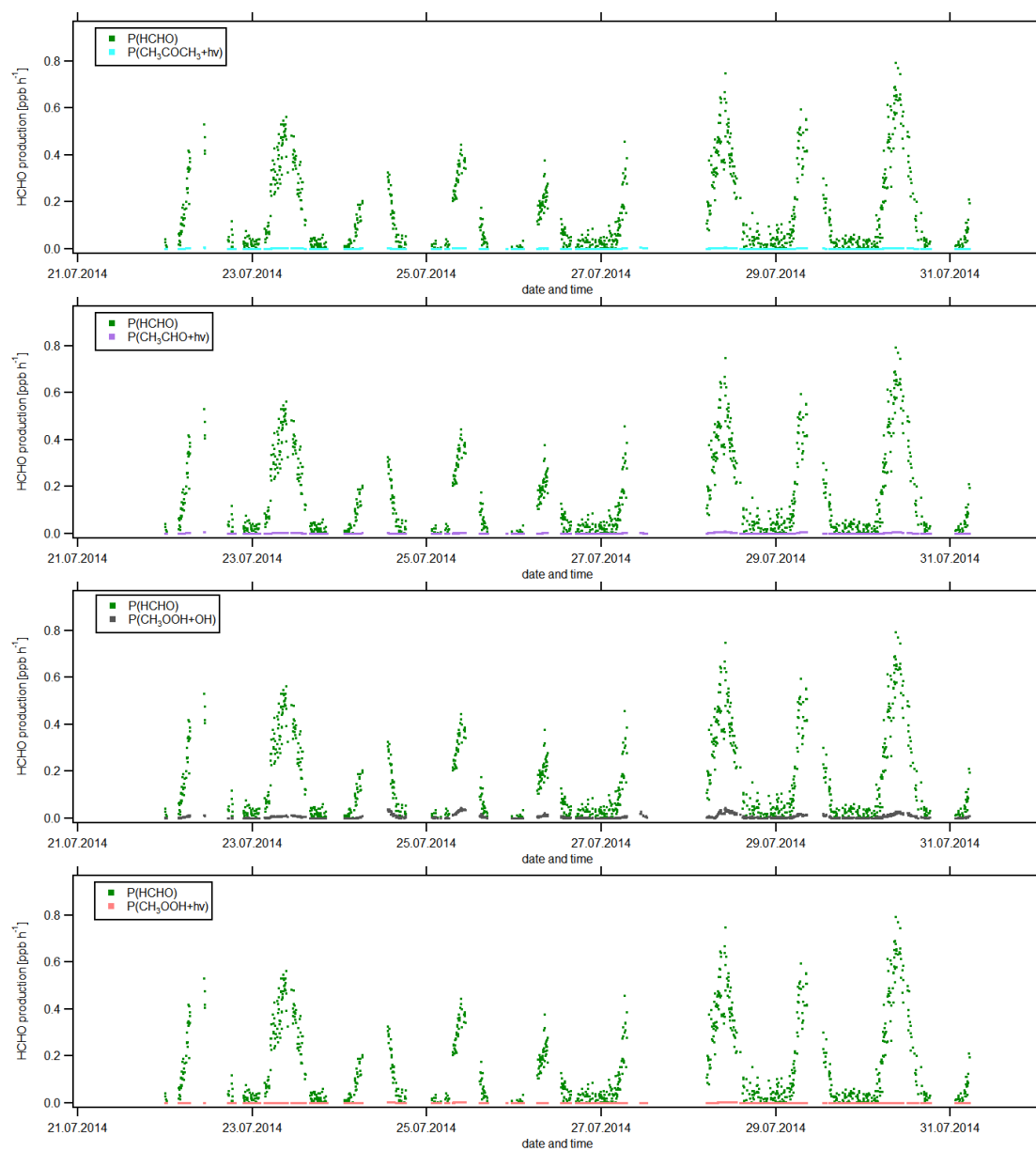


Figure S4. Diurnal average of HCHO concentrations including the rate of change $dHCHO/dt$.





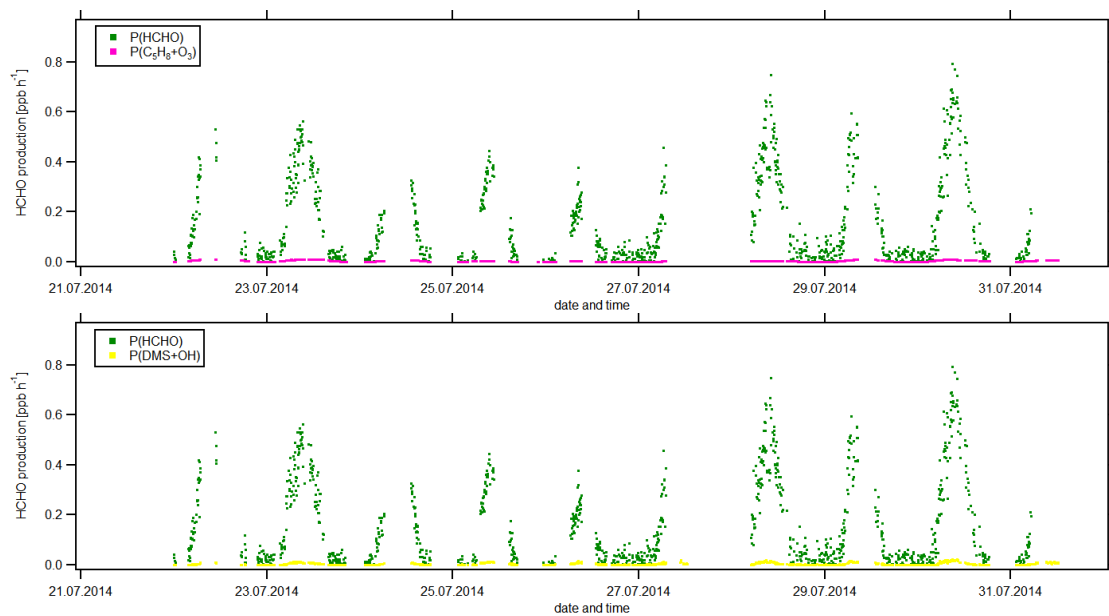


Figure S5. Individual panels of all HCHO production terms.

Table S4. Calculated uncertainties resulting from the measurement uncertainties (MU) and from the atmospheric variability (AV). All uncertainties were calculated via Gaussian error propagation. For CYPHEX, AV1 relates to the point-by-point calculation and AV2 relates to preaveraging and subsequent diurnal calculations. All values are in %. For the atmospheric variability, the number in brackets refers to the all-day average and the number without brackets refers to the daytime average. α_1 is $\alpha_{CH_3O_2}$ and α_2 is α_{CH_3CHO} .

		CYPHEX			HOPE		HUMPPA	
term	calculation	MU	AV1	AV2	MU	AV	MU	AV
HCHO								
P(CH ₄ +OH)	k×[CH ₄]×[OH]×α ₁	29	37 (61)	33 (54)	30	52 (62)	30	49 (49)
P(CH ₃ CHO+OH)	k×[CH ₃ CHO]×[OH]×α ₁ × α ₂	39	57 (79)	50 (67)	33	75 (80)	36	71 (71)
P(CH ₃ OH+OH)	k×[CH ₃ OH]×[OH]	50	41 (60)	39 (59)	33	65 (74)	36	85 (81)
P(C ₅ H ₈ +OH)	k×[C ₅ H ₈]×[OH]× yield	32	55 (71)	54 (71)	34	92 (96)	34	96 (104)
P(HCHO) _{basic}	∑ P _n (basic)	31	40 (61)	22 (34)	31	42 (45)	31	38 (39)
P(HCHO) _{all}	∑ P _n (all)	28	38 (58)	-	-	-	-	-
L(HCHO+OH)	k×[HCHO]×[OH]	33	44 (64)	42 (62)	34	65 (76)	45	113 (118)
L(HCHO+hν)	j(HCHO)×[HCHO]	26	32 (-)	31 (-)	26	59 (-)	39	111 (-)
L(HCHO) deposition	[HCHO]× $\frac{v_d}{BLH}$	-	-	-	63	69 (73)	58	112 (117)
L(HCHO)	∑ L _n	26	34 (57)	25 (52)	34	40 (51)	44	77 (87)
O ₃								
P(NO ₂ +hν)	j(NO ₂)×[NO ₂]	32	59 (-)	57 (-)	14	58 (-)	12	44 (-)
P(O ₃)	P(NO ₂ +hν)	32	59 (-)	57 (-)	14	58 (-)	12	44 (-)
L(O ₃ +NO)	k×[O ₃]×[NO]	21	46 (51)	42 (55)	11	97 (119)	11	63 (93)
L(O ₃ +hν)	j(O ¹ D)×[O ₃]×α	11	32 (-)	30 (-)	11	71 (-)	14	50 (-)
L(O ₃ +OH)	k×[O ₃]×[OH]	29	37 (58)	35 (57)	30	58 (66)	32	53 (54)
L(O ₃ +HO ₂)	k×[O ₃]×[HO ₂]	36	27 (41)	23 (35)	40	57 (55)	41	42 (56)
L(O ₃) deposition	[O ₃]× $\frac{v_d}{BLH}$	-	-	-	21	24 (24)	22	21 (23)
L(O ₃)	∑ L _n	16	37 (44)	35 (49)	10	90 (98)	13	51 (49)

Uncertainty Calculations: We exemplarily present the calculation of the uncertainties of P_{CH_4+OH} in Equations (S1)-(S4) and of $P(HCHO)_{basic}$ in Equations (S5)-(S7) according to gaussian error propagation. All other calculations are accordingly.

10 Example 1:

$$P_{CH_4+OH} = k_{CH_4+OH} \times [CH_4] \times [OH] \times \alpha_{CH_3O_2} \quad (S2)$$

$$\begin{aligned} \Delta P_{CH_4+OH}^2 &= \left(\frac{dP(CH_4+OH)}{d[CH_4]} \right)^2 \times \Delta[CH_4]^2 + \left(\frac{dP(CH_4+OH)}{d[OH]} \right)^2 \times \Delta[OH]^2 \\ &= k_{CH_4+OH}^2 \times [CH_4]^2 \times \alpha_{CH_3O_2}^2 \times \Delta[OH]^2 + k_{CH_4+OH}^2 \times [OH]^2 \times \alpha_{CH_3O_2}^2 \times \Delta[CH_4]^2 \end{aligned} \quad (S3)$$

$$\begin{aligned} \frac{\Delta P_{CH_4+OH}^2}{P_{CH_4+OH}^2} &= \frac{k_{CH_4+OH}^2 \times [CH_4]^2 \times \alpha_{CH_3O_2}^2 \times \Delta[OH]^2 + k_{CH_4+OH}^2 \times [OH]^2 \times \alpha_{CH_3O_2}^2 \times \Delta[CH_4]^2}{k_{CH_4+OH}^2 \times [CH_4]^2 \times [OH]^2 \times \alpha_{CH_3O_2}^2} \\ &= \frac{[CH_4]^2 \times \Delta[OH]^2 + [OH]^2 \times \Delta[CH_4]^2}{[CH_4]^2 \times [OH]^2} \end{aligned} \quad (S4)$$

$$\frac{\Delta P_{CH_4+OH}}{P_{CH_4+OH}} = \sqrt{\frac{\Delta[OH]^2}{[OH]^2} + \frac{\Delta[CH_4]^2}{[CH_4]^2}} \quad (S5)$$

15 Example 2:

$$\begin{aligned} P(HCHO)_{basic} &= P_{CH_4+OH} + P_{CH_3CHO+OH} + P_{CH_3OH+OH} + P_{C_5H_8+OH} \\ &= [OH] \times ([CH_4] \times k_{CH_4+OH} \times \alpha_{CH_3O_2} + [CH_3CHO] \times k_{CH_3CHO+OH} \times \alpha_{CH_3O_2} \times \alpha_{CH_3CHO} \\ &\quad + [CH_3OH] \times k_{CH_3OH+OH} + [C_5H_8] \times k_{C_5H_8+OH} \times \alpha_{Isoprene}) \end{aligned} \quad (S6)$$

$$\begin{aligned} \Delta P(HCHO)_{basic}^2 &= \left(\frac{dP(HCHO)_{basic}}{d[OH]} \right)^2 \times \Delta[OH]^2 + \left(\frac{dP(HCHO)_{basic}}{d[CH_4]} \right)^2 \times \Delta[CH_4]^2 \\ &\quad + \left(\frac{dP(HCHO)_{basic}}{d[CH_3CHO]} \right)^2 \times \Delta[CH_3CHO]^2 + \left(\frac{dP(HCHO)_{basic}}{d[CH_3OH]} \right)^2 \times \Delta[CH_3OH]^2 \\ &\quad + \left(\frac{dP(HCHO)_{basic}}{d[C_5H_8]} \right)^2 \times \Delta[C_5H_8]^2 \\ &= ([CH_4] \times k_{CH_4+OH} \times \alpha_{CH_3O_2} + [CH_3CHO] \times k_{CH_3CHO+OH} \times \alpha_{CH_3O_2} \times \alpha_{CH_3CHO} \\ &\quad + [CH_3OH] \times k_{CH_3OH+OH} + [C_5H_8] \times k_{C_5H_8+OH} \times \alpha_{Isoprene})^2 \times \Delta[OH]^2 \\ &\quad + k_{CH_4+OH}^2 \times \alpha_{CH_3O_2}^2 \times [OH]^2 \times \Delta[CH_4]^2 + k_{CH_3CHO+OH}^2 \times \alpha_{CH_3O_2}^2 \times \alpha_{CH_3CHO}^2 \\ &\quad \times [OH]^2 \times \Delta[CH_3CHO]^2 + k_{CH_3OH+OH}^2 \times [OH]^2 \times \Delta[CH_3OH]^2 \\ &\quad + k_{C_5H_8+OH}^2 \times \alpha_{Isoprene}^2 \times [OH]^2 \times \Delta[C_5H_8]^2 \end{aligned} \quad (S7)$$

$$\begin{aligned}
\frac{\Delta P(HCHO)_{basic}}{P(HCHO)_{basic}} &= \sqrt{\frac{\Delta P(HCHO)_{basic}^2}{P(HCHO)_{basic}^2}} \\
&= \sqrt{\frac{([CH_4] \times k_{CH_4+OH} \times \alpha_{CH_3O_2} + [CH_3CHO] \times k_{CH_3CHO+OH} \times \alpha_{CH_3O_2} \times \alpha_{CH_3CHO} \\
&\quad + [CH_3OH] \times k_{CH_3OH+OH} + [C_5H_8] \times k_{C_5H_8+OH} \times \alpha_{Isoprene})^2 \times \Delta[OH]^2}{+ k_{CH_4+OH}^2 \times \alpha_{CH_3O_2}^2 \times [OH]^2 \times \Delta[CH_4]^2 + k_{CH_3CHO+OH}^2 \times \alpha_{CH_3O_2}^2 \times \alpha_{CH_3CHO}^2 \times [OH]^2 \\
&\quad \times \Delta[CH_3CHO]^2 + k_{CH_3OH+OH}^2 \times [OH]^2 \times \Delta[CH_3OH]^2 + k_{C_5H_8+OH}^2 \times \alpha_{Isoprene}^2 \times [OH]^2)}} \\
&\quad \times \Delta[C_5H_8]^2 \times \frac{1}{(P_{CH_4+OH} + P_{CH_3CHO+OH} + P_{CH_3OH+OH} + P_{C_5H_8+OH})^2}} \tag{S8}
\end{aligned}$$

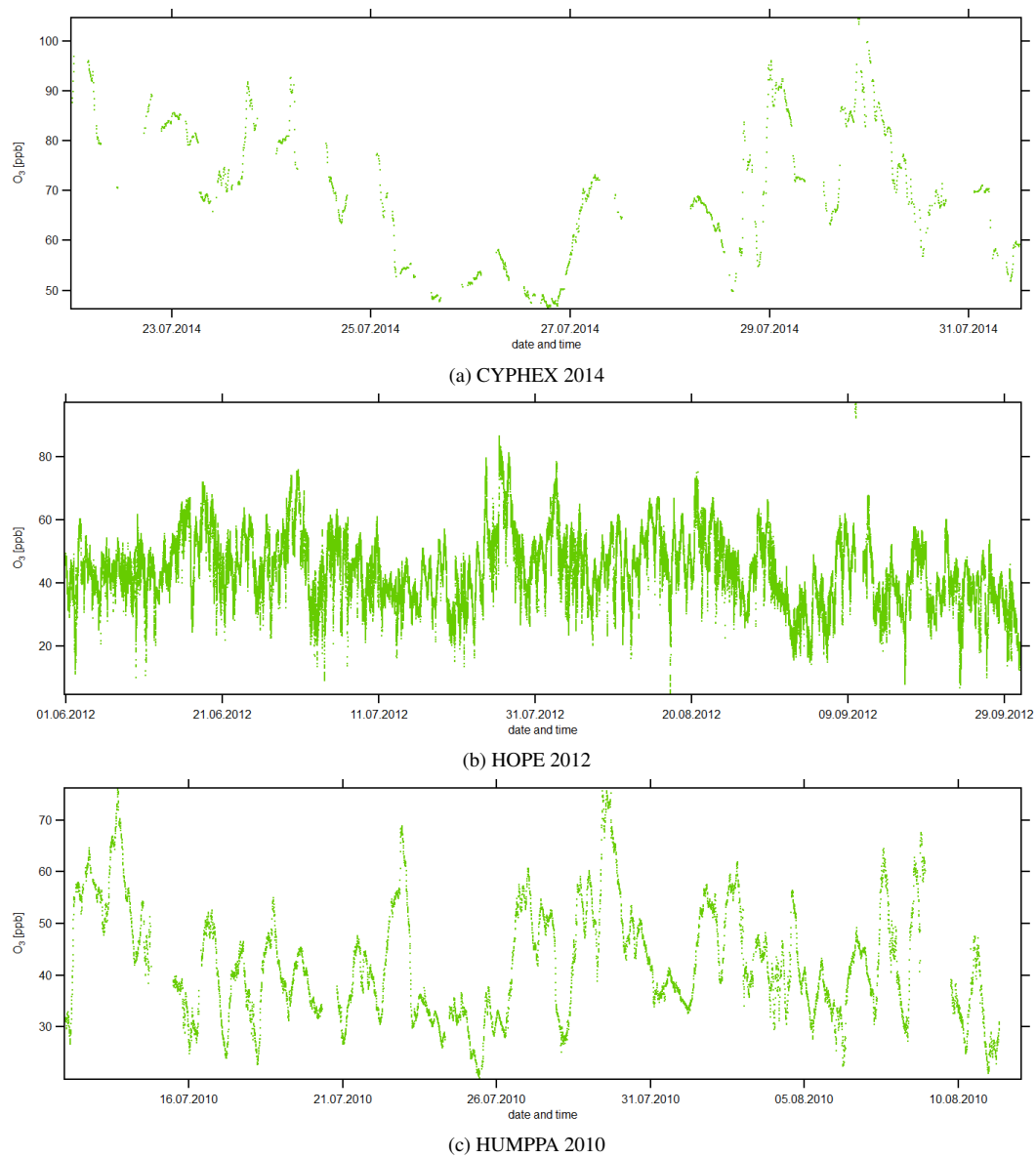


Figure S6. Temporal development of the O_3 concentration in the scope of each research campaign.

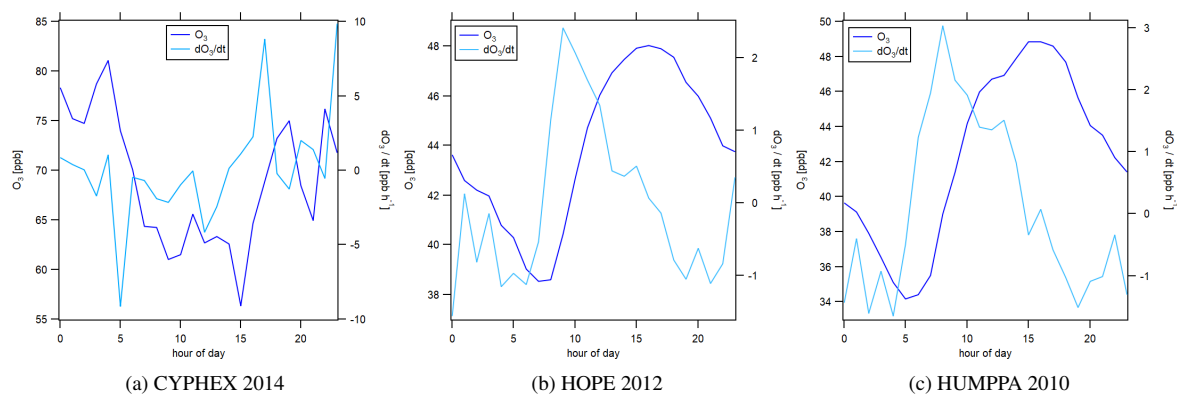


Figure S7. Diurnal average of O_3 concentrations including the rate of change dO_3/dt .

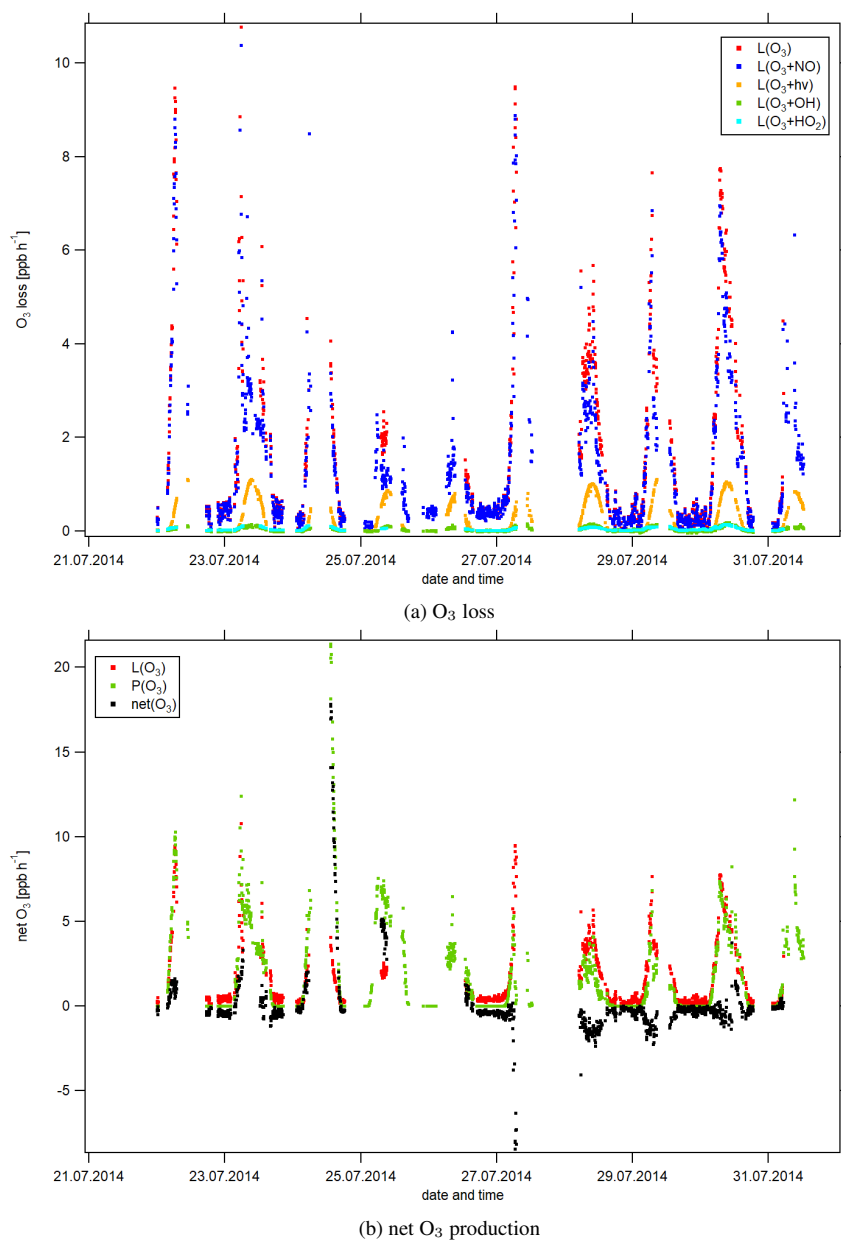


Figure S8. Temporal development of O₃ production and loss terms from July 22 to July 31, 2014 during the research campaign CYPHEX in Cyprus.

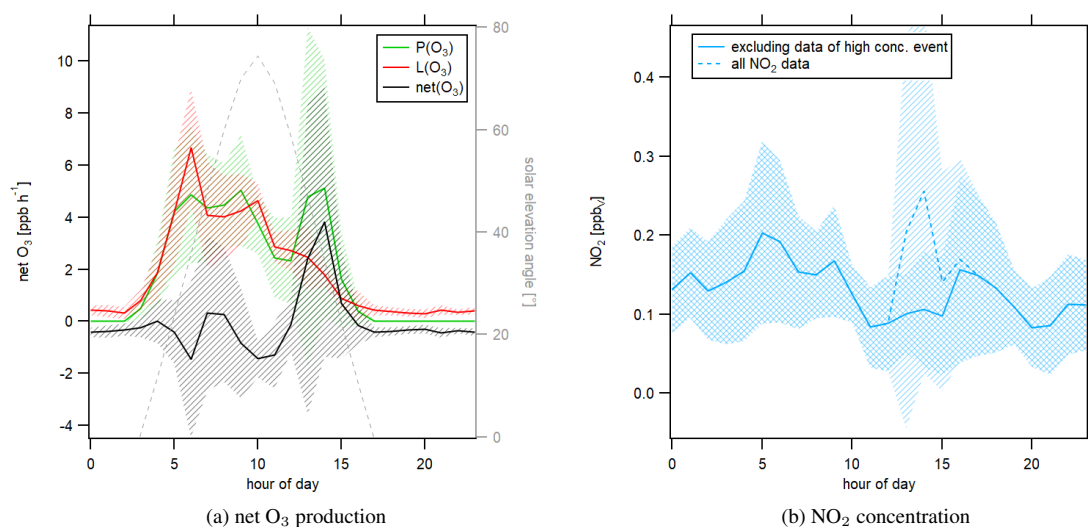


Figure S9. (a) Diurnal O₃ production and loss during CYPHEX, including all data points. (b) Diurnal NO₂ concentrations with and without afternoon peak caused by a singular high concentration event on July 24 (13:15 - 16.15 UTC).

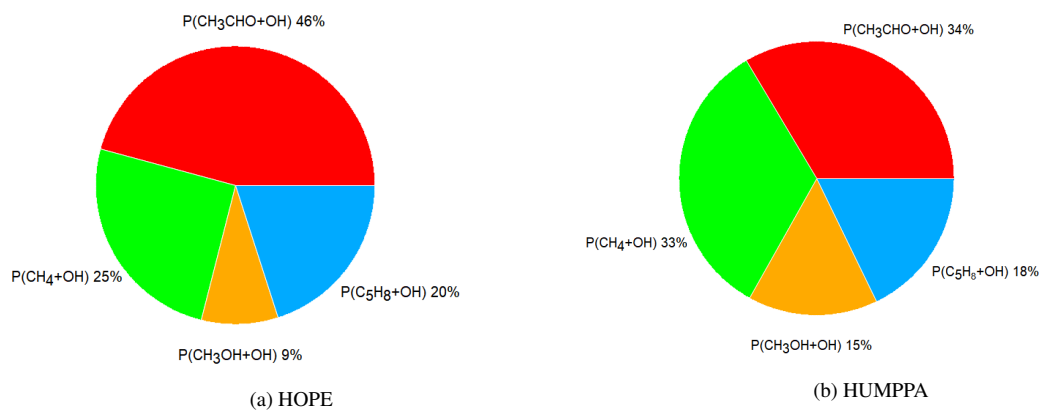


Figure S10. Chemical production terms of HCHO during (a) HOPE and (b) HUMPPA.

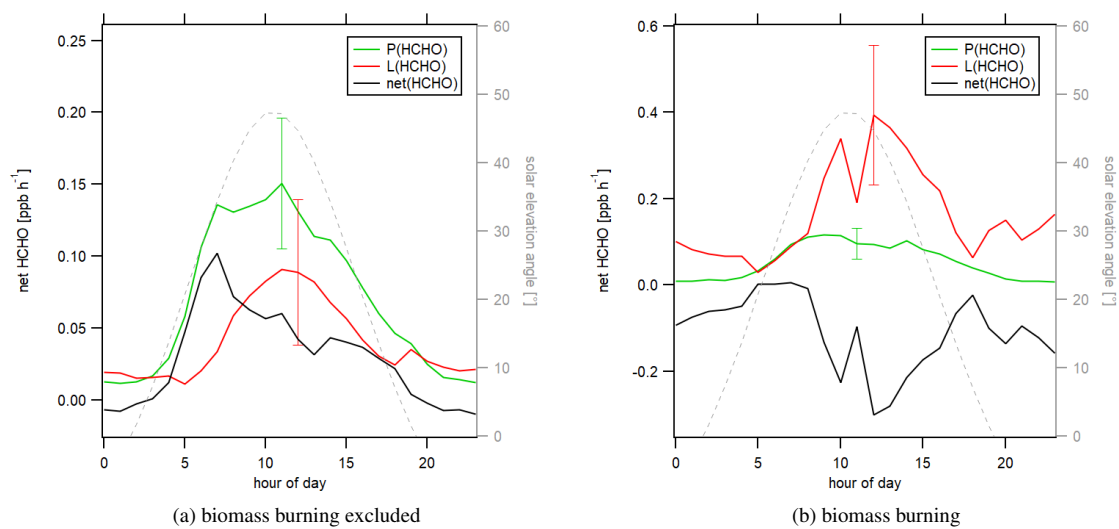


Figure S11. Diurnal HCHO production and loss during HUMPPA (a) considering only data which were impacted by biomass burning (BB) and (b) excluding data with BB impact.

4.4 Supplement of Section 3.5

This chapter provides the Supplement of *Tropospheric ozone production and chemical regime analysis during the COVID-19 lockdown over Europe*, available at:

<https://doi.org/10.5194/acp-22-6151-2022-supplement>

Supplement of Atmos. Chem. Phys., 22, 6151–6165, 2022
<https://doi.org/10.5194/acp-22-6151-2022-supplement>
© Author(s) 2022. CC BY 4.0 License.



Atmospheric
Chemistry
and Physics
Open Access
EGU

Supplement of

Tropospheric ozone production and chemical regime analysis during the COVID-19 lockdown over Europe

Clara M. Nussbaumer et al.

Correspondence to: Clara M. Nussbaumer (clara.nussbaumer@mpic.de)

The copyright of individual parts of the supplement might differ from the article licence.

Table S1. Number of data points averaged per altitude bin for the HOOVER experimental values.

altitude [m]	NO	O ₃	CO	HO ₂	OH	CH ₄	CH ₃ O ₂	j(NO ₂)	j(O ¹ D)	P(O ₃)
0 - 1000	5	10	10	5	4	8	4	10	10	3
1000 - 2000	11	20	15	18	17	15	14	19	19	10
2000 - 3000	3	8	4	7	6	4	3	8	7	2
3000 - 4000	5	7	5	6	5	4	3	7	7	2
4000 - 5000	4	8	5	6	6	5	4	8	8	3
5000 - 6000	7	10	9	9	8	9	8	9	9	6
6000 - 7000	10	18	12	16	14	11	10	18	18	7
7000 - 8000	20	31	27	29	28	27	26	31	31	19
8000 - 9000	48	62	47	61	46	47	45	62	62	37
9000 - 10000	21	40	30	24	31	30	15	33	33	12
10000 - 11000	7	17	7	18	18	7	7	18	18	7
11000 - 12000	3	6	3	6	6	3	3	6	6	3

Table S2. Number of data points averaged per altitude bin for the model values. The number is identical for all species and calculations.

altitude [m]	HOOVER	UTOPIHAN	BLUESKY
0 - 1000	10	19	71
1000 - 2000	20	36	50
2000 - 3000	8	11	35
3000 - 4000	7	16	24
4000 - 5000	8	9	53
5000 - 6000	10	16	32
6000 - 7000	18	16	14
7000 - 8000	31	32	21
8000 - 9000	63	68	29
9000 - 10000	40	78	52
10000 - 11000	18	32	64
11000 - 12000	6	10	42
12000 - 13000	1	9	24

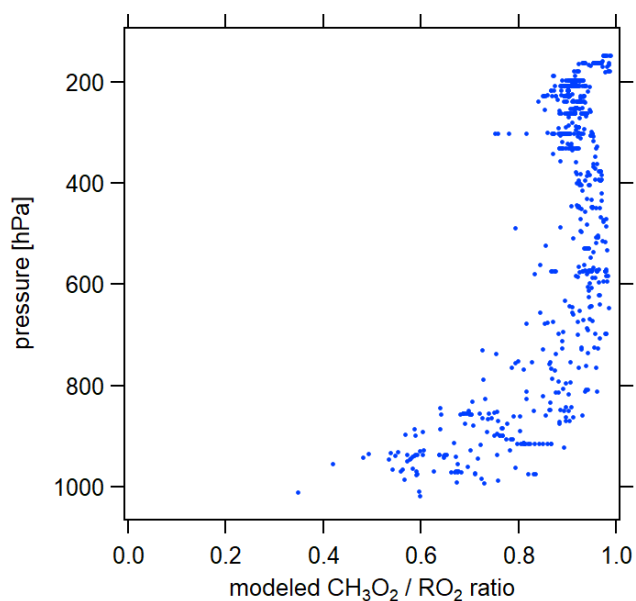


Figure S1. Proportion of modeled CH_3O_2 in the overall modeled RO_2 as a function of the pressure level. Above 800 hPa, CH_3O_2 accounts for more than 90 % of RO_2 .

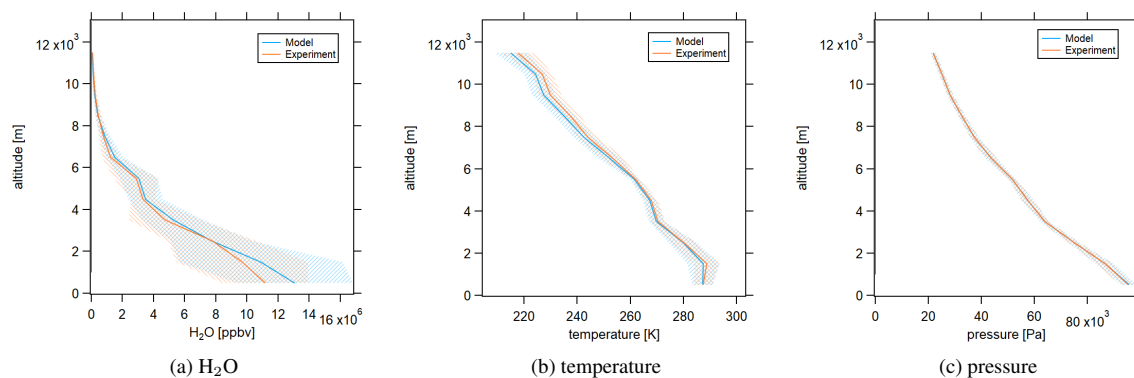


Figure S2. Vertical profiles of water, temperature and pressure for observations (orange) and model simulations (blue) during the HOOVER campaign. All three parameters show close agreement for model and experiment.

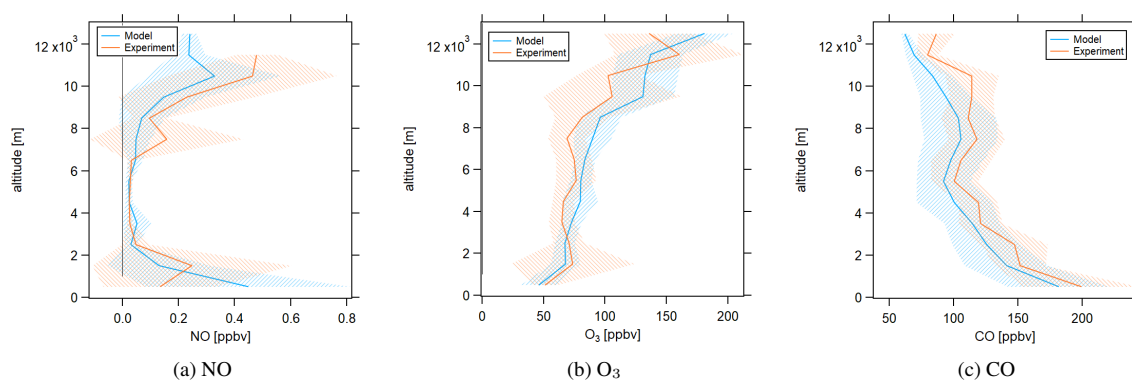


Figure S3. Vertical profiles of NO, O₃ and CO for observations (orange) and model simulations (blue) during the UTOPIHAN campaign. All three trace gases show close agreement for model and experiment.

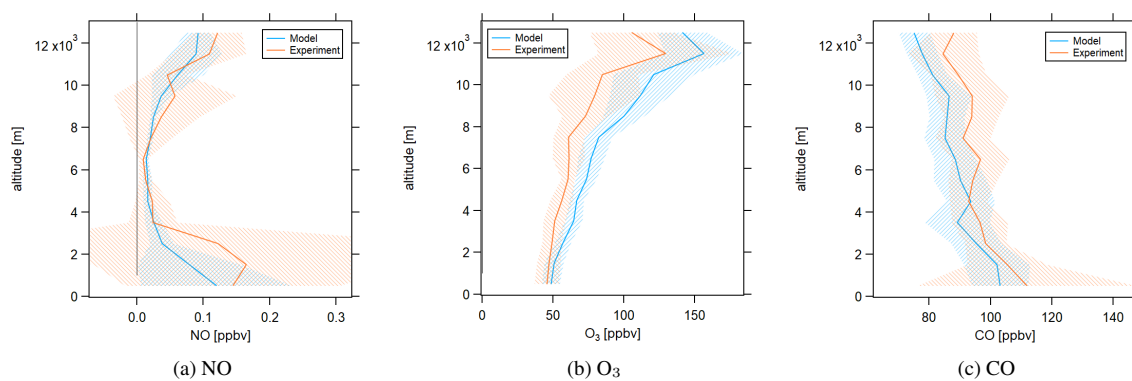


Figure S4. Vertical profiles of NO, O₃ and CO for observations (orange) and model simulations (blue) during the BLUESKY campaign. All three trace gases show close agreement for model and experiment.

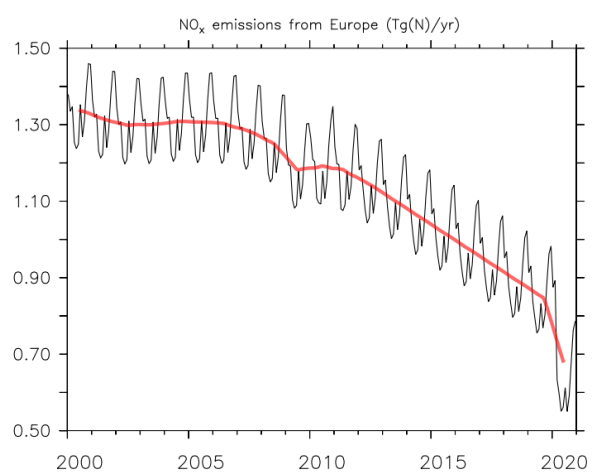


Figure S5. Modeled NO_x emissions across Europe over the past two decades. Monthly values are shown in black and annual means are presented in red.

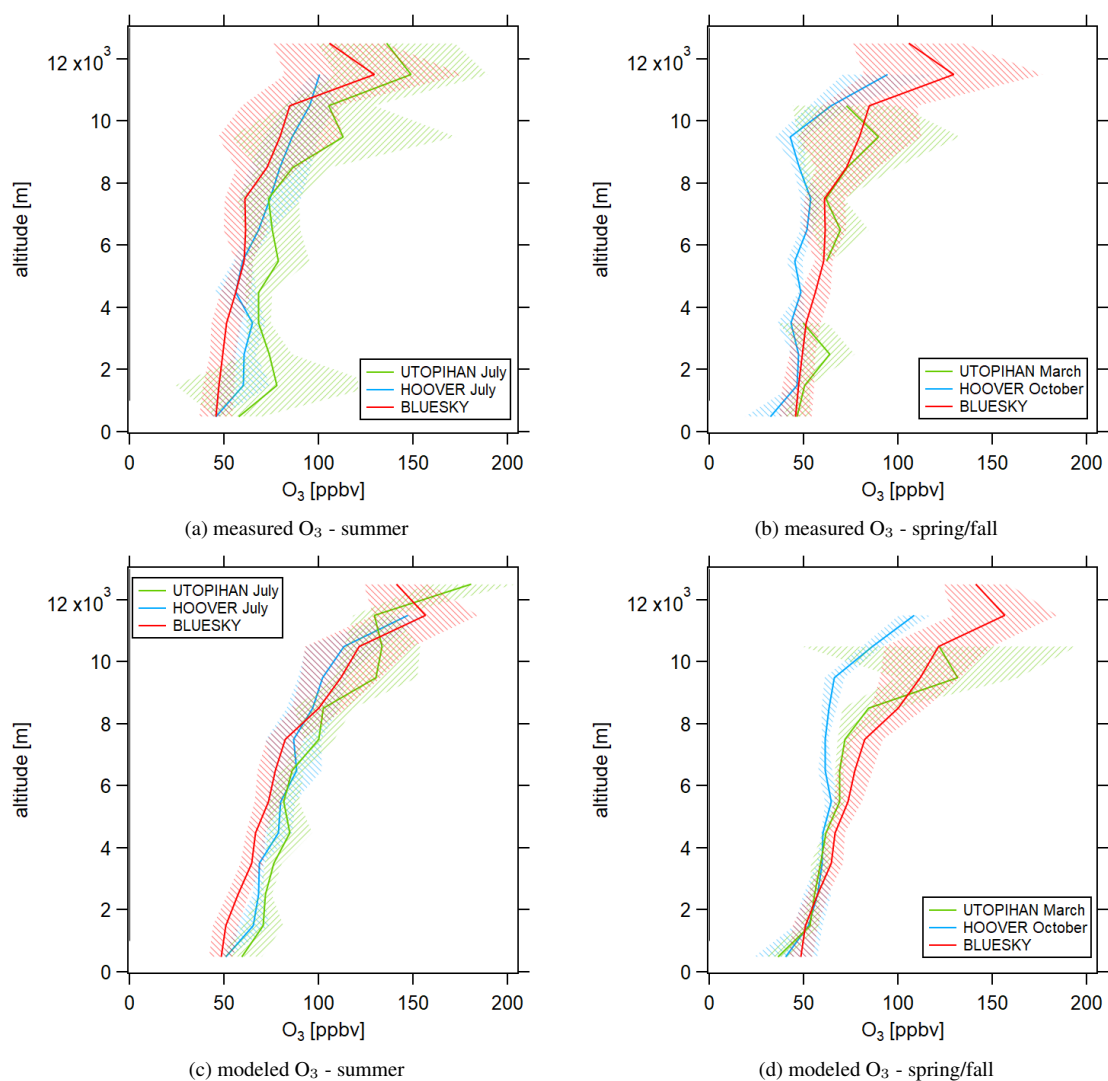


Figure S6. Measured and modeled vertical profiles of O_3 separated into different seasons for HOOVER and UTOPIHAN. BLUESKY data are always from May/June.

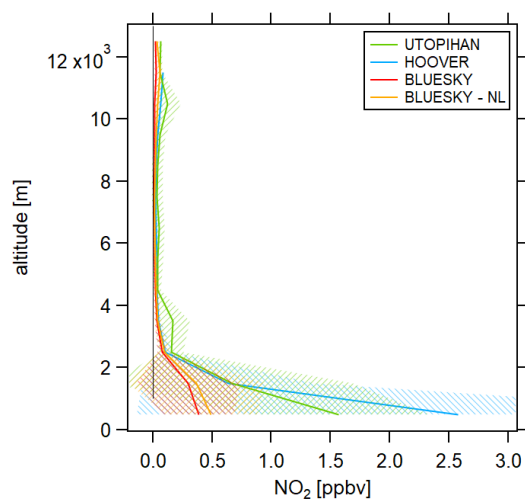


Figure S7. NO_2 vertical profiles during UTOPIHAN, HOOVER, BLUESKY with and without lockdown scenario as in Figure 3d of the main manuscript, but showing the full x-axis range.

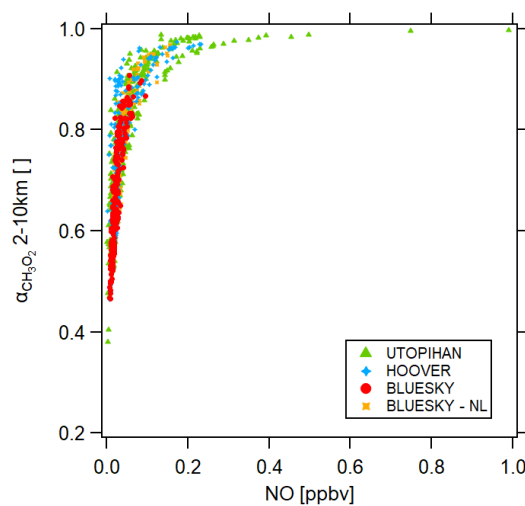


Figure S8. $\alpha_{\text{CH}_3\text{O}_2}$ for the campaigns UTOPIHAN (green), HOOVER (blue), BLUESKY (red) and the no-lockdown (NL) scenario (yellow) in correlation with NO between 2 and 10 km altitude.

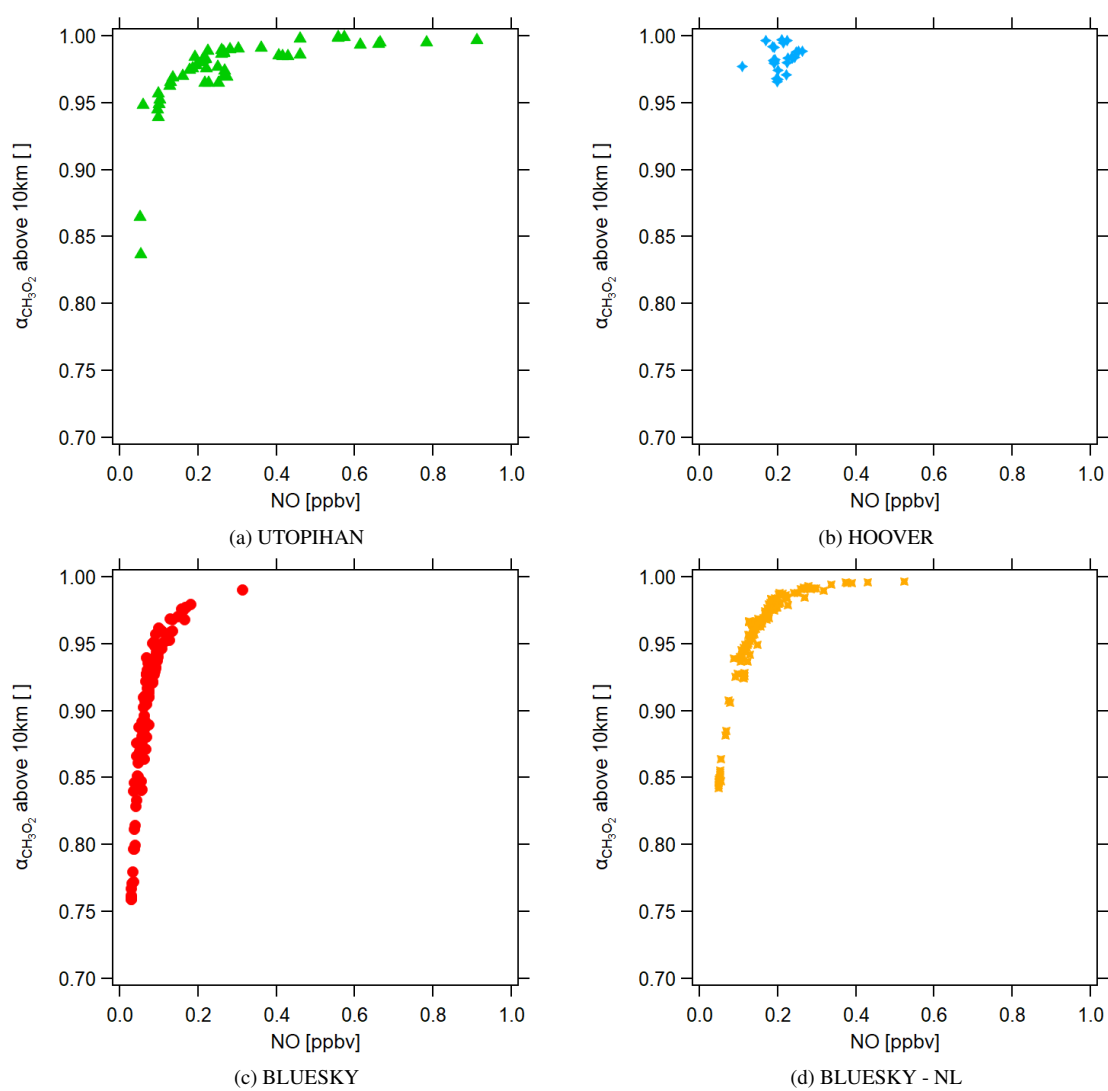


Figure S9. $\alpha_{\text{CH}_3\text{O}_2}$ correlated with NO mixing ratios for all campaigns as shown in Figure 5c of the manuscript in individual panels.

4.5 Supplement of Section 3.6

This chapter provides the Supplement of *What controls ozone sensitivity in the upper tropical troposphere?*, available at:

<https://doi.org/10.5194/egusphere-2023-816-supplement>

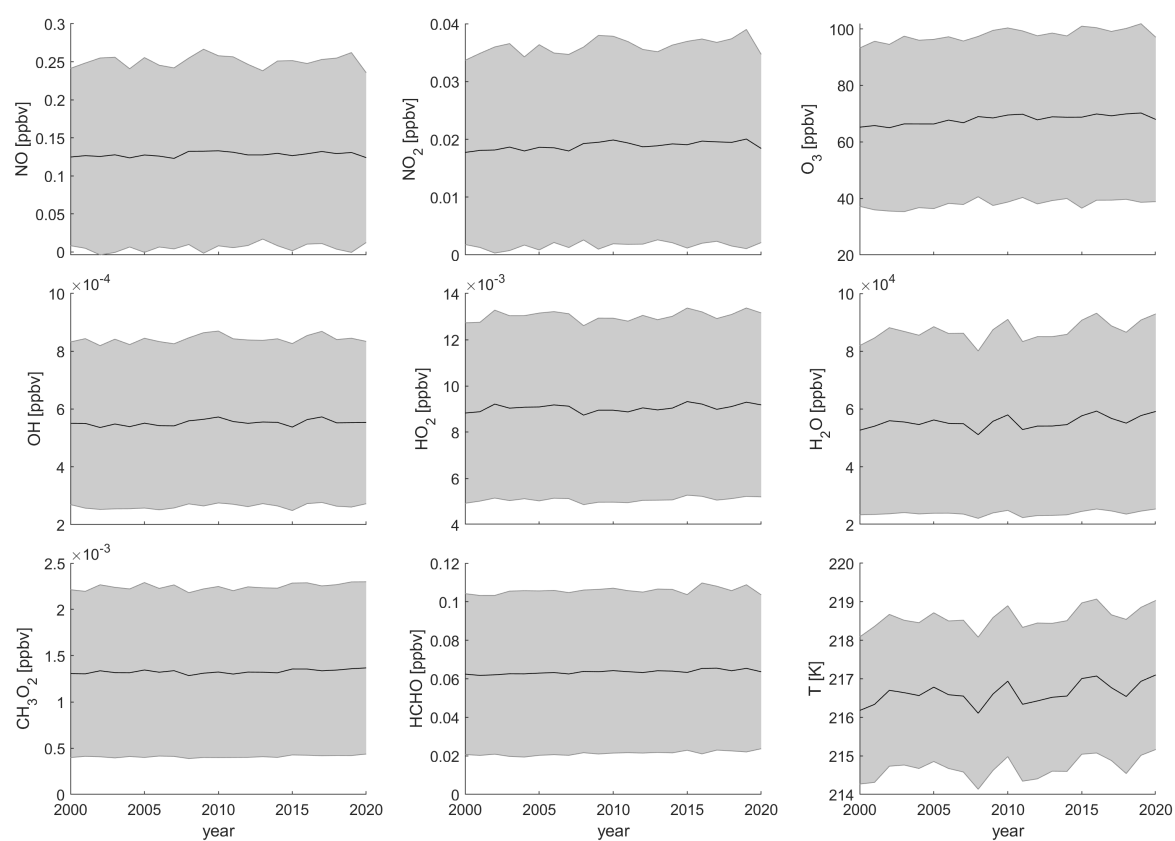


Figure S1. Development of modeled trace gas concentrations in the upper tropical troposphere from 2000 to 2020.

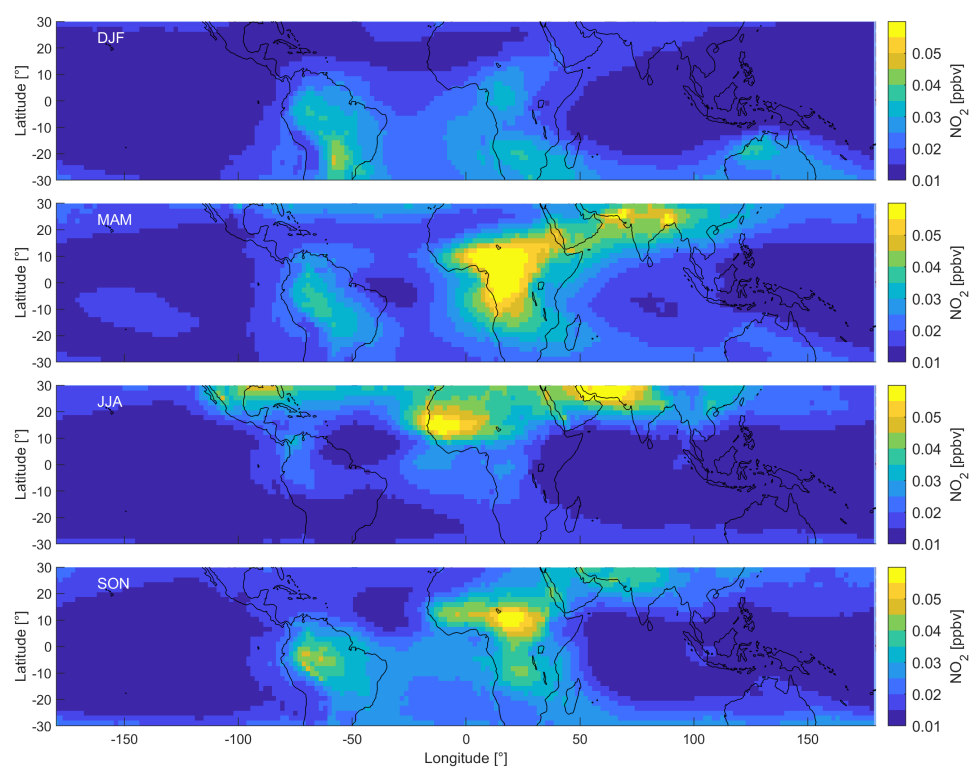


Figure S2. Distribution of NO₂ in the tropics between 30 ° S and 30 ° N for all periods.

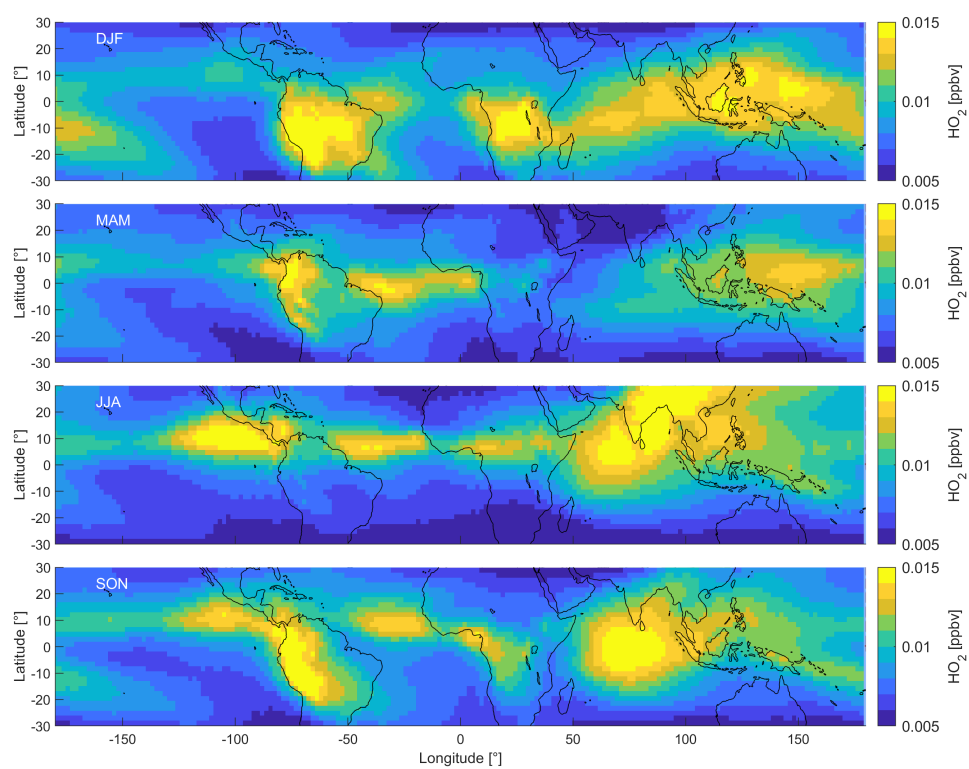


Figure S3. Distribution of HO_2 in the tropics between 30° S and 30° N for all periods.

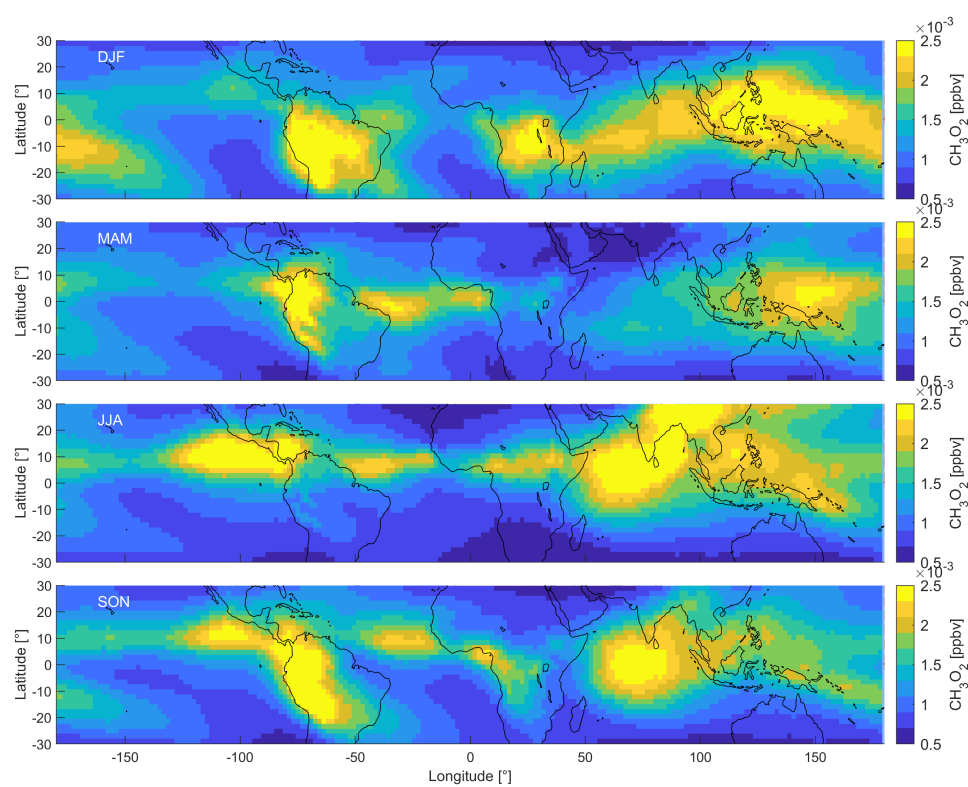


Figure S4. Distribution of CH_3O_2 in the tropics between 30° S and 30° N for all periods.

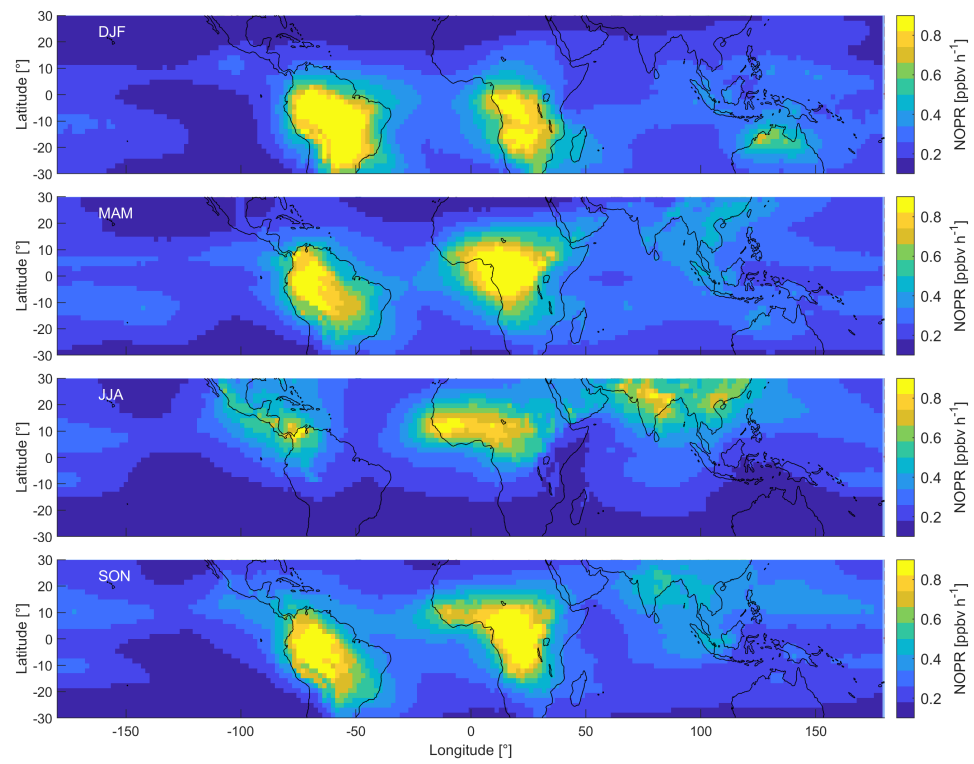


Figure S5. Distribution of NOPR in the tropics between 30 ° S and 30 ° N for all periods.

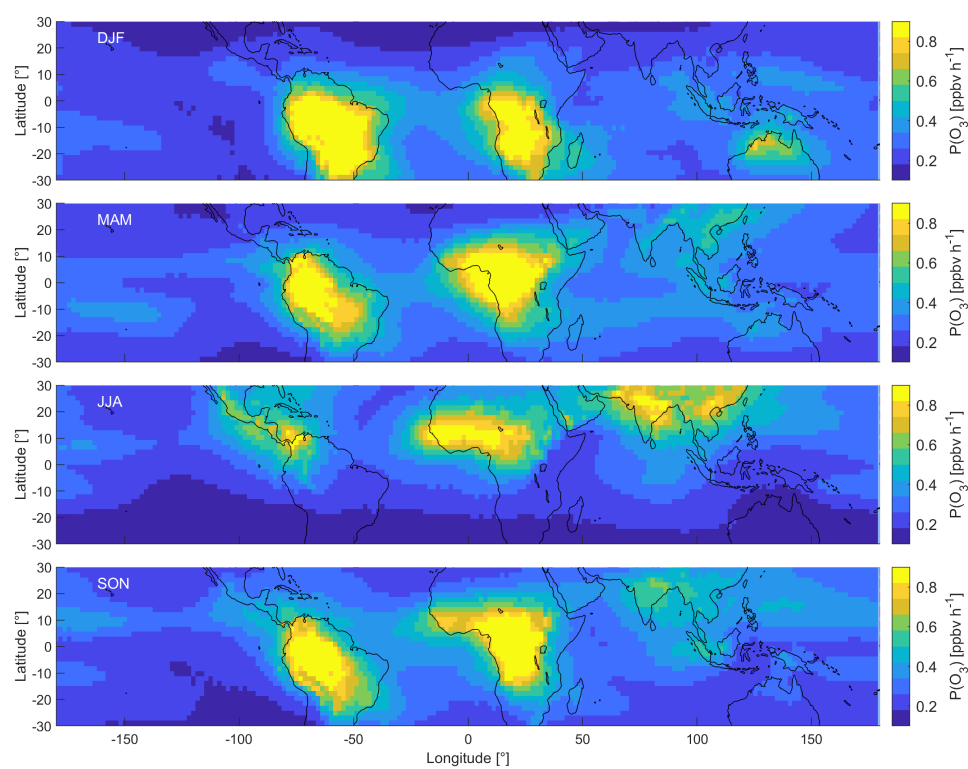


Figure S6. Distribution of $P(O_3)$ in the tropics between 30° S and 30° N for all periods.

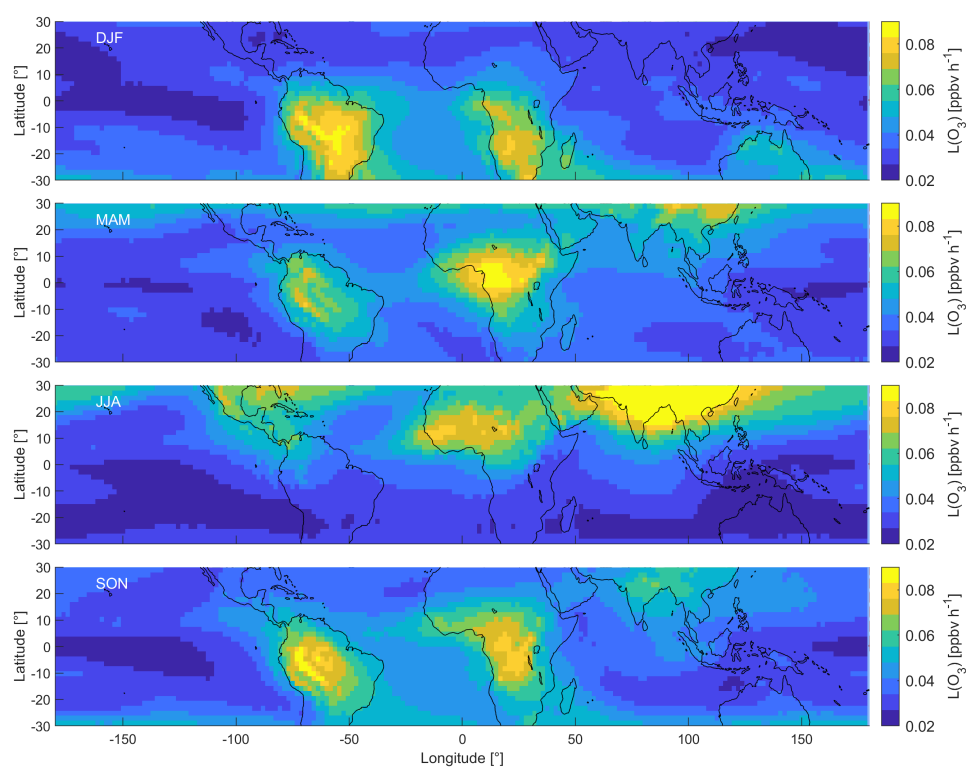


Figure S7. Distribution of $L(O_3)$ in the tropics between 30° S and 30° N for all periods.

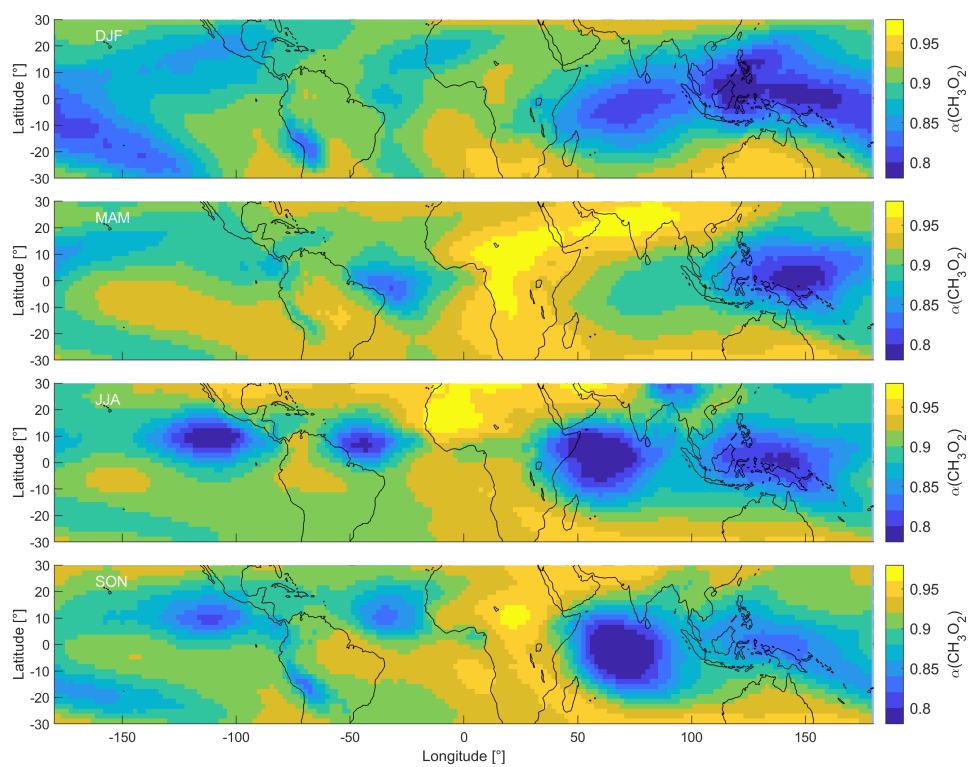


Figure S8. Distribution of $\alpha(\text{CH}_3\text{O}_2)$ in the tropics between 30° S and 30° N for all periods.

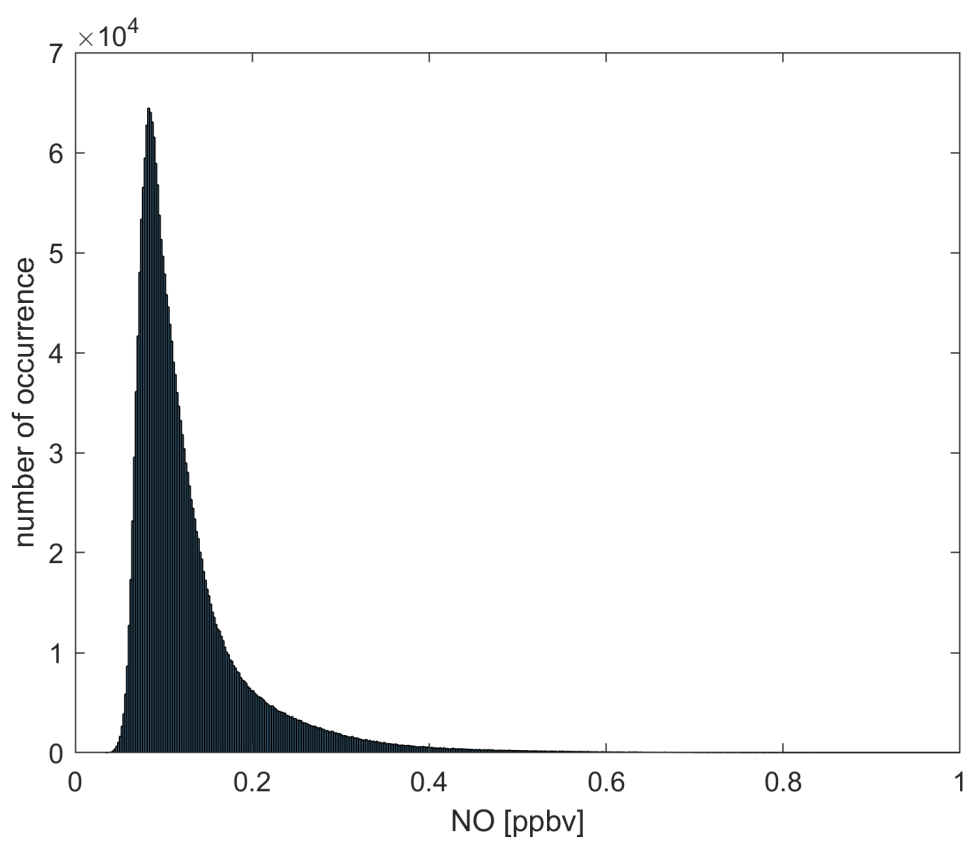


Figure S9. Size distribution for NO concentrations. 99.6 % of the data points show ≤ 0.5 ppbv NO.

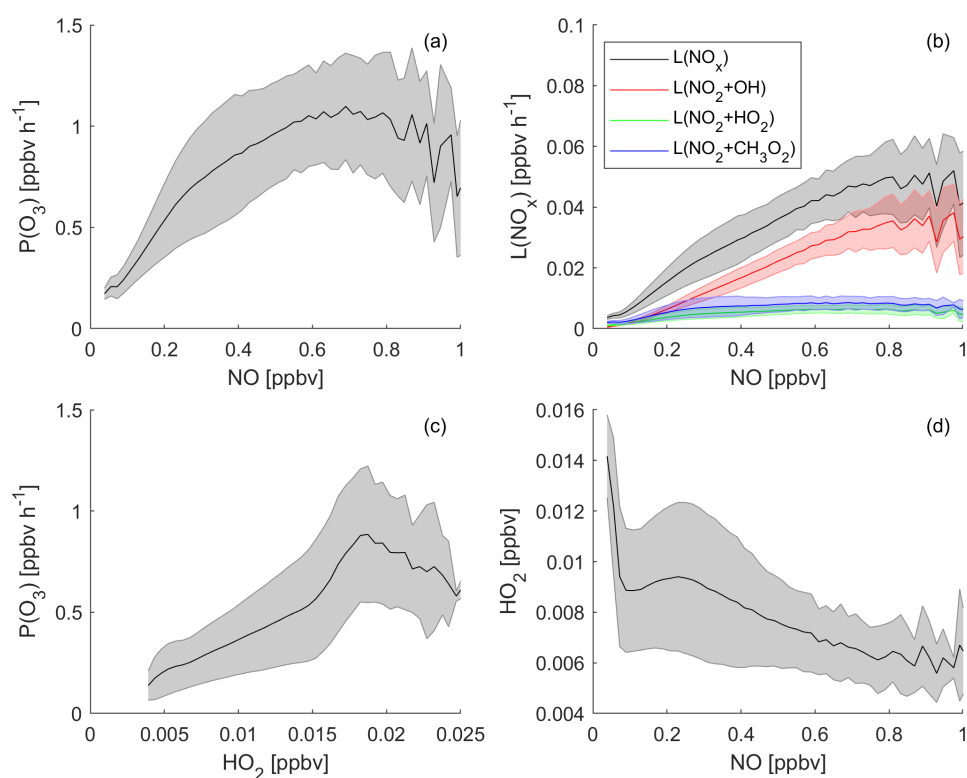


Figure S10. (a) $P(O_3)$ binned to NO concentrations up to 1 ppbv NO, (b) NO_x loss binned to NO concentrations and separated into loss via OH, HO_2 and CH_3O_2 , (c) $P(O_3)$ binned to HO_2 concentrations and (d) HO_2 binned to NO concentrations. Lines show averages of all data points and error shades present the 1 σ standard deviation.

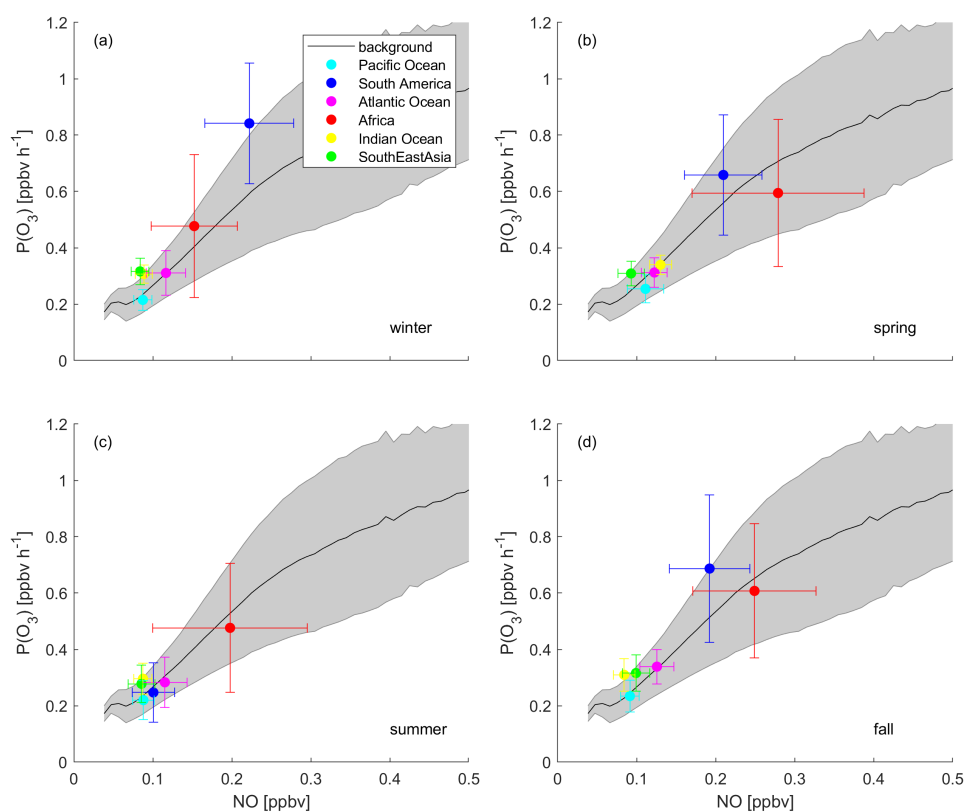


Figure S11. $P(O_3)$ binned to NO concentrations, separated into four periods. Black lines show averages of all data points and grey error shades present the 1 σ standard deviation. Colored data points show the averages for the indicated areas with the 1 σ error.

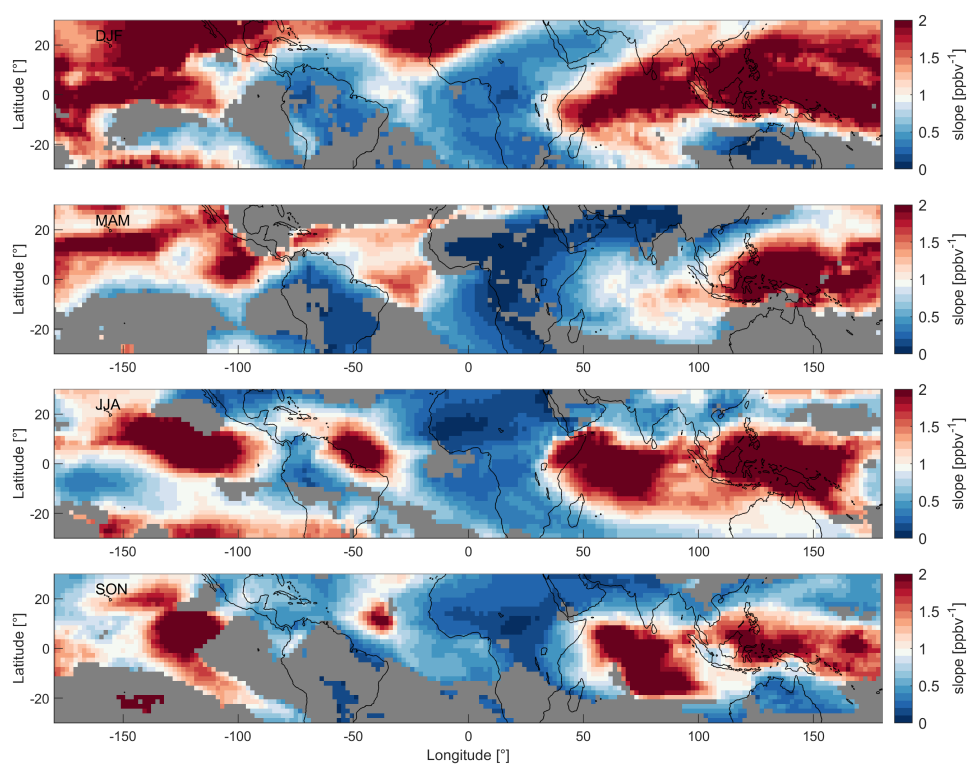


Figure S12. Map of the tropical UT between 30°S and 30°N for each period colored by the slopes of NO vs $\alpha(\text{CH}_3\text{O}_2)$ of the data in each pixel. Red colors indicate a NO_x and blue colors a VOC limitation. For grey pixels the R^2 of the fit is below 30 %.

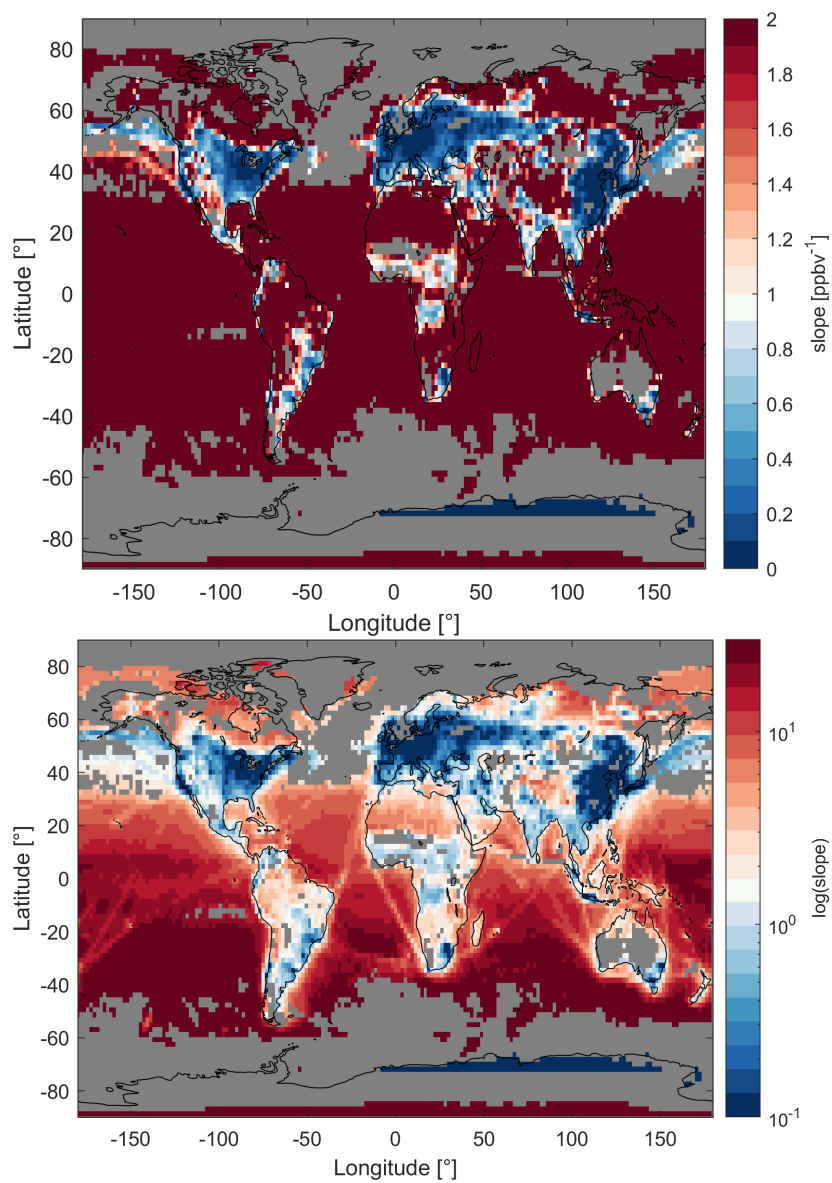


Figure S13. Determination of the dominant chemical regime at the surface for all latitudes, using the slope of NO vs $\alpha(\text{CH}_3\text{O}_2)$ as indicator - exemplary for MAM (March - May) data (upper panel). For grey pixels the R^2 of the fit is below 30 %. The lower panel shows the same data as the upper panel on a log scale which allows for a more detailed view of areas with strong NO_x sensitivity.

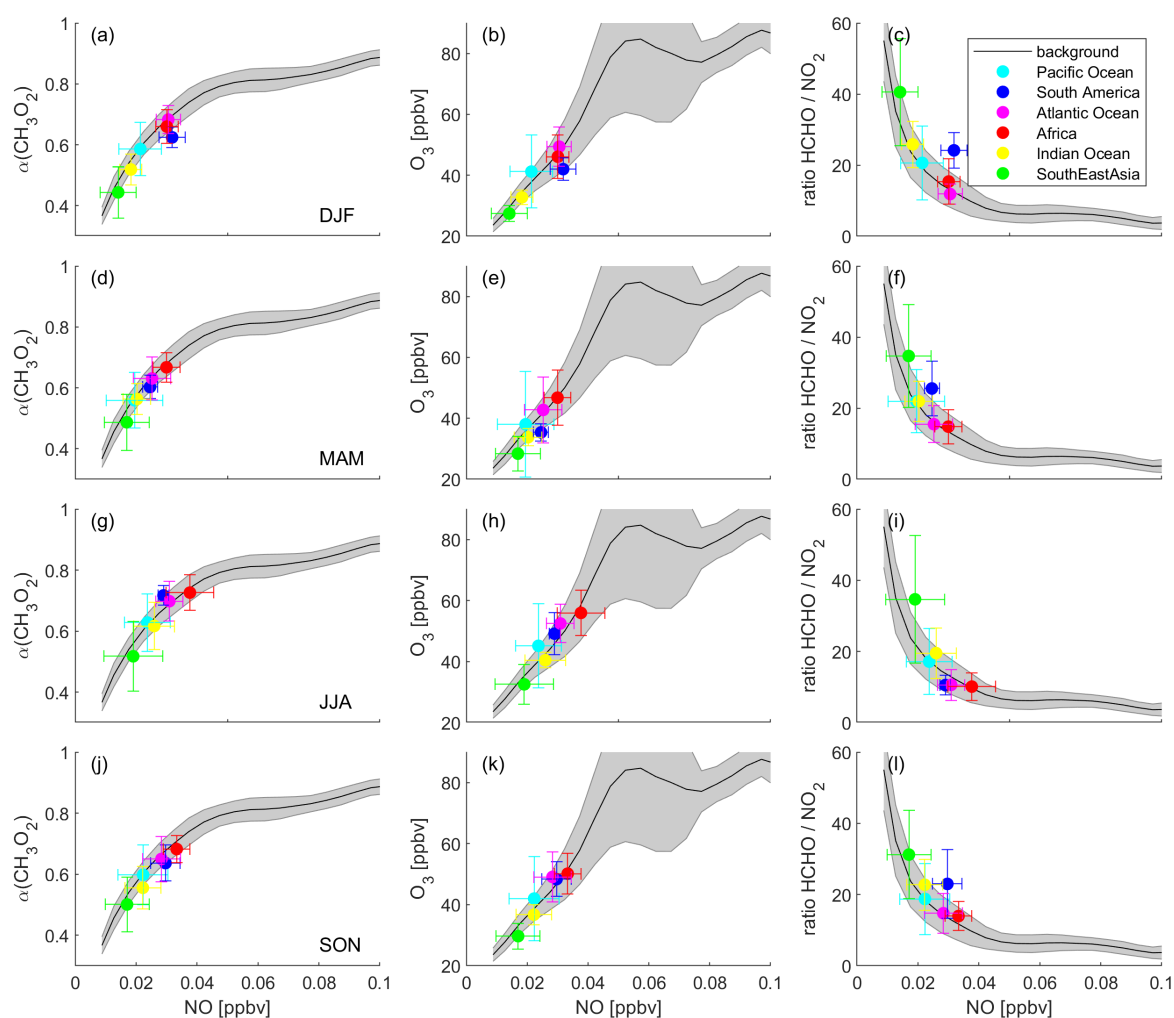


Figure S14. Determination of the dominant chemical regime in the tropical UT in the no lightning scenario via $\alpha(\text{CH}_3\text{O}_2)$, O_3 and the HCHO/NO_2 ratio binned to NO concentrations, separated into four periods. Black lines show averages of all data points and grey error shades present the 1σ standard deviation. Colored data points show the averages for the indicated areas with the 1σ error.

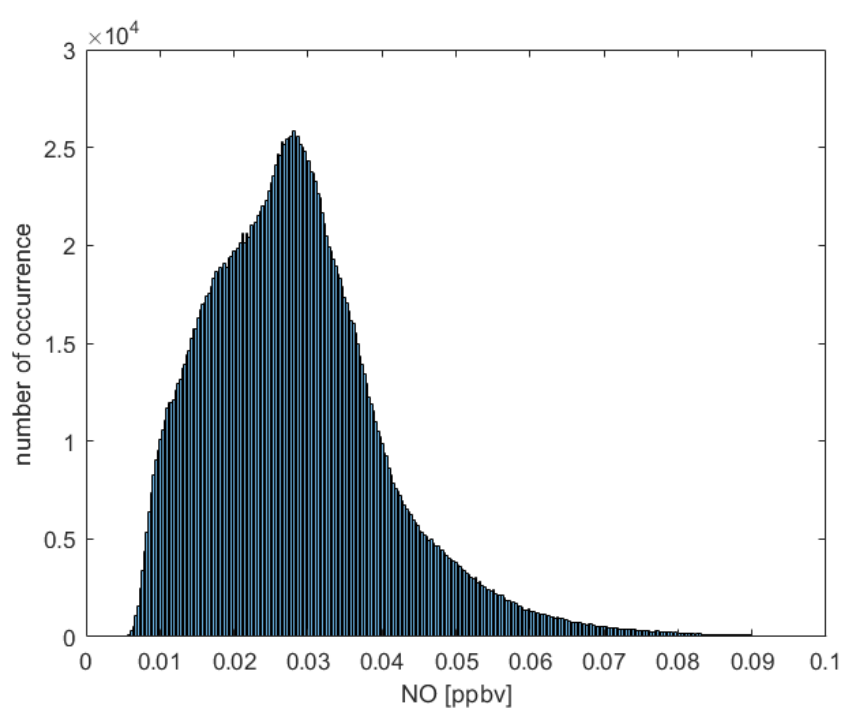


Figure S15. Size distribution for NO concentrations in the no lightning scenario.

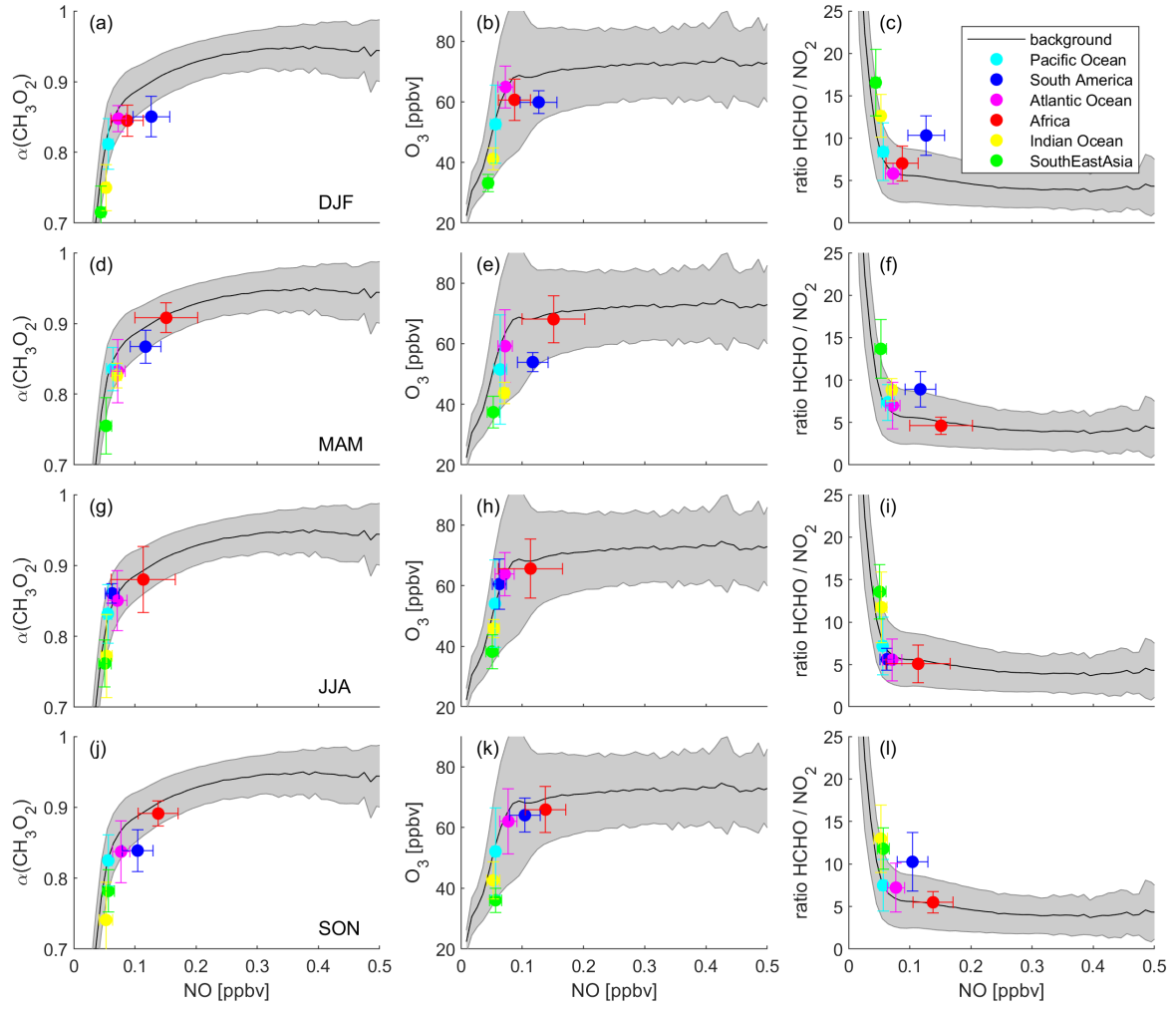


Figure S16. Determination of the dominant chemical regime in the tropical UT in the scenario with halved lightning via $\alpha(\text{CH}_3\text{O}_2)$, O_3 and the HCHO/NO_2 ratio binned to NO concentrations, separated into four periods. Black lines show averages of all data points and grey error shades present the 1σ standard deviation. Colored data points show the averages for the indicated areas with the 1σ error.

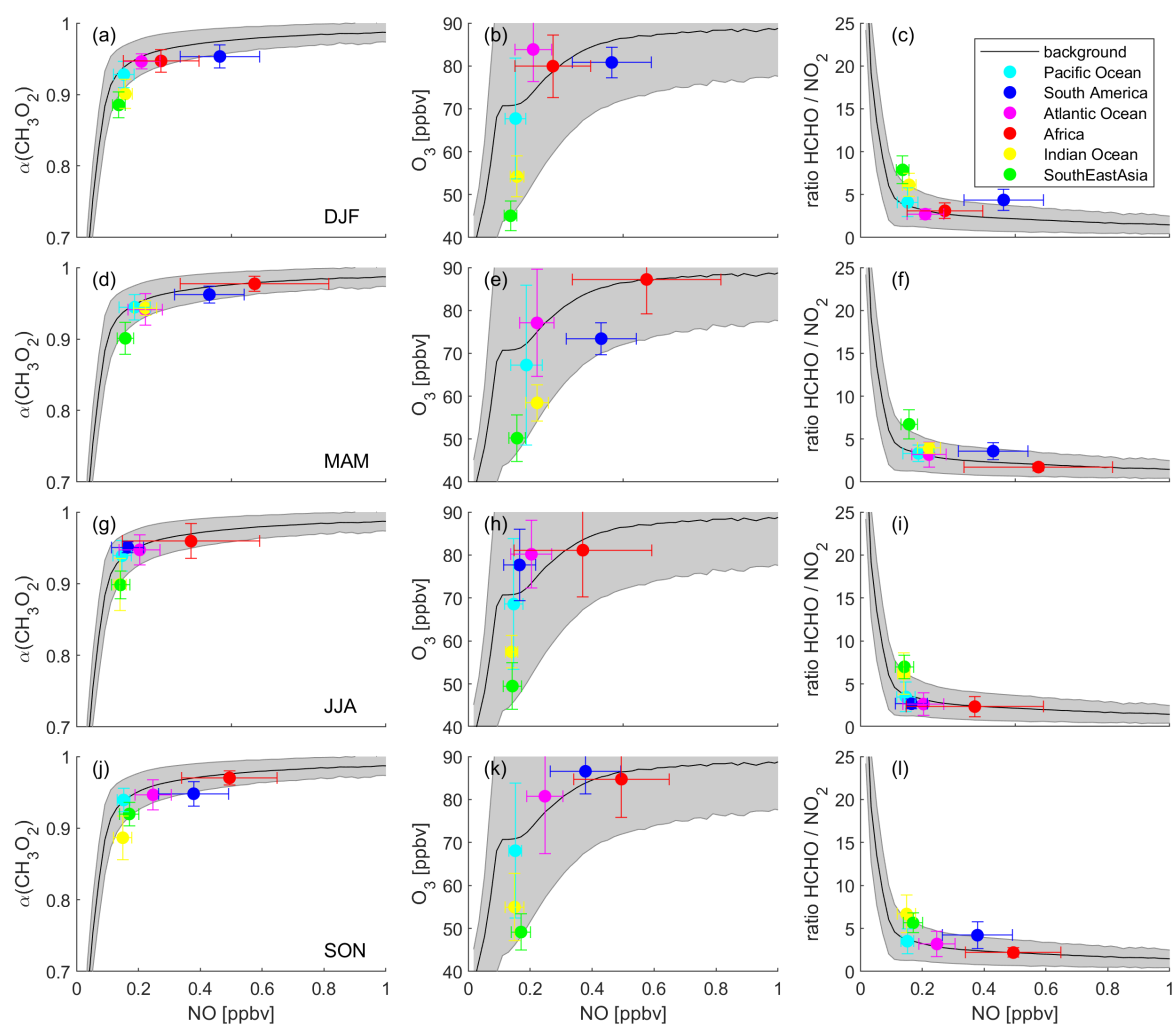


Figure S17. Determination of the dominant chemical regime in the tropical UT in the scenario with doubled lightning via $\alpha(\text{CH}_3\text{O}_2)$, O_3 and the HCHO/NO_2 ratio binned to NO concentrations, separated into four periods. Black lines show averages of all data points and grey error shades present the 1σ standard deviation. Colored data points show the averages for the indicated areas with the 1σ error.

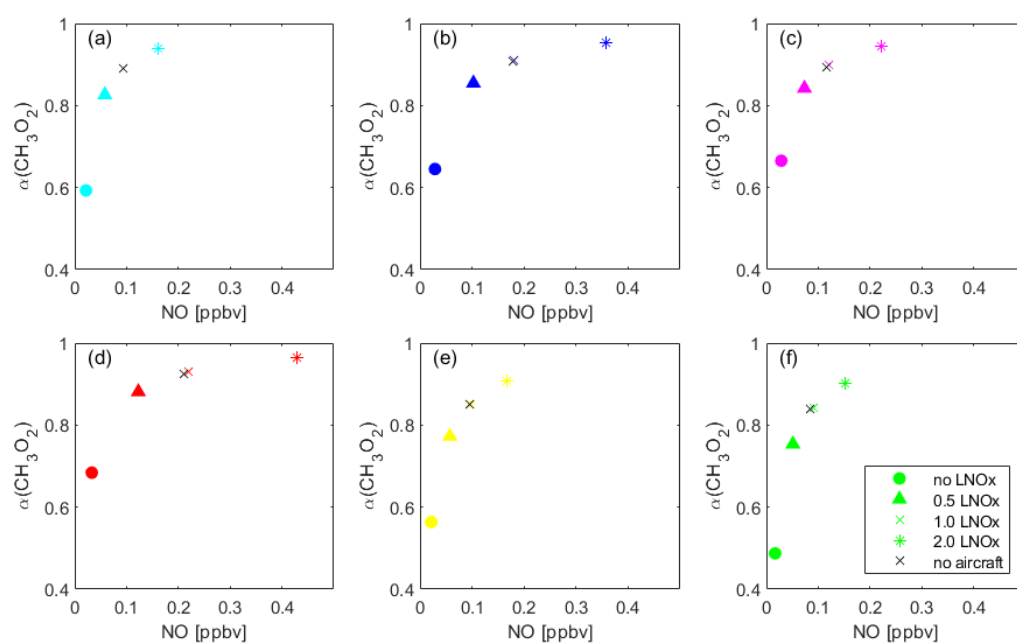


Figure S18. Overview of the impact of lightning NO_x on the dominant regime. The data points present the average NO vs $\alpha(\text{CH}_3\text{O}_2)$ of all data points located in each of the six regions (a) Pacific Ocean, (b) South America, (c) Atlantic Ocean, (d) Africa, (e) Indian Ocean, (f) South East Asia for the baseline scenario (crosses), excluding lightning (circles), halved lightning (triangles) and doubled lightning (stars).

4.6 Supplement of Section 3.7

This chapter provides the Supplement of *Measurement report: Airborne measurements of NO_x fluxes over Los Angeles during the RECAP-CA 2021 campaign*, available at:

<https://doi.org/10.5194/egusphere-2023-601-supplement>



Figure S1. NPS Twin Otter aircraft, including the mounted inlet for air sampling.

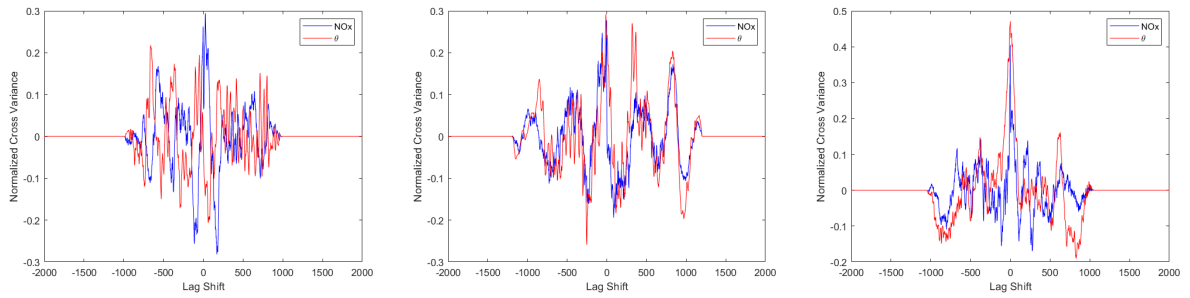


Figure S2. Example covariance peak for NO_x (green) and potential temperature θ (red) with the vertical windspeed for three segments on June 6.

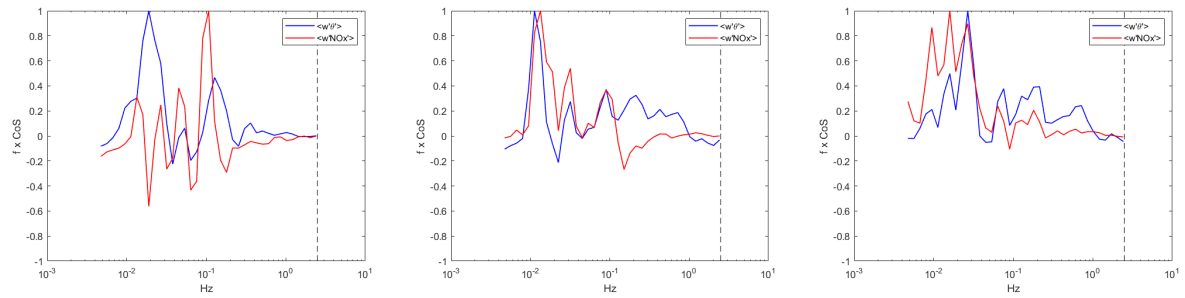


Figure S3. Example co-spectra (normalized) for the NO_x flux (green) and the heat flux (red) for three segments on June 6.

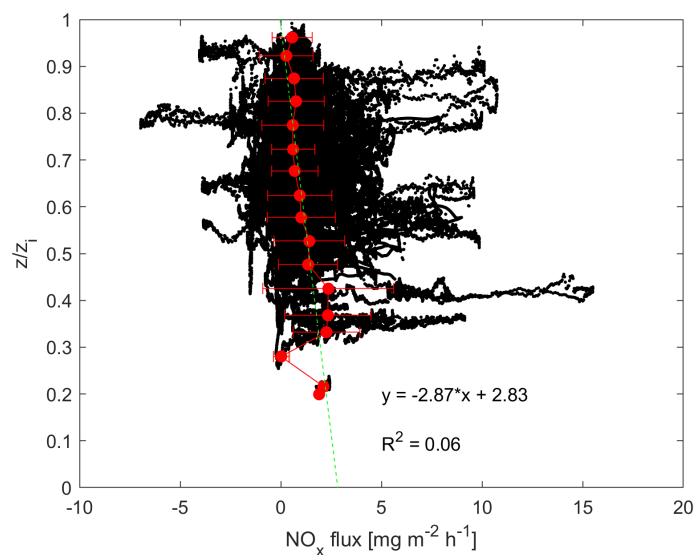


Figure S4. Dimensionless altitude z/z_i versus the NO_x flux to investigate vertical divergence. Black dots represent all data points. The green dashed line shows the linear fit of all data points. The red points and errorbars represent the binned means with the 1σ variability.

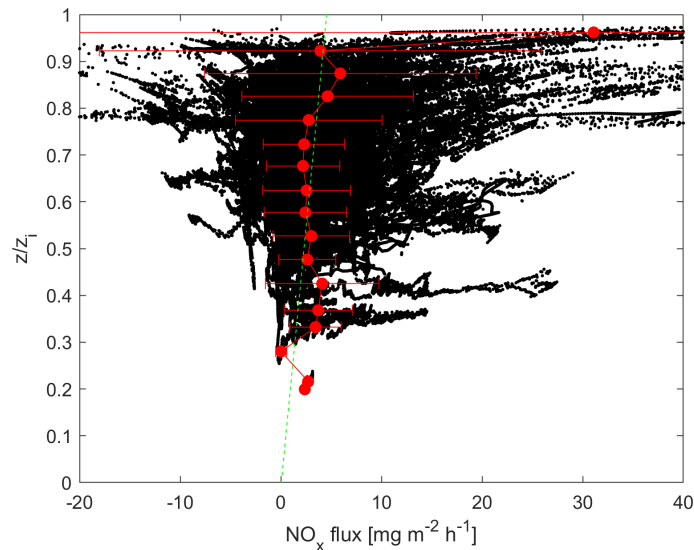


Figure S5. Dimensionless altitude z/z_i versus the corrected NO_x flux according to Figure S4. Black dots represent all data points. The green dashed line shows the linear fit of all data points. The red points and errorbars represent the binned means with the 1σ variability.

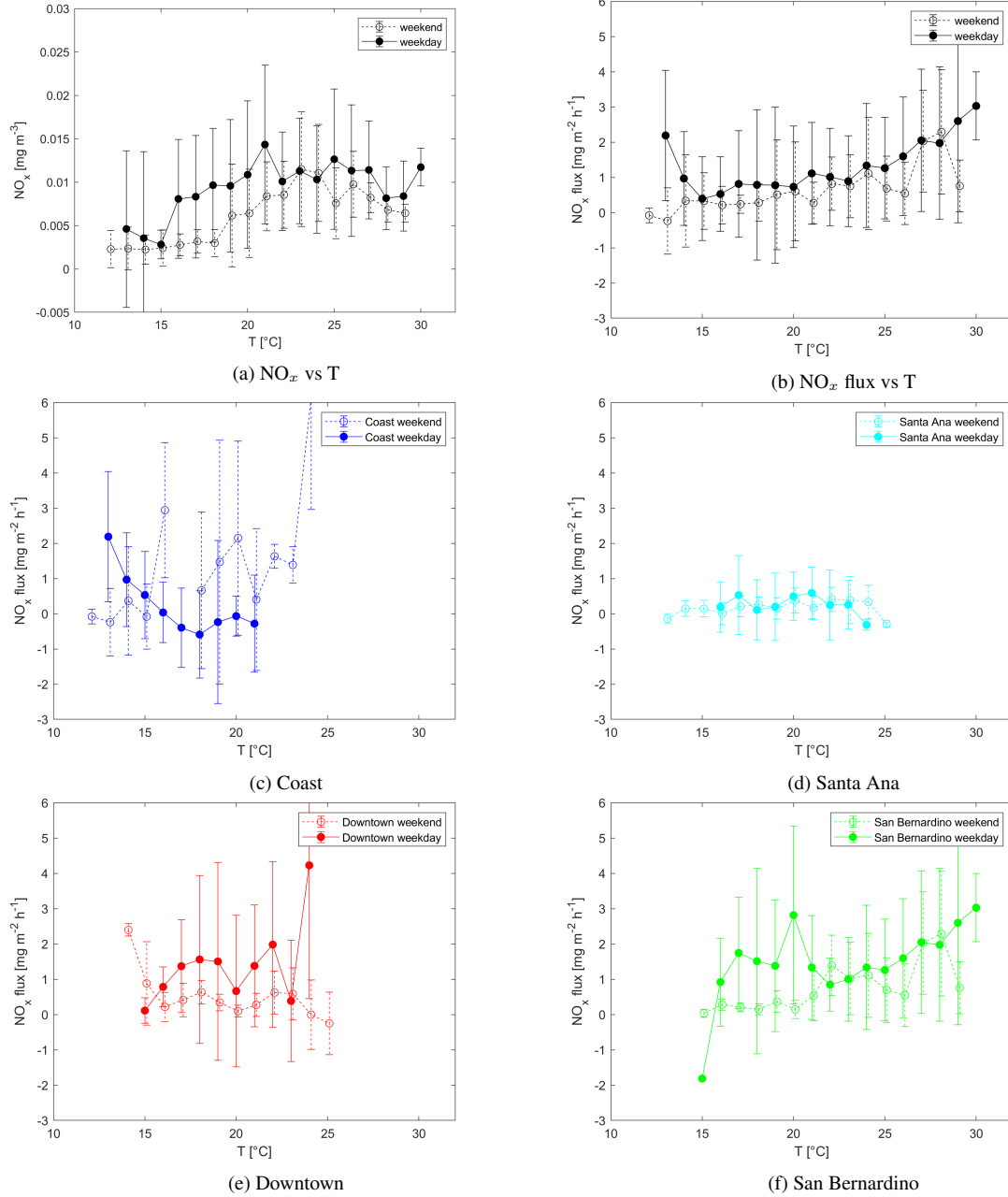


Figure S6. Temperature correlation of NO_x concentrations and NO_x fluxes for all data points ((a)&(b)) and separated into the four regions ((c)-(f)).



Figure S7. Highway emission grid based on the information from the California Department of Transportation (2015). Highway grid cells are shown in green. © Google Maps 2023.

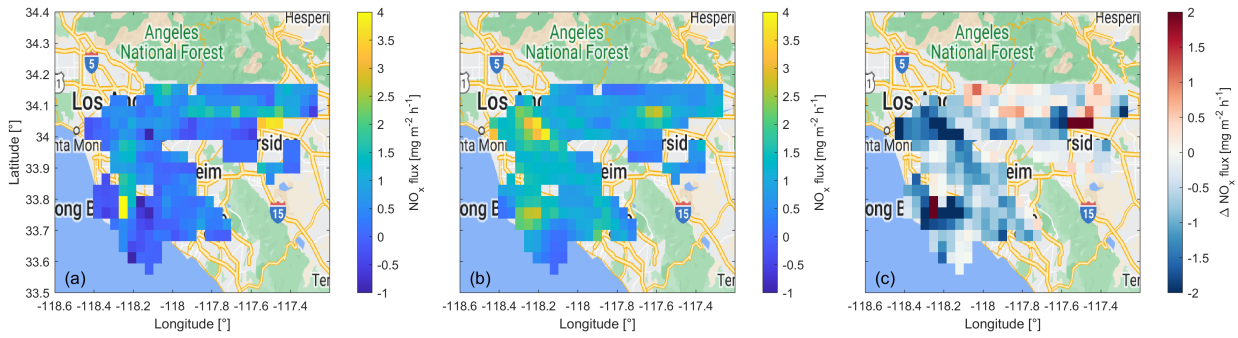


Figure S8. Weekend averages of NO_x emissions across Los Angeles with a $4 \text{ km} \times 4 \text{ km}$ spatial resolution (a) during the RECAP-CA campaign, (b) from the CARB emission inventory and (c) the difference between RECAP-CA and CARB NO_x fluxes. © Google Maps 2023.

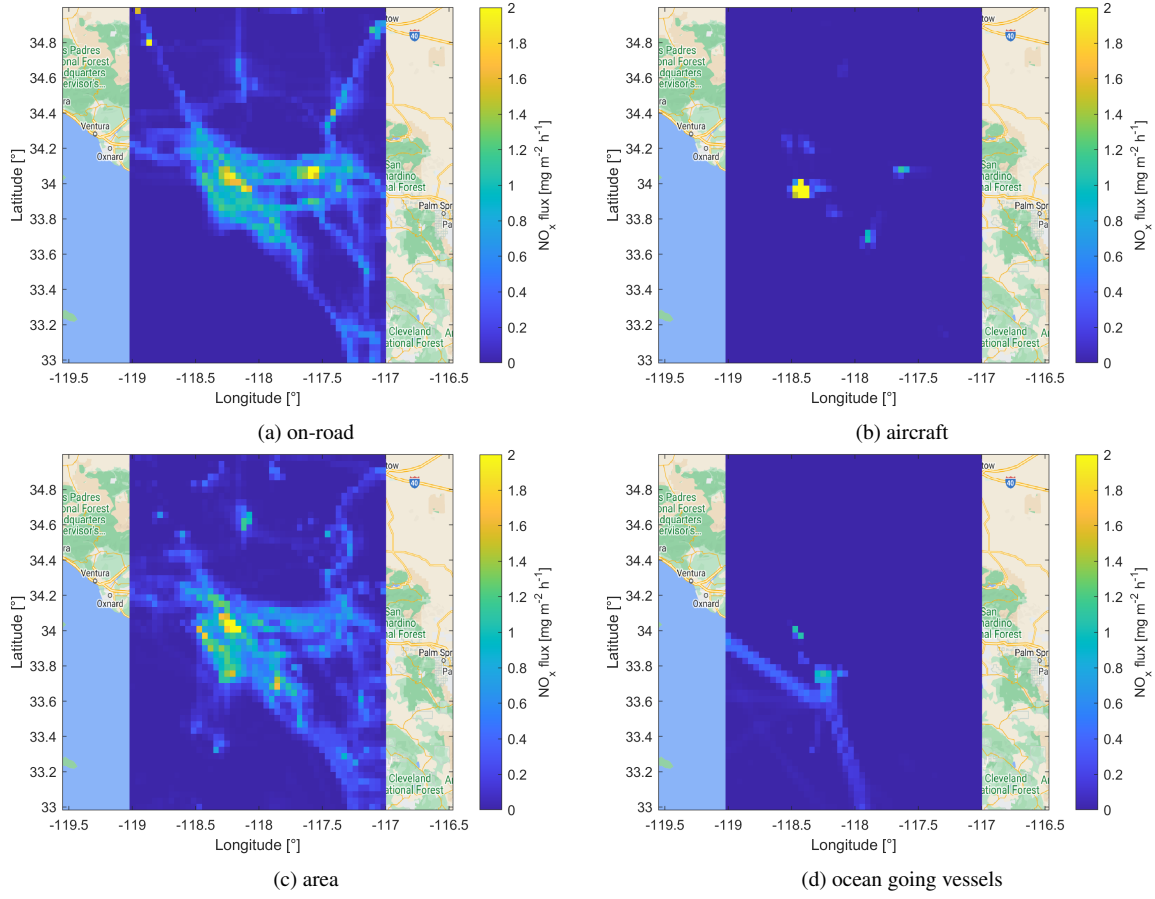


Figure S9. CARB emission inventory, separated into different sectors. © Google Maps 2023.

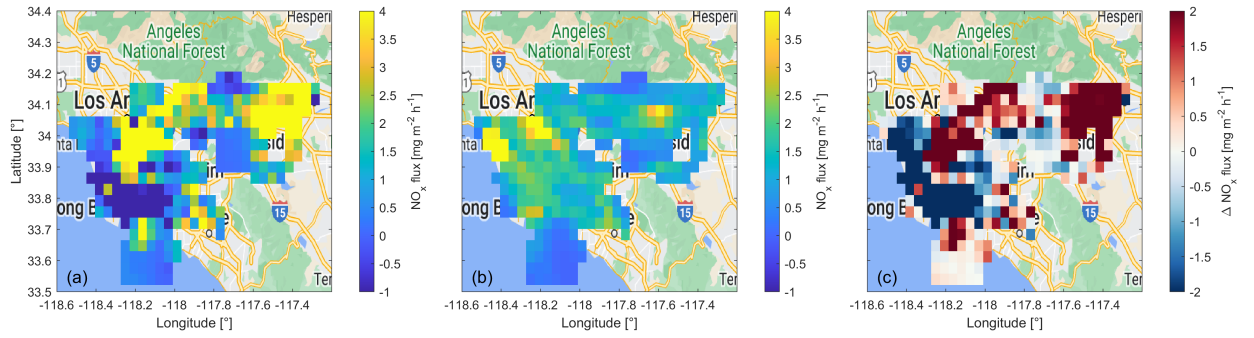


Figure S10. Weekday averages of vertical divergence corrected NO_x emissions across Los Angeles with a $4 \text{ km} \times 4 \text{ km}$ spatial resolution (a) during the RECAP-CA campaign, (b) from the CARB emission inventory and (c) the difference between RECAP-CA and CARB NO_x fluxes. © Google Maps 2023.

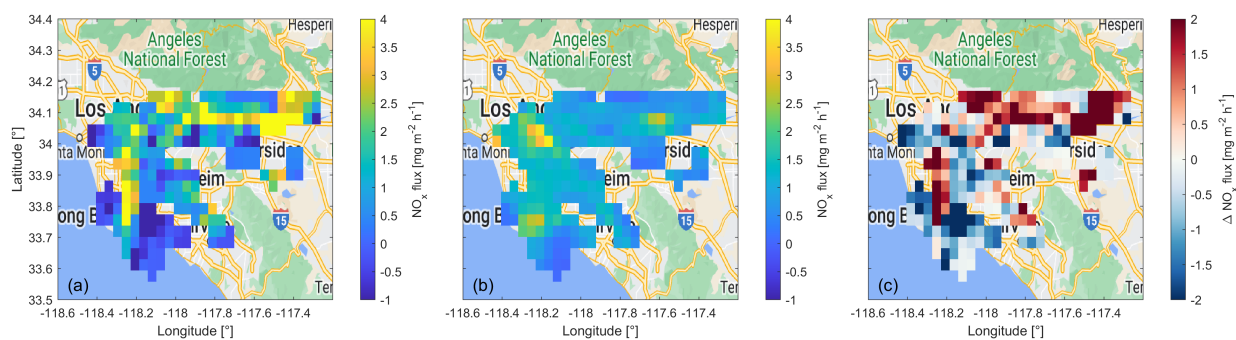


Figure S11. Weekend averages of vertical divergence corrected NO_x emissions across Los Angeles with a 4 km × 4 km spatial resolution (a) during the RECAP-CA campaign, (b) from the CARB emission inventory and (c) the difference between RECAP-CA and CARB NO_x fluxes. © Google Maps 2023.

References

- [1] C. Reed, M. J. Evans, P. D. Carlo, J. D. Lee, and L. J. Carpenter, “Interferences in photolytic NO₂ measurements: explanation for an apparent missing oxidant?,” *Atmospheric Chemistry and Physics*, vol. 16, no. 7, pp. 4707–4724, 2016. <https://doi.org/10.5194/acp-16-4707-2016>.
- [2] C. M. Nussbaumer, U. Parchatka, I. Tadic, B. Bohn, D. Marno, M. Martinez, R. Rohloff, H. Harder, F. Kluge, K. Pfeilsticker, F. Obersteiner, M. Zöger, J. N. Doerich, Raphael Crowley, J. Lelieveld, and H. Fischer, “Modification of a conventional photolytic converter for improving aircraft measurements of NO₂ via chemiluminescence,” *Atmospheric measurement techniques*, vol. 14, no. 10, pp. 6759–6776, 2021. <https://doi.org/10.5194/amt-14-6759-2021>.
- [3] J. Lelieveld and R. van Dorland, “Ozone chemistry changes in the troposphere and consequent radiative forcing of climate,” in *Atmospheric Ozone as a Climate Gas: General Circulation Model Simulations*, pp. 227–258, Springer, 1995. https://doi.org/10.1007/978-3-642-79869-6_16.
- [4] F. Iglesias-Suarez, D. E. Kinnison, A. Rap, A. C. Maycock, O. Wild, and P. J. Young, “Key drivers of ozone change and its radiative forcing over the 21st century,” *Atmospheric Chemistry and Physics*, vol. 18, no. 9, pp. 6121–6139, 2018. <https://doi.org/10.5194/acp-18-6121-2018>.
- [5] D. Nuvolone, D. Petri, and F. Voller, “The effects of ozone on human health,” *Environmental Science and Pollution Research*, vol. 25, no. 9, pp. 8074–8088, 2018. <https://doi.org/10.1007/s11356-017-9239-3>.
- [6] C. M. Nussbaumer, J. N. Crowley, J. Schuladen, J. Williams, S. Hafermann, A. Reiffs, R. Axinte, H. Harder, C. Ernest, A. Novelli, K. Sala, M. Martinez, C. Mallik, L. Tomsche, C. Plass-Dülmer, B. Bohn, J. Lelieveld, and H. Fischer, “Measurement report: Photochemical production and loss rates of formaldehyde and ozone across Europe,” *Atmospheric Chemistry and Physics*, vol. 21, no. 24, pp. 18413–18432, 2021. <https://doi.org/10.5194/acp-21-18413-2021>.
- [7] C. M. Nussbaumer, A. Pozzer, I. Tadic, L. Röder, F. Obersteiner, H. Harder, J. Lelieveld, and H. Fischer, “Tropospheric ozone production and chemical regime analysis during the COVID-19 lockdown over Europe,” *Atmospheric Chemistry and Physics*, vol. 22, no. 9, pp. 6151–6165, 2022. <https://doi.org/10.5194/acp-22-6151-2022>.
- [8] C. M. Nussbaumer, H. Fischer, J. Lelieveld, and A. Pozzer, “What controls ozone sensitivity in the upper tropical troposphere?,” *EGUsphere [preprint]*, 2023. <https://doi.org/10.5194/egusphere-2023-816>.
- [9] C. M. Nussbaumer, I. Tadic, D. Dienhart, N. Wang, A. Edtbauer, L. Ernle, J. Williams, F. Obersteiner, I. Gutiérrez-Álvarez, H. Harder, J. Lelieveld, and H. Fischer, “Measurement report: In situ observations of deep convection without lightning during the tropical cyclone Florence 2018,” *Atmospheric Chemistry and Physics*, vol. 21, no. 10, pp. 7933–7945, 2021. <https://doi.org/10.5194/acp-2021-79>.

-
- [10] C. M. Nussbaumer, B. K. Place, Q. Zhu, E. Y. Pfannerstill, P. Wooldridge, B. C. Schulze, C. Arata, R. Ward, A. Bucholtz, J. H. Seinfeld, A. H. Goldstein, and R. C. Cohen, “Measurement report: Airborne measurements of NO_x fluxes over Los Angeles during the RECAP-CA 2021 campaign,” *EGUsphere [preprint]*, 2023. <https://doi.org/10.5194/egusphere-2023-601>.
- [11] J. H. Seinfeld and S. N. Pandis, *Atmospheric chemistry and physics: from air pollution to climate change*. John Wiley & Sons, 1998.
- [12] J. M. Wallace and P. V. Hobbs, *Atmospheric science: an introductory survey*, vol. 92. Elsevier, 2006. ISBN: 978-0-12-732951-2.
- [13] National Weather Service, “Layers of the atmosphere.” Online available at: <https://www.weather.gov/jetstream/layer>, accessed on 2023-03-09.
- [14] Deutscher Wetterdienst, “Wetter- und Klimalexikon - Troposphäre.” Online available at: <https://www.dwd.de/DE/service/lexikon/Functions/glossar.html?lv2=102672&lv3=102820>, accessed on 2023-03-09.
- [15] D. J. Jacob, *Introduction to atmospheric chemistry*. Princeton university press, 1999.
- [16] Deutscher Wetterdienst, “Wetter- und Klimalexikon - Adiabatische Zustandsänderung.” Online available at: <https://www.dwd.de/DE/service/lexikon/Functions/glossar.html?nn=103346&lv2=100072&lv3=603138> accessed on 2023-03-09.
- [17] Deutscher Wetterdienst, “Wetter- und Klimalexikon - Stratosphäre.” Online available at: <https://www.dwd.de/DE/service/lexikon/Functions/glossar.html?lv2=102248&lv3=102632>, accessed on 2023-03-10.
- [18] National Geographic, “Ozone Layer.” Online available at: <https://education.nationalgeographic.org/resource/ozone-layer/>, accessed on 2023-03-10.
- [19] P. Leighton, *Photochemistry of air pollution*. New York: Academic Press, Inc., 1961.
- [20] K. Mannschreck, S. Gilge, C. Plass-Duelmer, W. Fricke, and H. Berresheim, “Assessment of the applicability of NO-NO₂-O₃ photostationary state to long-term measurements at the Hohenpeissenberg GAW Station, Germany,” *Atmospheric Chemistry and Physics*, vol. 4, no. 5, pp. 1265–1277, 2004. <https://doi.org/10.5194/acp-4-1265-2004>.
- [21] R. J. Griffin, P. J. Beckman, R. W. Talbot, B. C. Sive, and R. K. Varner, “Deviations from ozone photostationary state during the International Consortium for Atmospheric Research on Transport and Transformation 2004 campaign: Use of measurements and photochemical modeling to assess potential causes,” *Journal of Geophysical Research: Atmospheres*, vol. 112, no. D10, 2007. <https://doi.org/10.1029/2006JD007604>.
- [22] I. Tadic, C. Nussbaumer, B. Bohn, H. Harder, D. Marno, M. Martinez, F. Obersteiner, U. Parchatka, A. Pozzer, R. Rohloff, M. Zöger, J. Lelieveld, and H. Fischer, “Central role of nitric oxide in ozone production in the upper tropical troposphere over the Atlantic Ocean and West Africa,” *Atmospheric Chemistry and Physics*, vol. 21, no. 10, pp. 8195–8211, 2021. <https://doi.org/10.5194/acp-2021-52>.

- [23] S. E. Pusede, A. L. Steiner, and R. C. Cohen, "Temperature and recent trends in the chemistry of continental surface ozone," *Chemical reviews*, vol. 115, no. 10, pp. 3898–3918, 2015. <https://doi.org/10.1021/cr5006815>.
- [24] P. Jöckel, H. Tost, A. Pozzer, M. Kunze, O. Kirner, C. A. Brenninkmeijer, S. Brinkop, D. S. Cai, C. Dyroff, J. Eckstein, F. Frank, H. Garny, K.-D. Gottschaldt, P. Graf, V. Grewe, A. Kerkweg, B. Kern, S. Matthes, M. Mertens, S. Meul, M. Neumaier, M. Nützel, S. Oberländer-Hayn, R. Ruhnke, T. Runde, R. Sander, D. Scharffe, and A. Zahn, "Earth system chemistry integrated modelling (ESCiMo) with the modular earth submodel system (MESSy) version 2.51," *Geoscientific Model Development*, vol. 9, no. 3, pp. 1153–1200, 2016. <https://doi.org/10.5194/gmd-9-1153-2016>.
- [25] A. R. Vaughan, J. D. Lee, S. Metzger, D. Durden, A. C. Lewis, M. D. Shaw, W. S. Drysdale, R. M. Purvis, B. Davison, and C. N. Hewitt, "Spatially and temporally resolved measurements of NO_x fluxes by airborne eddy covariance over Greater London," *Atmospheric Chemistry and Physics*, vol. 21, no. 19, pp. 15283–15298, 2021. <https://doi.org/10.5194/acp-21-15283-2021>.
- [26] R. Zhang, X. Tie, and D. W. Bond, "Impacts of anthropogenic and natural NO_x sources over the US on tropospheric chemistry," *Proceedings of the National Academy of Sciences*, vol. 100, no. 4, pp. 1505–1509, 2003. <https://doi.org/10.1073/pnas.252763799>.
- [27] Schumann, Ulrich and Huntrieser, Heidi, "The global lightning-induced nitrogen oxides source," *Atmos. Chem. Phys. Discuss*, vol. 7, pp. 2623–2818, 2007. <https://doi.org/10.5194/acp-7-3823-2007>.
- [28] H. J. Christian, R. J. Blakeslee, D. J. Boccippio, W. L. Boeck, D. E. Buechler, K. T. Driscoll, S. J. Goodman, J. M. Hall, W. J. Koshak, D. M. Mach, and M. F. Stewart, "Global frequency and distribution of lightning as observed from space by the Optical Transient Detector," *Journal of Geophysical Research: Atmospheres*, vol. 108, no. D1, pp. ACL-4, 2003. <https://doi.org/10.1029/2002JD002347>.
- [29] S. Sillman, "The relation between ozone, NO_x and hydrocarbons in urban and polluted rural environments," *Atmospheric Environment*, vol. 33, no. 12, pp. 1821–1845, 1999. [https://doi.org/10.1016/S1352-2310\(98\)00345-8](https://doi.org/10.1016/S1352-2310(98)00345-8).
- [30] J. Lelieveld and F. J. Dentener, "What controls tropospheric ozone?," *Journal of Geophysical Research: Atmospheres*, vol. 105, no. D3, pp. 3531–3551, 2000. <https://doi.org/10.1029/1999JD901011>.
- [31] G. Mills, H. Pleijel, C. S. Malley, B. Sinha, O. R. Cooper, M. G. Schultz, H. S. Neufeld, D. Simpson, K. Sharps, Z. Feng, G. Gerosa, H. Harmens, K. Kobayashi, P. Saxena, E. Paoletti, V. Sinha, and X. Xu, "Tropospheric Ozone Assessment Report: Present-day tropospheric ozone distribution and trends relevant to vegetation," *Elementa: Science of the Anthropocene*, vol. 6, 2018. <https://doi.org/10.1525/elementa.302>.
- [32] C. M. Nussbaumer and R. C. Cohen, "The Role of Temperature and NO_x in Ozone Trends in the Los Angeles Basin," *Environmental Science & Technology*, vol. 54, pp. 15652–15659, 2020. <https://doi.org/10.1021/acs.est.0c04910>.

- [33] P. J. Crutzen, *Tropospheric ozone: An overview*. Springer, 1988. https://doi.org/10.1007/978-94-009-2913-5_1.
- [34] H. Bozem, T. M. Butler, M. G. Lawrence, H. Harder, M. Martinez, D. Kubistin, J. Lelieveld, and H. Fischer, “Chemical processes related to net ozone tendencies in the free troposphere,” *Atmospheric Chemistry and Physics*, vol. 17, no. 17, pp. 10565–10582, 2017. <https://doi.org/10.5194/acp-17-10565-2017>.
- [35] I. Tadic, J. N. Crowley, D. Dienhart, P. Eger, H. Harder, B. Hottmann, M. Martinez, U. Parchatka, J.-D. Paris, A. Pozzer, R. Rohloff, J. Schuladen, J. Shenolikar, S. Tauer, J. Lelieveld, and H. Fischer, “Net ozone production and its relationship to nitrogen oxides and volatile organic compounds in the marine boundary layer around the Arabian Peninsula,” *Atmospheric Chemistry and Physics*, vol. 20, no. 11, pp. 6769–6787, 2020. <https://doi.org/10.5194/acp-20-6769-2020>.
- [36] A. L. Sumner, P. B. Shepson, T. L. Couch, T. Thornberry, M. A. Carroll, S. Sillman, M. Pippin, S. Bertman, D. Tan, I. Faloon, W. Brune, V. Young, O. Cooper, J. Moody, , and W. Stockwell, “A study of formaldehyde chemistry above a forest canopy,” *Journal of Geophysical Research: Atmospheres*, vol. 106, no. D20, pp. 24387–24405, 2001. <https://doi.org/10.1029/2000JD900761>.
- [37] A. Stickler, H. Fischer, J. Williams, M. De Reus, R. Sander, M. Lawrence, J. Crowley, and J. Lelieveld, “Influence of summertime deep convection on formaldehyde in the middle and upper troposphere over Europe,” *Journal of Geophysical Research: Atmospheres*, vol. 111, no. D14, 2006. <https://doi.org/10.1029/2005JD007001>.
- [38] D. Anderson, J. Nicely, G. Wolfe, T. Hanisco, R. Salawitch, T. Canty, R. Dickerson, E. Apel, S. Baidar, T. Bannan, N. J. Blake, D. Chen, B. Dix, R. P. Fernandez, S. R. Hall, R. S. Hornbrook, L. G. Huey, B. Josse, P. Jöckel, D. E. Kinnison, T. K. Koenig, M. L. Breton, V. Marécal, O. Morgenstern, L. D. Oman, L. L. Pan, C. Percival, D. Plummer, L. E. Revell, E. Rozanov, A. Saiz-Lopez, A. Stenke, K. Sudo, S. Tilmes, K. Ullmann, R. Volkamer, A. J. Weinheimer, , and G. Zeng, “Formaldehyde in the tropical western Pacific: Chemical sources and sinks, convective transport, and representation in CAM-Chem and the CCMI models,” *Journal of Geophysical Research: Atmospheres*, vol. 122, no. 20, pp. 11,201–11,226, 2017. <https://doi.org/10.1002/2016JD026121>.
- [39] S. Sillman, J. A. Logan, and S. C. Wofsy, “The sensitivity of ozone to nitrogen oxides and hydrocarbons in regional ozone episodes,” *Journal of Geophysical Research: Atmospheres*, vol. 95, no. D2, pp. 1837–1851, 1990. <https://doi.org/10.1029/JD095iD02p01837>.
- [40] J. H. Seinfeld, “Air pollution: A half century of progress,” *AIChE Journal*, vol. 50, no. 6, pp. 1096–1108, 2004. <https://doi.org/10.1002/aic.10102>.
- [41] S. Pusede and R. Cohen, “On the observed response of ozone to NO_x and VOC reactivity reductions in San Joaquin Valley California 1995–present,” *Atmospheric Chemistry and Physics*, vol. 12, no. 18, pp. 8323–8339, 2012. <https://doi.org/10.5194/acp-12-8323-2012>.

- [42] National Research Council, *Rethinking the ozone problem in urban and regional air pollution*. National Academies Press, 1992. <https://doi.org/10.17226/1889>.
- [43] S. Liu, M. Trainer, F. Fehsenfeld, D. Parrish, E. Williams, D. W. Fahey, G. Hübner, and P. C. Murphy, “Ozone production in the rural troposphere and the implications for regional and global ozone distributions,” *Journal of Geophysical Research: Atmospheres*, vol. 92, no. D4, pp. 4191–4207, 1987. <https://doi.org/10.1029/JD092iD04p04191>.
- [44] S. Sillman, “The use of NO_y, H₂O₂, and HNO₃ as indicators for ozone-NO_x-hydrocarbon sensitivity in urban locations,” *Journal of Geophysical Research: Atmospheres*, vol. 100, no. D7, pp. 14175–14188, 1995. <https://doi.org/10.1029/94JD02953>.
- [45] W. A. Gough and V. Anderson, “Changing Air Quality and the Ozone Weekend Effect during the COVID-19 Pandemic in Toronto, Ontario, Canada,” *Climate*, vol. 10, no. 3, p. 41, 2022. <https://doi.org/10.3390/cli10030041>.
- [46] J. Xue, T. Zhao, Y. Luo, C. Miao, P. Su, F. Liu, G. Zhang, S. Qin, Y. Song, N. Bu, and C. Xing, “Identification of ozone sensitivity for NO₂ and secondary HCHO based on MAX-DOAS measurements in northeast China,” *Environment International*, vol. 160, p. 107048, 2022. <https://doi.org/10.1016/j.envint.2021.107048>.
- [47] J. D. Allan, H. Coe, R. C. Cohen, A. Fried, J. F. Hamilton, D. E. Heard, A. Hofzumahaus, A. C. Lewis, J. M. C. Plane, D. Richter, A. Saiz-Lopez, A. J. Weinheimer, J. Williams, and E. C. Wood, *Analytical techniques for atmospheric measurement*. Blackwell Publishing, 2006. <https://doi.org/978-1-4051-2357-0>.
- [48] J. A. Thornton, P. J. Wooldridge, and R. C. Cohen, “Atmospheric NO₂: In situ laser-induced fluorescence detection at parts per trillion mixing ratios,” *Analytical Chemistry*, vol. 72, no. 3, pp. 528–539, 2000. <https://doi.org/10.1021/ac9908905>.
- [49] D. Day, P. Wooldridge, M. Dillon, J. Thornton, and R. Cohen, “A thermal dissociation laser-induced fluorescence instrument for in situ detection of NO₂, peroxy nitrates, alkyl nitrates, and HNO₃,” *Journal of Geophysical Research: Atmospheres*, vol. 107, no. D6, pp. ACH-4, 2002. <https://doi.org/10.1029/2001JD000779>.
- [50] T. L. Sparks, C. J. Ebben, P. J. Wooldridge, F. D. Lopez-Hilfiker, B. H. Lee, J. A. Thornton, E. E. McDuffie, D. L. Fibiger, S. S. Brown, D. D. Montzka, J. C. Weinheimer, Andrew J. an Schroder, P. Campuzano-Jost, and R. C. Jimenez, Jose L. Cohen, “Comparison of airborne reactive nitrogen measurements during WINTER,” *Journal of Geophysical Research: Atmospheres*, vol. 124, no. 19, pp. 10483–10502, 2019. <https://doi.org/10.1029/2019JD030700>.
- [51] Q. Zhu, B. Place, E. Y. Pfannerstill, S. Tong, H. Zhang, J. Wang, C. M. Nussbaumer, P. Wooldridge, B. C. Schulze, C. Arata, A. Bucholtz, J. H. Seinfeld, A. H. Goldstein, and R. C. Cohen, “Direct observations of NO_x emissions over the San Joaquin Valley using airborne flux measurements during RECAP-CA 2021 field campaign,” *Atmospheric Chemistry and Physics Discussions*, pp. 1–21, 2023. <https://doi.org/10.5194/acp-2023-3>.

- [52] I. B. Pollack, B. M. Lerner, and T. B. Ryerson, “Evaluation of ultraviolet light-emitting diodes for detection of atmospheric NO₂ by photolysis-chemiluminescence,” *Journal of Atmospheric Chemistry*, vol. 65, no. 2-3, pp. 111–125, 2010. <https://doi.org/10.1007/s10874-011-9184-3>.
- [53] G. Villena, I. Bejan, R. Kurtenbach, P. Wiesen, and J. Kleffmann, “Interferences of commercial NO₂ instruments in the urban atmosphere and in a smog chamber,” *Atmospheric Measurement Techniques*, vol. 5, no. 1, pp. 149–159, 2012. <https://doi.org/10.5194/amt-5-149-2012>.
- [54] J. Jung, J. Lee, B. Kim, and S. Oh, “Seasonal variations in the NO₂ artifact from chemiluminescence measurements with a molybdenum converter at a suburban site in Korea (downwind of the Asian continental outflow) during 2015–2016,” *Atmospheric Environment*, vol. 165, pp. 290–300, 2017. <https://doi.org/10.1016/j.atmosenv.2017.07.0101352-2310>.
- [55] V. Shah, D. J. Jacob, R. Dang, L. N. Lamsal, S. A. Strode, S. D. Steenrod, K. F. Boersma, S. D. Eastham, T. M. Fritz, C. Thompson, J. Peischl, I. B. Bourgeois, I. B. P. Pollack, B. A. Nault, R. C. Cohen, P. Campuzano-Jost, J. L. Jimenez, S. T. Andersen, L. J. Carpenter, T. Sherwen, and M. J. Evans, “Nitrogen oxides in the free troposphere: implications for tropospheric oxidants and the interpretation of satellite NO₂ measurements,” *Atmospheric Chemistry and Physics*, vol. 23, no. 2, pp. 1227–1257, 2023. <https://doi.org/10.5194/acp-23-1227-2023>.
- [56] N. Jordan, N. M. Garner, L. C. Matchett, T. W. Tokarek, H. D. Osthoff, C. A. Odame-Ankrah, C. E. Grimm, K. N. Pickrell, C. Swainson, and B. W. Rosentreter, “Potential interferences in photolytic nitrogen dioxide converters for ambient air monitoring: Evaluation of a prototype,” *Journal of the Air & Waste Management Association*, vol. 70, no. 8, pp. 753–764, 2020. <https://doi.org/10.1080/10962247.2020.1769770>.
- [57] S. T. Andersen, L. J. Carpenter, B. S. Nelson, L. Neves, K. A. Read, C. Reed, M. Ward, M. J. Rowlinson, and J. D. Lee, “Long-term NO_x measurements in the remote marine tropical troposphere,” *Atmospheric Measurement Techniques*, vol. 14, pp. 3071–3085, 2021. <https://doi.org/10.5194/amt-14-3071-2021>.